Universidade de São Paulo
Instituto de Astronomia, Geofísica e Ciências Atmosféricas
Departamento de Astronomia

Bruno Correia Mota

BeAtlas: A grid of synthetic spectra for Be stars

Bayesian inference of physical properties of B Stars

São Paulo
2018

Bruno Correia Mota

BeAtlas: A grid of synthetic spectra for Be stars

Bayesian inference of physical properties of B Stars

Tese apresentada ao Departamento de Astronomia do Instituto de Astronomia, Geofísica e Ciências Atmosféricas da Universidade de São Paulo como requisito parcial para a obtenção do título de Mestre/Doutor em Ciências.

Área de Concentração: Astronomia
Orientador(a): Prof. Dr. Alex Cavaliéri Carciofi

São Paulo

2018

Acknowledgements

Se você está lendo os agradecimentos, muito provavelmente você deseja saber se me lembrei de você. Não se preocupe, pois saiba que, mesmo seu nome não estando listado aqui, eu sou muito grato por ter te conhecido. Não tenho como recompensar sua amizade, por isso deixo um singelo presente, uma música que gosto muito, espero que goste ;-)

TOCANDO EM FRENTE

Ando devagar
Porque já tive pressa
E levo esse sorriso
Porque já chorei demais
Hoje me sinto mais forte
Mais feliz, quem sabe
Só levo a certeza
De que muito pouco sei
Ou nada sei
Conhecer as manhas
E as manhãs
O sabor das massas
E das maçãs
É preciso amor
Pra poder pulsar
É preciso paz pra poder sorrir
É preciso a chuva para florir
Penso que cumprir a vida
Seja simplesmente
Compreender a marcha
E ir tocando em frente
Como um velho boiadeiro
Levando a boiada
Eu vou tocando os dias
Pela longa estrada, eu vou
Estrada eu sou
Conhecer as manhas
E as manhãs
O sabor das massas
E das maçãs
É preciso amor
Pra poder pulsar
É preciso paz pra poder sorrir
É preciso a chuva para florir
Todo mundo ama um dia
Todo mundo chora
Um dia a gente chega
E no outro vai embora
Cada um de nós compõe a sua história

Cada ser em si
Carrega o dom de ser capaz
E ser feliz
Conhecer as manhas
E as manhãs
O sabor das massas
E das maçãs
É preciso amor
Pra poder pulsar
É preciso paz pra poder sorrir
É preciso a chuva para florir
Ando devagar
Porque já tive pressa
E levo esse sorriso
Porque já chorei demais
Cada um de nós compõe a sua história
Cada ser em si
Carrega o dom de ser capaz
E ser feliz
Composição: Almir Sater / Renato Teixeira

"*... meu pai chegou lá, os médicos todos de branco, aí entraram os doidos com os carrinhos de mão que tinham sido adquiridos pelo Governo para iniciar a psicoterapia pelo trabalho. E um dos doidos estava com o carrinho de mão de cabeça para baixo. Aí papai chamou e disse,*

_Oh, não é assim não que se carrega, é assim!

_Eu sei doutor, mas se eu fizer assim, eles colocam pedra pra eu carregar. - Respondeu o doido."

Ariano Suassuna

"*Ardan: _Vejam só a distância das estrelas! A estrela Vega e a estrela Sírius estão a bilhões e bilhões de quilômetros de distância! E ainda há quem me venha falar da distância que separa os planetas do Sol! E ainda há os que afirmam que essa distância existe! Isso é um erro! Sabem o que penso do mundo que me começa no astro radiosos e termina em Netuno? Querem conhecer minha teoria? Ela é bem simples! Para mim, o mundo solar é um corpo sólido, homogêneo; os planetas se tocam, se juntam e o espaço existe entre eles é como o espaço que separa as moléculas do metal mais compacto, seja ele prata ou ferro, ouro ou platina. Portanto, posso afirmar e repito com convicação: a distância é uma coisa vã, a distância não existe! ... E fez um movimento tão violento que quase caiu do estrado. Mas conseguiu recuperar o equilíbrio e evitar uma queda que lhe provaria, de forma brutal, que a distância não é uma coisa vã.*"

Julio Verne, Da Terra à Lua

Abstract

Classical Be stars are the only Main Sequence stars that possess Keplerian decretion circumstellar disks ruled by viscous processes. The physical properties of the disk can be studied by modeling its structure and solving the radiative transfer problem. In this point, the production of synthetic observables arises as a tool to investigate the physical quantities of the system. Among the proposed models to the disk formation, the Viscous Decretion Disk model is the current paradigm, correctly describing a large set of evidences that implies viscous shear is the mechanism driving the disk outflow.

The modeling of stars is a challenger that demands, sometimes, very elaborate tricks to achieve confident results. Despite this, when we include other elements to the model (e.g. magnetic fields and rotation), the modeling can become very complex. In our study, we aim to study classical Be stars which are known by its rapid rotation rate and non-radial pulsations. These elements are, in some way, at the origin of circumstellar decretion disks.

Our main goal is to infer stellar, disk, geometrical parameters, and the interstellar extinction, without neglecting their uncertainties and correlations, for two specific cases (α Arae and β CMi) and for a set of 111 rapid rotating main sequence stars. For such a purpose, we make use of different observables, basically photometric and polarimetric data.

We use a modern statistical procedure employed by the code EMCEE, stellar parameters based on evolutionary models of the astrophysics group of the University of Geneva, and the code HDUST used to model the physical processes that occur into Be disks. To constrain the solutions, domain knowledge of $v \sin i$ and parallax were adopted.

We provide a inference tool for the Monte Carlo Markov Chain modeling of `Be` stars and hot main-sequence O, B and A stars. Our tool includes important effects due to the rapid rotation. The potential of the observables in constraining the stellar parameters is discussed. A catalog of

the inferred parameters and a discussion about their correlations are shown. We also present the first multi-technique treatment of a late- and early-type Be star, β CMi and α Arae.

The correlations found show that the parameters are coupled. This corroborates the hypothesis that an independent inference of any parameter could propagate errors. For β CMi, the analysis reveals a circumstellar disk truncated by a companion or a dissipating disk. Moreover, our results suggest the sub-spectral type B8e for this star. For α Arae, the analysis also indicates a truncated disk, a thick circumstellar disk and B2e as spectral-type.

The thesis is organized as follows. First, we introduce essential topics in Chapter 1. The tools and the grid used are shown in Chapters 2 and 3. In Chapter 4, we describe the adopted Bayesian approach used. After, we list observational dataset gathered into groups based on their features (Chap. 5). We discuss and analyze the results in Chapters 6 and 7. We summarize our conclusions in Chapter 8. The published articles, tutorials, and tables are in the appendices..

List of Figures

List of Tables

Contents

Chapter 1

Introduction: The Be phenomenon

1.1 Chapter summary

This Chapter presents a synopsis of the scientific problem and its astrophysical relevance (Sec. 1.2), following by a discussion about the stellar rotation (Sec. 1.3). Thereafter, in Sect. 1.4, we introduce additional classes of stars that were studied alongside the Be stars. A detailed description of the circumstellar disks of Be stars and its current paradigm is given in Section 1.5. We sum up our objectives in Sect. 1.6.

1.2 Classical Be Stars

The class of peculiar hot stars are known to present spectroscopic peculiarities (e.g. emission lines) in their spectra (e.g. Smith, 1996). The B spectral domain comprises complex subclasses of hot peculiar stars, including the non-supergiant, main-sequence B whose spectrum has, or had at some time, one or more Balmer lines in emission (Jaschek et al., 1981; Collins, 1987), the Classical Be stars (hereafter, CBe)[1]. They are notoriously recognized by their outwardly diffusing gaseous, dust-free Keplerian circumstellar disk that arises in active phases (Rivinius et al., 2013) and by show the highest rotation rates among the main-sequence (MS) stars ($W \simeq 0.75$, e.g. Townsend et al. 2004; Frémat et al. 2005; Granada and Haemmerlé 2014). Table 1.1 summarizes the stellar parameters of the Be stars for each subtype.

Since the discovery of the CBe, many efforts have been made in order to understand their distinguishing characteristics. For instance, the observational techniques progress in the last decades, such as photometry, polarimetry, spectroscopy, and interferometry have provided the

[1] Supergiant stars, Herbig Ae/Be, mass transfer binaries, B[e] and stars with line emission caused by a magnetosphere can be confused with CBe at first sight due to their similar peculiar features (Rivinius et al., 2013).

Table 1.1 - Stellar parameters of MS Be stars obtained from Townsend et al. (2004).

Sp. Subtype	$M_\star$ [$M_\odot$]	R_{pole} [$R_\odot$]	v_{crit} [km s^{-1}]	log $L_\star$ [dex $L_\odot$]
B0	17.5	7.7	538	4.64
B0.5	14.6	6.9	519	4.41
B1	12.5	6.3	502	4.21
B1.5	10.8	5.7	491	4.01
B2	9.6	5.4	475	3.85
B2.5	8.6	5.0	468	3.68
B3	7.7	4.7	456	3.52
B4	6.4	4.2	440	3.24
B5	5.5	3.8	429	3.00
B6	4.8	3.5	418	2.78
B7	4.2	3.2	408	2.56
B8	3.8	3.0	401	2.39
B9	3.4	2.8	393	2.20

basis data to study these objects in detail (Rivinius et al., 2013). Adding this to the advances in our understanding of Be star theory and in the computational simulations, our knowledge of the physics of Be stars and their detailed theoretical models reached an unprecedented level (Sect. 3.3). These efforts allowed us to draw a wide overview regarding the *Be phenomenon*, i.e. the theory about the disk. A literature review about Be stars can be seen in Underhill and Doazan (1982), Slettebak (1988), Porter and Rivinius (2003) and Rivinius et al. (2013).

The study of Be stars is essential for several reasons, for instance, the spectral limits of the *Be phenomenon* are still uncertain which demands a cautious investigation of neighboring spectral types, i.e. O and A spectral types. Despite the paucity of massive stars[2], they play a crucial role in the evolution of the Universe, being regarded as one of the main sources of heavy elements and UV radiation (Massey, 2003), even so our understanding of massive star formation is still incomplete. Moreover, they rarely born isolated (Sect. 1.2.2), in such case the combined effects of winds, massive outflows of nearby companions, gravitational interaction, and supernova of these objects provide energy that can trigger processes of mixing and formation of turbulence into the interstellar medium (Martins et al., 2005), as well as affect their global evolution (Zinnecker

[2] The terms massive star and high-mass star denote OB stars sufficiently massive to produce type II supernovae ($M_\star / M_\odot > 8$) to the solar abundances. Then, the term high-mass protostar denotes objects with $M_\star / M_\odot > 8$ which have not started the hydrogen burning.

and Yorke, 2007). Additionally, the fraction of Be among B stars is not negligible, ranging from 3 to ~ 50 % (e.g. Wisniewski and Bjorkman 2006; McSwain and Gies 2005; Zorec and Briot 1997; Keller et al. 1999; Maeder et al. 1999; Marco and Negueruela 2013; Bastian et al. 2017), actually approximately 10% of the MS B stars in the Galaxy are Be stars (Rivinius et al., 2013). Finally, regarding the evolutionary study of stellar rotation, the relative abundance of the B-type stars, compared to massive O-type stars, makes them the best targets to explore rotational effects (Huang et al., 2010). Therefore, a good knowledge of their properties is crucial and requires the development of either evolutionary or atmosphere models.

In stellar modeling, one of the most challenging problems involving the study of Be, Bn (Lamers et al., 1980), B normal, Oe (e.g. Conti and Leep 1974; Negueruela et al. 2004) and Ae stars (Bohlender, 2016) is the inference of their fundamental parameters (i.e., mass, temperature, rotation rate, radius, inclination, etc). This task becomes more complex in our case due to an important evolutionary element, the stellar rotation (Sect. 1.3). Additionally, we must emphasize the influence of the disk common in active Be stars, in such cases the star is veiled by the disk, making the problem more complex. We have, then, a coupled problem: the apparent stellar parameters are changed by the disk, while the disk structure depends on the stellar characteristics. Still in Be context, the current paradigm model was tested only for a handful of Be stars to-date (Sect. 3.3). As such, more detailed studies of individual Be stars and main-sequence O, B and A subclasses are necessary to provide further validation of the paradigm and a improvement of our knowledge about the *Be phenomenon*.

1.2.1 Variability of Be stars

Be stars are also subject to different variabilities, both intrinsic and extrinsic, which manifest in several observables and cover various time-scales. For instance, the *short-term variations* (~ hours-days), observed in emission lines, are associated with non-radial stellar pulsations (NRP) (Rivinius et al., 2013). In larger timescales, there are *intermediate-term variations* (~ months-years) seen in the V/R variations of emission lines and associated with global disk oscillations (e.g. Okazaki 1997; Carciofi et al. 2009). Recently, Labadie-Bartz et al. (2017) provided evidences that photometric outbursts correspond to disk build-up events. These events can be generated by some internal mechanism or by a companion (Sect. 1.2.2). Finally, *longer term variabilities* (~ years-decades) represent the complete process of formation and dissipation of the disk (e.g. Bjorkman et al. 2002). We summarize the variabilities described in Table 1.2.

Table 1.2 - Typical types of variability observed in CBe. NRP: Non-rotational pulsations. O: Outburst. QPO: Outbursts and quasi-periodic oscillations.

Type	Timescale	Cause
Shorter	Hours to days (0.1 to 2 days)	NRP
Intermediate	Days to months (2 and 200 days)	O or QPO
Long	Occasionally have duration of years	O

1.2.2 Binarity and Disk Truncation

Most of the massive O stars are binaries ($\sim 75\%$) or were in some moment of their lives (Sana et al., 2012). For the case of B stars, the binary fraction can reach up to $\sim 40\%$ (Chini et al., 2012) or 29 ± 8 % (Oudmaijer and Parr, 2010). This fraction is higher among Be stars, ranging from 27 (Sterken et al., 1996) to 30 ± 8 % (Oudmaijer and Parr, 2010). Hence the interaction might be a common component in massive star evolution, being associated with a variety of astrophysical processes such as γ-ray bursts, X-ray binaries, pulsars and double-neutron stars (Chini et al., 2012). In this context, a close companion can significantly influence the massive star evolution (e.g. Langer et al. 2008). The mass transfer in such a system is also an ingredient that must be considered (Dunstall et al., 2015). All these relevant aspects made the search for binary fractions increase in the last decades (e.g. Chini et al. 2012). As a result, it led to the conclusion that most massive stars may be born as part of multiple systems (Sana et al., 2012).

It was recently raised the possibility (e.g. Baade 1992) that Be stars and supergiant sgB[e] might be binary evolutionary products (Vanbeveren and Mennekens, 2017). Some observational evidences point out to the fact that gravitational interactions between a Be star and a companion could induce periodic variability and ellipsoidal precession of the disk (Labadie-Bartz et al., 2017). In addition, the companion might act on the disk by tidal effects or in its thermal properties (Panoglou et al., 2016). A list of some known binary Be stars is shown in Table A.1.

Long-baseline interferometry is the most powerful technique to detect companions (Meilland et al., 2012). Although it is powerful, the detection of very close companions ($\lesssim 100$ mas) has an observational limit (Sana et al., 2014). To investigate this issue, Chini et al. (2012), using another technique, performed a high-resolution radial velocity study of a spectroscopic survey containing ~ 250 O stars and ~ 540 B stars in the southern Milky Way. They found that $> 82\%$ with $M > 16\,M_\odot$ form close binary systems, this fraction drops to only 20% for $M \sim 3\,M_\odot$. The smallest orbital period found in their study was of only a few days, corresponding to critical

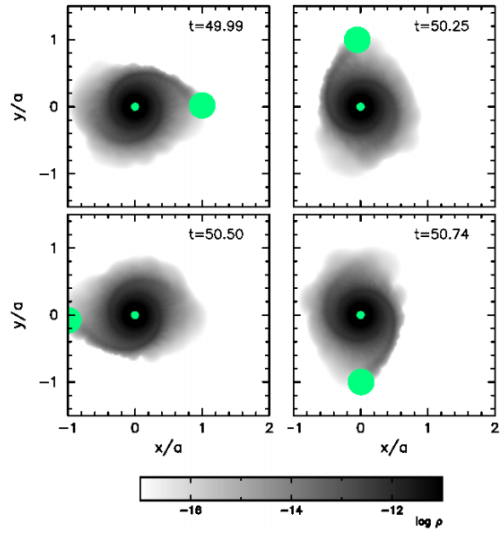

Figure 1.1: Snapshots of a complete cycle of the reference binary system at quasi-steady state simulated by Panoglou et al. (2016). The distances are given in semi-major axis, a, units.

separations of $\sim$ 0.2 AU. This is the limit in which the system could merge into a single object. *In summary, the multiplicity fraction seems to decrease with decreasing stellar mass*.

A peculiar phenomenon in binary Be systems is that the secondary could truncate the disk to a radius dependent on the orbital parameters (eccentricity and semi-major axis) (e.g. Rivinius et al. 2013; Okazaki et al. 2002). This hypothesis is still difficult to be directly confirmed due to the flux contrast between the primary and the faint companion (Peters et al., 2016). The SED turndown, as evidenced by Klement et al. (2017), occurs due to the truncation of the outer disk. However, there are two main hypothesis for the truncation: the *tidal influence from a close companion* and the *transonic transition*. The second is defined by the radius where the resonant torque is larger than the viscous torque, resulting in a sudden drop in the gas density profile (Okazaki et al., 2002). As mentioned by Klement et al. (2017), this transition is expected to occur only at wavelengths at roughly a magnitude longer than the cm data in Be disks.

Recently, Klement et al. (2015a) found relevant evidences of disk truncation in the Be star β CMi. Interestingly, by modeling its full SED from the UV through radio, it was detected a flux deficiency at long-wavelength measurements when compared to what was expected for the disk based on the inferred IR excess from the disk. More recently, still exploring the disk truncation problem, Klement et al. (2017) reported the discovery of a SED turndown, somewhere between mid-IR and radio wavelengths, for a set of stars by using radio measurements. They concluded that the most likely mechanism to truncate the disk is a close companion.

This problem was profoundly explored by Panoglou et al. (2016). They examined theoretically the cases of circular and eccentric coplanar orbits, both prograde and retrograde, using the same 3D SPH code adopted by Okazaki et al. (2002). Their main conclusions were:

1. In near circular binaries, the disk preserves a constant structure (azimuthal symmetry) in phase with the orbital motion of the companion (see Fig. 1.1). In such cases, the truncation region might be independent of the orbital phase;

2. A small disk could be present even for very close binaries, for instance, a companion with $P_{\rm orb} = 5$ days could have an observable disk with truncation radius, $R_{\rm t} = 2.5\,R_{\star}$;

3. From circular to moderately eccentric ($\epsilon \sim 0.6$) orbits, the inner disk preservers its structure. In highly eccentric orbits, the disk structure could present spiral arms induced by the companion as it passes the periastron;

4. The effects of binarity in the disk continuum emission induces an accumulation of material in the inner region limited by the truncation radius. It generates an inner density exponent lower than the steady-state value for isolated Be disks.

1.3 Stellar Rotation

Stellar rotation is defined as the angular motion of a star around its axis. A star may acquire angular momentum during the pre-MS phase, when its formation cloud contracts or through collisions with other protostars (e.g. Huang and Struve, 1954). In this phase, the accreting protostar can break up due to the centrifugal force. When a star enters the MS, it is believed that its magnetic field can interact with the stellar wind, carrying away its primordial angular momentum. Over time this gradually slows the stellar rotation rate (e.g. Ferreira et al., 2000).

The rotation slowing mechanism discussed above do not apply to CBe. Actually, this is an important ingredient to differentiate magnetic common stars from CBe, since the detection of large-scale magnetic fields has not been detected in any CBe star, which strongly indicates that the *Be phenomenon* could be independent of magnetism (Grunhut et al., 2012). As an example, we illustrate the modulus of the magnetic field of several MS stars in Figure 1.2. This figure shows that the stronger magnetic fields appears around the A spectral types decreasing towards the early spectral types B and O. Therefore, it is seen a clear dependence of the spectral type with strengh of the magnetic field, showing a maximum around A type stars dropping in several

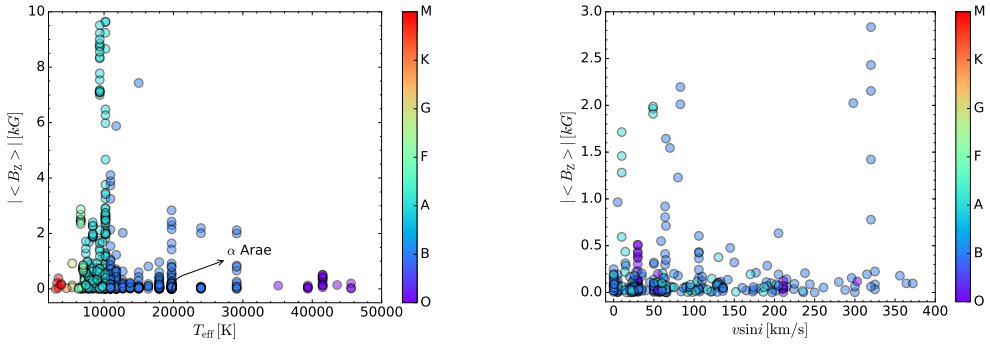

(a) *(b)*

Figure 1.2: Left: Magnetic field versus effective temperature for main sequence stars taken from Bagnulo et al., 2015. B_z refers to mean of the line of sight component. Right: Magnetic field versus projected rotational velocity for main sequence stars taken from Bagnulo et al., 2015. B_z refers to mean of the line of sight component.

magnitudes in B type stars. When we plot the $< B_z >$ field versus $v \sin i$ (Right panel of the Fig. 1.2) there is no clear evidence of correlation between these physical quantities.

The equatorial rotational velocity, $v_{\rm eq}$, is the main parameter to describe the rotation. This physical quantity can not be measured directly. Actually, what is measured is the projected rotational velocity, $v_{\rm eq} \sin i$, which depends on the inclination of the stellar rotation axis with the line of sight, i. Among the usual techniques to determine the $v \sin i$, there are: (i) measure by tracking the movement of magnetic starspots; (ii) from Doppler broadening caused by the stellar rotation in line profiles in the stellar spectrum (Shajn and Struve, 1929).

The break-up or critical velocity of a star is used to describe when the centrifugal force at the equator is equal to the gravitational force. While the equatorial rotational velocity is below this value, the star remains stable (Hardorp and Strittmatter, 1970). The critical velocity is given by,

$$V_{\rm crit} = \sqrt{\frac{2\,G\,M_\star}{3\,R_{\rm pole}}} = \sqrt{\frac{G\,M_\star}{R_{\rm eq}}}, \tag{1.1}$$

where $M_\star$ is the stellar mass, $R_{\rm pole}$ and $R_{\rm eq}$ are the polar and equatorial radii, respectively.

In our work, we employed the stellar rotation rate definition,

$$W = \frac{v_{\rm rot}}{v_{\rm orb}}, \tag{1.2}$$

where $v_{\rm orb}$ is the Keplerian circular orbital velocity at the equator and $v_{\rm rot}$ is the rotational velocity at the equator (Rivinius et al., 2013).

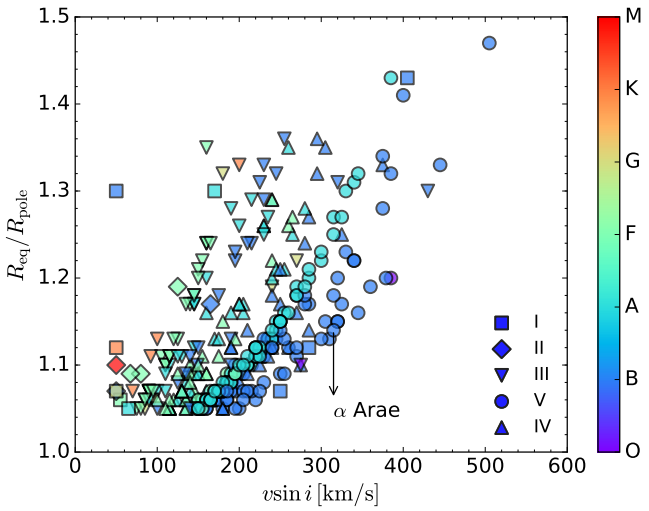

Figure 1.3: Oblateness versus projected velocity for several spectral types. The different colors represents the spectral types and the different symbols the luminosity classes (data from van Belle, 2012). The position occupied by α Arae is indicated just for further comparison.

1.3.1 Fast rotation in stars

The rotation is an important ingredient to understand the formation and evolution of stars (e.g. Granada et al. 2013; Cranmer 2005), being the main cause of several physical effects observed in stars. It is specially relevant in our case, since high-rotation rates are expected to be more common among early spectral types (Cranmer, 2005). As pointed out by Ekström et al. (2011), the effects on the stellar structure during its evolution are several: oblateness (e.g. Maeder 2009; Collins and Harrington 1966), mixing, and gravity darkening (Collins, 1963). For these reasons, in principle, the *gravity darkening* and *oblateness* must be considered in any modeling, once its effects produces relevant changes upon the disk thermal structure of Be stars (e.g. McGill et al. 2011; Frémat et al. 2005), on the `SED` (Townsend et al., 2004) and on its brightness distribution (von Zeipel, 1924). In addition, the evolutionary tracks (Ekström et al., 2012) shows that rotating hot stars and non-rotating models have not negligible evolutionary differences.

Figure 1.3 shows the estimated oblateness versus v sin i for several spectral types and luminosity classes. Some relevant aspects are: i) the most of the `MS` early-type stars (circles) occupies high-velocity regions ($\gtrsim 200$ km/s), while the late-type stars are more concentrated in low-velocity regions; ii) giant, subgiant, and `MS` early-type stars have larger oblateness. These results strengthens the view that the fast rotation is important to understand the formation and evolution of stars, being more common among early-type O, B and A stars (Cranmer, 2005).

The typical rotation rates associated with B spectral types play an instrumental role in the formation of the disk, allowing photospheric material to be ejected into orbit and so triggering the *Be phenomenon* (Struve, 1931). The higher initial rotation rates support various spin up mechanisms, which enable the Be star to reach nearly critical rotation rates as they evolve (Grudzinska et al., 2015). Among these mechanisms is the *spin up during the* MS evolution, associated with the second half of the MS lifetime of the B stars (McSwain and Gies, 2005). Besides, Huang et al. (2010) concluded from V_{eq}/V_{crit} distributions that low-mass B stars are born with a larger proportion of rapid rotators than high-mass B stars. Their results suggest that high-mass B stars experience angular momentum losses across the pre-MS and during the MS phase. In this context, recent statistical studies (e.g. Cranmer 2005) present evidence that cooler Be stars are more likely to be critical rotators. Furthermore, according to Massey (2003) the rotation might also be responsible for transporting stellar material from the core to the photosphere (Meynet and Maeder, 2000). This could exert a profound effect on the stellar mass loss rates (Maeder, 2009).

There are possibly other mechanisms that characterizes whether a star becomes a Be star. An evidence is given by the amount of Be stars rotating below the critical limit ($W \sim 1$), which indicates that the rotation alone can not trigger the *Be phenomenon*. Therefore, additional mechanisms, to push the photospheric material to forming the disk, are needed (Sect. 1.5.1).

1.3.2 Gravity Darkening

The gravity darkening (GD) is one of the main effects caused by rotation. McGill et al. (2011) studied the effect of the GD upon the thermal structure of Be star disks models covering a wide range of spectral types and rotation rates. They showed that the GD produces relevant changes in the temperature structure of Be disks. This effect weights the slow rotating polar regions, producing narrower line profiles (Cranmer, 2005). Beyond that, rapidly rotating stars can present strong GD levels in their equatorial regions leading to an underestimate of the actual $v \sin i$ (Townsend et al., 2004). Therefore, systematic errors in rotational rate determinations and inclination angles depend on whether the GD is adopted (Frémat et al., 2005).

1.4 Other Peculiar Hot Stars

Beyond the CBe (Sect. 1.2), there are several other stellar groups classified as peculiar stars. These groups were summarized by Rivinius et al., 2013 and, sometimes, have their properties associated with the presence of non-negligible magnetic fields. This constitutes an important ingredient to differentiate them from the CBe, since the detection of large-scale magnetic fields has not been detected in any CBe star, which strongly indicates that the *Be phenomenon* could be independent of magnetism (Grunhut et al., 2012).

In our specific case, we focus on the peculiar stars related with high-rotation. Beyond the Be stars, we included Oe, Bn and Ae stars. Next, we discuss their general characteristics.

1.4.1 Classical Oe stars

Even the hottest stars can present signals of decretion disks, this is the case of Oe stars. Oe stars are rapidly rotating O stars with narrow Balmer and helium emission lines along with broad absorption lines, but not the characteristic emission features of Of stars, in HeII λ4686 and NIII λ4634-40-42, associated with strong stellar winds (Conti and Leep, 1974). They also present V/R and Balmer line variability (e.g. Rauw et al., 2007) and can present HeI emission lines (e.g., Frost and Conti, 1976). In the context of the VDD model, Golden-Marx et al., 2016 confirms that Oe stars are the high-mass extension of the *Be phenomenon*, however it still appears not to be widely accepted (e.g, Rauw et al., 2015). Oe stars have stronger radiative forces, reducing their disk lifetime to order of days[3]. This can explain the rarity of the *Be phenomenon* among earlier spectral types (e.g. see Fig. 12 in Kee et al., 2016). From Figure 1.4 it is possible to note that the lifetime of a disk decreases by a factor of ~ 250 when we compare B3 to O7 spectral types.

The existence of disks around Oe stars remains a wide open question, because we have just indirect evidences of the disk around these stars as their high projected rotational velocities (Negueruela et al., 2004). Another interesting point is the scarcity of the *Be phenomenon* in spectral types earlier than B0, which might be related with: i) the force that their fast radiative winds exert on the circumstellar material; ii) models of fast-rotating stars (Meynet and Maeder, 2000) predict that the rotation rates increases during the lifetime for $M_\star < 15 M_\odot$, and decreases for $M_\star > 15 M_\odot$ because of angular momentum loss caused by their strong winds.

[3] Johnston et al., 2015 published the discovery of a keplerian-like disk around the forming O-type star AFGL 4176 from ALMA data in 1.2 mm.

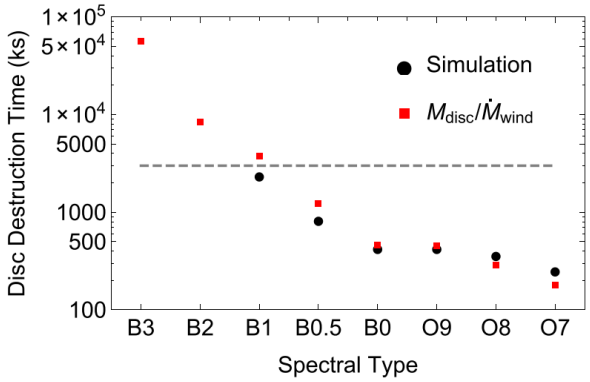

Figure 1.4: Time to destroy an optically thin disk as predicted by $M_{\rm disc}/\bar{M}_{\rm wind}$ (red squares) compared with the time from simulations (black circles) made by Kee et al. (2016).

Table 1.3 - Stellar parameters of late MS O stars obtained from Martins et al. (2005).

Spectral Class	$T_{\rm eff}$ [K]	$\log g_{\rm spec}$ [cm s^{-2}]	$M_{\rm V}$	BC	$\log L/L_{\odot}$	$R_{\star}$ [R$_{\odot}$]	$M_{\rm spec}$ [M$_{\odot}$]
5	40,862	3.92	5.21	3.77	5.49	11.20	38.08
6	38,867	3.92	4.92	3.62	5.32	10.11	30.98
7	36,872	3.92	4.63	3.47	5.14	9.15	25.29
7.5	35,874	3.92	4.48	3.39	5.05	8.70	22.90
8	34,877	3.92	4.34	3.30	4.96	8.29	20.76
8.5	33,879	3.92	4.19	3.22	4.86	7.90	18.80
9	32,882	3.92	4.05	3.13	4.77	7.53	17.08
9.5	31,884	3.92	3.90	3.04	4.68	7.18	15.55

For the purpose of study the presence of the Be phenomenon in late-type O stars, we made use of a new calibration of the stellar parameters of O stars given by Martins et al. (2005). In their work, contrary to previous works (e.g. Vacca et al. 1996), it were considered new ingredients such as solar metallicity, wind, and line-blanketing effect (they did not consider the oblateness). Their results are shown in two types of effective temperature scales: a) a *observational scale* derived from a compilation based in recent spectroscopic studies studies; b) *theoretical scale*: calculated directly from interpolations on a CMFGEN (Hillier and Miller, 1998) grid of non-LTE spherically extended line-blanketed models. They obtained a good agreement between the theoretical and observational scales for dwarfs and super-giants stars. We show their stellar parameters in Table 1.3.

Table 1.4 - Stellar parameters of early MS A stars obtained from Adelman (2004).

Stellar	$M_\star$	$R_\star$	$T_{\rm eff}$
Class	[$M_\odot$]	[$R_\odot$]	[K]
A0V	2.40	1.87	9,727
A2V	2.19	1.78	8,820
A5V	1.86	1.69	7,880
A6V	1.80	1.66	7,672
A7V	1.74	1.63	7,483
A8V	1.66	1.60	7,305
A9V	1.62	1.55	7,112

1.4.2 Bn Stars

The rapidly-rotating Bn stars have nebulous absorption lines and absence of emission lines (Lamers et al., 1980). They are not a negligible subgroup of the B stars, for instance, Baade (1992) pointed that there is for every Be star listed in the Bright Star Catalogue (Hoffleit and Jaschek, 1982) a correspondent Bn star with the same spectral and projected velocity, $v \sin i$.

The occurrence of Be/Bn transitions appears to be absent. In summary, there are three main characteristics that differentiate Be and Bn stellar types and point to independent evolutionary paths: (i) no record of Bn stars observations displaying any circumstellar emission; (ii) the complete absence of magnetic fields in Be stars, in contrast with a high incidence among Bn stars; and (iii) the absence of non-radial pulsation in Bn stars, in contrast with the relatively high incidence among Be stars (Baade, 1992).

1.4.3 Ae and A shell Stars

The A spectral class has two peculiar interesting spectral types: Ae and A shell stars. They might present emission in the Balmer lines and strong IR excess. Bohlender (2016) found an increase in the frequency of Hα emission and shell phenomena in the most rapidly-rotating A-type stars and a decrease as the $T_{\rm eff}$ decreases. These trends are also seen in CBe and might be ascribed to the presence of a disk. These evidences made the Ae stars being regarded as the late-type extension of Be stars, although some of them might be β Pictoris objects, in this case, their disks would be pre-MS primordial disks (Rivinius et al., 2013). We show their stellar parameters in Table 1.4.

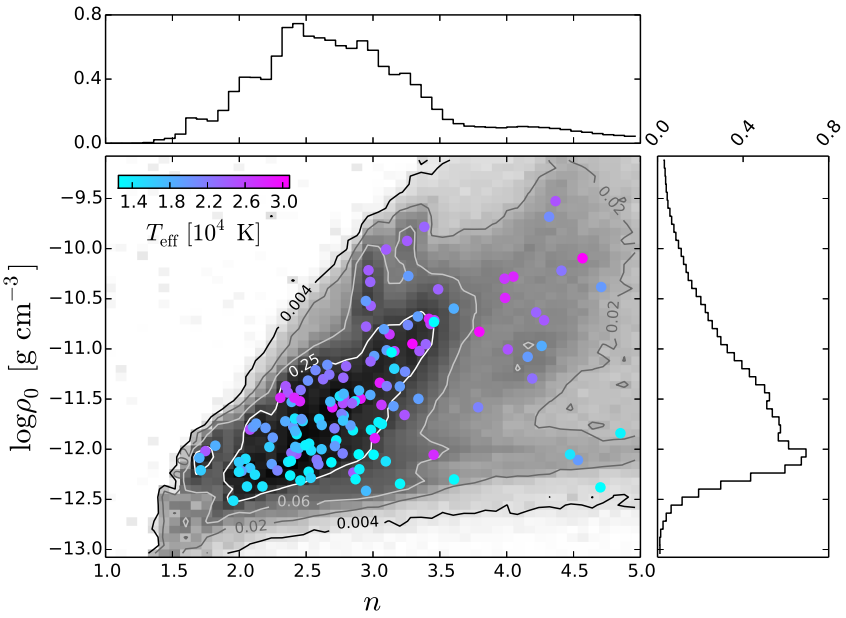

Figure 1.5: Distribution of $< n >$ and $< \log \rho_0 >$ for Be stars with emission line profiles.

1.5 The Circumstellar Disk of Be Stars

Disks are natural consequences of accretion systems, being present in the formation of Young Stellar Objects and in close binary systems with mass exchange (Owocki, 2006). In this context, Be stars are too old to have kept a protostellar disk. The disk of Be stars becomes apparent at optical wavelengths mainly by the presence of hydrogen (first Balmer lines) and metallic emission lines (stronger HeI and FeII lines) (Lamers et al., 1980). These observables arise from emission and recombination processes in the IR range by continuous bound-free and free-free thermal emission (e.g. Cote and Waters, 1987), and by the polarization of the stellar light by the disk (e.g., Kjurkchieva et al., 2016; Yudin, 2001). Basically, all B stars with a circumstellar material of density bigger than 10^{-13} g cm^{-3} are in this category, regardless of the mechanism responsible for that. A more precise definition was not found yet, given that the process that creates the disk has not yet been explained (Rivinius et al., 2013).

The disk geometry and physics of Be stars are well known. For instance, the confirmation that the disk shape was not spherically symmetric came from polarimetric and optical interferometric observations (e.g. McLean and Brown, 1978; Porter, 1996; Quirrenbach et al., 1997). These facts have been recently strengthened by the measurements of opening half-angles of disks of CBe (Cyr et al., 2015). The values range from 0.15° to 4.0° in thin disks, being able to reach larger values (3.7° to 14°) in thicker disks, which agrees with the current paradigm (Sect. 1.5.1).

The life cycle of a Be disk is quite complex, since vast majority of Be stars show variability in different temporal scales (Rivinius et al., 2013; Okazaki 1997; Carciofi et al. 2009), the dynamical evolution of the disk depends strongly on the mass injection rates. Different scenarios of mass injection rates have already been studied by Haubois et al. (2012) and are beyond the scope of this thesis. Conceptually, the disk formation starts from material ejected from the star through some still unknown process (Sect. 1.5.1). After being ejected, the material starts to be diffused outwards by viscous torques resulting in the formation of a decretion disk. The disk dissipation, after cease the injection of matter, may display both behaviors, i.e. accretion and decretion (e.g. Ghoreyshi et al. 2018). The current paradigm that comprises the theory behind the disk of CBe is the viscous decretion disk model (VDD, Sect. 1.5.1).

Recently, the physical disk parameters were revisited. Vieira and Carciofi (2017) inferred the disk density parameters (Fig. 1.5), the basis disk density (ρ_0) and the slope of the density profile (n) for a sample of 80 Be stars in the VDD context. They found that $1.5 < n < 3.5$ with the most frequent values spanning from 2.0 to 2.5 for all spectral types, corresponding to $10^{-12} < \rho_0 < 10^{-10}\,[\mathrm{g\,cm^{-3}}]$, which agrees with Arcos et al. (2017). Both studies established that the disk are denser around early-type than in late-type stars. These ranges would represent the dynamical state of the disk. Hence, according to dynamical models (Haubois et al., 2012) and assuming additional effects such as cooling by heavier elements, the index n would indicate different mass-loss scenarios. In summary, a disk with $n \geq 3.5$ shows growing disks, n between 3.0 and 3.5 disks in steady-state and dissipating disks for $n < 3.0$. These results agrees with the Huang et al. (2010), i.e. that the disk formation process may be different for both: low- and high-mass cases.

According to Huang et al. (2010), the low-mass case ($M < 4\,M_\odot$) needs a higher rotation rate $V_{\rm eq}\,/\,V_{\rm crit} > 0.96$ to become a Be star, while that for high-mass cases ($M > 8.6\,M_\odot$) this lower limit decreases to $V_{\rm eq}\,/\,V_{\rm crit} > 0.64$. Still, earlier statistical studies endorse this hypothesis. An example is the study performed by Yudin (2001). They identified that larger values of polarization and IR excesses are more present among early spectral types. Moreover, they found that about 95% of the Be stars in their sample exhibit intrinsic polarization on the level $0\% < p_\star < 1.5\%$ (Fig. 1.6a). The behaviour of the polarization and the near IR excesses of the Be stars revealed a maximum mean value between B1-B2 spectral types, decreasing toward late spectral types (1.6b).

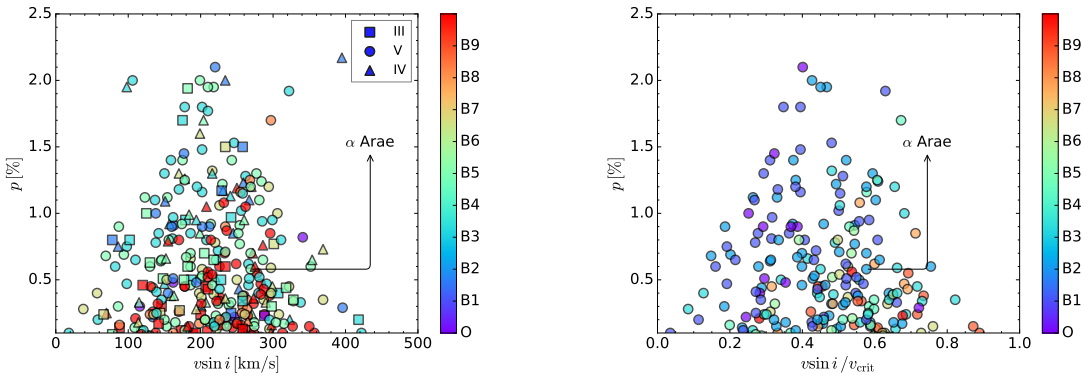

(a) *(b)*

Figure 1.6: Left: Linear polarization level versus projected velocity for III, IV and V luminosity classes. Right: Linear polarization level versus projected velocity over critical velocity for MS stars. Data from Yudin, 2001.

1.5.1 Viscous Decretion Disk Model

In the last decade, emerged a consensus of how Be disks are structured thanks to observational and theoretical advances. Undoubtedly, the only theory capable of explaining the global picture presented by observations of Be disks (both direct and indirect) is the Viscous Decretion Disk model (VDD), proposed by Lee (1991) and developed by several other authors (Porter 1999; Okazaki 2001; Bjorkman and Carciofi 2005b). The VDD model is similar to that employed to protostellar disks (Pringle, 1981); the difference being that Be disks varies between *outflowing* and *inflowing*, while pre-MS disks are *inflowing*. In the VDD model, it is supposed that an unknown mechanism injects material in the disk basis in an orbital keplerian velocity. Remarkably, non-radial pulsation, a combination of frequencies of different pulsation modes (Baade et al., 2016), binarity (Sect. 1.2.2) or small scale magnetic fields (Rivinius et al., 2013) are likely the ingredients responsible in triggering the *Be phenomenon*. After the material being ejected, the turbulent viscosity transports angular momentum from the inner material to the outer disk regions. Therefore, the density rises faster in the inner disk regions during its growth.

The VDD model has been employed in the study of individual Be stars (e.g. Carciofi et al. 2006; Carciofi et al. 2009; Tycner et al. 2008; Wheelwright et al. 2012; Carciofi et al. 2012; Wheelwright et al. 2012; Faes et al. 2015; Escolano et al. 2015; Klement et al. 2015b; Ghoreyshi et al. 2018) and samples of Be stars (e.g. Haubois et al. 2012; Haubois et al. 2014; Vieira et al. 2015; Panoglou et al. 2016; Vieira et al. 2017; Klement et al. 2017; Rímulo et al. 2018).

1.6 Aims

There are currently no synthetic Be spectral grids available for general application in the literature. Aiming to remedy this deficiency, we based on state-of-the-art theoretical and computational tools to offer an embracing grid model of Be stars and an useful new tool, capable of quantifying characteristics of hot O, B, and A stars by reproducing simultaneously available observables and the correlations among the inferred parameters through suitable statistical tools. Our method does not neglect the effects due to the rapid rotation, which is largely ignored in the literature, and allowed us to assess the universality of the `VDD` scenario with a larger, statistically significant sample of targets. Such studies serve three broad goals: i) to revisit the physical parameters of β CMi, a well-known Be system (Klement et al., 2015b); ii) it is the first time an analysis of the `VDD` is presented for the early-type star α Arae; iii) to form a statistical description of the physical conditions of Be disks by investigating the parameters of 162 `MS` stars, including Be, Bn, B, Ae and Oe spectral types.

Chapter 2

Tools

2.1 Chapter summary

This Chapter shows the theoretical and statistical tools adopted in our study. We present the EMCEE code used in the inference procedure. The visualizing tools are shown in Section 2.4. We end this chapter by showing an example of application (Sect. 2.5).

2.2 Astrostatistics

Astrostatistics arises from ancient studies developed by Thales of Miletus (624 - 546 BC) (Hilbe et al., 2017). Notoriously, he predicted a total solar eclipse in central Lydia in May 585 BC. Similarly, Hipparchus (190-120 BC) also applied statistical primitive principles in his analysis. It looks that, at least from these examples, that statistics always accompanied our studies being essential for the development of our knowledge. In principle, we can say statistics refers to a science designed to summarize[1] a set of collected finite raw data, providing useful information that allows us to decide. Therefore, each measurement, and their respective parameter or derived values, accompanied or not of an error estimate, is the end desired product of a statistical analysis.

2.2.1 Machine Learning

The term Machine learning refers to a set of techniques for interpreting data. These techniques essentially work by comparing data with models through several inference methods, for

[1] Here, it is implicit the process of analyzing the data for "the purpose of classification, prediction, and of attempting to quantify and understand the uncertainty inherent in phenomena underlying data" J. M. Hilbe 2014.

instance: regression, supervised classification, maximum likelihood estimators, or Bayesian inference (Ishak, 2017). In the Machine Learning context, there is a set of techniques for analyzing and describing structured data called *Data mining* which is used, for example, to find patterns in large data sets.

Next, we will revisit essential statistics concepts to draw an overview didactic picture of our inference problem.

2.2.2 Probability Distributions

Wall and Jenkins (2012) arguments that the concept of probability is the keystone in statistics, providing crucial information to make a decision. For our purposes, i.e. the *Data mining context*, it composes the problem of how to estimate the distribution $h(x)$ from which the values of a continuous random variable x are drawn. The distribution, $h(x)$, also called probability density function (PDF), simply quantifies the probability, $h(x)dx$, of a value be between x and $x + dx$. The PDF has the following properties,

(i) $p(a < x < b) = \int_a^b h(x)dx$;

(ii) $\int_{-\infty}^{\infty} h(x)dx = 1$;

(iii) $h(x)$ is a single-valued non-negative number for all real x.

The integral of the PDF from minus infinity to x, in the case of a continuous distribution,

$$H(x) = \int_{-\infty}^{x} h(x')dx' \tag{2.1}$$

is called the "cumulative distribution function", CDF. For a random variable Y or a distribution function $h(Y)$ is the probability that Y will be less than or equal to x.

The *quantile function*, which specifies the value of a random variable being less than or equal a given probability, is the inverse of the CDF. In other words, the quantiles are values that limit a certain percentage of the observations of a given variable. The notation for a quantile is q_d, where d indicates the defined percentage. For instance, $q_{12\%}$ is the quantile that delimits 12% of the inferior values of the data.

2.2.3 Bayes' Theorem

Thomas Bayes (1702 - 1761) was an English vicar, mathematician, and statistician. His work as a statistician was, probably published posthumously, is the *Essay Towards Solving a Problem in the Doctrine of Chances*. Bayes theorem allows us to make inferences from data, by considering what is known about each free explored parameter. Therefore, Bayesian method yields optimum results assuming that all the supplied info is correct.

Currently, the Bayes inference is applied to estimate parameters and their uncertainties from a set of model parameters when the shape and scale of their probability density distribution are unknown (Astrobites - "Your Gateway to the Bayesian Realm"[2]). Opposite to descriptive statistics[3], in the Bayesian context, we have a probability distribution $f(\text{data}|\vec{\alpha})$[4] and we wish to know the parameter vector $\vec{\alpha}$). The Bayesian route is clear, it should compute the posterior distribution of $\vec{\alpha}$.

$$p(\Theta|x) = \frac{p(x|\Theta)p(\Theta)}{p(x)} \tag{2.2}$$

We have $p(\Theta|x)$, the probability of our model parameters Θ given the data x and thus our quantity of interest also known as posterior probability. To compute this we multiply the prior $P(\Theta)$ (what we think about Θ before we have seen any data) and the likelihood $p(x|\Theta)$, i.e. how we think our data is distributed.

2.2.3.1 Likelihood function

We can rewrite the Bayes' theorem as,

$$p(M, \Theta|D, I) = \frac{p(D|M, \Theta, I)p(M, \Theta|I)}{p(D|I)} \tag{2.3}$$

where D represents the experimental data, M the set of models, $\Theta = \Theta_1, ..., \Theta_k$ the model parameters and I additional information.

The term $p(D|M, \Theta, I)$ is the distribution that is used to explain the predictor and parameter data called likelihood. Given by some model $M(\Theta)$ and all prior information I.

As an example of likelihood, let's consider the function,

[2] astrobites.org/2011/11/26/your-gateway-to-the-bayesian-realm;

[3] The math of determining mean, median, mode, range, tabulations, frequency distributions, were closely tied together until early nineteenth century;

[4] The conditional probability of A, given that we know B is given by, $p(A|B)$.

$$p(D|\Theta) = \Sigma \frac{(f_\mathrm{i} - f_{\Theta,i})^2}{\sigma_\mathrm{i}^2}. \tag{2.4}$$

This function represents the probability of getting a set of N observations, D, given a theoretical model $f_{\Theta,i}$ that fits the dataset. Therefore, the likelihood is a function of the model parameters, Θ.

2.2.3.2 Priors

The term $p(M, \Theta|I)$ in Eq. 2.3 is called *prior* or "initial belief". It is *a priori* information that summarizes something about a particular parameter model. Therefore, a prior is essentially used to constrain model parameters. Although the term "prior" suggests "before the inference process" actually it summarizes what it is known about the data.

2.2.3.3 Posterior

The product of the prior and likelihood distributions defines the posterior ($p(M, \Theta|D, I)$), our "improved belief". We can quantify the uncertainty in our model's parameters using this posterior distribution. A common solution is to apply some numerical technique that draw samples from the posterior so we can characterize the shape of the distributions. This is where Markov Chain Monte Carlo comes in.

2.3 Markov Chain Monte Carlo

`MCMC` methods were developed for sampling `PDF`s. The most common implementation of `MCMC` is a random-walk algorithm that estimates the posterior distribution that allows us to get the uncertainties for each of our model parameters.

In essence, it is taken a single model in a "state", then its parameters are perturbed. After, we determine whether this new model is better or worse. A "chain" of states is created through this process. Note that the next step only depends on the current step. This is fundamental since it guarantees the Markov Chain to explore all parameter space. Through this process, we build a "chain" of states that can be used to generate parameter distributions. In summary, the typical procedure is:

1. Initially, identify an acceptable model solution as a starting point. From here, we gauge

how the model parameters are constrained and use this information to assign a list of "walkers", and the scale length to perturb each parameter value;

2. It is calculated the posterior probability of this state, $p(\Theta_{\rm old}|D)$;

3. Next, we apply a random step to our current state, and calculate the posterior probability for this new trial state $p(\Theta_{\rm new}|D)$;

4. We compare the two posteriors. If $p(\Theta_{\rm new}|D)$ is better than $p(\Theta_{\rm old}|D)$, we accept it as a new state. If it is worse, there is no change it will still get accepted based on the ratio of their posterior probabilities. Note that because we are taking this ratio for the same physical model, it is not necessary to compute the evidence term, $p(D)$;

5. Go back to step 3. Keep repeating until a "chain" of states is assembled. Sampling the chain will result in an approximation of the posterior distribution.

2.3.1 *Metropolis-Hastings* `MCMC`

Metropolis-Hastings algorithm (`M H MCMC`) (Metropolis et al., 1953) constitutes the simplest `MCMC` algorithm. It depends on two inputs: (i) a set of models to be sampled, $f(\Theta)$; (ii) a proposal function $q(\Theta'|\Theta)$ that delivers samples. By using this two inputs, the algorithm is able to evaluate $f(\Theta)$[5] for any set of the parameters Θ. Then, the algorithm proceeds drawing a new position Θ' in the parameter space starting from a previous position Θ. This procedure allows us to random-walk around the parameter space.

In summary, the algorithm is:

1. Initialization: choose an arbitrary point Θ_0;

2. For each interaction k and considering a function $f(x) \propto P(x)$:

   (a) For the next sample, generate a candidate Θ' from the distribution $g(\Theta'|\Theta_{\rm k})$. $g(\Theta'|\Theta_{\rm k})$ is an arbitrary probability density function that suggests a candidate for the next sample value Θ' given the previous sample value $\Theta_{\rm k}$;

   (b) Acceptance fraction calculation: $\alpha = f(\Theta')/f(\Theta_{\rm k}) = P(\Theta')/P(\Theta_{\rm k})$. It allows us to decide if we accept or reject the current candidate;

[5] In our context, this function would be the posterior function evaluated at the observed data D.

3. Accept or Reject:

   (a) Generate a random number u between 0 and 1;

   (b) If $u \leq \alpha$ the candidate is accepted ($\Theta_{k+1} = \Theta'$);

   (c) If $u > \alpha$ the candidate is rejected ($\Theta_{k+1} = \Theta_k$).

2.3.2 EMCEE

`emcee` is a high performance open source PYTHON module[6]. It uses variations of a `MCMC` method developed by Goodman and Weare (2010) where multiple "walkers" are used to propagating multiple chains simultaneously for the parameters determination, correlations and error estimates. The algorithm has several advantages in relation with traditional `MCMC` sampling methods (Foreman-Mackey et al., 2013), as the Metropolis-Hastings (Sect. 2.3.1), being more efficient even in parameters spaces with many dimensions. Another advantage of the algorithm is that it requires hand-tuning of only 1 or 2 parameters compared to $\sim N^2$ for a traditional algorithm in an N-dimensional parameter space. The parameters used as input consists of a model grid and observational values to be fitted.

The EMCEE code uses the following definition for the posterior probability,

$$p(\Theta, \alpha|D) = \frac{1}{Z} p(\Theta, \alpha) p(D|\Theta, \alpha); \tag{2.5}$$

where $p(\Theta, \alpha)$ is the distribution *a priori*, $p(\Theta, \alpha|D)$ is the likelihood, and $Z = p(D)$ is a normalization factor.

Therefore, having defined the likelihood and prior functions, together with the models and the observations, the `MCMC` generates a *random walk* in the parameter space and returning parameters to draw samples $\{\Theta_i\}$ from the posterior probability density.

2.3.2.1 *Estimator of performance and reliability*

The quality of each simulation done with the EMCEE code is given by an important measurement: the acceptance fraction a_f. It corresponds to the number of accepted steps over the total number of steps of each walker. Hence, each walker, after finishing the chain, will carry a proper acceptances fraction. As a rule of thumb, the mean acceptance fraction, $\bar{a}_f$, must be between

[6] It is available online: `http://dan.iel.fm/emcee` under the `MIT` License.

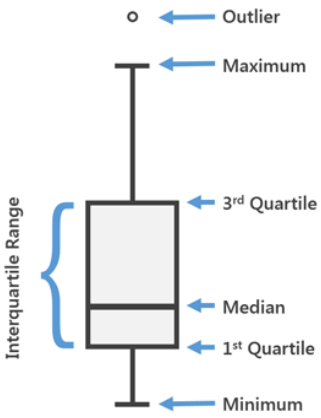

Figure 2.1: Box plot example.

0.2-0.5 (Foreman-Mackey et al., 2013). Whether $\bar{a_f} \sim 0$, then nearly all proposed steps are rejected, so the chain will have few independent samples and the sampling will not represent the target density. Typically, a low mean acceptance fraction means that the posterior probability is multi-modal, with the modes separated by wide, low probability "valleys". Conversely, whether $\bar{a_f} \sim 1$ then nearly all steps are accepted and the chain will not produce representative samples.

2.4 Viewing Tools

2.4.1 Box plot

A box plot is a graph representation involving quantiles. It allows the visualization of position, variability, asymmetry and the occurrence of atypical values of distributions.

To build a box plot, we define a rectangle ("box") in which the lower edge coincides with the first quartile (Q_1)[7] and the superior edge coincides with the third quartile (Q_3)[8]. The interquartile range is defined as $IQR = Q_3 - Q_1$ and comprises 50% of the data. The median is represented by a horizontal trace positioned between Q_1 and Q_3. Outside the box we include the "whiskers" (see Fig. 2.1) that indicates the data between $[Q_1 - 1.5IQ; Q_3 + 1.5IQ]$. Values outside this range are called "outliers".

[7] About 25% of the numbers in the dataset lie below Q_1;
[8] About 75% of the numbers in the dataset lie below Q_1.

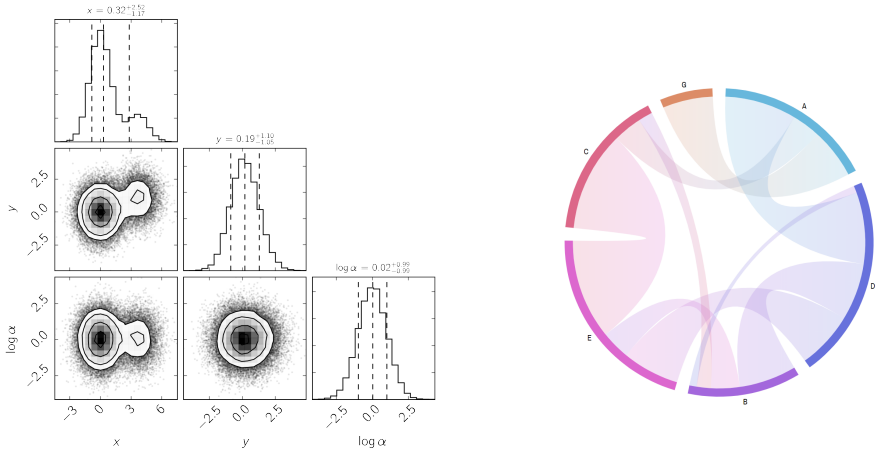

(a) (b)

Figure 2.2: Left: Box plot example. Right: chord plot example.

2.4.2 Corner Plot and Chord Plots

A corner plot is an illustrative representation to visualize multidimensional samples. Each dimensional projection of the sample is plotted to reveal covariances. In Figure 2.2a, we show an example of corner plot where it is seen the distributions of three parameters: x, y and $\log \alpha$. The dashed lines in the diagonal subplots correspond to the 16th, 50th, and 84th percentiles of the distributions. The subplots under the diagonal subplots show the probability densities correlations between the pairs of parameters. The way traveled by the walkers in the parameter space is also shown by smoothed black points.

A chord diagram is a graphical method used to display the inter-relationships between data in a matrix. The data are arranged in circumference sectors with the relationships between the data drawn as arcs connecting the data (Fig. 2.2b).

2.5 Example of Application

2.5.1 Bayesian Approach

To illustrate the Bayesian process, we must adopt a set of models and some observational data. We adopted the Kurucz atlas of model atmospheres [9]. This atlas contains about 7,600 models for a large range of metallicities, effective temperatures ($3,500\,\mathrm{K} \leq T_{\mathrm{eff}} \leq 50,000\,\mathrm{K}$), superficial gravities ($0.0 \leq \log\, g \leq 5.0$) and stellar radius ($1\,R_{\odot} \leq R_{\star} \leq 2,500\,R_{\odot}$).

[9] Available at http://kurucz.harvard.edu/grids.html.

The observational data were gathered from the VizieR photometry tool[10] and the Virtual Observatory (VO) tool SED Analyzer (VOSA, Bayo et al. 2008), for a the star Cl* Westerlund 1 W7 (hereafter W7), which represents an hypergiant cluster star that has been studied in other project (see Appendix K). These tools allow an easy visualization of photometry points extracted around a position or object name from several catalogs.

2.5.2 Likelihood

The observed flux at earth is given by the equation,

$$F_{\odot}(\lambda) = F(\alpha)(\lambda) \times \left(\frac{R_{\star}}{d}\right)^2 \times f_{\rm unred}, \tag{2.6}$$

where $F(\alpha)$ is the model flux interpolated to the free parameters $\alpha = (T_{\rm eff}, \log\, g)$, $(R_{\star}/D)^2$ is the normalizing factor[11], which takes into account the stellar radius, $R_{\star}$, and the distance star-earth, D, and $f_{\rm unred}$ is the reddening correction law used.

The reddening correction is fundamental since it affects significantly the determination of the stellar parameters. We adopted the correction suggested by Fitzpatrick (1999) (term $f_{\rm unred}$ in Eq. 2.6). This correction is valid for a large wavelength range, going from the far-UV (0.1μm) up to the IR (3.5μm). Therefore, the interstellar extinction is evaluated inside each interaction. For this, a progressive dereddening is calculated by taking interactively different values of $E(B-V)$ and $R_{\rm V}$ upon the flux models (see Eq. 2.6).

From the above assumptions, we define our likelihood functions as,

$$\log p(D|\Theta, \alpha) = -0.5 \left[\frac{\log(F_{\odot}/F_{\rm mod})}{\sigma_{F_{\odot}}/F_{\odot}}\right]^2. \tag{2.7}$$

Therefore, until now we have a 6-dimensional parameter space: $T_{\rm eff}$, $\log\, g$, $R_{\star}$, D, $E(B-V)$ and $R_{\rm V}$. In terms of code, it is written as,

```
def lnlike(params, lbd, flux, dflux):
    # Model Parameters
    Teff, logg, Rstar, dist, ebmv, rv = params[0], params[1], params[2],\
        params[3], params[4], params[5]
    # Corresponding model
```

[10] http://vizier.u-strasbg.fr/vizier/sed/;

[11] The term $(R/D)^2$ comes from the ratio $F_{\odot}/F_{\star}$.

```
    wave_mod, flux_mod = kurucz_models_interp(10**Teff, logg, 10**Rstar,
                                              10**dist, np.min(lbd),
                                              np.max(lbd))
    # Reading observational data
    lbd1, dlogF, logF, logF_mod = log_flux(lbd, dflux, flux,
                                           wave_mod, flux_mod)
    # Derredening the model
    flux_mod = pyasl.unred(1e4 * lbd1, 10**logF_mod, ebv=-1 * ebmv, R_V=rv)
    logF_mod = np.log10(flux_mod)
    chi2 = np.sum(((logF - logF_mod)**2 / (dlogF)**2.))
    return -0.5 * chi2
```

2.5.3 *Prior's Assumption*

For this example, we used as priors the Hipparcos parallax (van Leeuwen, 2007). We could say that the adopted ranges for the $E(B-V)$ and for R_V are some kind of prior($0.0 \leq E(B-V) \leq 20$ and $0.0 \leq R_V \leq 6.0$). We adopted as prior the function,

$$\log p_{\pi}(\Theta, \alpha) = -0.5 \left(\frac{\pi_{\dot{+}} - \pi_{\rm mod}}{\sigma_{\pi_{\dot{+}}}} \right)^2 , \tag{2.8}$$

where $\pi_{\rm mod}$ is the random parallax generated in each step of the inference; $\pi_{\dot{+}}$ and $\sigma_{\pi_{\dot{+}}}$ are the observed parallax and its uncertainty, respectively.

Once having defined the fluxes, the best-fitting model, in a first stage, is obtained by solving the equation 2.5, with the likelihood and the prior functions given by Eq. 2.7 and Eq. 2.8), respectively, for all set of parameters simultaneously. Thereafter, the code returns samples from the posterior probability density for each free parameter.

The representation of the prior in Python is,

```
def lnprior(params, dist_pc, sig_dist_pc):
    # Read distance free parameter
    dist = params[3]
    # Determine prior from the observed distance
    chi2_prior = ((dist_pc - dist) / sig_dist_pc)**2
    return -0.5 * chi2_prior
```

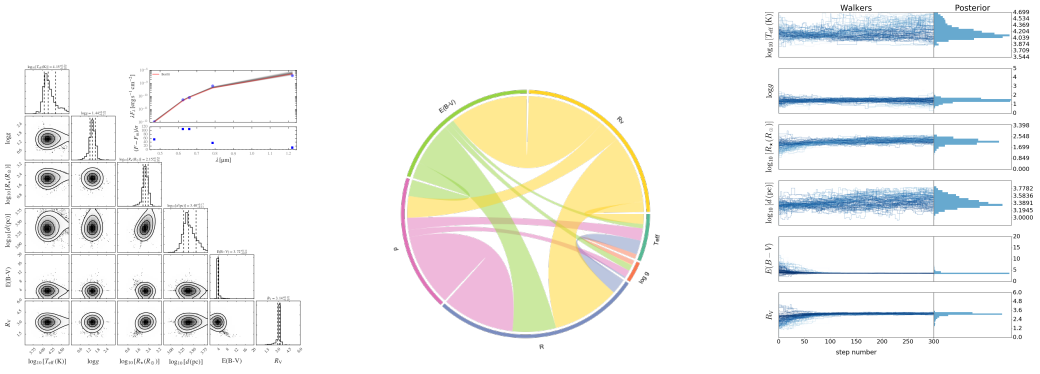

(a) (b) (c)

Figure 2.3: (a) Corner plot of W7. (b): Chord diagram for W7. Right: Convergence plot of W7.

The representation of the posterior in Python is,

```
def lnprob(params, lbd, flux_obs, dflux_obs, dist_pc, sig_dist_pc, ranges):
    # Prior
    lp = lnprior(params, dist_pc, sig_dist_pc)
    # Likelihood
    lk = lnlike(params, lbd, flux_obs, dflux_obs)
    # Posterior
    lpost = lp + lk
    return lpost
```

2.5.4 Results

Using the EMCEE and the functions defined, we obtained the results shown in Figure 2.3. It is worth pointing out These results are only illustrative of the Bayesian inference process, because of that we do not concern in analyze it. The Figure 2.3a represents the corner plot, where we can see the resulting PDFs, the histogram parameters, and the best fit. The Figure 2.3b shows the corresponding chord plot. From it is seen, for instance, that the extinction parameter R_V is strongly linked with the $E(B-V)$ parameter, as expected. Moreover, it is seen a strong correlation between the stellar radius, R, and the parallax, p, which occur due to the normalization considered in Eq. 2.6. In Figure 2.3c, we show, for each abscissa value (i.e. step), the position occupied by each walker. Note we can see a clear convergence of some free parameters ($\log g$, $R_\star$, $E(B-V)$, R_V).

Chapter 3

Model Description: BeAtlas Grid

3.1 Chapter summary

This Chapter presents a brief discussion about model photosphere (Sect. 3.2), followed by an introduction to the Geneva stellar evolution models (Sect. 3.2.1). The BeAtlas grid of models is presented in Section 3.3. The radiative transfer code used to compute the models is briefly described in Sect. 3.3.1. The model description and grid definition are presented in the subsequent sections, for both stellar grid (Sect. 3.3.2) and star plus disk grid (Sect. 3.3.3).

3.2 Model Photosphere

The photosphere denotes the stellar surface layer from which the stellar radiation is irradiated to space. Different computer techniques can model this radiation based on the theory about stellar photospheres (Gray, 2005).

The model photospheres are typically applied to produce synthetic spectra. They allow the study, for instance, of the stellar evolution, because of the effects generated by changes in the internal structure which results in photospheric changes. Then, the comparison of a set of synthetic spectra with observed spectra can, in principle, establish the properties of studied stars. Figure 3.1 shows a summary scheme of a typical processes of how a model photosphere is created and how it is applied.

3.2.1 Geneva grids of stellar evolution models

In model photospheres, we have the extensive and homogeneous database of stellar evolution models, the *Geneva stellar evolution models*. Among its features are highlighted the evolutionary

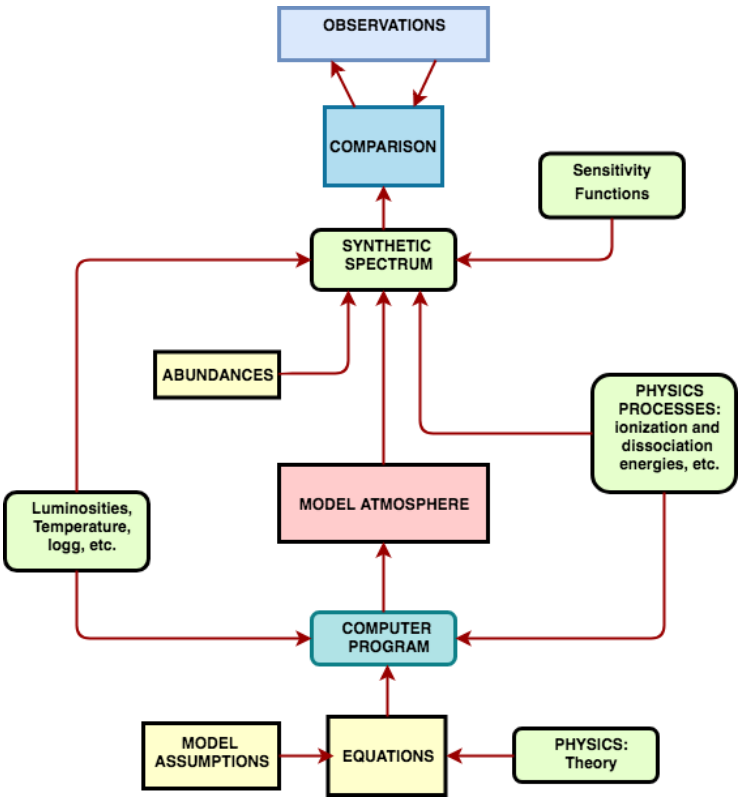

Figure 3.1: Overview of the conception of a model atmosphere and its application.

phases from the MS up to the end of carbon burning for massive stars, the early asymptotic giant branch phase for intermediate-mass stars, or core helium flash for low-mass stars. Predictions regarding the spectral evolution of massive stars can also be obtained [1].

B-type stars are known to rotate at various velocities, including very fast rotators near the critical velocity as the Be stars (Sect. 1.2). Hence, any analysis should take into account these rotational effects. To satisfy these conditions, we have chosen the rotating models described by Georgy et al. (2013) and Granada et al. (2013). We selected from them the models with solar metallicity (i.e., $Z = 0.014$), according to Grevesse and Sauval (1998). Their models include the populations of rotating star covering the mass range from 1.7 to 15 $M_{\odot}$ and Ω/Ω_{crit} encompassing from 0 to 1. The range mass includes typical masses of known Be stars as well as the transition from massive and energetic late-O stars, with strong stellar winds, to the less massive early-A stars in the regime of negligible winds Georgy et al. (2013).

To illustrate the importance of the rotation for the models, we will see some results published by Georgy et al. 2013. Figure 3.2a shows the evolution of the angular rotation rate ($\omega = \Omega/\Omega_{\rm crit}$) models published by Georgy et al. 2013 for a main-sequence star with 9 $M_{\odot}$ entering the ZAMS

[1] https://www.unige.ch/sciences/astro/evolution/fr/base-de-donnees/syclist/.

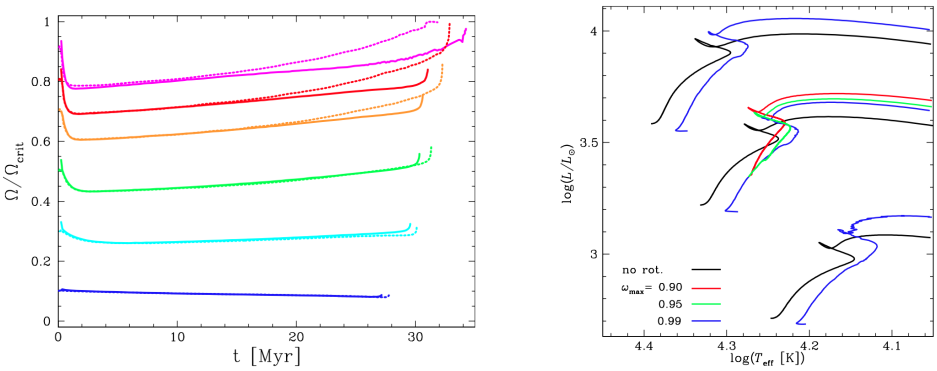

(a) *(b)*

Figure 3.2: (a) Evolution of the ω ratio for 9 $M_{\odot}$ at Z = 0.002, during the MS phase. The solid lines show the Georgy et al. 2013 models, the dotted lines the models by Ekström et al. 2008. (b) HR diagram for 5, 7, 9 $M_{\odot}$ models at solar metallicity (blue: ω = 0.99, green: ω = 0.95, and red: ω = 0.90).

with different rotation rates. In Figure 3.2b, it is shown the HR Diagram for stars with 5, 7 and 9 $M_{\odot}$ for different values of ω. These figures show basically two aspects of these models: (i) the high dependence with the rotation during the stellar evolution, and (ii) the effects of the rotation in the stellar parameters throughout their evolution. These characteristics motivated us to adopt the grid of Geneva in our study.

3.3 The BeAtlas Grid

The BeAtlas project arises in the context of grid based modelling, routinely applied to the determination of physical model parameters. The BeAtlas comprises two systematic grids of models: a photospheric-only (i.e., diskless) grid, and a star plus disk grid (hereafter referred to as "disk models"), computed according to the VDD formulation.

The initial aims of the BeAtlas project are: (i) interpreting the observations of large samples of B and Be stars (and part of the underlying spectral types); (ii) detailed modelling of individual objects; (iii) allowing theoretical studies on the physical properties of disks (e.g., disk thermal structure, correlations between parameters, etc.); and (iv) planning of new observations. Finally, we naturally expect that many other applications will arise from such a comprehensive project.

3.3.1 Radiative transfer calculations

The models were calculated with the Monte Carlo radiative transfer code HDUST (Carciofi and Bjorkman, 2006, 2008). It has been successfully applied in several previous works to interpret multi-technique observations, being the most recent examples: the interferometric study of Achernar (Dalla Vedova et al., 2017), the computation of Be disk line profiles subjected to a companion (Panoglou et al., 2018), and the interpretation of optical Be star light curves using the VDD model (Rímulo et al., 2018; Ghoreyshi et al., 2018).

For this work, we adopted a spectral coverage ranging from 1,000 Å (ultraviolet domain) up to 75 cm (radio wavelength), for both photospheric-only and disk models. Finally, we computed each model at ten different orientations with respect to the observer (i.e., angle between rotation axis and line-of-sight), ranging from the edge-on to the pole-on case with cosine-spaced steps. The grid repository can be accessed via the VIZIER service or through our website[2].

3.3.2 Stellar Description

For the photospheric models, we adopted a Roche equipotential (e.g., Cranmer, 1996) to describe the rotating stellar geometry. The limb darkening follows the prescription given by Claret (2000), and the gravity darkening effect is described by the modified von Zeipel law (see Cranmer, 1996):

$$T_{\rm eff}(\theta) = \left(\frac{L/\sigma_{\rm B}}{\oint g^{4b} {\rm d}A} \right)^{1/4} g^b(\theta), \tag{3.1}$$

where θ is the polar angle (spherical coordinates), $\sigma_{\rm B}$ is the Stefan-Boltzmann constant, and b is the GD exponent. As mentioned in Sect.3.3.1, all these ingredients are included in HDUST code.

Two possibilities were considered to define the stellar grid parameters: an empirical grid or a theoretically oriented grid. An empirical grid is defined by the typical ranges of parameters found in the literature for B-type stars, in or close to the main-sequence. It may be specified by the following four parameters: stellar mass ($M_\star$), polar radius ($R_{\rm pole}$), stellar luminosity (L) and the rotation rate (W). The choice of these parameters rely in principle on the ranges typically found in the literature for B stars on the main-sequence or close to it (e.g. Schmidt-Kaler, 1982; Harmanec, 1988). Consequently, the correlation between $M_\star$, $R_{\rm pole}$ and L are taken into account implicitly. On the other hand, the theoretically oriented grid is defined to be constrained by stellar

[2] http://beacon.iag.usp.br/joomla/.

evolution models. The advantages of such approach are both reducing the number of parameters necessary to specify a given model, and associating a specific evolutionary stage to it.

For this work, we adopted the theoretically oriented option. In particular, we chose the parameters $M_\star$, W, and $t/t_{\rm MS}$ to completely describe each model, where $t/t_{\rm MS}$ represents the time fraction spent in the main-sequence. The remaining parameters necessary for the radiative transfer calculations, $R_{\rm pole}$ and L, can be subsequently determined from the adopted stellar models.

To constrain the stellar parameters, we adopted the Geneva stellar evolution models (Sect. 3.2.1). In particular, the selected grid provides models at solar metallicity, stellar masses ranging from 1.7 to 20 $M_\odot$ [3] (roughly from early-A to late-O spectral types), and rotation rate values from the non-rotating case up to a quasi-critical case ($W \simeq 0.99$, where $W \equiv v_{\rm rot}/v_{\rm orb}$).

To constrain the gravity darkening exponent, we adopted the model presented by Espinosa Lara and Rieutord (2011), where b is function of rotation rate W only. Such model has provided a successful description for many cases in the literature (e.g., Domiciano de Souza et al., 2014).

For the disk model grid, we decided to set the mass range lower limit at 3 $M_\odot$, due to convergence difficulties of the Monte Carlo radiative transfer approach at lower masses. Also, we decided to restrict the disk models to the $W \geq 0.5$ subset, since no Be star disk was ever detected around slow rotators (see the compilation presented in Rivinius et al., 2013).

Finally, both grids also include different ages in the `MS`, from the `ZAMS` to the `TAMS`. A total of 770 photospheric models were computed, and the adopted parameters are summarized in Tab. 3.1. The table also contains the adopted disk parameters, discussed in the next section.

3.3.3 *Disk models*

Despite of being a simple approximation of the `VDD` model, a power law parametrization of the disk radial density profile represents a useful description, which is readily comparable to several results in the literature. Besides, part of the dynamical information contained in the time dependent solutions of the `VDD` model can be extracted from this particular formulation, since different intervals of the power law exponent can be associated to specific disk dynamical states (Vieira et al., 2017). The adopted parametric expression for the mass density may be written as:

$$\rho(r,z) = \frac{\Sigma_0}{H\sqrt{2\pi}}\left(\frac{r}{R_{\rm eq}}\right)^{-n} \exp\left[-\frac{z^2}{2\,H^2}\right], \tag{3.2}$$

[3] The original grid ranges up to 15 $M_\odot$, being the 20 $M_\odot$ model gently made available by C. Georgy in private communication.

Table 3.1 - BeAtlas stellar parameters of the photospheric grid model (third column) and BeAtlas parameters of the disk models (fourth column). [a] defined as $W = v_{\rm rot}/v_{\rm orb}$, where $v_{\rm rot}$ is the rotational velocity at the stellar surface and $v_{\rm orb}$ is the Keplerian orbital velocity directly above the stellar surface. [b] Based on the parametric prescription of $\rho_0\,(R_{\rm eq}/r)^n$. The spectral types are in agreement to Martins et al. (2005), Townsend et al. (2004), and Adelman (2004), for O, B and A spectral types, respectively.

	Parameters	Ranges	
		Stellar	Disk
ST	Spec. Type	O8 - A7	O8 - B9
$M_\star$	Mass ($M_\odot$)	1.7 - 20	3 - 20
W	Rotation Rate[a]	0.00 - 0.99	0.5 - 0.99
$t/t_{\rm ms}$	Stellar Age	0 - 1	0 - 1
n_0	Numerical base density (cm^{-3})	-	1.5 - 4.5
$R_{\rm D}$	Disk radius ($R_{\rm eq}$)	-	10 - 100
n	Mass density radial exponent[b]	-	1.5 - 4.5
i	Inclination angle (°)	0.0 - 90.0	0.0 - 90.0

where Σ_0 is the disk base surface density, $R_{\rm eq}$ is the equatorial stellar radius, r and z are respectively the radial and vertical cylindrical coordinates in the stellar frame of reference, and H is the disk scaleheight. In particular, H is a function of the radius given by:

$$H(r) = H_0 \left(\frac{r}{R_{\rm eq}}\right)^{\beta}, \tag{3.3}$$

where $H_0 = (c_{\rm s}/V_{\rm crit})\,R_{\rm eq}$, $c_{\rm s} = (k\,T_{\rm d}/\mu\,m_{\rm H})^{1/2}$ is the isothermal sound speed, $V_{\rm crit} = (G\,M_\star/R_{\rm eq})^{1/2}$ is the critical velocity, k is the Boltzmann constant, μ is the the molecular weight of the gas, $m_{\rm H}$ is the hydrogen atom mass, $T_{\rm d}$ is the disk temperature, and β is the disk flaring exponent. Since the disk temperature is actually highly non-isothermal, we adopt $T_{\rm d} = 0.72\,T_{\rm pole}$ as an educated guess to compute H_0 (Carciofi and Bjorkman, 2006). Additionally, β is fixed at 1.5 in the present work, which corresponds to the `VDD` model isothermal solution (e.g., Bjorkman and Carciofi, 2005a). Future grid versions are planned to have self-consistent scaleheights (Carciofi and Bjorkman, 2008).

The adopted upper and lower limits of the disk surface base density were defined as functions of the stellar mass, and can be written as,

$$\Sigma_0^{\rm upper}(M) = \begin{cases} \exp(-aM^2 + bM + c), & M \leq 8.6\,{\rm M}_\odot, \\ \exp(dM + e), & M > 8.6\,{\rm M}_\odot, \end{cases} \tag{3.4}$$

and

$$\Sigma_0^{\text{lower}}(M) = \exp(-fM^2 + gM + h). \tag{3.5}$$

The upper limits correspond to the `hdust` convergence limits, and were estimated from previous experiences with the code, while the lower limits roughly correspond to the detection limit of an Hα emission line. Notice that the convergence limitation does not impose a severe restriction, since a similar trend of increasing Σ_0 upper limit with stellar mass is also observed in nature (Vieira et al., 2017).

For the power law exponent n, we adopted the values ranging from 1.5 to 4.5, which are in agreement with those found by Vieira et al. (2017). Finally, the disk size is defined by a truncation radius, $R_{\rm D}$, ranging from 10 to 100 $R_{\rm eq}$.

For this work, we computed only lower mass sub-sample of the disk models grid ($3 \leq M_\star/M_\odot \leq 9$), constituting a total of ? models. As a first application, this sub-grid allowed the interpretation of the SED of β CMi (Sect. 6.3), a Be star of late B spectral type (B8Ve).

3.3.3.1 The Steady-State `VDD` Model

In our study, we adopted the parametric description of the `VDD` density profile given by Bjorkman and Carciofi (2005a), in which the radial disk density profile is a power law and has hydrostatic equilibrium structure in the vertical direction,

$$\rho(r,z) = \rho_0 \left(\frac{r}{R_{\rm eq}}\right)^{-n} \exp\left[-\frac{z^2}{2\,H^2(r)}\right]. \tag{3.6}$$

The constant ρ_0 is the disk base density, $R_{\rm eq}$ is the equatorial stellar radius, r is the radial coordinate, and z is the vertical cylindrical coordinate in the stellar frame of reference. Where the disk scaleheight, $H(r)$, and the surface base density, Σ_0, are given by the Eq. 3.3 and,

$$\Sigma_0 = \sqrt{2\pi}\rho_0 H_0 R_{\rm eq}^{n-\beta}, \tag{3.7}$$

where $H_0 = (c_{\rm s}/V_{\rm crit})\,R_{\rm eq}$, $c_{\rm s} = (k\,T_{\rm d}/\mu\,m_{\rm H})^{1/2}$ is the isothermal sound speed and $V_{\rm crit} = (G\,M_\star/R_{\rm eq})^{1/2}$ is the critical velocity. k is the Boltzmann constant, μ is the the molecular weight of the gas, $m_{\rm H}$ is the hydrogen atom mass, $M_\star$ is the stellar mass, β is the disk flaring exponent (Vieira et al., 2017), and $T_{\rm d}$ is the disk temperature.

Chapter 4

Methodology

4.1 Chapter summary

This Chapter shows the Bayesian Approach method used (Sect. 4.2). In Sections 4.2.1 and 4.2.2 we present the likelihood and prior functions used, respectively. The developed code is summed up in Sect. 4.3. In addition, we discuss an alternative method used to the spectral classification of Be stars in Section 4.4.

4.2 Bayesian Approach

Recent efforts (e.g. Rímulo et al., 2018; Vieira and Carciofi, 2017) showed that a grid, no matter how much science has been put to it, is useless without a statistical engine that allows exploring all the solutions. This problem arises in the context of *machine learning* or *inference techniques*, this is of the set of techniques used for interpreting and comparing observational data with models (Ivezić et al., 2014), and, naturally, leads to the employment of Bayesian inference techniques (Sect. 2.2). An additional reason for choosing the Bayesian approach is its capacity to combine the data with prior knowledge.

4.2.1 EMCEE Implementation

We adopted as likelihood the following function,

$$\log p(D|\Theta,\alpha) = -0.5\left[\frac{\log(F_{\rm obs}/F_{\rm mod})}{\sigma_{F_{\rm obs}}/F_{\rm obs}}\right]^2 \tag{4.1}$$

where $F_{\rm obs}$ and $F_{\rm mod} = F_{\rm mod}(\Theta)$ are the observed and model fluxes.

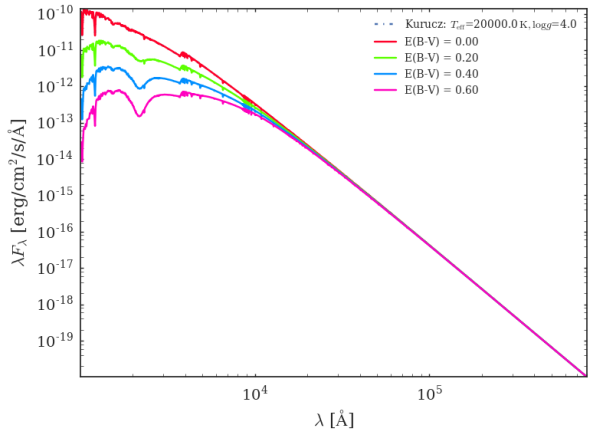

Figure 4.1: Extinction effect on the stellar spectrum.

In more detail, the fitting procedure is performed with the grid of models ($F_{\rm mod}$) and the observed fluxes ($F_{\rm obs}$) in Eq. 4.1. These observables can be converted to the fluxes received at the Earth by,

$$F(\lambda) = F_0(\alpha)(\lambda) \times \left(\frac{10}{d}\right)^2 \times f_{\rm unred}, \tag{4.2}$$

where $F(\alpha)(\lambda)$ is the emergent stellar flux, α is the set of intrinsic physical stellar properties, d is the distance to the star, and $f_{\rm unred}$ is the correction of the total extinction along the line of sight.

The reddening correction, represented by the function $f_{\rm unred}$, is fundamental since it affects significantly the determination of the stellar parameters. Recent articles attest the complexity of the extinction determination by lines for Be stars (McEvoy et al., 2015). For this reason, the use of alternative techniques for estimating $E(B-V)_{\rm IS}$ that are independent of circumstellar material (e.g. Beeckmans and Hubert-Delplace 1980) becomes essential in our study. Zagury (2013) studying a large absorption feature centered at 2 175Å called UV bump, showed that the duality between the forms of curves in the bump region, linear or with a bump, could be used to investigate the parameter $E(B-V)$ even in circumstances of low column density directions, and stars close to the obscuring material (see Figure 1 of Zagury 2013). Beyond the UV region, the extinction can be evaluated even beyond the near-infrared. As an example, Figure 4.1 shows the extinction effect upon the spectrum of a Kurucz photosphere model with $T_{\rm eff} = 20000$ K and $\log g = 4.0$. This result illustrates that as the extinction increases, the original spectrum becomes fainter in the UV domain, it makes the resulting spectrum be confusing with later spectral types than the original. Therefore, even without the bump region, the function can constrain the extinction parameters.

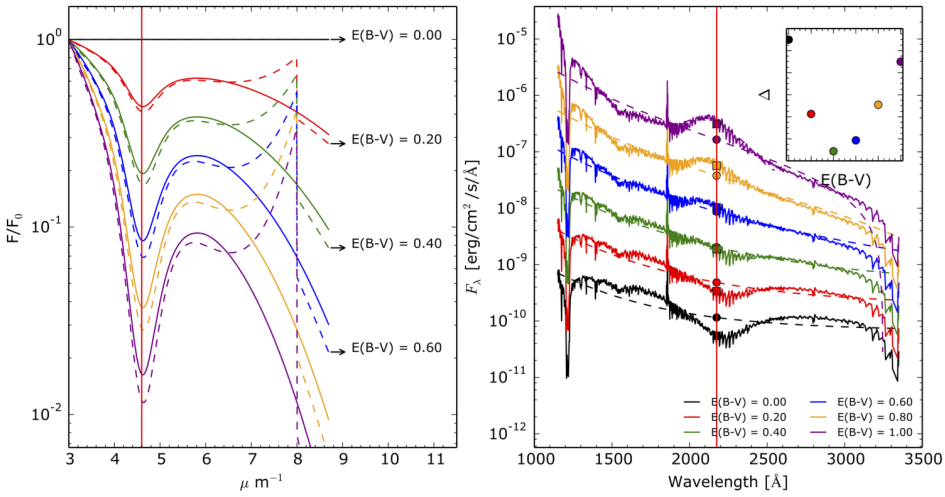

Figure 4.2: Comparison of the Fitzpatrick 1999's and Cardelli et al. 1989's laws applied for the star ρ Ophiuchi.

To implement this method of correction, first, we studied the extinction corrections that have the parametrization of the bump (Cardelli et al. 1989; Fitzpatrick 1999). Among them, we adopted the parametrization suggested by Fitzpatrick (1999) (see Fig. 4.2). Next, we calculated the interstellar extinction inside each interaction. For this, a progressive dereddening is calculated by taking interactively random values of $E(B-V)$ upon the flux models in the region of the bump (see Eq. 4.2). We adopted a typical value of $R_V = 3.1$ for all spectra (Schultz and Wiemer, 1975). We discuss the priors adopted during the `MCMC` procedure in the next section.

4.2.2 *Prior Choice Description*

We used as priors the Hipparcos parallax (van Leeuwen, 2007) and measurements of $v \sin i$ taken from several sources (Frémat et al. 2005; Levenhagen and Leister 2006; Abt et al. 2002; Challouf et al. 2015; Nieva, Mara-Fernanda and Przybilla, Norbert 2014; Spectroscopic survey of COROT[1] Be stars). We did not use the GAIA DR2 parallaxes (Gaia Collaboration, 2018) (see Discussion in Sect. 4.2.2.1).

[1] http://www.astrosurf.com/buil/us/bestar.htm.

The chosen prior distance function was,

$$\log p_{\pi}(\Theta, \alpha) = -0.5 \left(\frac{\pi_{\rm obs} - \pi_{\rm mod}}{\sigma_{\pi_{\rm obs}}} \right)^2, \tag{4.3}$$

where $\pi_{\rm mod}$ is the random parallax generated in each step of the inference; $\pi_{\rm obs}$ and $\sigma_{\pi_{\rm obs}}$ are the observed parallax and its uncertainty, respectively.

By providing $v \sin i$ values to the code, we can constrain the values of the likely inclinations, masses and oblateness, i.e. physical quantities directly related with. To implement such a prior, it was calculated for each interaction a $v \sin i(\Theta)$. For the stars with $v \sin i(\Theta)$ without uncertainty, we fixed the errors as 10 % of the measurement. Here, it is important to highlight the fact pointed by Townsend et al. (2004), i.e. that the classic $v \sin i$ values, which did not consider the gravity darkening effect, could be underestimated by 9 to 33% at $W = 0.75$ for B0 to B9-type stars. Therefore, some $v \sin i$ employed could propagate error in the inference of studied parameters. The prior function used to the $v \sin i$ was,

$$\log p_{\rm v \sin i}(\Theta, \alpha) = -0.5 \left(\frac{v \sin i_{\rm obs} - v \sin i_{\rm mod}}{\sigma_{v \sin i_{\rm obs}}} \right)^2. \tag{4.4}$$

where $v \sin i_{\rm mod}$ is the random $v \sin i$ generated in each step of the inference; $v \sin i_{\rm obs}$ and $\sigma_{v \sin i_{\rm obs}}$ are the observed $v \sin i$ and its uncertainty, respectively.

Once having defined the fluxes, the best-fitting model, in a first stage, is obtained by solving the Eq. 2.5 with the likelihood given by the Eq. 4.1 together with the prior functions (Eq. 4.4 and 4.3) for all set of parameters simultaneously. Thereafter, the code returns samples from the posterior probability density for each free parameter.

The posterior probability defines, for a set of parameters (D), the probability of them being true. Therefore, once the samples produced by EMCEE are available, the marginalized constraints on Θ can be approximated by the histogram of the samples projected into the parameter subspace spanned by Θ. The uncertainties on each parameter were defined as the measuring of percentiles of 16 and 84 % on the marginalized PDFs, and the best fit as the median.

4.2.2.1 Gaia parallaxes

We tested the quality of the GAIA data release 2, initially, by comparing with the Hipparcos parallaxes (Fig. 4.3). We noticed that there is no global agreement among the parallaxes, which is showed by the high dispersion of the measurements around the dashed line in Fig. 4.3.

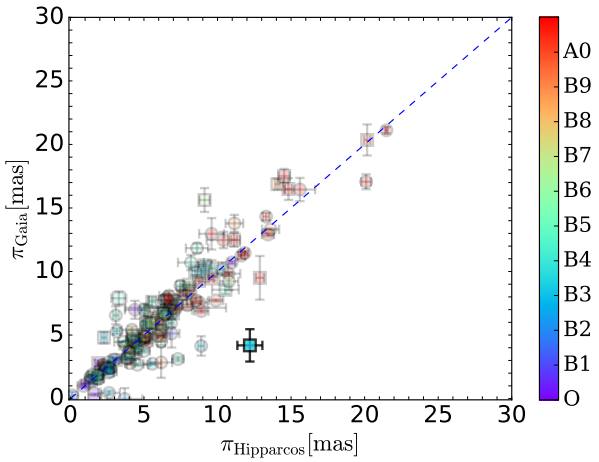

Figure 4.3: Comparison of Hipparcos and Gaia parallaxes for our survey of stars.

GAIA DR2 already indicates limitations in the published data (Gaia Collaboration et al., 2018). Nevertheless, this release is still intermediate, being based on a limited amount of input data ($\sim$ 22 months) and submitted to simplifications in the data processing. This introduces shortcomings in the calibrations that propagate systematic errors.

The *duplicated source* quality field of the GAIA DR2 indicates that the source was identified as duplicated during data processing. It may indicate: observational cross-matching, processing problems, stellar multiplicity (near companions), astrometric or photometric problems. Hence, GAIA DR2 might indicate incorrect parallaxes for multiple systems. This may explain the incompatibility among GAIA DR2 and Hipparcos parallaxes for many cases (e.g. α Arae, α Col). A counterexample is Pleione, which is a simple star that show compatible values ($\pi_{\rm hip} = 8.54 \pm 0.31$ mas and $\pi_{\rm gaia} = 7.72 \pm 0.20$ mas).

Since we do not know exactly the binary fraction among Be stars (Sect. 1.2.2), the GAIA DR2 parallaxes were rejected in our study.

4.3 Bemcee

The Bemcee open-source code comprises all modules developed during this Ph.D. It is a community effort (Beacon's group) to develop a common core package for the inference of Be stars parameters in Python. It is available online in the github[2] repository through the https://github.com/tangodaum/bemcee[3]. We present its tutorial in Appendix B.

[2] It support collaborative development of software and the tracking of changes to software source code over time.
[3] https://github.com/tangodaum/bemcee.

4.4 BCD System

The BCD System is a consolidated method for obtain the photosphere parameters of "normal" stars, i.e. objects whose atmospheres can be studied in the framework of hydrostatic and radiative equilibrium approximations. However, since both circumstellar and photospheric components of the Balmer Discontinuity (hereafter BD) are spectroscopically distinct, the BCD System is usually applied to "peculiar" stars as the Be stars (e.g. Divan et al. 1982; Zorec and Briot 1991; Shokry et al. 2018).

It is based on measurable quantities that are sensitive to the ionization balance and gas pressure in stellar photospheres. This makes the method ideal to indicate $T_{\rm eff}$ and log g. In summary, the method is based in four quantities taken from the spectrum around the Balmer Discontinuity (hereafter, BD):

1. D: the Balmer jump at $\lambda 3,700$ Å given in dex; this parameter is a strong function of $T_{\rm eff}$;
2. λ_1: the mean spectral position of the BD, usually defined as $\lambda_1 - 3,700$ Å; this parameter is very sensitive to log g;
3. $\Phi_{\rm UV}$: the gradient of the Balmer energy distribution in the near-UV from $\lambda 3,100$ to $\lambda 3,700$ Å in μm;
4. $\Phi_{\rm rb}$: the gradient of the Paschen energy distribution in the range $\lambda\lambda 4,000 - 6,200$ Å in μm.

The BCD parameters ($_1$, D) can be measured even in spectra of low resolution and in cases of high ISM extinction, which makes the method applicable also for distant objects.

During this Ph.D., we worked with this method, developing a Python Code (PharaUS) to apply the BCD method. The code is available at the GitHub link[4]. This contribution helped in the work published by Shokry et al. 2018. This article is in Appendix D.

[4] https://github.com/tangodaum/pyxshooter.

Chapter 5

Observational and Data Reduction

5.1 Chapter summary

There are different physical processes operating in Be disks, each of them being associated with distinct observables. Then, the multiplicity of observations could, in principle, creates complementary results, providing support for the modeling process. In this Chapter, we present the studied objects (Sect. 5.2). Next, the observational measurements are shown, and the reduction made when necessary (Sect. 5.3). Following, we show the set of developed tools made (Sect. 5.4) used to look for these objects and some of the observational data in VO tools.

5.2 Selected Stars

5.2.1 Sample of stars

Our sample of stars comprises O, B and A stars, including the peculiar classes Be, Bn, Ae, A shell and Oe stars. Each selected peculiar class is detailed in Section 1.4. Basically, we selected stars from the Bright Star Catalogue (Hoffleit and Jaschek, 1982) and from Jaschek and Egret (1982). After, we selected just the luminosity classes V and IV (MS and subgiants). Naturally, the stars without UV data were discarded. The selection is shown in Table A.11.

5.2.2 β CMi

We selected the nearby late-type (B8Ve) Be star β CMi has a stable low-density disk. β CMi was the target of pioneer interferometric studies, for instance, Quirrenbach et al., 1997 published the disk and stellar diameters from interferometric measurements. They also estimated the equatorial radius, $R_{\rm eq}3.6\,R_\odot$, and a lower limit for the disk size, $R_{\rm D} = 13\,R_\odot$. Later, Tycner

Table 5.1 - Recent results of β CMi.

Parameter	Klement et al., 2015b	Klement et al., 2017
$R_{\rm pole}[R_\odot]$	2.8	2.8 ± 0.2
$M\,[M_\odot]$	3.5	3.5
$L\,[L_\odot]$	185	185 ± 5
W	0.98	1.0
β	$0.1367^{+0.0025}_{-0.0013}$	-
$\log_{10}\rho_0[{\rm g}\cdot{\rm cm}^{-3}]$	-11.70	$-11.78^{+0.18}_{-0.30}$
$R_{\rm out}[R_{\rm eq}]$	35^{+10}_{-5}	40^{+10}_{-5}
$i\,[^{\rm o}]$	43^{+3}_{-2}	-
$d\,[{\rm pc}]$	49.6	-
$E(B-V)[{\rm mag}]$	-	$0.01^{+0.02}_{-0.01}$
n	-	2.9 ± 0.1

et al., 2005, also through long-baseline interferometric data, determined the rotation rate ($W = 0.85 \pm 0.21$) and the equatorial radius, $R_{\rm eq} = 3.6 \pm 0.3\,R_\odot$.

Recently, multi-technique analyzes were applied for β CMi (Klement et al., 2015b; Klement et al., 2017). These studies kept the same stellar parameters. Table 5.1 shows the best-fit parameters of each study. For comparison, we adopted the results from Klement et al., 2017 since it resulted from a improved version of the HDUST code and from additional VLA measurements.

5.2.3 α Arae

The southern star α Arae (HD 158427, HR 6510) is a MS star of spectral type B2Vne[1]. Its proximity (74.3 pc, van Leeuwen 2007) allowed the constitution of a rich observational history, offering unique opportunities to perform a detailed study of the process that governs the dynamic of Be disks. Furthermore, Arae region seems suitable to the search of distant objects, since dark clouds are not as important there (Vega et al., 1980), resulting in lower extinction levels.

Recently, Bagnulo et al., 2015 using FORS1 instrument on the ESO Very Large Telescope (VLT) measured the mean longitudinal magnetic field from low-resolution circular polarised spectra of nearly a thousand different stars. In Figure 1.2, we show the MS stars studied by them showing the position occupied by α Arae ($< B_z > (G) = -27 \pm 38$, $MJD = 53869.353$) which constitute another piece of evidence that it is a Be star. α Arae has also shown a relatively stable behavior in the last years (Sect. 7.4.1.1). This allowed us to adopt the VDD model (Section 1.5.1) from which we can assume two possibilities to the α Arae's disk: i) a large disk (non-

[1] http://simbad.u-strasbg.fr/simbad/sim-id?Ident=alf+ara.

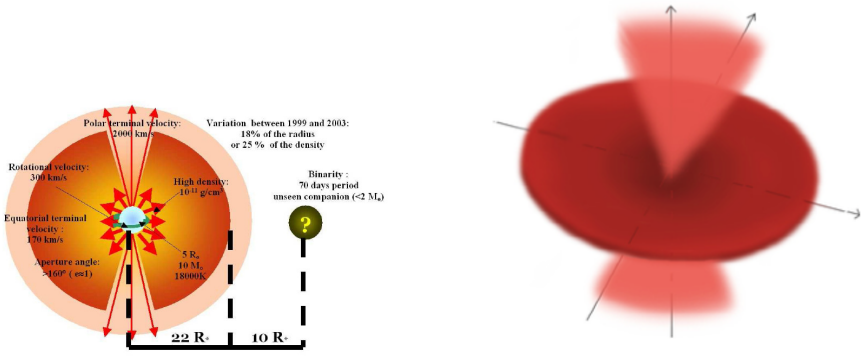

(a) *(b)*

Figure 5.1: Left: Model with a polar dense wind proposed by Chesneau et al. (2005). Right: 3D artist view of the best model achieved by Meilland and Stee (2006).

binary case); ii) a truncated disk (see Sect. 1.2.2) (binary case). The results derived by previous studies of α Arae are summarized in Tables A.2 and A.3.

The binarity of α Arae was first suggested from studies performed with data taken with the instruments `MIDI` and `AMBER` (Meilland and Stee, 2006). Interpreting these results, first done outside the `VDD` context, suggested a *dense polar wind* along its rotational axis and a thin disk truncated by an unseen binary. These previous models suggested a period of $\sim$ 74 days and a semi-major axis of 32 $R_\star$ for the companion ($M_\star < 2\,M_\odot$) (e.g. Chesneau et al. 2005, Vinicius et al. 2007, Meilland et al. 2007).

Recently, Meilland et al. (2012) concluded that the disk-size does not differ in the range 8 - 12 μm from `VLTI/MIDI` measurements. Their results are supported by Hamed and Sigut (2013). These authors found out that the α Arae's disk, between 2.1 and 12 μm, does not change considerably. This corroborates the hypothesis of a truncated disk by an unseen companion.

About the α Arae stellar wind (Fig. 5.1), the recent review of Rivinius et al. (2013) argues that the evidence proposed by Chesneau et al. (2005) is fragile, once it was based on a single interferometric measurement [2]. Here, a simple calibration bias could fluctuate deeply the wind features. Apparently, the only case of wind in Be stars that deserves to be checked is Achernar (Faes, 2015). Despite this, the interplay between winds and rotation should be better investigated. These effects, when combined, could affect, for example, the stellar evolution and the mass injection to the circumstellar environment (Georgy et al., 2013). Previous results of α Arae are summarized in the Appendix A.2.

[2] These results were obtained by means of the code `SIMECA` (SIMulation pour Étoiles Chaudes Actives).

5.3 Observational Data Overview

A diversity in data would interest to explore different system parameters since different physical processes appear in distinct spectral domains. The disk of Be stars becomes clear at optical wavelengths by hydrogen (first Balmer lines) and metallic emission lines (stronger HeI and FeII lines) in their spectrum (Lamers et al., 1980). These observables arise from emission and recombination processes. In the IR range, the emission arises from continuous bound-free and free-free thermal emission (e.g. Cote and Waters, 1987). Beyond these processes, the polarization of the stellar light by the disk is also present (e.g., Kjurkchieva et al., 2016; Yudin, 2001).

To support our simulations, we combined data from the literature, including photometric, polarimetric and spectroscopic data. Most data were accessed through online Virtual Observatory Tools (VO): Bess[3], VO SED Analyzer (VOSA, Bayo et al. 2008), Spectral Analysis Tool (VOSpec; Arviset et al. 2008), MAST[4], VAO[5], SDSS[6], AAVSO[7], ESO archive[8], US Virtual Astronomical Observatory[9], and from VizieR Photometry viewer (Ochsenbein et al., 2000). All the routines used to read and plot the observational data are available in the GitHub Repository Link[10].

5.3.1 UV data selection

There are several missions covering the UV domain: EUVE (70 – 760 Å), CHIPS (90 – 260 Å), ORFEUS (400 – 1 250 Å), Astro 2 (425 – 3 200 Å), FUSE (905 – 1 187 Å), IUE (1 145 – 3 300 Å), and GALEX (1 300 – 3 000 Å). Among these missions, we adopted data from the International Ultraviolet Explorer spatial mission - IUE. The IUE has two cameras: the SWP camera (1 145 – 1 975 Å) and the long-wavelength LWP/LWR cameras (1 850 – 3 300 Å).

The data selection followed the procedure described by Freire Ferrero et al. (2012), this is, there were selected high-dispersion large-aperture observations, because they can be calibrated in flux units. Another caution was to select data with exposure time < 60 s. After that, we selected the IUE fits re-binned files from INES Archive Data Center[11], maintained by ESA.

[3] http://basebe.obspm.fr;
[4] http://archive.stsci.edu;
[5] http://vao.stsci.edu;
[6] http://www.sdss.org;
[7] http://www.aavso.org;
[8] http://archive.eso.org;
[9] http://vao.stsci.edu;
[10] https://github.com/tangodaum/AstroPLOT;
[11] http://sdc.cab.inta-csic.es/cgi-ines/IUEdbsMY.

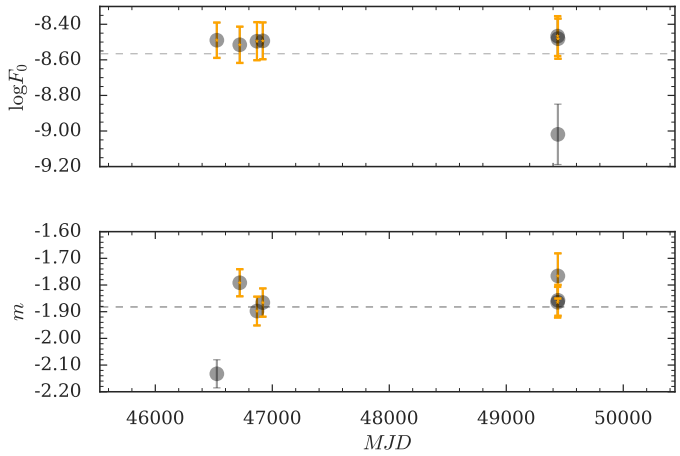

Figure 5.2: Parameters F_0 and m found to α Arae. Modified Julian Date (MJD) are in abscissas and F_0 and m parameters in ordinates. Dashed lines represent the mean values.

After the data selection, we calculated the flux level (F_0) and its inclination m for each selected spectrum for each selected stars by fitting a exponential function,

$$f = F_0 \left(\frac{\lambda}{\lambda_0} \right)^m . \tag{5.1}$$

It allowed us to verify through the UV domain, whether the stellar emission suffered some variation in the period it was observed. Hence, the resulting complete UV spectrum is the combination of the spectra that showed levels and inclinations inside three times the standard deviation (σ) calculated using all the fluxes. Therefore, *for each selected star, we removed the spectra which were out of the 3 σ of the mean values obtained for the inclination and level, respectively*.

As an example, the adjusted parameters F_0 and m obtained from each SED of α Arae are shown in Fig. 5.2. These results show that α Arae can be considered stable in the UV domain. We see that only two spectra are out of the average values (dashed lines) in the dates 1994-03-30 and 1986-04-06 (points with black error bars). These spectra were removed from the analysis.

5.3.2 Photometric data

VO Tools can provide the SED of an object by searching in several catalogues. Our photometric data comprises results of several observational missions: Ducati (2002), Hipparcos (ESA, 1997), Mermilliod (1994), IUE, 2MASS, TYCHO (Hog et al., 2000) in the visual domain, DENIS, IRAS, WISE (Cutri and et al., 2014) in the IR domain, AKARI (AKARI/IRC mid-IR all-sky Survey; Ishihara et al. 2010), MSX (MSX6C Infrared Point Source Catalog; Egan et al. 2003), SDSS, and from the Catalogue of Homogeneous Means in the UBV System (Mermilliod, 1994). We

also added radio APEX observations made with the LABOCA bolometer at 870 μm and radio data from the Very Large Array (VLA). The selected photometric data of α Are is in Table A.5. The photometric data of β CMi is listed in Klement et al., 2015a.

5.3.3 Linear Polarization Data

Linear polarization of starlight can be intrinsic to the star, its environment or due to interstellar contribution. This measurement is the most sensitive quantity to detect circumstellar activity (Faes, 2015). The interstellar polarization results from dust[12] particles aligned to the Galactic fossil magnetic field (Cotton et al., 2016). In contrast, the intrinsic polarization arises from the scatters present in the disk. The basic ingredient to occur the polarization of the light by the disk is the existence of free electrons that, by means of the Thompson scattering, produces the polarization. This polarization is strongly connected with the stellar subspectral type, the density scale and with the inclination angle.

Cotton et al. (2016) reported the linear polarization of 50 nearby ($d \lesssim 100$ pc) southern stars without considering the interstellar extinction. One of the main results of their study is illustrated in Figure 5.3. Notably, the most highly polarized stars were four Be stars: α Eri, α Col, η Cen and α Ara. Thereafter, they showed the trend of the polarization with spectral type; exhibiting the remarkable polarization levels among Be stars and a clear division between A and B-type stars that suggests a peculiar mechanism in B stars.

We made use of polarimetric data from the Pico dos Dias Observatory (OPD-LNA) (Tab. A.8 and A.6), and from the HPOL Spectropolarimeter at the University of Wisconsin-Madison Pine Bluff Observatory (PBO) (Tab. A.9). The OPD-LNA data was reduced with packages developed by our research group. We obtained the HPOL data from MAST Archive[13].

For the case of α Arae, we have estimated the interstellar polarization in its line of sight by measuring a set of field stars (Tab. A.4). The five main sequence selected field stars showed that the average interstellar polarization does not exceed 0.05%, which is consistent with previous studies of McLean and Clarke (1979) ($p_{\max} \sim 0.03\%$) and Dachs et al. (1988) ($E_{IS}(B-V) = 0.0$). Due to the small amount of interstellar contribution, we performed none interstellar polarization correction. We also used additional polarimetric data for α Arae (Tab. 5.2).

[12] Dust is formed in the circumstellar environment of giant stars. Pulsations in the outer envelope carry molecular gas to the surface, then the stellar wind blows it radially outward to condense as grains (Morris, 1987);

[13] https://archive.stsci.edu/hpol/.

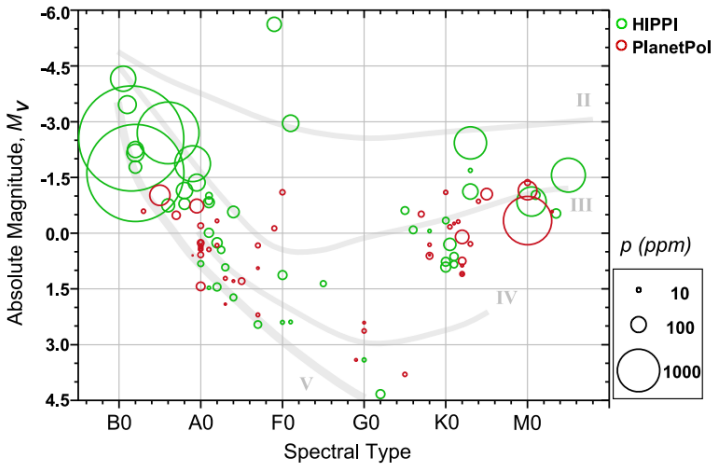

Figure 5.3: H-R Diagram of Cotton et al., 2016. The gray lines represent the main sequence (V), sub-giant (IV), giant (III), and bright giant (II) branches. The diameter of the bubbles represents the degree of polarization for HIPPI and PlanePol surveys.

Table 5.2 - Polarimetric dataset. `OPD-LNA` data obtained in the period $54260 < MJD < 57624$. Historical data published by Serkowski (1970) and McLean (1979) ($40085 < MJD < 42877$).

Date/MJD	Filters	$P_{\rm int}$ [%]	$PA_{\rm int}$ [°]	$P_{\rm IM}$ [%]	$PA_{\rm IM}$ [°]	Ref.
-	-	0.58	166	0.15	-	Yudin, 2001
12/5/2014		0.62400 ± 0.00034	172.0 ± 0.0	-	-	Cotton et al., 2016
54260 to 57624	`UBVRI`	0.50 (average)	-	-	-	`OPD-LNA`
40085 to 42877	`UBV`	0.50 (average)	-	-	-	McLean, 1979

5.3.4 *Spectroscopic data*

The reason why the spectra shown by Be stars have an excess in the continuum or emission lines is that the disk material acts as a "pseudo-photosphere" larger than the stellar photosphere (Carciofi, 2011). Such lines strongly depend on the inclination angle.

The study of lines has been the source of fundamental information about the disk. For instance, evidence of variability in emission line profiles of Be stars is quite common. Curious cases are the V/R variations that can show peaks intensities change in relation to each other in timescales of weeks to months. These variations can be understood in terms of density patterns in the disk. In such a scenario, the approaching of the high-density region to the observer could enhance the violet peak (V), when it is moving away from the observer the red peak (R) becomes prominent (e.g. Labadie-Bartz et al. 2017). These variations might arise from binary effects (Rivinius et al., 2013).

The hydrogen lines are the most prominent ones and constitute one of the best diagnostic-lines. Depending on the density level there will be also emission by the lines: Hα (6562.8 Å),

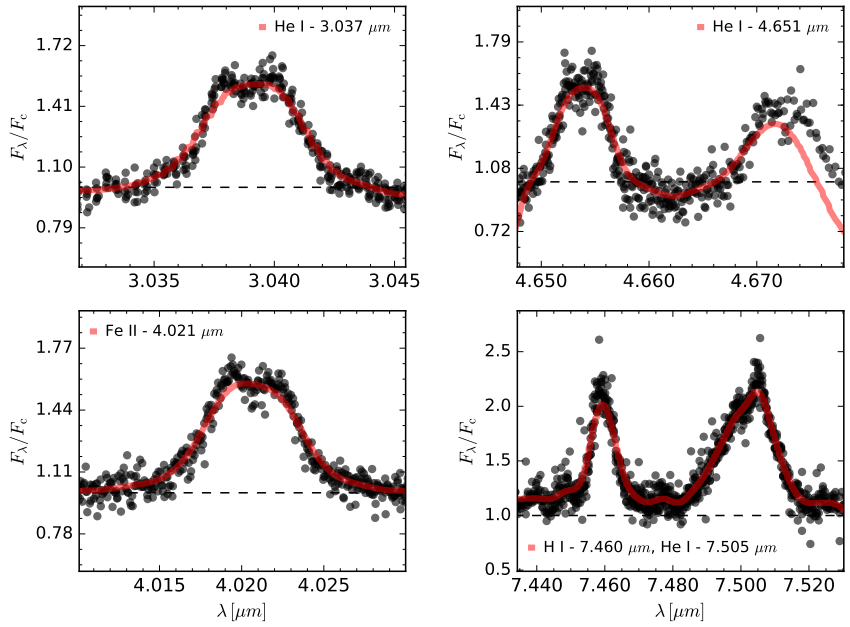

Figure 5.4: Infrared Space Observatory (ISO) spectra of α Arae (1996-02-17). We detached some lines (He I, Fe II and H I) found in the spectrum. Red curves are the smoothed lines.

Hβ (4861.3 Å), Hγ (4340.5 Å). Hδ (4101.7 Å), Hϵ (3970.1 Å). Neutral helium HeI can also be seen in emission at 4009.3, 4026.2, 4143.7, 4387.9, 4437.5, 4471.5, 4713.1, 4921.9, 5875.6 and 6678.2 Å. Beyond these lines another wide group of lines are observed, such as: CII (3920, 4267, 4738, 4745, 6578, 6583 Å), NII (3995, 4630 Å), OII (4119, 4367, 4415, 4642, 4649, 4662 Å), MgII (4481 Å), SiIII (4552, 4568 and 4575 Å triplet; several lines around 3800; also at 3924, 4338, 4813, 4829 and 5740 Å), SiII (3856, 3863, 4128, 4131, 5041, 5056, 6347, 6371 Å), and sometimes FeII lines[14] (Fig. 5.4).

We search for spectroscopic data only for the star α Arae. It was gathered from several sources as VO tools. In addition, we have own data from the Brazilian observatory Pico dos Dias OPD-LNA. These data were obtained using the ECass, a long slit Cassegrain spectrograph and the MUSICOS (Multi-SIte Continuous Spectroscopy)[15]. The Flash and Heros data, covering from 3 500 Å to 9 000 Å where accessed through the German VO tool GAVO[16]. Our compilation includes historical hydrogen lines (Hα and Hβ) published by Dachs et al. (1981) (1978-11-02 to 1977-07-08), Hanuschik et al. (1996) (1982-08-30 to 1993-09-09), Banerjee et al. (2000) (1999-04-13) and by Dachs et al. (1986) (1982-02-27 to 1983-03-17).

[14] http://www.shelyak.com/dossier.php?id_dossier=24&lang=2;
[15] http://www.lna.br/opd/instrum/instr.html;
[16] http://dc.zah.uni-heidelberg.de/.

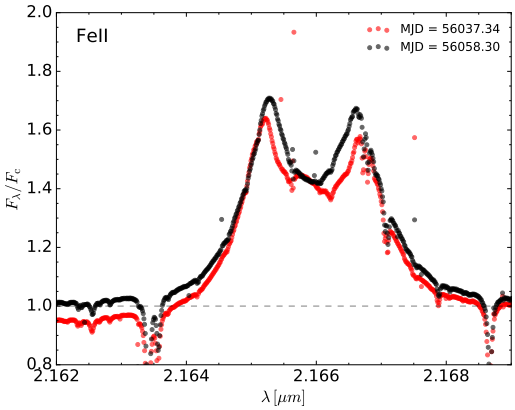

Figure 5.5: α Arae Fe II lines from CRIRES spectrograph from 2012-04-20 to 2012-07-05.

The reduction chain used for all instruments of the ESO followed the sequence: 1) classify/organize the data, a process called "data association", which uses, in principle, FITS headers information present in "association keywords". 2) Next, the instrument pipeline is called by a standard ESO application, i.e. Gasgano (ESO, 2012), Reflex or Esorex (Freudling et al., 2013).

From the ESO facility we obtained UVES data. UVES is a two-arm cross-dispersed echelle spectrograph. It covers 3 000-5 000 Å (blue arm) and 4 200-1 1000 Å (red arm). The spectral resolution can reach up to 80 000 (blue arm) or 110 000 (red arm) (Dekker et al., 2000). The data reduction was done through the UVES pipeline described in the UVES-Tutorial[17](version 5.7.0). We used the typical UVES data reduction sequence with the UVES pipeline.

Additionally, CRIRES[18] instrument provided high-resolution data from 1 to 5 μm (Kaeufl et al., 2004). These results were reduced by the EsoRex platform (201, 2015) as described in CRIRES-Tutorial[19] (see Tab. A.7). The smoothed lines obtained are shown in Fig. 5.5

We also selected reduced data from Harps and Feros downloaded from the ESO archive. We summarized in Table A.7 our spectroscopic data of α Arae.

In our study, we focus basically at the Hα line. During the Be state, the Hα line profile comprises a central absorption core and two emission peaks (red and blue) displaced almost symmetrically around the absorption core. In the B state, we can expect pure absorption[20].

[17] ftp://ftp.eso.org/pub/dfs/pipelines/uves/uves-pipeline-manual-22.12.pdf;

[18] CRyogenic high-resolution InfraRed Echelle Spectrograph;

[19] https://www.eso.org/public/teles-instr/paranal-observatory/vlt/vlt-instr/crires/;

[20] Class I profiles show symmetric, double-peak profiles ($V \sim R$). Class II profiles has a dominant single peak (Hanuschik et al., 1995);

5.3.5 Interferometric data

For the case of α Arae, we also collected interferometric data obtained by the instruments: PIONIER, MIDI and AMBER. PIONIER[21] is an instrument on the VLTI together with AMBER[22] and MIDI[23] (PIONIER-Tutorial)[24]. It has a wavelength coverage of 1.5-2.4 μm at low spectral resolution. We downloaded the reduced data from the facility Optical interferometry DataBase[25] and are shown at Table A.10.

MIDI is an interferometer and spectrograph covering the mid-infrared (8-13 μm) (MIDI-Tutorial)[26]. The reduced data published by Chesneau et al. (2005) were in this paper (details about the observations can be seen at their Table 1).

AMBER is an interferometer and spectrograph operating in the near-infrared domain (1.0 - 2.4 μm) with variable spectral resolution ($R = 30$, $R = 1500$ or $R = 12000$). AMBER data were reduced using the VLTI/AMBER pipeline, AMDLIB v3.0.9 (e.g. Tatulli and Duvert 2007). For more details about the reduction we recommend the examples of the VLTI Scholl Site (2013)[27].

5.4 BeFaVOr Tools

This tool started with a Scientific Initiation Project (Appendix I). It uses "Web Service" PYTHON routines to get data and a list of stars given some conditions. The routines are available at the GITHUB link[28]. A detailed description is given in Appendix J.

Figure 5.6 illustrates the workflow showing in a simplified form the main relations between the routines and their dependencies.

[21] Precision Integrated-Optics Near-infrared Imaging ExpeRiment;
[22] Astronomical Multi-BEam combineR;
[23] MID-infrared Interferometric instrument;
[24] https://www.eso.org/public/teles-instr/paranal-observatory/vlt/vlt-instr/pionier/;
[25] http://oidb.jmmc.fr/index.html;
[26] https://www.eso.org/public/teles-instr/paranal-observatory/vlt/vlt-instr/midi/;
[27] http://www.jmmc.fr/twiki/pub/Jmmc/VltiSchool2013/SchoolTutorials/;
[28] https://github.com/tangodaum/BeFaVOr-WEB.

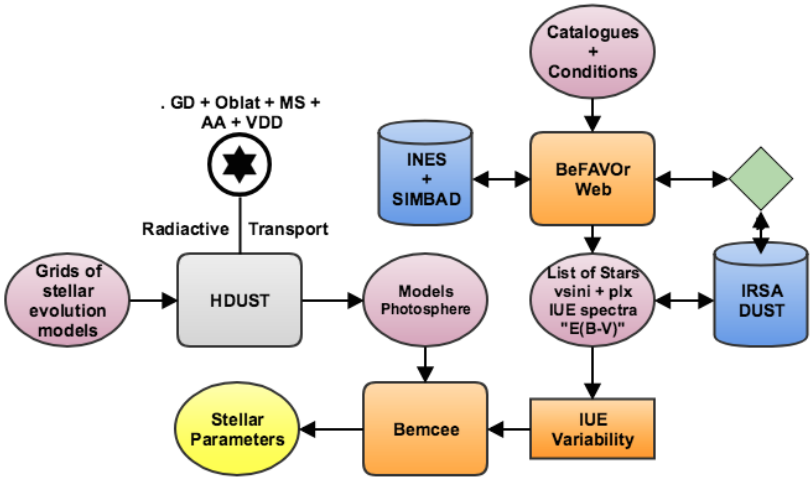

Figure 5.6: Workflow of the developed routines. GD: gravity darkening. Oblat: oblateness. MS: multiple scattering. AA: auto-absorption by the disk. INES: http://sdc.cab.inta-csic.es/cgi-ines/IUEdbsMY. IRSA DUST: https://irsa.ipac.caltech.edu/applications/DUST/. SIMBAD: http://simbad.u-strasbg.fr/simbad/sim-fbasic.

Chapter 6

Results

6.1 Chapter summary

In this Chapter, we applied our inference method for a set of 111 stars (Sect. 6.2). This procedure allowed us to examine a diversity of theoretical and methodological problems. After, we show the results achieved for the stars β CMi and α Arae (Sect. 6.3 and 6.4).

6.2 UV description

Our start point was to use the UV spectral domain (Sect. 5.3.1) in the procedure described in the Sect. 4.2. At first sight, the choice of the UV domain appears to be a natural first step, however there are two main reasons for that, namely: (i) B stars emit most of their energy (70% - 100%) in the UV (e.g. Fitzpatrick and Massa 1999; Bless and Percival 1997); (ii) for Be stars, the contribution of the disk to the spectra is minimum in the UV (e.g. see Fig. 2 of Klement et al. 2015b and Fig. 1 of Briot 1978). Therefore, regarding the study of the stellar properties, the UV domain might provide one of the best observational available data to our method.

6.2.1 UV disk excess

Despite these previous results already pointed to a weak influence of the disk in the UV domain, we revisited this problem by using our grid models, exploring different scenarios. In order to do that, we define the disk excess as the mean taken in the UV domain,

$$\left\langle \frac{\Delta F}{F_\star} \right\rangle_{\rm UV} = \frac{1}{\Delta\lambda} \int_{\lambda_{\rm min}}^{\lambda_{\rm max}} \frac{|F_\lambda - F_\lambda^\star|}{F_\lambda^\star} d\lambda; \tag{6.1}$$

where $\lambda_{\rm min} = 1000$ Å, $\lambda_{\rm max} = 3000$ Å, $F_\lambda^\star$ is the specific stellar flux and F_λ the total flux.

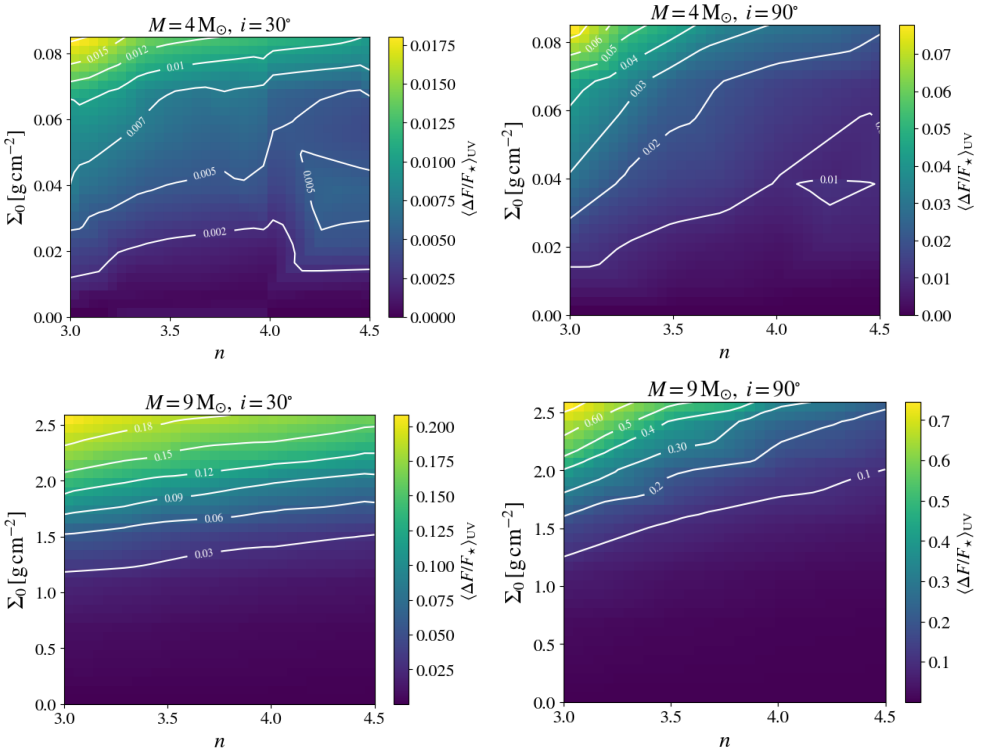

Figure 6.1: Top: UV disk excess of a typical late-type Be star ($M = 4\,M_\odot$) at different orientations. Left: $i = 30°$. Middle: $i = 70°$. Right: $i = 90°$. Bottom: UV disk excess of a typical early-type Be star ($M = 9\,M_\odot$) at different orientations. Left: $i = 30°$. Middle: $i = 70°$. Right: $i = 90°$.

Figure 6.1 shows the defined measure of UV excess for a few representative cases of Be star disks. As expected, we see that in general either larger Σ_0 or smaller n values are associated to larger UV excesses. We also observe larger excess values for the edge-on cases. In particular, the 4 $M_\odot$ model excess has as upper limit of 1% of disk contribution, while the 9 $M_\odot$ model reaches a 10% UV excess only for large densities ($\Sigma_0 \gtrsim 1.5$) at edge-on orientation.

These results demonstrate that the disk contribution can be neglected in the UV domain. This is an important realization, since it allows one to use UV observations to independently constrain the photospheric parameters, in spite of the presence of a circumstellar disk. This is the main hypothesis of the present BeAtlas application, which will be developed in the next sections.

6.2.2 *The influence of the priors*

In this section, we explore what the UV spectrum can provide alone and with a v sin i prior. For this purpose, we adopted a typical Be star, α Arae (see Sect 5.2.3).

Initially, we compute the stellar, geometrical and extinction parameters of α Arae, using as input only its IUE data. Figure 6.2a shows the corner plot obtained. The posterior probability

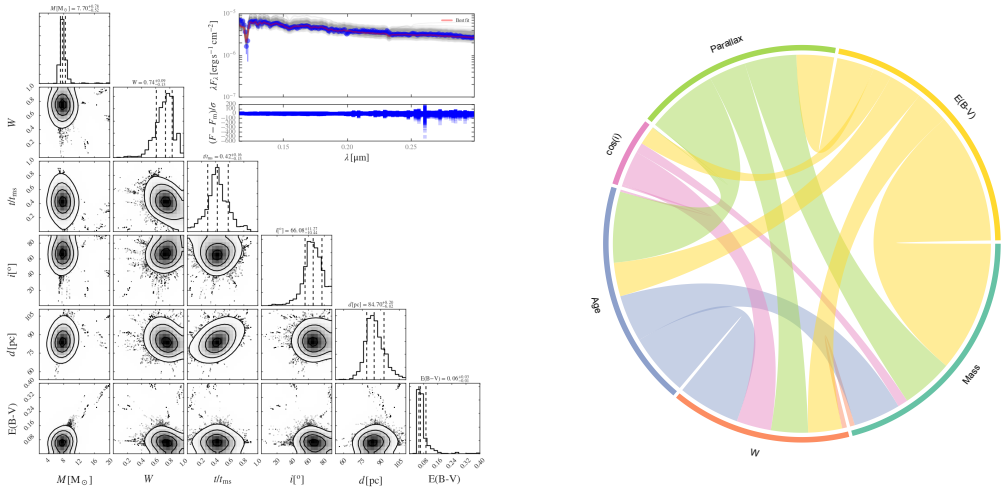

(a) (b)

Figure 6.2: (a) Posterior probability distributions computed using `IUE` data. The `SED` fit is shown inset within the main panel, the solid gray lines represent the sample of total fluxes interpolated, and the red line represents the best adjust. The dashed lines in the diagonal subplots correspond to the 16th, 50th, and 84th percentiles of the distributions. The subplots under the diagonal subplots show the probability densities correlations between several pairs of parameters. (b) Chord diagram for the corner plot on the left.

distributions indicate that all the parameters were constrained. In this figure, it is also possible to verify the correlations among the parameters. However, it involves a certain effort because the reader should look at each `2D` correlation map to understand the link between any two parameters. A way to work around this issue is the chord diagram (Fig. 6.2b). Its circular layout has been promoted as one of the best visualizing methods to describe inter-relationships between parameters (Sect. 2.4). The connections (bands) shared between the parameters indicates they share something in common, showing correlations more easily.

As a second step, we redo the procedure, but now considering the v sin i prior. The results are shown in Figure 6.3. At first sight, the posterior probability distributions appear narrower when compared with the distributions shown in Fig. 6.2. This indicates that the v sin i prior, in fact, improves the Bayesian approach. However, it becomes a difficult task to differentiate how much the adoption interfere in the correlations.

Comparing the two chord diagrams (Figures 6.2b and 6.3b), it is notable that including the v sin i prior broadens almost all bonds. Remarkably, the correlation among the inclination angle, rotation rate, age, and mass are improved. This was expected, since the v sin i involves, beyond the inclination angle (sin i), the stellar mass and radius, which are coupled with the stellar age. This comparative work led us to consider the v sin i in all studied cases.

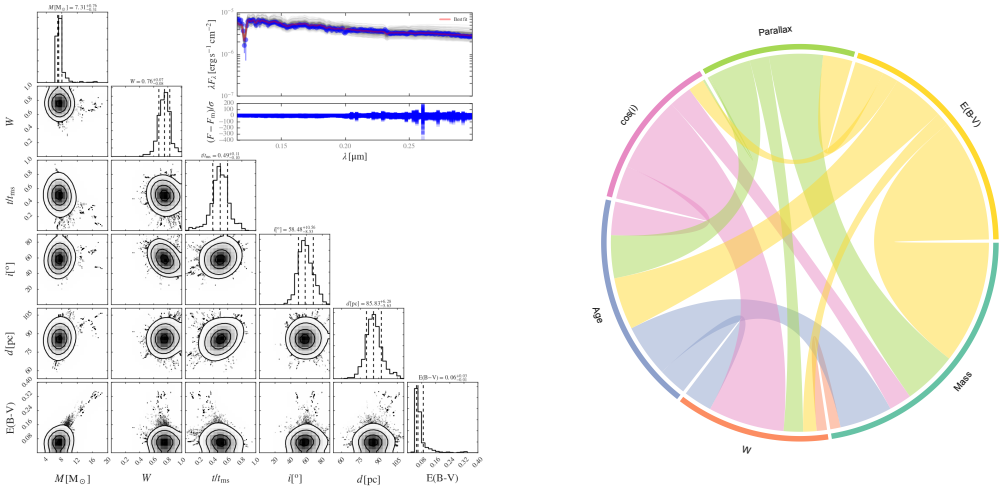

(a) (b)

Figure 6.3: (a) Posterior probability distributions computed using IUE data and the v sin i prior. The SED fit is shown inset within the main panel, the solid gray lines represent the sample of total fluxes interpolated, and the red line represents the best adjust. The dashed lines in the diagonal subplots correspond to the 16th, 50th, and 84th percentiles of the distributions. The subplots under the diagonal subplots show the probability densities correlations between several pairs of parameters. (b) Chord diagram for the corner plot on the left.

6.2.3 Results

The steps followed in this section were directed to explore the spectral limits of the *Be phenomenon*, evolutionary links among peculiar stars (Bn, Be, Ae and Oe stars); and to have a global overview of stellar properties of these stars, including rotational effects. We proceeded with the inference of the stellar parameters of the sample of stars shown in Section 5.2.1. The UV data of the selected stars were used in the procedure detailed in the Section 4.2.1. The table A.12 shows the stellar parameters inferred from this analysis. Thereafter, we compare our results with those from the literature (Frémat et al. 2005; Levenhagen and Leister 2006; Zorec et al. 2016)[1].

We compared the temperatures and log g inferred by our method with the values found in the literature in Fig. 6.4. In Figure 6.5, we show the comparison of the inferred luminosity and age compared with the literature. Both inferred values, log $T_{\rm eff}$ and log $L_\star$, agree, inside the error values, with the reference values present in the literature. Another important point is the trend for lower values found in the reference values for some stars, which might be caused by the difference between the methods. The luminosity, as well as the $t/t_{\rm ms}$, is a multiplicative factor, then it does not change the slope of the spectrum, only the flux level. The change in the

[1] Levenhagen and Leister (2006) did not consider the rotational effects on the SED.

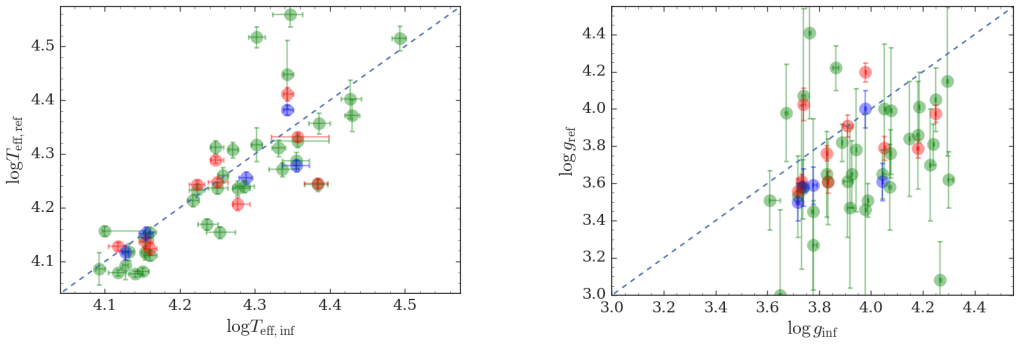

(a) *(b)*

Figure 6.4: (a) Plot of the log $T_{\rm eff}$ calculated and from the references for each star. (b) Plot of the log (g) calculated and from the references for each star. Blue: data from Levenhagen and Leister (2006). Red: data from Frémat et al. (2005). Green: data from Zorec et al. (2016).

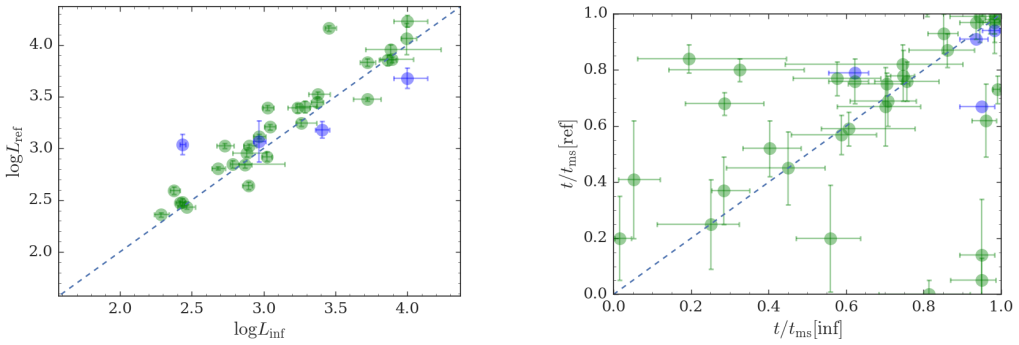

(a) *(b)*

Figure 6.5: (a) Plot of the log $L_\star$ calculated and from the references for each star. (b) Plot of the $t/t_{\rm ms}$. Blue: data from Levenhagen and Leister (2006). Red: data from Frémat et al. (2005). Green: data from Zorec et al. (2016). Pink: data from Meilland et al. (2012). Orange: data from Gies et al. (2007). Purple: data from Touhami et al. (2014). Yellow: data from Tycner et al. (2006).

luminosity is generated by the increase of the rotation as the star gets older, inflating its equatorial radius and, respectively, decreasing its polar radius by a few percents (2% at critical rotation for typical B; Ekström et al. 2008). Regarding the $\log g$, the inferred values are compared with the literature (Fig. 6.4b). Although most reference values do not agree with our inferences, our inferred values are inside the typical range for B-type stars ($3.7 \lesssim \log g \lesssim 4.2$) (e.g. Silaj et al. 2014). The high precision inference of this measure comes mainly from the UV domain. It means that having the UV slope, we can determine the mass and the temperature with precision.

The inclination angle determination has a relative importance. It is justified by the degeneracy between the inclination and the luminosity. In principle, a star with $i \sim 0^{\rm o}$ and late spectral type

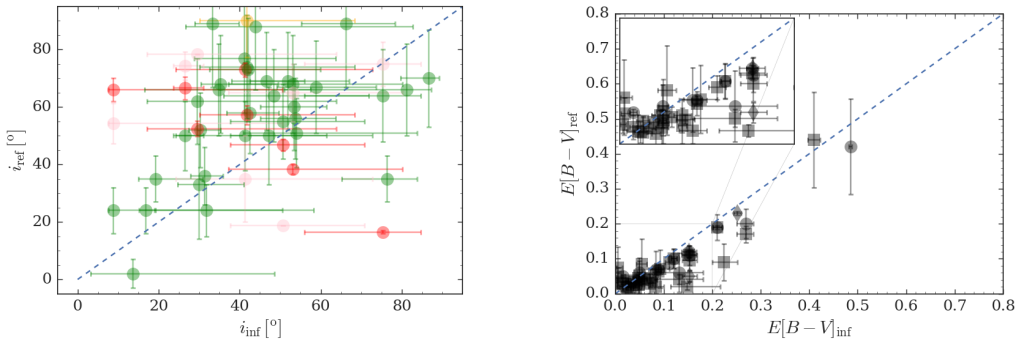

(a) *(b)*

Figure 6.6: (a) Plot of the i calculated and from the references for each star. (b) Plot of the $E(B-V)$ calculated and from the references for each star (♦: Hunter et al. (2006), •: Dougherty et al. (1994) calculated using the 2 200 bump. ■: Zorec et al. (2016)).

could appear like a star with $i \sim 90^{\rm o}$ and an earlier spectral type. Therefore, the inference of the i might influence substantially the determination of the temperature, which might present a variation of over 50% between the polar and equatorial temperatures (Vinicius et al., 2007). This could explain the trend observed in Fig. 6.4a. In Fig. 6.6a, we present a comparison between the inclination angles inferred with the values found in the literature (Frémat et al., 2005). Our error bars are larger, but the results agree. The trend of the inferred inclinations to high values and the larger errors were caused by the $v \sin i$ prior adopted (see Sect. 4.2.2).

Some inferred $E(B-V)$ are shown in Figure 6.6a together with their respective reference values (e.g. di Benedetto 1998; Dougherty et al. 1994; Hunter et al. 2006; Zorec et al. 2016). The reference values are lower than the inferred, but they agree when we consider the error bars.

Examining the relationship of the rotation rate with the mass, we verified no clear dependence between them as shown in Figure 6.7b. This Figure also shows that all selected Be have $W \gtrsim 0.4$. Furthermore, the selected stars cover all the MS (Fig. 6.8) and present a lower limit to the rotation rate. The lower limit found to Be stars is ~ 0.4 and for Bn is ~ 0.1. Our results corroborate well-known results, e.g. the presence of few Be stars with masses $M \leq 7\,{\rm M}_{\odot}$, $\sim 14\%$ of the studied Be stars, in the first half of the MS phase (Frémat et al., 2005). Actually, most of our Be stars (~ 76 %) belong to the second half of the MS phase. The most likely mechanism for that is the *spin up during the* MS evolution, associated with the second half of the MS lifetime of the B stars (McSwain and Gies, 2005). This mechanism is supported by higher initial rotation rates, which enable the Be stars to reach nearly critical rotation rates as they evolve (Grudzinska et al., 2015). Our results also indicate that high-mass B stars experience angular momentum losses during the

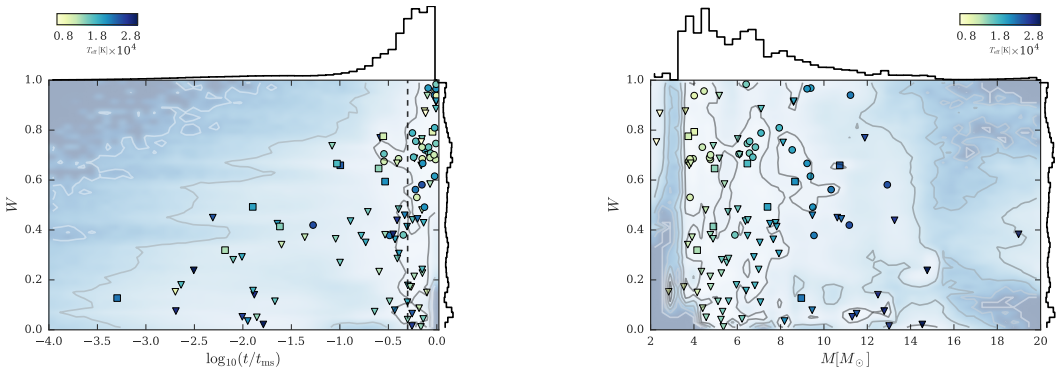

(a) *(b)*

Figure 6.7: (a) Rotation rate, W, versus MS lifetime, $t/t_{\rm ms}$. (b) Mass versus rotation rate, W.

MS phase and the fact that low-mass B stars are born with a larger proportion of rapid rotators than high-mass B stars (Huang et al., 2010). Moreover, our results point out to a wide range ($0.0 \lesssim t/t_{\rm ms} \lesssim 0.95$) occupied by Bn stars. This result disagrees with earlier studies that discuss the occurrence of Bn stars in the first MS evolutionary phases (Zorec et al., 2007).

In a recent study, Granada et al., 2013 demonstrate a fact confirmed by current models, that the critical velocity is reached at TAMS (see Fig. 1 of their work). They showed that lower-mass models frequently reach the critical rotation, when compared with their massive counterparts, expending up to $\sim 30\%\, t/t_{\rm MS}$ at this stage. In contrast, high-mass stars have stellar winds dense enough to remove superficial angular momentum, leading to $V_{\rm orb} < V_{\rm crit}$ (Granada et al., 2013). They also shows that after a star reach its critical limit, it preserves the rotation until reach the TAMS. These results are also reproduced by our method.

We know that the stellar shape depends on several parameters (critical velocity, latitudinal differential rotation, etc., see e.g. Zorec et al., 2011). Even so, we can constrain the oblateness, knowing how the oblateness varies through the MS. Figure 6.7a shows the correlation between oblateness and the age in terms of fraction of the MS lifetime. The results corroborate the conclusion of Martayan et al. (2007), this is, that the *Be phenomenon* appears earlier ($t/t_{\rm ms} \sim 0.05$) in the MS for early B-types than for their late counterparts ($t/t_{\rm ms} \sim 0.30$). These results show that there must be some evolutionary mechanism that activates the *Be phenomenon* during the MS lifetime which also agrees with conclusions reported by previous works (e.g. Levenhagen and Leister, 2006; McSwain and Gies, 2005; Zorec et al., 2005; Zorec et al., 2007). Therefore, our results also show that there must be some evolutionary mechanism that activates the *Be phenomenon* during the MS lifetime.

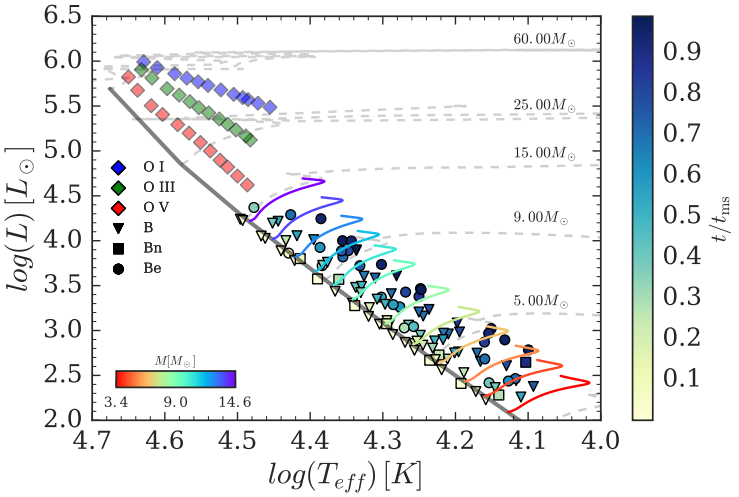

Figure 6.8: HR Diagram constructed using the data shown in Table A.12. The gray curve indicates the zero age main sequence ZAMS. Each evolutionary track extends from ZAMS through to terminal age TAMS, defined by the cessation of core hydrogen burning. The vertical colorbar at the right represent the MS lifetime fraction. The colorbar at left lower corner represents the stellar mass. The different symbols are representative of the object type and they are denoted in the figure. The O-type stars are put just for comparison (data from Martins et al. 2005).

The results shown in this section show that our method, even dealing with a large set of parameters and just one observable (UV spectrum), can reproduce fundamental stellar parameters and the $E(B-V)$ from an aleatory sample, returning consistent errors. This was already expected to slow-rotators, since there is a clear unicity among them and their correspondent UV spectra, which is the cause of, for instance, the MS be a line instead of a band (Fig. 6.8). On the other hand, initially it was not obvious that the UV alone would be enough non-degenerated to provide good results. Hence, we showed that the $v \sin i$ prior improves the inference, i.e. we degenerate the UV spectra in an away it becomes useful. We could reproduce important effects such as the *spin up during the* MS and the evidence that cooler Be stars are more likely to be critical rotators (e.g. Cranmer 2005). These results strengths the hypothesis that the disk formation process may be different for both: low and high-mass cases. The low-mass case ($M < 4\,M_\odot$) needs a higher rotation rate $V_{eq}\,/\,V_{crit} > 0.96$ to become a Be star, while that for high-mass cases ($M > 8.6\,M_\odot$) this lower limit decreases to $V_{eq}\,/\,V_{crit} > 0.64$ (Huang et al., 2010).

6.3 Application: The case of β CMi

6.3.1 Initial estimates from the SED

We applied the method described in Sect. 3.3 for all available photometric data of β CMi. The results are summarized in Figure 6.9a. We can notice that all parameters are well constrained, however, this direct procedure prevents us to understand the real contribution provided by each band. Hence, to explore properly the correlation among the parameters and each photometric data and, consequently, enrich the discussion, we computed different corner plots for isolated bands or groups of bands. This procedure allows us to explore the pseudo-photosphere effect (Carciofi, 2011).

Box plots were used to visualize the inference (Sect. 2.4). Figure 6.10 shows the box plot obtained from each analyzed band. For instance, the upper plot in the first column represents the inference of the stellar mass for each spectral domain analyzed. In general, we verify that shorter wavelengths (UV and visible) sample better some stellar parameters: M, W, and $t/t_{\rm ms}$. Adding the UV, Visible and the NIR domains, it is not seen any considerable change in the inferred parameters. By another side, when we include the MIR band it is seen a global improvement, especially in the disk parameters: $\log n_0$, $R_{\rm D}$ and n. The inference precision and accuracy of the stellar parameters becomes worst as we remove shorter wavelengths than the NIR. Overall, this procedure showed that the observed SED of a Be star might provide information about the star (photospheric emission) and from the absorption/emission by the disk, being that each photometry band should provide complementary information about the system.

6.3.2 The optical polarization

The linear polarization is strongly dependent on the inclination angle, the disk size and the inclination angle (Teses-USP[2]). Naturally, we might expect to infer these parameters from the linear polarization data. However, the linear polarization level and shape also depends on the subspectral type, for instance, by fixing the inclination angle and disk size, it is seen an increasing of the polarization level towards early spectral types. Considering this scenario, we applied the method described in Chapter 4 for the linear polarimetric data of β CMi (Tab. A.8). The results are shown in Figure 6.9b. As expected, the polarimetric data could not constrain the stellar parameters. It impacts the inference of the disk size and the index n (see Eq. 3.6).

[2] http://www.teses.usp.br/teses/disponiveis/14/14131/tde-30082013-140129/pt-br.php.

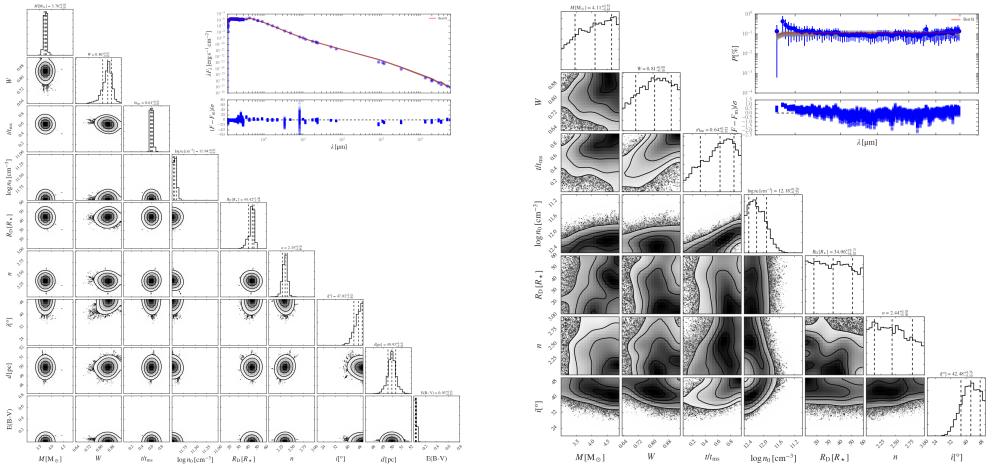

(a) (b)

Figure 6.9: (a) Posterior probability distributions computed using the complete range of photometric data. The SED fit is shown inset within the main panel, the solid gray lines represent the sample of total fluxes interpolated, and the red line represents the best adjust. (b) Same as the right plot, but for the linear polarization.

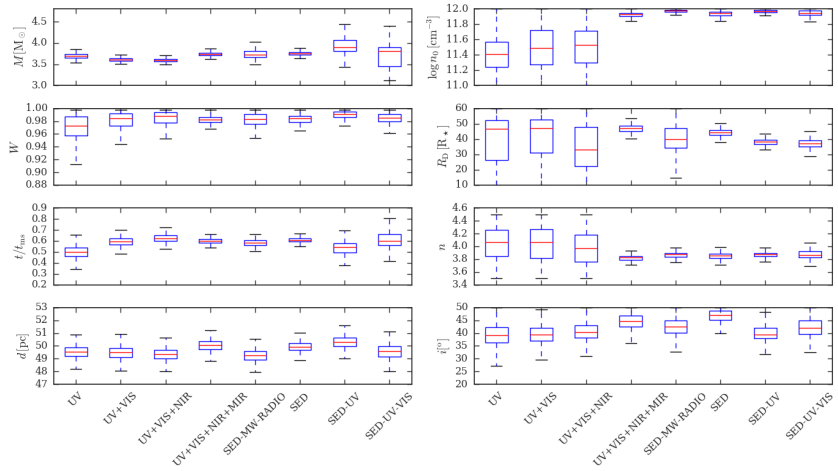

Figure 6.10: Box plot of the PDFs of different spectral domains for all parameters.

Interestingly, we can use additional priors based on the previous results obtained from the entire SED. For our case, we can adopt a Gaussian kernel density estimator (KDE) for each stellar PDF (M, W and $t/t_{\rm ms}$) got previously. This additional prior function becomes,

$$\log p_\star(\Theta, \alpha) = -0.5 \left[\hat{f}_{\rm M}(M) + \hat{f}_{\rm W}(W) + \hat{f}_{\rm t/t_{ms}}({\rm t/t_{ms}})\right]^2, \tag{6.2}$$

where $\hat{f}_{\rm M}$, $\hat{f}_{\rm W}$ and $\hat{f}_{\rm t/t_{ms}}$ are the inverse of the KDE distributions.

The resulting corner plot is shown in Figure 6.11a. Note that by considering the stellar prior a reasonable inference was achieved for all parameters.

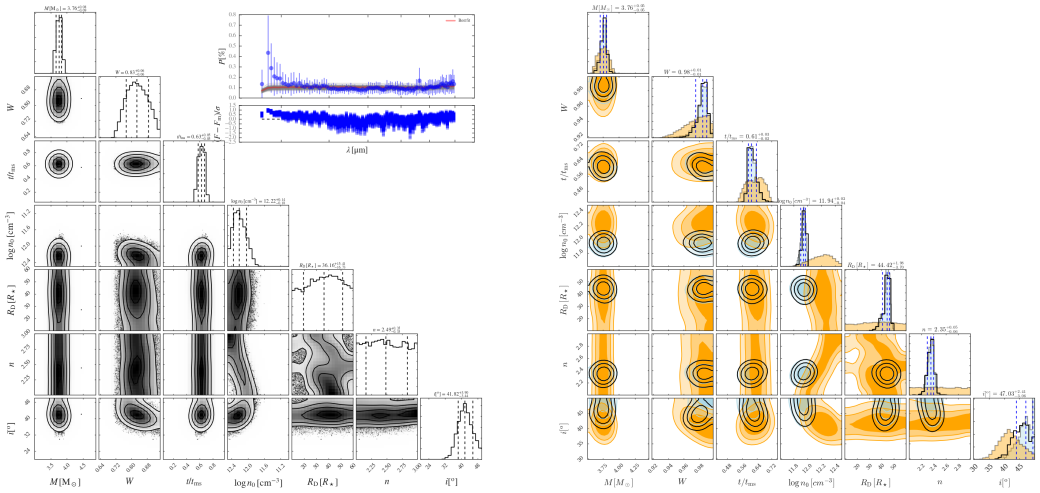

(a) (b)

Figure 6.11: (a) Posterior probability distributions computed using the polarimetric data and the KDE priors. (b) The contours in the diagram were obtained by combining the posterior probabilities of the fitted SEDs and polarization and normalizing its integral over the plane to unity.

Table 6.1 - Best fit parameters of β CMi.

Parameter	Value	Parameter	Value
M [$M_\odot$]	$3.76^{+0.05}_{-0.05}$	$\log\, n_0$	$11.94^{+0.03}_{-0.04}$
$\log g$	$4.0795^{0.00005}_{-0.00010}$	R_D [$R_\star$]	$44.42^{+1.98}_{-3.70}$
R_{pole} [$R_\odot$]	$2.92^{+0.05}_{-0.03}$	n	$2.35^{+0.05}_{-0.06}$
L [$L_\odot$]	$233.01^{+32.40}_{-20.69}$	i [°]	$47.03^{+2.41}_{-3.06}$
T_{eff} [K]	$18215.61^{+496.07}_{-482.92}$	d [pc]	$49.93^{+0.42}_{-0.41}$
W	$0.98^{+0.01}_{-0.01}$	β_{GD}	$0.20^{+0.05}_{-0.05}$
t/t_{ms}	$0.61^{+0.03}_{-0.02}$	$E(B-V)$ [mag]	$0.03^{+0.01}_{-0.01}$

6.3.3 *Best-fit Parameters*

The corner diagram shown in Fig. 6.11b represents the combination of each PDF shown in Fig. 6.9a and 6.11a. The results obtained from this combination were adopted as the best-fit parameters of β CMi (Tab. 6.1).

6.4 *Application: the case of α Arae*

In this section, we show the results for α Arae. The procedure is the same described in Sect. 6.3. We analyzed the SED and polarimetric data (see Chap. 5).

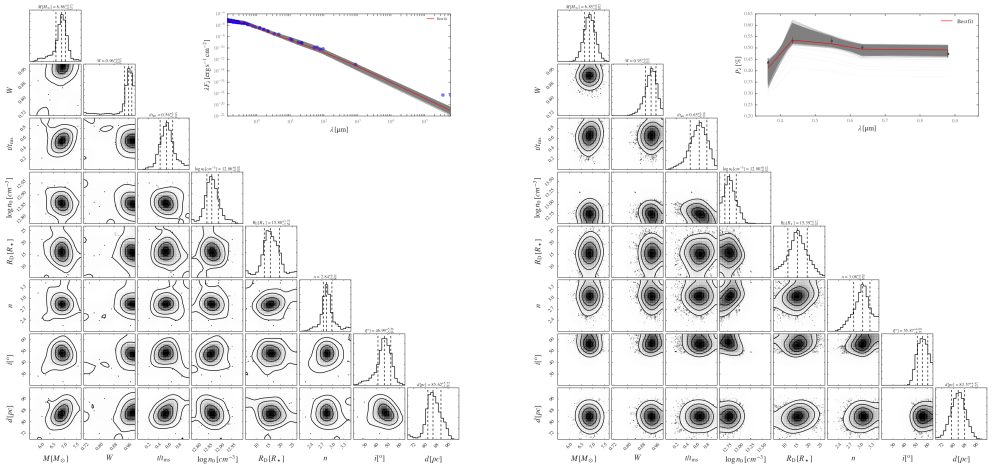

(a) (b)

Figure 6.12: (a) Posterior probability distributions computed using the complete range of photometric data (see Table. A.5). The SED fit is shown inset within the main panel, the solid gray lines represent the sample of total fluxes interpolated, and the red line represents the best adjust. The dashed lines in the diagonal subplots correspond to the 16th, 50th, and 84th percentiles of the distributions. The subplots under the diagonal subplots show the probability densities correlations between several pairs of parameters. (b) Same as the right plot, but for the linear polarization.

6.4.1 *Initial estimates from the SED and from the Polarimetric data*

Figure 6.12a shows the results obtained by considering all the photometric data. We see that all the parameters are well constrained. In addition, we show the results obtained from the polarimetric data (Tab. A.6) combined with the KDE stellar prior in Figure 6.12b.

The box plot for all parameters and for each band analyzed of α Arae is illustrated in Fig. 6.13. In general, we verify that shorter wavelengths (UV and visible) sample better the parameters: M, W, $t/t_{\rm ms}$, log n_0, n and d. Removing the UV from the complete SED, we lose precision in the inference of the M, on the other hand, the precision in the W, $t/t_{\rm ms}$ and $R_{\rm D}$ are improved. Now, removing the UV and the visible of the SED, it is seen a loss of precision in the inference of all parameters. The precision becomes worst as we continue to remove shorter wavelengths until remain just the bands FIR, radio and centimeter. These results show that the absence of information about the central star propagates to the other parameters, whose cause might be the broad PDFs seen for the M, W, $t/t_{\rm ms}$ and log n_0. These parameters are strongly connected with the stellar radius, then without a good precision in such parameters, naturally we lose precision in the inference of all other parameters.

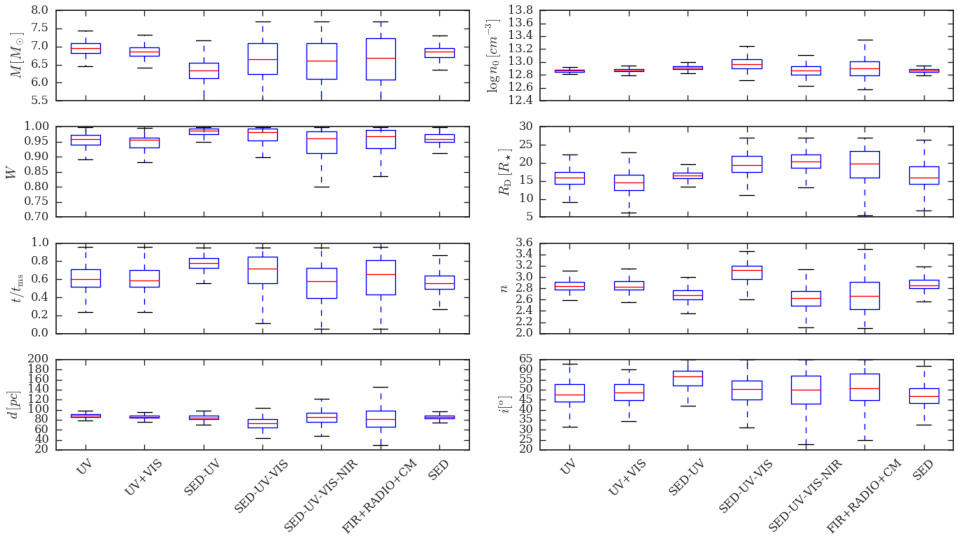

Figure 6.13: Boxplot of the PDFs of different spectral domains for all parameters.

6.4.2 *Best-fit Parameters*

Figure 6.14 has the combination of the previous results with the results presented in Figure 6.12a. We adopted these results as the best-fit parameters of α Arae (Tab. 6.2).

To compare our results with previous studies, we discarded the results of Levenhagen and Leister (2006) (see Tab. A.2), due to the large discrepancy of this study with other studies. Considering 1 σ range of our results, it is seen a compatibility among our inferences and previous results. For the temperature, our results are compatible with the results published by Dachs et al. (1988, 1990), Chauville et al. (2001), Frémat et al. (2005), Meilland and Stee (2006), Meilland et al. (2007), Meilland et al. (2009), Hamed and Sigut (2013). For the inclination angle, our result agrees with Chesneau et al. (2005) and Frémat et al. (2005). The inferred luminosity is in agreement with Chesneau et al. (2005). Increasing 2 and 3 times the σ range, we have an agreement with the literature for the previous results obtained for the temperature and the inclination angle. In the case of the stellar mass, our result just agrees with the values published by Zorec et al. (2005) and Meilland et al. (2009). Our inferred stellar radius also agrees with the result inferred by Zorec et al. (2005). The MS lifetime obtained for α Arae ($t/t_{\rm MS} = 0.55^{+0.15}_{-0.10}$) is compatible with Zorec et al., 2005 ($t/t_{\rm MS} = 0.43$) and Levenhagen and Leister, 2006 ($t/t_{\rm MS} = 0.74$).

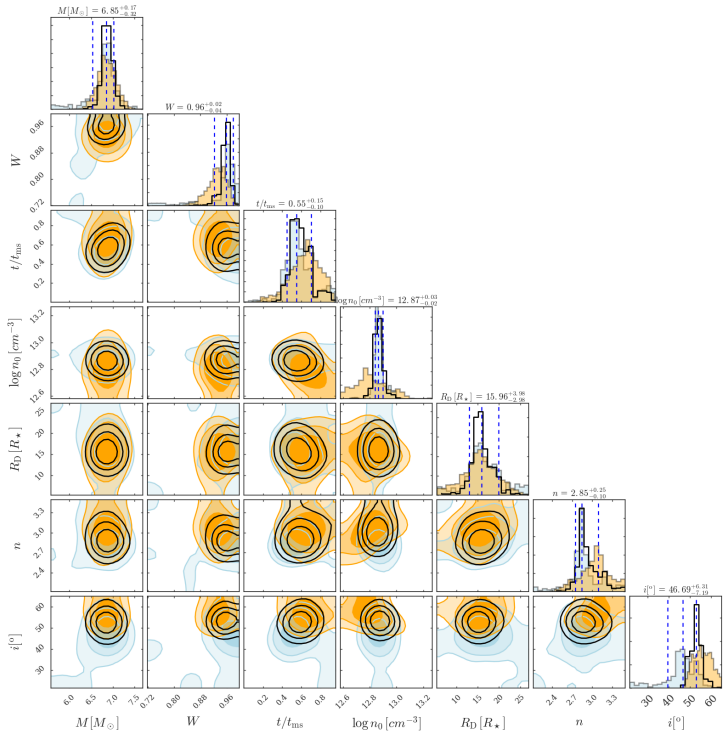

Figure 6.14: The contours in the diagram were obtained by combining the posterior probabilities of the fitted SEDs and polarization and normalizing its integral over the plane to unity.

Table 6.2 - Best fit parameters of α Arae.

Parameter	Value	Parameter	Value
M [$M_\odot$]	$6.85^{+0.17}_{-0.32}$	$\log\, n_0$	$12.87^{+0.03}_{-0.02}$
$\log g$	$4.1115^{+0.0003}_{-0.0008}$	R_D [$R_\star$]	$15.96^{+3.98}_{-2.98}$
R_{pole} [$R_\odot$]	$3.81^{+0.09}_{-0.09}$	n	$2.85^{+0.25}_{-0.10}$
L [$L_\odot$]	$1940.54^{+323.17}_{-277.03}$	i [°]	$46.69^{+6.31}_{-7.19}$
T_{eff} [K]	$18215.61^{+496.07}_{-482.92}$	d [pc]	$86.12^{+5.06}_{-3.97}$
W	$0.96^{+0.02}_{-0.04}$	β_{GD}	$0.177^{+0.010}_{-0.012}$
t/t_{ms}	$0.55^{+0.15}_{-0.10}$	$E(B-V)$ [mag]	$0.03^{+0.01}_{-0.01}$

Chapter 7

Analysis

7.1 Chapter summary

We present in this Chapter the analysis of the results obtained from our sample of stars (Sect. 7.2). In Section 7.3 the results achieved for the Be stars β CMi are analyzed. Finally, we discuss the results of α Arae in Section 7.4).

7.2 Sample of Stars

We saw in Chapter 6 that the disk excess in the UV domain can be ignored in the analysis for both early and late spectral types. For instance, Fig. 6.1 (first line) shows the disk excess for a low-mass case ($3\,M_\odot$). In that case, the disk excess in the UV domain increases with the inclination angle substantially for $n \gtrsim 3.5$, reaching the maximum excess of ~ 0.0175, in pole-on orientation, and ~ 0.070 for edge-on cases. In Figure 6.1 (second line) we look at a typical early-type star ($9\,M_\odot$). An interesting aspect shown by this class is that the disk excess is not so dependent (being almost constant at $i = 70^o$) on the n, except for the edge-on case. Actually, in the edge-on case, the disk excess can reach up to 0.70 for disks with a superficial base density of $\sim 2.5\,g\,cm^{-3}$. This represents an extreme case where we are seeing at a star immerse in a thick disk. By other side, stars seeing at pole-on orientation can have disk excess ranging from 0 to 0.24, corresponding to base densities of ~ 1.3 to $\sim 2.5\,g\,cm^{-3}$.

From these results, it was possible to verify that a disk can create a disk excess very dependent on the superficial base density, the index n and of the inclination angle, i. In a nutshell, the disk excess increases towards early-spectral types and edge-on orientations, showing a complex dependence on n. For late-type cases, the maximum disk excess is just $\sim 2\%$ in the range $0^o \leq i \leq 70^o$, reaching $\sim 7\%$ for thick disks ($\Sigma_0 \simeq 0.08\,g\,cm^{-2}$) edge-on orientation. For early-

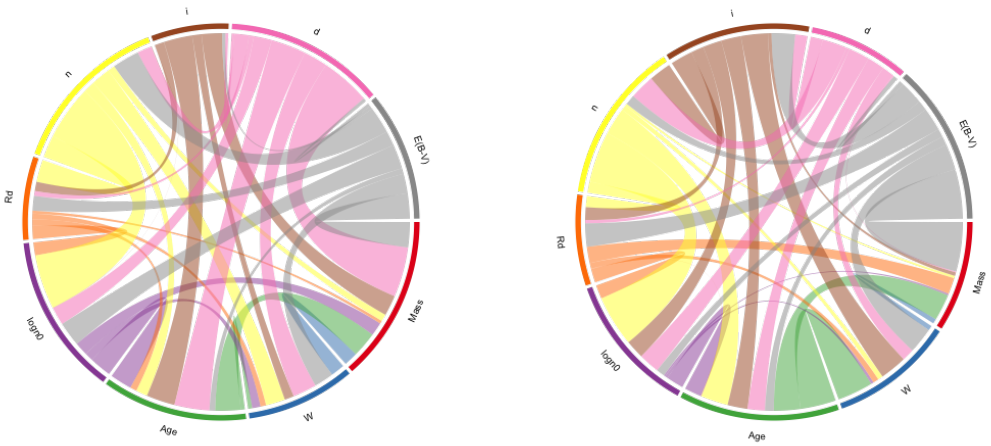

(a) *(b)*

Figure 7.1: (a) Chord diagram of α Arae and (b) β CMi.

type cases, the maximum disk excess is between $\sim 10-24\%$ in the range $0^{o} \leq i \leq 70^{o}$, reaching $\sim 70\%$ for thick disks ($\Sigma_0 \simeq 2.5\,\mathrm{g\,cm^{-2}}$) at edge-on orientation. Except for the thick disks at edge-on orientation, we considered our photospheric models as a good approach to study the physical parameters of our sample of stars.

7.2.1 *Interpretation of the correlations*

The results shown in Sect. 6 presents some important correlations. As an example of the correlations shown by all free studied parameters (disk and stellar) see Figure 7.1a. This figure shows the global correlations among all studied parameters. It helps us conceive the Table 7.1 where we illustrate the degree of dependence for each pair of parameters for the α Arae's case. Note that the chord diagrams obtained for α Arae and β CMi are quite similar (Fig. 7.1) because of that we proceed our analysis considering just the correlations obtained from α Arae's results.

To simplify this discussion, we selected some interesting correlations and grouped them into categories in the next sections.

7.2.1.1 *Stellar Mass*

- The first interesting feature is the correlation between M and W where (1) low-mass models (i.e. lower stellar radii) with low-rotation rates and (2) high-mass models (i.e. larger stellar radii) with high-rotation rates are correlated. For instance, if case (1) had a weaker gravity darkening than the case (2), they would have equivalent fluxes;

Table 7.1 - Color map of the parameter correlations of α Arae. Red: strong correlation. Orange: medium correlation. Green: weak correlation. Purple: no correlation.

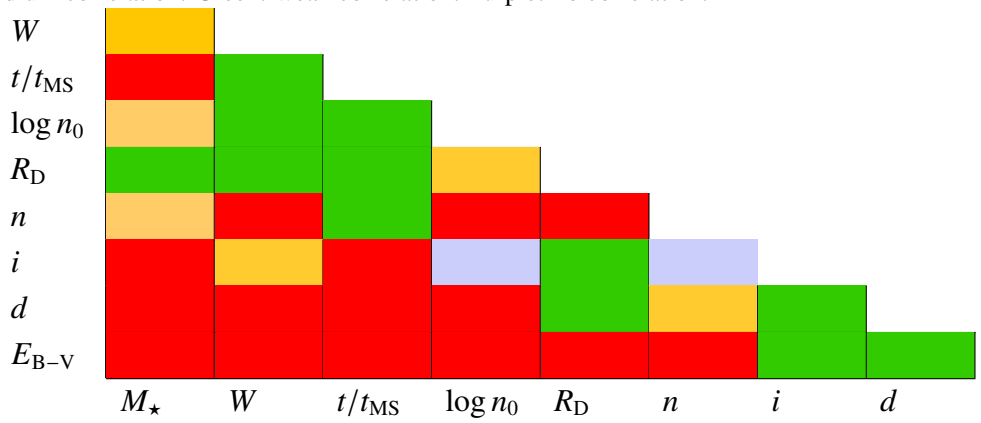

- M and t/t_{MS}: the models assume that the star increases it rotation rate as they get older. In other words, an older low-mass star (small stellar radii and high luminosity) would have equivalent fluxes than a young massive star (larger radius and low luminosity);

- M and i are also correlated. Low-mass stars seen at low-inclination angles (towards pole-on orientation) produces fluxes equivalent to high-mass stars seen at high-inclination angles (towards edge-on orientation). This is explained because a less massive star seen pole-on will present a luminosity larger than when it is seen from the equatorial region. Equivalently, a high-mass star seen at its equatorial region will have a lower luminosity. Then, different configurations would produce equivalent fluxes;

- M and d: a low-mass nearby star (i.e. high observed flux) is equivalent to a high-mass distant star (i.e. low observed flux);

- The E_{B-V} strongly affects the UV domain, this perturbs the inference of M.

7.2.1.2 Rotation Rate

- W and t/t_{ms}: (1) An older low-rotating star would be equivalent to (2) an younger high-rotating star. As the star gets older, it increases its luminosity, in that case, the gravity darkening effect decrease with the rotation, increasing the photospheric flux, which might generate an equivalent flux observed in the case (2);

- W and n: we saw in Chapter 1 that different values of n would indicate distinct mass-loss scenarios. This would explain the correlation between these parameters;

- W and d: A distant high-rotating star (larger stellar radii) could produce an equivalent observed flux than a nearby low-rotating star (low stellar radii);

- W and $E_{\mathrm{B-V}}$ are anti-correlated: a high-rotating star in an environment of low interstellar extinction produces equivalent observed flux than a low-rotating star suffering high interstellar extinction. This might be related to the gravity darkening effect.

7.2.1.3 Main-sequence lifetime

- t/t_{ms} and $\log n_0$ are anti-correlated. (1) younger stars (lower luminosities) with thick disks are equivalent to (2) older stars (higher luminosities) with thin disks. Here, we are not considering the absorption by the disk, but the excess of flux due to the disk (emitting area);

- t/t_{ms} and i are correlated: edge-on younger stars (lower stellar radii + lower GD) could be confused with a pole-on older star (larger stellar radii + high GD);

- t/t_{ms} and d are correlated. (1) nearby younger stars (lower luminosities) are equivalent to older stars (higher luminosities) seeing at larger distances;

- t/t_{ms} and $E_{\mathrm{B-V}}$ are correlated. A young star (lower luminosity + low extinction) is like an older star (high luminosity + high extinction).

7.2.1.4 Disk base density

- $\log n_0$ and n are correlated. Disks with smaller n and small base density will have equivalent density profiles to disks with large n's and high base density, both would have equivalent disks;

- $\log n_0$ and i are anti-correlated. Thinking in terms of the density of scatters, we can expect that thicker disks (larger $\log n_0$ values) seen at high-inclination angles (towards the edge-on orientation) would emit the same that thin disks seen at inclinations directed towards the pole-on region. A denser disk seeing at pole-on (absorption decreases) is similar to a thin disk seeing at edge-on angles.

7.2.1.5 Disk size

- R_D and log n_0 are correlated. The fluxes of large thin disks should be reproduced by small thick disks because of the equivalent emitting area of them;
- R_D and n. Small disks with a small n would emit the same than larger disks with a large n;
- R_D and i. There is an anti-correlation between these parameters. We could reproduce the observed fluxes by either, a model of a large disk seeing at high-inclination angles (i.e. small emitting area) or by models with a lower disk seeing at low-inclination angles (i.e. larger emitting area);

7.2.1.6 Inclination Angle

- i and d are anti-correlated. Distant disks seeing towards the pole-on region are equivalent to nearby disks seeing towards the edge-on region.

7.3 β CMi

7.3.1 Discussion

The best-fit parameters of β CMi (Tab. 6.1) agree with previous recent results (see Tab. 5.1), suggesting it is a B8e. We see that, contrary to previous studies, our results suggest a range around each inferred result. Overall, there is a slight difference in part of the parameters (e.g. i, n, and log n_0) and a good agreement among the other. Our results also agree with some previous results of Zorec et al. 2005 (log $g = 3.88$, $t/t_{MS} = 0.58$, $M = 3.6\,M_\odot$).

7.3.2 Binarity

The results from Table 6.1 allowed us to estimate the period and the semi-major axis of the binary system. For this purpose, we assumed the companion's mass of 0.42 $M_\odot$), giving a period of $P = 105.96 \pm 34.18$ days. Here, we applied the correction proposed by Panoglou et al. (2016). This value agree with the previous estimate of $P \sim 170.4$ days (Dulaney et al., 2017). These results corroborate the hypothesis that β CMi has indeed a companion (Fig.7.2a). It supports the hypothesis that β CMi may be product of a binary evolution process (Dulaney et al., 2017), likely resulting in a hot subdwarf or white dwarf companion.

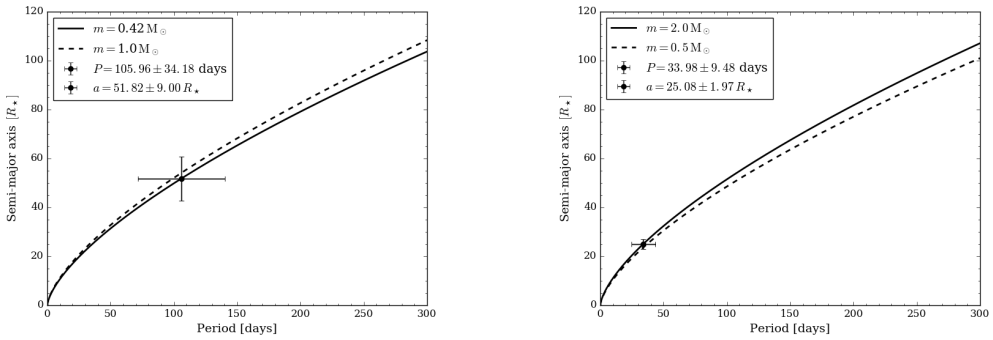

(a) *(b)*

Figure 7.2: (a) Estimation of the period of β CMi's companion. (b) Estimation of the period of α Arae's companion.

7.4 α Arae

7.4.1 Discussion

Regarding the α Arae's disk, we found $n \sim 2.85$ and $\log n_0 \simeq 12.87$, which according to Vieira et al. (2017) are inside the typical values for Be stars. Our result also agrees to the affirmation that disks around early-type stars are denser (Chap. 1). By another side, whether we consider the errors in the n parameters, it put α Arae in two possible cases: a steady-state disk (i.e. $3.0 < n < 3.5$) or a dissipating disk ($n < 3.0$). Beyond that, as discussed before (Sect. 1.2.2), a binary might cause an accumulation of material in the inner region limited by the size of the truncation radius, resulting in a lower density exponent than the steady-state value.

The truncation radius and the mass shown in Table 6.2, enabled us to estimate roughly the period and the semi-major axis of the binary system. For this purpose, we assume two masses for the companion (0.5 and 2.0 $M_\odot$), which gives a period of $P = 33.98 \pm 9.48$ days. Here, we applied the correction proposed by Panoglou et al. (2016). These values do not agree with previous values, this is $R_D = 32\,R_\star$ and $P \sim 74$ days (Chap. 1). However, our estimation could encompass the period obtained by Mennickent and Vogt (1991), i.e. 47.5 days. These results corroborate the hypothesis that α Arae has indeed a companion, but a more detailed observational temporal series should prove it.

The full SED of α Arae is displayed in Fig. 7.3, where are shown the best models to the star and to the system, i.e. considering the disk. We can see clearly that the shorter wavelength range is dominated by the stellar flux (zooming region) and the larger wavelengths are dominated by the disk emission. The truncation caused by the unseen companion can also be observed around

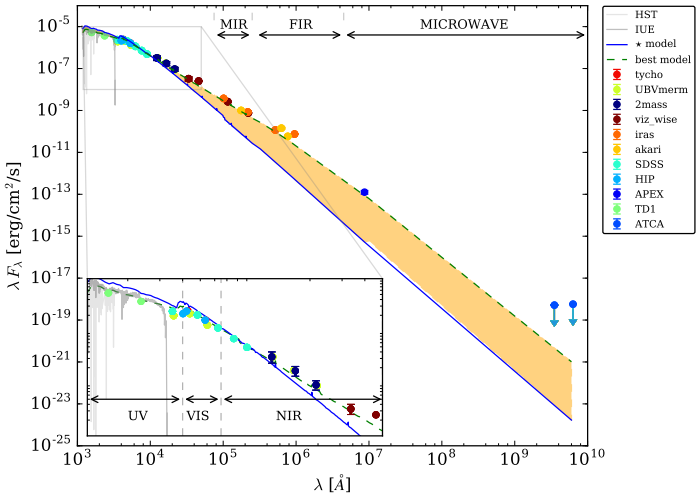

Figure 7.3: SED of α Arae showing the best photospheric model (blue line) and the system (star + disk) best model (green dashed line). The red region show the IR excess. The spectral regions are highlighted in order to facilitate the identification of the different spectral regions.

the wavelength 10^6 Å. The position of the turndown is not well defined, it includes a range of wavelength where the SED changes. Even so, we can estimate the likely range radius by using equation D1 from Vieira et al. (2017). This equation put the effective radius between $\sim$ 12.43 and $\sim$ 28.38 $R_\star$ for the wavelengths of 400 and 2000 μm (where the turndown appears) respectively. Therefore, our result for the truncation radius is consistent with the current theory.

7.4.1.1 *Temporal evolution of the observables*

Both polarization and spectroscopy corroborate the assumption that α Arae's disk has been relatively stable in the past few years ($\sim$ 20 years). For instance, α Arae was reported to be stable on long time-scales (e.g. Dachs et al. 1981) and still seems to represent an active Be star in a well-balanced equilibrium state (Hanuschik et al., 1988). Its stability was reported by the study of V/R variability and global oscillations by (Hanuschik et al., 1995), showing almost no variability in the line profiles over 7 years (see Fig. 12 in Hanuschik et al. 1995) and an Equivalent Width (EW) of about 20-30 Å over the same period. Earlier, (Mennickent and Vogt, 1991) detected rapid V/R variations from high time-resolution ($\sim$ 7 days) between 1984 and 1989, having detected a quasi-period of 0.13 yr ($\sim$ 47.5 days) using data from (Hanuschik et al., 1988). In another study, (Mennickent, 1991) showed that α Arae had a relatively constant and moderate Balmer emission, through double-peaked Hβ line profiles (see their Fig. 12) with V/R variations of small amplitude, only slight changes in strength of emission and mean EW relatively constant

between 1977-87, except for a decrease in 1982. In summary, these previous studies concluded that α Arae might have had variations in timescales of months, however without showing a clear, organized long-term pattern.

To confirm the recent long-term stability of the α Arae's disk, we looked for periods in several polarimetric and photometric observables. These time series data allowed us to determine periodic components of the data that might be related to the physical properties of the system.

We performed the calculus of periods by using the photometric, polarization and spectroscopic data. Initially, we applied the Lomb-Scargle (LS) method VanderPlas (2017), which assumes a sinusoidal variability pattern, but without success. After, we applied two methods independent of the signal shape, the PMD[1] (e.g. Stellingwerf 1978; Rivinius et al. 1998) and the Supersmoother method (e.g. VanderPlas and Ivezić 2015; Reimann 1994). Neither the Supersmoother algorithm nor the PDM method requires *a priori* knowledge of the light curve shape.

Additional light curves were obtained from the tools AAVSO[2], VSX[3] and from the Hipparcos mission (Hipparcos VizieR Table[4]).

In Fig. 7.4, we show temporal evolution of the apparent magnitudes of four filters taken from various sources, covering $\sim$ 1 000 days, $\sim$ 40 days, $\sim$ 1 800 days, and $\sim$ 40 days respectively. The LS analysis applied to these data is shown in Fig. 7.4. The results point out to periods of 12.2, 12.98 and 12.75 days for the u, y and v apparent magnitudes, respectively. Because of the short time coverage of the data, relative to these filters, our estimates could point out to a period shorter than the real one. In most cases, the period with the highest Lomb-Scargle power was chosen as the best system period.

Given the short time coverage and the low time-resolution, we applied a method of determination of periods through the analysis of multi-band Lomb-Scargle (VanderPlas and Ivezić, 2015) using only the filters with larger coverage, that are b and v filters. This procedure provided a period of 55.83 days and a semi-major axis of $\sim 22\,R_{\rm eq}$ for the companion. Both values might correspond to an upper limit. We also tried to apply the Supersmoother multi-band analysis using the b and v filters, but it returned none relevant result.

Concerning the polarization, Fig. 7.6 represents the temporal evolution of the linear polarization measurements of the star α Arae (see Sect. 5.3). We performed a median absolute deviation

[1] Period determination using phase dispersion minimization.
[2] https://www.aavso.org/lcg;
[3] https://www.aavso.org/vsx/;
[4] http://vizier.cfa.harvard.edu/viz-bin/VizieR-3?-source=I/239/hip_main.

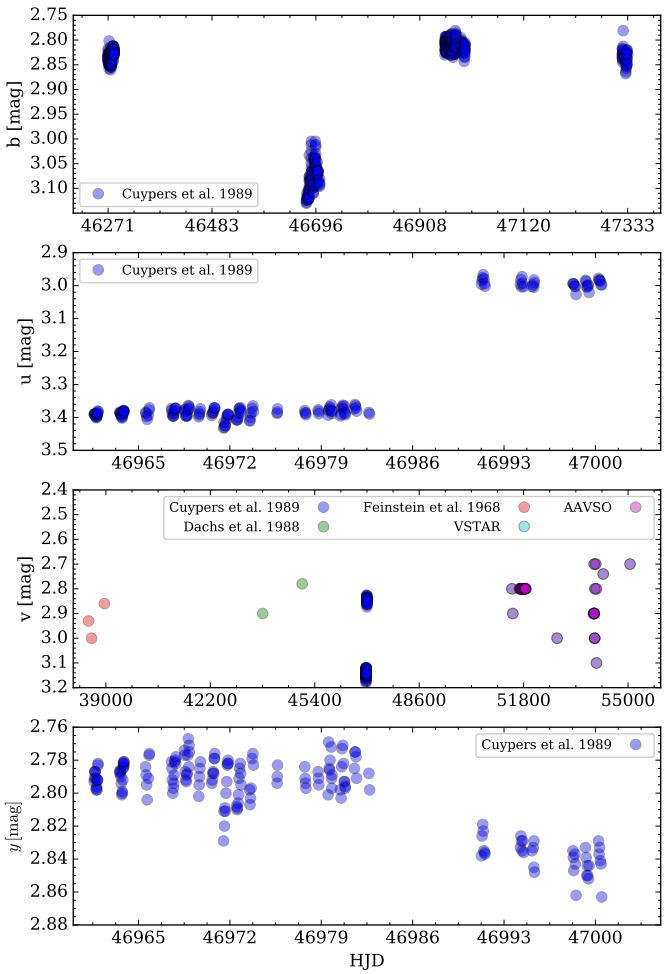

Figure 7.4: Compilation of the light curves of α Arae from top to bottom: b filter, u filter, v filter and y filter. Data from Cuypers et al. (1989), Feinstein (1968) and Dachs et al. (1988).

determination to set the ranges shown in the figure as dashed lines. By another side, we have adopted as an average representation the median of the data. From above to the bottom, we have the temporal evolution of the linear polarization in the filters U, B, V, R and I. This data presents a global mean polarization level equal to 0.50 ± 0.14 %, that means there were no significant variations in time of the polarization measurements. For this reason, we adopted the mean polarimetric data in the modeling (Sect. 3.3). We also applied multi-band paradigm analysis for the polarimetric data, but we found none relevant period.

Fig. 7.7 shows the temporal evolution of the spectral parameters measured from Hα lines. Applying the periodogram analysis to these data and to the radial velocities (V_r) taken from the

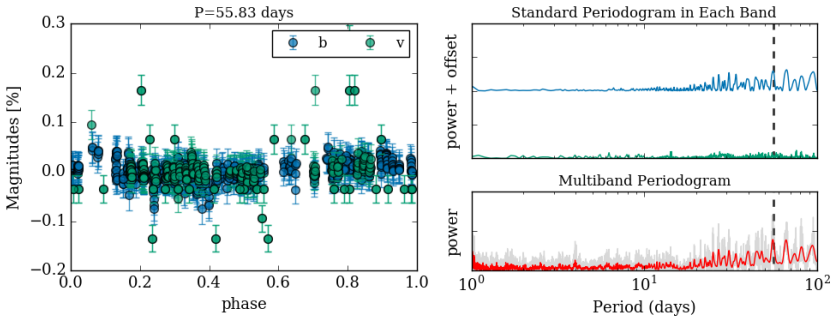

Figure 7.5: Lomb-Scargle Multi-band periodogram made using the *b* and *v* filters.

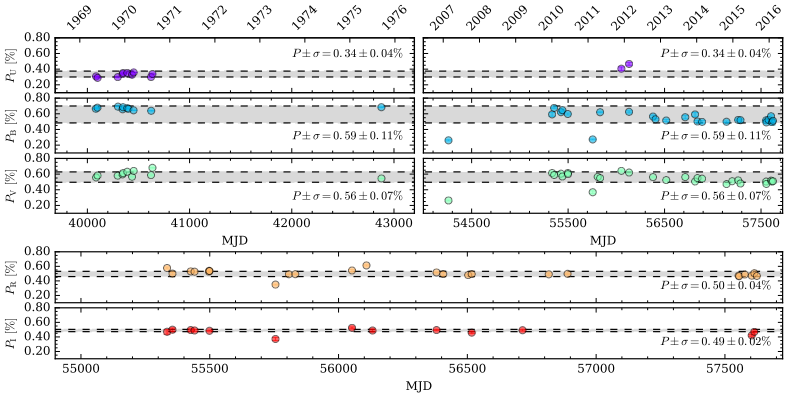

Figure 7.6: Temporal evolution of the polarimetric measurements. From the top to bottom: linear polarization in the filters: U, B, V, R and I. The mean values are represented in each panel together with their respective errors.

lines observed by the instrument `Heros`, we could not find any signal of variability. Nevertheless, comparing these results with the polarimetric values shown in Fig. 7.6, it is clear from nearly 2012 a decrease in the polarization which is also seen in the spectral parameters: EW and maximum emission/continuum ratio (E/C). This behavior could be interpreted as an effect caused by the dimming of the stellar brightness due to some sort of variability. In this case, all the `SED` flux decreases, but emission lines, for instance, the Hα, remain at the same level. This means that the two peaks, V and R, preserve the same previous levels, but as the continuum decrease, the E/C increases and the EW decreases. The time distribution of these parameters might represent two distinct phases: a high-density ($MJD \gtrsim 56000$) and a low-density ($MJD \lesssim 56000$). However, most of the points drop inside the limits delimited by dashed lines, which corroborates to our initial assumption that the disk is stable.

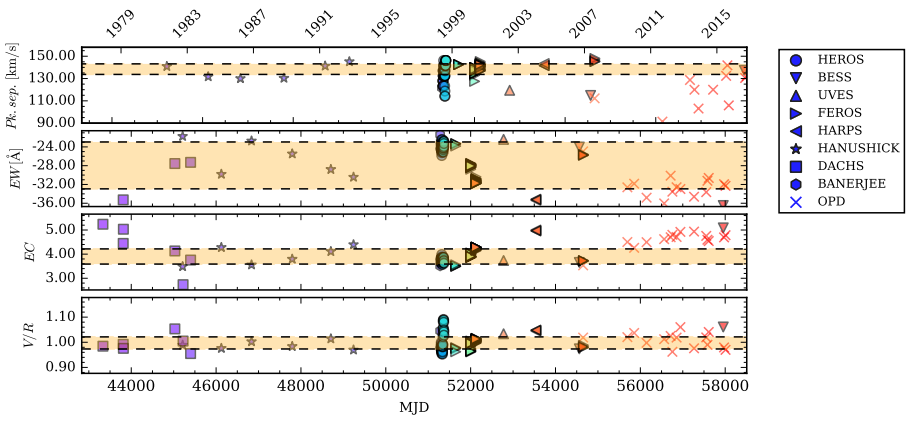

Figure 7.7: Temporal evolution of the spectral measurements. Top panel: peak separation ($\Delta v_{\rm peak} = v_{\rm P_V} - v_{\rm P_R}$). Second panel: Equivalent width. Third panel: emission over the continuum. Bottom panel: V/R ratio ($V/R = F(\lambda_{\rm V})/F(\lambda_{\rm R})$). The median absolute deviation determination was adopt to set the ranges shown as dashed lines.

Chapter 8

Conclusions

Stellar parameters are fundamental aspects of stars, even so, it is a difficult task to determine them since it involves the use of models and various techniques. These parameters are determined by analyzing data by either making calculations or through comparison to theoretical models. The analysis becomes more complex in the case of Be stars, because of the additional physical characteristics present by these objects, for instance, their typical rapid rotation and the presence of circumstellar keplerian disks, in active phases, ruled by viscous processes (Chap. 1). These additional elements imply in a profound modification of the photospheric parameters whose impact on the observables are not fully characterized.

In the present work, we presented the BeAtlas homogeneous grid of models spectra (Chap. 3) . It comprises two systematic grids of models: a photospheric-only (i.e., diskless) grid, and a star plus disk grid ("disk models"), computed according to the VDD formulation. We also presented a new robust method for the determination of parameters of rapid-rotating main-sequence stars based on Bayesian-MCMC methods. These methods are projected to get efficiently correlations and estimates of parameters, even in parameters spaces with several dimensions. A key advantage of our approach was the use of prior information, for instance, the $v \sin i$ and parallaxes from the Hipparcos catalog. The method we developed uses a large grid of synthetic spectra, calculated using a modern grid of stellar evolution models coupled with three-dimensional NLTE radiative transfer calculations.

We derived the stellar parameters, extinction and geometrical parameters of 111 stars (Oe, Be, Bn, B and Ae spectral types), by using just the UV domain, whose showed itself as a powerful constraint of the stellar parameters including the rotation rate and main-sequence lifetime when we applied the $v \sin i$ as a prior. This was expected, since the $v \sin i$ is an implicit function of the inclination angle, mass, and stellar radius. Profound changes occur in different observ-

ables, especially in cases where the rotation rate is close to the critical limit. These changes can lead to stellar misclassifications in simple catalogs mainly when assigning a spectral type and luminosity. In such a scenario, our results can greatly differ to the inferences done considering non-rotating effects. Additionally, from the global combination of our results, we could reproduce well-known statistical proprieties of B-type stars that served to consolidate our method.

The multi-technique analysis of the Be stars α Arae and β CMi provided the stellar, disk and geometrical parameters along with their uncertainties. It helped us to understand better how the different spectral domains and observational measures can be used to extract independent or correlated information about several parameters that describe these peculiar systems. The results indicate that these stars have truncated disks, probably caused by unseen companions. The proprieties of the companions lack of additional information to be completely defined. Our parameters agree with previous estimations for both stars. Regarding the evolutionary state of the α Arae's disk, we have two possible cases, namely: a dissipating disk or a disk truncated by a binary. For β CMi, our results suggest a dissipating disk.

Bibliography

2015 EsoRex: ESO Recipe Execution Tool Astrophysics Source Code Library

Abt H. A., Levato H., Grosso M., Rotational Velocities of B Stars, ApJ, 2002, vol. 573, p. 359

Adelman S. J., The physical properties of normal A stars. In The A-Star Puzzle , vol. 224 of IAU Symposium, 2004, p. 1

Ammler-von Eiff M., Reiners A., New measurements of rotation and differential rotation in A-F stars: are there two populations of differentially rotating stars?, A&A, 2012, vol. 542, p. A116

Arcos C., Jones C. E., Sigut T. A. A., Kanaan S., Curé M., Evidence for Different Disk Mass Distributions Between Early and Late-Type Be Stars in the BeSOS Survey, ArXiv e-prints, 2017

Arviset C., Barbarisi I., de La Calle I., Fajersztejn N., Freschi M., Gabriel C., Gomez P., Guainazzi M., Ibarra A., Laruelo A., Leon I., Micol A., Parrilla E., Ortiz I., Osuna P., Salgado J., Stebe A., Tapiador D., ESA Science Archives, VO tools and remote Scientific Data reduction in Grid Architectures. In Astronomical Data Analysis Software and Systems XVII , vol. 394 of Astronomical Society of the Pacific Conference Series, 2008, p. 227

Baade D., Binary Be-Stars and Be-Binaries. In Evolutionary Processes in Interacting Binary Stars , vol. 151 of IAU Symposium, 1992, p. 147

Baade D., Martayan C., Rivinius T., Be Stars as Seen Through Telescopes in Survey Mode Invited Review. In Bright Emissaries: Be Stars as Messengers of Star-Disk Physics , vol. 506 of Astronomical Society of the Pacific Conference Series, 2016, p. 175

Bagnulo S., Fossati L., Landstreet J. D., Izzo C., The FORS1 catalogue of stellar magnetic field measurements, A&A, 2015, vol. 583, p. A115

Bailey J. D., Landstreet J. D., Abundances determined using Si ii and Si iii in B-type stars: evidence for stratification, A&A, 2013, vol. 551, p. A30

Banerjee D. P. K., Rawat S. D., Janardhan P., Hα observations of Be stars, A&AS, 2000, vol. 147, p. 229

Bastian N., Cabrera-Ziri I., Niederhofer F., de Mink S., Georgy C., Baade D., Correnti M., Usher C., Romaniello M., A high fraction of Be stars in young massive clusters: evidence for a large population of near-critically rotating stars, MNRAS, 2017, vol. 465, p. 4795

Bayo A., Rodrigo C., Barrado y Navascues D., Solano E., Gutierrez R., Morales-Calderon M., Allard F., VizieR Online Data Catalog: VOSA: virtual observatory SED analyzer (Bayo+, 2008), VizieR Online Data Catalog, 2008, vol. 349

Beeckmans F., Hubert-Delplace A. M., Absolute ultraviolet spectrophotometry with the TD-1 satellite. XI - Spectrophotometric study of Be and shell stars with the S 2/68 experiment, A&A, 1980, vol. 86, p. 72

Bernacca P. L., Perinotto M., A catalogue of stellar rotational velocities: I. Main sequence single stars. II. Main sequence spectroscopic binaries and eclipsing systems., Contributi dell'Osservatorio Astrofisica dell'Universita di Padova in Asiago, 1970, vol. 239, p. 1

Bhat S. S., Paul K. T., Subramaniam A., Mathew B., Spectroscopic study of Be-shell stars: 4 Her and 88 Her, Research in Astronomy and Astrophysics, 2016, vol. 16, p. 76

Bjorkman J. E., Carciofi A. C., Modeling the Structure of Hot Star Disks. In The Nature and Evolution of Disks Around Hot Stars , vol. 337, 2005a, p. 75

Bjorkman J. E., Carciofi A. C., NLTE Monte Carlo Models of the Polarization of Circumstellar Disks. In Astronomical Polarimetry: Current Status and Future Directions , vol. 343 of Astronomical Society of the Pacific Conference Series, 2005b, p. 270

Bjorkman K. S., Miroshnichenko A. S., McDavid D., Pogrosheva T. M., A Study of π Aquarii during a Quasi-normal Star Phase: Refined Fundamental Parameters and Evidence for Binarity, ApJ, 2002, vol. 573, p. 812

Bless R. C., Percival J. W., The bolometric luminosities of stars.. In IAU Symposium , vol. 189 of IAU Symposium, 1997, p. 73

Bohlender D., Searching For and Monitoring Ae and A Shell Stars at the DAO. In Bright Emissaries: Be Stars as Messengers of Star-Disk Physics , vol. 506 of Astronomical Society of the Pacific Conference Series, 2016, p. 275

Bragança G. A., Daflon S., Cunha K., Bensby T., Oey M. S., Walth G., Projected Rotational Velocities and Stellar Characterization of 350 B Stars in the Nearby Galactic Disk, AJ, 2012, vol. 144, p. 130

Briot D., Ultraviolet fluxes of Be stars, A&A, 1978, vol. 66, p. 197

Carciofi A. C., The circumstellar discs of Be stars. In IAU Symposium , vol. 272 of IAU Symposium, 2011, p. 325

Carciofi A. C., Bjorkman J. E., Non-LTE Monte Carlo Radiative Transfer. I. The Thermal Properties of Keplerian Disks around Classical Be Stars, ApJ, 2006, vol. 639, p. 1081

Carciofi A. C., Bjorkman J. E., Non-LTE Monte Carlo Radiative Transfer. II. Nonisothermal Solutions for Viscous Keplerian Disks, apj, 2008, vol. 684, p. 1374

Carciofi A. C., Bjorkman J. E., Otero S. A., Okazaki A. T., Štefl S., Rivinius T., Baade D., Haubois X., The First Determination of the Viscosity Parameter in the Circumstellar Disk of a Be Star, apjl, 2012, vol. 744, p. L15

Carciofi A. C., Miroshnichenko A. S., Kusakin A. V., Bjorkman J. E., Bjorkman K. S., Marang F., Kuratov K. S., García-Lario P., Calderón J. V. P., Fabregat J., Magalhães A. M., Properties of the δ Scorpii Circumstellar Disk from Continuum Modeling, apj, 2006, vol. 652, p. 1617

Carciofi A. C., Okazaki A. T., Le Bouquin J.-B., Štefl S., Rivinius T., Baade D., Bjorkman J. E., Hummel C. A., Cyclic variability of the circumstellar disk of the Be star ζ Tauri. II. Testing the 2D global disk oscillation model, aap, 2009, vol. 504, p. 915

Cardelli J. A., Clayton G. C., Mathis J. S., The relationship between infrared, optical, and ultraviolet extinction, ApJ, 1989, vol. 345, p. 245

Challouf M., Nardetto N., Domiciano de Souza A., Mourard D., Aroui H., Stee P., Delaa O., Graczyk D., Pietrzyński G., Gieren W., Theoretical impact of fast rotation on calibrating the surface brightness-color relation for early-type stars, A&A, 2015, vol. 579, p. A107

Chauville J., Zorec J., Ballereau D., Morrell N., Cidale L., Garcia A., High and intermediate-resolution spectroscopy of Be stars 4481 lines, A&A, 2001, vol. 378, p. 861

Chesneau O., Meilland A., Rivinius T., Stee P., Jankov S., Domiciano de Souza A., Graser U., Herbst T., Janot-Pacheco E., Koehler R., Leinert C., Morel S., Paresce F., Richichi A., Robbe-Dubois S., First VLTI/MIDI observations of a Be star: Alpha Arae, aap, 2005, vol. 435, p. 275

Chini R., Hoffmeister V. H., Nasseri A., Stahl O., Zinnecker H., A spectroscopic survey on the multiplicity of high-mass stars, MNRAS, 2012, vol. 424, p. 1925

Claret A., A new non-linear limb-darkening law for LTE stellar atmosphere models. Calculations for -5.0 = log[M/H] = +1, 2000 K = T_{eff} = 50000 K at several surface gravities, A&A, 2000, vol. 363, p. 1081

Clark J. S., Steele I. A., Fender R. P., Radio observations of IRAS-selected Southern hemisphere classical Be stars, MNRAS, 1998, vol. 299, p. 1119

Collins II G. W., Continuum Emission from a Rapidly Rotating Stellar Atmosphere., ApJ, 1963, vol. 138, p. 1134

Collins II G. W., The use of terms and definitions in the study of Be stars. In IAU Colloq. 92: Physics of Be Stars , 1987, p. 3

Collins II G. W., Harrington J. P., Theoretical H-Beta Line Profiles and Related Parameters for Rotating B Stars, ApJ, 1966, vol. 146, p. 152

Conti P. S., Leep E. M., Spectroscopic observations of O-type stars. V. The hydrogen lines and lambda 4686 He II., ApJ, 1974, vol. 193, p. 113

Cote J., Waters L. B. F. M., IRAS observations of Be stars. I - Statistical study of the IR excess of 101 Be stars, A&A, 1987, vol. 176, p. 93

Cotton D. V., Bailey J., Kedziora-Chudczer L., Bott K., Lucas P. W., Hough J. H., Marshall J. P., The linear polarization of Southern bright stars measured at the parts-per-million level, MNRAS, 2016, vol. 455, p. 1607

Cranmer S. R., Dynamical Models of Winds from Rotating Hot Stars, Bartol Research Institute, University of Delaware, 1996, Ph.D. Thesis

Cranmer S. R., A Statistical Study of Threshold Rotation Rates for the Formation of Disks around Be Stars, ApJ, 2005, vol. 634, p. 585

Cutri R. M., et al. VizieR Online Data Catalog: AllWISE Data Release (Cutri+ 2013), VizieR Online Data Catalog, 2014, vol. 2328

Cuypers J., Balona L. A., Marang F., Intensive photometry of southern Be variables. I - Winter objects, A&AS, 1989, vol. 81, p. 151

Cyr R. P., Jones C. E., Tycner C., Statistical Analysis of Interferometric Measurements of Axis Ratios for Classical Be Stars, ApJ, 2015, vol. 799, p. 33

Dachs J., Eichendorf W., Schleicher H., Schmidt-Kaler T., Stift M., Tug H., Photoelectric scanner measurements of Balmer emission line profiles for southern Be stars. II - A survey for variations, A&AS, 1981, vol. 43, p. 427

Dachs J., Hanuschik R., Kaiser D., Ballereau D., Bouchet P., Kiehling R., Kozok J., Rudolph R., Schlosser W., Measurements of Balmer emission line profiles for southern Be stars. II. New data and radial velocities., Astronomy and Astrophysics Supplement Series, 1986, vol. 63, p. 87

Dachs J., Kiehling R., Engels D., Optical and infrared continua of southern Be stars, A&A, 1988, vol. 194, p. 167

Dachs J., Rohe D., Loose A. S., A study of Balmer decrements in Be star emission-line spectra, A&A, 1990, vol. 238, p. 227

Dalla Vedova G., Millour F., Domiciano de Souza A., Petrov R. G., Moser Faes D., Carciofi A. C., Kervella P., Rivinius T., VLTI/PIONIER images the Achernar disk swell, A&A, 2017, vol. 601, p. A118

Dekker H., D'Odorico S., Kaufer A., Delabre B., Kotzlowski H., Design, construction, and performance of UVES, the echelle spectrograph for the UT2 Kueyen Telescope at the ESO Paranal Observatory. In Optical and IR Telescope Instrumentation and Detectors , vol. 4008, 2000, p. 534

di Benedetto G. P., Towards a fundamental calibration of stellar parameters of A, F, G, K dwarfs and giants, A&A, 1998, vol. 339, p. 858

Divan L., Zorec J., Briot D., Correlations between BCD parameters of the continuous spectrum and the Balmer decrement of Be stars. In Be Stars , vol. 98, 1982, p. 53

Domiciano de Souza A., Kervella P., Moser Faes D., Dalla Vedova G., Mérand A., Le Bouquin J. B., Espinosa Lara F., Rieutord M., Bendjoya P., Carciofi A. C., Hadjara M., Millour F., Vakili F., The environment of the fast rotating star Achernar. III. Photospheric parameters revealed by the VLTI, A&A, 2014, vol. 569, p. A10

Dougherty S. M., Waters L. B. F. M., Burki G., Cote J., Cramer N., van Kerkwijk M. H., Taylor A. R., Near-IR excess of Be stars., A&A, 1994, vol. 290

Ducati J. R., VizieR Online Data Catalog: Catalogue of Stellar Photometry in Johnson's 11-color system., VizieR Online Data Catalog, 2002, vol. 2237

Dulaney N. A., Richardson N. D., Gerhartz C. J., Bjorkman J. E., Bjorkman K. S., Carciofi A. C., Klement R., Wang L., Morrison N. D., Bratcher A. D., Greco J. J., Hardegree-Ullman K. K., Lembryk L., Oswald W. L., Trucks J. L., A Spectroscopic Orbit for the Late-type Be Star β CMi, ApJ, 2017, vol. 836, p. 112

Dunstall P. R., Dufton P. L., Sana H., Evans C. J., Howarth I. D., Simón-Díaz S., de Mink S. E., Langer N., Maíz Apellániz J., Taylor W. D., The VLT-FLAMES Tarantula Survey. XXII. Multiplicity properties of the B-type stars, A&A, 2015, vol. 580, p. A93

Egan M. P., Price S. D., Kraemer K. E., Mizuno D. R., Carey S. J., Wright C. O., Engelke C. W., Cohen M., Gugliotti M. G., VizieR Online Data Catalog: MSX6C Infrared Point Source Catalog. The Midcourse Space Experiment Point Source Catalog Version 2.3 (October 2003), VizieR Online Data Catalog, 2003, vol. 5114

Ekström S., Georgy C., Eggenberger P., Meynet G., Mowlavi N., Wyttenbach A., Granada A., Decressin T., Hirschi R., Frischknecht U., Charbonnel C., Maeder A., Grids of stellar models with rotation. I. Models from 0.8 to 120 M at solar metallicity (Z = 0.014), A&A, 2012, vol. 537, p. A146

Ekström S., Georgy C., Meynet G., Maeder A., Granada A., Massive stellar models: rotational evolution, metallicity effects. In Active OB Stars: Structure, Evolution, Mass Loss, and Critical Limits , vol. 272 of IAU Symposium, 2011, p. 62

Ekström S., Meynet G., Maeder A., Barblan F., Evolution towards the critical limit and the origin of Be stars, A&A, 2008, vol. 478, p. 467

ESA VizieR Online Data Catalog: The Hipparcos and Tycho Catalogues (ESA 1997), VizieR Online Data Catalog, 1997, vol. 1239

Escolano C., Carciofi A. C., Okazaki A. T., Rivinius T., Baade D., Štefl S., 2.5D global-disk oscillation models of the Be shell star ζ Tauri. I. Spectroscopic and polarimetric analysis, A&A, 2015, vol. 576, p. A112

ESO, 2012 GASGANO: Data File Organizer Astrophysics Source Code Library

Espinosa Lara F., Rieutord M., Gravity darkening in rotating stars, A&A, 2011, vol. 533, p. A43

Faes D. M., An interferometric view of hot star disks, IAG-Universidade de Sao Paulo (Brazil), Lagrange-Universite de Nice (France) ¡EMAIL¿dmfaes@gmail.com¡/EMAIL¿, 2015, Ph.D. Thesis

Faes D. M., Domiciano de Souza A., Carciofi A. C., Bendjoya P., The photosphere and circumstellar environment of the Be star Achernar. In New Windows on Massive Stars , vol. 307 of IAU Symposium, 2015, p. 261

Feinstein A., A Survey of Southern Be Stars. II. Photometric data, ZAp, 1968, vol. 68, p. 29

Ferreira J., Pelletier G., Appl S., Reconnection X-winds: spin-down of low-mass protostars, MNRAS, 2000, vol. 312, p. 387

Fitzpatrick E. L., Correcting for the Effects of Interstellar Extinction, PASP, 1999, vol. 111, p. 63

Fitzpatrick E. L., Massa D., Determining the Physical Properties of the B Stars. I. Methodology and First Results, ApJ, 1999, vol. 525, p. 1011

Foreman-Mackey D., Hogg D. W., Lang D., Goodman J., emcee: The MCMC Hammer, PASP, 2013, vol. 125, p. 306

Freire Ferrero R., Morales Durán C., Halbwachs J.-L., Cabo Cubeiro A. M., High Ionization Species in the Nearby Interstellar Medium from an Exhaustive Analysis of the IUE INES Database, AJ, 2012, vol. 143, p. 28

Frémat Y., Zorec J., Hubert A.-M., Floquet M., Effects of gravitational darkening on the determination of fundamental parameters in fast-rotating B-type stars, A&A, 2005, vol. 440, p. 305

Freudling W., Romaniello M., Bramich D. M., Ballester P., Forchi V., García-Dabló C. E., Moehler S., Neeser M. J., Automated data reduction workflows for astronomy. The ESO Reflex environment, A&A, 2013, vol. 559, p. A96

Frost S. A., Conti P. S., The Relationship of the OE to the be Stars. In Be and Shell Stars , vol. 70 of IAU Symposium, 1976, p. 139

Gaia Collaboration VizieR Online Data Catalog: Gaia DR2 (Gaia Collaboration, 2018), VizieR Online Data Catalog, 2018, vol. 1345

Gaia Collaboration Brown A. G. A., Vallenari A., Prusti T., de Bruijne J. H. J., Babusiaux C., Bailer-Jones C. A. L., Biermann M., Evans D. W., Eyer L., Jansen Gaia Data Release 2. Summary of the contents and survey properties, A&A, 2018, vol. 616, p. A1

Georgy C., Ekström S., Granada A., Meynet G., Mowlavi N., Eggenberger P., Maeder A., Populations of rotating stars. I. Models from 1.7 to 15 $M_Ł$ at Z = 0.014, 0.006, and 0.002 with Ω/Ω_{crit} between 0 and 1, A&A, 2013, vol. 553, p. A24

Ghoreyshi M. R., Carciofi A. C., Rímulo L. R., Vieira R. G., Faes D. M., Baade D., Bjorkman J. E., Otero S., Rivinius T., The life cycles of Be viscous decretion discs: The case of ω CMa, MNRAS, 2018

Gies D. R., Bagnuolo Jr. W. G., Baines CHARA Array K'-Band Measurements of the Angular Dimensions of Be Star Disks, ApJ, 2007, vol. 654, p. 527

Gies D. R., Bagnuolo Jr. W. G., Ferrara E. C., Kaye A. B., Thaller M. L., Penny L. R., Peters G. J., Hubble Space Telescope Goddard High Resolution Spectrograph Observations of the Be + sdO Binary Persei, ApJ, 1998, vol. 493, p. 440

Golden-Marx J. B., Oey M. S., Lamb J. B., Graus A. S., White A. S., Classical Oe Stars in the Field of the Small Magellanic Cloud, ApJ, 2016, vol. 819, p. 55

Goodman J., Weare J., Ensemble samplers with affine invariance, Communications in Applied Mathematics and Computational Science, Vol. 5, No. 1, p. 65-80, 2010, 2010, vol. 5, p. 65

Granada A., Ekström S., Georgy C., Krtička J., Owocki S., Meynet G., Maeder A., Populations of rotating stars. II. Rapid rotators and their link to Be-type stars, A&A, 2013, vol. 553, p. A25

Granada A., Haemmerlé L., Evolution of single B-type stars with a large angular momentum content, A&A, 2014, vol. 570, p. A18

Gray D. F., The Observation and Analysis of Stellar Photospheres, 2005

Grevesse N., Sauval A. J., Standard Solar Composition, Space Sci. Rev., 1998, vol. 85, p. 161

Grudzinska M., Belczynski K., Casares J., de Mink S. E., Ziolkowski J., Negueruela I., Ribó M., Ribas I., Paredes J. M., Herrero A., Benacquista M., On the formation and evolution of the first Be star in a black hole binary MWC 656, MNRAS, 2015, vol. 452, p. 2773

Grunhut J. H., Wade G. A., MiMeS Collaboration The incidence of magnetic fields in massive stars: An overview of the MiMeS survey component. In American Institute of Physics Conference Series , vol. 1429 of American Institute of Physics Conference Series, 2012, p. 67

Hamed G. E., Sigut T. A. A., Theoretical infrared continuum images for Be star disks, NRIAG Journal of Astronomy and Geophysics, 2013, vol. 2, p. 125

Hanuschik R. W., Hummel W., Dietle O., Sutorius E., V/R variability and global oscillations in Be star disks., A&A, 1995, vol. 300, p. 163

Hanuschik R. W., Hummel W., Sutorius E., Dietle O., Thimm G., Atlas of high-resolution emission and shell lines in Be stars. Line profiles and short-term variability., A&AS, 1996, vol. 116, p. 309

Hanuschik R. W., Kozok J. R., Kaiser D., High-resolution emission-line spectroscopy of Be stars. III - Balmer line profiles, A&A, 1988, vol. 189, p. 147

Hardorp J., Strittmatter P. A., Rotation and Evolution of be Stars. In IAU Colloq. 4: Stellar Rotation , 1970, p. 48

Harmanec P., Stellar masses and radii based on modern binary data, Bulletin of the Astronomical Institutes of Czechoslovakia, 1988, vol. 39, p. 329

Harmanec P., Hill G. M., Walker G. A. H., Dinshaw N., Yang S., Is Omicron Andromedae a quadruple or even quintuple system?, Publications of the Astronomical Institute of the Czechoslovak Academy of Sciences, 1987, vol. 70, p. 115

Hartkopf W. I., Tokovinin A., Mason B. D., Speckle Interferometry at SOAR in 2010 and 2011: Measures, Orbits, and Rectilinear Fits, AJ, 2012, vol. 143, p. 42

Haubois X., Carciofi A. C., Rivinius T., Okazaki A. T., Bjorkman J. E., Dynamical Evolution of Viscous Disks around Be Stars. I. Photometry, apj, 2012, vol. 756, p. 156

Haubois X., Mota B. C., Carciofi A. C., Draper Z. H., Wisniewski J. P., Bednarski D., Rivinius T., Dynamical Evolution of Viscous Disks around Be Stars. II. Polarimetry, ApJ, 2014, vol. 785, p. 12

Henry G. W., Smith M. A., Rotational and Cyclical Variability in γ Cassiopeiae. II. Fifteen Seasons, ApJ, 2012, vol. 760, p. 10

Hilbe J. M., de Souza R. S., Ishida E. E. O., Bayesian Models for Astrophysical Data Using R, JAGS, Python, and Stan, 2017

Hillier D. J., Miller D. L., The Treatment of Non-LTE Line Blanketing in Spherically Expanding Outflows, ApJ, 1998, vol. 496, p. 407

Hoffleit D., Jaschek C., The Bright Star Catalogue, 1982

Hog E., Fabricius C., Makarov V. V., Urban S., Corbin T., Wycoff G., Bastian U., Schwekendiek P., Wicenec A., VizieR Online Data Catalog: The Tycho-2 Catalogue (Hog+ 2000), VizieR Online Data Catalog, 2000, vol. 1259

Huang S.-S., Struve O., Stellar rotation, Annales d'Astrophysique, 1954, vol. 17, p. 85

Huang W., Gies D. R., Stellar Rotation in Young Clusters. I. Evolution of Projected Rotational Velocity Distributions, ApJ, 2006, vol. 648, p. 580

Huang W., Gies D. R., McSwain M. V., A Stellar Rotation Census of B Stars: From ZAMS to TAMS, ApJ, 2010, vol. 722, p. 605

Hunter I., Smoker J. V., Keenan F. P., Ledoux C., Jehin E., Cabanac R., Melo C., Bagnulo S., Early-type stars observed in the ESO UVES Paranal Observatory Project - I. Interstellar NaI UV, TiII and CaII K observations*, MNRAS, 2006, vol. 367, p. 1478

Ishak B., Statistics, data mining, and machine learning in astronomy: a practical Python guide for the analysis of survey data, by Željko Ivezić, Andrew J. Connolly, Jacob T. VanderPlas and Alexander Gray, Contemporary Physics, 2017, vol. 58, p. 99

Ishihara D., Onaka T., Kataza H., Salama A., Alfageme C., Cassatella The AKARI/IRC mid-infrared all-sky survey, A&A, 2010, vol. 514, p. A1

Ivezić Ž., Connelly A. J., VanderPlas J. T., Gray A., Statistics, Data Mining, and Machine Learningin Astronomy, 2014

Jarad M. M., Hilditch R. W., Skillen I., A radial-velocity study of 18 emission-line B stars, MNRAS, 1989, vol. 238, p. 1085

Jaschek M., Egret D., A Catalogue of Be-Stars. In Be Stars , vol. 98 of IAU Symposium, 1982, p. 261

Jaschek M., Slettebak A., Jaschek C., , 1981 Be star terminology. Be Star Newsletter

Johnston K. G., Robitaille T. P., Beuther H., Linz H., Boley P., Kuiper R., Keto E., Hoare M. G., van Boekel R., A Keplerian-like Disk around the Forming O-type Star AFGL 4176, ApJ, 2015, vol. 813, p. L19

Kaeufl H.-U., Ballester P., Biereichel P., Delabre B., Donaldson R., Dorn R., Fedrigo E., Finger G., Fischer CRIRES: a high-resolution infrared spectrograph for ESO's VLT. In Ground-based Instrumentation for Astronomy , vol. 5492, 2004, p. 1218

Katahira J.-I., Hirata R., Ito M., Katoh M., Ballereau D., Chauville J., Period Analysis of the Radial Velocity in PLEIONE, PASJ, 1996, vol. 48, p. 317

Kee N. D., Owocki S., Sundqvist J. O., Line-driven ablation of circumstellar discs - I. Optically thin decretion discs of classical Oe/Be stars, MNRAS, 2016, vol. 458, p. 2323

Keller S. C., Wood P. R., Bessell M. S., Be stars in and around young clusters in the Magellanic Clouds, A&AS, 1999, vol. 134, p. 489

Kervella P., Domiciano de Souza A., Bendjoya P., The close-in companion of the fast rotating Be star Achernar, A&A, 2008, vol. 484, p. L13

Kjurkchieva D., Marchev D., Sigut T. A. A., Dimitrov D., The B and Be States of the Star EM Cepheus, AJ, 2016, vol. 152, p. 56

Klement R., Carciofi A. C., Rivinius T., Matthews L. D., Vieira R. G., Ignace R., Bjorkman J. E., Mota B. C., Faes D. M., Bratcher A. D., Curé M., Štefl S., Revealing the structure of the outer disks of Be stars, A&A, 2017, vol. 601, p. A74

Klement R., Carciofi A. C., Rivinius T., Panoglou D., Vieira R. G., Bjorkman J. E., Štefl S., Tycner C., Faes D. M., Korčáková D., Müller A., Zavala R. T., Curé M., Multitechnique testing of the viscous decretion disk model I. The stable and tenuous disk of the late-type Be star β CMi, ArXiv e-prints, 2015a

Klement R., Carciofi A. C., Rivinius T., Panoglou D., Vieira R. G., Bjorkman J. E., Štefl S., Tycner C., Faes D. M., Korčáková D., Müller A., Zavala R. T., Curé M., Multitechnique testing of the viscous decretion disk model. I. The stable and tenuous disk of the late-type Be star β CMi, A&A, 2015b, vol. 584, p. A85

Koubský P., Kotková L., Votruba V., Šlechta M., Dvořáková Š., o Puppis: another Be+sdO binary?, A&A, 2012, vol. 545, p. A121

Labadie-Bartz J., Pepper J., McSwain M. V., Bjorkman J. E., Bjorkman K. S., Lund M. B., Rodriguez J. E., Stassun K. G., Stevens D. J., James D. J., Kuhn R. B., Siverd R. J., Beatty T. G., Photometric Variability of the Be Star Population, AJ, 2017, vol. 153, p. 252

Lamers H. J. G. L. M., Faraggiana R., Burger M., Observations of the mid-ultraviolet spectrum of peculiar A and B stars and of Be stars, BN stars and shell stars, A&A, 1980, vol. 82, p. 48

Langer N., Cantiello M., Yoon S.-C., Hunter I., Brott I., Lennon D., de Mink S., Verheijdt M., Rotation and Massive Close Binary Evolution. In Massive Stars as Cosmic Engines , vol. 250 of IAU Symposium, 2008, p. 167

Lee R. W., ed., 1991 A review of spectral line broadening relevant to hot dense plasmas

Levenhagen R. S., Leister N. V., Spectroscopic analysis of southern B and Be stars, MNRAS, 2006, vol. 371, p. 252

Maeder A., Physics, Formation and Evolution of Rotating Stars, 2009

Maeder A., Grebel E. K., Mermilliod J.-C., Differences in the fractions of Be stars in galaxies, A&A, 1999, vol. 346, p. 459

Marco A., Negueruela I., NGC 7419 as a template for red supergiant clusters, A&A, 2013, vol. 552, p. A92

Martayan C., Frémat Y., Hubert A.-M., Floquet M., Zorec J., Neiner C., Effects of metallicity, star-formation conditions, and evolution in B and Be stars. II. Small Magellanic Cloud, field of NGC330, A&A, 2007, vol. 462, p. 683

Martins F., Schaerer D., Hillier D. J., A new calibration of stellar parameters of Galactic O stars, A&A, 2005, vol. 436, p. 1049

Mason B. D., ten Brummelaar T., Gies D. R., Hartkopf W. I., Thaller M. L., , 1997 A Speckle Survey of Southern Be Stars Be Star Newsletter

Mason B. D., Wycoff G. L., Hartkopf W. I., Douglass G. G., Worley C. E., The 2001 US Naval Observatory Double Star CD-ROM. I. The Washington Double Star Catalog, AJ, 2001, vol. 122, p. 3466

Massey P., MASSIVE STARS IN THE LOCAL GROUP: Implications for Stellar Evolution and Star Formation, ARA&A, 2003, vol. 41, p. 15

McEvoy C. M., Smoker J. V., Dufton P. L., Smith K. T., Kennedy M. B., Keenan F. P., Lambert D. L., Welty D. E., Lauroesch J. T., Early-type stars observed in the ESO UVES Paranal Observatory Project - V. Time-variable interstellar absorption, MNRAS, 2015, vol. 451, p. 1396

McGill M. A., Sigut T. A. A., Jones C. E., The Thermal Structure of Gravitationally Darkened Classical Be Star Disks, ApJ, 2011, vol. 743, p. 111

McLean I. S., Interpretation of the intrinsic polarizations of early-type emission-line stars, MNRAS, 1979, vol. 186, p. 265

McLean I. S., Brown J. C., Polarisation by Thomson scattering in optically thin stellar envelopes. III. A statistical study of the oblateness and rotation of Be star envelopes., A&A, 1978, vol. 69, p. 291

McLean I. S., Clarke D., Separation of the intrinsic and interstellar linear polarization components of southern hemisphere early-type emission-line stars., MNRAS, 1979, vol. 186, p. 245

McSwain M. V., Gies D. R., The Evolutionary Status of Be Stars: Results from a Photometric Study of Southern Open Clusters, ApJS, 2005, vol. 161, p. 118

Meilland A., Millour F., Kanaan S., Stee P., Petrov R., Hofmann K.-H., Natta A., Perraut K., First spectro-interferometric survey of Be stars. I. Observations and constraints on the disk geometry and kinematics, A&A, 2012, vol. 538, p. A110

Meilland A., Stee P., Recent results from the SIMECA code and VLTI observations. In EAS Publications Series , vol. 18 of EAS Publications Series, 2006, p. 273

Meilland A., Stee P., Chesneau O., Jones C., VLTI/MIDI observations of 7 classical Be stars, aap, 2009, vol. 505, p. 687

Meilland A., Stee P., Vannier M., Millour F., Domiciano de Souza A., Malbet F., Martayan C., Paresce F., Petrov R. G., Richichi A., Spang A., First direct detection of a Keplerian rotating disk around the Be star α Arae using AMBER/VLTI, aap, 2007, vol. 464, p. 59

Mennickent R. E., H-beta line profile variability of seven southern Be stars, A&AS, 1991, vol. 88, p. 1

Mennickent R. E., Vogt N., V/R variations in H-beta emission profiles of Be stars, A&A, 1991, vol. 241, p. 159

Mermilliod J.-C., VizieR Online Data Catalog: UBV Photoelectric Cat: Data 1986-1992 (Mermilliod 1994), VizieR Online Data Catalog, 1994, vol. 2193

Metropolis N., Rosenbluth A. W., Rosenbluth M. N., Teller A. H., Teller E., Equation of State Calculations by Fast Computing Machines, J. Chem. Phys., 1953, vol. 21, p. 1087

Meynet G., Maeder A., Stellar evolution with rotation. V. Changes in all the outputs of massive star models, A&A, 2000, vol. 361, p. 101

Miroshnichenko A. S., Pasechnik A. V., Manset N., The 2011 Periastron Passage of the Be Binary δ Scorpii, ApJ, 2013, vol. 766, p. 119

Morris M., Mechanisms for mass loss from cool stars, PASP, 1987, vol. 99, p. 1115

Negueruela I., Steele I. A., Bernabeu G., On the class of Oe stars, Astronomische Nachrichten, 2004, vol. 325, p. 749

Nieva, Mara-Fernanda Przybilla, Norbert Fundamental properties of nearby single early B-type stars*, A&A, 2014, vol. 566, p. A7

Ochsenbein F., Bauer P., Marcout J., The VizieR database of astronomical catalogues, A&AS, 2000, vol. 143, p. 23

Okazaki A. T., On the confinement of one-armed oscillations in discs of Be stars., A&A, 1997, vol. 318, p. 548

Okazaki A. T., Viscous Transonic Decretion in Disks of Be Stars, pasj, 2001, vol. 53, p. 119

Okazaki A. T., Bate M. R., Ogilvie G. I., Pringle J. E., Evolution of truncated decretion disks in Be/X-Ray binaries. In The Physics of Cataclysmic Variables and Related Objects , vol. 261 of Astronomical Society of the Pacific Conference Series, 2002, p. 519

Oudmaijer R. D., Parr A. M., The binary fraction and mass ratio of Be and B stars: a comparative Very Large Telescope/NACO study, MNRAS, 2010, vol. 405, p. 2439

Owocki S., Formation and Evolution of Disks around Classical Be Stars. In Stars with the B[e] Phenomenon , vol. 355 of Astronomical Society of the Pacific Conference Series, 2006, p. 219

Panoglou D., Carciofi A. C., Vieira R. G., Cyr I. H., Jones C. E., Okazaki A. T., Rivinius T., Be discs in binary systems - I. Coplanar orbits, MNRAS, 2016, vol. 461, p. 2616

Panoglou D., Faes D. M., Carciofi A. C., Okazaki A. T., Baade D., Rivinius T., Borges Fernandes M., Be discs in coplanar circular binaries: Phase-locked variations of emission lines, MNRAS, 2018, vol. 473, p. 3039

Peters G. J., Gies D. R., Grundstrom E. D., McSwain M. V., Detection of a Hot Subdwarf Companion to the Be Star FY Canis Majoris, ApJ, 2008, vol. 686, p. 1280

Peters G. J., Pewett T. D., Gies D. R., Touhami Y. N., Grundstrom E. D., Far-ultraviolet Detection of the Suspected Subdwarf Companion to the Be Star 59 Cygni, ApJ, 2013, vol. 765, p. 2

Peters G. J., Wang L., Gies D. R., Grundstrom E. D., The Hot Companion and Circumbinary Disk of the Be Star HR 2142, ApJ, 2016, vol. 828, p. 47

Pollmann E., Period analysis of the Halpha line profile variation of the Be binary star pi Aqr, Information Bulletin on Variable Stars, 2012, vol. 6023, p. 1

Porter J. M., On the rotational velocities of Be and Be-shell stars, MNRAS, 1996, vol. 280, p. L31

Porter J. M., On outflowing viscous disc models for Be stars, aap, 1999, vol. 348, p. 512

Porter J. M., Rivinius T., Classical Be Stars, pasp, 2003, vol. 115, p. 1153

Pringle J. E., Accretion discs in astrophysics, araa, 1981, vol. 19, p. 137

Quirrenbach A., Bjorkman K. S., Bjorkman J. E., Hummel C. A., Buscher D. F., Armstrong J. T., Mozurkewich D., Elias II N. M., Babler B. L., Constraints on the Geometry of Circumstellar Envelopes: Optical Interferometric and Spectropolarimetric Observations of Seven Be Stars, apj, 1997, vol. 479, p. 477

Rauw G., Morel T., Nazé Y., Eversberg T., Alves F., Arnold W., Bergmann T., Spectroscopic variability of two Oe stars, A&A, 2015, vol. 575, p. A99

Rauw G., Naze Y., Marique P. X., De Becker M., Sana H., Vreux J.-M., Long-term Spectroscopic Variability of Two Oe Stars, Information Bulletin on Variable Stars, 2007, vol. 5773

Reimann J. D., Frequency Estimation Using Unequally-Spaced Astronomical Data., UNIVERSITY OF CALIFORNIA, BERKELEY., 1994, Ph.D. Thesis

Rímulo L. R., Carciofi A. C., Vieira R. G., Rivinius T., Faes D. M., Figueiredo A. L., Bjorkman J. E., Georgy C., Ghoreyshi M. R., Soszyński I., The life cycles of Be viscous decretion discs: fundamental disc parameters of 54 SMC Be stars, MNRAS, 2018, vol. 476, p. 3555

Rivinius T., Baade D., Stefl S., Stahl O., Wolf B., Kaufer A., Stellar and circumstellar activity of the Be star MU Centauri. II. Multiperiodic low-order line-profile variability, A&A, 1998, vol. 336, p. 177

Rivinius T., Carciofi A. C., Martayan C., Classical Be stars. Rapidly rotating B stars with viscous Keplerian decretion disks, aapr, 2013, vol. 21, p. 69

Rivinius T., Štefl S., Baade D., Central quasi-emission peaks in shell spectra and the rotation of disks of Be stars, A&A, 1999, vol. 348, p. 831

Royer F., Grenier S., Baylac M.-O., Gómez A. E., Zorec J., Rotational velocities of A-type stars in the northern hemisphere. II. Measurement of v sin i, A&A, 2002, vol. 393, p. 897

Royer F., Zorec J., Gómez A. E., Rotational velocities of A-type stars. III. Velocity distributions, A&A, 2007, vol. 463, p. 671

Ruždjak D., Božić H., Harmanec P., Fiřt R., Chadima P., Bjorkman K., Gies D. R., Kaye A. B., Koubský P., McDavid D., Richardson N., Sudar D., Šlechta M., Wolf M., Yang S., Properties and nature of Be stars. 26. Long-term and orbital changes of ζ Tauri, A&A, 2009, vol. 506, p. 1319

Sana H., de Mink S. E., de Koter A., Langer N., Evans C. J., Gieles M., Gosset E., Izzard R. G., Le Bouquin J.-B., Schneider F. R. N., Binary Interaction Dominates the Evolution of Massive Stars, Science, 2012, vol. 337, p. 444

Sana H., Le Bouquin J.-B., Lacour S., Berger J.-P., Duvert G., Gauchet L., Norris B., Olofsson J., Pickel D., Zins G., Absil O., de Koter A., Kratter K., Schnurr O., Zinnecker H., Southern Massive Stars at High Angular Resolution: Observational Campaign and Companion Detection, ApJS, 2014, vol. 215, p. 15

Schmidt-Kaler T., , 1982 4.1.2 Intrinsic colors and visual absolute magnitudes (calibration of the MK system): Datasheet from Landolt-Börnstein - Group VI Astronomy and Astrophysics

· Volume 2B: “Stars and Star Clusters” in SpringerMaterials, publisher=”Springer-Verlag Berlin Heidelberg

Schultz G. V., Wiemer W., Interstellar reddening and IR-excesses of O and B stars., A&A, 1975, vol. 43, p. 133

Serkowski K., Intrinsic Polarization of Early-Type Stars with Extended Atmospheres, ApJ, 1970, vol. 160, p. 1083

Shajn G., Struve O., On the rotation of the stars, MNRAS, 1929, vol. 89, p. 222

Shokry A., Rivinius T., Mehner A., Martayan C., Hummel W., Townsend R. H. D., Mérand A., Mota B., Faes D. M., Hamdy M. A., Beheary M. M., Gadallah K. A. K., Abo-Elazm M. S., Stellar parameters of Be stars observed with X-shooter, A&A, 2018, vol. 609, p. A108

Silaj J., Jones C. E., Sigut T. A. A., Tycner C., The Hα Profiles of Be Shell Stars, ApJ, 2014, vol. 795, p. 82

Simón-Díaz S., Herrero A., The IACOB project. I. Rotational velocities in northern Galactic O- and early B-type stars revisited. The impact of other sources of line-broadening, A&A, 2014, vol. 562, p. A135

Slettebak A., The Be stars, pasp, 1988, vol. 100, p. 770

Smith K. C., Chemically Peculiar Hot Stars, Ap&SS, 1996, vol. 237, p. 77

Stellingwerf R. F., Period determination using phase dispersion minimization, ApJ, 1978, vol. 224, p. 953

Sterken C., Vogt N., Mennickent R. E., Long-term photometry of Be stars. II. Periodic variations on time scales of days to months., A&A, 1996, vol. 311, p. 579

Struve O., On the Origin of Bright Lines in Spectra of Stars of Class B, apj, 1931, vol. 73, p. 94

Tatulli E., Duvert G., AMBER data reduction, New A Rev., 2007, vol. 51, p. 682

Touhami Y., Gies D. R., Schaefer G. H., Richardson N. D., McAlister H. A., Ridgway S. T., Brummelaar T. A. t., Goldfinger P. J., Sturmann L., Sturmann J., Turner N. H., Farrington C. D., A CHARA Array Long Baseline Interferometric Survey of Circumstellar Disks of Be

Stars. In Resolving The Future Of Astronomy With Long-Baseline Interferometry , vol. 487 of Astronomical Society of the Pacific Conference Series, 2014, p. 395

Townsend R. H. D., Owocki S. P., Howarth I. D., Be-star rotation: how close to critical?, mnras, 2004, vol. 350, p. 189

Tycner C., Gilbreath G. C., Zavala R. T., Armstrong J. T., Benson J. A., Hajian A. R., Hutter D. J., Jones C. E., Pauls T. A., White N. M., Constraining Disk Parameters of Be Stars using Narrowband Hα Interferometry with the Navy Prototype Optical Interferometer, AJ, 2006, vol. 131, p. 2710

Tycner C., Jones C. E., Sigut T. A. A., Schmitt H. R., Benson J. A., Hutter D. J., Zavala R. T., Constraining the Physical Parameters of the Circumstellar Disk of χ Ophiuchi, apj, 2008, vol. 689, p. 461

Tycner C., Lester J. B., Hajian A. R., Armstrong J. T., Benson J. A., Gilbreath G. C., Hutter D. J., Pauls T. A., White N. M., Properties of the Hα-emitting Circumstellar Regions of Be Stars, ApJ, 2005, vol. 624, p. 359

Uesugi A., Fukuda I., Catalogue of rotational velocities of the stars, 1970

Underhill A., Doazan V., B Stars with and without emission lines, parts 1 and 2, 1982

Vacca W. D., Garmany C. D., Shull J. M., The Lyman-Continuum Fluxes and Stellar Parameters of O and Early B-Type Stars, ApJ, 1996, vol. 460, p. 914

van Belle G. T., Interferometric observations of rapidly rotating stars, A&A Rev., 2012, vol. 20, p. 51

van Leeuwen F., Validation of the new Hipparcos reduction, A&A, 2007, vol. 474, p. 653

Vanbeveren D., Mennekens N., Evolution of Intermediate Mass and Massive Binary Stars: Physics, Mass Loss, and Rotation. In The B[e] Phenomenon: Forty Years of Studies , vol. 508 of Astronomical Society of the Pacific Conference Series, 2017, p. 121

VanderPlas J. T., Understanding the Lomb-Scargle Periodogram, ArXiv e-prints, 2017

VanderPlas J. T., Ivezić Ž., Periodograms for Multiband Astronomical Time Series, ApJ, 2015, vol. 812, p. 18

Vega E. I., Rabolli M., Feinstein A., Muzzio J. C., A search for H-alpha-emission objects in a region in ARA, AJ, 1980, vol. 85, p. 1207

Vieira R. G., Carciofi A. C., The viscous disk properties of 80 Be stars, ArXiv e-prints, 2017

Vieira R. G., Carciofi A. C., Bjorkman J. E., The pseudo-photosphere model for the continuum emission of gaseous discs, MNRAS, 2015, vol. 454, p. 2107

Vieira R. G., Carciofi A. C., Bjorkman J. E., Rivinius T., Baade D., Rímulo L. R., The life cycles of Be viscous decretion discs: time-dependent modelling of infrared continuum observations, MNRAS, 2017, vol. 464, p. 3071

Vinicius M.-M. F., Townsend R. H. D., Leister N. V., Determination of Be-star Inclinations from Gravity-Darkened Photospheric Spectra. In Active OB-Stars: Laboratories for Stellare and Circumstellar Physics , vol. 361 of Astronomical Society of the Pacific Conference Series, 2007, p. 518

von Zeipel H., The radiative equilibrium of a slightly oblate rotating star, MNRAS, 1924, vol. 84, p. 684

Wall J. V., Jenkins C. R., Practical Statistics for Astronomers, 2012

Waters L. B. F. M., Boland W., Taylor A. R., van de Stadt H., Lamers H. J. G. L. M., Millimeter observations of the Be stars Psi Persei and Gamma Cassiopeiae, A&A, 1989, vol. 213, p. L19

Wheelwright H. E., Bjorkman J. E., Oudmaijer R. D., Carciofi A. C., Bjorkman K. S., Porter J. M., Probing the properties of Be star discs with spectroastrometry and NLTE radiative transfer modelling: β CMi, mnras, 2012, vol. 423, p. L11

Wisniewski J. P., Bjorkman K. S., The Role of Evolutionary Age and Metallicity in the Formation of Classical Be Circumstellar Disks. I. New Candidate Be Stars in the LMC, SMC, and Milky Way, ApJ, 2006, vol. 652, p. 458

Yudin R. V., Statistical analysis of intrinsic polarization, IR excess and projected rotational velocity distributions of classical Be stars, A&A, 2001, vol. 368, p. 912

Zagury F., The 2200Å bump and the interstellar extinction curve, Astronomische Nachrichten, 2013, vol. 334, p. 1107

Zinnecker H., Yorke H. W., Toward Understanding Massive Star Formation, ARA&A, 2007, vol. 45, p. 481

Zorec J., Briot D., Absolute magnitudes of B emission line stars : correlation between the luminosity excess and the effective temperature., A&A, 1991, vol. 245, p. 150

Zorec J., Briot D., Critical study of the frequency of Be stars taking into account their outstanding characteristics., A&A, 1997, vol. 318, p. 443

Zorec J., Frémat Y., Cidale L., On the evolutionary status of Be stars. I. Field Be stars near the Sun, A&A, 2005, vol. 441, p. 235

Zorec J., Frémat Y., Domiciano de Souza A., Delaa O., Stee P., Mourard D., Cidale L., Martayan C., Georgy C., Ekström S., Differential rotation in rapidly rotating early-type stars. I. Motivations for combined spectroscopic and interferometric studies, A&A, 2011, vol. 526, p. A87

Zorec J., Frémat Y., Domiciano de Souza A., Royer F., Cidale L., Hubert A.-M., Semaan T., Martayan C., Cochetti Y. R., Arias M. L., Aidelman Y., Stee P., Critical study of the distribution of rotational velocities of Be stars. I. Deconvolution methods, effects due to gravity darkening, macroturbulence, and binarity, A&A, 2016, vol. 595, p. A132

Zorec J., Frémat Y., Martayan C., Cidale L. S., Torres A. F., Rotation in the ZAMS: Be and Bn stars. In Active OB-Stars: Laboratories for Stellare and Circumstellar Physics , vol. 361 of Astronomical Society of the Pacific Conference Series, 2007, p. 539

Appendix

Appendix A

Additional Tables

A.1 Binary Be Stars

Table A.1 - : Some Be stars known as binaries.

Star	ST	Period	Ref.
FY CMa	B0.5IVe	-	Peters et al., 2008
γ Cas	B0.5IVpe	203.5 days	Henry and Smith, 2012
o Pup	B1IVe	29	Koubský et al., 2012
ζ Tau	B1IVe_shell	133 days	Ruždjak et al., 2009
η Tau	B7III	4.2 days	Jarad et al., 1989
59 Cyg	B1.5Vnne	29 days	Peters et al., 2013
κ CMa	B1.5Ve	~ years	Meilland et al., 2012
δ Cen	B2Vne	~ years	Meilland et al., 2012
μ Cen	B2Vnpe	-	Meilland et al., 2012
α Ara	B2Vne	74 days	Chesneau et al., 2005
HD 81654	B2/3V(e)	-	Labadie-Bartz et al., 2017
HR 2142	B3/5Vnne	~ 81 days	Peters et al., 2016
p Car	B4Vne	-	Meilland et al., 2012
ψ Per	B5Ve	-	Waters et al., 1989
κ Dra	B6IIIe	61.55 days	Gies et al., 2007
Achernar	B6Vpe	15 years	Kervella et al., 2008
o Aqr	B7IVe	-	Meilland et al., 2012
o And	B6III	33.1 days	Harmanec et al., 1987
ω Car	B8IIIe	-	Meilland et al., 2012

α Col	B9Ve	-	Meilland et al., 2012
δ Sco	B0.3IV	10.8 years	Miroshnichenko et al., 2013
17 Tau	B6III	4.3 days	Jarad et al., 1989
β Mon A	B3V	-	Hartkopf et al., 2012
π Aqr	B1III-IVe	$\sim$ 80 days	Pollmann, 2012
66 Oph	B2Ve	-	Mason et al., 2001
θ Circ	B2IV/V	-	Mason et al., 1997
ϕ Per	B1.5Ve-shell	127 days	Gies et al., 1998
28 Tau	B8Vne	218 days	Katahira et al., 1996
4 Her	B9pe	46 days	Bhat et al., 2016
88 Her	B6IIInp_sh	87 days	Bhat et al., 2016
ϵ Cap	B3V	95 days	Rivinius et al., 1999
β CMi	B3V	170.4 days	Dulaney et al., 2017

A.2 Previous results of α Arae

Table A.2 - α Arae's stellar parameters determined previously.

Source	M [$M_\odot$]	$T_{\rm eff}$ [K]	R [$R_\odot$]	L [$L_\odot$]	i[°]	d[pc]	$v \sin i$[km s^{-1}]	ST
Dachs et al., 1988	9.5	18 000	5.1	-	-	-	-	-
Dachs et al., 1990	-	18 000	-	-	-	-	-	-
Chauville et al., 2001	-	18 000	-	-	-	-	-	-
Chesneau et al., 2005	-	19 010	4.8	2.2×10^3	45 ± 5	105	-	-
Zorec et al., 2005	6.2	17 360	3.94	-	-	-	-	-
Frémat et al., 2005	-	18 044	-	-	51.3 ±3.2	-	-	-
Levenhagen and Leister, 2006	11.9	22 150	9.60	22908	-	-	270 ± 25	B2Vne
Meilland and Stee, 2006	9.6	18 000	4.8	5.8×10^3	-	105	-	B3Ve
Meilland et al., 2007	9.6	18 000	4.8	5.8×10^3	55	105	375	-
Meilland et al., 2009	7.2	18 044	4.5	-	-	81	-	-
Hamed and Sigut, 2013[1]	9.6	18 044	4.8	2.2×10^3	55, 45, 75	-	-	B3Ve

Table A.3 - Disk parameters determined by previous works. $R_{\rm D}$ [2 μm]: Disk size at 2 μm. $R_{\rm D}$ [8 μm]: Disk size at 8 μm. $R_{\rm D}$ [12 μm]: Disk size at 12 μm. ρ_0: volumetric density at the disk basis. [1] from Meilland et al., 2007.

Source	$R_{\rm D}$	$R_{\rm D}$ [mas]			n	$10^{-10} \times \rho_0$
	[$R_\star$]	(2 μm)	(8 μm)	(12 μm)		[g/cm^3]
Meilland et al., 2009	-	7.3 ± 2 [1]	5.5 ± 0.3	8.1 ± 0.6	-	-
Hamed and Sigut, 2013	5.0	7.6 ± 1.4	4.0 ± 1.8	5.9 ± 2.98	2 and 3	0.75 to 1.0

A.3 Field stars used to infer the interstellar polarization

Table A.4 - Field stars used to infer the interstellar polarization in the region of α Arae.

Field Star	$P_{\rm max}$ [%]	$\lambda_{\rm max}$ [μm]	$< \theta >$ [°]	N
HIP 84956	$0.018^{+0.005}_{-0.005}$	$0.80^{+0.15}_{-0.46}$	64 ± 34	4
HIP 85241	$0.029^{+0.005}_{-0.004}$	$0.44^{+0.20}_{-0.16}$	97.5 ± 6.5	4
HIP 85610	$0.018^{+0.006}_{-0.005}$	$0.34^{+0.27}_{-0.18}$	105 ± 24	4
HIP 86248	$0.040^{+0.005}_{-0.005}$	$0.59^{+0.14}_{-0.14}$	94.5 ± 5.2	4
HIP 86247	$0.056^{+0.004}_{-0.004}$	$0.981^{+0.014}_{-0.030}$	93.0 ± 7.1	4
HIP 86247 (B)	$0.036^{+0.007}_{-0.006}$	$0.58^{+0.24}_{-0.24}$	109.6 ± 7.3	4
HIP 86516	$0.034^{+0.004}_{-0.004}$	$0.54^{+0.15}_{-0.16}$	104.2 ± 4.8	4

A.4 Photometric data of α Arae

Table A.5 - Photometric dataset.

Filter	λ (Å)	F (erg/s/cm^2/Å)	σF (erg/s/cm^2/Å)	Source (Mission/Instrument)	Obs.Date (VO) (Gregorian)
Generic/Stromgren.u	3447.51	1.630×10^{-10}	-	Paunzen 2015	-
Generic/Johnson.U	3570.65	5.496×10^{-10}	1.538×10^{-11}	UBV, Mermilliod 1991	-
Generic/Stromgren.v	4110.37	4.818×10^{-10}	-	Paunzen 2015	-
TYCHO/TYCHO.B	4280.00	5.632×10^{-10}	7.262×10^{-12}	Tycho	-
Generic/Johnson.B	4378.12	4.908×10^{-10}	1.072×10^{-11}	UBV, Mermilliod 1991	-
Generic/Stromgren.b	4663.26	3.847×10^{-10}	-	Paunzen 2015	-
TYCHO/TYCHO.V	5340.00	3.041×10^{-10}	2.521×10^{-12}	Tycho	-
Generic/Johnson.V	5466.11	2.384×10^{-10}	4.610×10^{-12}	UBV, Mermilliod 1991	-
Generic/Stromgren.y	5472.42	2.280×10^{-10}	-	Paunzen 2015	-
2MASS/2MASS.J	12350.00	2.605×10^{-11}	6.334×10^{-12}	2MASS	2000-08-04
2MASS/2MASS.H	16620.00	1.049×10^{-11}	2.221×10^{-12}	2MASS	2000-08-04
2MASS/2MASS.Ks	21590.00	4.335×10^{-12}	8.783×10^{-13}	2MASS	2000-08-04
IRAS/IRAS.12mu	101464.58	3.698×10^{-14}	1.479×10^{-15}	IRAS	-
WISE/WISE.W3	115608.00	2.379×10^{-14}	8.325×10^{-16}	WISE	-
AKARI/IRC.L18W	176094.90	5.692×10^{-15}	2.852×10^{-16}	AKARI/IRC	-
IRAS/IRAS.25mu	217265.49	3.893×10^{-15}	2.336×10^{-16}	IRAS	-
WISE/WISE.W4	220883.00	3.457×10^{-15}	3.821×10^{-17}	WISE	-
IRAS/IRAS.60mu	519887.31	2.241×10^{-16}	2.016×10^{-17}	IRAS	-
AKARI/FIS.N60	629506.72	2.264×10^{-16}	2.133×10^{-17}	AKARI/FIS	-
AKARI/FIS.WIDE-S	769035.21	7.538×10^{-17}	2.443×10^{-18}	AKARI/FIS	-
SDSS	7634.91	9.412×10^{-11}	-	SDSS	-
SDSS	6246.98	1.836×10^{-10}	-	SDSS	-
SDSS	4819.97	4.207×10^{-10}	-	SDSS	-
SDSS	9017.94	5.419×10^{-11}	-	SDSS	-
SDSS	3518.98	6.754×10^{-10}	-	SDSS	-
HIP	4020.01	5.343×10^{-10}	-	HIP	-
HIP	5318.96	3.041×10^{-10}	-	HIP	-
HIP	4203.01	5.719×10^{-10}	-	HIP	-
APEX	8695652.17	1.452×10^{-20}	2.857×10^{-21}	APEX	-
TD	1565.00	3.395×10^{-09}	1.800×10^{-11}	TD	-
TD1	2365.00	1.555×10^{-09}	1.900×10^{-12}	TD1	-
Clark et al., 1998	3.5×10^{9}	1.469×10^{-28}	-	ATCA	-
Clark et al., 1998	6.3×10^{9}	9.070×10^{-29}	-	ATCA	-

A.5 α Arae polarimetric data

Table A.6 - : Polarimetric data from OPD (54260 < MJD < 57624) and historical data published by Serkowski, 1970 and McLean, 1979 (40085 < MJD < 42877).

MJD	Filter	P_{obs}[%]	PA_{Pobs}	σ_P[%]	σ_{PA}	MJD	Filter	P_{obs}[%]	PA_{Pobs}	σ_P[%]	σ_{PA}
54260.19	b	0.2614	145.96	0.0077	0.84	56816.22	r	0.4904	140.33	0.0171	1
54260.22	v	0.2635	142.97	0.0062	0.67	56816.22	i	0.4713	140.79	0.0038	0.23
54289.14	b	0.1488	142.38	0.0471	9.07	56817.28	b	0.5356	151.07	0.0185	0.99
54720.97	b	0.5985	145.72	0.0336	1.61	56840.24	b	0.5068	146.03	0.0205	1.16
55012.18	b	0.6397	141.52	0.0132	0.59	56840.25	v	0.5205	143.5	0.0259	1.43
55012.20	r	0.5082	142.01	0.0099	0.56	56840.26	r	0.4763	142.3	0.005	0.3
55334.30	b	0.5926	139.73	0.0244	1.18	56840.27	i	0.4789	142.36	0.0018	0.11
55334.30	v	0.6137	139.5	0.0169	0.79	56841.08	b	0.502	141.68	0.014	0.8
55334.31	r	0.5769	142.35	0.013	0.65	56841.09	v	0.5495	140.51	0.0128	0.67
55334.32	i	0.4705	143.34	0.0336	2.05	56841.09	r	0.4921	137.55	0.007	0.41
55355.21	b	0.6748	142.41	0.0089	0.38	56841.10	i	0.4706	138.22	0.0091	0.55
55355.22	v	0.5887	143.51	0.0115	0.56	56889.11	b	0.4968	143.72	0.0159	0.92
55355.23	r	0.4996	140.62	0.0151	0.87	56889.14	v	0.5416	142.39	0.0246	1.3
55355.24	i	0.4988	140.13	0.0224	1.29	56889.16	r	0.4969	142.78	0.0088	0.51
55426.03	b	0.6209	143.49	0.0145	0.67	56890.16	i	0.4177	146.24	0.0387	2.65
55426.04	v	0.605	139.49	0.0155	0.73	57142.24	b	0.4982	141.9	0.0096	0.55
55426.06	r	0.5304	144.62	0.0137	0.74	57142.25	v	0.473	141.27	0.0092	0.56
55426.07	i	0.4945	142.45	0.0158	0.92	57142.25	r	0.4472	141.44	0.0073	0.47
55441.00	i	0.4888	141.58	0.0125	0.73	57142.25	i	0.4568	141.31	0.0049	0.31
55441.01	r	0.5261	142.62	0.0097	0.53	57201.20	r	0.4648	140.14	0.0085	0.52
55441.02	v	0.5697	144.47	0.0086	0.43	57201.21	v	0.5096	136.28	0.0099	0.56
55441.02	b	0.6461	143.28	0.0134	0.59	57201.21	b	0.4979	141	0.0162	0.93
55496.90	v	0.5791	142.2	0.0076	0.38	57201.22	i	0.4421	138.45	0.0052	0.34
55496.91	r	0.5278	141.02	0.0065	0.35	57263.05	i	0.4512	140.66	0.0077	0.49
55496.91	i	0.4792	141.75	0.0089	0.53	57263.06	r	0.4983	138.96	0.0074	0.43
55496.92	b	0.5974	143.3	0.0126	0.6	57263.06	v	0.5202	141.18	0.0052	0.29
55497.94	v	0.6139	142.54	0.0065	0.3	57263.07	b	0.5218	143.01	0.0096	0.53
55497.94	r	0.5379	141.78	0.0085	0.45	57286.92	v	0.48	140.51	0.0205	1.22
55497.95	i	0.4956	141.92	0.0071	0.41	57286.93	b	0.5185	140.85	0.0141	0.78

55497.96	b	0.6107	143.62	0.0051	0.24	57286.94	r	0.4425	141.66	0.0151	0.98
55498.90	v	0.6	143.64	0.0069	0.33	57286.95	i	0.3993	140.84	0.0089	0.64
55498.91	r	0.5354	136.84	0.007	0.37	57553.15	r	0.4706	144.61	0.0128	0.78
55498.91	i	0.4843	138.15	0.005	0.3	57553.15	i	0.476	142.43	0.0118	0.71
55498.92	b	0.6035	144.63	0.0107	0.51	57553.15	v	0.5045	138.79	0.0121	0.69
55741.24	v	0.3671	142.82	0.0139	1.08	57553.16	b	0.5175	141.71	0.0069	0.38
55741.25	r	0.306	142.76	0.0135	1.26	57555.28	v	0.4745	143.13	0.0121	0.73
55741.26	i	0.3077	144.3	0.0082	0.76	57555.29	r	0.465	141.78	0.0098	0.6
55741.26	b	0.3833	144.48	0.0255	1.91	57555.30	b	0.4907	143.75	0.0094	0.55
55755.23	b	0.2728	145.52	0.0056	0.59	57577.16	i	0.4672	140.99	0.0169	1.04
55755.24	v	0.3686	140.05	0.0176	1.37	57577.16	r	0.4874	141.25	0.0095	0.56
55755.24	r	0.349	141.7	0.0068	0.56	57577.17	v	0.5182	139.7	0.012	0.66
55755.25	i	0.3719	141.11	0.0222	1.71	57577.18	b	0.5222	139.79	0.0088	0.48
55807.12	b	0.6035	139.33	0.0179	0.85	57604.05	i	0.421	143.39	0.0113	0.77
55807.13	v	0.5649	139.73	0.0076	0.39	57604.05	r	0.4714	144.11	0.0147	0.89
55807.13	r	0.4918	138.42	0.0035	0.2	57604.06	v	0.5159	145.22	0.0101	0.56
55807.14	i	0.4266	140.78	0.006	0.4	57604.06	b	0.5687	148.49	0.017	0.86
55832.00	b	0.6202	142.68	0.0052	0.24	57614.10	v	0.506	142.63	0.0162	0.92
55832.01	v	0.5487	140.67	0.0171	0.89	57614.10	r	0.506	142.09	0.0049	0.28
55832.02	r	0.4925	140.93	0.0043	0.25	57614.11	i	0.4695	142.14	0.0089	0.54
55832.03	i	0.4367	140.85	0.0039	0.26	57614.12	b	0.4938	143.66	0.0373	2.16
56052.30	b	0.6485	142.77	0.0081	0.36	57623.98	i	0.4854	141.99	0.0165	0.97
56052.30	v	0.6414	139.76	0.0098	0.44	57623.99	r	0.4682	143.07	0.0095	0.58
56052.31	r	0.5429	138.92	0.013	0.69	57623.99	v	0.5095	142.93	0.0195	1.1
56052.32	i	0.5243	138.6	0.012	0.66	57624.00	b	0.5098	144.36	0.0073	0.41
56052.32	u	0.4054	147.81	0.0227	1.6	40085	u	0.3076	-	-	-
56108.21	u	0.4842	150.99	0.0391	2.31	40100	u	0.2886	-	-	-
56108.22	b	0.626	144.84	0.03	1.37	40297	u	0.2984	-	-	-
56108.23	v	0.5897	138.99	0.024	1.17	40344	u	0.3370	-	-	-
56108.24	r	0.6127	141.57	0.0085	0.4	40349	u	0.3505	-	-	-
56108.25	i	0.5365	139.15	0.0044	0.23	40390	u	0.3520	-	-	-
56132.00	v	0.6198	142.38	0.0118	0.55	40437	u	0.3281	-	-	-
56132.01	r	0.5202	142.04	0.0364	2	40453	u	0.3581	-	-	-
56132.01	i	0.4882	145.57	0.0179	1.05	40623	u	0.2993	-	-	-

56132.02	b	0.625	142.82	0.0127	0.58	40637	u	0.3378	-	-	-
56132.03	u	0.4664	150.11	0.0171	1.05	40085.23	v	0.5578	-	-	-
56380.32	b	0.5652	139.54	0.018	0.91	40100	v	0.5814	-	-	-
56380.34	v	0.5617	139.56	0.0055	0.28	40296.92	v	0.5799	-	-	-
56380.35	r	0.5159	140.07	0.0061	0.34	40343.69	v	0.5969	-	-	-
56380.35	i	0.4945	139.36	0.0069	0.4	40348.61	v	0.6124	-	-	-
56406.24	b	0.5301	144.86	0.0118	0.64	40390.46	v	0.6296	-	-	-
56406.24	v	0.5272	141.15	0.0312	1.7	40437.23	v	0.5660	-	-	-
56406.25	r	0.4936	142.62	0.0218	1.27	40453.23	v	0.6407	-	-	-
56406.26	i	0.4857	140.35	0.0045	0.27	40623.07	v	0.5869	-	-	-
56503.13	b	0.5306	145.55	0.0138	0.75	40636.61	v	0.6799	-	-	-
56503.14	v	0.5209	141.49	0.0075	0.41	42877	v	0.5445	-	-	-
56503.15	r	0.4797	142.15	0.0122	0.73	40082.76	b	0.6644	-	-	-
56503.17	i	0.4515	139.16	0.0181	1.15	40098.76	b	0.6776	-	-	-
56517.07	b	0.5144	142	0.0141	0.79	40299.38	b	0.6907	-	-	-
56517.08	v	0.5235	141.99	0.0071	0.39	40344.92	b	0.6578	-	-	-
56517.08	r	0.4932	142.75	0.0098	0.57	40348.61	b	0.6842	-	-	-
56517.09	i	0.4587	142.41	0.0123	0.77	40389.23	b	0.6710	-	-	-
56714.33	v	0.5623	141.34	0.0197	1	40401.53	b	0.6644	-	-	-
56714.33	b	0.5562	140.27	0.0204	1.05	40452	b	0.6447	-	-	-
56714.33	i	0.4924	144.4	0.0112	0.65	40624.30	b	0.6381	-	-	-
56816.19	b	0.5916	144.31	0.0252	1.22	42877	b	0.6842	-	-	-
56816.21	v	0.506	140.52	0.009	0.51						

A.6 α Arae spectroscopic

Table A.7 - : Spectroscopic data from several sources ($43332.72 \leq MJD \leq 58008.08$.

Instrument	MJD	Instrument	MJD	Instrument	MJD
HEROS	43332.72	FEROS	52003.35	OPD	53537.31
HEROS	43810.52	FEROS	52003.36	OPD	53537.31
HEROS	43814.52	FEROS	52004.27	OPD	53537.31
HEROS	45027.91	FEROS	52004.27	OPD	54562.10
HEROS	45211.00	FEROS	52004.28	OPD	54651.22
HEROS	45221.56	FEROS	52004.28	OPD	54658.14
HEROS	45398.88	FEROS	52004.28	OPD	54658.14
HEROS	46124.00	FEROS	52004.29	OPD	54658.14
HEROS	46835.00	FEROS	52004.29	OPD	54658.14
HEROS	47795.00	FEROS	52004.29	OPD	55694.00
HEROS	48705.00	FEROS	52004.30	OPD	55854.00
HEROS	49239.00	FEROS	52004.30	Hanuschik et al., 1996	56147.11
HEROS	51281.00	FEROS	52004.30	Hanuschik et al., 1996	56561.50
HEROS	51300.36	FEROS	52004.31	Hanuschik et al., 1996	56714.30
HEROS	51304.40	FEROS	52004.31	Hanuschik et al., 1996	56755.25
HEROS	51305.43	FEROS	52004.31	Hanuschik et al., 1996	56854.12
HEROS	51306.39	FEROS	52004.31	Hanuschik et al., 1996	56943.96
HEROS	51307.39	FEROS	52004.32	Dachs et al., 1981	57266.02
HEROS	51308.40	FEROS	52004.32	Dachs et al., 1981	57553.18
HEROS	51309.35	FEROS	52004.32	Dachs et al., 1981	57581.08
HEROS	51310.43	FEROS	52004.33	Dachs et al., 1981	57612.04
HEROS	51311.40	FEROS	52004.33	Dachs et al., 1981	57954.53
HEROS	51312.44	FEROS	52127.10	Dachs et al., 1981	57973.05
HEROS	51313.40	FEROS	52127.11	FEROS	51366.37
HEROS	51314.42	FEROS	52127.11	FEROS	51367.37
HEROS	51316.42	FEROS	52127.11	FEROS	51369.35
HEROS	51319.42	FEROS	52127.12	FEROS	51648.21
HEROS	51320.43	FEROS	52127.12	FEROS	51648.25

HEROS	51321.40	FEROS	52127.13	FEROS	51648.26
HEROS	51327.36	FEROS	52127.13	FEROS	51648.33
HEROS	51329.42	FEROS	52127.13	FEROS	52002.21
HEROS	51330.40	FEROS	52127.14	FEROS	52002.22
HEROS	51331.43	FEROS	52127.14	FEROS	52002.23
HEROS	51332.41	FEROS	52127.14	FEROS	52002.24
HEROS	51333.32	FEROS	52127.15	FEROS	52002.25
HEROS	51334.44	FEROS	52127.15	FEROS	52002.26
HEROS	51335.34	FEROS	52127.15	FEROS	52002.27
HEROS	51336.34	FEROS	52127.16	FEROS	52002.28
HEROS	51338.35	FEROS	52127.16	FEROS	52002.29
HEROS	51339.41	FEROS	52127.17	FEROS	52002.30
HEROS	51340.41	FEROS	52127.17	FEROS	52002.31
HEROS	51341.39	FEROS	52127.17	FEROS	52002.32
HEROS	51343.42	FEROS	52127.18	FEROS	52003.32
BESS	51347.36	FEROS	52127.18	FEROS	52003.32
BESS	51349.32	FEROS	52127.18	FEROS	52003.33
UVES	51350.38	FEROS	52127.19	FEROS	52003.34
FEROS	51352.38	FEROS	52127.19	FEROS	52003.34
FEROS	51353.33	HARPS	52127.20	FEROS	52003.34
FEROS	51354.39	HARPS	52127.20	FEROS	52003.35
FEROS	51355.39	HARPS	52127.21	Banerjee et al., 2000	58008.08
FEROS	51360.36	OPD	52127.21	Banerjee et al., 2000	58008.08
FEROS	51363.38	OPD	52127.21	BESS	55443.41
FEROS	51364.36	OPD	52127.22	BESS	54562.62
FEROS	52003.35	OPD	52776.25	BESS	56168.06

A.7 β CMi polarimetric data

Table A.8 - : Polarimetric data from OPD-LNA taken with the IAGPOL polarimeter.

MJD	Filter	$P_{\rm obs}[\%]$	$PA_{\rm Pobs}$	$\sigma_P[\%]$	σ_{PA}
55855.33	b	0.0365	65.33	0.0038	2.98
55855.34	r	0.0512	88.90	0.0040	2.24
55855.37	i	0.0714	78.06	0.0195	7.82
56022.03	i	0.0488	1.53	0.0151	8.87
56022.04	b	0.0194	72.54	0.0129	19.05
56022.05	v	0.0288	92.40	0.0152	15.12
56022.06	r	0.0425	17.03	0.0171	11.53
56610.19	v	0.0488	3.48	0.0111	6.52
56610.22	i	0.0567	0.00	0.0042	2.12
56610.23	r	0.0526	3.66	0.0242	13.18
56610.25	b	0.0637	1.90	0.0351	15.79
56714.09	v	0.1242	85.81	0.0127	2.93
56726.08	b	0.0601	75.52	0.0260	12.39
56726.09	v	0.0410	75.25	0.0233	16.28
56726.10	r	0.0656	80.67	0.0239	10.44
56726.11	i	0.0379	5.24	0.0209	15.8
56946.28	b	0.0826	86.66	0.0070	2.43
56946.30	v	0.0401	106.55	0.0152	10.86
56946.31	r	0.0601	79.15	0.0084	4.00
56946.32	i	0.0306	1.22	0.0136	12.73
56981.29	v	0.0823	3.00	0.0267	9.29
56981.30	r	0.0624	6.25	0.0089	4.09
56981.30	i	0.0505	12.85	0.0144	8.17

Table A.9 - : Spectro-polarimetric data from HPOL.

Data ID	Obs. Start Time	Exp. Time
bet-cmi_19910422	1991-04-22 02:07:32	3277
bet-cmi_19950208b	1995-02-08 00:00:00	768
bet-cmi_19950208r	1995-02-08 00:00:00	640
bet-cmi_19950325b	1995-03-25 00:00:00	1920
bet-cmi_19950325r	1995-03-25 00:00:00	640
bet-cmi_20000207r	2000-02-07 00:00:00	600
bet-cmi_20000212b	2000-02-12 00:00:00	1536
bet-cmi_20000212r	2000-02-12 00:00:00	640

Table A.10 - Interferometric observations of α Arae from VLTI.

MJD	Instrument	MJD	Instrument
57485.40	PIONIER	54236.00	AMBER
56920.96	PIONIER	54257.00	AMBER
56921.02	PIONIER	54260.00	AMBER
56921.06	PIONIER	54309.00	AMBER
56393.40	PIONIER	54350.00	AMBER
56393.42	PIONIER	54375.00	AMBER
56404.35	PIONIER	55734.00	AMBER
56404.38	PIONIER	55739.00	AMBER
53425.00	AMBER	55741.00	AMBER
54438.00	AMBER		

A.8 Selected stars.

Table A.11 - : Stars used in the validation process.

main ID	Star	π (mas)	σ_π (mas)	v sin i (km s^{-1})	$\sigma_{v \sin i}$ (mas)	Sp. type (Simbad)	RA (J2000) (h:m:s)	DEC (J2000) (^{o}, ', ")	Ref. v sin i
* π And	HD3369	5.939	0.3628	25	-	B5V	00 36 52.8512	+33 43 09.651	Abt et al., 2002
* ν And	HD4727	6.9259	0.46	20	-	B5V	00 49 48.8460	+41 04 44.045	Abt et al., 2002
* π Ari	HD17543	4.18	0.69	51	20	B6V	02 49 17.5592	+17 27 51.516	Huang et al., 2010
HD 18537	HD18537	6.9745	0.1205	90	-	B7V	03 00 52.2119	+52 21 06.247	Abt et al., 2002
* 53 Ari	HD19374	3.1669	0.0881	0	24	B1.5V	03 07 25.6726	+17 52 47.971	Huang et al., 2010
* ksi Tau	HD21364	16.4494	0.9165	231	-	B9Vn	03 27 10.1384	+09 43 57.862	Royer et al., 2007
* ψ Per	HD22192	5.9627	0.873	200	-	B5Ve	03 36 29.3784	+48 11 33.508	Abt et al., 2002
* τ05 Eri	HD22203	12.4912	0.5487	73	-	B9V	03 33 47.2721	-21 37 58.375	Royer et al., 2007
* o Per	HD22951	3.031	0.2274	10	-	B0.5V	03 42 22.6477	+33 57 54.111	Abt et al., 2002
* 18 Tau	HD23324	7.3405	0.1237	185	-	B8V	03 45 09.7395	+24 50 21.349	Abt et al., 2002
* 24 Eri	HD23363	4.8394	0.1452	140	-	B7IV	03 44 30.5099	-01 09 47.120	Abt et al., 2002
* 21 Tau	HD23432	7.5658	0.1321	160	-	B8V	03 45 54.4767	+24 33 16.241	Abt et al., 2002
* 28 Tau	HD23862	7.7229	0.2039	220	-	B8Vne	03 49 11.2175	+24 08 12.172	Abt et al., 2002
* c Per	HD25940	5.9344	0.3278	155	-	B3Ve	04 08 39.6888	+47 42 45.042	Abt et al., 2002
HD 26326	HD26326	4.9039	0.1056	5	-	B5IV	04 09 17.8360	-16 23 09.075	Abt et al., 2002
* 62 Tau	HD27778	4.4566	0.0474	101	10	B3V	04 23 59.7629	+24 18 03.527	Huang et al., 2010
V* HU Tau	HD29365	7.7218	0.0851	70	-	B8V	04 38 15.8302	+20 41 05.011	Abt et al., 2002
* τ Tau	HD29763	10.7072	0.6001	100	-	B3V	04 42 14.6926	+22 57 24.894	Uesugi and Fukuda, 1970
HD 31726	HD31726	2.5701	0.1017	26	8	B2V	04 57 44.6843	-14 13 54.892	Bragança et al., 2012

* ψ Eri	HD32249	3.9274	0.2514	52	8	B3IV	05 01 26.3456	-07 10 26.271	Bragança et al., 2012
* 11 Cam	HD32343	4.6189	0.162	55	-	B3Ve	05 06 08.4523	+58 58 20.548	Abt et al., 2002
* 105 Tau	HD32991	3.0763	0.0908	175	-	B2Ve	05 07 55.4350	+21 42 17.350	Abt et al., 2002
HD 34748	HD34748	2.6618	0.0992	295	-	B3V	05 19 35.2871	-01 24 42.883	Abt et al., 2002
HD 34798	HD34798	4.1424	0.0643	30	-	B5Vs	05 19 17.4368	-18 31 11.696	Abt et al., 2002
* 113 Tau	HD35532	2.7358	0.0923	281	7	B2Vn	05 26 05.7215	+16 42 00.584	Huang et al., 2010
* κ Pic	HD35580	4.8587	0.0765	264	-	B8/9V	05 22 22.1470	-56 08 03.825	Royer et al., 2002
HD 35588	HD35588	2.8528	0.0774	170	-	B2V	05 25 47.0186	+00 31 12.875	Abt et al., 2002
* 115 Tau	HD35671	4.9316	0.2069	125	8	B5V	05 27 10.0943	+17 57 43.947	Huang et al., 2010
* 32 Ori	HD36267	10.77	0.64	155	-	B5V	05 30 47.0509	+05 56 53.292	Abt et al., 2002
* 35 Ori	HD36653	3.1116	0.1814	118	10	B3V	05 33 54.2872	+14 18 20.086	Bragança et al., 2012
V* VV Ori	HD36695	2.6531	0.2153	120	-	B9IV/V	05 33 31.4472	-01 09 21.859	Abt et al., 2002
V* V1046 Ori	HD37017	0.4468	0.1712	165	-	B2/3V	05 35 21.8676	-04 29 39.040	Abt et al., 2002
* c Ori	HD37018	3.69	1.2	20	-	B1V	05 35 23.1642	-04 50 18.088	Abt et al., 2002
HD 37303	HD37303	2.4339	0.1159	265	-	B2V(n)	05 37 27.3574	-05 56 18.197	Abt et al., 2002
HD 37744	HD37744	2.3209	0.0954	37	-	B2IV	05 40 37.2961	-02 49 30.847	Simón-Díaz and Herrero, 2014
* ζ Tau	HD37202	7.33	0.82	125	-	B1IVe_shell	05 37 38.6870	+21 08 32.834	Abt et al., 2002
* ω Ori	HD37490	3.1596	0.3589	180	-	B3Ve	05 39 11.1455	+04 07 17.290	Abt et al., 2002
* α Col	HD37795	7.2328	1.0229	195	-	B9Ve	05 39 38.9390	-34 04 26.750	Abt et al., 2002
* 57 Ori	HD39698	1.5872	0.1401	115	-	B2V	05 54 56.6871	+19 44 58.629	Abt et al., 2002
* ν Ori	HD41753	6.7656	0.3931	30	-	B3V	06 07 34.3252	+14 46 06.511	Abt et al., 2002
* f01 Ori	HD42545	4.4787	0.28	245	-	B5Vn	06 12 03.2806	+16 07 49.458	Abt et al., 2002

* ζ CMa	HD44402	9.9047	0.7158	25	-	B2.5V	06 20 18.7878	-30 03 48.121	Abt et al., 2002
HD 44506	HD44506	1.6226	0.1024	241	11	B3V	06 20 36.2399	-34 08 38.915	Bragança et al., 2012
HD 47054	HD47054	4.4762	0.128	220	-	B8IVe	06 36 35.3296	-05 12 40.100	Abt et al., 2002
* 16 Mon	HD48977	3.1699	0.1518	20	-	B3V	06 46 32.4144	+08 35 13.781	Abt et al., 2002
HD 49662	HD49662	6.17	0.75	90	-	B7IV	06 48 57.7366	-15 08 41.000	Abt et al., 2002
* κ CMa	HD50013	4.7425	0.3295	210	-	B1.5Ve	06 49 50.4601	-32 30 30.532	Abt et al., 2002
* ω CMa	HD56139	4.8816	0.4238	105	-	B2IV-Ve	07 14 48.6531	-26 46 21.556	Abt et al., 2002
* β CMi	HD58715	20.3535	1.222	210	-	B8Ve	07 27 09.0497	+08 17 21.488	Abt et al., 2002
HD 60098	HD60098	3.549	0.0422	41	5	B3V	07 31 25.7671	-36 09 11.729	Bragança et al., 2012
HD 60848	HD60848	0.3128	0.0839	362	-	O8:V:pe	07 37 05.7328	+16 54 15.303	Uesugi and Fukuda, 1970
HD 60855	HD60855	2.0486	0.1038	244	8	B2Ve	07 36 03.8931	-14 29 33.982	Huang and Gies, 2006
HD 67536	HD67536	2.3923	0.0519	292	-	B2Vn	08 04 42.9316	-62 50 10.842	Uesugi and Fukuda, 1970
* r Pup	HD68980	2.1661	0.1724	167	-	B2ne	08 13 29.5169	-35 53 58.260	Uesugi and Fukuda, 1970
HD 71459	HD71459	4.0543	0.1218	38	1	B3/5IV	08 25 51.9109	-42 09 11.067	Bragança et al., 2012
HD 74234	HD74234	1.3915	0.0511	192	11	B2IV	08 40 53.3999	-48 13 31.814	Bragança et al., 2012
* η Hya	HD74280	7.6128	0.3517	99.2	5	B3V	08 43 13.4759	+03 23 55.184	Ammler-von Eiff and Reiners, 2012
* κ Hya	HD83754	8.8837	0.3752	150	-	B3/5IV/V	09 40 18.3596	-14 19 56.215	Abt et al., 2002
* I Hya	HD83953	6.5733	0.2851	240	-	B5V	09 41 17.0078	-23 35 29.432	Abt et al., 2002
* α Leo	HD87901	41.13	0.35	300	-	B8IVn	10 08 22.3109	+11 58 01.951	Abt et al., 2002
* β Sex	HD90994	8.9613	0.2448	80	-	B5IV/V	10 30 17.4798	-00 38 13.303	Abt et al., 2002
* tet Car	HD93030	7.16	0.21	202	-	B0Vp	10 42 57.3575	-64 23 39.865	Uesugi and Fukuda, 1970
* π Cen	HD98718	9.12	0.34	350	-	B5Vn	11 21 00.4061	-54 29 27.665	Uesugi and Fukuda, 1970

* ρ Cen	HD105937	11.8348	0.3746	147	-	B3V	12 11 39.1280	-52 22 06.406	Uesugi and Fukuda, 1970
* ζ Cru	HD106983	10.4901	0.3308	188	-	B2/3V	12 18 26.2361	-64 00 11.114	Uesugi and Fukuda, 1970
HD 110432	HD110432	2.3834	0.1228	213	-	B0.5IVpe	12 42 50.2655	-63 03 31.048	Bernacca and Perinotto, 1970
HD 110956	HD110956	10.0283	0.3413	22	3	B2/3V	12 46 22.7143	-56 29 19.738	Bragança et al., 2012
* chi Cen	HD122980	7.7536	0.3819	16	7	B2V	14 06 02.7692	-41 10 46.676	Bragança et al., 2012
* ρ Lup	HD128345	10.1866	0.5381	240	-	B3/4V	14 37 53.2256	-49 25 33.025	Uesugi and Fukuda, 1970
* b Cen	HD129116	10.2435	0.6426	197	-	B3V	14 41 57.5930	-37 47 36.588	Uesugi and Fukuda, 1970
* λ Lup	HD133955	3.5406	0.5961	169	-	B3V	15 08 50.6128	-45 16 47.500	Uesugi and Fukuda, 1970
* mu. Lup	HD135734	9.72	0.71	308	-	B8Ve	15 18 32.0229	-47 52 30.995	Uesugi and Fukuda, 1970
* β Lib	HD135742	17.62	0.16	250	-	B8Vn	15 17 00.4138	-09 22 58.491	Abt et al., 2002
* phi02 Lup	HD136664	6.28	0.2	141	6	B4V	15 23 09.3275	-36 51 30.875	Bragança et al., 2012
* ζ04 Lib	HD138485	4.5302	0.1902	203	19	B3V	15 32 55.2197	-16 51 10.247	Bragança et al., 2012
* τ Lib	HD139365	4.1418	0.7621	100	-	B2.5V	15 38 39.3637	-29 46 39.988	Uesugi and Fukuda, 1970
* b Sco	HD141637	6.8954	0.2438	225	-	B1.5Vn	15 50 58.7451	-25 45 04.662	Abt et al., 2002
* 4 Her	HD142926	5.8913	0.0804	275	-	B9pe	15 55 30.5918	+42 33 58.287	Abt et al., 2002
* ω Sco	HD144470	7.0596	0.3975	95	7	B1V	16 06 48.4226	-20 40 09.118	Bragança et al., 2012
* ν Sco	HD145502	6.88	0.76	115	-	B2V	16 11 59.7356	-19 27 38.536	Abt et al., 2002
* 25 Her	HD148283	12.9109	0.1359	280	-	A5V	16 25 24.1681	+37 23 38.579	Royer et al., 2007
* i Sco	HD148605	8.5602	0.3723	169	4	B3V	16 30 12.4745	-25 06 54.811	Bragança et al., 2012
* τ Sco	HD149438	5.1232	1.11	3	2	B0.2V	16 35 52.9508	-28 12 57.730	Bragança et al., 2012
HD 155806	HD155806	1.0057	0.1306	211	-	O7.5V((f))z(e)	17 15 19.2484	-33 32 54.307	Uesugi and Fukuda, 1970
V* U Oph	HD156247	3.7432	0.1307	50	-	B3V	17 16 31.7132	+01 12 37.996	Abt et al., 2002

* α Ara	HD158427	4.1865	1.2735	288	-	B2Vne	17 31 50.5006	-49 52 34.093	Uesugi and Fukuda, 1970
* 66 Oph	HD164284	6.9762	0.5037	250	-	B2Ve	18 00 15.7981	+04 22 07.139	Abt et al., 2002
* λ Pav	HD173948	4.8003	0.4471	217	-	B2Ve	18 52 13.0368	-62 11 15.339	Uesugi and Fukuda, 1970
* β01 Sgr	HD181454	12.4748	0.6401	94	-	B9V	19 22 38.2988	-44 27 32.347	Uesugi and Fukuda, 1970
HD 183362	HD183362	1.7248	0.0538	220	-	B3Ve	19 27 36.3963	+37 56 28.304	Abt et al., 2002
* β Cyg B	HD183914	8.3779	0.1696	215	-	B8Ve	19 30 45.3960	+27 57 54.973	Abt et al., 2002
HD 183656	HD183656	3.6705	0.0607	186	-	B7III	19 30 33.1219	+03 26 39.858	Royer et al., 2002
* ι Cyg	HD184006	27.0603	0.3278	240	-	A5V	19 29 42.3595	+51 43 47.206	Royer et al., 2007
* 12 Vul	HD187811	5.7966	0.2206	195	-	B2.5Ve	19 51 04.1087	+22 36 36.165	Abt et al., 2002
* 57 Aql A	HD188293	7.2437	0.1495	190	-	B7Vn	19 54 37.6522	-08 13 38.244	Abt et al., 2002
* 23 Cyg	HD188665	5.9155	0.1728	105	-	B5V	19 53 17.3787	+57 31 24.480	Abt et al., 2002
* 17 Vul	HD190993	6.6847	0.2047	75	-	B3V	20 06 53.4080	+23 36 51.927	Abt et al., 2002
* b02 Cyg	HD191610	5.2947	0.2255	250	-	B2.5Ve	20 09 25.6190	+36 50 22.596	Abt et al., 2002
* 20 Vul	HD192044	2.7904	0.0726	205	-	B7Ve	20 12 00.7017	+26 28 43.698	Abt et al., 2002
HD 192685	HD192685	7.8952	0.5496	160	-	B3V	20 15 15.8976	+25 35 31.045	Abt et al., 2002
* λ Cyg	HD198183	4.24	0.43	100	-	B5V	20 47 24.5376	+36 29 26.573	Abt et al., 2002
HD 198625	HD198625	2.2256	0.0456	250	-	B4Ve	20 49 54.6433	+46 39 40.814	Abt et al., 2002
* 57 Cyg	HD199081	6.688	0.2395	30	-	B5V	20 53 14.7592	+44 23 14.138	Abt et al., 2002
* ϵ Cap	HD205637	6.5495	0.7048	210	-	B3V	21 37 04.8309	-19 27 57.627	Abt et al., 2002
* 16 Peg	HD208057	5.8309	0.264	110	-	B3Ve	21 53 03.7679	+25 55 30.506	Abt et al., 2002
* o Aqr	HD209409	6.9205	0.2583	205	-	B7IVe	22 03 18.8435	-02 09 19.320	Abt et al., 2002
HD 209522	HD209522	3.0964	0.119	260	-	B4IVe	22 04 36.7670	-26 49 20.492	Abt et al., 2002

HD 214240	HD214240	1.5419	0.067	55	-	B3V	22 35 53.3823	+50 04 14.835	Abt et al., 2002
* ϵ PsA	HD214748	8.0981	0.3582	185	-	B8Ve	22 40 39.3446	-27 02 36.967	Abt et al., 2002
* ι And	HD222173	7.8999	0.3357	67	5	B8V	23 38 08.1998	+43 16 05.073	Bailey and Landstreet, 2013
* ϵ Tuc	HD224686	9.2645	0.2741	174	-	B8V	23 59 54.9800	-65 34 37.666	Uesugi and Fukuda, 1970

A.9 Inferred parameters of the survey of stars

Table A.12 - : Stellar parameters and $E(B-V)$ inferred from the UV domain.

star	$\log(g)$ (dex)	W	$t/t_{\rm ms}$	$T_{\rm eff}$ (K)	L ($L_\odot$)	$R_{\rm pole}$ ($R_\odot$)	i ($^{\rm o}$)	$\beta_{\rm GD}$	d (pc)	$E(B-V)$ (mag)
HD3369	$3.987^{+0.000}_{-0.000}$	$0.76^{+0.09}_{-0.07}$	$0.70^{+0.04}_{-0.08}$	$17553.53^{+295.40}_{-280.61}$	$1450.40^{+142.19}_{-125.89}$	$4.13^{+0.06}_{-0.05}$	$3.99^{+0.49}_{-0.46}$	$0.21^{+-0.03}_{-0.03}$	$182.56^{+9.96}_{-8.41}$	$0.06^{+0.01}_{-0.01}$
HD4727	$3.980^{+0.001}_{-0.001}$	$0.04^{+0.01}_{-0.01}$	$0.72^{+0.03}_{-0.04}$	$17794.49^{+219.79}_{-236.09}$	$1607.06^{+115.22}_{-117.12}$	$4.23^{+0.04}_{-0.05}$	$62.85^{+18.55}_{-21.61}$	$0.25^{+-0.00}_{-0.00}$	$187.84^{+6.12}_{-5.56}$	$0.03^{+0.00}_{-0.00}$
HD17543	$4.074^{+0.004}_{-0.004}$	$0.44^{+0.22}_{-0.24}$	$0.56^{+0.14}_{-0.12}$	$18941.41^{+632.04}_{-625.03}$	$1733.12^{+360.91}_{-308.48}$	$3.88^{+0.11}_{-0.12}$	$14.86^{+19.48}_{-6.15}$	$0.24^{+-0.01}_{-0.01}$	$215.36^{+28.62}_{-25.68}$	$0.18^{+0.01}_{-0.01}$
HD18537	$4.089^{+0.001}_{-0.001}$	$0.21^{+0.27}_{-0.04}$	$0.58^{+0.11}_{-0.11}$	$15694.46^{+482.16}_{-499.83}$	$577.04^{+104.27}_{-94.11}$	$3.26^{+0.07}_{-0.08}$	$58.81^{+20.53}_{-36.74}$	$0.25^{+0.00}_{-0.00}$	$154.15^{+21.25}_{-18.71}$	$0.13^{+0.01}_{-0.01}$
HD19374	$4.317^{+0.002}_{-0.002}$	$0.05^{+0.06}_{-0.03}$	$0.01^{+0.02}_{-0.01}$	$27546.15^{+681.45}_{-648.02}$	$7718.59^{+1204.99}_{-1021.78}$	$3.87^{+0.09}_{-0.09}$	$41.15^{+38.93}_{-27.08}$	$0.25^{+0.00}_{-0.00}$	$377.29^{+20.72}_{-17.88}$	$0.19^{+0.01}_{-0.01}$
HD21364	$4.367^{+0.000}_{-0.000}$	$0.32^{+0.02}_{-0.03}$	$0.01^{+0.01}_{-0.01}$	$15573.43^{+136.86}_{-139.48}$	$257.44^{+13.51}_{-13.24}$	$2.21^{+0.02}_{-0.02}$	$78.37^{+8.47}_{-10.65}$	$0.24^{+-0.01}_{-0.01}$	$83.51^{+1.34}_{-1.92}$	$0.08^{+0.01}_{-0.01}$
HD22192	$3.829^{+0.002}_{-0.001}$	$0.71^{+0.21}_{-0.20}$	$0.86^{+0.07}_{-0.10}$	$17789.69^{+572.97}_{-526.07}$	$2394.24^{+454.46}_{-366.24}$	$5.16^{+0.12}_{-0.12}$	$41.76^{+26.66}_{-11.60}$	$0.22^{+-0.03}_{-0.03}$	$179.21^{+6.99}_{-6.94}$	$0.15^{+0.01}_{-0.01}$
HD22203	$4.119^{+0.000}_{-0.000}$	$0.17^{+0.15}_{-0.03}$	$0.55^{+0.04}_{-0.06}$	$12880.64^{+97.27}_{-90.94}$	$181.68^{+7.65}_{-6.87}$	$2.71^{+0.02}_{-0.01}$	$64.66^{+17.57}_{-35.46}$	$0.25^{+-0.00}_{-0.00}$	$90.14^{+1.69}_{-1.77}$	$0.03^{+0.00}_{-0.00}$
HD22951	$4.064^{+0.003}_{-0.001}$	$0.02^{+0.00}_{-0.00}$	$0.55^{+0.02}_{-0.03}$	$27798.42^{+562.08}_{-313.27}$	$16466.88^{+2301.40}_{-1166.00}$	$5.55^{+0.14}_{-0.08}$	$65.24^{+7.74}_{-3.10}$	$0.25^{+-0.00}_{-0.00}$	$309.70^{+14.94}_{-14.52}$	$0.23^{+0.00}_{-0.01}$
HD23324	$4.350^{+0.002}_{-0.002}$	$0.37^{+0.11}_{-0.05}$	$0.04^{+0.05}_{-0.03}$	$14855.50^{+205.89}_{-173.54}$	$209.19^{+17.00}_{-13.55}$	$2.19^{+0.03}_{-0.02}$	$58.19^{+16.78}_{-16.28}$	$0.24^{+-0.01}_{-0.01}$	$121.81^{+5.78}_{-4.75}$	$0.11^{+0.01}_{-0.01}$
HD23363	$3.981^{+0.001}_{-0.001}$	$0.48^{+0.28}_{-0.15}$	$0.70^{+0.06}_{-0.14}$	$14801.03^{+233.06}_{-214.97}$	$558.95^{+48.69}_{-42.19}$	$3.60^{+0.04}_{-0.04}$	$39.37^{+29.74}_{-15.65}$	$0.24^{+-0.01}_{-0.01}$	$196.45^{+8.95}_{-9.44}$	$0.06^{+0.01}_{-0.01}$
HD23432	$4.366^{+0.002}_{-0.001}$	$0.34^{+0.10}_{-0.06}$	$0.03^{+0.04}_{-0.02}$	$14396.81^{+218.60}_{-211.13}$	$169.10^{+15.14}_{-13.43}$	$2.10^{+0.03}_{-0.02}$	$55.20^{+26.10}_{-15.76}$	$0.24^{+-0.01}_{-0.01}$	$122.66^{+5.84}_{-4.75}$	$0.13^{+0.01}_{-0.01}$
HD23862	$3.979^{+0.001}_{-0.001}$	$0.68^{+0.24}_{-0.15}$	$0.71^{+0.07}_{-0.10}$	$13109.42^{+335.04}_{-383.11}$	$291.29^{+40.48}_{-41.34}$	$3.32^{+0.05}_{-0.06}$	$53.14^{+27.03}_{-15.96}$	$0.22^{+-0.02}_{-0.03}$	$117.10^{+4.21}_{-4.25}$	$0.09^{+0.02}_{-0.02}$
HD25940	$4.181^{+0.002}_{-0.004}$	$0.38^{+0.23}_{-0.12}$	$0.33^{+0.17}_{-0.18}$	$24179.70^{+768.97}_{-970.74}$	$5279.61^{+1141.62}_{-1192.23}$	$4.15^{+0.15}_{-0.19}$	$41.33^{+31.51}_{-17.09}$	$0.24^{+-0.00}_{-0.01}$	$146.15^{+3.53}_{-3.49}$	$0.27^{+0.02}_{-0.02}$
HD26326	$4.016^{+0.002}_{-0.000}$	$0.01^{+0.01}_{-0.00}$	$0.69^{+0.05}_{-0.06}$	$16463.26^{+704.43}_{-367.69}$	$932.95^{+261.58}_{-117.04}$	$3.76^{+0.15}_{-0.08}$	$58.85^{+18.74}_{-25.86}$	$0.25^{+-0.00}_{-0.00}$	$203.68^{+14.96}_{-11.09}$	$0.05^{+0.02}_{-0.01}$

HD27778	$3.831^{+0.003}_{-0.003}$	$0.58^{+0.28}_{-0.31}$	$0.85^{+0.09}_{-0.18}$	$15762.72^{+1220.70}_{-943.96}$	$1210.58^{+618.40}_{-351.50}$	$4.68^{+0.28}_{-0.22}$	$24.78^{+28.39}_{-8.48}$	$0.23^{+-0.01}_{-0.01}$	$254.72^{+40.28}_{-50.07}$	$0.40^{+0.03}_{-0.03}$
HD29365	$4.385^{+0.000}_{-0.000}$	$0.15^{+0.03}_{-0.02}$	$0.00^{+0.01}_{-0.00}$	$12152.84^{+80.01}_{-73.84}$	$62.55^{+2.25}_{-2.02}$	$1.79^{+0.01}_{-0.01}$	$47.82^{+19.15}_{-5.50}$	$0.25^{+-0.00}_{-0.00}$	$126.42^{+0.19}_{-0.72}$	$0.08^{+0.01}_{-0.01}$
HD29763	$4.356^{+0.000}_{-0.000}$	$0.18^{+0.03}_{-0.02}$	$0.00^{+0.00}_{-0.00}$	$19332.49^{+52.84}_{-72.66}$	$901.94^{+14.84}_{-20.11}$	$2.68^{+0.01}_{-0.01}$	$53.80^{+17.69}_{-7.40}$	$0.25^{+-0.00}_{-0.00}$	$187.10^{+0.48}_{-1.14}$	$0.05^{+0.00}_{-0.00}$
HD31726	$4.172^{+0.002}_{-0.002}$	$0.08^{+0.14}_{-0.03}$	$0.37^{+0.14}_{-0.24}$	$24139.37^{+580.32}_{-579.37}$	$5316.76^{+855.29}_{-758.25}$	$4.18^{+0.11}_{-0.12}$	$33.47^{+36.72}_{-22.63}$	$0.25^{+0.00}_{-0.00}$	$483.39^{+50.49}_{-65.04}$	$0.02^{+0.01}_{-0.01}$
HD32249	$4.159^{+0.001}_{-0.001}$	$0.31^{+0.39}_{-0.20}$	$0.41^{+0.13}_{-0.20}$	$21743.36^{+319.61}_{-343.33}$	$3017.43^{+273.38}_{-272.66}$	$3.88^{+0.06}_{-0.06}$	$16.60^{+37.58}_{-9.15}$	$0.25^{+0.00}_{-0.00}$	$225.72^{+13.40}_{-12.09}$	$0.04^{+0.00}_{-0.00}$
HD32343	$4.052^{+0.004}_{-0.001}$	$0.76^{+0.04}_{-0.62}$	$0.61^{+0.17}_{-0.07}$	$18909.01^{+730.74}_{-269.85}$	$1831.06^{+439.07}_{-144.64}$	$4.00^{+0.13}_{-0.05}$	$8.79^{+41.69}_{-1.19}$	$0.22^{+-0.03}_{-0.01}$	$228.65^{+11.13}_{-8.43}$	$0.12^{+0.01}_{-0.01}$
HD32991	$4.025^{+0.003}_{-0.003}$	$0.56^{+0.03}_{-0.03}$	$0.60^{+0.05}_{-0.08}$	$24347.15^{+424.76}_{-445.39}$	$8427.84^{+985.89}_{-949.15}$	$5.17^{+0.11}_{-0.12}$	$35.95^{+8.17}_{-8.03}$	$0.23^{+-0.02}_{-0.02}$	$283.75^{+15.03}_{-22.98}$	$0.49^{+0.00}_{-0.00}$
HD34748	$4.324^{+0.001}_{-0.001}$	$0.45^{+0.02}_{-0.03}$	$0.00^{+0.01}_{-0.00}$	$26389.03^{+192.38}_{-246.84}$	$6006.26^{+269.01}_{-332.40}$	$3.72^{+0.03}_{-0.04}$	$67.53^{+14.78}_{-10.84}$	$0.24^{+-0.01}_{-0.01}$	$392.26^{+2.10}_{-4.28}$	$0.19^{+0.00}_{-0.00}$
HD34798	$4.260^{+0.001}_{-0.000}$	$0.07^{+0.12}_{-0.02}$	$0.23^{+0.13}_{-0.12}$	$17570.92^{+522.41}_{-455.31}$	$686.12^{+130.56}_{-100.42}$	$2.83^{+0.08}_{-0.07}$	$44.29^{+34.67}_{-28.87}$	$0.25^{+0.00}_{-0.00}$	$266.62^{+28.37}_{-22.11}$	$0.04^{+0.01}_{-0.01}$
HD35532	$4.337^{+0.001}_{-0.001}$	$0.49^{+0.07}_{-0.05}$	$0.01^{+0.02}_{-0.01}$	$21808.81^{+234.06}_{-242.72}$	$1892.70^{+130.39}_{-128.55}$	$3.06^{+0.04}_{-0.04}$	$64.09^{+12.01}_{-11.40}$	$0.24^{+-0.01}_{-0.01}$	$268.52^{+5.38}_{-7.57}$	$0.18^{+0.00}_{-0.00}$
HD35580	$4.194^{+0.001}_{-0.001}$	$0.67^{+0.12}_{-0.09}$	$0.39^{+0.09}_{-0.11}$	$13974.12^{+248.78}_{-247.89}$	$231.53^{+23.06}_{-21.34}$	$2.60^{+0.03}_{-0.03}$	$62.43^{+17.53}_{-14.59}$	$0.22^{+-0.02}_{-0.02}$	$196.62^{+9.96}_{-9.47}$	$0.02^{+0.01}_{-0.01}$
HD35588	$4.109^{+0.002}_{-0.002}$	$0.41^{+0.20}_{-0.09}$	$0.49^{+0.14}_{-0.24}$	$21344.41^{+490.17}_{-500.58}$	$3105.46^{+451.26}_{-415.10}$	$4.09^{+0.09}_{-0.10}$	$44.96^{+22.77}_{-15.57}$	$0.24^{+-0.01}_{-0.01}$	$411.47^{+48.88}_{-41.33}$	$0.05^{+0.00}_{-0.00}$
HD35671	$4.304^{+0.002}_{-0.001}$	$0.27^{+0.11}_{-0.05}$	$0.10^{+0.08}_{-0.07}$	$18046.34^{+311.27}_{-321.73}$	$714.29^{+77.80}_{-74.27}$	$2.74^{+0.05}_{-0.05}$	$50.23^{+20.83}_{-18.06}$	$0.25^{+-0.00}_{-0.00}$	$160.08^{+7.99}_{-7.76}$	$0.10^{+0.01}_{-0.01}$
HD36267	$4.231^{+0.001}_{-0.001}$	$0.38^{+0.09}_{-0.06}$	$0.29^{+0.09}_{-0.07}$	$16255.06^{+193.45}_{-196.80}$	$480.23^{+33.11}_{-31.99}$	$2.77^{+0.03}_{-0.03}$	$48.05^{+14.28}_{-10.99}$	$0.24^{+-0.01}_{-0.01}$	$98.97^{+5.09}_{-4.89}$	$0.00^{+0.00}_{-0.00}$
HD36653	$4.359^{+0.001}_{-0.001}$	$0.28^{+0.05}_{-0.09}$	$0.01^{+0.01}_{-0.01}$	$18048.01^{+194.82}_{-242.63}$	$602.01^{+41.22}_{-48.56}$	$2.52^{+0.03}_{-0.04}$	$43.63^{+36.86}_{-7.34}$	$0.25^{+-0.00}_{-0.00}$	$161.48^{+5.22}_{-5.41}$	$0.06^{+0.00}_{-0.00}$
HD36695	$3.993^{+0.011}_{-0.006}$	$0.44^{+0.31}_{-0.20}$	$0.63^{+0.13}_{-0.21}$	$24841.45^{+1075.04}_{-976.48}$	$10266.28^{+3221.33}_{-2289.24}$	$5.48^{+0.29}_{-0.25}$	$28.25^{+31.77}_{-12.26}$	$0.24^{+-0.01}_{-0.01}$	$433.71^{+66.56}_{-56.96}$	$0.06^{+0.01}_{-0.01}$
HD37017	$4.175^{+0.004}_{-0.001}$	$0.36^{+0.16}_{-0.08}$	$0.37^{+0.19}_{-0.18}$	$21398.43^{+813.39}_{-738.10}$	$2641.87^{+673.51}_{-501.25}$	$3.75^{+0.15}_{-0.13}$	$50.96^{+25.55}_{-18.61}$	$0.24^{+-0.01}_{-0.01}$	$453.24^{+73.82}_{-55.68}$	$0.06^{+0.01}_{-0.01}$

HD37018	$4.198^{+0.002}_{-0.003}$	$0.77^{+0.03}_{-0.03}$	$0.26^{+0.04}_{-0.03}$	$27127.72^{+532.50}_{-593.78}$	$10036.13^{+1325.31}_{-1251.94}$	$4.55^{+0.11}_{-0.10}$	$2.47^{+0.26}_{-0.24}$	$0.21^{+-0.04}_{-0.04}$	$314.95^{+19.17}_{-23.21}$	$0.06^{+0.00}_{-0.00}$
HD37303	$4.275^{+0.002}_{-0.001}$	$0.66^{+0.01}_{-0.01}$	$0.10^{+0.10}_{-0.07}$	$25922.78^{+674.69}_{-470.83}$	$6325.08^{+1059.93}_{-669.20}$	$3.95^{+0.10}_{-0.08}$	$54.51^{+3.77}_{-8.53}$	$0.23^{+-0.02}_{-0.02}$	$488.32^{+42.38}_{-24.92}$	$0.01^{+0.01}_{-0.01}$
HD37744	$4.069^{+0.003}_{-0.003}$	$0.06^{+0.02}_{-0.01}$	$0.56^{+0.08}_{-0.07}$	$26194.78^{+508.56}_{-542.43}$	$11359.18^{+1397.78}_{-1361.30}$	$5.19^{+0.10}_{-0.11}$	$65.76^{+13.68}_{-22.00}$	$0.25^{+-0.00}_{-0.00}$	$644.43^{+53.00}_{-41.96}$	$0.04^{+0.01}_{-0.01}$
HD37202	$3.909^{+0.020}_{-0.016}$	$0.49^{+0.35}_{-0.23}$	$0.75^{+0.15}_{-0.30}$	$22746.58^{+2169.89}_{-1820.30}$	$7694.85^{+6202.02}_{-3133.52}$	$5.66^{+0.68}_{-0.51}$	$29.53^{+34.27}_{-12.35}$	$0.24^{+-0.01}_{-0.01}$	$134.98^{+15.33}_{-14.43}$	$0.13^{+0.05}_{-0.05}$
HD37490	$3.776^{+0.014}_{-0.001}$	$0.97^{+0.03}_{-0.09}$	$0.98^{+0.01}_{-0.03}$	$22667.90^{+895.94}_{-998.01}$	$10018.19^{+3179.30}_{-2208.66}$	$6.51^{+0.40}_{-0.22}$	$26.49^{+4.58}_{-2.89}$	$0.17^{+-0.08}_{-0.08}$	$347.36^{+33.54}_{-33.91}$	$0.15^{+0.02}_{-0.01}$
HD37795	$3.717^{+0.006}_{-0.006}$	$0.70^{+0.17}_{-0.11}$	$0.94^{+0.03}_{-0.04}$	$14267.17^{+326.89}_{-290.48}$	$930.96^{+102.09}_{-84.01}$	$5.01^{+0.03}_{-0.03}$	$50.77^{+20.00}_{-13.00}$	$0.22^{+-0.03}_{-0.03}$	$80.99^{+2.06}_{-1.89}$	$0.02^{+0.01}_{-0.01}$
HD39698	$3.758^{+0.001}_{-0.008}$	$0.89^{+0.09}_{-0.12}$	$0.98^{+0.02}_{-0.04}$	$19105.21^{+481.70}_{-608.86}$	$4060.27^{+652.30}_{-580.46}$	$5.83^{+0.15}_{-0.07}$	$19.45^{+3.78}_{-2.46}$	$0.20^{+-0.05}_{-0.05}$	$703.00^{+49.82}_{-55.87}$	$0.04^{+0.01}_{-0.01}$
HD41753	$4.185^{+0.001}_{-0.001}$	$0.29^{+0.20}_{-0.23}$	$0.39^{+0.11}_{-0.15}$	$17716.00^{+257.61}_{-245.25}$	$884.51^{+79.98}_{-71.42}$	$3.17^{+0.05}_{-0.04}$	$11.26^{+52.72}_{-4.92}$	$0.25^{+-0.00}_{-0.00}$	$164.43^{+7.68}_{-6.87}$	$0.01^{+0.01}_{-0.01}$
HD42545	$4.249^{+0.001}_{-0.002}$	$0.65^{+0.09}_{-0.24}$	$0.25^{+0.07}_{-0.14}$	$16701.05^{+391.37}_{-403.49}$	$533.82^{+78.39}_{-67.93}$	$2.77^{+0.06}_{-0.05}$	$75.39^{+9.34}_{-19.41}$	$0.23^{+-0.02}_{-0.02}$	$167.88^{+9.38}_{-11.15}$	$0.03^{+0.01}_{-0.01}$
HD44402	$4.122^{+0.000}_{-0.001}$	$0.11^{+0.26}_{-0.06}$	$0.50^{+0.06}_{-0.10}$	$20312.47^{+257.48}_{-256.94}$	$2235.17^{+178.53}_{-158.78}$	$3.83^{+0.05}_{-0.04}$	$22.81^{+42.72}_{-16.15}$	$0.25^{+0.00}_{-0.00}$	$111.37^{+1.67}_{-1.61}$	$0.04^{+0.01}_{-0.01}$
HD44506	$3.776^{+0.003}_{-0.003}$	$0.92^{+0.06}_{-0.15}$	$0.98^{+0.01}_{-0.03}$	$21724.35^{+439.32}_{-406.75}$	$7892.53^{+827.75}_{-710.81}$	$6.29^{+0.06}_{-0.06}$	$40.19^{+8.13}_{-3.55}$	$0.19^{+-0.06}_{-0.06}$	$551.15^{+35.71}_{-41.47}$	$0.03^{+0.01}_{-0.01}$
HD47054	$3.834^{+0.001}_{-0.001}$	$0.69^{+0.12}_{-0.04}$	$0.85^{+0.04}_{-0.04}$	$14456.70^{+291.89}_{-299.71}$	$743.72^{+81.36}_{-77.36}$	$4.36^{+0.05}_{-0.06}$	$58.92^{+14.77}_{-9.75}$	$0.22^{+-0.03}_{-0.03}$	$256.41^{+15.87}_{-15.63}$	$0.06^{+0.01}_{-0.00}$
HD48977	$4.142^{+0.001}_{-0.001}$	$0.04^{+0.04}_{-0.01}$	$0.50^{+0.01}_{-0.02}$	$16930.28^{+122.00}_{-117.24}$	$764.96^{+34.43}_{-32.03}$	$3.22^{+0.02}_{-0.02}$	$66.76^{+16.16}_{-37.81}$	$0.25^{+-0.00}_{-0.00}$	$304.00^{+6.16}_{-5.68}$	$0.00^{+0.00}_{-0.00}$
HD49662	$4.124^{+0.002}_{-0.001}$	$0.17^{+0.02}_{-0.02}$	$0.53^{+0.12}_{-0.08}$	$15893.43^{+540.42}_{-383.32}$	$562.70^{+114.85}_{-70.84}$	$3.14^{+0.08}_{-0.06}$	$81.00^{+5.85}_{-5.58}$	$0.25^{+-0.00}_{-0.00}$	$164.19^{+24.40}_{-11.82}$	$0.05^{+0.01}_{-0.01}$
HD50013	$3.738^{+0.009}_{-0.006}$	$0.62^{+0.11}_{-0.11}$	$0.95^{+0.03}_{-0.06}$	$22039.86^{+419.24}_{-271.05}$	$9939.94^{+1508.53}_{-895.35}$	$6.86^{+0.23}_{-0.15}$	$47.22^{+14.24}_{-9.50}$	$0.23^{+-0.02}_{-0.02}$	$203.37^{+3.79}_{-3.70}$	$0.05^{+0.01}_{-0.01}$
HD56139	$3.731^{+0.009}_{-0.006}$	$0.98^{+0.01}_{-0.14}$	$0.98^{+0.01}_{-0.02}$	$17670.45^{+429.15}_{-258.62}$	$2855.55^{+317.87}_{-179.37}$	$5.72^{+0.03}_{-0.02}$	$16.85^{+2.35}_{-1.73}$	$0.16^{+-0.09}_{-0.08}$	$290.35^{+7.16}_{-9.39}$	$0.01^{+0.01}_{-0.00}$
HD58715	$4.044^{+0.000}_{-0.000}$	$0.53^{+0.16}_{-0.04}$	$0.62^{+0.04}_{-0.07}$	$13402.12^{+112.77}_{-121.25}$	$273.60^{+12.52}_{-12.96}$	$3.08^{+0.02}_{-0.02}$	$81.28^{+6.07}_{-30.27}$	$0.24^{+-0.01}_{-0.01}$	$49.64^{+0.49}_{-0.48}$	$0.03^{+0.00}_{-0.00}$

HD60098	$4.221^{+0.001}_{-0.001}$	$0.11^{+0.21}_{-0.04}$	$0.33^{+0.09}_{-0.16}$	$17039.26^{+258.67}_{-295.25}$	$636.23^{+61.48}_{-62.65}$	$2.90^{+0.05}_{-0.05}$	$39.85^{+38.02}_{-27.20}$	$0.25^{+0.00}_{-0.00}$	$287.66^{+16.14}_{-17.69}$	$0.07^{+0.00}_{-0.00}$
HD60848	$3.864^{+0.011}_{-0.011}$	$0.97^{+0.02}_{-0.06}$	$0.81^{+0.10}_{-0.13}$	$22257.01^{+827.34}_{-1229.17}$	$7758.22^{+2219.70}_{-2333.70}$	$5.94^{+0.32}_{-0.38}$	$76.44^{+7.32}_{-11.30}$	$0.17^{+-0.08}_{-0.08}$	$722.91^{+106.22}_{-111.41}$	$0.01^{+0.01}_{-0.00}$
HD60855	$3.956^{+0.007}_{-0.005}$	$0.67^{+0.21}_{-0.16}$	$0.72^{+0.13}_{-0.18}$	$22644.73^{+654.37}_{-600.24}$	$6595.34^{+1420.49}_{-1032.05}$	$5.29^{+0.22}_{-0.16}$	$45.74^{+24.94}_{-13.25}$	$0.22^{+-0.02}_{-0.02}$	$389.89^{+47.39}_{-46.28}$	$0.19^{+0.01}_{-0.01}$
HD67536	$4.201^{+0.003}_{-0.004}$	$0.59^{+0.07}_{-0.10}$	$0.29^{+0.15}_{-0.17}$	$22940.77^{+593.35}_{-619.89}$	$3717.46^{+607.49}_{-561.37}$	$3.87^{+0.10}_{-0.10}$	$59.68^{+15.41}_{-13.72}$	$0.23^{+-0.02}_{-0.02}$	$374.03^{+24.55}_{-26.61}$	$0.15^{+0.01}_{-0.01}$
HD68980	$3.762^{+0.004}_{-0.002}$	$0.81^{+0.16}_{-0.22}$	$0.95^{+0.04}_{-0.08}$	$20038.59^{+553.95}_{-459.73}$	$5440.75^{+809.54}_{-704.39}$	$6.14^{+0.09}_{-0.14}$	$30.03^{+11.02}_{-5.36}$	$0.21^{+-0.04}_{-0.04}$	$293.01^{+7.74}_{-8.07}$	$0.05^{+0.01}_{-0.01}$
HD71459	$4.349^{+0.001}_{-0.001}$	$0.11^{+0.04}_{-0.03}$	$0.02^{+0.04}_{-0.02}$	$18593.40^{+247.96}_{-261.75}$	$736.51^{+61.29}_{-60.81}$	$2.62^{+0.04}_{-0.04}$	$31.47^{+11.20}_{-9.28}$	$0.25^{+-0.00}_{-0.00}$	$241.58^{+6.91}_{-6.38}$	$0.03^{+0.01}_{-0.01}$
HD74234	$4.111^{+0.004}_{-0.002}$	$0.46^{+0.15}_{-0.10}$	$0.47^{+0.13}_{-0.15}$	$23774.35^{+800.39}_{-698.79}$	$5754.84^{+1343.59}_{-980.99}$	$4.48^{+0.18}_{-0.15}$	$43.89^{+21.33}_{-12.42}$	$0.24^{+-0.01}_{-0.01}$	$926.14^{+129.95}_{-85.97}$	$0.07^{+0.01}_{-0.01}$
HD74280	$3.979^{+0.000}_{-0.003}$	$0.24^{+0.20}_{-0.05}$	$0.71^{+0.04}_{-0.08}$	$19420.50^{+354.63}_{-417.76}$	$2564.83^{+292.03}_{-300.07}$	$4.49^{+0.08}_{-0.08}$	$50.13^{+28.05}_{-24.78}$	$0.25^{+-0.00}_{-0.00}$	$178.77^{+8.73}_{-7.78}$	$0.02^{+0.01}_{-0.01}$
HD83754	$4.314^{+0.001}_{-0.001}$	$0.36^{+0.12}_{-0.09}$	$0.09^{+0.06}_{-0.06}$	$16893.92^{+208.79}_{-167.44}$	$473.92^{+34.03}_{-26.01}$	$2.55^{+0.03}_{-0.02}$	$45.67^{+28.17}_{-13.05}$	$0.24^{+-0.01}_{-0.01}$	$137.99^{+4.61}_{-4.65}$	$0.02^{+0.00}_{-0.00}$
HD83953	$4.075^{+0.000}_{-0.001}$	$0.69^{+0.19}_{-0.15}$	$0.59^{+0.09}_{-0.13}$	$16484.28^{+312.60}_{-258.23}$	$791.45^{+92.48}_{-69.49}$	$3.46^{+0.06}_{-0.05}$	$48.46^{+23.44}_{-12.39}$	$0.22^{+-0.03}_{-0.03}$	$155.75^{+4.69}_{-4.67}$	$0.05^{+0.01}_{-0.01}$
HD87901	$4.243^{+0.001}_{-0.001}$	$0.78^{+0.05}_{-0.04}$	$0.28^{+0.05}_{-0.05}$	$13813.83^{+225.27}_{-221.70}$	$191.24^{+17.86}_{-16.41}$	$2.42^{+0.03}_{-0.03}$	$67.82^{+11.10}_{-9.45}$	$0.21^{+-0.04}_{-0.04}$	$24.38^{+0.21}_{-0.21}$	$0.03^{+0.00}_{-0.00}$
HD90994	$4.253^{+0.001}_{-0.000}$	$0.23^{+0.29}_{-0.07}$	$0.25^{+0.10}_{-0.16}$	$15434.85^{+232.42}_{-240.19}$	$338.75^{+29.98}_{-29.00}$	$2.58^{+0.03}_{-0.03}$	$38.91^{+22.04}_{-22.78}$	$0.25^{+0.00}_{-0.00}$	$122.41^{+5.47}_{-5.53}$	$0.04^{+0.01}_{-0.01}$
HD93030	$4.125^{+0.004}_{-0.004}$	$0.44^{+0.15}_{-0.12}$	$0.39^{+0.11}_{-0.14}$	$28297.86^{+603.08}_{-524.97}$	$15678.31^{+2355.82}_{-1864.05}$	$5.22^{+0.15}_{-0.13}$	$44.55^{+26.77}_{-14.00}$	$0.24^{+-0.01}_{-0.01}$	$139.04^{+4.10}_{-4.05}$	$0.03^{+0.01}_{-0.01}$
HD98718	$4.304^{+0.002}_{-0.002}$	$0.67^{+0.05}_{-0.05}$	$0.09^{+0.07}_{-0.06}$	$19711.77^{+333.69}_{-328.18}$	$1190.38^{+120.52}_{-110.14}$	$2.97^{+0.04}_{-0.04}$	$65.43^{+7.50}_{-9.22}$	$0.23^{+-0.02}_{-0.02}$	$110.15^{+4.29}_{-3.49}$	$0.03^{+0.00}_{-0.01}$
HD105937	$4.169^{+0.001}_{-0.001}$	$0.48^{+0.13}_{-0.16}$	$0.40^{+0.17}_{-0.13}$	$18387.10^{+298.17}_{-296.73}$	$1146.19^{+112.68}_{-104.39}$	$3.34^{+0.05}_{-0.05}$	$34.90^{+25.74}_{-8.96}$	$0.24^{+-0.01}_{-0.01}$	$124.71^{+10.16}_{-9.02}$	$0.00^{+0.00}_{-0.00}$
HD106983	$4.269^{+0.001}_{-0.002}$	$0.38^{+0.10}_{-0.06}$	$0.17^{+0.07}_{-0.09}$	$19690.45^{+220.17}_{-233.21}$	$1288.48^{+86.10}_{-86.69}$	$3.09^{+0.03}_{-0.03}$	$57.22^{+21.40}_{-14.82}$	$0.24^{+-0.01}_{-0.01}$	$120.19^{+4.53}_{-4.84}$	$0.00^{+0.00}_{-0.00}$
HD110432	$3.919^{+0.012}_{-0.009}$	$0.58^{+0.18}_{-0.17}$	$0.70^{+0.09}_{-0.12}$	$26716.55^{+919.51}_{-724.47}$	$19500.74^{+5289.63}_{-3562.92}$	$6.54^{+0.35}_{-0.29}$	$41.10^{+22.67}_{-12.32}$	$0.23^{+-0.02}_{-0.02}$	$344.99^{+36.60}_{-33.12}$	$0.41^{+0.01}_{-0.01}$

HD110956	$4.363^{+0.001}_{-0.001}$	$0.05^{+0.05}_{-0.01}$	$0.01^{+0.02}_{-0.01}$	$16560.38^{+185.91}_{-167.75}$	$365.58^{+24.05}_{-20.72}$	$2.33^{+0.02}_{-0.02}$	$47.37^{+29.28}_{-26.76}$	$0.25^{+0.00}_{-0.00}$	$124.11^{+2.51}_{-2.46}$	$0.01^{+0.01}_{-0.01}$
HD122980	$4.329^{+0.001}_{-0.001}$	$0.04^{+0.09}_{-0.01}$	$0.01^{+0.02}_{-0.01}$	$23206.92^{+229.17}_{-223.27}$	$2735.07^{+166.98}_{-155.67}$	$3.24^{+0.03}_{-0.03}$	$59.56^{+23.74}_{-47.31}$	$0.25^{+0.00}_{-0.00}$	$156.40^{+4.01}_{-3.63}$	$0.04^{+0.00}_{-0.00}$
HD128345	$4.322^{+0.001}_{-0.001}$	$0.74^{+0.02}_{-0.03}$	$0.08^{+0.05}_{-0.06}$	$16857.32^{+113.06}_{-113.48}$	$462.92^{+17.93}_{-17.48}$	$2.53^{+0.01}_{-0.01}$	$34.80^{+5.81}_{-4.55}$	$0.22^{+-0.03}_{-0.03}$	$95.87^{+1.73}_{-1.56}$	$0.00^{+0.00}_{-0.00}$
HD129116	$4.287^{+0.001}_{-0.001}$	$0.44^{+0.11}_{-0.08}$	$0.13^{+0.07}_{-0.08}$	$19533.85^{+206.36}_{-204.71}$	$1178.22^{+74.45}_{-69.55}$	$3.00^{+0.03}_{-0.03}$	$53.46^{+22.43}_{-15.73}$	$0.24^{+-0.01}_{-0.01}$	$105.42^{+1.84}_{-1.92}$	$0.03^{+0.00}_{-0.00}$
HD133955	$3.999^{+0.003}_{-0.002}$	$0.75^{+0.05}_{-0.22}$	$0.67^{+0.07}_{-0.11}$	$21175.32^{+489.21}_{-477.35}$	$4023.69^{+586.85}_{-516.78}$	$4.73^{+0.11}_{-0.11}$	$27.80^{+12.55}_{-3.69}$	$0.22^{+-0.03}_{-0.03}$	$216.38^{+21.80}_{-21.77}$	$0.03^{+0.00}_{-0.00}$
HD135734	$3.673^{+0.004}_{-0.005}$	$0.96^{+0.02}_{-0.04}$	$0.96^{+0.03}_{-0.04}$	$13555.47^{+176.73}_{-288.21}$	$786.88^{+48.12}_{-77.72}$	$5.10^{+0.02}_{-0.05}$	$86.72^{+2.55}_{-6.96}$	$0.18^{+-0.07}_{-0.07}$	$126.56^{+5.45}_{-6.59}$	$0.00^{+0.00}_{-0.00}$
HD135742	$3.761^{+0.003}_{-0.002}$	$0.79^{+0.08}_{-0.08}$	$0.90^{+0.02}_{-0.02}$	$12684.88^{+236.27}_{-224.03}$	$442.69^{+44.51}_{-37.19}$	$4.37^{+0.05}_{-0.04}$	$71.24^{+11.80}_{-13.83}$	$0.21^{+-0.04}_{-0.04}$	$56.82^{+0.54}_{-0.54}$	$0.02^{+0.01}_{-0.01}$
HD136664	$4.257^{+0.000}_{-0.001}$	$0.35^{+0.19}_{-0.10}$	$0.18^{+0.11}_{-0.11}$	$20818.33^{+230.69}_{-246.56}$	$1801.00^{+123.69}_{-119.92}$	$3.27^{+0.04}_{-0.03}$	$40.75^{+22.55}_{-15.71}$	$0.24^{+-0.00}_{-0.01}$	$159.72^{+4.90}_{-5.02}$	$0.06^{+0.00}_{-0.00}$
HD138485	$4.330^{+0.002}_{-0.002}$	$0.43^{+0.08}_{-0.10}$	$0.02^{+0.03}_{-0.02}$	$21957.69^{+350.61}_{-426.96}$	$2007.10^{+206.36}_{-231.64}$	$3.10^{+0.05}_{-0.07}$	$46.91^{+30.35}_{-10.24}$	$0.24^{+-0.01}_{-0.01}$	$223.10^{+13.01}_{-11.59}$	$0.08^{+0.01}_{-0.01}$
HD139365	$4.120^{+0.001}_{-0.001}$	$0.18^{+0.03}_{-0.02}$	$0.50^{+0.04}_{-0.05}$	$19807.09^{+213.42}_{-200.96}$	$1955.94^{+122.32}_{-110.09}$	$3.77^{+0.03}_{-0.03}$	$77.09^{+9.64}_{-22.98}$	$0.25^{+-0.00}_{-0.00}$	$112.72^{+2.64}_{-2.43}$	$0.03^{+0.00}_{-0.00}$
HD141637	$4.327^{+0.000}_{-0.001}$	$0.13^{+0.01}_{-0.02}$	$0.00^{+0.00}_{-0.00}$	$24538.76^{+96.84}_{-137.69}$	$3756.10^{+90.22}_{-123.27}$	$3.40^{+0.01}_{-0.02}$	$84.48^{+4.13}_{-7.86}$	$0.25^{+-0.00}_{-0.00}$	$182.65^{+0.13}_{-0.46}$	$0.21^{+0.00}_{-0.00}$
HD142926	$4.241^{+0.001}_{-0.001}$	$0.67^{+0.09}_{-0.11}$	$0.29^{+0.10}_{-0.10}$	$13823.53^{+299.09}_{-286.00}$	$193.17^{+24.17}_{-21.13}$	$2.43^{+0.04}_{-0.04}$	$66.28^{+12.04}_{-10.99}$	$0.22^{+-0.03}_{-0.03}$	$168.70^{+6.26}_{-6.21}$	$0.02^{+0.02}_{-0.01}$
HD144470	$4.305^{+0.001}_{-0.003}$	$0.24^{+0.04}_{-0.03}$	$0.00^{+0.01}_{-0.00}$	$31339.74^{+385.43}_{-618.65}$	$17336.96^{+1129.65}_{-2077.82}$	$4.48^{+0.03}_{-0.11}$	$31.19^{+5.32}_{-6.18}$	$0.25^{+-0.00}_{-0.00}$	$162.81^{+3.58}_{-7.71}$	$0.28^{+0.00}_{-0.00}$
HD145502	$4.309^{+0.003}_{-0.001}$	$0.14^{+0.01}_{-0.01}$	$0.01^{+0.02}_{-0.01}$	$28963.21^{+948.74}_{-395.10}$	$10604.04^{+2455.27}_{-916.30}$	$4.10^{+0.17}_{-0.07}$	$76.84^{+7.08}_{-7.74}$	$0.25^{+-0.00}_{-0.00}$	$180.36^{+11.32}_{-5.73}$	$0.23^{+0.01}_{-0.01}$
HD148283	$3.912^{+0.004}_{-0.008}$	$0.87^{+0.10}_{-0.11}$	$0.76^{+0.06}_{-0.10}$	$9240.66^{+467.18}_{-351.00}$	$53.13^{+16.72}_{-10.66}$	$2.85^{+0.11}_{-0.10}$	$72.53^{+13.46}_{-16.12}$	$0.20^{+-0.05}_{-0.05}$	$74.63^{+2.19}_{-2.24}$	$0.15^{+0.05}_{-0.04}$
HD148605	$4.343^{+0.003}_{-0.004}$	$0.29^{+0.21}_{-0.03}$	$0.01^{+0.09}_{-0.01}$	$20874.05^{+419.60}_{-649.66}$	$1435.01^{+175.83}_{-239.42}$	$2.90^{+0.05}_{-0.08}$	$63.21^{+23.64}_{-28.10}$	$0.25^{+-0.00}_{-0.00}$	$140.81^{+2.82}_{-4.11}$	$0.08^{+0.01}_{-0.01}$
HD149438	$4.300^{+0.015}_{-0.003}$	$0.02^{+0.06}_{-0.01}$	$0.02^{+0.03}_{-0.01}$	$31113.86^{+611.30}_{-755.49}$	$16781.49^{+1685.11}_{-2401.61}$	$4.47^{+0.04}_{-0.12}$	$13.65^{+34.95}_{-10.44}$	$0.25^{+0.00}_{-0.00}$	$138.26^{+9.37}_{-8.19}$	$0.03^{+0.01}_{-0.01}$

HD155806	$4.208^{+0.017}_{-0.033}$	$0.38^{+0.12}_{-0.11}$	$0.35^{+0.15}_{-0.31}$	$30018.89^{+0.00}_{-0.00}$	$23463.42^{+0.00}_{-0.00}$	$5.68^{+0.00}_{-0.00}$	$45.86^{+19.77}_{-13.61}$	$0.24^{+-0.01}_{-0.01}$	$540.61^{+65.55}_{-62.53}$	$0.25^{+0.01}_{-0.01}$
HD156247	$4.314^{+0.001}_{-0.004}$	$0.08^{+0.04}_{-0.01}$	$0.00^{+0.00}_{-0.00}$	$29336.47^{+170.60}_{-1122.74}$	$11284.21^{+433.74}_{-2483.80}$	$4.12^{+0.03}_{-0.19}$	$57.64^{+24.13}_{-23.48}$	$0.25^{+-0.00}_{-0.00}$	$279.44^{+2.79}_{-23.04}$	$0.46^{+0.00}_{-0.01}$
HD158427	$4.078^{+0.000}_{-0.002}$	$0.79^{+0.04}_{-0.06}$	$0.56^{+0.08}_{-0.09}$	$20047.41^{+333.76}_{-347.66}$	$2354.15^{+247.01}_{-229.21}$	$4.03^{+0.07}_{-0.06}$	$53.74^{+9.94}_{-8.63}$	$0.21^{+-0.04}_{-0.04}$	$88.70^{+5.11}_{-5.13}$	$0.05^{+0.00}_{-0.00}$
HD164284	$4.295^{+0.003}_{-0.003}$	$0.42^{+0.12}_{-0.08}$	$0.05^{+0.07}_{-0.04}$	$26889.74^{+592.62}_{-604.77}$	$7278.74^{+1030.71}_{-950.42}$	$3.94^{+0.09}_{-0.10}$	$54.02^{+29.81}_{-13.09}$	$0.24^{+-0.01}_{-0.01}$	$198.51^{+9.32}_{-10.16}$	$0.21^{+0.01}_{-0.01}$
HD173948	$3.736^{+0.010}_{-0.010}$	$0.94^{+0.04}_{-0.08}$	$0.95^{+0.04}_{-0.08}$	$24275.80^{+824.57}_{-779.42}$	$17585.97^{+4170.28}_{-3392.61}$	$7.52^{+0.30}_{-0.31}$	$31.27^{+4.66}_{-3.45}$	$0.18^{+-0.07}_{-0.07}$	$364.66^{+28.32}_{-29.13}$	$0.11^{+0.01}_{-0.01}$
HD181454	$3.993^{+0.000}_{-0.000}$	$0.66^{+0.14}_{-0.23}$	$0.69^{+0.06}_{-0.11}$	$13077.44^{+228.01}_{-326.10}$	$276.89^{+26.08}_{-34.45}$	$3.25^{+0.03}_{-0.05}$	$19.84^{+10.49}_{-4.10}$	$0.23^{+-0.02}_{-0.02}$	$91.62^{+7.59}_{-12.30}$	$0.02^{+0.01}_{-0.01}$
HD183362	$3.727^{+0.006}_{-0.008}$	$0.75^{+0.03}_{-0.03}$	$0.98^{+0.02}_{-0.07}$	$17706.44^{+325.13}_{-410.45}$	$2931.37^{+252.27}_{-296.12}$	$5.77^{+0.03}_{-0.04}$	$61.01^{+7.15}_{-7.50}$	$0.22^{+-0.03}_{-0.03}$	$505.15^{+19.61}_{-43.39}$	$0.05^{+0.01}_{-0.01}$
HD183914	$4.186^{+0.000}_{-0.000}$	$0.69^{+0.04}_{-0.03}$	$0.40^{+0.08}_{-0.07}$	$14251.12^{+183.03}_{-180.34}$	$261.77^{+19.13}_{-17.27}$	$2.66^{+0.03}_{-0.02}$	$42.52^{+7.15}_{-5.81}$	$0.22^{+-0.03}_{-0.03}$	$123.64^{+4.08}_{-3.68}$	$0.07^{+0.00}_{-0.00}$
HD183656	$4.267^{+0.004}_{-0.003}$	$0.47^{+0.30}_{-0.15}$	$0.19^{+0.25}_{-0.13}$	$17908.96^{+837.64}_{-726.30}$	$761.62^{+239.09}_{-170.20}$	$2.87^{+0.13}_{-0.12}$	$43.83^{+38.89}_{-17.21}$	$0.24^{+-0.01}_{-0.01}$	$250.25^{+18.71}_{-19.11}$	$0.22^{+0.03}_{-0.03}$
HD184006	$3.996^{+0.004}_{-0.004}$	$0.75^{+0.18}_{-0.12}$	$0.69^{+0.07}_{-0.09}$	$9040.58^{+317.53}_{-296.01}$	$37.59^{+8.00}_{-6.45}$	$2.51^{+0.07}_{-0.07}$	$63.43^{+19.53}_{-15.56}$	$0.22^{+-0.03}_{-0.03}$	$37.32^{+0.14}_{-0.13}$	$0.08^{+0.04}_{-0.03}$
HD187811	$4.228^{+0.002}_{-0.001}$	$0.70^{+0.01}_{-0.01}$	$0.28^{+0.07}_{-0.03}$	$18640.39^{+294.54}_{-265.79}$	$1069.41^{+102.96}_{-86.91}$	$3.14^{+0.05}_{-0.04}$	$30.27^{+5.07}_{-2.79}$	$0.22^{+-0.03}_{-0.03}$	$184.48^{+6.06}_{-5.61}$	$0.04^{+0.01}_{-0.00}$
HD188293	$4.353^{+0.002}_{-0.002}$	$0.41^{+0.09}_{-0.10}$	$0.02^{+0.03}_{-0.02}$	$17196.05^{+222.80}_{-260.13}$	$466.54^{+35.83}_{-39.34}$	$2.44^{+0.03}_{-0.03}$	$50.04^{+32.30}_{-9.70}$	$0.24^{+-0.01}_{-0.01}$	$161.14^{+6.43}_{-7.23}$	$0.11^{+0.01}_{-0.01}$
HD188665	$3.990^{+0.001}_{-0.000}$	$0.23^{+0.03}_{-0.03}$	$0.71^{+0.03}_{-0.05}$	$16210.20^{+517.19}_{-240.09}$	$914.52^{+184.65}_{-77.27}$	$3.84^{+0.11}_{-0.05}$	$73.26^{+8.90}_{-7.15}$	$0.25^{+-0.00}_{-0.00}$	$190.92^{+6.90}_{-6.36}$	$0.03^{+0.01}_{-0.01}$
HD190993	$4.345^{+0.001}_{-0.001}$	$0.16^{+0.08}_{-0.04}$	$0.01^{+0.02}_{-0.01}$	$20157.46^{+223.28}_{-232.16}$	$1174.31^{+77.94}_{-77.09}$	$2.82^{+0.03}_{-0.03}$	$47.85^{+34.60}_{-18.82}$	$0.25^{+-0.00}_{-0.00}$	$161.91^{+4.22}_{-4.17}$	$0.05^{+0.00}_{-0.00}$
HD191610	$3.926^{+0.002}_{-0.002}$	$0.72^{+0.08}_{-0.06}$	$0.76^{+0.08}_{-0.08}$	$21456.75^{+443.14}_{-440.29}$	$5268.49^{+671.18}_{-608.56}$	$5.27^{+0.10}_{-0.10}$	$46.55^{+9.39}_{-8.52}$	$0.22^{+-0.03}_{-0.03}$	$317.86^{+18.00}_{-19.72}$	$0.09^{+0.01}_{-0.01}$
HD192044	$3.608^{+0.040}_{-0.001}$	$0.94^{+0.04}_{-0.02}$	$0.99^{+0.01}_{-0.01}$	$12576.55^{+1764.51}_{-98.90}$	$608.45^{+505.65}_{-22.61}$	$5.21^{+0.21}_{-0.02}$	$34.84^{+22.74}_{-18.28}$	$0.18^{+-0.07}_{-0.07}$	$223.24^{+17.87}_{-34.13}$	$0.15^{+0.07}_{-0.03}$
HD192685	$3.939^{+0.003}_{-0.002}$	$0.43^{+0.26}_{-0.11}$	$0.73^{+0.09}_{-0.16}$	$20440.65^{+800.31}_{-783.13}$	$3834.75^{+972.13}_{-800.19}$	$4.95^{+0.18}_{-0.19}$	$48.78^{+29.58}_{-21.36}$	$0.24^{+-0.01}_{-0.01}$	$275.86^{+41.85}_{-40.73}$	$0.03^{+0.01}_{-0.01}$

HD198183	$3.888^{+0.000}_{-0.000}$	$0.70^{+0.16}_{-0.27}$	$0.81^{+0.08}_{-0.10}$	$17234.79^{+573.92}_{-503.57}$	$1715.77^{+340.21}_{-261.10}$	$4.66^{+0.12}_{-0.11}$	$19.22^{+11.72}_{-4.16}$	$0.22^{+-0.03}_{-0.02}$	$221.48^{+26.81}_{-28.34}$	$0.08^{+0.01}_{-0.01}$
HD198625	$3.872^{+0.002}_{-0.002}$	$0.73^{+0.13}_{-0.15}$	$0.82^{+0.10}_{-0.14}$	$18562.38^{+591.89}_{-607.91}$	$2678.80^{+535.20}_{-453.54}$	$5.02^{+0.14}_{-0.13}$	$50.69^{+19.64}_{-12.03}$	$0.22^{+-0.03}_{-0.03}$	$485.78^{+57.07}_{-67.06}$	$0.15^{+0.01}_{-0.01}$
HD199081	$4.042^{+0.000}_{-0.001}$	$0.09^{+0.71}_{-0.02}$	$0.66^{+0.06}_{-0.25}$	$14641.70^{+291.66}_{-309.23}$	$452.06^{+52.20}_{-49.72}$	$3.31^{+0.05}_{-0.05}$	$44.47^{+26.82}_{-39.88}$	$0.25^{+0.03}_{-0.00}$	$160.21^{+5.99}_{-5.66}$	$0.02^{+0.01}_{-0.01}$
HD205637	$3.776^{+0.002}_{-0.007}$	$0.91^{+0.06}_{-0.29}$	$0.98^{+0.01}_{-0.03}$	$21682.22^{+1129.81}_{-893.35}$	$7829.22^{+2668.92}_{-1485.55}$	$6.29^{+0.29}_{-0.13}$	$35.21^{+14.33}_{-4.81}$	$0.19^{+-0.06}_{-0.05}$	$303.20^{+21.36}_{-21.43}$	$0.08^{+0.02}_{-0.02}$
HD208057	$4.148^{+0.001}_{-0.001}$	$0.38^{+0.25}_{-0.14}$	$0.45^{+0.09}_{-0.16}$	$18099.35^{+269.72}_{-271.65}$	$1105.65^{+99.86}_{-93.32}$	$3.39^{+0.05}_{-0.05}$	$31.86^{+26.35}_{-12.97}$	$0.24^{+-0.00}_{-0.01}$	$194.46^{+8.67}_{-8.57}$	$0.02^{+0.00}_{-0.00}$
HD209409	$3.988^{+0.000}_{-0.001}$	$0.73^{+0.18}_{-0.16}$	$0.70^{+0.06}_{-0.10}$	$14443.70^{+294.17}_{-288.53}$	$482.42^{+57.47}_{-50.54}$	$3.52^{+0.06}_{-0.05}$	$42.15^{+17.75}_{-9.67}$	$0.22^{+-0.03}_{-0.03}$	$134.94^{+3.63}_{-3.39}$	$0.07^{+0.01}_{-0.01}$
HD209522	$4.072^{+0.004}_{-0.004}$	$0.69^{+0.06}_{-0.11}$	$0.58^{+0.11}_{-0.11}$	$19305.26^{+573.92}_{-540.79}$	$1942.60^{+353.62}_{-293.77}$	$3.95^{+0.10}_{-0.10}$	$51.93^{+15.13}_{-9.36}$	$0.22^{+-0.03}_{-0.03}$	$344.97^{+45.09}_{-33.94}$	$0.05^{+0.01}_{-0.01}$
HD214240	$3.898^{+0.001}_{-0.001}$	$0.94^{+0.03}_{-0.04}$	$0.80^{+0.13}_{-0.10}$	$15647.52^{+235.05}_{-301.90}$	$962.97^{+86.19}_{-100.87}$	$4.23^{+0.06}_{-0.07}$	$8.80^{+1.02}_{-0.74}$	$0.18^{+-0.07}_{-0.07}$	$372.23^{+75.88}_{-39.90}$	$0.12^{+0.01}_{-0.01}$
HD214748	$3.649^{+0.005}_{-0.005}$	$0.68^{+0.09}_{-0.03}$	$0.97^{+0.02}_{-0.04}$	$14149.56^{+249.96}_{-249.73}$	$1052.17^{+87.13}_{-82.67}$	$5.41^{+0.03}_{-0.03}$	$53.43^{+7.93}_{-8.40}$	$0.22^{+-0.03}_{-0.03}$	$174.96^{+7.86}_{-9.56}$	$0.04^{+0.01}_{-0.00}$
HD222173	$3.921^{+0.000}_{-0.001}$	$0.15^{+0.02}_{-0.01}$	$0.79^{+0.01}_{-0.02}$	$13484.49^{+173.08}_{-236.23}$	$405.00^{+29.64}_{-37.20}$	$3.70^{+0.04}_{-0.05}$	$83.47^{+4.34}_{-15.47}$	$0.25^{+-0.00}_{-0.00}$	$152.84^{+4.48}_{-3.89}$	$0.05^{+0.01}_{-0.01}$
HD224686	$3.942^{+0.000}_{-0.000}$	$0.88^{+0.07}_{-0.08}$	$0.75^{+0.03}_{-0.03}$	$12380.41^{+219.25}_{-152.92}$	$238.15^{+23.15}_{-15.18}$	$3.36^{+0.04}_{-0.03}$	$33.37^{+6.39}_{-4.47}$	$0.20^{+-0.05}_{-0.05}$	$114.74^{+2.32}_{-2.25}$	$0.05^{+0.01}_{-0.01}$

Appendix B

Bemcee Tutorial

Bemcee Documentation

Beacon

Oct 20, 2018

CONTENTS

ii

CHAPTER

ONE

THE BEMCEE CODE

In this document we present a brief documentation of the developed code Bemcee. All the routines can be acessed thought the GitHub link: **https://github.com/tangodaum/bemcee**.

1.1 Main Routine: bemcee.py

Having defined properly all folders and options, the code can be runned in terminal by typing

```
python3 bemcee.py list_of_stars.txt
```

The file list_of_stars.txt has the format #star plx splx vsini svsi ebmv inc bump HD23466 5.31 0.24 90.0 8.0 0.0 nan True HD23793 7.74 0.17 20.0 0.0 0.0 nan True HD23862 7.72 0.20 220.0 0.0 0.0 nan True

star	plx	sig_plx	vsini	sig_vsini
HDXXXXXX	parallax	plx error	vsini value	vsini error

The main code is

```
# ================================================================================
# -*- coding:utf-8 -*-
# ================================================================================
# importing packages
from reading_routines import read_stars, read_models
from emcee.utils import MPIPool
from emcee_routines import run
import sys
# import matplotlib
from sys import argv
# matplotlib.use('Agg')

# ================================================================================
# General Options
a_parameter = 2  # Set internal steps of each walker
extension = '.png'  # Figure extension to be saved
include_rv = False  # If False: fix Rv = 3.1, else Rv will be inferead
af_filter = True  # Remove walkers outside the range 0.2 < af < 0.5
long_process = True  # Run with few walkers or many?
list_of_stars = argv[1]  # 'bcmi.txt', 'aara.txt', argv[1]
plot_fits = True  # Include fits in the corner plot
Nsigma_dis = 5.  # Set the range of values for the distance
```

(continues on next page)

Bemcee Documentation

(continued from previous page)

```
# 'beatlas', 'befavor', 'befavor_new' 'aara', 'bcmi' or 'acol' (equals)
# 'bcmi_pol'
# model = 'bcmi'
model = 'bcmi_pol'
tag = '+' + model + '_xdr' + '+hip+hpol'  # Suffix for the figures

# General Options
doconvpol = False
table_csv = 'hpol.npy'  # 'bcmi_iscor.csv', 'bcmi_iscor_2.csv'

# ------------------------------------------------------------------------
# Alphacrucis' options
acrux = False  # If True, it will run in Nproc processors in the cluster
Nproc = 24  # Number of processors to be used in the cluster

# ------------------------------------------------------------------------
# if True: M, Age, Oblat are set as priors for the choosen input, npy_star
stellar_prior = False
npy_star = 'Walkers_500_Nmcmc_1000_af_0.28_a_1.4_rv_false+hip.npy'

# lbd_range = 'UV'
# lbd_range = 'UV+VIS+NIR+MIR+FIR+MICROW+RADIO'
lbd_range = 'MIR+FIR+MICROW+RADIO'

if lbd_range == 'UV':
    votable = False
else:
    votable = True

if lbd_range == 'bcmi_pol':
    lbd_range = ''

if lbd_range == 'UV' or lbd_range == 'UV+VIS' or\
   lbd_range == 'UV+VIS+NIR' or lbd_range == 'UV+VIS+NIR+MIR' or\
   lbd_range == 'FIR+MICROW+RADIO' or lbd_range == 'MICROW+RADIO' or\
   lbd_range == 'RADIO':
    plot_in_log_scale = False  # yscale in log for fits
else:
    plot_in_log_scale = True

# ========================================================================
# Acrux
if acrux is True:
    pool = MPIPool()
    if not pool.is_master():
        pool.wait()
        sys.exit(0)
else:
    pool = False

# ========================================================================
# Reading the list of stars
stars, list_plx, list_sig_plx, list_vsini_obs, list_sig_vsin_obs,\
    list_pre_ebmv, incl0, bump0 = read_stars(list_of_stars)

# Reading Models
ctrlarr, minfo, models, lbdarr, listpar, dims, isig = read_models(model)
```

(continues on next page)

(continued from previous page)

```
# ============================================================================
# Run code
input_params = stars, list_plx, list_sig_plx, list_vsini_obs,\
    list_sig_vsin_obs, list_pre_ebmv, lbd_range,\
    Nsigma_dis, include_rv, model, ctrlarr, minfo, models,\
    lbdarr, listpar, dims, isig, a_parameter, af_filter,\
    tag, plot_fits, plot_in_log_scale, long_process,\
    extension, acrux, pool, Nproc, stellar_prior, npy_star, votable,\
    table_csv

run(input_params)

# ============================================================================
# The End
print(75 * '=')
print('\nSimulation Finished\n')
print(75 * '=')

if acrux is True:
    pool.close()

# ============================================================================
```

1.2 Routine: emcee_routines

It is the main module of our code.

emcee_routines.**emcee_inference**(*star*, *Ndim*, *ranges*, *lbdarr*, *wave*, *logF*, *dlogF*, *minfo*, *listpar*, *logF_grid*, *vsin_obs*, *sig_vsin_obs*, *dist_pc*, *sig_dist_pc*, *isig*, *dims*, *include_rv*, *a_parameter*, *af_filter*, *tag*, *plot_fits*, *long_process*, *log_scale*, *model*, *acrux*, *pool*, *Nproc*, *stellar_prior*, *npy_star*, *pdf_mas*, *pdf_obl*, *pdf_age*, *pdf_dis*, *pdf_ebv*, *grid_mas*, *grid_obl*, *grid_age*, *band*)

Returns the posterior probability function. :param star: star name (string) :param Ndim: number of dimensions (integer) :param lbdarr: model wavelength (array) :param wave: observed wavelength (array) :param logF: observed flux (array) :param dlogF: observed flux error (array) :param minfo: models info (array) :param listpar: list of parameters (array) :param logF_grid: flux model (array) :param vsin_obs: observed vsini (float) :param sig_vsin_obs: observed vsini error (float) :param dist_pc: distance in parsec (float) :param sig_dist_pc: distance error (float) :param isig: float :param dims: float :param include_rv: to set rv as a free parameter (boolean) :param a_parameter: internal paramenter (float) :param af_filter: remove bad walkers (boolean) :param tag: string to be added to the final results :param plot_fits: plot fits? (boolean) :param long_process: long mcmc process? (boolean) :param log_scale: log scale? (boolean) :param model: grid model adopted (string) :param acrux: use acrux? (boolean) :param pool: internal paramenter (function) :param Nproc: number of processors (integer) :param stellar_prior: use stellar prior? (boolean) :param npy_star: npy file (string) :param pdf_mas: (float) :param pdf_obl: (float) :param pdf_age: (float) :param pdf_dis: (float) :param pdf_ebv: (float) :param grid_mas: (float) :param grid_obl: (float) :param grid_age: (float) :param band: wavelength range (string)

:return : results

emcee_routines.**lnlike**(*params*, *lbd*, *logF*, *dlogF*, *logF_mod*, *include_rv*, *model*)

Returns the likelihood probability function.

Parameters

- **params** – mass, oblat, age, inclination, ebmv, distance
- **lbd** – wavelength (float)
- **logF** – flux (float)
- **dlogF** – flux error (float)
- **logF_mod** – model flux (float)
- **include_rv** – distance (float)
- **model** – grid model (string)

:return : likelihood

emcee_routines.**lnprior**(*params*, *vsin_obs*, *sig_vsin_obs*, *dist_pc*, *sig_dist_pc*, *model*, *stellar_prior*, *npy_star*, *pdf_mas*, *pdf_obl*, *pdf_age*, *pdf_dis*, *pdf_ebv*, *grid_mas*, *grid_obl*, *grid_age*, *grid_dis*, *grid_ebv*)

Returns the prior probability function. :param params: mass, oblat, age, inclination, ebmv, distance :param vsin_obs: observed vsini (float) :param sig_vsin_obs: observed vsini error (float) :param dist_pc: distance in parsec (float) :param sig_dist_pc: distance error (float) :param model: grid model adopted (string) :param stellar_prior: use stellar prior? (boolean) :param npy_star: npy file (string) :param pdf_mas: (float) :param pdf_obl: (float) :param pdf_age: (float) :param pdf_dis: (float) :param pdf_ebv: (float) :param grid_mas: (float) :param grid_obl: (float) :param grid_age: (float) :param grid_dis: (float) :param grid_ebv: (float)

:return : prior

emcee_routines.**lnprob**(*params*, *lbd*, *logF*, *dlogF*, *minfo*, *listpar*, *logF_grid*, *vsin_obs*, *sig_vsin_obs*, *dist_pc*, *sig_dist_pc*, *isig*, *ranges*, *dims*, *include_rv*, *model*, *stellar_prior*, *npy_star*, *pdf_mas*, *pdf_obl*, *pdf_age*, *pdf_dis*, *pdf_ebv*, *grid_mas*, *grid_obl*, *grid_age*)

Returns the posterior probability function. :param params: mass, oblat, age, inclination, ebmv, distance :param lbd: wavelength (array) :param logF: observed flux (array) :param dlogF: observed flux error (array) :param minfo: models info (array) :param listpar: list of parameters (array) :param logF_grid: flux model (array) :param vsin_obs: observed vsini (float) :param sig_vsin_obs: observed vsini error (float) :param dist_pc: distance in parsec (float) :param sig_dist_pc: distance error (float) :param isig: float :param ranges: paramter's ranges :param dims: float :param model: grid model adopted (string) :param stellar_prior: use stellar prior? (boolean) :param npy_star: npy file (string) :param pdf_mas: (float) :param pdf_obl: (float) :param pdf_age: (float) :param pdf_dis: (float) :param pdf_ebv: (float) :param grid_mas: (float) :param grid_obl: (float) :param grid_age: (float)

:return : posterior

emcee_routines.**run**(*input_params*)

Main function :param input_params: array :return : Final results

emcee_routines.**run_emcee**(*p0*, *sampler*, *nib*, *nimc*, *Ndim*, *file_name*)

Core emcee code :params p0: initial position of the walkers (matrix) :params sampler: sampler (matrix) :params nib: number of steps in the burning phase (integer) :params nimc: number of steps in the mcmc (integer) :params Ndim: number of dimensions (integer) :params file_name: file name (string) :return : arrays

1.3 Routine: utils

Module with math functions envolved in different processes as: interpolation, binning, etc.

utils.**bin_data**(*x*, *y*, *nbins*, *xran=None*, *exclude_empty=True*)

Bins data

Usage: xbin, ybin, dybin = bin_data(x, y, nbins, xran=None, exclude_empty=True)

where dybin is the standard deviation inside the bins. Find the nearest value inside an array

Parameters

- **x** – array
- **y** – array
- **nbins** – number of bins
- **xran** – x range
- **exclude_empty** – remove empty values

:return : array

utils.**find_nearest**(*array*, *value*)
Find the nearest value inside an array :param array: array :param value: value (float) :return : array

utils.**find_neighbours**(*par*, *par_grid*, *ranges*)
Finds neighbours' positions of par in par_grid.

Usage: keep, out, inside_ranges, par_new, par_grid_new = find_neighbours(par, par_grid, ranges):

where redundant columns in 'new' values are excluded, but length is preserved (i.e., par_grid[keep] in griddata call).

Parameters

- **par** – list of parameters (array)
- **par_grid** – grid of parameters (float)
- **ranges** – parameter ranges

:return : array

utils.**geneva_interp_fast**(*Par*, *oblat*, *t*, *neighbours_only=True*, *isRpole=False*)
Interpolates Geneva stellar models, from grid of pre-computed interpolations.

Usage: Rpole, logL = geneva_interp_fast(Mstar, oblat, t,

neighbours_only=True, isRpole=False)

or Mstar, logL = geneva_interp_fast(Rpole, oblat, t,

neighbours_only=True, isRpole=True)

(in this case, the option 'neighbours_only' will be set to 'False')

where t is given in tMS, and tar is the open tar file. For now, only Z=0.014 is available.

Parameters

- **Par** – list of parameters (array)
- **oblat** – oblateness (float)
- **t** – stellar age
- **neighbours_only** – boolean
- **isRpole** – boolean

:return : array

utils.**griddataBA**(*minfo*, *models*, *params*, *listpar*, *dims*)
Moser's routine to interpolate BeAtlas models obs: last argument ('listpar') had to be included here :param

minfo: model's info (matrix) :param models: matrix of models :param params: free parameters (array) :param listpar: list of parameters (array) :param dims: array :return : array

utils.**griddataBA_new**(*minfo*, *models*, *params*, *isig*, *silent=True*)
Interpolates model grid

Usage: model_interp = griddata(minfo, models, params, isig, silent=True)

where minfo = grid of parameters models = grid of models params = parameters, isig = (normalized) sigma0 index

Ex: # read grid xdrpath = 'beatlas/disk_flx.xdr' listpar, lbdarr, minfo, models = bat.readBAsed(xdrpath, quiet=True) # find isig dims = ['M', 'ob', 'sig0', 'nr', 'cosi'] dims = dict(zip(dims, range(len(dims)))) isig = dims["sig0"] # interpolation params = [12.4, 1.44, 0.9, 4.4, 0.1] model_interp = np.exp(griddataBA(minfo, np.log(models), params, isig))

If photospheric models are interpolated, let isig=None. For spectra, it is recommended to enter the log of the grid of spectra as input, as shown in the example above.

Parameters

- **minfo** – model info (matrix)
- **models** – list of models (matrix)
- **params** – free parameters (array)
- **isig** – internal value (float)
- **silet** – boolean

:return : array

utils.**griddataBAtlas**(*minfo*, *models*, *params*, *listpar*, *dims*, *isig*)
Interpolation routine

Parameters

- **minfo** – model info (matrix)
- **models** – list of models (matrix)
- **params** – free parameters (array)
- **listpar** – list of parameters (array)
- **dims** – internal value (float)
- **isigt** – boolean

:return : array

utils.**hfrac2tms**(*Hfrac*, *inverse=False*)
Converts nuclear hydrogen fraction into fractional time in the main-sequence, (and vice-versa) based on the polynomial fit of the average of this relation for all B spectral types and rotational velocities.

Usage: t = hfrac2tms(Hfrac, inverse=False) or Hfrac = hfrac2tms(t, inverse=True) :param Hfrac: core hydrogen fraction (float) :param isigt: calculate inverse (boolean) :return : array

utils.**kde_scipy**(*x*, *x_grid*, *bandwidth=0.2*)
Kernel Density Estimation with Scipy :param x: array :param x: x grind :param bandwidth: band width :return : kde distribution

1.4 Routine: be_theory

The module be_theory is a Python routine that comprises the basic physical functions regarding Be stars. Their functions are read

be_theory.**W2oblat**(*W*)
Calculates oblateness from W = v/v_orb :param W: rotation rate (W = v/v_orb) :return: oblateness

be_theory.**hfrac2tms**(*Hfrac*, *inverse=False*)
Converts nuclear hydrogen fraction into fractional time in the main-sequence, (and vice-versa) based on the polynomial fit of the average of this relation for all B spectral types and rotational velocities.

Usage: t = hfrac2tms(Hfrac, inverse=False) or Hfrac = hfrac2tms(t, inverse=True)

Parameters

- **Hfrac** – hydrogen fraction in the core (float)
- **Inverse** – If you wish to convert from ttms to hfrac (boolean)

Returns main sequence lifetime

be_theory.**obl2W**(*oblat*)
Calculates rotation range (W = v/v_orb) from oblateness :param oblat: oblateness (Req/Rpole) :return: rotation rate (W)

be_theory.**oblat2w**(*oblat*)
Converts oblateness (Req/Rpole) into w=Omega/Omega_crit Ekstrom et al. 2008, Eq. 9

Usage: w = oblat2w(oblat)

Parameters **oblat** – oblateness (Req/Rpole) (float)

Returns angular rotation rate (omega)

be_theory.**t_tms_from_Xc**(*M*, *savefig=None*, *plot_fig=None*, *ttms_true=None*, *Xc=None*)
Calculates the t(tms) for a given Xc and mass :param Xc: hydrogen fraction in the core (float) :param M: stellar mass (Msun) :param plot_fig: plot figure? (boolean) :param ttms_true: a fixed value :return: main sequence lifetime

1.5 Routine: Reading Routines

Set of functions for: reading lists of stars, informations about the targets, models, observational data, VO catalogues, etc.

reading_routines.**npy2csv**(*npy_file*)
Function to convert npy file to csv table :param npy_file: npy file (string) :return : csv_file

reading_routines.**read_acol_xdr**(*xdr_name*)
Function to read the grid model (alpha col grid model) :param xdr_name: xdr name (string) :return : array

reading_routines.**read_bcmi_pol**()
Function to read the grid model (alpha col polarimetric grid model) :param xdr_name: xdr name (string) :return : array

reading_routines.**read_beatlas_xdr**()
Function to read the grid model (V1-Beatlas) :return : array

reading_routines.**read_befavor_xdr**()
Function to read the grid model (stellar models) :return : array

reading_routines.**read_befavor_xdr_complete**()
Function to read the grid model (stellar models) :return : array

reading_routines.**read_befavor_xdr_new**()
Function to read the grid model (stellar models) :return : array

reading_routines.**read_iue**(*models*, *lbdarr*, *wave0*, *flux0*, *sigma0*, *folder_data*, *folder_fig*, *star*, *cut_iue_regions*, *model*, *lbd_range*)
Function to read IUE data :param models: adopted grid model :param lbdarr: model wavelenght (array) :param wave0: wavelength (array) :param flux0: observed flux (array) :param sigma0: observed flux error (array) :param folder_data: folder data (string) :param folder_fig: folder figure (string) :param star: star name (string) :param cut_iue_regions: cut regions with large errors (boolean) :param model: string :param lbd_range: wavelength range :return : array

reading_routines.**read_models**(*model*)
Function to read models :param models: model name (string) :return : array

reading_routines.**read_opd_pol**(*folder_data*, *star*, *table_csv*)
Function to read OPD polarimetric data :param folder_data: folder data (string) :param star: star name (string) :param table_csv: boolean :return : wave, flux, sigma

reading_routines.**read_star_info**(*stars*, *list_plx*, *list_sig_plx*, *list_vsini_obs*, *list_sig_vsin_obs*, *list_pre_ebmv*, *lbd_range*, *listpar*, *Nsigma_dis*, *include_rv*, *model*)
Function to read the info about the stars :param stars: list of stars (array) :param list_plx: list of parallaxes (array) :param list_sig_plx: list of parallaxes errors (array) :param list_vsini_obs: list of observed vsini (array) :param list_sig_vsin_obs: list of observed vsini errors (array) :param list_pre_ebmv: list of previous ebmv values (array) :param lbd_range: wavelengths ranges :param listpar: list of parameters (array) :param Nsigma_dis: define the distance range :param include_rv: set rv as a free parameter :param model: adopted grid model :return : array

reading_routines.**read_stars**(*stars_table*)
Function to read the list of stars :param stars_table: list name (string) :return : array

reading_routines.**read_votable**(*folder_data*, *star*)
Function to read VO tables :param folder_data: folder data (string) :param star: star name (string) :return : wave, flux, sigma

1.6 Routine: Plotting Routines

Group of routines developed to plot the outputs of the inference process.

plot_routines.**par_errors**(*flatchain*)
Most likely parameters and respective asymmetric errors

Usage: par, errors = par_errors(flatchain)

Parameters **flatchain** – array

:return : par, errors

plot_routines.**plot_fit_last**(*par*, *lbd*, *logF*, *dlogF*, *minfo*, *listpar*, *lbdarr*, *logF_grid*, *isig*, *dims*, *Nwalk*, *Nmcmc*, *ranges*, *include_rv*, *npy*, *log_scale*, *model*)
Plots best model fit over data

Usage: plot_fit(par, lbd, logF, dlogF, minfo, logF_grid, isig, Nwalk, Nmcmc) where par = np.array([Mstar, oblat, Sig0, Rd, n, cosi, dist])

Parameters

- **par** – free parameters (array)

- **lbd** – observed wavelength (array)
- **logF** – observed flux (array)
- **dlogF** – observed flux error (array)
- **minfo** – models informations (matrix)
- **listpar** – list of parameters (array)
- **lbdarr** – model wavelenght (array)
- **logF_grid** – grid of models (array)
- **isig** – internal parameter
- **dims** – internal parameter
- **Nwalk** – number of walkers (integer)
- **Nmcmc** – number of steps (integer)
- **ranges** – ranges of the grid parameters (array)
- **include_rv** – set rv as free parameter (boolean)
- **npy** – npy file (string)
- **log_scale** – boolean
- **model** – grid model (string)

:return : figures

plot_routines.**plot_residuals**(*par*, *lbd*, *logF*, *dlogF*, *minfo*, *listpar*, *lbdarr*, *logF_grid*, *isig*, *dims*, *Nwalk*, *Nmcmc*, *ranges*, *include_rv*, *npy*, *log_scale*, *model*)

Plots best model fit over data

Usage: plot_fit(par, lbd, logF, dlogF, minfo, logF_grid, isig, Nwalk, Nmcmc) where par = np.array([Mstar, oblat, Sig0, Rd, n, cosi, dist])

Parameters

- **par** – free parameters (array)
- **lbd** – observed wavelength (array)
- **logF** – observed flux (array)
- **dlogF** – observed flux error (array)
- **minfo** – models informations (matrix)
- **listpar** – list of parameters (array)
- **lbdarr** – model wavelenght (array)
- **logF_grid** – grid of models (array)
- **isig** – internal parameter
- **dims** – internal parameter
- **Nwalk** – number of walkers (integer)
- **Nmcmc** – number of steps (integer)
- **ranges** – ranges of the grid parameters (array)
- **include_rv** – set rv as free parameter (boolean)

- **npy** – npy file (string)
- **log_scale** – boolean
- **model** – grid model (string)

:return : figures

plot_routines.**print_output**(*params_fit*, *errors_fit*)
Function to print output results :param params_fit: array :param errors_fit: array :return : results

1.6.1 Routine: Chord Diagram

Module with the functions used to create the chord diagram.

chord_diagram.**chord_plot**(*folder*, *file*)
Function that plots the chord plot for the stellar grid :param Xc: folder data (string) :param file: file name (string) :return: figure

chord_diagram.**chord_plot_complete**(*folder*, *file*)
Function that plots the chord plot for the disk+star grid :param Xc: folder data (string) :param file: file name (string) :return: figure

chord_diagram.**chord_plot_pol**(*folder*, *file*)
Function that plots the chord plot for polarization measurements :param Xc: folder data (string) :param file: file name (string) :return: figure

1.6.2 Routine: Convergence Routines

Module with the functions developed to make the convergence routines.

convergence_routines.**plot_convergence**(*npy*, *file_name*, *model*)
Function to plot the convergence :param npy: npy file (string) :param file_name: file name (string) :param model : model name (string) :return: figure

CHAPTER

TWO

INDICES AND TABLES

- genindex
- modindex
- search

PYTHON MODULE INDEX

INDEX

Appendix C

Thesis article

Astronomy & Astrophysics manuscript no. output
October 21, 2018

BeAtlas: A grid of synthetic spectra for Be stars

I. Application: the Bayesian inference of physical properties of main-sequence hot stars

B. C. Mota[1], A. C. Carciofi[1], R. G. Vieira[1], D. M. Faes[1], M. R. Ghoreyshi[1], L. R. Rímulo[1], D. Bednarski[1], A. L. Figueiredo[1], D. B. Seriacopi[1] and A. Rubio[1].

Instituto de Astronomia, Geofísica e Ciências Atmosféricas, Universidade de São Paulo, Rua do Matão 1226, Cidade Universitária, 05508-900, São Paulo, SP, Brazil, bruno.mota@usp.br, carciofi@usp.br, moser@usp.br

Received July 20, 2018; accepted November 05, 2018

ABSTRACT

Context. Be, Bn, Ae and Oe stars are fast rotators in the main sequence phase or at the beginning of the subgiant phase. The rapid rotation and the presence of circumstellar disks in active phases imply in a profound modification of the photospheric parameters whose impact on the observables are not fully characterized.
Aims. Our goal is to infer stellar, disk, geometrical parameters, and the interstellar extinction, without neglecting their uncertainties and correlations, for one specific case (β CMi) and for a set of rapid rotating main sequence stars. For such a purpose, we make use of different observables.
Methods. The modern statistical procedure employed by the code EMCEE and stellar parameters based on evolutionary models of the astrophysics group of University of Geneva are used. To constrain the solutions, domain knowledge of $v \sin i$ and parallax are applied.
Results. We provide a useful new inference tool for the Monte Carlo Markov Chain modeling of Be stars and hot main-sequence O, B and A stars. Our tool includes important effects due to the rapid rotation. The potential of the observables in constraining the stellar parameters is discussed. A catalog of the inferred parameters and a discussion about their correlations are shown. We also present the first multi-technique treatment of an late-type Be star, β CMi.
Conclusions. The correlations found show that the parameters are coupled. This corroborates the hypothesis that an independent inference of any parameter could propagate errors. For β CMi, the analysis reveals a circumstellar disk truncated by a companion or a dissipating disk. Moreover, our results suggest a later sub-spectral type (B3/4) than the inferred from previous studies.

Key words. Stars: emission-line, Be, Oe, Ae, Bn, B, circumstellar matter, rotation, fundamental parameters, β CMi, HD58715, HR2845. ISM: dust, extinction. Astronomical databases: miscellaneous. Techniques: photometric, polarimetric. Methods: statistical.

1. Introduction

The B spectral domain comprises several complex subclasses of stars, including the non-supergiant, main-sequence B whose spectrum has, or had at some time, one or more Balmer lines in emission (Jaschek et al. 1981; Collins 1987), the Classical Be stars (hereafter, CBe). They are notoriously recognized by their outwardly diffusing gaseous, dust-free Keplerian circumstellar disk (hereafter, CSD) that arises in active phases (Rivinius et al. 2013) and by showing the highest rotation rates among the main-sequence (MS) stars (Granada & Haemmerlé 2014) (e.g. Townsend et al. 2004; Frémat et al. 2005).

Since the discovery of the CBe, many efforts have been made to understand their characteristics. For instance, the observational techniques progress in the last decades has provided the basis data to study these objects. Adding this to the advances in our understanding of Be star theory and in the computational simulations, our knowledge of the physics of Be stars and their detailed theoretical models reached an unprecedented level (Sect. 2). These efforts allowed us to draw a wide overview regarding the *Be phenomenon*. The current status progress is partially summarized in the review paper Rivinius et al. (2013), but since then many other theoretical and observational works have added to our knowledge (Sect. 1.1).

The life cycle of a Be CSD is quite complex, since the vast majority of Be stars shows variability in different temporal scales (e.g. Rivinius et al. 2001; Draper et al. 2011), the dynamical evolution of the disk depends strongly on the mass injection rates. Different scenarios of mass injection rates have already been studied by Haubois et al. (2012) and are beyond the scope of this paper. Conceptually, the disk formation starts from material ejected from the star through some still unknown process (Sect. 1.1). After being ejected, the material starts to be diffused outwards by viscous torques resulting in the formation of a decretion CSD. The dissipation of the CSD, after cease the injection of matter, part of the material in the inner disk is re-accreted onto the star, providing the necessary angular momentum to diffuse the disk outwardly (e.g. Ghoreyshi et al. 2018). The current paradigm that comprises the theory behind the CSD of CBe is the viscous decretion disk model (VDD, Sect. 1.1).

The study of Be stars is essential for several reasons. For instance, despite the paucity of massive stars[1], they play a crucial role in the evolution of the Universe, being regarded as one of

[1] The terms massive star and high-mass star denote OB stars sufficiently massive to produce type II supernovae ($M_\star / M_\odot > 8$) to the solar abundances. Then, the term high-mass protostar denotes objects with $M_\star / M_\odot > 8$ which have not started the hydrogen burning.

the main sources of heavy elements and UV radiation (Massey 2003), even so our understanding of massive star formation is still incomplete. Moreover, they rarely born isolated, in such case the combined effects of winds, massive outflows of nearby companions, gravitational interaction, and supernova of these objects provide energy that can trigger processes of mixing and formation of turbulence into the interstellar medium (Martins et al. 2005), as well as affect their global evolution (Zinnecker & Yorke 2007). Additionally, the fraction of Be among B stars is not negligible, ranging from 3 to ∼ 50 % (e.g. Wisniewski & Bjorkman 2006; McSwain & Gies 2005; Zorec & Briot 1997; Keller et al. 1999; Maeder et al. 1999; Marco & Negueruela 2013; Bastian et al. 2017). Finally, regarding the evolutionary study of stellar rotation, the relative abundance of the B-type stars, compared to massive O-type stars, makes them the best targets to explore rotational effects (Huang et al. 2010). Therefore, a good knowledge of their properties is crucial and requires the development of either evolutionary or atmosphere models.

In stellar modeling, one of the most challenging problems involving the study of Be, Bn (Lamers et al. 1980), B, Oe (e.g. Conti & Leep 1974; Negueruela et al. 2004) and Ae stars (Bohlender 2016) is the inference of their fundamental parameters (i.e., mass, temperature, rotation rate, radius, inclination, etc). This task becomes difficult due to their peculiar high rotation rates and their disk excess, which could explain the absence of synthetic Be spectral grids available for general application in the literature. In fact, the fast rotation is an important ingredient to understand the formation and evolution of stars (e.g. Collins 1963; Granada et al. 2013; Cranmer 2005). It is especially relevant in our case, since high-rotation rates are expected to be more common among early spectral types (O and B stars) (Cranmer 2005). As pointed out by Ekström et al. (2011), the effects on the stellar structure during its evolution are several: oblateness (e.g. Maeder 2009; Collins & Harrington 1966), mixing, anisotropic winds, and *gravity darkening* (Collins 1963). For these reasons, in principle, the gravity darkening and oblateness must be considered in any modeling, once its effects produce relevant changes upon the disk thermal structure (e.g. McGill et al. 2011; Frémat et al. 2005), on the SED (Townsend et al. 2004) and on its brightness distribution (von Zeipel 1924). Additionally, we must emphasize the influence of the circumstellar disk common in active Be stars, in such cases the star is veiled by the disk, making the problem more complex. The, we have a coupled problem: the apparent stellar parameters are changed by the disk, while the disk structure depends on the stellar characteristics. Still, in this context, more detailed studies of individual Be stars and MS O, B and A subclasses are necessary to provide further comprehension about the origins of the *Be phenomenon*.

Departing from the computation of an extensive grid of realistic models (Sect. 2) and modern statistical inference tools, we present a new and robust method to self-consistently and simultaneously determine both photospheric and disk parameters of Be stars from multi-technique observations. Our method considers effects due to the rapid rotation, which is largely ignored in the literature. Subsequently, we present two applications to exemplify the use of the method. Initially, we access the universality of the VDD scenario with a statistically significant sample of 111 main-sequence stars, including Be, Bn, B, Ae and Oe spectral types. Including O and A spectral types are needed, since the spectral limits of the *Be phenomenon* are still uncertain (e.g. Golden-Marx et al. 2016; Bohlender 2016). These results provide a statistical description of the physical conditions of Be disks. Finally, we revisit the physical parameters of the well-known Be star β CMi (Klement et al. 2015a);

The paper is organized as follows. First, we discuss the model disk adopted (Sect. 1.1). The tools and the grid of models used are shown in Sect. 2. In Sect. 3, we describe the adopted procedure used in the determination of the parameters of interest. We discuss and analyze the results in Sections 4 and 5. We summarize our conclusions in Sect. 6.

1.1. Viscous Decretion Disk Model

Disks are natural consequences of accretion systems, being present in the formation of Young Stellar Objects and in close binary systems with mass exchange (Owocki 2006). In this context, Be stars are too old to have kept a protostellar disk. Our conception about the properties of the circumstellar material around Be stars has evolved significantly since the pioneer works by Struve (1931). In the last decade, emerged a consensus of how Be disks are structured thanks to observational and theoretical advances. For instance, the confirmation that the CSD shape was not spherically symmetric came from polarimetric and optical interferometric observations (e.g. McLean & Brown 1978; Porter 1996; Quirrenbach et al. 1997). These facts have been recently strengthened by measurements of opening half-angles of CBe (Cyr et al. 2015). The values range from 0.15° to 4.0° in thin disks, reaching larger values (3.7° to 14°) in thicker disks.

Undoubtedly, the only theory capable of explaining the global picture presented by observations of Be disks is the Viscous Decretion Disk model (VDD), proposed by Lee (1991) and developed by several other authors (Porter 1999; Okazaki 2001; Bjorkman & Carciofi 2005b). The VDD model is similar to that employed to protostellar disks (Pringle 1981); the difference being that Be disks varies between *outflowing* and *inflowing*, while pre-MS disks are *inflowing*. In the VDD model, it is supposed that an unknown mechanism injects material in the disk basis in an orbital keplerian velocity. Remarkably, non-radial pulsation (Baade et al. 2016) is likely the ingredient responsible in triggering the *Be phenomenon*. After the material being ejected, the turbulent viscosity transports angular momentum from the inner material to the outer disk regions. Therefore, the density rises faster in the inner disk regions during its growth.

Depending on the scenario, for instance in the cases of long period of constant mass injection, the disk will reach a steady-state density profile with radial power-law with $n = 3.5$ in Eq. 6. Here, the density profile of the disk can be considered constant and independent of the previous evolutionary history of the disk (Haubois et al. 2012). Likewise, different ranges of n would indicate other evolutionary phases. However, we must take into account that the index n can also change whether other effects are present, as non-isothermal viscous diffusion (Carciofi & Bjorkman 2008) or due the presence of a companion.

A peculiar phenomenon in binary Be systems is that the secondary could truncate the disk to a radius dependent on the orbital parameters (eccentricity and semi-major axis) (e.g. Rivinius et al. 2013; Okazaki et al. 2002). This hypothesis is still difficult to be directly confirmed due to the flux contrast between the primary and the faint companion (Peters et al. 2016). The SED turndown, as evidenced by Klement et al. (2017), occurs due to the truncation of the outer disk. However, there are two main hypothesis for the truncation: the *tidal influence from a close companion* and the *transonic transition*. The second is defined by the radius where the resonant torque is larger than the viscous torque, resulting in a sudden drop in the gas density profile (Okazaki et al. 2002). As mentioned by Klement et al. (2017), this transition is expected to occur only at wavelengths at roughly a magnitude longer than the cm data in Be disks.

The VDD model employed successfully in the study of individual Be stars (e.g. Carciofi et al. 2006; Carciofi et al. 2009; Tycner et al. 2008; Wheelwright et al. 2012; Carciofi et al. 2012; Wheelwright et al. 2012; Faes et al. 2015; Escolano et al. 2015; Klement et al. 2015a; Ghoreyshi et al. 2018) and samples of Be stars (e.g. Haubois et al. 2012; Haubois et al. 2014; Vieira et al. 2015; Panoglou et al. 2016; Vieira et al. 2017; Klement et al. 2017; Rímulo et al. 2018).

2. The BeAtlas Grid

The BeAtlas project arises in the context of grid based modelling, routinely applied to the determination of physical model parameters. The BeAtlas comprises two systematic grids of models: a photospheric-only (i.e., diskless) grid, and a star plus disk grid (hereafter referred to as "disk models"), computed according to the VDD formulation.

The initial aims of the BeAtlas project are: (i) interpreting the observations of large samples of B and Be stars (and part of the underlying spectral types); (ii) detailed modelling of individual objects; (iii) allowing theoretical studies on the physical properties of disks (e.g., disk thermal structure, correlations between parameters, etc.); and (iv) planning of new observations. Finally, we naturally expect that many other applications will arise from such a comprehensive project.

The radiative transfer code used to compute the models is briefly described in Sect. 2.1. The model description and grid definition are presented in the subsequent sections, for both stellar grid (Sect.2.2) and star plus disk grid (Sect.2.3).

2.1. Radiative transfer calculations

The models were calculated with the Monte Carlo radiative transfer code HDUST (Carciofi & Bjorkman 2006, 2008). It has been successfully applied in several previous works to interpret multi-technique observations, being the most recent examples: the interferometric study of Achernar (Dalla Vedova et al. 2017), the computation of Be disk line profiles subjected to a companion (Panoglou et al. 2018), and the interpretation of optical Be star light curves using the VDD model (Rímulo et al. 2018; Ghoreyshi et al. 2018).

Based on an iterative method, HDUST is capable of simultaneously computing the radiative and statistical equilibrium in circumstellar media, besides hydrostatic equilibrium for thin disk models. The code accepts arbitrary 3D geometry and kinematics, and assumes a NLTE regime. The circumstellar chemistry is composed by atomic hydrogen and/or dust grains, and the inclusion of other atomic species is currently under development (Carciofi et al. 2017). The implemented gas opacity sources are: Thomson scattering, bound-bound, bound-free and free-free mechanisms, while the dust grains opacity is computed using Mie theory. The code also offers a realistic description of the star, which includes limb darkening, gravity darkening, and rotational flattening according to the Roche model (see details in Sect. 2.2). As result, HDUST computes the emergent spectrum (both continuum and emission lines), the polarized spectrum, and synthetic images.

For this work, we adopted a spectral coverage ranging from 1,000 Å (ultraviolet domain) up to 75 cm (radio wavelength), for both photospheric-only and disk models. Finally, we computed each model at ten different orientations with respect to the observer (i.e., angle between rotation axis and line-of-sight), ranging from the edge-on to the pole-on case with cosine-spaced steps. The grid repository can be accessed via the VIZIER service or through our website[2].

2.2. Stellar Description

For the photospheric models, we adopted a Roche equipotential (e.g., Cranmer 1996) to describe the rotating stellar geometry. The limb darkening follows the prescription given by Claret (2000), and the gravity darkening effect is described by the modified von Zeipel law (see Cranmer 1996):

$$T_{\rm eff}(\theta) = \left(\frac{L/\sigma_{\rm B}}{\oint g^{4b} {\rm d}A} \right)^{1/4} g^b(\theta), \quad (1)$$

where θ is the polar angle (spherical coordinates), $\sigma_{\rm B}$ is the Stefan-Boltzmann constant, and b is the gravity darkening exponent. As mentioned in Sect.2.1, all these ingredients are included in HDUST code.

Two possibilities were considered to define the stellar grid parameters: an empirical grid or a theoretically oriented grid. An empirical grid is defined by the typical ranges of parameters found in the literature for B-type stars, in or close to the main-sequence. It may be specified by the following four parameters: stellar mass ($M_\star$), polar radius ($R_{\rm pole}$), stellar luminosity (L) and the rotation rate (W). The choice of these parameters rely in principle on the ranges typically found in the literature for B stars on the main-sequence or close to it (e.g. Schmidt-Kaler 1982; Harmanec 1988). Consequently, the correlation between $M_\star$, $R_{\rm pole}$ and L are taken into account implicitly. On the other hand, the theoretically oriented grid is defined to be constrained by stellar evolution models. The advantages of such approach are both reducing the number of parameters necessary to specify a given model, and associating a specific evolutionary stage to it.

For this work, we adopted the theoretically oriented option. In particular, we chose the parameters $M_\star$, W, and $t/t_{\rm MS}$ to completely describe each model, where $t/t_{\rm MS}$ represents the time fraction spent in the main-sequence. The remaining parameters necessary for the radiative transfer calculations, $R_{\rm pole}$ and L, can be subsequently determined from the adopted stellar models.

To constrain the stellar parameters, we adopted the Geneva stellar evolution models [3] (Georgy et al. 2013). In particular, the selected grid provides models at solar metallicity, stellar masses ranging from 1.7 to 20 $M_\odot$ [4] (roughly from early-A to late-O spectral types), and rotation rate values from the non-rotating case up to a quasi-critical case ($W \simeq 0.99$, where $W \equiv v_{\rm rot}/v_{\rm orb}$).

To constrain the gravity darkening exponent, we adopted the model presented by Espinosa Lara & Rieutord (2011), where b is function of rotation rate W only. Such model has provided a successful description for many cases in the literature (e.g., Domiciano de Souza et al. 2014).

For the disk model grid, we decided to set the mass range lower limit at 3 $M_\odot$, due to convergence difficulties of the Monte Carlo radiative transfer approach at lower masses. Also, we decided to restrict the disk models to the $W \geq 0.5$ subset, since no Be star disk was ever detected around slow rotators (see the compilation presented in Rivinius et al. 2013).

Finally, both grids also include different ages in the main-sequence, from the ZAMS to the TAMS. A total of 770 photospheric models was computed, and the adopted parameters are

[2] http://beacon.iag.usp.br/joomla/

[3] https://www.unige.ch/sciences/astro/evolution/fr/base-de-donnees/syclist/.

[4] The original grid ranges up to 15 $M_\odot$, being the 20 $M_\odot$ model gently made available by C. Georgy in private communication.

summarized in Table 1. The table also contains the adopted disk parameters, which are described in the next section.

2.3. Disk models

Despite of being a simple approximation of the VDD model, a power law parametrization of the disk radial density profile represents a useful description, which is readily comparable to several results in the literature. Besides, part of the dynamical information contained in the time dependent solutions of the VDD model can be extracted from this particular formulation, since different intervals of the power law exponent can be associated to specific disk dynamical states (Vieira et al. 2017). The adopted parametric expression for the mass density may be written as:

$$\rho(r,z) = \frac{\Sigma_0}{H\sqrt{2\pi}}\left(\frac{r}{R_{\rm eq}}\right)^{-n} \exp\left[-\frac{z^2}{2\,H^2}\right], \tag{2}$$

where Σ_0 is the disk base surface density, $R_{\rm eq}$ is the equatorial stellar radius, r and z are respectively the radial and vertical cylindrical coordinates in the stellar frame of reference, and H is the disk scaleheight. In particular, H is a function of the radius given by:

$$H(r) = H_0\left(\frac{r}{R_{\rm eq}}\right)^{\beta}, \tag{3}$$

where $H_0 = (c_{\rm s}/V_{\rm crit})\,R_{\rm eq}$, $c_{\rm s} = (k\,T_{\rm d}/\mu\,m_{\rm H})^{1/2}$ is the isothermal sound speed, $V_{\rm crit} = (G\,M_\star/R_{\rm eq})^{1/2}$ is the critical velocity, k is the Boltzmann constant, μ is the the molecular weight of the gas, $m_{\rm H}$ is the hydrogen atom mass, $T_{\rm d}$ is the disk temperature, and β is the disk flaring exponent. Since the disk temperature is actually highly non-isothermal, we adopt $T_{\rm d} = 0.72\,T_{\rm pole}$ as an educated guess to compute H_0 (Carciofi & Bjorkman 2006). Additionally, β is fixed at 1.5 in the present work, which corresponds to the VDD model isothermal solution (e.g., Bjorkman & Carciofi 2005a). Future grid versions are planned to have self-consistent scaleheights (Carciofi & Bjorkman 2008).

The adopted upper and lower limits of the disk surface base density were defined as functions of the stellar mass, and can be written as (vou derivar estas expressões nos próximos dias...)

$$\Sigma_0^{\rm upper}(M) = \begin{cases} \exp(-aM^2 + bM + c), & M \le 8.6\,{\rm M}_\odot, \\ \exp(dM + e), & M > 8.6\,{\rm M}_\odot, \end{cases} \tag{4}$$

and

$$\Sigma_0^{\rm lower}(M) = \exp(-fM^2 + gM + h). \tag{5}$$

The upper limits correspond to the hdust convergence limits, and were estimated from previous experiences with the code, while the lower limits roughly correspond to the detection limit of an Hα emission line. Notice that the convergence limitation does not impose a severe restriction, since a similar trend of increasing Σ_0 upper limit with stellar mass is also observed in nature (Vieira et al. 2017).

For the power law exponent n, we adopted the values ranging from 1.5 to 4.5, which are in agreement with those found by Vieira et al. (2017). Finally, the disk size is defined by a truncation radius, $R_{\rm D}$, ranging from 10 to 100 $R_{\rm eq}$.

For this work, we computed only lower mass sub-sample of the disk models grid ($3 \le M_\star/M_\odot \le$?), constituting a total of ? models. As a first application, this sub-grid allowed the interpretation of the SED of β CMi (Sect. 4.2), a Be star of late B spectral type (B8Ve).

2.3.1. The Steady-State VDD Model

In our study, we adopted the parametric description of the VDD density profile given by Bjorkman & Carciofi (2005a), in which the radial disk density profile is a power law and has hydrostatic equilibrium structure in the vertical direction,

$$\rho(r,z) = \rho_0\left(\frac{r}{R_{\rm eq}}\right)^{-n} \exp\left[-\frac{z^2}{2\,H^2(r)}\right]. \tag{6}$$

The constant ρ_0 is the disk base density, $R_{\rm eq}$ is the equatorial stellar radius, r is the radial coordinate, and z is the vertical cylindrical coordinate in the stellar frame of reference. Where the disk scaleheight, $H(r)$, and the surface base density, Σ_0, are given by,

$$H(r) = H_0\left(\frac{r}{R_{\rm eq}}\right)^{\beta}, \tag{7}$$

$$\Sigma_0 = \sqrt{2\pi}\rho_0 H_0 R_{\rm eq}^{n-\beta}, \tag{8}$$

where $H_0 = (c_{\rm s}/V_{\rm crit})\,R_{\rm eq}$, $c_{\rm s} = (k\,T_{\rm d}/\mu\,m_{\rm H})^{1/2}$ is the isothermal sound speed and $V_{\rm crit} = (G\,M_\star/R_{\rm eq})^{1/2}$ is the critical velocity. k is the Boltzmann constant, μ is the the molecular weight of the gas, $m_{\rm H}$ is the hydrogen atom mass, $M_\star$ is the stellar mass, β is the disk flaring exponent (Vieira et al. 2017), and $T_{\rm d}$ is the disk temperature.

3. Bayesian Approach

Recent efforts (e.g. Rímulo et al. 2018; Vieira & Carciofi 2017) showed that a grid, no matter how much science has been put to it, is useless without a statistical engine that allows exploring all the solutions. This problem arises in the context of *machine learning* or *inference techniques*, this is of the set of techniques used for interpreting and comparing observational data with models (Ivezić et al. 2014), and, naturally, leads to the employment of Bayesian inference techniques. An additional reason for choosing the Bayesian approach is its capacity to combine the data with prior knowledge.

In our problem, we adopted the EMCEE inference tool (Foreman-Mackey et al. 2013). EMCEE is a high-performance open source PYTHON module[5]. It uses variations of a MCMC method developed by Goodman & Weare (2010) where they use several "walkers" to propagate multiple chains simultaneously for the parameters determination, correlations and error estimate. This procedure reduces the degeneracy cases. Next, we discuss the procedure adopted.

3.1. General Description

MCMC methods are projected to get efficiently correlations and estimates of parameters, even in parameters spaces with many dimensions. This procedure uses random numbers to generate parameters to a determined probability density function (PDF). Formally, the a MCMC code gets the parameters Θ from a PDF, given known measurements. The result is the marginalized probability function[6], $p(\Theta, \alpha|D)$, of the set of model parameters (Θ)

[5] It is available online: http://dan.iel.fm/emcee under the MIT License;

[6] Marginalization: process of integrating over all possible parameter values and propagating the uncertainties until the final result is reached.

Table 1. BeAtlas stellar parameters of the photospheric grid model (third column) and BeAtlas parameters of the disk models (fourth column). [a] defined as $W = v_{\rm rot}/v_{\rm orb}$, where $v_{\rm rot}$ is the rotational velocity at the stellar surface and $v_{\rm orb}$ is the Keplerian orbital velocity directly above the stellar surface. [b] Based on the parametric prescription of $\rho_0\,(R_{\rm eq}/r)^n$. The spectral types are in agreement to Martins et al. (2005), Townsend et al. (2004), and Adelman (2004), for O, B and A spectral types, respectively.

	Parameters	Ranges	
		Stellar	Disk
ST	Spec. Type	O8 - A7	O8 - B9
$M_\star$	Mass ($M_\odot$)	1.7 - 20	3 - 20
W	Rotation Rate[a]	0.00 - 0.99	0.5 - 0.99
$t/t_{\rm ms}$	Stellar Age	0 - 1	0 - 1
n_0	Numerical base density (cm^{-3})	-	1.5 - 4.5
$R_{\rm D}$	Disk radius ($R_{\rm eq}$)	-	10 - 100
n	Mass density radial exponent[b]	-	1.5 - 4.5
i	Inclination angle (°)	0.0 - 90.0	0.0 - 90.0

for a set of observations (D) and a list of nuisance parameters (α),

$$p(\Theta,\alpha|D) = \frac{1}{Z}p(\Theta,\alpha)p(D|\Theta,\alpha); \tag{9}$$

where $p(\Theta,\alpha)$ is the distribution *a priori*, $p(\Theta,\alpha|D)$ is the likelihood, and $Z = p(D)$ is a normalization factor.

Having defined the likelihood and prior functions, together with the models and the observations, the `MCMC` generates a *random walk* in the parameter space and returning parameters to draw samples $\{\Theta_i\}$ from the posterior probability density.

The posterior probability defines, for a set of parameters (D), the probability of them being true. Therefore, once the samples produced by `MCMC` are available, the marginalized constraints on Θ can be approximated by the histogram of the samples projected into the parameter subspace spanned by Θ. The uncertainties on each parameter were defined as the measuring of percentiles of 16 and 84 % on the marginalized `PDF`s, and the best fit as the median.

3.2. EMCEE Implementation

We adopted as likelihood the following function,

$$\log p(D|\Theta,\alpha) = -0.5\left[\frac{\log(F_{\rm obs}/F_{\rm mod})}{\sigma_{F_{\rm obs}}/F_{\rm obs}}\right]^2 \tag{10}$$

where $F_{\rm obs}$ and $F_{\rm mod} = F_{\rm mod}(\Theta)$ are the observed and model fluxes.

In more detail, the fitting procedure is performed with the grid of models ($F_{\rm mod}$ in Eq. 10) and the observed fluxes ($F_{\rm obs}$ in Eq. 10). These observables can be converted to the fluxes received at the Earth by,

$$F(\lambda) = F_0(\alpha)(\lambda)\times\left(\frac{10}{d}\right)^2\times f_{\rm unred}, \tag{11}$$

where $F(\alpha)(\lambda)$ is the emergent stellar flux, α is the set of intrinsic physical stellar properties, d is the distance to the star, and $f_{\rm unred}$ is the correction of the total extinction along the line of sight.

The reddening correction, represented by the function $f_{\rm unred}$, is fundamental since it affects significantly the determination of the stellar parameters. Recent articles attests the complexity of the extinction determination by lines for Be stars (McEvoy et al. 2015). For this reason, the use of alternative techniques for estimating $E(B-V)_{\rm IS}$ that are independent of circumstellar material (e.g. Beeckmans & Hubert-Delplace 1980) becomes essential in our study. Zagury (2013) studying a large absorption feature centered at 2 175Å called `UV` bump, showed that the duality between the forms of curves in the bump region, linear or with a bump, could be used to investigate the parameter $E(B-V)$ even in circumstances of low column density directions, and stars close to the obscuring material (see Figure 1 of Zagury 2013). To implement this method of correction, first, we studied the extinction corrections that have the parametrization of the bump (Cardelli et al. 1989; Fitzpatrick 1999), among them we adopted the parametrization suggested by Fitzpatrick (1999). Next, we evaluated the interstellar extinction inside each interaction. For this, a progressive dereddening is calculated by taking interactively random values of $E(B-V)$ upon the flux models in the region of the bump (see Eq. 11). We adopted a typical value of $R_{\rm V} = 3.1$ for all spectra (Schultz & Wiemer 1975). Next, we discuss the priors adopted during the `MCMC` procedure.

3.3. Prior Choice Description

We used as priors the HIPPARCOS parallax (van Leeuwen 2007) and measurements of $v\sin i$ taken from several sources (Frémat et al. 2005; Levenhagen & Leister 2006; Abt et al. 2002; Challouf et al. 2015; Nieva, María-Fernanda & Przybilla, Norbert 2014; Spectroscopic survey of `COROT`[7] Be stars). When available, the GAIA DR2 parallaxes (201 2018) also were used.

The chosen prior distance function was,

$$\log p_\pi(\Theta,\alpha) = -0.5\left(\frac{\pi_{\rm obs}-\pi_{\rm mod}}{\sigma_{\pi_{\rm obs}}}\right)^2, \tag{12}$$

where $\pi_{\rm mod}$ is the random parallax generated in each step of the inference; $\pi_{\rm obs}$ and $\sigma_{\pi_{\rm obs}}$ are the observed parallax and its uncertainty, respectively.

By providing $v\sin i$ values to the code, we can constrain the values of the likely inclinations, masses and oblateness, i.e. physical quantities directly related with. To implement such a prior, it was calculated for each interaction a $v\sin i(\Theta)$. For the stars with $v\sin i(\Theta)$ without uncertainty, we fixed the errors as 10 % of the measurement. Here, it is important to highlight the fact pointed by Townsend et al. (2004), i.e. that the classic $v\sin i$ values, which did not consider the gravity darkening effect, could be underestimated by 9 to 33% at $W = 0.75$ for B0 to B9-type

[7] `http://www.astrosurf.com/buil/us/bestar.htm`;

stars. Therefore, some $v \sin i$ employed could propagate error in the inference of studied parameters. The prior function used to the $v \sin i$ was,

$$\log p_{v \sin i}(\Theta, \alpha) = -0.5 \left(\frac{v \sin i_{\rm obs} - v \sin i_{\rm mod}}{\sigma_{v \sin i_{\rm obs}}} \right)^2 . \quad (13)$$

where $v \sin i_{\rm mod}$ is the random $v \sin i$ generated in each step of the inference; $v \sin i_{\rm obs}$ and $\sigma_{v \sin i_{\rm obs}}$ are the observed $v \sin i$ and its uncertainty, respectively.

Once having defined the fluxes, the best-fitting model, in a first stage, is obtained by solving the Eq. 9 with the likelihood given by the Eq. 10 together with the prior functions (Eq. 13 and 12) for all set of parameters simultaneously. Thereafter, the code returns samples from the posterior probability density for each free parameter.

4. Applications

In this section, we applied our inference method for a set of 162 early-type stars (O, B, and A spectral types) (Sect. 4.1). This procedure have not been applied just to check the validity of our method, but also to allow us to examine a diversity of theoretical and methodological problems. After, we show the results obtained for the star β CMi (Sect. 4.2).

4.1. UV description

Our start point was to use the UV spectral domain (1 150 - 3 200 Å) in the procedure described in the Sect. 3. At first sight, the choice of the UV domain appears to be a natural first step, however there are two main reasons for that, namely: (i) in this spectral domain B stars emit most of their energy (70% - 100%) (e.g. Fitzpatrick & Massa 1999; Bless & Percival 1997); (ii) in the case of Be stars, the contribution of the disk to the spectra is minimum in this domain (e.g. see Fig. 2 of Klement et al. 2015a and Fig. 1 of Briot 1978). Therefore, regarding the study of the stellar properties of the stars, the UV domain might provide one of the best observational available data to our method.

4.1.1. UV disk excess

Despite these previous results already pointed to a weak influence of the disk in the UV domain, we revisited this problem by using our grid models, exploring different scenarios. In order to do that, we define the disk excess as the mean taken in the UV domain,

$$\left\langle \frac{\Delta F}{F_\star} \right\rangle_{\rm UV} = \frac{1}{\Delta\lambda} \int_{\lambda_{\rm min}}^{\lambda_{\rm max}} \frac{|F_\lambda - F_\lambda^\star|}{F_\lambda^\star} d\lambda; \quad (14)$$

where $\lambda_{\rm min} = 1000$ Å, $\lambda_{\rm max} = 3000$ Å, $\Delta\lambda = \lambda_{\rm max} - \lambda_{\rm min}$, $F_\lambda^\star$ is the specific stellar flux and F_λ the total flux.

Figure 1 shows the defined measure of UV excess for a few representative cases of Be star disks. As expected, we see that in general either larger Σ_0 or smaller n values are associated to larger UV excesses. We also observe larger excess values for the edge-on cases. In particular, the 4 $M_\odot$ model excess has as upper limit of 1% of disk contribution, while the 9 $M_\odot$ model reaches a 10% UV excess only for large densities ($\Sigma_0 \gtrsim 1.5$) at edge-on orientation.

These results demonstrate that the disk contribution can be neglected in the UV domain. This is an important realization, since it allows one to use UV observations to independently constrain the photospheric parameters, in spite of the presence of a circumstellar disk. This is the main hypothesis of the present BeAtlas application, which will be developed in the next sections.

4.1.2. UV data selection

There are several missions covering the UV domain: EUVE (70 – 760 Å), CHIPS (90 – 260 Å), ORFEUS (400 – 1 250 Å), Astro 2 (425 – 3 200 Å), FUSE (905 – 1 187 Å), IUE (1 145 – 3 300 Å), and GALEX (1 300 – 3 000 Å). Among these missions, we adopted data from the International Ultraviolet Explorer spatial mission - IUE, which operated between 1978 and 1996. The IUE has two cameras: the SWP camera (1 145 – 1 975 Å) and the long-wavelength LWP/LWR cameras (1 850 – 3 300 Å).

The data selection followed the procedure described by Freire Ferrero et al. (2012), this is, there were selected high-dispersion large-aperture observations, because they can be calibrated in flux units. Another caution was to select data with exposure time < 60 s. After that, we selected the IUE fits re-binned files from INES Archive Data Center[8], maintained by ESA.

After the data selection, we calculated the flux level (F_0) and its inclination m for each selected spectrum for each selected stars by fitting a exponential function,

$$f = F_0 \left(\frac{\lambda}{\lambda_0} \right)^m . \quad (15)$$

This procedure allowed us to verify through the UV domain, whether the stellar emission suffered some variation in the period it was observed. Hence, the resulting complete UV spectrum is the combination of the spectra that showed levels and inclinations inside three times the standard deviation (σ) calculated using all the fluxes. Therefore, *for all selected stars, we removed the spectra which were out of the 3 σ of the mean values obtained for the inclination and level, respectively*.

As an example, the adjusted parameters F_0 and m obtained from each SED of α Arae are shown in Fig. 2. These results show that α Arae can be considered stable in the UV domain. We see that only two spectra are out of the average values (dashed lines) in the dates 1994-03-30 and 1986-04-06 (points with black error bars). These spectra were removed from the analysis.

4.1.3. Sample of stars

Our sample of stars comprises O, B and A stars, including the peculiar classes Be, Bn, Ae, A shell and Oe stars. Each selected peculiar class is detailed ahead in this section. Basically, we selected stars from the Bright Star Catalogue (Hoffleit & Jaschek 1982) and from Jaschek & Egret (1982). After, we selected just the luminosity classes V and IV (MS and subgiants); the exception was the star ϕ And (HD 6811). Naturally, the stars without UV data were discarded. The selection is shown in Table C.1.

The rapidly-rotating Bn stars are remarkably known to have nebulous absorption lines and absence of emission lines (Lamers et al. 1980). They are not a negligible subgroup of the B stars, for instance, Baade (1992) pointed that there is for every Be star listed in the Bright Star Catalogue a correspondent Bn star with

[8] http://sdc.cab.inta-csic.es/cgi-ines/IUEdbsMY.

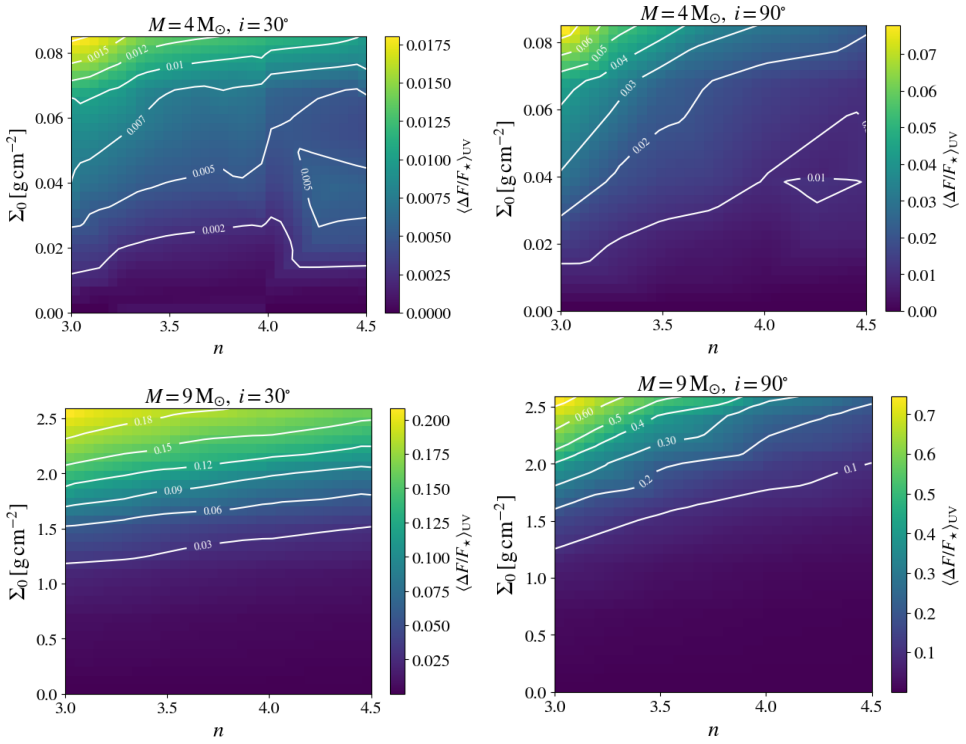

Fig. 1. Top: UV disk excess of a typical late-type Be star ($M = 4\,M_\odot$) at different orientations. Left: $i = 30°$. Middle: $i = 70°$. Right: $i = 90°$. Bottom: UV disk excess of a typical early-type Be star ($M = 9\,M_\odot$) at different orientations. Left: $i = 30°$. Middle: $i = 70°$. Right: $i = 90°$.

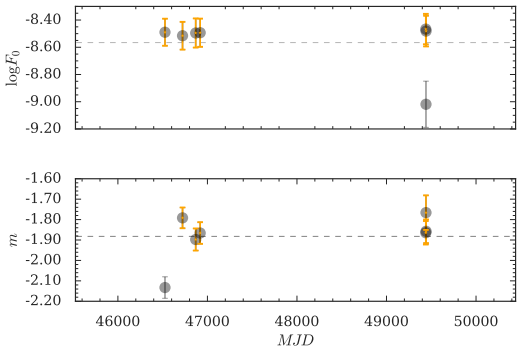

Fig. 2. Parameters F_0 and m found to α Arae. Modified Julian Date (MJD) are in abscissas and F_0 and m parameters in ordinates. Dashed lines represent the mean values.

the same spectral-type and projected velocity, $v \sin i$. Whether or not this group has an evolutionary link with the Be stars is still an open question. However, the occurrence of Be/Bn transitions appears to be absent. In summary, there are three main characteristics that differentiate Be and Bn stellar types which point to independent evolutionary paths: (i) no record of Bn stars observations displaying any circumstellar emission; (ii) the complete absence of magnetic fields in Be stars, in contrast with a high incidence among Bn stars; and (iii) the absence of non-radial pulsation in Bn stars, in contrast with the relatively high incidence among Be stars (Baade 1992).

Even the hottest stars can present signals of decretion disks, this is the case of Oe stars. Oe stars are rapidly rotating O stars with narrow Balmer and helium emission lines along with broad absorption lines, but not the characteristic emission features of Of stars, in HeII λ4686 and NIII λ4634-40-42, which are associated with strong stellar winds (e.g., Conti & Leep 1974; Walborn et al. 2010). They also present V/R and Balmer line variability (e.g. Rauw et al. 2007) and can present HeI emission lines (e.g., Frost & Conti 1976). In the context of the VDD model, Golden-Marx et al. 2016 confirmed that Oe stars are the high-mass extension of the *Be phenomenon*, however it still appears not to be widely accepted (e.g, Rauw et al. 2015). Oe stars have stronger radiative forces, reducing their disk lifetime to the order of days[9]. This can explain the rarity of the *Be phenomenon* among earlier spectral types (e.g. see Fig. 12 in Kee et al. 2016). Actually, the lifetime of a disk decreases by a factor of ~ 250 when we compare B3 and O7 spectral types (Kee et al. 2016).

[9] Johnston et al. 2015 published the discovery of a keplerian-like disk around the forming O-type star AFGL 4176 from ALMA data in 1.2 mm.

The question about the existence of a disk around Oe stars remains a wide open question, because we have just indirect evidences of the disk around these stars as their high projected rotational velocities (Negueruela et al. 2004). Another interesting point is the rarity of the *Be phenomenon* in spectral types earlier than B0, which might be related with: (i) the force that their fast radiative winds provoke on the circumstellar material (Negueruela et al. 2004); (ii) models of fast-rotating stars (Meynet & Maeder 2000) predict that the rotation rates increases during the lifetime for $M_\star < 15\,M_\odot$, and decrease for $M_\star > 15\,M_\odot$ because of angular momentum loss caused by their strong winds.

For the purpose of study the presence of the Be phenomenon in late-type O stars, we made use of a new calibration of the stellar parameters of O stars given by Martins et al. (2005). In their work, contrary to previous works (e.g. Vacca et al. 1996), they considered new ingredients such as solar metallicity, wind, and line-blanketing effect, but ignored the oblateness. They show their results in two types of effective temperature scales: a) an *observational scale* derived from a compilation based in recent spectroscopic studies; b) *theoretical scale*: calculated directly from interpolations on a CMFGEN (Hillier & Miller 1998) grid of non-LTE spherically extended line-blanketed models. They obtained a good agreement between the theoretical and observational scales for dwarfs and supergiant stars.

The A spectral class has two peculiar interesting spectral types: Ae and A shell stars. They might present emission in the Balmer lines and a strong IR excess. Bohlender (2016) found an increase in the frequency of Hα emission and shell phenomena in the most rapidly rotating A-type stars and a decrease as the $T_{\rm eff}$ decreases. These trends are also seen in CBe and might be ascribed to a disk. These peace of evidence made the Ae stars being regarded as the late-type extension of Be stars, although some of them might be β Pictoris objects, in this case, their disk would be pre-MS primordial disks (Rivinius et al. 2013).

4.1.4. The influence of the priors

In this section, we explore what the UV spectrum can provide alone and with a $v \sin i$ prior. For this purpose, we adopted a typical Be star, α Arae (HD 158427, HR 6510). This southern Be star is classified as a B2Vne[10]. Several reasons can be listed for its choice: (i) it has shown a relatively stable behavior in the last years; (ii) furthermore, Arae region seems suitable to the search of distant objects, since dark clouds are not as important there (Vega et al. 1980), resulting in lower extinction levels and, consequently, good S/N in the UV domain; (iii) its proximity (74.3 pc, van Leeuwen 2007) allowed the constitution of a rich observational history; (iv) recently, Bagnulo et al. (2015) determined a low magnetic field for α Arae ($< B_z > (G) = -27 \pm 38$, $MJD = 53869.353$), which strongly indicates that the *Be phenomenon* is present in α Arae (Grunhut et al. 2012).

Initially, we compute the stellar, geometrical and extinction parameters of α Arae, using as input only its IUE data. The left panel of the Figure 3 shows the corner plot obtained. The posterior probability distributions indicate that all the parameters were constrained. In this figure, it is also possible to verify the correlations among the parameters. However, it involves a certain effort because the reader should look at each 2D correlation map to understand the link between any two parameters. A way to work around this issue is the chord diagram (right panel of Fig. 3). Its circular layout has been promoted as one of the best visualizing methods to describe inter-relationships between parameters. The connections (bands) shared between the parameters indicates they share something in common, showing correlations more easily.

As a second step, we redo the procedure, but now considering the $v \sin i$ prior. The results are shown in Figure 4. At first sight, the posterior probability distributions appear narrower when compared with the distributions shown in Fig. 3. This indicates that the $v \sin i$ prior, in fact, improves the Bayesian approach. However, it becomes a difficult task to differentiate how much the adoption interfere in the correlations.

Comparing the two chord diagrams (right panels of the Figures 3 and 4), it is notable that including the $v \sin i$ prior broadens almost all bonds. Remarkably, the correlation among the inclination angle, rotation rate, age, and mass are improved. This was expected, since the $v \sin i$ involves, beyond the inclination angle ($\sin i$), the stellar mass and radius, which are coupled with the stellar age. This comparative work led us to consider the $v \sin i$ in all studied cases.

4.1.5. Results

The steps followed in this section were directed to explore the spectral limits of the *Be phenomenon*, evolutionary links among peculiar stars (Bn, Be, Ae and Oe stars); and to have a global overview of stellar properties of these stars, including rotational effects. We proceeded with the inference of the stellar parameters of the sample of stars shown in Section 4.1.3. The UV data of the selected stars were used in the procedure detailed in the Section 3.2. The table D.1 shows the stellar parameters inferred from this analysis. Thereafter, we compare our results with those from the literature (Frémat et al. 2005; Levenhagen & Leister 2006; Zorec et al. 2016)[11].

We compared the temperatures, luminosities and $\log g$ inferred by our method with the values found in the literature in Fig. 5. Both inferred values, $\log T_{\rm eff}$ and $\log L_\star$, agree, inside the error values, with the reference values present in the literature. Another important point is the trend for lower values found in the reference values for some stars, which might be caused by the difference between the methods. The luminosity, as well as the $t/t_{\rm ms}$, is a multiplicative factor, then it does not change the slope of the spectrum, only the flux level. The change in the luminosity is generated by the increase of the rotation as the star gets older, inflating its equatorial radius and, respectively, decreasing its polar radius by a few percents (2% at critical rotation for typical B; Ekström et al. 2008). Regarding the $\log g$, the inferred values are compared with the literature in the right panel of the Fig. 5. Although most reference values do not agree with our inferences, our inferred values are inside the typical range for B-type stars ($3.7 \lesssim \log g \lesssim 4.2$) (e.g. Silaj et al. 2014). The high precision inference of this measure comes mainly from the UV domain. It means that having the UV slope, independently of any other parameter, we can determine the mass and the temperature with precision.

The inclination angle, i, determination has a relative importance. It is justified by the degeneracy between the i and the luminosity. In principle, a star with $i \sim 0^o$ and late spectral type could appear like a star with $i \sim 90^o$ and an earlier spectral type. Therefore, the inference of the i might influence substantially the determination of the temperature, which might present a variation of over 50% between the polar and equatorial tem-

[10] http://simbad.u-strasbg.fr/simbad/sim-id?Ident=alf+ara.

[11] Levenhagen & Leister (2006) did not consider the rotational effects on the SED.

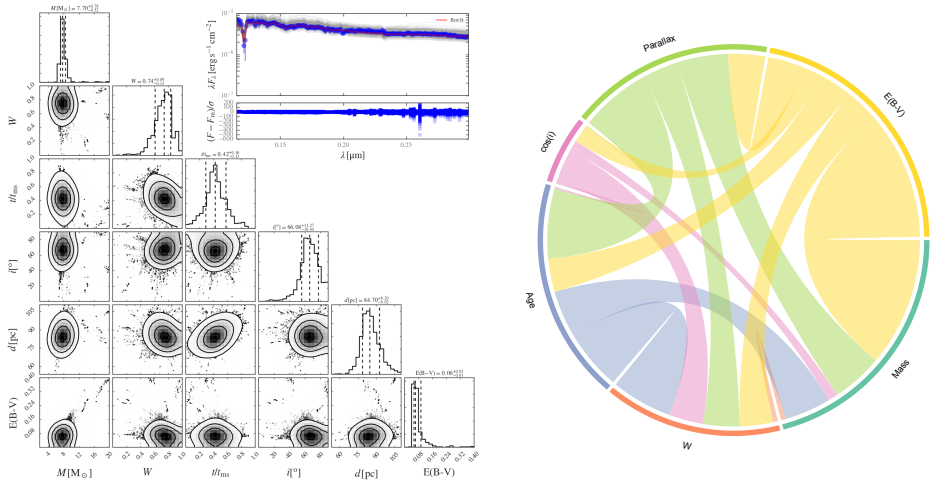

Fig. 3. Left: posterior probability distributions computed using `IUE` data. The `SED` fit is shown inset within the main panel, the solid gray lines represent the sample of total fluxes interpolated, and the red line represents the best adjust. The dashed lines in the diagonal subplots correspond to the 16th, 50th, and 84th percentiles of the distributions. The subplots under the diagonal subplots show the probability densities correlations between several pairs of parameters. Right: Chord diagram for the corner plot on the left.

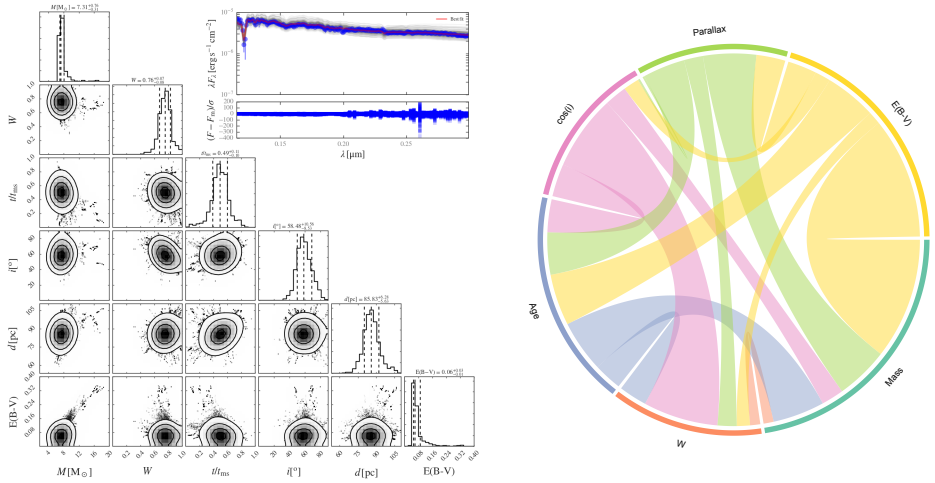

Fig. 4. Left: posterior probability distributions computed using `IUE` data and the v sin i prior. The `SED` fit is shown inset within the main panel, the solid gray lines represent the sample of total fluxes interpolated, and the red line represents the best adjust. The dashed lines in the diagonal subplots correspond to the 16th, 50th, and 84th percentiles of the distributions. The subplots under the diagonal subplots show the probability densities correlations between several pairs of parameters. Right: Chord diagram for the corner plot on the left.

peratures (Vinicius et al. 2007). This could explain the trend observed in the left panel of the Fig. 5. In the left panel of the Fig. 6, we present a comparison between the inclination angles inferred with the values found in the literature (Frémat et al. 2005). Our error bars are larger, but the results agree. The trend of the inferred inclinations to high values and the larger errors were caused by the v sin i prior adopted (see Sect. 3.3).

Some inferred $E(B-V)$ values are shown in the left panel of Fig. 6 together with their respective reference values (e.g. di Benedetto 1998; Dougherty et al. 1994; Hunter et al. 2006; Zorec et al. 2016). The reference values are lower than the inferred, but they agree when we consider the error bars.

Examining the relationship of the rotation rate with the mass, we verified no clear dependence between them as shown in the right panel of the Figure 7. This Figure also shows that all selected Be have $W \gtrsim 0.4$. Furthermore, the selected stars cover all the `MS` (see right panel of Fig. 8) and present a lower limit to the rotation rate. The lower limit found to Be stars is ~ 0.4 and for Bn is ~ 0.1. Our results corroborate well-known results, e.g. the presence of few Be stars with masses $M \leq 7\,M_{\odot}$, $\sim 14\%$ of

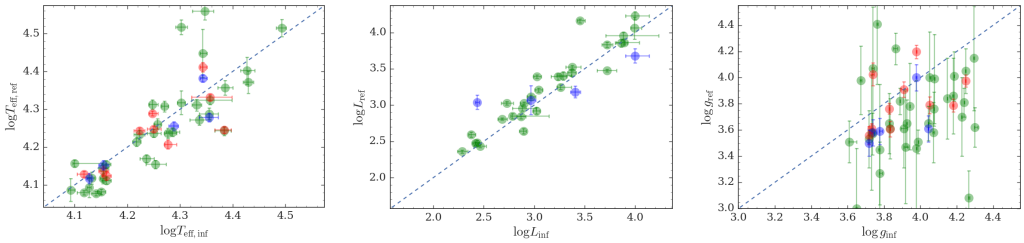

Fig. 5. Left: Plot of the log $T_{\rm eff}$ calculated and from the references, for each star used in the validation. Center: Plot of the log $L_\star$ calculated and from the references, for each star used in the validation. Right: Plot of the log (g) calculated and from the references for each star used in the validation. Blue: data from Levenhagen & Leister (2006). Red: data from Frémat et al. (2005). Green: data from Zorec et al. (2016).

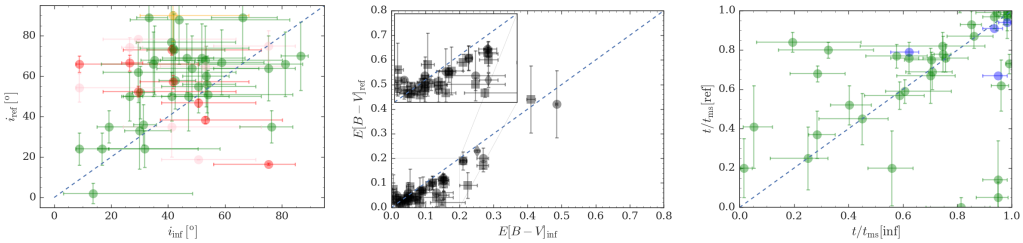

Fig. 6. Left: Plot of the i calculated and from the references for each star used in the validation. Center: Plot of the $E(B-V)$ calculated and from the references, for each star used in the validation (♦: Hunter et al. (2006), •: Dougherty et al. (1994) calculated using the 2 200 bump. ■: Zorec et al. (2016)). Right: Plot of the $t/t_{\rm ms}$. Blue: data from Levenhagen & Leister (2006). Red: data from Frémat et al. (2005). Green: data from Zorec et al. (2016). Pink: data from Meilland et al. (2012). Orange: data from Gies et al. (2007). Purple: data from Touhami et al. (2014). Yellow: data from Tycner et al. (2006).

the studied Be stars[12], in the first half of the MS phase (Frémat et al. 2005). Actually, most of our Be stars (∼ 76 %) belong to the second half of the MS phase. The most likely mechanism for that is the *spin up during the* MS evolution, associated with the second half of the MS lifetime of the B stars (McSwain & Gies 2005). This mechanism is supported by higher initial rotation rates, which enable the Be stars to reach nearly critical rotation rates as they evolve (Grudzinska et al. 2015). Our results also indicate that high-mass B stars experience angular momentum losses during the MS phase and the fact that low-mass B stars are born with a larger proportion of rapid rotators than high-mass B stars (Huang et al. 2010). Moreover, our results point out to a wide range ($0.0 \lesssim t/t_{\rm ms} \lesssim 0.95$) occupied by Bn stars. This result disagrees with earlier studies that discuss the occurrence of Bn stars in the first MS evolutionary phases (Zorec et al. 2007).

In a recent study, Granada et al. 2013 demonstrate a fact confirmed by current models, that the critical velocity is reached at TAMS (see Fig. 1 of their work). They showed that lower-mass models frequently reach the critical rotation, when compared with their massive counterparts, expending up to ∼ 30%$t/t_{\rm MS}$ at this stage. In contrast, high-mass stars have stellar winds dense enough to remove superficial angular momentum, leading to $V_{\rm orb} < V_{\rm crit}$ (Granada et al. 2013). They also shows that after a star reach its critical limit, it preserves the rotation until reach the TAMS. These results are also reproduced by our method.

We know that the stellar shape depends on several parameters (critical velocity, latitudinal differential rotation, etc., see e.g. Zorec et al. 2011). Even so, we can constrain the oblateness, knowing how the oblateness varies through the MS. The left panel of the Figure 7 shows the correlation between oblateness and the age in terms of fraction of the MS lifetime. The results corroborate the conclusion of Martayan et al. (2007), this is, that the *Be phenomenon* appears earlier ($t/t_{\rm ms} \sim 0.05$) in the MS for early B-types than for their late counterparts ($t/t_{\rm ms} \sim 0.30$). These results show that there must be some evolutionary mechanism that activates the *Be phenomenon* during the MS lifetime which also agrees with conclusions reported by previous works (e.g. Levenhagen & Leister 2006; McSwain & Gies 2005; Zorec et al. 2005; Zorec et al. 2007). Therefore, our results also show that there must be some evolutionary mechanism that activates the *Be phenomenon* during the MS lifetime.

The results shown in this section show that our method, even dealing with a large set of parameters and just one observable (UV spectrum), can reproduce fundamental stellar parameters and the $E(B-V)$ from an aleatory sample, returning consistent errors. This was already expected to slow-rotators, since there is a clear unicity among them and their correspondent UV spectra, which is the cause of, for instance, the MS be a line instead of a band (see Fig. 8). On the other hand, initially it was not obvious that the UV alone would be enough non-degenerated to provide good results. Hence, we showed that the v sin i prior is a good mechanism to improve the inference, this is, we degenerate the UV spectra in an away it becomes useful. We could reproduce important effects such as the *spin up during the* MS and the evidence that cooler Be stars are more likely to be critical rotators (e.g. Cranmer 2005). These results strengths the hypothesis that the disk formation process may be different for both: low-mass and high-mass cases. The low-mass case ($M < 4\,{\rm M}_\odot$) needs a higher

[12] The stars: HD142926, HD183914, HD187811, HD208057.

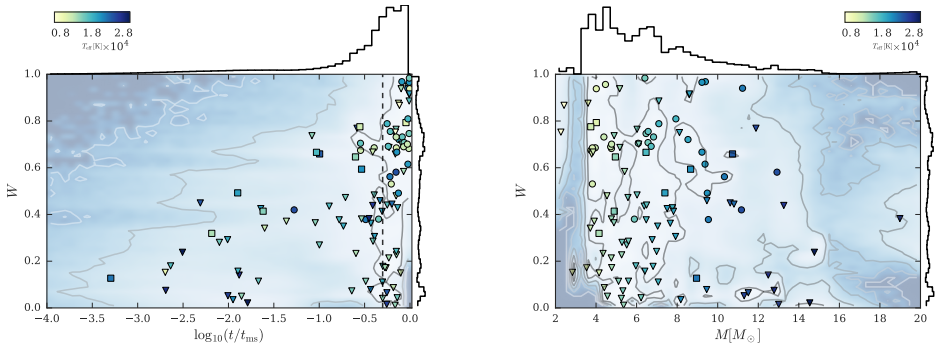

Fig. 7. Left: Oblateness, R_{eq}/R_{pole}, versus MS lifetime, t/t_{ms}. Right: Mass versus rotation rate, W.

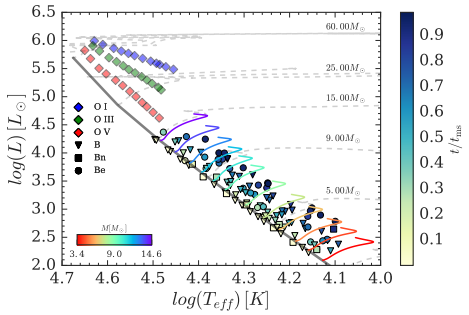

Fig. 8. Left: Oblateness, R_{eq}/R_{pole}, versus MS lifetime, t/t_{ms}. Right: HR Diagram constructed using the data shown in Table D.1. The gray curve indicates the zero age main sequence ZAMS. Each evolutionary track extends from ZAMS through to terminal age TAMS, defined by the cessation of core hydrogen burning. The vertical colorbar at the right represent the MS lifetime fraction. The colorbar at left lower corner represents the stellar mass. The different symbols are representative of the object type and they are denoted in the figure. The O-type stars are put just for comparison (data from Martins et al. 2005). Correlations for the results shown in Table **??**.

rotation rate V_{eq} / V_{crit} > 0.96 to become a Be star, while that for high-mass cases ($M > 8.6\,M_\odot$) this lower limit decreases to V_{eq} / V_{crit} > 0.64 (Huang et al. 2010).

4.2. Application: The case of β CMi

4.2.1. Observational data and Data Reduction

A diversity in data would be of interest to explore different system parameters, since different physical processes appear in distinct spetral domains. The disk of Be stars becomes clear at optical wavelengths by hydrogen (first Balmer lines) and metallic emission lines (stronger HeI and FeII lines) in their spectrum (Lamers et al. 1980). These observables arise from emission and recombination processes. In the IR range, the emission arises from continuous bound-free and free-free thermal emission (e.g. Cote & Waters 1987). Beyond these processes, the polarization of the stellar light by the disk is also present (e.g., Kjurkchieva et al. 2016; Yudin 2001).

To support our simulations, we combined data from the literature, including photometric and polarimetric data. Most data were accessed through online Virtual Observatory Tools (VO): [13], VO SED Analyzer (VOSA, Bayo et al. 2008), Spectral Analysis Tool (VOSpec; Arviset et al. 2008), and from VizieR Photometry viewer (Ochsenbein et al. 2000). VO Tools can provide the SED of an object by searching in several catalogues. Our photometric data comprises results of several observational missions: Ducati (2002), Hipparcos (ESA 1997), Mermilliod (1994), IUE, 2MASS, TYCHO (Hog et al. 2000) in the visual domain, DENIS, IRAS, WISE (Cutri & et al. 2014) in the IR domain, AKARI (AKARI/IRC mid-IR all-sky Survey; Ishihara et al. 2010), MSX (MSX6C Infrared Point Source Catalog; Egan et al. 2003), SDSS, and from the Catalogue of Homogeneous Means in the UBV System (Mermilliod 1994). We also added radio APEX observations made with the LABOCA bolometer at 870 μm and radio data from the Very Large Array (VLA).

We made use of polarimetric data from the Pico dos Dias Observatory (OPD-LNA) (Tab. B.1), and data from the HPOL Spectropolarimeter at the University of Wisconsin-Madison Pine Bluff Observatory (PBO) (Tab. B.2). The OPD-LNA data was reduced with packages developed by our research group. We got the HPOL data from the MAST archiveMAST[14]. Due to the small amount of interstellar contribution, we performed none interstellar polarization correction.

4.2.2. Initial estimates from the SED

Initially, we applied the method described in Sect. 2 for all available photometric data of β CMi. The result is summarized in the right panel of Fig. 9. We can notice that all parameters are well constrained, however, this direct procedure prevents us to understand the real contribution provided by each band. Hence, to explore properly the correlation among the parameters and each photometric data and, consequently, enrich the discussion, we computed different corner plots for isolated bands or groups of bands. This procedure allows us to explore the pseudo-photosphere effect (Carciofi 2011).

Box plots are the better way to see how the precision in the inference varies among the analyzed bands. In Fig. 10, we show the box plot for all parameters for each band analyzed. For instance, the upper plot in the first column represents the inference

[13] http://basebe.obspm.fr;
[14] https://archive.stsci.edu/hpol/

of the stellar mass for each spectral domain analyzed. In general, we verify that shorter wavelengths (UV and visible) sample better some stellar parameters: M, W, and $t/t_{\rm ms}$. Adding the UV, Visible and the NIR domains, it is not seen any considerable change in the inferred parameters. By another side, when we include the MIR band it is seen a global improvement, especially in the disk parameters: $\log n_0$, R_D and n. The inference precision and accuracy of the stellar parameters becomes worst as we remove shorter wavelengths than the NIR. Overall, this procedure showed that the observed SED of a Be star might provide information about the star (photospheric emission) and from the absorption/emission by the disk, being that each photometry band should provide complementary information about the system.

4.2.3. The optical polarization

The linear polarization is strongly dependent on the inclination angle, the disk size and the inclination angle (Teses-USP[15]). Naturally, we might expect to infer these parameters from the linear polarization data. However, the linear polarization level and shape also depends on the subspectral type, for instance, by fixing the inclination angle and disk size, it is seen an increasing of the polarization level towards early spectral types. Considering this scenario, we applied the method described in Section 3 for the linear polarimetric data of β CMi (Sect. 4.2.1). The results are shown in the left panel of the Figure 11. As expected, the polarimetric data could not constrain the stellar parameters. Consequently, this impacts the determination of the disk size, which depends on the stellar parameters, and the n index (Eq. 6), that is associated with the stellar age.

Interestingly, we can use additional priors based on the previous results obtained from the entire SED. For our case, we can adopt a Gaussian kernel density estimator (KDE) for each stellar PDF (M, W and $t/t_{\rm ms}$) got previously (left panel of the Fig. 9). This prior function becomes,

$$\log p_\star(\Theta, \alpha) = -0.5 \left[\hat{f}_{\rm M}(M) + \hat{f}_{\rm W}(W) + \hat{f}_{\rm t/t_{ms}}({\rm t/t_{ms}})\right]^2, \qquad (16)$$

where $\hat{f}_{\rm M}$, $\hat{f}_{\rm W}$ and $\hat{f}_{\rm t/t_{ms}}$ are the KDE distributions.

The resulting corner plot is shown in left panel of Fig. 11. Note that by considering the stellar prior a reasonable inference was achieved for all parameters.

4.2.4. Interpretation of the correlations

The corner diagram shown in Fig. 12 represent the combination of each of the PDFs shown in Fig. 9 and **??**. The 2D distributions of this figure are useful to understand some interesting aspects of the models. To simplify this discussion, we selected some interesting correlations and grouped them into categories.

Gravity Darkening:

- The first interesting feature is the correlation of the M and W, where (1) low-mass models (i.e. lower stellar radii) with low-rotation rates and (2) high-mass models (i.e. larger stellar radii) with high-rotation rates are correlated. For instance, if case (1) had a weaker gravity darkening than the case (2), they would have equivalent fluxes.
- M and i are correlated. Low-mass stars seen at low-inclination angles (towards pole-on orientation) produces fluxes equivalent to high-mass stars seen at high-inclination angles (towards edge-on orientation). This is explained by the fact that a less massive star seen pole-on will present a luminosity larger than when it is seen from the equatorial region. Equivalently, a high-mass star seen at its equatorial region will have a lower luminosity. Then, different configurations would produce equivalent fluxes.

Luminosity:

- Expected correlation between M and d. For instance, a low-mass near star (i.e. less luminous) is equivalent to a high-mass distant star (i.e. more luminous).
- Correlation between M and the $t/t_{\rm ms}$. In this case, an older low-mass star (small stellar radii and high luminosity) would have equivalent fluxes than young massive star (larger radius and low luminosity).
- Anti-correlation between W and $t/t_{\rm ms}$. (1) An older low-rotating star would be equivalent to (2) an younger high-rotating star. As the star becomes older, it increases its luminosity, in that case, the gravity darkening effect decrease with the rotation, increasing the photospheric flux, which might generate an equivalent flux observed in the case (2).
- $t/t_{\rm ms}$ and d are correlated. (1) younger stars (lower luminosities) seeing at smaller distances are equivalent to older stars (higher luminosities) seeing at larger distances.

Stellar Radii:

- The anti-correlation between the M and the $R_{\rm D}$ is due to the parametrization adopted for the disk size. The disk size is proportional to the stellar polar radius in our models, then a low-mass star (i.e. small radius) with large disks might produce equivalent fluxes than high-mass stars (i.e. large stellar radius) with small disks.

Distance:

- W and d are correlated. (1) low-rotating stars (i.e. low luminosity) seeing at small distances are equivalent to (2) high-rotating stars (i.e. high luminosity) seeing at larger distances.

Emitting area/Absorption by the disk:

- $t/t_{\rm ms}$ and $\log n_0$ are anti-correlated. (1) younger stars (lower luminosities) with thick disks are equivalent to (2) older stars (higher luminosities) with thin disks. In this case, we are not considering the absorption by the disk, but the excess of flux due to the disk (emitting area).
- $R_{\rm D}$ and $\log n_0$ are correlated. The fluxes of large thin disks should be reproduced by small thick disks, because of the equivalent emitting area of them.
- $\log n_0$ and n are correlated. Disks with smaller n and small base density will have equivalent density profiles to disks with large n's and high base density, both would have equivalent disks.
- $\log n_0$ and i are anti-correlated. Thinking in terms of the density of scatters, we can expect that thicker disks (larger $\log n_0$ values) seen at high-inclination angles (towards the edge-on orientation) would emit the same that thin disks seen at inclinations directed towards the pole-on. A denser disk seeing at pole-on (absorption decreases) is similar to a thin disk seeing at edge-on angles.

[15] http://www.teses.usp.br/teses/disponiveis/14/14131/tde-30082013-140129/pt-br.php

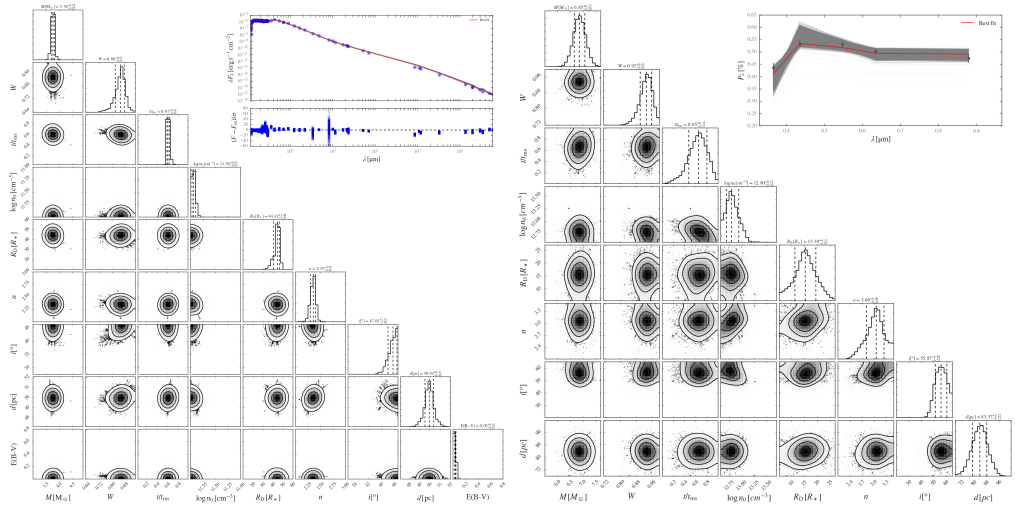

Fig. 9. Left: posterior probability distributions computed using the complete range of photometric data (see Table. A.1). The SED fit is shown inset within the main panel, the solid gray lines represent the sample of total fluxes interpolated, and the red line represents the best adjust. The dashed lines in the diagonal subplots correspond to the 16th, 50th, and 84th percentiles of the distributions. The subplots under the diagonal subplots show the probability densities correlations between several pairs of parameters. Right: same as the right plot, but for the linear polarization.

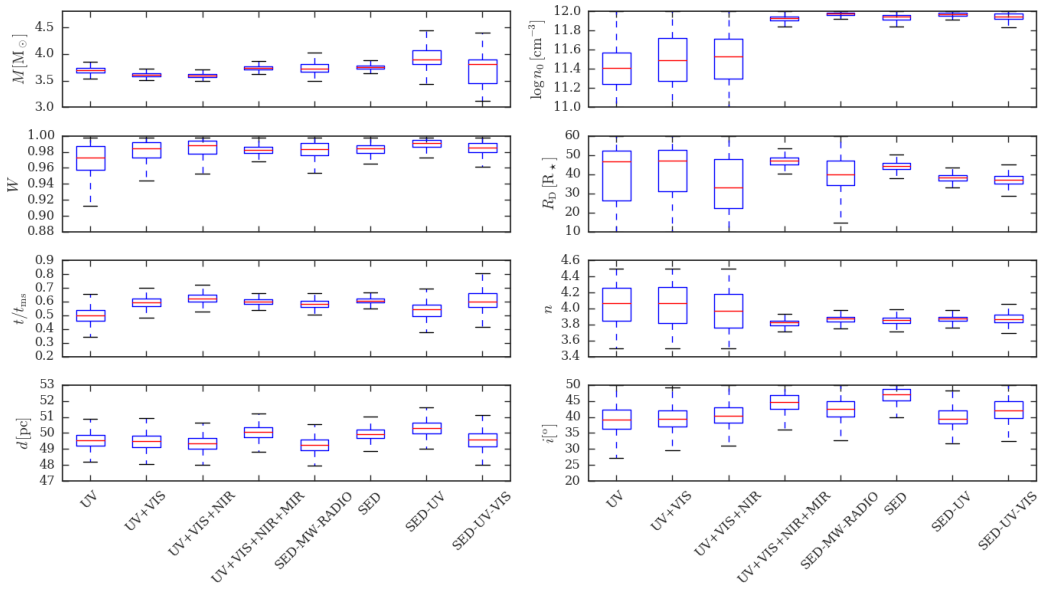

Fig. 10. Box plot of the PDFs of different spectral domains for all parameters. The red horizontal lines represents the medians. The size of the blue boxes represent the interquartile range. The lines extending vertically from the boxes are the whiskers, extending to the most extreme, non-outlier data points.

Fig. 11. Left: Oblateness, $R_{\rm eq}/R_{\rm pole}$, versus MS lifetime, $t/t_{\rm ms}$. Right: Mass versus rotation rate, W.

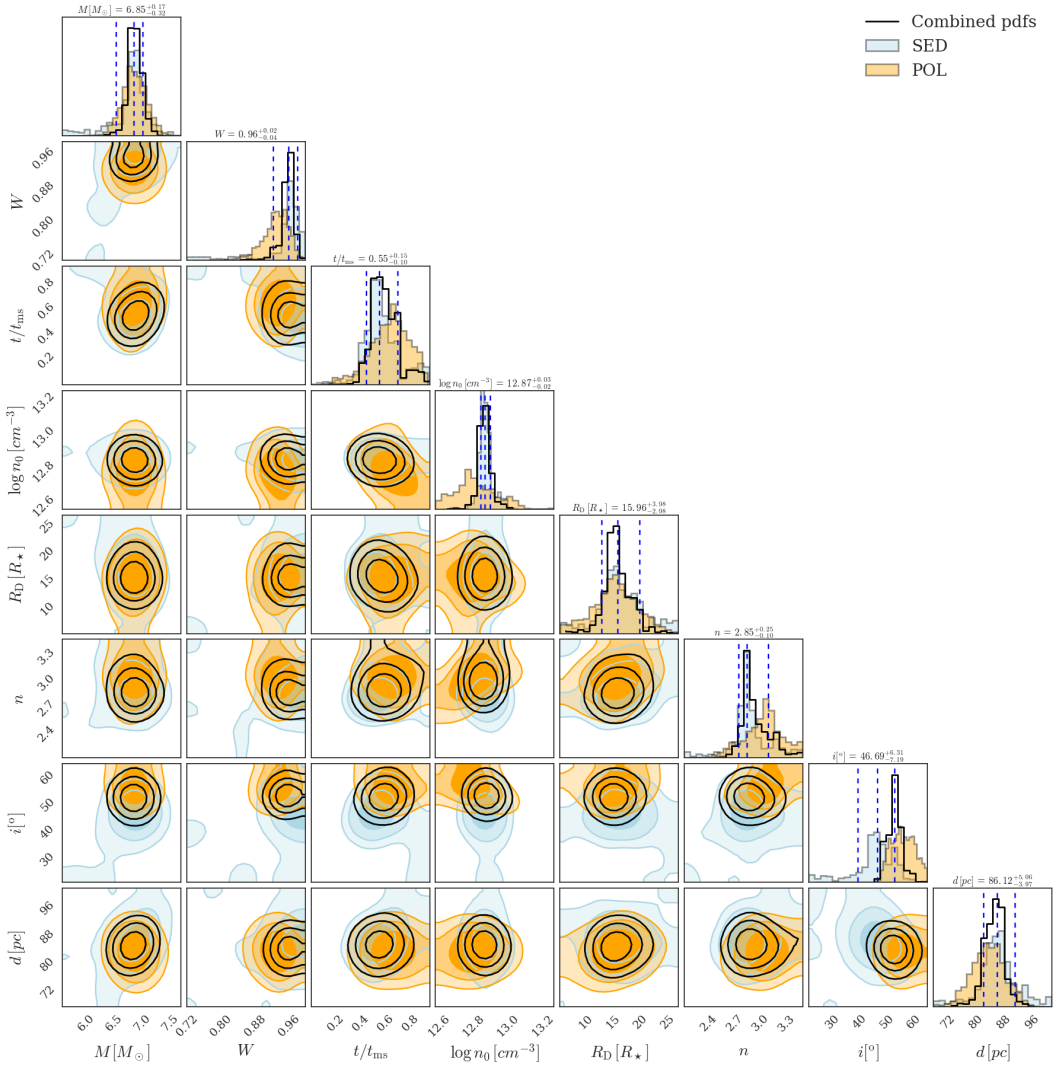

Fig. 12. The contours in the diagram were obtained by combining the posterior probabilities of the fitted SEDs and polarization and normalizing its integral over the plane to unity.

- $R_{\rm D}$ and n are correlated. Small disks with small n would emit the same than larger disks with large n.
- $R_{\rm D}$ and i. There is an anti-correlation between these parameters. We could reproduce the observed fluxes by either, a model of a large disk seeing at high-inclination angles (i.e. small emitting area) or by models with a lower disk seeing at low-inclination angles (i.e. larger emitting are).
- $R_{\rm D}$ and d are correlated. Large-distant disks will have emitting areas equivalent to small-near disks.
- i and d are anti-correlated. Distant disks seeing towards the pole-on region are equivalent to a near disk seeing towards the edge-on region.

Table 2. Best fit parameters of α Arae.

Parameter	Value
Spectral Type	B3/4Ve
M [$M_\odot$]	$6.85^{+0.17}_{-0.32}$
$\log g$	$4.1115^{+0.0003}_{-0.0008}$
$R_{\rm pole}$ [$R_\odot$]	$3.81^{+0.09}_{-0.09}$
L [$L_\odot$]	$1940.54^{+323.17}_{-277.03}$
$T_{\rm eff}$ [K]	$18215.61^{+496.07}_{-482.92}$
W	$0.96^{+0.02}_{-0.04}$
$t/t_{\rm ms}$	$0.55^{+0.15}_{-0.10}$
$\log\ n_0$	$12.87^{+0.03}_{-0.02}$
$R_{\rm D}$ [$R_\star$]	$15.96^{+3.98}_{-2.98}$
n	$2.85^{+0.25}_{-0.10}$
i [°]	$46.69^{+6.31}_{-7.19}$
d [pc]	$86.12^{+5.06}_{-3.97}$
$\beta_{\rm GD}$	$0.177^{+0.010}_{-0.012}$
$E(B-V)$ [mag]	$0.03^{+0.01}_{-0.01}$

5. Discussion

The best fit parameters of α Arae are shown in Table 2. To compare our results with previous studies, we discarded the results of Levenhagen & Leister (2006) (see Table **??**), due to the large discrepancy with other studies. Considering 1 σ range of our results, it is seen a compatibility among our inferences and previous results. For the temperature, T, our results are compatible with the results shown by Dachs et al. (1988, 1990), Chauville et al. (2001), Frémat et al. (2005), Meilland & Stee (2006), Meilland et al. (2007), Meilland et al. (2009), Hamed & Sigut (2013). For the inclination angle, i, our result is compatible with Chesneau et al. (2005) and Frémat et al. (2005). For the luminosity, L, the values agree with the Chesneau et al. (2005). Increasing 2 and 3 times the σ range, we have an agreement for all previous results obtained for T and i. In the case of the stellar mass, our result just agrees with the values published by Zorec et al. (2005) and Meilland et al. (2009). After increasing the confidence level, the only stellar radius that is in concordance with our estimating is the one inferred by Zorec et al. (2005).

Regarding the disk, we found $n \sim 2.85$ and $\log n_0 \simeq 12.87$, which according to Vieira et al. (2017) are inside the typical values for Be stars. Our result also agrees to the affirmation that disk around early-type stars are denser (Sect. 1). By another side, whether we consider the errors in the n parameters, it put α Arae in two possible cases: a steady-state disk (i.e. $3.0 < n < 3.5$) or a dissipating disk ($n < 3.0$). Beyond that, as discussed before, a binary might cause an accumulation of material in the inner region limited by the size of the truncation radius, resulting in a lower density exponent than the steady-state value.

It was recently raised again the possibility (e.g. Baade 1992) that Be-stars and supergiant sgB[e] might be binary evolutionary products (Vanbeveren & Mennekens 2017). Some observational evidences point out to the fact that gravitational interactions between a Be star and a binary companion could induce periodic variability and ellipsoidal precession of the disk (Labadie-Bartz et al. 2017). In addition, the companion might act on the disk by tidal effects or in its thermal properties.

A peculiar phenomenon in binary Be systems is that the secondary could truncate the disk to a radius dependent on the orbital parameters (eccentricity and semi-major axis) (e.g. Rivinius et al. 2013; Okazaki et al. 2002). This hypothesis is still difficult to be directly confirmed due to the flux contrast between the primary and the faint companion (Peters et al. 2016). The SED turndown, as evidenced by Klement et al. (2017), occurs due to the truncation of the outer disk. However, there are two main hypothesis for the truncation: the *tidal influence from a close companion* and the *transonic transition*. The second is defined by the radius where the resonant torque is larger than the viscous torque, resulting in a sudden drop in the gas density profile (Okazaki et al. 2002). As mentioned by Klement et al. (2017), this transition is expected to occur only at wavelengths at roughly a magnitude longer than the cm data in Be disks.

Recently, Klement et al. (2015b) found relevant evidence of disk truncation in the Be star β CMi. Interestingly, by modeling its full SED from the UV through radio, it was detected a flux deficiency at long-wavelength measurements when compared to what was expected for the disk based on the inferred IR excess from the disk. More recently, still exploring the disk truncation problem, Klement et al. (2017) discussed that radio measurements allowed the discovery of a SED turndown, somewhere between mid-IR and radio wavelengths, for a set of stars. They concluded that the most likely mechanism to truncate the disk is a close companion.

This problem was profoundly explored by Panoglou et al. (2016). They examined theoretically the cases of circular and eccentric coplanar orbits, both prograde and retrograde, using the same 3D SPH code adopted by Okazaki et al. (2002). Their main conclusions were:

1. In near circular binaries, the disk preserves a constant structure (azimuthal symmetry) in phase with the orbital motion of the companion. In such cases, the truncation region might be independent of the orbital phase;
2. A small disk could be present even for very close binaries, for instance, a companion with $P_{\rm orb} = 5$ days could have an observable disk with $R_{\rm t} = 2.5\,R_\star$;
3. From circular to moderately eccentric ($\epsilon \sim 0.6$) orbits, the inner disk preservers its structure. In highly eccentric orbits, the disk structure could present spiral arms induced by the companion as it passes the periastron;
4. The effects of binarity in the disk continuum emission induces an accumulation of material in the inner region limited by the truncation radius. It generates an inner density exponent lower than the steady-state value for isolated Be disks.

(***) In this context, the truncation radius and the mass shown in Table 2, enable us to estimate roughly the period and the semi-major axis of the binary system. For this purpose, we assume two masses for the companion (0.5 and 2.0 $M_\odot$), which gives a period of $P = 24.27 \pm 15.91$ days. Here, we applied the correction proposed by Panoglou et al. (2016). These values do not agree with previous values, this is $R_{\rm D} = 32\,R_\star$ and $P \sim 74$ days (Sect. 1). However, our estimation could encompass the period obtained by Mennickent & Vogt (1991), i.e. 47.5 days. These results corroborate the hypothesis that α Arae has indeed a companion, but a more detailed observational temporal series should prove it.

The full SED of α Arae is displayed in Fig. 13, where are shown the best models to the star and to the system, i.e. considering the disk. We can see clearly that the shorter wavelength range is dominated by the stellar flux (zooming region) and the larger wavelengths are dominated by the disk emission. The truncation caused by the unseen companion can also be observed around the wavelength 10^6 Å. The position of the turndown is not well defined, it includes a range of wavelength where the SED changes. Even so, we can estimate the likely range radius by using the

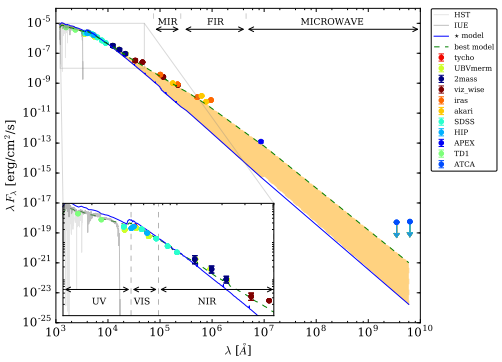

Fig. 13. SED of α Arae showing the best photospheric model (blue line) and the system (star + disk) best model (green dashed line). The red regions show the IR excess. The spectral regions are highlighted in order to facilitate the identification of the spectral regions used.

equation D1 from Vieira et al. (2017). This equation put the effective radius between $\sim$ 12.43 and $\sim$ 28.38 $R_\star$ for the the wavelengths of 400 and 2000 μm (where the turndown appears) respectively. Therefore, our result for the truncation radius is consistent with the current theory.

6. Conclusions

Stellar parameters are fundamental aspects of stars, even so, it is a difficult task to determine them since it involves the use of models and various techniques. These parameters are determined by analyzing data by either making calculations or through comparison to theoretical models. To solve this problematic, in this work we adopted the second method in the context of a Bayesian analysis, where the parameters were derived interactively, in a fully self-consistent manner. This method proved itself as a good tool in the determination of parameters of B-type stars. A key advantage of our approach was the use of priors information, for instance, the $v \sin i$, which improve the determination of photometric quantities, as well as the distance from Hipparcos catalog.

We derived the stellar parameters, $E(B-V)$ and geometrical parameters of 128 stars (Be, Bn and B), by using just the UV domain, whose showed itself as powerful constraint of the stellar parameters including the rotation rate when we applied the $v \sin i$ as a prior. Profound changes occur in different observables, especially in cases where rotation rate is close to the critical limit. These changes can lead to stellar misclassifications in simple catalogs, especially when assigning a spectral type and luminosity value. In such a scenario, our results can greatly differ to the inferences done considering non-rotating effects. In general, the results showed that the stellar and geometrical parameters were well determined for all stars used in the validation. Additionally, from the global combination of the results, we were able to reproduce well-known statistical proprieties of B-type stars, which served to consolidate our method.

Most of the massive O stars are binaries ($\sim$ 75%) or were in some moment of their lives (Sana et al. 2012). For the case of B stars, the binary fraction can reach up to $\sim$ 40% (Chini et al. 2012) or 29 $\pm$ 8 % (Oudmaijer & Parr 2010). This fraction is higher among Be stars, ranging from 27 (Sterken et al. 1996) to 30 $\pm$ 8 % (Oudmaijer & Parr 2010). Hence the interaction might be a common component in massive star evolution, being associated with a variety of astrophysical processes such as γ-ray bursts, X-ray binaries, pulsars and double-neutron stars (Chini et al. 2012). In this context, a close companion can significantly influence the massive star evolution (e.g. Langer et al. 2008). The mass transfer in such a system is also an ingredient that must be considered (Dunstall et al. 2015). All these relevant aspects made the search for binary fractions increase in the last decades (e.g. Chini et al. 2012). As a result, it led to the conclusion that most massive stars may be born as part of multiple systems (Sana et al. 2012).

The multi-technique analysis of the CBe β CMi provides the stellar, disk and geometrical parameters along with their uncertainties. It helped us to understand better how the different spectral domains and observational measures can be used in order to extract independent or correlated information about the several parameters that describe these peculiar systems. The results indicate that this star has a truncated disk at $15.96^{+3.98}_{-2.98}$, which could be caused by an unseen companion. The proprieties of the binary lack of additional information to be completely defined. The comparison of our parameters with previous estimations shows that α Arae has later sub-spectral type (B3/4) than presented by other authors (B2). Regarding the evolutionary state do it disk, $n = 2.85^{+0.25}_{-0.10}$, it put α Arae in two possible cases, namely: a dissipating disk or a disk truncated by a binary.

Acknowledgements. This study was financed in part by the "Conselho Nacional de Desenvolvimento Científico e Tecnológico" - Brasil (CNPq) - Finance Code 140171/2015-0.".

References

2018, VizieR Online Data Catalog, I/345
Abt, H. A., Levato, H., & Grosso, M. 2002, ApJ, 573, 359
Adelman, S. J. 2004, in IAU Symposium, Vol. 224, The A-Star Puzzle, ed. J. Zverko, J. Ziznovsky, S. J. Adelman, & W. W. Weiss, 1–11
Ammler-von Eiff, M. & Reiners, A. 2012, A&A, 542, A116
Arviset, C., Barbarisi, I., de La Calle, I., et al. 2008, in Astronomical Society of the Pacific Conference Series, Vol. 394, Astronomical Data Analysis Software and Systems XVII, ed. R. W. Argyle, P. S. Bunclark, & J. R. Lewis, 227
Baade, D. 1992, in IAU Symposium, Vol. 151, Evolutionary Processes in Interacting Binary Stars, ed. Y. Kondo, R. Sistero, & R. S. Polidan, 147
Baade, D., Martayan, C., & Rivinius, T. 2016, in Astronomical Society of the Pacific Conference Series, Vol. 506, Bright Emissaries: Be Stars as Messengers of Star-Disk Physics, ed. T. A. A. Sigut & C. E. Jones, 175
Bagnulo, S., Fossati, L., Landstreet, J. D., & Izzo, C. 2015, A&A, 583, A115
Bailey, J. D. & Landstreet, J. D. 2013, A&A, 551, A30
Bastian, N., Cabrera-Ziri, I., Niederhofer, F., et al. 2017, MNRAS, 465, 4795
Bayo, A., Rodrigo, C., Barrado y Navascues, D., et al. 2008, VizieR Online Data Catalog, 349
Beeckmans, F. & Hubert-Delplace, A. M. 1980, A&A, 86, 72
Bernacca, P. L. & Perinotto, M. 1970, Contributi dell'Osservatorio Astrofisica dell'Universita di Padova in Asiago, 239, 1
Bjorkman, J. E. & Carciofi, A. C. 2005a, in Astronomical Society of the Pacific Conference Series, Vol. 337, The Nature and Evolution of Disks Around Hot Stars, ed. R. Ignace & K. G. Gayley, 75
Bjorkman, J. E. & Carciofi, A. C. 2005b, in Astronomical Society of the Pacific Conference Series, Vol. 343, Astronomical Polarimetry: Current Status and Future Directions, ed. A. Adamson, C. Aspin, C. Davis, & T. Fujiyoshi, 270
Bless, R. C. & Percival, J. W. 1997, in IAU Symposium, Vol. 189, IAU Symposium, ed. T. R. Bedding, A. J. Booth, & J. Davis, 73–82
Bohlender, D. 2016, in Astronomical Society of the Pacific Conference Series, Vol. 506, Bright Emissaries: Be Stars as Messengers of Star-Disk Physics, ed. T. A. A. Sigut & C. E. Jones, 275
Bragança, G. A., Daflon, S., Cunha, K., et al. 2012, AJ, 144, 130
Briot, D. 1978, A&A, 66, 197
Carciofi, A. C. 2011, in Active OB Stars: Structure, Evolution, Mass Loss, and Critical Limits, ed. C. Neiner, G. Wade, G. Meynet, & G. Peters, Vol. 272, 325–336
Carciofi, A. C. & Bjorkman, J. E. 2006, ApJ, 639, 1081

Carciofi, A. C. & Bjorkman, J. E. 2008, apj, 684, 1374
Carciofi, A. C., Bjorkman, J. E., Otero, S. A., et al. 2012, apjl, 744, L15
Carciofi, A. C., Bjorkman, J. E., & Zsargó, J. 2017, in IAU Symposium, Vol. 329, The Lives and Death-Throes of Massive Stars, ed. J. J. Eldridge, J. C. Bray, L. A. S. McClelland, & L. Xiao, 390–390
Carciofi, A. C., Miroshnichenko, A. S., Kusakin, A. V., et al. 2006, apj, 652, 1617
Carciofi, A. C., Okazaki, A. T., Le Bouquin, J.-B., et al. 2009, aap, 504, 915
Cardelli, J. A., Clayton, G. C., & Mathis, J. S. 1989, ApJ, 345, 245
Challouf, M., Nardetto, N., Domiciano de Souza, A., et al. 2015, A&A, 579, A107
Chauville, J., Zorec, J., Ballereau, D., et al. 2001, A&A, 378, 861
Chesneau, O., Meilland, A., Rivinius, T., et al. 2005, aap, 435, 275
Chini, R., Hoffmeister, V. H., Nasseri, A., Stahl, O., & Zinnecker, H. 2012, MNRAS, 424, 1925
Claret, A. 2000, A&A, 363, 1081
Clark, J. S., Steele, I. A., & Fender, R. P. 1998, MNRAS, 299, 1119
Collins, II, G. W. 1963, ApJ, 138, 1134
Collins, II, G. W. 1987, in IAU Colloq. 92: Physics of Be Stars, ed. A. Slettebak & T. P. Snow, 3–19
Collins, II, G. W. & Harrington, J. P. 1966, ApJ, 146, 152
Conti, P. S. & Leep, E. M. 1974, ApJ, 193, 113
Cote, J. & Waters, L. B. F. M. 1987, A&A, 176, 93
Cranmer, S. R. 1996, PhD thesis, Bartol Research Institute, University of Delaware
Cranmer, S. R. 2005, ApJ, 634, 585
Cutri, R. M. & et al. 2014, VizieR Online Data Catalog, 2328
Cyr, R. P., Jones, C. E., & Tycner, C. 2015, ApJ, 799, 33
Dachs, J., Kiehling, R., & Engels, D. 1988, A&A, 194, 167
Dalla Vedova, G., Millour, F., Domiciano de Souza, A., et al. 2017, A&A, 601, A118
di Benedetto, G. P. 1998, A&A, 339, 858
Domiciano de Souza, A., Kervella, P., Moser Faes, D., et al. 2014, A&A, 569, A10
Dougherty, S. M., Waters, L. B. F. M., Burki, G., et al. 1994, A&A, 290
Draper, Z. H., Wisniewski, J. P., Bjorkman, K. S., et al. 2011, in Active OB Stars: Structure, Evolution, Mass Loss, and Critical Limits, ed. C. Neiner, G. Wade, G. Meynet, & G. Peters, Vol. 272, 388–389
Ducati, J. R. 2002, VizieR Online Data Catalog, 2237
Dunstall, P. R., Dufton, P. L., Sana, H., et al. 2015, A&A, 580, A93
Egan, M. P., Price, S. D., Kraemer, K. E., et al. 2003, VizieR Online Data Catalog, 5114
Ekström, S., Georgy, C., Meynet, G., Maeder, A., & Granada, A. 2011, in IAU Symposium, Vol. 272, Active OB Stars: Structure, Evolution, Mass Loss, and Critical Limits, ed. C. Neiner, G. Wade, G. Meynet, & G. Peters, 62–72
Ekström, S., Meynet, G., Maeder, A., & Barblan, F. 2008, A&A, 478, 467
ESA. 1997, VizieR Online Data Catalog, 1239
Escolano, C., Carciofi, A. C., Okazaki, A. T., et al. 2015, A&A, 576, A112
Espinosa Lara, F. & Rieutord, M. 2011, A&A, 533, A43
Faes, D. M., Domiciano de Souza, A., Carciofi, A. C., & Bendjoya, P. 2015, in IAU Symposium, Vol. 307, New Windows on Massive Stars, ed. G. Meynet, C. Georgy, J. Groh, & P. Stee, 261–266
Fitzpatrick, E. L. 1999, PASP, 111, 63
Fitzpatrick, E. L. & Massa, D. 1999, ApJ, 525, 1011
Foreman-Mackey, D., Hogg, D. W., Lang, D., & Goodman, J. 2013, PASP, 125, 306
Freire Ferrero, R., Morales Durán, C., Halbwachs, J.-L., & Cabo Cubeiro, A. M. 2012, AJ, 143, 28
Frémat, Y., Zorec, J., Hubert, A.-M., & Floquet, M. 2005, A&A, 440, 305
Frost, S. A. & Conti, P. S. 1976, in IAU Symposium, Vol. 70, Be and Shell Stars, ed. A. Slettebak, 139
Georgy, C., Ekström, S., Granada, A., et al. 2013, A&A, 553, A24
Ghoreyshi, M. R., Carciofi, A. C., Rímulo, L. R., et al. 2018, MNRAS
Gies, D. R., Bagnuolo, Jr., W. G., Baines, E. K., et al. 2007, ApJ, 654, 527
Golden-Marx, J. B., Oey, M. S., Lamb, J. B., Graus, A. S., & White, A. S. 2016, ApJ, 819, 55
Goodman, J. & Weare, J. 2010, Communications in Applied Mathematics and Computational Science, Vol. 5, No. 1, p. 65-80, 2010, 5, 65
Granada, A., Ekström, S., Georgy, C., et al. 2013, A&A, 553, A25
Granada, A. & Haemmerlé, L. 2014, A&A, 570, A18
Grudzinska, M., Belczynski, K., Casares, J., et al. 2015, MNRAS, 452, 2773
Grunhut, J. H., Wade, G. A., & MiMeS Collaboration. 2012, in American Institute of Physics Conference Series, Vol. 1429, American Institute of Physics Conference Series, ed. J. L. Hoffman, J. Bjorkman, & B. Whitney, 67–74
Hamed, G. E. & Sigut, T. A. A. 2013, NRIAG Journal of Astronomy and Geophysics, 2, 125
Harmanec, P. 1988, Bulletin of the Astronomical Institutes of Czechoslovakia, 39, 329
Haubois, X., Carciofi, A. C., Rivinius, T., Okazaki, A. T., & Bjorkman, J. E. 2012, apj, 756, 156
Haubois, X., Mota, B. C., Carciofi, A. C., et al. 2014, ApJ, 785, 12
Hillier, D. J. & Miller, D. L. 1998, ApJ, 496, 407
Hoffleit, D. & Jaschek, C. 1982, The Bright Star Catalogue
Hog, E., Fabricius, C., Makarov, V. V., et al. 2000, VizieR Online Data Catalog, 1259
Huang, W. & Gies, D. R. 2006, ApJ, 648, 580
Huang, W., Gies, D. R., & McSwain, M. V. 2010, ApJ, 722, 605
Hunter, I., Smoker, J. V., Keenan, F. P., et al. 2006, MNRAS, 367, 1478
Ishihara, D., Onaka, T., Kataza, H., et al. 2010, A&A, 514, A1
Ivezić, Ž., Connelly, A. J., VanderPlas, J. T., & Gray, A. 2014, Statistics, Data Mining, and Machine Learningin Astronomy
Jaschek, M. & Egret, D. 1982, in IAU Symposium, Vol. 98, Be Stars, ed. M. Jaschek & H.-G. Groth, 261
Jaschek, M., Slettebak, A., & Jaschek, C. 1981, Be star terminology., Be Star Newsletter
Johnston, K. G., Robitaille, T. P., Beuther, H., et al. 2015, ApJ, 813, L19
Kee, N. D., Owocki, S., & Sundqvist, J. O. 2016, MNRAS, 458, 2323
Keller, S. C., Wood, P. R., & Bessell, M. S. 1999, A&AS, 134, 489
Kjurkchieva, D., Marchev, D., Sigut, T. A. A., & Dimitrov, D. 2016, AJ, 152, 56
Klement, R., Carciofi, A. C., Rivinius, T., et al. 2017, A&A, 601, A74
Klement, R., Carciofi, A. C., Rivinius, T., et al. 2015a, A&A, 584, A85
Klement, R., Carciofi, A. C., Rivinius, T., et al. 2015b, ArXiv e-prints
Labadie-Bartz, J., Pepper, J., McSwain, M. V., et al. 2017, AJ, 153, 252
Lamers, H. J. G. L. M., Faraggiana, R., & Burger, M. 1980, A&A, 82, 48
Langer, N., Cantiello, M., Yoon, S.-C., et al. 2008, in IAU Symposium, Vol. 250, Massive Stars as Cosmic Engines, ed. F. Bresolin, P. A. Crowther, & J. Puls, 167–178
Lee, R. W., ed. 1991, A review of spectral line broadening relevant to hot dense plasmas
Levenhagen, R. S. & Leister, N. V. 2006, MNRAS, 371, 252
Maeder, A. 2009, Physics, Formation and Evolution of Rotating Stars
Maeder, A., Grebel, E. K., & Mermilliod, J.-C. 1999, A&A, 346, 459
Marco, A. & Negueruela, I. 2013, A&A, 552, A92
Martayan, C., Frémat, Y., Hubert, A.-M., et al. 2007, A&A, 462, 683
Martins, F., Schaerer, D., & Hillier, D. J. 2005, A&A, 436, 1049
Massey, P. 2003, ARA&A, 41, 15
McEvoy, C. M., Smoker, J. V., Dufton, P. L., et al. 2015, MNRAS, 451, 1396
McGill, M. A., Sigut, T. A. A., & Jones, C. E. 2011, ApJ, 743, 111
McLean, I. S. & Brown, J. C. 1978, A&A, 69, 291
McSwain, M. V. & Gies, D. R. 2005, ApJS, 161, 118
Meilland, A., Millour, F., Kanaan, S., et al. 2012, A&A, 538, A110
Meilland, A. & Stee, P. 2006, in EAS Publications Series, Vol. 18, EAS Publications Series, ed. P. Stee, 273–290
Meilland, A., Stee, P., Chesneau, O., & Jones, C. 2009, aap, 505, 687
Meilland, A., Stee, P., Vannier, M., et al. 2007, aap, 464, 59
Mennickent, R. E. & Vogt, N. 1991, A&A, 241, 159
Mermilliod, J.-C. 1994, VizieR Online Data Catalog, 2193
Meynet, G. & Maeder, A. 2000, A&A, 361, 101
Negueruela, I., Steele, I. A., & Bernabeu, G. 2004, Astronomische Nachrichten, 325, 749
Nieva, María-Fernanda & Przybilla, Norbert. 2014, A&A, 566, A7
Ochsenbein, F., Bauer, P., & Marcout, J. 2000, A&AS, 143, 23
Okazaki, A. T. 2001, pasj, 53, 119
Okazaki, A. T., Bate, M. R., Ogilvie, G. I., & Pringle, J. E. 2002, in Astronomical Society of the Pacific Conference Series, Vol. 261, The Physics of Cataclysmic Variables and Related Objects, ed. B. T. Gänsicke, K. Beuermann, & K. Reinsch, 519
Oudmaijer, R. D. & Parr, A. M. 2010, MNRAS, 405, 2439
Owocki, S. 2006, in Astronomical Society of the Pacific Conference Series, Vol. 355, Stars with the B[e] Phenomenon, ed. M. Kraus & A. S. Miroshnichenko, 219
Panoglou, D., Carciofi, A. C., Vieira, R. G., et al. 2016, MNRAS, 461, 2616
Panoglou, D., Faes, D. M., Carciofi, A. C., et al. 2018, MNRAS, 473, 3039
Peters, G. J., Wang, L., Gies, D. R., & Grundstrom, E. D. 2016, ApJ, 828, 47
Porter, J. M. 1996, MNRAS, 280, L31
Porter, J. M. 1999, aap, 348, 512
Pringle, J. E. 1981, araa, 19, 137
Quirrenbach, A., Bjorkman, K. S., Bjorkman, J. E., et al. 1997, apj, 479, 477
Rauw, G., Morel, T., Nazé, Y., et al. 2015, A&A, 575, A99
Rauw, G., Naze, Y., Marique, P. X., et al. 2007, Information Bulletin on Variable Stars, 5773
Rímulo, L. R., Carciofi, A. C., Vieira, R. G., et al. 2018, MNRAS, 476, 3555
Rivinius, T., Baade, D., Štefl, S., & Maintz, M. 2001, A&A, 379, 257
Rivinius, T., Carciofi, A. C., & Martayan, C. 2013, aapr, 21, 69
Royer, F., Grenier, S., Baylac, M.-O., Gómez, A. E., & Zorec, J. 2002, A&A, 393, 897
Royer, F., Zorec, J., & Gómez, A. E. 2007, A&A, 463, 671
Sana, H., de Mink, S. E., de Koter, A., et al. 2012, Science, 337, 444

Schmidt-Kaler, T. 1982, 4.1.2 Intrinsic colors and visual absolute magnitudes (calibration of the MK system): Datasheet from Landolt-Börnstein - Group VI Astronomy and Astrophysics · Volume 2B: "Stars and Star Clusters" in SpringerMaterials, Berlin Heidelberg, Copyright 1982 Springer-Verlag Berlin Heidelberg
Schultz, G. V. & Wiemer, W. 1975, A&A, 43, 133
Silaj, J., Jones, C. E., Sigut, T. A. A., & Tycner, C. 2014, ApJ, 795, 82
Simón-Díaz, S. & Herrero, A. 2014, A&A, 562, A135
Sterken, C., Vogt, N., & Mennickent, R. E. 1996, A&A, 311, 579
Struve, O. 1931, apj, 73, 94
Touhami, Y., Gies, D. R., Schaefer, G. H., et al. 2014, in Astronomical Society of the Pacific Conference Series, Vol. 487, Resolving The Future Of Astronomy With Long-Baseline Interferometry, ed. M. J. Creech-Eakman, J. A. Guzik, & R. E. Stencel, 395
Townsend, R. H. D., Owocki, S. P., & Howarth, I. D. 2004, mnras, 350, 189
Tycner, C., Gilbreath, G. C., Zavala, R. T., et al. 2006, AJ, 131, 2710
Tycner, C., Jones, C. E., Sigut, T. A. A., et al. 2008, apj, 689, 461
Uesugi, A. & Fukuda, I. 1970, Catalogue of rotational velocities of the stars
Vacca, W. D., Garmany, C. D., & Shull, J. M. 1996, ApJ, 460, 914
van Leeuwen, F. 2007, A&A, 474, 653
Vanbeveren, D. & Mennekens, N. 2017, in Astronomical Society of the Pacific Conference Series, Vol. 508, The B[e] Phenomenon: Forty Years of Studies, ed. A. Miroshnichenko, S. Zharikov, D. Korčáková, & M. Wolf, 121
Vega, E. I., Rabolli, M., Feinstein, A., & Muzzio, J. C. 1980, AJ, 85, 1207
Vieira, R. G. & Carciofi, A. C. 2017, ArXiv e-prints
Vieira, R. G., Carciofi, A. C., & Bjorkman, J. E. 2015, MNRAS, 454, 2107
Vieira, R. G., Carciofi, A. C., Bjorkman, J. E., et al. 2017, MNRAS, 464, 3071
Vinicius, M.-M. F., Townsend, R. H. D., & Leister, N. V. 2007, in Astronomical Society of the Pacific Conference Series, Vol. 361, Active OB-Stars: Laboratories for Stellare and Circumstellar Physics, ed. A. T. Okazaki, S. P. Owocki, & S. Stefl, 518
von Zeipel, H. 1924, MNRAS, 84, 684
Walborn, N. R., Sota, A., Maíz Apellániz, J., et al. 2010, ApJ, 711, L143
Wheelwright, H. E., Bjorkman, J. E., Oudmaijer, R. D., et al. 2012, mnras, 423, L11
Wisniewski, J. P. & Bjorkman, K. S. 2006, ApJ, 652, 458
Yudin, R. V. 2001, A&A, 368, 912
Zagury, F. 2013, Astronomische Nachrichten, 334, 1107
Zinnecker, H. & Yorke, H. W. 2007, ARA&A, 45, 481
Zorec, J. & Briot, D. 1997, A&A, 318, 443
Zorec, J., Frémat, Y., & Cidale, L. 2005, A&A, 441, 235
Zorec, J., Frémat, Y., Domiciano de Souza, A., et al. 2011, A&A, 526, A87
Zorec, J., Frémat, Y., Domiciano de Souza, A., et al. 2016, A&A, 595, A132
Zorec, J., Frémat, Y., Martayan, C., Cidale, L. S., & Torres, A. F. 2007, in Astronomical Society of the Pacific Conference Series, Vol. 361, Active OB-Stars: Laboratories for Stellare and Circumstellar Physics, ed. A. T. Okazaki, S. P. Owocki, & S. Stefl, 539

Appendix A: Photometric data of β CMi

*** MUDAR DADOS

Table A.1. Photometric dataset.

Filter	λ (Å)	F (erg/s/cm^2/Å)	σF (erg/s/cm^2/Å)	Source (Mission/Instrument)	Obs.Date (VO) (Gregorian)
Generic/Stromgren.u	3447.51	1.630×10^{-10}	-	Paunzen 2015	-
Generic/Johnson.U	3570.65	5.496×10^{-10}	1.538×10^{-11}	UBV, Mermilliod 1991	-
Generic/Stromgren.v	4110.37	4.818×10^{-10}	-	Paunzen 2015	-
TYCHO/TYCHO.B	4280.00	5.632×10^{-10}	7.262×10^{-12}	Tycho	-
Generic/Johnson.B	4378.12	4.908×10^{-10}	1.072×10^{-11}	UBV, Mermilliod 1991	-
Generic/Stromgren.b	4663.26	3.847×10^{-10}	-	Paunzen 2015	-
TYCHO/TYCHO.V	5340.00	3.041×10^{-10}	2.521×10^{-12}	Tycho	-
Generic/Johnson.V	5466.11	2.384×10^{-10}	4.610×10^{-12}	UBV, Mermilliod 1991	-
Generic/Stromgren.y	5472.42	2.280×10^{-10}	-	Paunzen 2015	-
2MASS/2MASS.J	12350.00	2.605×10^{-11}	6.334×10^{-12}	2MASS	2000-08-04
2MASS/2MASS.H	16620.00	1.049×10^{-11}	2.221×10^{-12}	2MASS	2000-08-04
2MASS/2MASS.Ks	21590.00	4.335×10^{-12}	8.783×10^{-13}	2MASS	2000-08-04
IRAS/IRAS.12mu	101464.58	3.698×10^{-14}	1.479×10^{-15}	IRAS	-
WISE/WISE.W3	115608.00	2.379×10^{-14}	8.325×10^{-16}	WISE	-
AKARI/IRC.L18W	176094.90	5.692×10^{-15}	2.852×10^{-16}	AKARI/IRC	-
IRAS/IRAS.25mu	217265.49	3.893×10^{-15}	2.336×10^{-16}	IRAS	-
WISE/WISE.W4	220883.00	3.457×10^{-15}	3.821×10^{-17}	WISE	-
IRAS/IRAS.60mu	519887.31	2.241×10^{-16}	2.016×10^{-17}	IRAS	-
AKARI/FIS.N60	629506.72	2.264×10^{-16}	2.133×10^{-17}	AKARI/FIS	-
AKARI/FIS.WIDE-S	769035.21	7.538×10^{-17}	2.443×10^{-18}	AKARI/FIS	-
SDSS	7634.91	9.412×10^{-11}	-	SDSS	-
SDSS	6246.98	1.836×10^{-10}	-	SDSS	-
SDSS	4819.97	4.207×10^{-10}	-	SDSS	-
SDSS	9017.94	5.419×10^{-11}	-	SDSS	-
SDSS	3518.98	6.754×10^{-10}	-	SDSS	-
HIP	4020.01	5.343×10^{-10}	-	HIP	-
HIP	5318.96	3.041×10^{-10}	-	HIP	-
HIP	4203.01	5.719×10^{-10}	-	HIP	-
APEX	8695652.17	1.452×10^{-20}	2.857×10^{-21}	APEX	-
TD	1565.00	3.395×10^{-09}	1.800×10^{-11}	TD	-
TD1	2365.00	1.555×10^{-09}	1.900×10^{-12}	TD1	-
Clark et al. 1998	3.5×10^{9}	1.469×10^{-28}	-	ATCA	-
Clark et al. 1998	6.3×10^{9}	9.070×10^{-29}	-	ATCA	-

A&A–output, *Online Material p 20*

Appendix B: β CMi polarimetric data

Table B.1. Polarimetric data from OPD-LNA taken with the IAGPOL polarimeter.

MJD	Filter	$P_{\rm obs}[\%]$	$PA_{\rm Pobs}$	$\sigma_P[\%]$	σ_{PA}
55855.33	b	0.0365	65.33	0.0038	2.98
55855.34	r	0.0512	88.90	0.0040	2.24
55855.37	i	0.0714	78.06	0.0195	7.82
56022.03	i	0.0488	1.53	0.0151	8.87
56022.04	b	0.0194	72.54	0.0129	19.05
56022.05	v	0.0288	92.40	0.0152	15.12
56022.06	r	0.0425	17.03	0.0171	11.53
56610.19	v	0.0488	3.48	0.0111	6.52
56610.22	i	0.0567	0.00	0.0042	2.12
56610.23	r	0.0526	3.66	0.0242	13.18
56610.25	b	0.0637	1.90	0.0351	15.79
56714.09	v	0.1242	85.81	0.0127	2.93
56726.08	b	0.0601	75.52	0.0260	12.39
56726.09	v	0.0410	75.25	0.0233	16.28
56726.10	r	0.0656	80.67	0.0239	10.44
56726.11	i	0.0379	5.24	0.0209	15.8
56946.28	b	0.0826	86.66	0.0070	2.43
56946.30	v	0.0401	106.55	0.0152	10.86
56946.31	r	0.0601	79.15	0.0084	4.00
56946.32	i	0.0306	1.22	0.0136	12.73
56981.29	v	0.0823	3.00	0.0267	9.29
56981.30	r	0.0624	6.25	0.0089	4.09
56981.30	i	0.0505	12.85	0.0144	8.17

Table B.2. Spetro-polarimetric data from HPOL.

Data ID	Obs. Start Time	Exp. Time
bet-cmi_19910422	1991-04-22 02:07:32	3277
bet-cmi_19950208b	1995-02-08 00:00:00	768
bet-cmi_19950208r	1995-02-08 00:00:00	640
bet-cmi_19950325b	1995-03-25 00:00:00	1920
bet-cmi_19950325r	1995-03-25 00:00:00	640
bet-cmi_20000207r	2000-02-07 00:00:00	600
bet-cmi_20000212b	2000-02-12 00:00:00	1536
bet-cmi_20000212r	2000-02-12 00:00:00	640

A&A–output, *Online Material p 21*

Appendix C: Selected stars.

Table C.1. Stars used in the validation process.

main ID	Star	π (mas)	σ_π (mas)	v sin i (km s^{-1})	$\sigma_{v \sin i}$ (mas)	Sp. type (Simbad)	RA (J2000) (h:m:s)	DEC (J2000) (°, ', '')	Ref. v sin i
* π And	HD3369	5.939	0.3628	25	-	B5V	00 36 52.8512	+33 43 09.651	Abt et al. 2002
* ν And	HD4727	6.9259	0.46	20	-	B5V	00 49 48.8460	+41 04 44.045	Abt et al. 2002
* π Ari	HD17543	4.18	0.69	51	20	B6V	02 49 17.5592	+17 27 51.516	Huang et al. 2010
HD 18537	HD18537	6.9745	0.1205	90	-	B7V	03 00 52.2119	+52 21 06.247	Abt et al. 2002
* 53 Ari	HD19374	3.1669	0.0881	0	24	B1.5V	03 07 25.6726	+17 52 47.971	Huang et al. 2010
* Tau	HD21364	16.4494	0.9165	231	-	B9Vn	03 27 10.1384	+09 43 57.862	Royer et al. 2007
* ψ Per	HD22192	5.9627	0.873	200	-	B5Ve	03 36 29.3784	+48 11 33.508	Abt et al. 2002
* τ05 Eri	HD22203	12.4912	0.5487	73	-	B9V	03 33 47.2721	-21 37 58.375	Royer et al. 2007
* o Per	HD22951	3.031	0.2274	10	-	B0.5V	03 42 22.6477	+33 57 54.111	Abt et al. 2002
* 18 Tau	HD23324	7.3405	0.1237	185	-	B8V	03 45 09.7395	+24 50 21.349	Abt et al. 2002
* 24 Eri	HD23363	4.8394	0.1452	140	-	B7IV	03 44 30.5099	-01 09 47.120	Abt et al. 2002
* 21 Tau	HD23432	7.5658	0.1321	160	-	B8V	03 45 54.4767	+24 33 16.241	Abt et al. 2002
* 28 Tau	HD23862	7.7229	0.2039	220	-	B8Vne	03 49 11.2175	+24 08 12.172	Abt et al. 2002
* c Per	HD25940	5.9344	0.3278	155	-	B3Ve	04 08 39.6888	+47 42 45.042	Abt et al. 2002
HD 26326	HD26326	4.9039	0.1056	5	-	B5IV	04 09 17.8360	-16 23 09.075	Abt et al. 2002
* 62 Tau	HD27778	4.4566	0.0474	101	10	B3V	04 23 59.7629	+24 18 03.527	Huang et al. 2010
V* HU Tau	HD29365	7.7218	0.0851	70	-	B8V	04 38 15.8302	+20 41 05.011	Abt et al. 2002
* τ Tau	HD29763	10.7072	0.6001	100	-	B3V	04 42 14.6926	+22 57 24.894	Uesugi & Fukuda 1970
HD 31726	HD31726	2.5701	0.1017	26	8	B2V	04 57 44.6843	-14 13 54.892	Bragança et al. 2012
* ψ Eri	HD32249	3.9274	0.2514	52	8	B3IV	05 01 26.3456	-07 10 26.271	Bragança et al. 2012
* 11 Cam	HD32343	4.6189	0.162	55	-	B3Ve	05 06 08.4523	+58 58 20.548	Abt et al. 2002
* 105 Tau	HD32991	3.0763	0.0908	175	-	B2Ve	05 07 55.4350	+21 42 17.350	Abt et al. 2002
HD 34748	HD34748	2.6618	0.0992	295	-	B3V	05 19 35.2871	-01 24 42.883	Abt et al. 2002
HD 34798	HD34798	4.1424	0.0643	30	-	B5Vs	05 19 17.4368	-18 31 11.696	Abt et al. 2002
* 113 Tau	HD35532	2.7358	0.0923	281	7	B2Vn	05 26 05.7215	+16 42 00.584	Huang et al. 2010
* κ Pic	HD35580	4.8587	0.0765	264	-	B8/9V	05 22 22.1470	-56 08 03.825	Royer et al. 2002
HD 35588	HD35588	2.8528	0.0774	170	-	B2V	05 25 47.0186	+00 31 12.875	Abt et al. 2002
* 115 Tau	HD35671	4.9316	0.2069	125	8	B5V	05 27 10.0943	+17 57 43.947	Huang et al. 2010
* 32 Ori	HD36267	10.77	0.64	155	-	B5V	05 30 47.0509	+05 56 53.292	Abt et al. 2002
* 35 Ori	HD36653	3.1116	0.1814	118	10	B3V	05 33 54.2872	+14 18 20.086	Bragança et al. 2012
V* VV Ori	HD36695	2.6531	0.2153	120	-	B9IV/V	05 33 31.4472	-01 09 21.859	Abt et al. 2002
V* V1046 Ori	HD37017	0.4468	0.1712	165	-	B2/3V	05 35 21.8676	-04 29 39.040	Abt et al. 2002
* c Ori	HD37018	3.69	1.2	20	-	B1V	05 35 23.1642	-04 50 18.088	Abt et al. 2002
HD 37303	HD37303	2.4339	0.1159	265	-	B2V(n)	05 37 27.3574	-05 56 18.197	Abt et al. 2002
HD 37744	HD37744	2.3209	0.0954	37	-	B2IV	05 40 37.2961	-02 49 30.847	Simón-Díaz & Herrero 2014
* ζ Tau	HD37202	7.33	0.82	125	-	B1IVe_shell	05 37 38.6870	+21 08 32.834	Abt et al. 2002
* ω Ori	HD37490	3.1596	0.3589	180	-	B3Ve	05 39 11.1455	+04 07 17.290	Abt et al. 2002
* α Col	HD37795	7.2328	1.0229	195	-	B9Ve	05 39 38.9390	-34 04 26.750	Abt et al. 2002
* 57 Ori	HD39698	1.5872	0.1401	115	-	B2V	05 54 56.6871	+19 44 58.629	Abt et al. 2002
* ν Ori	HD41753	6.7656	0.3931	30	-	B3V	06 07 34.3252	+14 46 06.511	Abt et al. 2002
* f01 Ori	HD42545	4.4787	0.28	245	-	B5Vn	06 12 03.2806	+16 07 49.458	Abt et al. 2002
* ζ CMa	HD44402	9.9047	0.7158	25	-	B2.5V	06 20 18.7878	-30 03 48.121	Abt et al. 2002
HD 44506	HD44506	1.6226	0.1024	241	11	B3V	06 20 36.2399	-34 08 38.915	Bragança et al. 2012

HD 47054	HD47054	4.4762	0.128	220	-	B8IVe	06 36 35.3296	-05 12 40.100	Abt et al. 2002
* 16 Mon	HD48977	3.1699	0.1518	20	-	B3V	06 46 32.4144	+08 35 13.781	Abt et al. 2002
HD 49662	HD49662	6.17	0.75	90	-	B7IV	06 48 57.7366	-15 08 41.000	Abt et al. 2002
* κ CMa	HD50013	4.7425	0.3295	210	-	B1.5Ve	06 49 50.4601	-32 30 30.532	Abt et al. 2002
* ω CMa	HD56139	4.8816	0.4238	105	-	B2IV-Ve	07 14 48.6531	-26 46 21.556	Abt et al. 2002
* β CMi	HD58715	20.3535	1.222	210	-	B8Ve	07 27 09.0497	+08 17 21.488	Abt et al. 2002
HD 60098	HD60098	3.549	0.0422	41	5	B3V	07 31 25.7671	-36 09 11.729	Bragança et al. 2012
HD 60848	HD60848	0.3128	0.0839	362	-	O8:V:pe	07 37 05.7328	+16 54 15.303	Uesugi & Fukuda 1970
HD 60855	HD60855	2.0486	0.1038	244	8	B2Ve	07 36 03.8931	-14 29 33.982	Huang & Gies 2006
HD 67536	HD67536	2.3923	0.0519	292	-	B2Vn	08 04 42.9316	-62 50 10.842	Uesugi & Fukuda 1970
* r Pup	HD68980	2.1661	0.1724	167	-	B2ne	08 13 29.5169	-35 53 58.260	Uesugi & Fukuda 1970
HD 71459	HD71459	4.0543	0.1218	38	1	B3/5IV	08 25 51.9109	-42 09 11.067	Bragança et al. 2012
HD 74234	HD74234	1.3915	0.0511	192	11	B2IV	08 40 53.3999	-48 13 31.814	Bragança et al. 2012
* η Hya	HD74280	7.6128	0.3517	99.2	5	B3V	08 43 13.4759	+03 23 55.184	Ammler-von Eiff & Reiners 2012
* κ Hya	HD83754	8.8837	0.3752	150	-	B3/5IV/V	09 40 18.3596	-14 19 56.215	Abt et al. 2002
* I Hya	HD83953	6.5733	0.2851	240	-	B5V	09 41 17.0078	-23 35 29.432	Abt et al. 2002
* α Leo	HD87901	41.13	0.35	300	-	B8IVn	10 08 22.3109	+11 58 01.951	Abt et al. 2002
* β Sex	HD90994	8.9613	0.2448	80	-	B5IV/V	10 30 17.4798	-00 38 13.303	Abt et al. 2002
* tet Car	HD93030	7.16	0.21	202	-	B0Vp	10 42 57.3575	-64 23 39.865	Uesugi & Fukuda 1970
* π Cen	HD98718	9.12	0.34	350	-	B5Vn	11 21 00.4061	-54 29 27.665	Uesugi & Fukuda 1970
* ρ Cen	HD105937	11.8348	0.3746	147	-	B3V	12 11 39.1280	-52 22 06.406	Uesugi & Fukuda 1970
* ζ Cru	HD106983	10.4901	0.3308	188	-	B2/3V	12 18 26.2361	-64 00 11.114	Uesugi & Fukuda 1970
HD 110432	HD110432	2.3834	0.1228	213	-	B0.5IVpe	12 42 50.2655	-63 03 31.048	Bernacca & Perinotto 1970
HD 110956	HD110956	10.0283	0.3413	22	3	B2/3V	12 46 22.7143	-56 29 19.738	Bragança et al. 2012
* chi Cen	HD122980	7.7536	0.3819	16	7	B2V	14 06 02.7692	-41 10 46.676	Bragança et al. 2012
* ρ Lup	HD128345	10.1866	0.5381	240	-	B3/4V	14 37 53.2256	-49 25 33.025	Uesugi & Fukuda 1970
* b Cen	HD129116	10.2435	0.6426	197	-	B3V	14 41 57.5930	-37 47 36.588	Uesugi & Fukuda 1970
* λ Lup	HD133955	3.5406	0.5961	169	-	B3V	15 08 50.6128	-45 16 47.500	Uesugi & Fukuda 1970
* mu. Lup	HD135734	9.72	0.71	308	-	B8Ve	15 18 32.0229	-47 52 30.995	Uesugi & Fukuda 1970
* β Lib	HD135742	17.62	0.16	250	-	B8Vn	15 17 00.4138	-09 22 58.491	Abt et al. 2002
* phi02 Lup	HD136664	6.28	0.2	141	6	B4V	15 23 09.3275	-36 51 30.875	Bragança et al. 2012
* ζ04 Lib	HD138485	4.5302	0.1902	203	19	B3V	15 32 55.2197	-16 51 10.247	Bragança et al. 2012
* τ Lib	HD139365	4.1418	0.7621	100	-	B2.5V	15 38 39.3637	-29 46 39.988	Uesugi & Fukuda 1970
* b Sco	HD141637	6.8954	0.2438	225	-	B1.5Vn	15 50 58.7451	-25 45 04.662	Abt et al. 2002
* 4 Her	HD142926	5.8913	0.0804	275	-	B9pe	15 55 30.5918	+42 33 58.287	Abt et al. 2002
* ω Sco	HD144470	7.0596	0.3975	95	7	B1V	16 06 48.4226	-20 40 09.118	Bragança et al. 2012
* ν Sco	HD145502	6.88	0.76	115	-	B2V	16 11 59.7356	-19 27 38.536	Abt et al. 2002
* 25 Her	HD148283	12.9109	0.1359	280	-	A5V	16 25 24.1681	+37 23 38.579	Royer et al. 2007
* i Sco	HD148605	8.5602	0.3723	169	4	B3V	16 30 12.4745	-25 06 54.811	Bragança et al. 2012
* τ Sco	HD149438	5.1232	1.11	3	2	B0.2V	16 35 52.9508	-28 12 57.730	Bragança et al. 2012
HD 155806	HD155806	1.0057	0.1306	211	-	O7.5V((f))z(e)	17 15 19.2484	-33 32 54.307	Uesugi & Fukuda 1970
V* U Oph	HD156247	3.7432	0.1307	50	-	B3V	17 16 31.7132	+01 12 37.996	Abt et al. 2002
* α Ara	HD158427	4.1865	1.2735	288	-	B2Vne	17 31 50.5006	-49 52 34.093	Uesugi & Fukuda 1970
* 66 Oph	HD164284	6.9762	0.5037	250	-	B2Ve	18 00 15.7981	+04 22 07.139	Abt et al. 2002
* λ Pav	HD173948	4.8003	0.4471	217	-	B2Ve	18 52 13.0368	-62 11 15.339	Uesugi & Fukuda 1970
* β01 Sgr	HD181454	12.4748	0.6401	94	-	B9V	19 22 38.2988	-44 27 32.347	Uesugi & Fukuda 1970
HD 183362	HD183362	1.7248	0.0538	220	-	B3Ve	19 27 36.3963	+37 56 28.304	Abt et al. 2002

* β Cyg B	HD183914	8.3779	0.1696	215	-	B8Ve	19 30 45.3960	+27 57 54.973	Abt et al. 2002
HD 183656	HD183656	3.6705	0.0607	186	-	B7III	19 30 33.1219	+03 26 39.858	Royer et al. 2002
* ι Cyg	HD184006	27.0603	0.3278	240	-	A5V	19 29 42.3595	+51 43 47.206	Royer et al. 2007
* 12 Vul	HD187811	5.7966	0.2206	195	-	B2.5Ve	19 51 04.1087	+22 36 36.165	Abt et al. 2002
* 57 Aql A	HD188293	7.2437	0.1495	190	-	B7Vn	19 54 37.6522	-08 13 38.244	Abt et al. 2002
* 23 Cyg	HD188665	5.9155	0.1728	105	-	B5V	19 53 17.3787	+57 31 24.480	Abt et al. 2002
* 17 Vul	HD190993	6.6847	0.2047	75	-	B3V	20 06 53.4080	+23 36 51.927	Abt et al. 2002
* b02 Cyg	HD191610	5.2947	0.2255	250	-	B2.5Ve	20 09 25.6190	+36 50 22.596	Abt et al. 2002
* 20 Vul	HD192044	2.7904	0.0726	205	-	B7Ve	20 12 00.7017	+26 28 43.698	Abt et al. 2002
HD 192685	HD192685	7.8952	0.5496	160	-	B3V	20 15 15.8976	+25 35 31.045	Abt et al. 2002
* λ Cyg	HD198183	4.24	0.43	100	-	B5V	20 47 24.5376	+36 29 26.573	Abt et al. 2002
HD 198625	HD198625	2.2256	0.0456	250	-	B4Ve	20 49 54.6433	+46 39 40.814	Abt et al. 2002
* 57 Cyg	HD199081	6.688	0.2395	30	-	B5V	20 53 14.7592	+44 23 14.138	Abt et al. 2002
* ϵ Cap	HD205637	6.5495	0.7048	210	-	B3V	21 37 04.8309	-19 27 57.627	Abt et al. 2002
* 16 Peg	HD208057	5.8309	0.264	110	-	B3Ve	21 53 03.7679	+25 55 30.506	Abt et al. 2002
* o Aqr	HD209409	6.9205	0.2583	205	-	B7IVe	22 03 18.8435	-02 09 19.320	Abt et al. 2002
HD 209522	HD209522	3.0964	0.119	260	-	B4IVe	22 04 36.7670	-26 49 20.492	Abt et al. 2002
HD 214240	HD214240	1.5419	0.067	55	-	B3V	22 35 53.3823	+50 04 14.835	Abt et al. 2002
* ϵ PsA	HD214748	8.0981	0.3582	185	-	B8Ve	22 40 39.3446	-27 02 36.967	Abt et al. 2002
* ι And	HD222173	7.8999	0.3357	67	5	B8V	23 38 08.1998	+43 16 05.073	Bailey & Landstreet 2013
* ϵ Tuc	HD224686	9.2645	0.2741	174	-	B8V	23 59 54.9800	-65 34 37.666	Uesugi & Fukuda 1970

A&A-output, *Online Material p 24*

A&A–output, *Online Material p 25*

Appendix D: Inferred parameters of the survey of stars

Table D.1. Stellar parameters and $E(B-V)$ inferred from the UV domain.

star	$\log(g)$ (dex)	W	$t/t_{\rm ms}$	$T_{\rm eff}$ (K)	L ($L_\odot$)	$R_{\rm pole}$ ($R_\odot$)	i (°)	$\beta_{\rm GD}$	d (pc)	$E(B-V)$ (mag)
HD3369	$3.987^{+0.000}_{-0.000}$	$0.76^{+0.09}_{-0.07}$	$0.70^{+0.04}_{-0.08}$	$17553.53^{+295.40}_{-280.61}$	$1450.40^{+142.19}_{-125.89}$	$4.13^{+0.06}_{-0.05}$	$3.99^{+0.49}_{-0.46}$	$0.21^{+-0.03}_{-0.03}$	$182.56^{+9.96}_{-8.41}$	$0.06^{+0.01}_{-0.01}$
HD4727	$3.980^{+0.001}_{-0.001}$	$0.04^{+0.01}_{-0.01}$	$0.72^{+0.03}_{-0.04}$	$17794.49^{+219.79}_{-236.09}$	$1607.06^{+115.22}_{-117.12}$	$4.23^{+0.04}_{-0.05}$	$62.85^{+18.55}_{-21.61}$	$0.25^{+-0.00}_{-0.00}$	$187.84^{+6.12}_{-5.56}$	$0.03^{+0.00}_{-0.00}$
HD17543	$4.074^{+0.004}_{-0.004}$	$0.44^{+0.22}_{-0.24}$	$0.56^{+0.14}_{-0.12}$	$18941.41^{+632.04}_{-625.03}$	$1733.12^{+360.91}_{-308.48}$	$3.88^{+0.11}_{-0.12}$	$14.86^{+19.48}_{-6.15}$	$0.24^{+-0.01}_{-0.01}$	$215.36^{+28.62}_{-25.68}$	$0.18^{+0.01}_{-0.01}$
HD18537	$4.089^{+0.001}_{-0.001}$	$0.21^{+0.27}_{-0.04}$	$0.58^{+0.11}_{-0.11}$	$15694.46^{+482.16}_{-499.83}$	$577.04^{+104.27}_{-94.11}$	$3.26^{+0.07}_{-0.08}$	$58.81^{+20.53}_{-36.74}$	$0.25^{+0.00}_{-0.00}$	$154.15^{+21.25}_{-18.71}$	$0.13^{+0.01}_{-0.01}$
HD19374	$4.317^{+0.002}_{-0.002}$	$0.05^{+0.06}_{-0.03}$	$0.01^{+0.02}_{-0.01}$	$27546.15^{+681.45}_{-648.02}$	$7718.59^{+1204.99}_{-1021.78}$	$3.87^{+0.09}_{-0.09}$	$41.15^{+38.93}_{-27.08}$	$0.25^{+0.00}_{-0.00}$	$377.29^{+20.72}_{-17.88}$	$0.19^{+0.01}_{-0.01}$
HD21364	$4.367^{+0.000}_{-0.000}$	$0.32^{+0.02}_{-0.03}$	$0.01^{+0.01}_{-0.01}$	$15573.43^{+136.86}_{-139.48}$	$257.44^{+13.51}_{-13.24}$	$2.21^{+0.02}_{-0.02}$	$78.37^{+8.47}_{-10.65}$	$0.24^{+-0.01}_{-0.01}$	$83.51^{+1.34}_{-1.92}$	$0.08^{+0.01}_{-0.01}$
HD22192	$3.829^{+0.002}_{-0.001}$	$0.71^{+0.21}_{-0.20}$	$0.86^{+0.07}_{-0.10}$	$17789.69^{+572.97}_{-526.07}$	$2394.24^{+454.46}_{-366.24}$	$5.16^{+0.12}_{-0.12}$	$41.76^{+26.66}_{-11.60}$	$0.22^{+-0.03}_{-0.03}$	$179.21^{+6.99}_{-6.94}$	$0.15^{+0.01}_{-0.01}$
HD22203	$4.119^{+0.000}_{-0.000}$	$0.17^{+0.15}_{-0.03}$	$0.55^{+0.04}_{-0.06}$	$12880.64^{+97.27}_{-90.94}$	$181.68^{+7.65}_{-6.87}$	$2.71^{+0.02}_{-0.01}$	$64.66^{+17.57}_{-35.46}$	$0.25^{+-0.00}_{-0.00}$	$90.14^{+1.69}_{-1.77}$	$0.03^{+0.00}_{-0.00}$
HD22951	$4.064^{+0.003}_{-0.001}$	$0.02^{+0.00}_{-0.00}$	$0.55^{+0.02}_{-0.03}$	$27798.42^{+562.08}_{-313.27}$	$16466.88^{+2301.40}_{-1166.00}$	$5.55^{+0.14}_{-0.08}$	$65.24^{+7.74}_{-3.10}$	$0.25^{+-0.00}_{-0.00}$	$309.70^{+14.94}_{-14.52}$	$0.23^{+0.00}_{-0.01}$
HD23324	$4.350^{+0.002}_{-0.002}$	$0.37^{+0.11}_{-0.05}$	$0.04^{+0.05}_{-0.03}$	$14855.50^{+205.89}_{-173.54}$	$209.19^{+17.00}_{-13.55}$	$2.19^{+0.03}_{-0.02}$	$58.19^{+16.78}_{-16.28}$	$0.24^{+-0.01}_{-0.01}$	$121.81^{+5.78}_{-4.75}$	$0.11^{+0.01}_{-0.01}$
HD23363	$3.981^{+0.001}_{-0.001}$	$0.48^{+0.28}_{-0.15}$	$0.70^{+0.06}_{-0.14}$	$14801.03^{+233.06}_{-214.97}$	$558.95^{+48.69}_{-42.19}$	$3.60^{+0.04}_{-0.04}$	$39.37^{+29.74}_{-15.65}$	$0.24^{+-0.01}_{-0.01}$	$196.45^{+8.95}_{-9.44}$	$0.06^{+0.01}_{-0.01}$
HD23432	$4.366^{+0.002}_{-0.001}$	$0.34^{+0.10}_{-0.06}$	$0.03^{+0.04}_{-0.02}$	$14396.81^{+218.60}_{-211.13}$	$169.10^{+15.14}_{-13.43}$	$2.10^{+0.03}_{-0.02}$	$55.20^{+26.10}_{-15.76}$	$0.24^{+-0.01}_{-0.01}$	$122.66^{+5.84}_{-4.75}$	$0.13^{+0.01}_{-0.01}$
HD23862	$3.979^{+0.001}_{-0.001}$	$0.68^{+0.24}_{-0.15}$	$0.71^{+0.07}_{-0.10}$	$13109.42^{+335.04}_{-383.11}$	$291.29^{+40.48}_{-41.34}$	$3.32^{+0.05}_{-0.06}$	$53.14^{+27.03}_{-15.96}$	$0.22^{+-0.02}_{-0.03}$	$117.10^{+4.21}_{-4.25}$	$0.09^{+0.02}_{-0.02}$
HD25940	$4.181^{+0.002}_{-0.004}$	$0.38^{+0.23}_{-0.12}$	$0.33^{+0.17}_{-0.18}$	$24179.70^{+768.97}_{-970.74}$	$5279.61^{+1141.62}_{-1192.23}$	$4.15^{+0.15}_{-0.19}$	$41.33^{+31.51}_{-17.09}$	$0.24^{+-0.00}_{-0.01}$	$146.15^{+3.53}_{-3.49}$	$0.27^{+0.02}_{-0.02}$
HD26326	$4.016^{+0.002}_{-0.000}$	$0.01^{+0.01}_{-0.00}$	$0.69^{+0.05}_{-0.06}$	$16463.26^{+704.43}_{-367.69}$	$932.95^{+261.58}_{-117.04}$	$3.76^{+0.15}_{-0.08}$	$58.85^{+18.74}_{-25.86}$	$0.25^{+-0.00}_{-0.00}$	$203.68^{+14.96}_{-11.09}$	$0.05^{+0.02}_{-0.01}$
HD27778	$3.831^{+0.003}_{-0.003}$	$0.58^{+0.28}_{-0.31}$	$0.85^{+0.09}_{-0.18}$	$15762.72^{+1220.70}_{-943.96}$	$1210.58^{+618.40}_{-351.50}$	$4.68^{+0.28}_{-0.22}$	$24.78^{+28.39}_{-8.48}$	$0.23^{+-0.01}_{-0.01}$	$254.72^{+40.28}_{-50.07}$	$0.40^{+0.03}_{-0.03}$
HD29365	$4.385^{+0.000}_{-0.000}$	$0.15^{+0.03}_{-0.02}$	$0.00^{+0.01}_{-0.00}$	$12152.84^{+80.01}_{-73.84}$	$62.55^{+2.25}_{-2.02}$	$1.79^{+0.01}_{-0.01}$	$47.82^{+19.15}_{-5.50}$	$0.25^{+-0.00}_{-0.00}$	$126.42^{+0.19}_{-0.72}$	$0.08^{+0.01}_{-0.01}$
HD29763	$4.356^{+0.000}_{-0.000}$	$0.18^{+0.03}_{-0.02}$	$0.00^{+0.00}_{-0.00}$	$19332.49^{+52.84}_{-72.66}$	$901.94^{+14.84}_{-20.11}$	$2.68^{+0.01}_{-0.01}$	$53.80^{+17.69}_{-7.40}$	$0.25^{+-0.00}_{-0.00}$	$187.10^{+0.48}_{-1.14}$	$0.05^{+0.00}_{-0.00}$
HD31726	$4.172^{+0.002}_{-0.002}$	$0.08^{+0.14}_{-0.03}$	$0.37^{+0.14}_{-0.24}$	$24139.37^{+580.32}_{-579.37}$	$5316.76^{+855.29}_{-758.25}$	$4.18^{+0.11}_{-0.12}$	$33.47^{+36.72}_{-22.63}$	$0.25^{+0.00}_{-0.00}$	$483.39^{+50.49}_{-65.04}$	$0.02^{+0.01}_{-0.01}$
HD32249	$4.159^{+0.001}_{-0.001}$	$0.31^{+0.39}_{-0.20}$	$0.41^{+0.13}_{-0.20}$	$21743.36^{+319.61}_{-343.33}$	$3017.43^{+273.38}_{-272.66}$	$3.88^{+0.06}_{-0.06}$	$16.60^{+37.58}_{-9.15}$	$0.25^{+0.00}_{-0.00}$	$225.72^{+13.40}_{-12.09}$	$0.04^{+0.00}_{-0.00}$
HD32343	$4.052^{+0.004}_{-0.001}$	$0.76^{+0.04}_{-0.62}$	$0.61^{+0.17}_{-0.07}$	$18909.01^{+730.74}_{-269.85}$	$1831.06^{+439.07}_{-144.64}$	$4.00^{+0.13}_{-0.05}$	$8.79^{+41.69}_{-1.19}$	$0.22^{+-0.03}_{-0.01}$	$228.65^{+11.13}_{-8.43}$	$0.12^{+0.01}_{-0.01}$
HD32991	$4.025^{+0.003}_{-0.003}$	$0.56^{+0.03}_{-0.03}$	$0.60^{+0.05}_{-0.08}$	$24347.15^{+424.76}_{-445.39}$	$8427.84^{+985.89}_{-949.15}$	$5.17^{+0.11}_{-0.12}$	$35.95^{+8.17}_{-8.03}$	$0.23^{+-0.02}_{-0.02}$	$283.75^{+15.03}_{-22.98}$	$0.49^{+0.00}_{-0.00}$
HD34748	$4.324^{+0.001}_{-0.001}$	$0.45^{+0.02}_{-0.03}$	$0.00^{+0.01}_{-0.00}$	$26389.03^{+192.38}_{-246.84}$	$6006.26^{+269.01}_{-332.40}$	$3.72^{+0.03}_{-0.04}$	$67.53^{+14.78}_{-10.84}$	$0.24^{+-0.01}_{-0.01}$	$392.26^{+2.10}_{-4.28}$	$0.19^{+0.00}_{-0.00}$
HD34798	$4.260^{+0.001}_{-0.000}$	$0.07^{+0.12}_{-0.02}$	$0.23^{+0.13}_{-0.12}$	$17570.92^{+522.41}_{-455.31}$	$686.12^{+130.56}_{-100.42}$	$2.83^{+0.08}_{-0.07}$	$44.29^{+34.67}_{-28.87}$	$0.25^{+0.00}_{-0.00}$	$266.62^{+28.37}_{-22.11}$	$0.04^{+0.01}_{-0.01}$
HD35532	$4.337^{+0.001}_{-0.001}$	$0.49^{+0.07}_{-0.05}$	$0.01^{+0.02}_{-0.01}$	$21808.81^{+234.06}_{-242.72}$	$1892.70^{+130.39}_{-128.55}$	$3.06^{+0.04}_{-0.04}$	$64.09^{+12.01}_{-11.40}$	$0.24^{+-0.01}_{-0.01}$	$268.52^{+5.38}_{-7.57}$	$0.18^{+0.00}_{-0.00}$
HD35580	$4.194^{+0.001}_{-0.001}$	$0.67^{+0.12}_{-0.09}$	$0.39^{+0.09}_{-0.11}$	$13974.12^{+248.78}_{-247.89}$	$231.53^{+23.06}_{-21.34}$	$2.60^{+0.03}_{-0.03}$	$62.43^{+17.53}_{-14.59}$	$0.22^{+-0.02}_{-0.02}$	$196.62^{+9.96}_{-9.47}$	$0.02^{+0.01}_{-0.01}$

HD35588	$4.109^{+0.002}_{-0.002}$	$0.41^{+0.20}_{-0.09}$	$0.49^{+0.14}_{-0.24}$	$21344.41^{+490.17}_{-500.58}$	$3105.46^{+451.26}_{-415.10}$	$4.09^{+0.09}_{-0.10}$	$44.96^{+22.77}_{-15.57}$	$0.24^{+-0.01}_{-0.01}$	$411.47^{+48.88}_{-41.33}$	$0.05^{+0.00}_{-0.00}$
HD35671	$4.304^{+0.002}_{-0.001}$	$0.27^{+0.11}_{-0.05}$	$0.10^{+0.08}_{-0.07}$	$18046.34^{+311.27}_{-321.73}$	$714.29^{+77.80}_{-74.27}$	$2.74^{+0.05}_{-0.05}$	$50.23^{+20.83}_{-18.06}$	$0.25^{+-0.00}_{-0.00}$	$160.08^{+7.99}_{-7.76}$	$0.10^{+0.01}_{-0.01}$
HD36267	$4.231^{+0.001}_{-0.001}$	$0.38^{+0.09}_{-0.06}$	$0.29^{+0.09}_{-0.07}$	$16255.06^{+193.45}_{-196.80}$	$480.23^{+33.11}_{-31.99}$	$2.77^{+0.03}_{-0.03}$	$48.05^{+14.28}_{-10.99}$	$0.24^{+-0.01}_{-0.01}$	$98.97^{+5.09}_{-4.89}$	$0.00^{+0.00}_{-0.00}$
HD36653	$4.359^{+0.001}_{-0.001}$	$0.28^{+0.05}_{-0.09}$	$0.01^{+0.01}_{-0.01}$	$18048.01^{+194.82}_{-242.63}$	$602.01^{+41.22}_{-48.56}$	$2.52^{+0.03}_{-0.04}$	$43.63^{+36.86}_{-7.34}$	$0.25^{+-0.00}_{-0.00}$	$161.48^{+5.22}_{-5.41}$	$0.06^{+0.00}_{-0.00}$
HD36695	$3.993^{+0.011}_{-0.006}$	$0.44^{+0.31}_{-0.20}$	$0.63^{+0.13}_{-0.21}$	$24841.45^{+1075.04}_{-976.48}$	$10266.28^{+3221.33}_{-2289.24}$	$5.48^{+0.29}_{-0.25}$	$28.25^{+31.77}_{-12.26}$	$0.24^{+-0.01}_{-0.01}$	$433.71^{+66.56}_{-56.96}$	$0.06^{+0.01}_{-0.01}$
HD37017	$4.175^{+0.004}_{-0.001}$	$0.36^{+0.16}_{-0.08}$	$0.37^{+0.19}_{-0.18}$	$21398.43^{+813.39}_{-738.10}$	$2641.87^{+673.51}_{-501.25}$	$3.75^{+0.15}_{-0.13}$	$50.96^{+25.55}_{-18.61}$	$0.24^{+-0.01}_{-0.01}$	$453.24^{+73.82}_{-55.68}$	$0.06^{+0.01}_{-0.01}$
HD37018	$4.198^{+0.002}_{-0.003}$	$0.77^{+0.03}_{-0.03}$	$0.26^{+0.04}_{-0.03}$	$27127.72^{+532.50}_{-593.78}$	$10036.13^{+1325.31}_{-1251.94}$	$4.55^{+0.11}_{-0.10}$	$2.47^{+0.26}_{-0.24}$	$0.21^{+-0.04}_{-0.04}$	$314.95^{+19.17}_{-23.21}$	$0.06^{+0.00}_{-0.00}$
HD37303	$4.275^{+0.002}_{-0.001}$	$0.66^{+0.01}_{-0.01}$	$0.10^{+0.10}_{-0.07}$	$25922.78^{+674.69}_{-470.83}$	$6325.08^{+1059.93}_{-669.20}$	$3.95^{+0.10}_{-0.08}$	$54.51^{+3.77}_{-8.53}$	$0.23^{+-0.02}_{-0.02}$	$488.32^{+42.38}_{-24.92}$	$0.01^{+0.01}_{-0.01}$
HD37744	$4.069^{+0.003}_{-0.003}$	$0.06^{+0.02}_{-0.01}$	$0.56^{+0.08}_{-0.07}$	$26194.78^{+508.56}_{-542.43}$	$11359.18^{+1397.78}_{-1361.30}$	$5.19^{+0.10}_{-0.11}$	$65.76^{+13.68}_{-22.00}$	$0.25^{+-0.00}_{-0.00}$	$644.43^{+53.00}_{-41.96}$	$0.04^{+0.01}_{-0.01}$
HD37202	$3.909^{+0.020}_{-0.016}$	$0.49^{+0.35}_{-0.23}$	$0.75^{+0.15}_{-0.30}$	$22746.58^{+2169.89}_{-1820.30}$	$7694.85^{+6202.02}_{-3133.52}$	$5.66^{+0.68}_{-0.51}$	$29.53^{+34.27}_{-12.35}$	$0.24^{+-0.01}_{-0.01}$	$134.98^{+15.33}_{-14.43}$	$0.13^{+0.05}_{-0.05}$
HD37490	$3.776^{+0.014}_{-0.001}$	$0.97^{+0.03}_{-0.09}$	$0.98^{+0.01}_{-0.03}$	$22667.90^{+895.94}_{-998.01}$	$10018.19^{+3179.30}_{-2208.66}$	$6.51^{+0.40}_{-0.22}$	$26.49^{+4.58}_{-2.89}$	$0.17^{+-0.08}_{-0.08}$	$347.36^{+33.54}_{-33.91}$	$0.15^{+0.02}_{-0.01}$
HD37795	$3.717^{+0.006}_{-0.006}$	$0.70^{+0.17}_{-0.11}$	$0.94^{+0.03}_{-0.04}$	$14267.17^{+326.89}_{-290.48}$	$930.96^{+102.09}_{-84.01}$	$5.01^{+0.03}_{-0.03}$	$50.77^{+20.00}_{-13.00}$	$0.22^{+-0.03}_{-0.03}$	$80.99^{+2.06}_{-1.89}$	$0.02^{+0.01}_{-0.01}$
HD39698	$3.758^{+0.001}_{-0.008}$	$0.89^{+0.09}_{-0.12}$	$0.98^{+0.02}_{-0.04}$	$19105.21^{+481.70}_{-608.86}$	$4060.27^{+652.30}_{-580.46}$	$5.83^{+0.15}_{-0.07}$	$19.45^{+3.78}_{-2.46}$	$0.20^{+-0.05}_{-0.05}$	$703.00^{+49.82}_{-55.87}$	$0.04^{+0.01}_{-0.01}$
HD41753	$4.185^{+0.001}_{-0.001}$	$0.29^{+0.20}_{-0.23}$	$0.39^{+0.11}_{-0.15}$	$17716.00^{+257.61}_{-245.25}$	$884.51^{+79.98}_{-71.42}$	$3.17^{+0.05}_{-0.04}$	$11.26^{+52.72}_{-4.92}$	$0.25^{+-0.00}_{-0.00}$	$164.43^{+7.68}_{-6.87}$	$0.01^{+0.01}_{-0.01}$
HD42545	$4.249^{+0.001}_{-0.002}$	$0.65^{+0.09}_{-0.24}$	$0.25^{+0.07}_{-0.14}$	$16701.05^{+391.37}_{-403.49}$	$533.82^{+78.39}_{-67.93}$	$2.77^{+0.06}_{-0.05}$	$75.39^{+9.34}_{-19.41}$	$0.23^{+-0.02}_{-0.02}$	$167.88^{+9.38}_{-11.15}$	$0.03^{+0.01}_{-0.01}$
HD44402	$4.122^{+0.000}_{-0.001}$	$0.11^{+0.26}_{-0.06}$	$0.50^{+0.06}_{-0.10}$	$20312.47^{+257.48}_{-256.94}$	$2235.17^{+178.53}_{-158.78}$	$3.83^{+0.05}_{-0.04}$	$22.81^{+42.72}_{-16.15}$	$0.25^{+0.00}_{-0.00}$	$111.37^{+1.67}_{-1.61}$	$0.04^{+0.01}_{-0.01}$
HD44506	$3.776^{+0.003}_{-0.003}$	$0.92^{+0.06}_{-0.15}$	$0.98^{+0.01}_{-0.03}$	$21724.35^{+439.32}_{-406.75}$	$7892.53^{+827.75}_{-710.81}$	$6.29^{+0.06}_{-0.06}$	$40.19^{+8.13}_{-3.55}$	$0.19^{+-0.06}_{-0.06}$	$551.15^{+35.71}_{-41.47}$	$0.03^{+0.01}_{-0.01}$
HD47054	$3.834^{+0.001}_{-0.001}$	$0.69^{+0.12}_{-0.04}$	$0.85^{+0.04}_{-0.04}$	$14456.70^{+291.89}_{-299.71}$	$743.72^{+81.36}_{-77.36}$	$4.36^{+0.05}_{-0.06}$	$58.92^{+14.77}_{-9.75}$	$0.22^{+-0.03}_{-0.03}$	$256.41^{+15.87}_{-15.63}$	$0.06^{+0.01}_{-0.00}$
HD48977	$4.142^{+0.001}_{-0.001}$	$0.04^{+0.04}_{-0.01}$	$0.50^{+0.01}_{-0.02}$	$16930.28^{+122.00}_{-117.24}$	$764.96^{+34.43}_{-32.03}$	$3.22^{+0.02}_{-0.02}$	$66.76^{+16.16}_{-37.81}$	$0.25^{+-0.00}_{-0.00}$	$304.00^{+6.16}_{-5.68}$	$0.00^{+0.00}_{-0.00}$
HD49662	$4.124^{+0.002}_{-0.001}$	$0.17^{+0.02}_{-0.02}$	$0.53^{+0.12}_{-0.08}$	$15893.43^{+540.42}_{-383.32}$	$562.70^{+114.85}_{-70.84}$	$3.14^{+0.08}_{-0.06}$	$81.00^{+5.85}_{-5.58}$	$0.25^{+-0.00}_{-0.00}$	$164.19^{+24.40}_{-11.82}$	$0.05^{+0.01}_{-0.01}$
HD50013	$3.738^{+0.009}_{-0.006}$	$0.62^{+0.11}_{-0.11}$	$0.95^{+0.03}_{-0.06}$	$22039.86^{+419.24}_{-271.05}$	$9939.94^{+1508.53}_{-895.35}$	$6.86^{+0.23}_{-0.15}$	$47.22^{+14.24}_{-9.50}$	$0.23^{+-0.02}_{-0.02}$	$203.37^{+3.79}_{-3.70}$	$0.05^{+0.01}_{-0.01}$
HD56139	$3.731^{+0.009}_{-0.006}$	$0.98^{+0.01}_{-0.14}$	$0.98^{+0.01}_{-0.02}$	$17670.45^{+429.15}_{-258.62}$	$2855.55^{+317.87}_{-179.37}$	$5.72^{+0.03}_{-0.02}$	$16.85^{+2.35}_{-1.73}$	$0.16^{+-0.09}_{-0.08}$	$290.35^{+7.16}_{-9.39}$	$0.01^{+0.01}_{-0.00}$
HD58715	$4.044^{+0.000}_{-0.000}$	$0.53^{+0.16}_{-0.04}$	$0.62^{+0.04}_{-0.07}$	$13402.12^{+112.77}_{-121.25}$	$273.60^{+12.52}_{-12.96}$	$3.08^{+0.02}_{-0.02}$	$81.28^{+6.07}_{-30.27}$	$0.24^{+-0.01}_{-0.01}$	$49.64^{+0.49}_{-0.48}$	$0.03^{+0.00}_{-0.00}$
HD60098	$4.221^{+0.001}_{-0.001}$	$0.11^{+0.21}_{-0.04}$	$0.33^{+0.09}_{-0.16}$	$17039.26^{+258.67}_{-295.25}$	$636.23^{+61.48}_{-62.65}$	$2.90^{+0.05}_{-0.05}$	$39.85^{+38.02}_{-27.20}$	$0.25^{+0.00}_{-0.00}$	$287.66^{+16.14}_{-17.69}$	$0.07^{+0.00}_{-0.00}$
HD60848	$3.864^{+0.011}_{-0.011}$	$0.97^{+0.02}_{-0.06}$	$0.81^{+0.10}_{-0.13}$	$22257.01^{+827.34}_{-1229.17}$	$7758.22^{+2219.70}_{-2333.70}$	$5.94^{+0.32}_{-0.38}$	$76.44^{+7.32}_{-11.30}$	$0.17^{+-0.08}_{-0.08}$	$722.91^{+106.22}_{-111.41}$	$0.01^{+0.01}_{-0.00}$
HD60855	$3.956^{+0.007}_{-0.005}$	$0.67^{+0.21}_{-0.16}$	$0.72^{+0.13}_{-0.18}$	$22644.73^{+654.37}_{-600.24}$	$6595.34^{+1420.49}_{-1032.05}$	$5.29^{+0.22}_{-0.16}$	$45.74^{+24.94}_{-13.25}$	$0.22^{+-0.02}_{-0.02}$	$389.89^{+47.39}_{-46.28}$	$0.19^{+0.01}_{-0.01}$
HD67536	$4.201^{+0.003}_{-0.004}$	$0.59^{+0.07}_{-0.10}$	$0.29^{+0.15}_{-0.17}$	$22940.77^{+593.35}_{-619.89}$	$3717.46^{+607.49}_{-561.37}$	$3.87^{+0.10}_{-0.10}$	$59.68^{+15.41}_{-13.72}$	$0.23^{+-0.02}_{-0.02}$	$374.03^{+24.55}_{-26.61}$	$0.15^{+0.01}_{-0.01}$
HD68980	$3.762^{+0.004}_{-0.002}$	$0.81^{+0.16}_{-0.22}$	$0.95^{+0.04}_{-0.08}$	$20038.59^{+553.95}_{-459.73}$	$5440.75^{+809.54}_{-704.39}$	$6.14^{+0.09}_{-0.14}$	$30.03^{+11.02}_{-5.36}$	$0.21^{+-0.04}_{-0.04}$	$293.01^{+7.74}_{-8.07}$	$0.05^{+0.01}_{-0.01}$
HD71459	$4.349^{+0.001}_{-0.001}$	$0.11^{+0.04}_{-0.03}$	$0.02^{+0.04}_{-0.02}$	$18593.40^{+247.96}_{-261.75}$	$736.51^{+61.29}_{-60.81}$	$2.62^{+0.04}_{-0.04}$	$31.47^{+11.20}_{-9.28}$	$0.25^{+-0.00}_{-0.00}$	$241.58^{+6.91}_{-6.38}$	$0.03^{+0.01}_{-0.01}$

HD74234	$4.111^{+0.004}_{-0.002}$	$0.46^{+0.15}_{-0.10}$	$0.47^{+0.13}_{-0.15}$	$23774.35^{+800.39}_{-698.79}$	$5754.84^{+1343.59}_{-980.99}$	$4.48^{+0.18}_{-0.15}$	$43.89^{+21.33}_{-12.42}$	$0.24^{+-0.01}_{-0.01}$	$926.14^{+129.95}_{-85.97}$	$0.07^{+0.01}_{-0.01}$
HD74280	$3.979^{+0.000}_{-0.003}$	$0.24^{+0.20}_{-0.05}$	$0.71^{+0.04}_{-0.08}$	$19420.50^{+354.63}_{-417.76}$	$2564.83^{+292.03}_{-300.07}$	$4.49^{+0.08}_{-0.08}$	$50.13^{+28.05}_{-24.78}$	$0.25^{+-0.00}_{-0.00}$	$178.77^{+8.73}_{-7.78}$	$0.02^{+0.01}_{-0.01}$
HD83754	$4.314^{+0.001}_{-0.001}$	$0.36^{+0.12}_{-0.09}$	$0.09^{+0.06}_{-0.06}$	$16893.92^{+208.79}_{-167.44}$	$473.92^{+34.03}_{-26.01}$	$2.55^{+0.03}_{-0.02}$	$45.67^{+28.17}_{-13.05}$	$0.24^{+-0.01}_{-0.01}$	$137.99^{+4.61}_{-4.65}$	$0.02^{+0.00}_{-0.00}$
HD83953	$4.075^{+0.000}_{-0.001}$	$0.69^{+0.19}_{-0.15}$	$0.59^{+0.09}_{-0.13}$	$16484.28^{+312.60}_{-258.23}$	$791.45^{+92.48}_{-69.49}$	$3.46^{+0.06}_{-0.05}$	$48.46^{+23.44}_{-12.39}$	$0.22^{+-0.03}_{-0.03}$	$155.75^{+4.69}_{-4.67}$	$0.05^{+0.01}_{-0.01}$
HD87901	$4.243^{+0.001}_{-0.001}$	$0.78^{+0.05}_{-0.04}$	$0.28^{+0.05}_{-0.05}$	$13813.83^{+225.27}_{-221.70}$	$191.24^{+17.86}_{-16.41}$	$2.42^{+0.03}_{-0.03}$	$67.82^{+11.10}_{-9.45}$	$0.21^{+-0.04}_{-0.04}$	$24.38^{+0.21}_{-0.21}$	$0.03^{+0.00}_{-0.00}$
HD90994	$4.253^{+0.001}_{-0.000}$	$0.23^{+0.29}_{-0.07}$	$0.25^{+0.10}_{-0.16}$	$15434.85^{+232.42}_{-240.19}$	$338.75^{+29.98}_{-29.00}$	$2.58^{+0.03}_{-0.03}$	$38.91^{+22.04}_{-22.78}$	$0.25^{+0.00}_{-0.00}$	$122.41^{+5.47}_{-5.53}$	$0.04^{+0.01}_{-0.01}$
HD93030	$4.125^{+0.004}_{-0.004}$	$0.44^{+0.15}_{-0.12}$	$0.39^{+0.11}_{-0.14}$	$28297.86^{+603.08}_{-524.97}$	$15678.31^{+2355.82}_{-1864.05}$	$5.22^{+0.15}_{-0.13}$	$44.55^{+26.77}_{-14.00}$	$0.24^{+-0.01}_{-0.01}$	$139.04^{+4.10}_{-4.05}$	$0.03^{+0.01}_{-0.01}$
HD98718	$4.304^{+0.002}_{-0.002}$	$0.67^{+0.05}_{-0.05}$	$0.09^{+0.07}_{-0.06}$	$19711.77^{+333.69}_{-328.18}$	$1190.38^{+120.52}_{-110.14}$	$2.97^{+0.04}_{-0.04}$	$65.43^{+7.50}_{-9.22}$	$0.23^{+-0.02}_{-0.02}$	$110.15^{+4.29}_{-3.49}$	$0.03^{+0.00}_{-0.01}$
HD105937	$4.169^{+0.001}_{-0.001}$	$0.48^{+0.13}_{-0.16}$	$0.40^{+0.17}_{-0.13}$	$18387.10^{+298.17}_{-296.73}$	$1146.19^{+112.68}_{-104.39}$	$3.34^{+0.05}_{-0.05}$	$34.90^{+25.74}_{-8.96}$	$0.24^{+-0.01}_{-0.01}$	$124.71^{+10.16}_{-9.02}$	$0.00^{+0.00}_{-0.00}$
HD106983	$4.269^{+0.001}_{-0.002}$	$0.38^{+0.10}_{-0.06}$	$0.17^{+0.07}_{-0.09}$	$19690.45^{+220.17}_{-233.21}$	$1288.48^{+86.10}_{-86.69}$	$3.09^{+0.03}_{-0.03}$	$57.22^{+21.40}_{-14.82}$	$0.24^{+-0.01}_{-0.01}$	$120.19^{+4.53}_{-4.84}$	$0.00^{+0.00}_{-0.00}$
HD110432	$3.919^{+0.012}_{-0.009}$	$0.58^{+0.18}_{-0.17}$	$0.70^{+0.09}_{-0.12}$	$26716.55^{+919.51}_{-724.47}$	$19500.74^{+5289.63}_{-3562.92}$	$6.54^{+0.35}_{-0.29}$	$41.10^{+22.67}_{-12.32}$	$0.23^{+-0.02}_{-0.02}$	$344.99^{+36.60}_{-33.12}$	$0.41^{+0.01}_{-0.01}$
HD110956	$4.363^{+0.001}_{-0.001}$	$0.05^{+0.05}_{-0.01}$	$0.01^{+0.02}_{-0.01}$	$16560.38^{+185.91}_{-167.75}$	$365.58^{+24.05}_{-20.72}$	$2.33^{+0.02}_{-0.02}$	$47.37^{+29.28}_{-26.76}$	$0.25^{+0.00}_{-0.00}$	$124.11^{+2.51}_{-2.46}$	$0.01^{+0.01}_{-0.01}$
HD122980	$4.329^{+0.001}_{-0.001}$	$0.04^{+0.09}_{-0.01}$	$0.01^{+0.02}_{-0.01}$	$23206.92^{+229.17}_{-223.27}$	$2735.07^{+166.98}_{-155.67}$	$3.24^{+0.03}_{-0.03}$	$59.56^{+23.74}_{-47.31}$	$0.25^{+0.00}_{-0.00}$	$156.40^{+4.01}_{-3.63}$	$0.04^{+0.00}_{-0.00}$
HD128345	$4.322^{+0.001}_{-0.001}$	$0.74^{+0.02}_{-0.03}$	$0.08^{+0.05}_{-0.06}$	$16857.32^{+113.06}_{-113.48}$	$462.92^{+17.93}_{-17.48}$	$2.53^{+0.01}_{-0.01}$	$34.80^{+5.81}_{-4.55}$	$0.22^{+-0.03}_{-0.03}$	$95.87^{+1.73}_{-1.56}$	$0.00^{+0.00}_{-0.00}$
HD129116	$4.287^{+0.001}_{-0.001}$	$0.44^{+0.11}_{-0.08}$	$0.13^{+0.07}_{-0.08}$	$19533.85^{+206.36}_{-204.71}$	$1178.22^{+74.45}_{-69.55}$	$3.00^{+0.03}_{-0.03}$	$53.46^{+22.43}_{-15.73}$	$0.24^{+-0.01}_{-0.01}$	$105.42^{+1.84}_{-1.92}$	$0.03^{+0.00}_{-0.00}$
HD133955	$3.999^{+0.003}_{-0.002}$	$0.75^{+0.05}_{-0.22}$	$0.67^{+0.07}_{-0.11}$	$21175.32^{+489.21}_{-477.35}$	$4023.69^{+586.85}_{-516.78}$	$4.73^{+0.11}_{-0.11}$	$27.80^{+12.55}_{-3.69}$	$0.22^{+-0.03}_{-0.03}$	$216.38^{+21.80}_{-21.77}$	$0.03^{+0.00}_{-0.00}$
HD135734	$3.673^{+0.004}_{-0.005}$	$0.96^{+0.02}_{-0.04}$	$0.96^{+0.03}_{-0.04}$	$13555.47^{+176.73}_{-288.21}$	$786.88^{+48.12}_{-77.72}$	$5.10^{+0.02}_{-0.05}$	$86.72^{+2.55}_{-6.96}$	$0.18^{+-0.07}_{-0.07}$	$126.56^{+5.45}_{-6.59}$	$0.00^{+0.00}_{-0.00}$
HD135742	$3.761^{+0.003}_{-0.002}$	$0.79^{+0.08}_{-0.08}$	$0.90^{+0.02}_{-0.02}$	$12684.88^{+236.27}_{-224.03}$	$442.69^{+44.51}_{-37.19}$	$4.37^{+0.05}_{-0.04}$	$71.24^{+11.80}_{-13.83}$	$0.21^{+-0.04}_{-0.04}$	$56.82^{+0.54}_{-0.54}$	$0.02^{+0.01}_{-0.01}$
HD136664	$4.257^{+0.000}_{-0.001}$	$0.35^{+0.19}_{-0.10}$	$0.18^{+0.11}_{-0.11}$	$20818.33^{+230.69}_{-246.56}$	$1801.00^{+123.69}_{-119.92}$	$3.27^{+0.04}_{-0.03}$	$40.75^{+22.55}_{-15.71}$	$0.24^{+-0.00}_{-0.01}$	$159.72^{+4.90}_{-5.02}$	$0.06^{+0.00}_{-0.00}$
HD138485	$4.330^{+0.002}_{-0.002}$	$0.43^{+0.08}_{-0.10}$	$0.02^{+0.03}_{-0.02}$	$21957.69^{+350.61}_{-426.96}$	$2007.10^{+206.36}_{-231.64}$	$3.10^{+0.05}_{-0.07}$	$46.91^{+30.35}_{-10.24}$	$0.24^{+-0.01}_{-0.01}$	$223.10^{+13.01}_{-11.59}$	$0.08^{+0.01}_{-0.01}$
HD139365	$4.120^{+0.001}_{-0.001}$	$0.18^{+0.03}_{-0.02}$	$0.50^{+0.04}_{-0.05}$	$19807.09^{+213.42}_{-200.96}$	$1955.94^{+122.32}_{-110.09}$	$3.77^{+0.03}_{-0.03}$	$77.09^{+9.64}_{-22.98}$	$0.25^{+-0.00}_{-0.00}$	$112.72^{+2.64}_{-2.43}$	$0.03^{+0.00}_{-0.00}$
HD141637	$4.327^{+0.000}_{-0.001}$	$0.13^{+0.01}_{-0.02}$	$0.00^{+0.00}_{-0.00}$	$24538.76^{+96.84}_{-137.69}$	$3756.10^{+90.22}_{-123.27}$	$3.40^{+0.01}_{-0.02}$	$84.48^{+4.13}_{-7.86}$	$0.25^{+-0.00}_{-0.00}$	$182.65^{+0.13}_{-0.46}$	$0.21^{+0.00}_{-0.00}$
HD142926	$4.241^{+0.001}_{-0.001}$	$0.67^{+0.09}_{-0.11}$	$0.29^{+0.10}_{-0.10}$	$13823.53^{+299.09}_{-286.00}$	$193.17^{+24.17}_{-21.13}$	$2.43^{+0.04}_{-0.04}$	$66.28^{+12.04}_{-10.99}$	$0.22^{+-0.03}_{-0.03}$	$168.70^{+6.26}_{-6.21}$	$0.02^{+0.02}_{-0.01}$
HD144470	$4.305^{+0.001}_{-0.003}$	$0.24^{+0.04}_{-0.03}$	$0.00^{+0.01}_{-0.00}$	$31339.74^{+385.43}_{-618.65}$	$17336.96^{+1129.65}_{-2077.82}$	$4.48^{+0.03}_{-0.11}$	$31.19^{+5.32}_{-6.18}$	$0.25^{+-0.00}_{-0.00}$	$162.81^{+3.58}_{-7.71}$	$0.28^{+0.00}_{-0.00}$
HD145502	$4.309^{+0.003}_{-0.001}$	$0.14^{+0.01}_{-0.01}$	$0.01^{+0.02}_{-0.01}$	$28963.21^{+948.74}_{-395.10}$	$10604.04^{+2455.27}_{-916.30}$	$4.10^{+0.17}_{-0.07}$	$76.84^{+7.08}_{-7.74}$	$0.25^{+-0.00}_{-0.00}$	$180.36^{+11.32}_{-5.73}$	$0.23^{+0.01}_{-0.01}$
HD148283	$3.912^{+0.004}_{-0.008}$	$0.87^{+0.10}_{-0.11}$	$0.76^{+0.06}_{-0.10}$	$9240.66^{+467.18}_{-351.00}$	$53.13^{+16.72}_{-10.66}$	$2.85^{+0.11}_{-0.10}$	$72.53^{+13.46}_{-16.12}$	$0.20^{+-0.05}_{-0.05}$	$74.63^{+2.19}_{-2.24}$	$0.15^{+0.05}_{-0.04}$
HD148605	$4.343^{+0.003}_{-0.004}$	$0.29^{+0.21}_{-0.03}$	$0.01^{+0.09}_{-0.01}$	$20874.05^{+419.60}_{-649.66}$	$1435.01^{+175.83}_{-239.42}$	$2.90^{+0.05}_{-0.08}$	$63.21^{+23.64}_{-28.10}$	$0.25^{+-0.00}_{-0.00}$	$140.81^{+2.82}_{-4.11}$	$0.08^{+0.01}_{-0.01}$
HD149438	$4.300^{+0.015}_{-0.003}$	$0.02^{+0.06}_{-0.01}$	$0.02^{+0.03}_{-0.01}$	$31113.86^{+611.30}_{-755.49}$	$16781.49^{+1685.11}_{-2401.61}$	$4.47^{+0.04}_{-0.12}$	$13.65^{+34.95}_{-10.44}$	$0.25^{+0.00}_{-0.00}$	$138.26^{+9.37}_{-8.19}$	$0.03^{+0.01}_{-0.01}$
HD155806	$4.208^{+0.017}_{-0.033}$	$0.38^{+0.12}_{-0.11}$	$0.35^{+0.15}_{-0.31}$	$30018.89^{+0.00}_{-0.00}$	$23463.42^{+0.00}_{-0.00}$	$5.68^{+0.00}_{-0.00}$	$45.86^{+19.77}_{-13.61}$	$0.24^{+-0.01}_{-0.01}$	$540.61^{+65.55}_{-62.53}$	$0.25^{+0.01}_{-0.01}$

HD156247	$4.314^{+0.001}_{-0.004}$	$0.08^{+0.04}_{-0.01}$	$0.00^{+0.00}_{-0.00}$	$29336.47^{+170.60}_{-1122.74}$	$11284.21^{+433.74}_{-2483.80}$	$4.12^{+0.03}_{-0.19}$	$57.64^{+24.13}_{-23.48}$	$0.25^{+-0.00}_{-0.00}$	$279.44^{+2.79}_{-23.04}$	$0.46^{+0.00}_{-0.01}$
HD158427	$4.078^{+0.000}_{-0.002}$	$0.79^{+0.04}_{-0.06}$	$0.56^{+0.08}_{-0.09}$	$20047.41^{+333.76}_{-347.66}$	$2354.15^{+247.01}_{-229.21}$	$4.03^{+0.07}_{-0.06}$	$53.74^{+9.94}_{-8.63}$	$0.21^{+-0.04}_{-0.04}$	$88.70^{+5.11}_{-5.13}$	$0.05^{+0.00}_{-0.00}$
HD164284	$4.295^{+0.003}_{-0.003}$	$0.42^{+0.12}_{-0.08}$	$0.05^{+0.07}_{-0.04}$	$26889.74^{+592.62}_{-604.77}$	$7278.74^{+1030.71}_{-950.42}$	$3.94^{+0.09}_{-0.10}$	$54.02^{+29.81}_{-13.09}$	$0.24^{+-0.01}_{-0.01}$	$198.51^{+9.32}_{-10.16}$	$0.21^{+0.01}_{-0.01}$
HD173948	$3.736^{+0.010}_{-0.010}$	$0.94^{+0.04}_{-0.08}$	$0.95^{+0.04}_{-0.08}$	$24275.80^{+824.57}_{-779.42}$	$17585.97^{+4170.28}_{-3392.61}$	$7.52^{+0.30}_{-0.31}$	$31.27^{+4.66}_{-3.45}$	$0.18^{+-0.07}_{-0.07}$	$364.66^{+28.32}_{-29.13}$	$0.11^{+0.01}_{-0.01}$
HD181454	$3.993^{+0.000}_{-0.000}$	$0.66^{+0.14}_{-0.23}$	$0.69^{+0.06}_{-0.11}$	$13077.44^{+228.01}_{-326.10}$	$276.89^{+26.08}_{-34.45}$	$3.25^{+0.03}_{-0.05}$	$19.84^{+10.49}_{-4.10}$	$0.23^{+-0.02}_{-0.02}$	$91.62^{+7.59}_{-12.30}$	$0.02^{+0.01}_{-0.01}$
HD183362	$3.727^{+0.006}_{-0.008}$	$0.75^{+0.03}_{-0.03}$	$0.98^{+0.02}_{-0.07}$	$17706.44^{+325.13}_{-410.45}$	$2931.37^{+252.27}_{-296.12}$	$5.77^{+0.03}_{-0.04}$	$61.01^{+7.15}_{-7.50}$	$0.22^{+-0.03}_{-0.03}$	$505.15^{+19.61}_{-43.39}$	$0.05^{+0.01}_{-0.01}$
HD183914	$4.186^{+0.000}_{-0.000}$	$0.69^{+0.04}_{-0.03}$	$0.40^{+0.08}_{-0.07}$	$14251.12^{+183.03}_{-180.34}$	$261.77^{+19.13}_{-17.27}$	$2.66^{+0.03}_{-0.02}$	$42.52^{+7.15}_{-5.81}$	$0.22^{+-0.03}_{-0.03}$	$123.64^{+4.08}_{-3.68}$	$0.07^{+0.00}_{-0.00}$
HD183656	$4.267^{+0.004}_{-0.003}$	$0.47^{+0.30}_{-0.15}$	$0.19^{+0.25}_{-0.13}$	$17908.96^{+837.64}_{-726.30}$	$761.62^{+239.09}_{-170.20}$	$2.87^{+0.13}_{-0.12}$	$43.83^{+38.89}_{-17.21}$	$0.24^{+-0.01}_{-0.01}$	$250.25^{+18.71}_{-19.11}$	$0.22^{+0.03}_{-0.03}$
HD184006	$3.996^{+0.004}_{-0.004}$	$0.75^{+0.18}_{-0.12}$	$0.69^{+0.07}_{-0.09}$	$9040.58^{+317.53}_{-296.01}$	$37.59^{+8.00}_{-6.45}$	$2.51^{+0.07}_{-0.07}$	$63.43^{+19.53}_{-15.56}$	$0.22^{+-0.03}_{-0.03}$	$37.32^{+0.14}_{-0.13}$	$0.08^{+0.04}_{-0.03}$
HD187811	$4.228^{+0.002}_{-0.001}$	$0.70^{+0.01}_{-0.01}$	$0.28^{+0.07}_{-0.03}$	$18640.39^{+294.54}_{-265.79}$	$1069.41^{+102.96}_{-86.91}$	$3.14^{+0.05}_{-0.04}$	$30.27^{+5.07}_{-2.79}$	$0.22^{+-0.03}_{-0.03}$	$184.48^{+6.06}_{-5.61}$	$0.04^{+0.01}_{-0.00}$
HD188293	$4.353^{+0.002}_{-0.002}$	$0.41^{+0.09}_{-0.10}$	$0.02^{+0.03}_{-0.02}$	$17196.05^{+222.80}_{-260.13}$	$466.54^{+35.83}_{-39.34}$	$2.44^{+0.03}_{-0.03}$	$50.04^{+32.30}_{-9.70}$	$0.24^{+-0.01}_{-0.01}$	$161.14^{+6.43}_{-7.23}$	$0.11^{+0.01}_{-0.01}$
HD188665	$3.990^{+0.001}_{-0.000}$	$0.23^{+0.03}_{-0.03}$	$0.71^{+0.03}_{-0.05}$	$16210.20^{+517.19}_{-240.09}$	$914.52^{+184.65}_{-77.27}$	$3.84^{+0.11}_{-0.05}$	$73.26^{+8.90}_{-7.15}$	$0.25^{+-0.00}_{-0.00}$	$190.92^{+6.90}_{-6.36}$	$0.03^{+0.01}_{-0.01}$
HD190993	$4.345^{+0.001}_{-0.001}$	$0.16^{+0.08}_{-0.04}$	$0.01^{+0.02}_{-0.01}$	$20157.46^{+223.28}_{-232.16}$	$1174.31^{+77.94}_{-77.09}$	$2.82^{+0.03}_{-0.03}$	$47.85^{+34.60}_{-18.82}$	$0.25^{+-0.00}_{-0.00}$	$161.91^{+4.22}_{-4.17}$	$0.05^{+0.00}_{-0.00}$
HD191610	$3.926^{+0.002}_{-0.002}$	$0.72^{+0.08}_{-0.06}$	$0.76^{+0.08}_{-0.08}$	$21456.75^{+443.14}_{-440.29}$	$5268.49^{+671.18}_{-608.56}$	$5.27^{+0.10}_{-0.10}$	$46.55^{+9.39}_{-8.52}$	$0.22^{+-0.03}_{-0.03}$	$317.86^{+18.00}_{-19.72}$	$0.09^{+0.01}_{-0.01}$
HD192044	$3.608^{+0.040}_{-0.001}$	$0.94^{+0.04}_{-0.02}$	$0.99^{+0.01}_{-0.01}$	$12576.55^{+1764.51}_{-98.90}$	$608.45^{+505.65}_{-22.61}$	$5.21^{+0.21}_{-0.02}$	$34.84^{+22.74}_{-18.28}$	$0.18^{+-0.07}_{-0.07}$	$223.24^{+17.87}_{-34.13}$	$0.15^{+0.07}_{-0.03}$
HD192685	$3.939^{+0.003}_{-0.002}$	$0.43^{+0.26}_{-0.11}$	$0.73^{+0.09}_{-0.16}$	$20440.65^{+800.31}_{-783.13}$	$3834.75^{+972.13}_{-800.19}$	$4.95^{+0.18}_{-0.19}$	$48.78^{+29.58}_{-21.36}$	$0.24^{+-0.01}_{-0.01}$	$275.86^{+41.85}_{-40.73}$	$0.03^{+0.01}_{-0.01}$
HD198183	$3.888^{+0.000}_{-0.000}$	$0.70^{+0.16}_{-0.27}$	$0.81^{+0.08}_{-0.10}$	$17234.79^{+573.92}_{-503.57}$	$1715.77^{+340.21}_{-261.10}$	$4.66^{+0.12}_{-0.11}$	$19.22^{+11.72}_{-4.16}$	$0.22^{+-0.03}_{-0.02}$	$221.48^{+26.81}_{-28.34}$	$0.08^{+0.01}_{-0.01}$
HD198625	$3.872^{+0.002}_{-0.002}$	$0.73^{+0.13}_{-0.15}$	$0.82^{+0.10}_{-0.14}$	$18562.38^{+591.89}_{-607.91}$	$2678.80^{+335.20}_{-453.54}$	$5.02^{+0.14}_{-0.13}$	$50.69^{+19.64}_{-12.03}$	$0.22^{+-0.03}_{-0.03}$	$485.78^{+57.07}_{-67.06}$	$0.15^{+0.01}_{-0.01}$
HD199081	$4.042^{+0.000}_{-0.001}$	$0.09^{+0.71}_{-0.02}$	$0.66^{+0.06}_{-0.25}$	$14641.70^{+291.66}_{-309.23}$	$452.06^{+52.20}_{-49.72}$	$3.31^{+0.05}_{-0.05}$	$44.47^{+26.82}_{-39.88}$	$0.25^{+0.03}_{-0.00}$	$160.21^{+5.99}_{-5.66}$	$0.02^{+0.01}_{-0.01}$
HD205637	$3.776^{+0.002}_{-0.007}$	$0.91^{+0.06}_{-0.29}$	$0.98^{+0.01}_{-0.03}$	$21682.22^{+1129.81}_{-893.35}$	$7829.22^{+2668.92}_{-1485.55}$	$6.29^{+0.29}_{-0.13}$	$35.21^{+14.33}_{-4.81}$	$0.19^{+-0.06}_{-0.05}$	$303.20^{+21.36}_{-21.43}$	$0.08^{+0.02}_{-0.02}$
HD208057	$4.148^{+0.001}_{-0.001}$	$0.38^{+0.25}_{-0.14}$	$0.45^{+0.09}_{-0.16}$	$18099.35^{+269.72}_{-271.65}$	$1105.65^{+99.86}_{-93.32}$	$3.39^{+0.05}_{-0.05}$	$31.86^{+26.35}_{-12.97}$	$0.24^{+-0.00}_{-0.01}$	$194.46^{+8.67}_{-8.57}$	$0.02^{+0.00}_{-0.00}$
HD209409	$3.988^{+0.000}_{-0.001}$	$0.73^{+0.18}_{-0.16}$	$0.70^{+0.06}_{-0.10}$	$14443.70^{+294.17}_{-288.53}$	$482.42^{+57.47}_{-50.54}$	$3.52^{+0.06}_{-0.05}$	$42.15^{+17.75}_{-9.67}$	$0.22^{+-0.03}_{-0.03}$	$134.94^{+3.63}_{-3.39}$	$0.07^{+0.01}_{-0.01}$
HD209522	$4.072^{+0.004}_{-0.004}$	$0.69^{+0.06}_{-0.11}$	$0.58^{+0.11}_{-0.11}$	$19305.26^{+573.92}_{-540.79}$	$1942.60^{+353.62}_{-293.77}$	$3.95^{+0.10}_{-0.10}$	$51.93^{+15.13}_{-9.36}$	$0.22^{+-0.03}_{-0.03}$	$344.97^{+45.09}_{-33.94}$	$0.05^{+0.01}_{-0.01}$
HD214240	$3.898^{+0.001}_{-0.001}$	$0.94^{+0.03}_{-0.04}$	$0.80^{+0.13}_{-0.10}$	$15647.52^{+235.05}_{-301.90}$	$962.97^{+86.19}_{-100.87}$	$4.23^{+0.06}_{-0.07}$	$8.80^{+1.02}_{-0.74}$	$0.18^{+-0.07}_{-0.07}$	$372.23^{+75.88}_{-39.90}$	$0.12^{+0.01}_{-0.01}$
HD214748	$3.649^{+0.005}_{-0.005}$	$0.68^{+0.09}_{-0.03}$	$0.97^{+0.02}_{-0.04}$	$14149.56^{+249.96}_{-249.73}$	$1052.17^{+87.13}_{-82.67}$	$5.41^{+0.03}_{-0.03}$	$53.43^{+7.93}_{-8.40}$	$0.22^{+-0.03}_{-0.03}$	$174.96^{+7.86}_{-9.56}$	$0.04^{+0.01}_{-0.00}$
HD222173	$3.921^{+0.000}_{-0.001}$	$0.15^{+0.02}_{-0.01}$	$0.79^{+0.01}_{-0.02}$	$13484.49^{+173.08}_{-236.23}$	$405.00^{+29.64}_{-37.20}$	$3.70^{+0.04}_{-0.05}$	$83.47^{+4.34}_{-15.47}$	$0.25^{+-0.00}_{-0.00}$	$152.84^{+4.48}_{-3.89}$	$0.05^{+0.01}_{-0.01}$
HD224686	$3.942^{+0.000}_{-0.000}$	$0.88^{+0.07}_{-0.08}$	$0.75^{+0.03}_{-0.03}$	$12380.41^{+219.25}_{-152.92}$	$238.15^{+23.15}_{-15.18}$	$3.36^{+0.04}_{-0.03}$	$33.37^{+6.39}_{-4.47}$	$0.20^{+-0.05}_{-0.05}$	$114.74^{+2.32}_{-2.25}$	$0.05^{+0.01}_{-0.01}$

Appendix D

Stellar parameters of Be stars observed with X-shooter

A&A 609, A108 (2018)
DOI: 10.1051/0004-6361/201731536

Astronomy & Astrophysics

Stellar parameters of Be stars observed with X-shooter[⋆,⋆⋆]

A. Shokry[1,2,3], Th. Rivinius[1], A. Mehner[1], C. Martayan[1], W. Hummel[4], R. H. D. Townsend[5], A. Mérand[1], B. Mota[6], D. M. Faes[6], M. A. Hamdy[2,⋆⋆⋆], M. M. Beheary[7], K. A. K Gadallah[7], and M. S. Abo-Elazm[2]

[1] ESO – European Organisation for Astronomical Research in the Southern Hemisphere, Casilla 19001, Santiago, Chile
e-mail: ahmedsh2911@gmail.com
[2] Astronomy Department, National Research Institute of Astronomy and Geophysics (NRIAG), 11421 Helwan, Cairo, Egypt
[3] Kottamia Center of Scientific Excellence in Astronomy and Space Science (KCScE, STDF, ASRT), Cairo, Egypt
[4] ESO – European Organisation for Astronomical Research in the Southern Hemisphere, Karl-Schwarzschild-Str. 2, Garchingnwt, Germany
[5] Department of Astronomy, University of Wisconsin-Madison, Madison, WI 53706, USA
[6] Instituto de Astronomia, Geofísica e Ciências Atmosféricas, Universidade de São Paulo (USP), Rua do Matão 1226, Cidade Universitária, 05508-900 São Paulo, Brazil
[7] Astronomy and Meteorology Department, Faculty of Science, Al-Azhar University, Cairo, Egypt

Received 9 July 2017 / Accepted 26 October 2017

ABSTRACT

Aims. The X-shooter archive of several thousand telluric standard star spectra was skimmed for Be and Be shell stars to derive the stellar fundamental parameters and statistical properties, in particular for the less investigated late-type Be stars and the extension of the Be phenomenon into early A stars.
Methods. An adapted version of the BCD method is used, using the Balmer discontinuity parameters to determine effective temperature and surface gravity. This method is optimally suited for late B stars. The projected rotational velocity was obtained by profile fitting to the Mg II lines of the targets, and the spectra were inspected visually for the presence of peculiar features such as the infrared Ca II triplet or the presence of a double Balmer discontinuity. The Balmer line equivalent widths were measured, but they are only useful for determining the pure emission contribution in a subsample of Be stars owing to uncertainties in determining the photospheric contribution.
Results. A total of 78, mostly late-type, Be stars, were identified in the X-shooter telluric standard star archive, out of which 48 had not been reported before. We confirm the general trend that late-type Be stars have more tenuous disks and are less variable than early-type Be stars. The relatively large number (48) of relatively bright ($V > 8.5$) additional Be stars casts some doubt on the statistics of late-type Be stars; they are more common than currently thought. The Be/B star fraction may not strongly depend on spectral subtype.

Key words. circumstellar matter – stars: emission-line, Be – stars: activity

1. Introduction

Be stars are non-supergiant B stars that show or have shown Hα emission, as defined by Jaschek et al. (1981). Emission does not only occur in the first members of the Balmer line series, but can affect the continuum and line profiles of other species as well, most often singly ionized metals, such as Fe II. It is generally agreed that, in classical Be stars, this emission is due to the presence of a gaseous Keplerian disk that is concentrated in the equatorial plane. This disk is a decretion disk, i.e., the source of the disk material is the central star, generated by the equatorial flow of stellar material. One of the key factors in creating the disk is supposed to be the very high rotational velocity. In fact, Be stars are known to have higher rotational velocities than normal B-type stars (Catanzaro 2013). For a complete review on the topic, see Porter & Rivinius (2003) and Rivinius et al. (2013a).

Classical Be stars are known to vary both in brightness and spectral line appearance with a large range of timescales from years to minutes (Okazaki 1997; Floquet et al. 2002; Kogure & Leung 2007). While long-term variations are associated with formation and dissipation of the disk (Okazaki 1997), the origin of short-term variability is usually attributed to pulsations within the B star photosphere (Baade 2000; Huat et al. 2009). Photometric studies show that earlier type Be stars are more likely to be variable (e.g., Hubert & Floquet 1998).

Chojnowski et al. (2015) have demonstrated that Be stars can often be found among stars observed for the purpose of removing telluric absorption in the near-infrared domain because main sequence B stars are among the preferred objects for this task. Inspired by this example, we decided to search for Be stars in a similarly extensive database of telluric standard star observations, namely that taken at the Very Large Telescope (VLT) with the X-shooter instrument.

2. Observations and data reduction

All spectra were acquired with the VLT/X-shooter instruments. Most data were taken as telluric standard stars for other observations from the commissioning of X-shooter in 2007 until

⋆ Based on observations made with ESO Telescopes at the La Silla Paranal Observatory under program IDs 60.A-9022, 60.A-9024, 077.D-0085, 085.A-0962, 185.D-0056, 091.B-0900, and 093.D-0415.
⋆⋆ Table 6 is only available at the CDS via anonymous ftp to cdsarc.u-strasbg.fr (130.79.128.5) or via http://cdsarc.u-strasbg.fr/viz-bin/qcat?J/A+A/609/A108
⋆⋆⋆ Deceased.

A&A 609, A108 (2018)

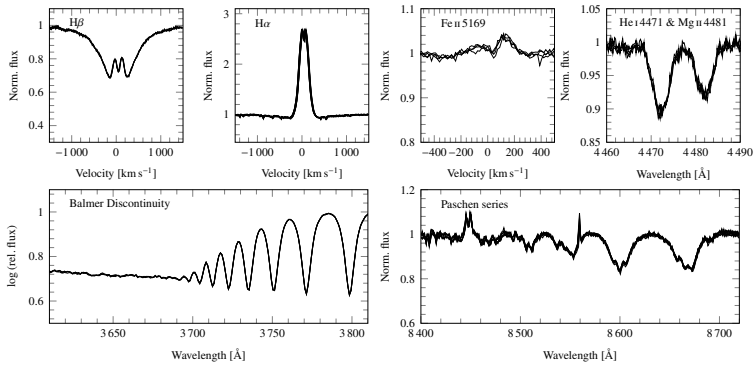

Fig. 1. Spectrum overview plot for HIP 11116. All available spectra are overplotted, giving an indication of the spectral variability. For the remaining 77 active Be stars, see Appendix C.

2015. Once the value of this database for science was realized, additional spectra of stars of interest were acquired in a dedicated observing program in ESO period 93. A few datasets of stars of interest were also taken under a number of different program IDs and were downloaded from the archive as well. The data observed for this work, however, are mainly from program IDs 60.A-9022, 60.A-9024, and 093.D-0415. The meteorological observing conditions, dates, and night-log excerpts are available from the ESO data archive together with the raw data.

X-shooter is a multiwavelength medium-resolution spectrograph mounted at the Cassegrain focus of UT2 of the VLT at ESO Paranal that has a mirror diameter of 8.2 m. The three arms of X-shooter are UVB, covering 300–550 nm; VIS, covering 550–1010 nm; and NIR, covering 1000–2500 nm. The resolution depends on the chosen slit width and ranges from $R = 1890$ to 9760 in the UVB, 3180 to 18110 in the VIS, and 3900 to 11490 in NIR arm, respectively (Vernet et al. 2011).

To select the Be stars and other possibly interesting objects from this huge archival sample, first the raw frames in the VIS arm were obtained. A window, containing only the spectral order with the Hα line, was cut from the entire raw frame. From the inter-order space in that window, the local background, effectively the sum of the bias, dark, and scattered light, was estimated and subtracted. The result was integrated into a 1D spectrum, divided by a generic blaze shape obtained from flat-field frames, and then divided by the counts in the continuum. This procedure yields an approximately normalized Hα line profile in the units of pixel vs. flux (i.e., without any wavelength calibration), which is sufficient to judge upon the line shape for the presence of emission and other features of interest.

The resulting more than 10 000 profiles of 1334 stars were inspected visually for emission or any other curious appearance, such as binarity or strong profile shape distortions. Of these stars, 1093 were found to be spectroscopically normal BA main sequence objects and 16 were of later spectral type. Of the remaining objects, 89 were spectroscopic binaries of type SB2 (as seen in Hα) and 48 were found to be supergiants with winds or otherwise not as expected for a single main sequence star. The procedure yielded a number of emission line stars for further inspection, of which two are known as Herbig Be stars (HIP 56379 and HIP 85755), and four are mass-transferring binaries of various types (HIP 33237, HIP 45311, HIP 88615, and HIP 93502). This leaves 78 Be stars identified from the X-shooter data. In addition, among the stars not showing emission four could be identified, with the SIMBAD database, as currently inactive Be stars and hence were added to the sample (HIP 15188, HIP 25950, HIP 108022, and HIP 108975), bringing the number to a total of 82 Be stars. We note that not all stars could be used for every analysis below, so the number of Be stars used for some results might be lower.

The spectra of the Be star sample, identified in the above way, were reduced with the ESO Recipe Flexible Execution Workbench (REFLEX) for X-shooter (Freudling et al. 2013), which is a workflow environment to run ESO VLT pipelines. This workflow provides an easy and interactive way to reduce VLT science data. The steps executed by the ESO X-shooter pipeline (v.2.6.0) include bias subtraction, flat fielding, wavelength and flux calibration, and order merging.

For the flux calibration the master response calibration provided by the ESO archive was used, except for UVB data obtained between 2009 and beginning of 2012. Using the master calibration on these spectra produces an obviously spurious dip in the region immediately blueward of the Balmer discontinuity. This is most likely due to the use of two flat-field lamps in the very blue, where their flux ratio was not entirely stable. To avoid the problem, spectra taken in these years were flux calibrated with a flux standard taken in the same night or not more than a few nights before or after, which was reduced with the same flat-field exposures.

Spectra that had obvious faults, such as bad flux calibration, too little flux, or overexposure in the relevant parts of the continuum, were discarded from the following analysis. This left 10 Be stars without suitable data to determine stellar parameters. For each spectrum, a flux calibrated version and a normalized version, using a global spline fit to continuum regions, were produced for analysis.

In Fig. 1 an overview of the data of the Be star HIP 11116 is shown. Similar plots for the remaining 77 identified Be stars are presented in Appendix C.

3. Analysis methods

3.1. Fundamental parameters via the BCD method

The primary goal of this work is to obtain fundamental parameters of Be stars. In addition the line broadening $v \sin i$ and Balmer emission equivalent widths (EW) were obtained.

3.1.1. Measuring the Balmer discontinuity

Stellar parameters were determined with a procedure akin to the BCD method, which is named after the main contributors to the method, Barbier, Chalonge, and Divan (see Appendix A of Zorec et al. 2009, for a description, and references in that work for the history of the method). The BCD method uses the height ($D_\star$) and position (λ_1) of the Balmer discontinuity for spectral classification. Some adaptations were necessary, however, since the original BCD method is designed to work on low-resolution photographic spectra with $\Delta\lambda = 8$ Å at the position of the BD, or about $R = 460$.

The height $D_\star$ is measured by extrapolating the Balmer and Paschen continua to a wavelength of 370 nm and taking the flux difference in dex; see the solid and dashed red lines in Fig. 2. For this, both spectra with relative flux calibration and traditionally normalized spectra were used. In the normalized spectrum, a selection was made to chose the points on which the continuum fit would be performed in the flux-calibrated spectrum. All points with a normalized intensity between 0.95 and and 1.05 were selected for this purpose; see the red points in Fig. 2.

- To determine the Paschen continuum, a selection of these points between $\lambda = 398$ and 450 nm was made. A linear regression was computed to the flux-calibrated spectrum in log-log space.
- For the Balmer continuum, and only in cases in which no double Balmer discontinuity (see below) was apparent, the wavelength selection was made between 350 and 368 nm, and then again a linear regression was computed in log-log space.

The difference between the two regressions at 370 nm, which corresponds to 3.568 in log scale, is then taken as $D_\star$.

A special problem for Be stars is that the Balmer discontinuity can appear twice: once due to the stellar photosphere and a second time due to the disk, blueward from the photospheric BD. A clearly visible second BD mostly occurs in strong shell and pole-on Be stars. This is due to the lower temperature and pressure broadening in the circumstellar environment (Kaiser 1987; Aidelman et al. 2012). The term shell star here denotes a Be star in which the photosphere is (partly) obscured by the disk. A pole-on star, to the contrary, is a Be star seen at very low inclination. In the shell star, the additional line opacity causes the second BD; in the pole-on star, the second BD is caused by the line emission, which is typically much higher in pole-on stars, in terms of units of the local continuum, than in Be stars of intermediate inclination. While this does not exclude a secondary BD in intermediate inclination Be stars, it makes it much harder to detect, as it is typically weaker. Indeed, all stars showing a strong secondary BD are either shell stars, or stars with very narrow photospheric and emission lines. The above method of determining the Balmer continuum would fail here, as it would inevitably focus on the second, circumstellar Balmer discontinuity. For stars that have such a clearly double Balmer discontinuity in their spectrum, the position of points for the linear regression for the Balmer continuum around 370 nm was defined by hand by selecting the points with the highest flux between Balmer line cores, as demonstrated in the lowermost panel of Fig. 2.

The second parameter measured in the BCD system, λ_1 is the mean spectral position of the Balmer discontinuity, usually given as differential from 370 nm, i.e., $\lambda_1 = \lambda_{\rm meanBD} - 370$. Following the original BCD convention, λ_1 is given in Ångström in this work. To measure λ_1, the two linear regressions to Paschen and Balmer continuum are averaged to a third linear function between the two. Next, the midpoints between the Balmer lines, which are local flux maxima, are used for a 4th order polynomial fit to estimate an upper envelope of the flux curve. The wavelength at which this upper envelope intersects the midpoint between Balmer and Paschen continuum is taken to measure λ_1. This position is not independent of the spectral resolution, in particular for lower resolutions as used in the original BCD system.

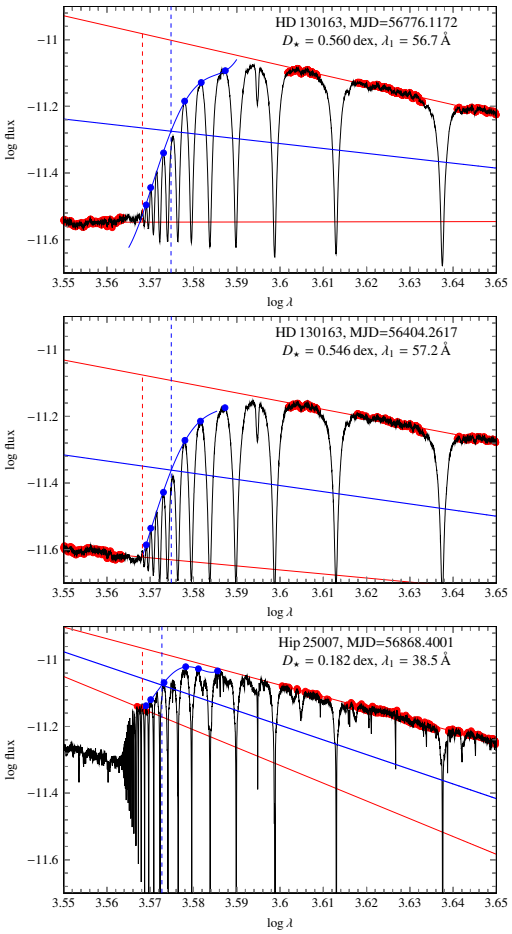

Fig. 2. *Two upper panels*: spectra for HD 130163 with the most discrepant calibration of the UV flux slope. The steps to determine $D_\star$ are indicated in red: selection of continuum points to fit the slopes and the difference between the two fits at 3700 Å as the value of $D_\star$. In blue for λ_1: the midpoints between the continuum fits in red, the upper envelope of the BD. The intersection of this envelope with the midpoints to determine λ_1. *Lower panel*: for HIP 25007, a clear double BD is present, and the Balmer continuum must be determined by choosing bona fide continuum points manually.

The principle of measurement is illustrated in Fig. 2. For the non-Be star HD 130163, the results and fit for the two most discrepant observations, in terms of slopes of the Balmer and Paschen continua, are compared. For the strong Be-shell star

HIP 25007 the procedure in case of a clear double Balmer discontinuity is illustrated.

3.1.2. Model grid

To determine stellar parameters, the measurements were compared against a model grid, rather than an existing calibration of the BCD method, since calibrations only exist for low resolution (much lower than the lowest available for X-shooter data). We used the B4 model, which in terms of physics is identical to the BRUCE3 model described in Sect. 3 of Rivinius et al. (2013b), but has been updated computationally to make use of GPU parallel computing. The model creates a surface grid of a rotating star based on the Roche model, and then assigns each point a local value of $\log g$ and $T_{\rm eff}$ using the Roche model and von Zeipel relations with a traditional value of $\beta = 0.25$. The computationally new code then interpolates these precomputed intensity spectra, taking the aspect angle of the line of sight into account. Finally, the numerically updated part integrates the surface grid over the visible surface, a task GPUs were explicitly designed for, into the observed spectrum. This is carried out first for input spectra including all spectral lines, and then for an input grid of spectra with continuum emission only. The resulting spectra can then either be normalized traditionally, i.e., in the same way as the observations, or in a perfect sense, using the computed, true continuum spectrum.

The set of stellar parameters for the input grid is based on Table 6 of Zorec et al. (2009), i.e., computing models based on their parameters for B0 to A1, and for LCs V to III. Any sufficiently dense and even sampling of the $D_\star$–λ_1-plane would have produced the same numerical results for the determined parameters, except it would not have been possible to give an estimate of spectral types. This grid of models was produced for five X-shooter instrumental resolutions in the UVB, which depend on slit width, as mentioned in Sect. 2.

For the spectrophotometric slit of 5″ the resolution is effectively governed by the seeing, for which a somewhat worse than typical value for Paranal observatory of 1.0″ is assumed. The BCD parameters were measured in the model spectra with the same method as the observed data.

To obtain the stellar parameters, the three models forming a triangle that encloses the observed value in the $D_\star$–λ_1-plane were chosen and the barycentric coordinates of the observational $(D_\star, \lambda_1)$ pair in this triangle were computed (see Fig. 3). With these coordinates, the physical parameters were interpolated. The spectral type is assigned as one of the most nearby grid points. This is not a spectral classification scheme, which would have to rely on actual standard stars, but is rather only meant as an indication. In a few cases where stars are outside the grid limits, but still close (see Fig. 4), extrapolation was used instead of the barycentric interpolation.

As Be stars are typically fast rotators, the grid was computed for two values of $\omega = \Omega/\Omega_{\rm crit}$, a slow rotation grid with $\omega = 0.25$ and a fast rotation grid with $\omega = 0.85$. The former was computed for only one value of $v \sin i = 20\,{\rm km\,s^{-1}}$, i.e., a total of 5×51 models, the latter for inclinations from a pole-on value of $v \sin i = 10\,{\rm km\,s^{-1}}$ to the equator in steps of $10\,{\rm kms^{-1}}$, i.e., a total of 5×651 models. For the fast rotation grid, at low temperatures and low surface gravities, the equatorial parameters were outside the grid of input spectra and no model spectra were produced for these parameters. The full grids are available at the CDS as Table 6

Most program stars are late type and some are at the very edge of the $D_\star$–λ_1-range covered by the models at $\omega = 0.85$.

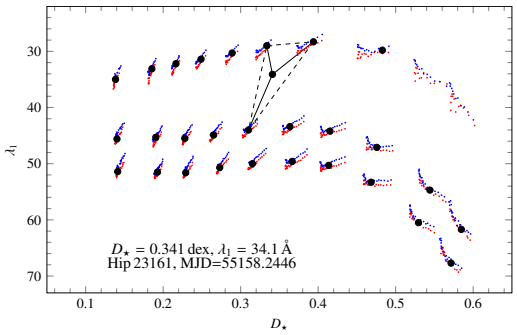

Fig. 3. Interpolation and BCD plane for one star. Shown are all $(D_\star, \lambda_1)$ points for all computed $v \sin i$ in the models for $R = 3300$ (red) and $R = 9100$ (blue). The chosen subgrid to analyze this observation ($R = 5100$ for 1″ slit width, $v \sin i = 150\,{\rm kms^{-1}}$) is shown in black, and the surrounding triangle is indicated by dashed lines, and the barycentric coordinates to obtain the weighted parameter values are indicated by solid lines. The nearest grid point, used to associate a spectral type, represents a B7 III star.

We investigated the influence of rapid rotation on the parameter determination first for a number of test stars only.

3.1.3. Test cases

Three non-Be stars with a large number of observations in various slit widths were selected from the archive for the purpose of assessing stability and reliability of the method. These are HIP 72362 (HD 130163, A0 V, $V = 6.9$ mag), HIP 98926 (HD 190285, A0 V, $V = 7.2$ mag), and HIP 01115 (HD 955, B3/5 V, $V = 7.4$ mag).

In addition, program stars with 10 or more observations were analyzed in a thorough way similar to the three test stars, before applying the method to the bulk of objects with fewer observations. All stars used for tests are given in Table 1.

An absolute flux calibration is not very reliable across the different slit widths, so we only assessed the relative flux calibration. For this, all spectra were normalized to the mean flux in the interval from 404 to 406 nm. The spectra have a large individual scatter, but the averages for the different slit widths are indistinguishable. This indicates that, at the resolutions offered by X-shooter, the differences in resolution do not have much influence on the method employed.

In particular, there is no systematic difference between the observation with the 5″ slit, which does not suffer from any slit loss vs. those with smaller slit widths. This is confirmed by measurements in the model grid, in which the differences between the resolutions turned out to be well below the scatter of the measurements and other systematic errors discussed here (see also Fig. 3). The last two columns of Table 1 give the mean and standard deviation of the measured BCD parameters. Both the height and position of the Balmer discontinuity $D_\star$ and λ_1 can be very well measured in X-shooter data. An imperfect flux calibration turns out not to be a problem, since, even if not perfect, it is reasonably stable across the region of interest. In a sense the fitting procedure can be regarded as self-calibrating, and only strong slopes, curvatures, or discontinuities in the flux calibration around 370 nm would have a strongly detrimental effect on the derived parameters.

In the next step, and for the non-Be stars only, we investigated how well the $D_\star$ and λ_1 values translate into physical parameters. As Table 2 shows, there are systematic effects between the slow rotation and the high rotation model grids. The same BCD parameters analyzed with the slow rotation grid give systematically higher effective temperatures, well outside the statistical scatter. For the effective gravity, the effect is less severe, giving lower $\log g$ for slow rotation, but still within the limit of the statistical error, by which the 3σ limit is meant, traditionally employed in astronomy vs. the more conservative 5σ limit often found in other fields of physics.

In turn, the differences of the BCD measurements with high rotation, but different inclinations, is negligible. In this context, it does not matter that we do not know the actual rotation of the non-Be test stars. It only matters that we know it for the Be stars, namely that they are rapid rotators, much closer to 85% than to 25%. It follows that the Be stars must be analyzed with the 85% grid to avoid the identified systematic errors. However, we do not need to know the inclination or even $v \sin i$ of the Be star with high precision, since this choice does not have a strong effect on the determined BCD parameters.

Combining the errors listed in Tables 1 and 2, one can estimate a typical error of about 50 K and 0.03 in $\log g$ for a late-type B stars, for which the BCD method has the highest power of distinction (since the BD parameters change steeply at this spectral type), and about 400 K and 0.05 in $\log g$ for a mid-type B star. Since for most targets only one or two spectra are available, we use these numbers as the typical accuracy.

3.2. Projected rotational velocity

When available, $v \sin i$ was taken from the literature; otherwise for each observed spectrum the rotational parameter $v \sin i$ was fitted using synthetic spectra to the Mg II 4481 Å line, which is reasonably strong across the entire range of spectral types investigated in this work, mostly B5 to B9 with a few stars of earlier types only.

For the fit the line profiles were computed with two different sets of underlying model atmospheres. For effective temperatures below 15 000 K ATLAS9 LTE model atmospheres (Kurucz 1969) were used. Above that temperature TLUSTY NLTE atmospheres (Lanz & Hubeny 2007) were used. As values for $T_{\rm eff}$ and $\log g$, those obtained by the BCD method were used.

The results of $v \sin i$ for each star are given in Table 3, and Appendix B shows the observed and fitted line profiles for each star.

3.3. Disk variability and other observations of interest

Often Be stars show variability in their EW and in the line profiles (Catanzaro 2013). This was checked visually in the spectra, as shown in Appendix C and flagged in Table 3.

In addition, equivalent widths were measured for the Balmer lines Hα and Hβ, together with the equivalent widths in the models for these stars, see Table 4. The goal to measure the Balmer decrement, i.e., the ratio of emission strength, however, was not achieved with acceptable accuracy. This is because the emission in general is often weak and the Balmer decrement is steep for late-type Be stars. This is seen in the total Hβ EWs in Table 4, none of which is negative, i.e., all are still dominated by the photospheric absorption. The values for Hβ after subtracting the model photospheric EW are dominated by the systematic errors arising from the stellar parameters and the resulting D34 Balmer decrement does not allow us to draw any reliable conclusion.

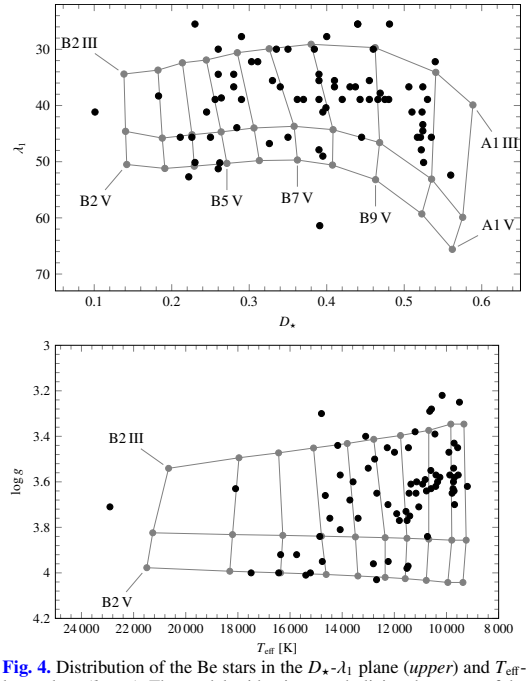

Fig. 4. Distribution of the Be stars in the $D_\star$-λ_1 plane (*upper*) and $T_{\rm eff}$-$\log g$ plane (*lower*). The model grid points symbolizing the center of the respective spectral types are shown in gray. The bias toward later type Be stars is clearly apparent from the lower panel, with only one star hotter than about 20 000 K.

Some stars show the infrared Ca II triplet in emission. It has been speculated that this is connected to binarity, in particular accretion onto a secondary (Polidan 1976). Koubský et al. (2012) reject this, but acceded that the presence of this line must be due to some peculiarity in the circumstellar environment that is not further specified. The stars for which a clear or possible Ca II triplet emission is observed are also flagged in Table 3.

4. Results

In this section, the overall results concerning the sample are reported; for notes and observations on individual stars, see Appendix A.

4.1. Incidence of Be stars

To assess the impact of this work on the statistics of Be stars, the selection biases of the sample need to be known and discussed. In fact, the target list is indeed heavily biased toward later type B stars, which is due to the selection policy for telluric standard stars at the VLT. Unless explicitly specified otherwise by the PI of the observations, late-type B and early-type A main sequence stars are preferred. Consequently, the distribution among the luminosity classes V to III is less biased, even though a bias favoring non-giant stars still exists, as not all observers are familiar with the broader definition of main sequence among B stars vs. solar-type telluric stars. Another bias is that

A&A 609, A108 (2018)

Table 1. Objects, their derived spectral types, and the number of observations at each slit width to test the method and obtain the statistical scatter and the mean measured $D_\star$ and λ_1 values.

Star	Sp Type	N of observations/slit						$D_\star$	λ_1-3700
		0.5″	0.8″	1.0″	1.3″	1.6″	5.0″	dex	Å
HD 130163	A1V	–	–	38	5	6	1	0.545 ± 0.006	63.65 ± 0.97
HD 190285	A1V	14	8	15	1	5	–	0.565 ± 0.013	68.16 ± 1.1
HIP 1115	B3IV	–	2	2	–	5	2	0.253 ± 0.006	45.65 ± 2.0
HIP 32474	A0IIIe	1	–	7	–	2	–	0.522 ± 0.01	44.525 ± 3.5
HIP 39483	B4IIIe	–	3	5	1	1	–	0.281 ± 0.008	34.44 ± 1.0
HIP 52977	B4IIIe	7	–	5	8	1	–	0.263 ± 0.017	34.44 ± 3.04
HIP 71974	A0IIIe	5	–	5	1	2	–	0.522 ± 0.007	47.89 ± 1.1
HIP 85138	B7IIIe	6	–	4	–	3	–	0.393 ± 0.011	34.44 ± 2.4
HIP 85195	B9IIIe	5	–	16	3	6	–	0.479 ± 0.007	38.92 ± 1.1
HIP 88374	B9IVe	1	2	10	2	2	2	0.443 ± 0.006	44.52 ± 2.07
HIP 89486	A0IIIe	4	–	6	–	4	–	0.512 ± 0.01	41.16 ± 0.88
HIP 94986	B4IIIe	8	5	7	1	5	–	0.278 ± 0.02	36.68 ± 3.52
Hip104508	B7IIIe	–	6	14	–	1	–	0.431 ± 0.014	36.68 ± 2.95

Table 2. Stellar parameter for the non-Be stars from Table 1, derived under various assumptions for the stellar rotation.

Star	$\omega = 0.25$, $v \sin i = 20$ km s^{-1}		$\omega = 0.85$, $v \sin i = 20$ km s^{-1}		$\omega = 0.85$, max converging or measured $v \sin i$		
	$T_{\rm eff}$ [K]	$\log g_{\rm pole}$	$T_{\rm eff}$ [K]	$\log g_{\rm pole}$	$v \sin i$ [km s^{-1}]	$T_{\rm eff}$ [K]	$\log g_{\rm pole}$
HD 130163	9763 ± 64	3.76 ± 0.03	9481 ± 63	3.89 ± 0.03	120	9592 ± 54	3.86 ± 0.03
HD 190285	outside of grid		outside of grid		130	9358 ± 32	3.94 ± 0.02
HIP 1115	15 296 ± 324	3.78 ± 0.05	14 970 ± 349	3.91 ± 0.05	150	15 119 ± 358	3.92 ± 0.05

Be stars are known to be unsuited as telluric standards, hence there is a bias against known Be stars. Two of those biases can be well seen from Table 5, in that there are generally fewer early-type stars and, among these, almost no Be stars even if the observed Be star incidence is highest among the early-type B stars (Zorec & Briot 1997).

Some care is needed to interpret Table 5, however. The spectral types for the non-Be stars were taken from SIMBAD, i.e., they are collected from a large number of inhomogeneous sources. For instance, the original definition of the MK spectral classification scheme did not include standard stars for all subtypes, in particular B4, B6, and B7 were missing and not classified in that scheme at all, while already early the intermediate type of B0.5 was included (see, e.g., Table 1 in Ardeberg 1979). The system has evolved since and more intermediate subtypes as well as standard stars for the missing integer subtypes have been proposed. Nevertheless, the first line of our Table 5 shows a lack of B4, B6, and B7 for exactly this reason. Also, for the purpose of the Table, all intermediate classifications have been rounded to the next earlier integer subtype.

Photometric or spectrophotometric classification systems, such as BCD, on the other hand, define B0 to B9 much more linearly, and also without intermediate types. Therefore, to avoid systematic effects arising from these inconsistencies as much as possible, the sample is grouped into early-, mid-, and late-type stars, which we define as B0–B2, B3–B6, and B7–A1. This amounts to 3 Be stars out of 99 early B stars, 21 out of 313 mid B stars, and 56 out of 681 late B stars.

This lack of early-type Be stars in the sample is because known Be stars have been avoided. The detection probability for an earlier type Be star is much higher, as discussed by, e.g., Zorec et al. (2007). The reason for this bias can be seen from Appendix C; almost all newly discovered Be stars have weak Hα emission and often no Hβ at all. Since the traditional spectral classification wavelength range does not include either, but only Hγ and bluer Balmer lines, the Be nature is easily missed for stars with steep Balmer decrement.

Figure 3 of Zorec et al. (2007) suggests that the statistics of Be stars is sufficiently complete for spectral types as late as about B6, but becomes increasingly incomplete for B8 and later subtypes. Updating the numbers of Zorec et al. (2007) with our findings does not entirely restore the suggested trend in their Fig. 3, but given that our search was not designed to achieve completeness, it certainly strengthens the suggestion of Zorec et al. (2007) that the probability of a B star to become a Be during its life star does not (strongly) depend on spectral subtype.

4.2. Stellar parameters

The values of $D_\star$ and λ_1, measured by the method described above, and the stellar parameters $T_{\rm eff}$ and $\log g$ obtained from these values are given in Table 3 and plotted in the upper panel of Fig. 4. Comparing this to Fig. 1 of Zorec et al. (2005) the values of λ_1 show a systematic offset. This is because of the much higher resolution of X-shooter data vs. nominal BCD method data. At the nominal resolution for the BCD method, the value of λ_1 is strongly affected by the convolution of the stellar spectrum with the instrumental resolution. This is why the original BCD method puts strong emphasis on using spectra at a given resolution of $\Delta\lambda = 8$ Å at the BD and the published BCD calibrations cannot be used for X-shooter data. On the other hand, the X-shooter instrumental resolution is so high that its contribution to the BCD parameters is negligible, and our mapping of

Table 3. Program stars with the number of valid observations, whether Hα variability, a single, or double BD; the Ca II IR triplet is observed; the measured $D_\star$ and λ_1, with mean values in case of more than one observation; and stellar parameters.

Star	# of obs. U/V/N	Sp Type	Hα var?	Double BD?	IR Ca II emiss.?	$D_\star$ [dex]	λ_1 –3700 [Å]	$T_{\rm eff}$ [K]	$\log g_{\rm pol}$ [dex]	$v \sin i$ [km s^{-1}]
HIP 11116	4/4/4	B8III	N	N	N	0.35	29.97	11 994	3.47	190
HIP 15188	1/1/1	B3:	–	–	N	–	–	–	–	–
HIP 23161	2/2/2	B7III	–	N	N	0.335	29.97	12 272	3.45	150
HIP 24475	3/4/3	B9II	Y	N	N	0.44	25.50	10 643	3.29	220
HIP 25007	6/6/6	B3IV	Y	Y	N	0.183	38.30	18 089	3.63	–
HIP 25690	4/4/4	A0IV	–	N	N	0.525	50.14	9691	3.70	90
HIP 25950	1/2/0	B7:	N	–	N	–	–	–	–	–
HIP 26368	2/2/2	A1III	N	N	Y	0.535	45.65	9550	3.57	190
HIP 26964	2/2/1	B4V	–	Y	N	0.262	50.2	15 220	4.00	200
HIP 28561	3/3/3	B8IV	Y	Y	Y	0.399	40.4	11 554	3.73	70
HIP 29635	8/8/9	B8IV	N	N	Y	0.395	41.16	11 409	3.75	230
HIP 31362	1/1/1	B8IV	–	N	N	0.443	38.92	10 769	3.64	270
HIP 32474	10/14/16	A0III	Y	N	N	0.524	44.52	9733	3.60	120
HIP 33509	1/1/1	B4V	–	Y	N	0.226	45.65	15 747	3.92	160
HIP 34144	1/1/1	B8III	–	N	N	0.4	27.73	11 204	3.38	200
HIP 36009	1/1/1	B4V	–	N	N	0.23	50.14	16 435	4.00	40
HIP 37007	6/6/6	B7IV	N	N	Y	0.34	36.68	12 245	3.70	230
HIP 39183	2/2/2	A0III	Y	N	:	0.481	25.50	10 167	3.22	190
HIP 39483	10/11/11	B6IV	Y	N	N	0.28	34.44	13 583	3.60	130
HIP 39595	1/1/1	B9IV	–	N	Y	0.455	38.92	10 592	3.63	240
HIP 41085	1/1/1	B5IV	–	Y	N	0.245	41.16	14 860	3.84	250
HIP 41268	2/2/2	B8III	–	Y	N	0.384	29.97	11 460	3.45	240
HIP 42060	1/1/1	B7V	–	N	N	0.35	45.65	12 235	3.95	250
HIP 43073	1/1/1	B9IV	–	N	N	0.466	38.92	10 413	3.62	250
HIP 43114	1/1/0	B5IV:	–	N	N	–	–	–	–	–
HIP 44423	2/3/3	B7IV	N	N	N	0.362	38.92	11 909	3.74	160
HIP 46329	2/2/2	B5IV	Y	N	N	0.25	45.65	14 763	3.95	160
HIP 47868	1/1/1	B0III:	–	N	N	0.067	23.70	–	–	–
HIP 47962	1/3/3	A0IV	N	N	N	0.517	45.65	9786	3.65	220
HIP 48582	4/6/6	B5IV	Y	Y	Y	0.26	51.26	15 396	4.01	–
HIP 48943	2/5/2	B5IV	N	Y	Y	0.284	43.95	14 077	3.81	190
HIP 51444	1/2/2	B5III	Y	N	N	0.23	25.50	14 795	3.30	250
HIP 51491	3/3/4	B9III	Y	N	Y	0.475	38.92	10 341	3.60	230
HIP 51546	2/2/2	A0V:	–	N	N	–	–	–	–	210
HIP 52977	21/21/21	B6III	Y	N	N	0.26	34.44	14 076	3.57	200
HIP 56393	1/1/1	A1IV	–	N	:	0.56	52.39	9200	3.62	270
HIP 57861	4/6/6	B6IV	Y	N	N	0.29	38.92	13 390	3.76	270
HIP 59970	2/2/2	A1IV-III	–	N	:	0.574	48.45	–	–	–
HIP 64501	2/2/2	B8IV	–	N	N	0.39	38.92	11 512	3.77	–
HIP 64867	5/6/6	A0III	N	N	N	0.524	36.68	9708	3.43	170
HIP 66339	1/1/1	B3V	–	Y	N	0.222	52.7	17 493	4.00	210
HIP 66351	2/2/2	B9III	–	N	N	0.469	37.80	10 404	3.57	140

Notes. For the double BD and Ca II flags "Y" and "N" are clear statements, ":" means uncertain, and "–" mean no suitable spectra were available. Newly identified Be stars are indicated in bold face. In case of Hα variability, "–" means that all spectra, even if more than one, were taken on the same night.

$T_{\rm eff}$ and $\log g$ onto $D_\star$ and λ_1 is valid for all medium- to high-resolution data.

Table 5 also confirms the finding of Zorec et al. (2005) that among the later type Be stars the higher luminosity classes are more common, i.e., later type Be stars are more likely found in the second half of their main sequence life. This is in agreement with the idea that the Be phase is a consequence of rotational evolution during the main sequence (e.g., Granada et al. 2013). In that hypothesis, a Be star with moderate rotation at the ZAMS, owing to the internal evolution and angular momentum transport from core to surface, at some point approaches critical rotation at the surface as the star ages. To prevent the surface rotation from going above the critical threshhold, angular momentum must be transported away. The means of this transport then is the circumstellar decretion disk (Krtička et al. 2011).

4.3. Disk properties as a function of spectral type

Although it was not possible to determine the Balmer decrement for our sample stars (see Table 4 for measurements of the equivalent widths), this still provides information. Because the emission is weak and the Balmer decrement too steep, the disks found by X-shooter are too tenuous to allow a reliable measurement of the Balmer decrement. This is in agreement with

A&A 609, A108 (2018)

Table 3. continued.

Star	# of obs. U/V/N	Sp Type	Hα var?	Double BD?	IR Ca II emiss.?	$D_\star$ [dex]	λ_1 –3700 [Å]	$T_{\rm eff}$ [K]	log $g_{\rm pol}$ [dex]	$v \sin i$ [km s^{-1}]
HIP 68100	2/2/2	B6V	–	N	N	0.326	46.77	12 804	3.96	100
HIP 69429	4/6/6	A0IV	N	N	N	0.521	45.65	9749	3.63	190
HIP 71668	3/3/3	B2V:	N	N	N	–	–	–	–	–
HIP 71974	12/141/4	A0IV	N	N	N	0.522	47.89	9709	3.64	160
HIP 78375	1/1/1	B9:	N	N	:	–	–	–	–	–
HIP 80577	3/3/3	B8IV	Y	N	N	0.39	47.89	11 472	3.97	100
HIP 80820	3/3/3	B9III	Y	N	N	0.44	25.50	10 576	3.28	150
HIP 81321	0/2/2	A0V:	–	–	N	–	–	–	–	–
HIP 82874	1/1/0	B7III	–	N	N	0.311	32.20	12 755	3.50	240
HIP 83278	3/3/3	B9IV	N	N	N	0.437	36.68	10 816	3.59	230
HIP 84184	3/3/3	B8IV	Y	Y	N	0.37	38.92	11 808	3.77	270
HIP 85138	14/15/15	B8IV	Y	N	N	0.39	34.44	11 365	3.61	180
HIP 85195	28/29/29	B9III	Y	N	N	0.48	38.92	10 253	3.58	250
HIP 85566	3/3/3	A1III	N	N	:	0.53	38.92	9572	3.45	240
HIP 87032	3/3/3	B8V:	N	N	Y	–	–	–	–	300
HIP 87698	1/2/2	A0III	N	N	N	0.523	41.16	9725	3.54	210
HIP 88172	2/5/3	B8IV	N	N	N	0.39	35.56	11 436	3.65	180
HIP 88374	21/25/25	B9IV	Y	N	N	0.445	45.65	10 730	3.84	140
HIP 89486	14/14/15	A0III	Y	N	N	0.51	41.16	9874	3.57	180
HIP 89500	5/5/5	B9III	N	N	N	0.46	29.97	10 443	3.39	240
HIP 90096	4/5/5	B8IV	N	N	N	0.41	36.68	11 170	3.65	200
HIP 90509	2/2/2	B8IV	–	N	:	0.42	38.92	11 062	3.71	250
HIP 91460	3/3/3	A1III	N	N	N	0.54	32.20	9503	3.25	150
HIP 91975	2/3/3	B9III	Y	N	:	0.455	35.56	10 600	3.55	250
HIP 92038	3/3/3	B7III	Y	Y	Y	0.303	32.20	13 002	3.54	170
HIP 93993	3/3/3	A0III	N	N	N	0.524	43.40	9694	3.58	10
HIP 94770	2/2/2	B8IV	–	N	Y	0.41	35.56	11 145	3.60	260
HIP 94859	1/3/3	B7III	Y	N	:	0.33	35.56	12673	3.65	240
HIP 94986	24/36/36	B6III	Y	N	N	0.28	36.68	13 706	3.68	120
HIP 95109	1/2/2	B8V	N	N	N	0.395	49.01	11 518	3.98	260
HIP 96453	1/3/3	B6III	Y	N	N	0.26	29.97	14 172	3.44	230
HIP 99457	7/9/3	B1IV	Y	N	N	0.101	41.16	22 907	3.71	–
HIP 100664	2/3/3	A0III	N	N	N	0.506	36.68	9908	3.47	190
HIP 104508	18/24/24	B9IV	Y	N	N	0.43	36.68	10915	3.61	270
HIP 108022	2/5/5	B6III	N	N	N	0.29	27.73	13 100	3.40	110
HIP 108402	5/5/5	B7V	N	Y	Y	0.391	61.39	12 682	4.03	250
HIP 108597	3/3/3	B5IV	N	Y	Y	0.256	38.92	14 473	3.76	–
HIP 108975	2/2/2	B4IV	N	N	N	0.264	38.65	14 648	3.66	–

Vieira et al. (2017), who found that disks of late-type Be stars are less dense than those of early-type stars. As mentioned above, there is also a general agreement that late-type Be stars show less variability than early-type stars. This is again confirmed by the numbers shown in Table 5, where two-thirds of early- and mid-type Be stars are found to be variable, but only about one-third are variable among the late subtypes.

4.4. Infrared Ca II triplet

We clearly detected the IR Ca II triplet in the emission of 13 stars. This is in agreement with the reported number of about 20% of Be stars showing this feature (e.g., Koubský et al. 2012). In absorption and possibly emission the IR Ca II triplet is seen in another 8 stars.

There is no obvious correlation of the presence of the IR Ca II triplet, in either emission or absorption, with spectral type of the Be star. Although our sample (heavily biased toward later type Be stars) does not include stars with Ca II triplet emission earlier than B5, a literature search does reveal such stars (Polidan & Peters 1976; Polidan 1976; Briot 1981; Koubský et al. 2012).

The emission morphology closely resembles that of the O I 8446 line, which is supposed to trace the hydrogen Lyβ formation region, since its upper level is excited by fluorescence from this transition (Mathew et al. 2012). However, while the O I 8446 can be clearly linked to processes originating in the Be star, this is not the case for the IR Ca II triplet.

The emission strength of the Ca II triplet can vary without similar changes taking place in O I 8446 or the Balmer lines. This emission strength can even be transient without a major change in the Balmer line emission properties; for example, the Ca II triplet was not detected in γ Cas by Briot (1981), but was reported to be present by Koubský et al. (2012) to be anti-correlated with the Balmer emission for the same star.

This suggests that while the formation region is the same as for the other lines, i.e., the disk around the Be star, the excitation process does not originate in the same source as for the other spectral lines formed in the disk. Koubský et al. (2012) investigated the correlation of the Ca II triplet with binarity and

Table 4. Equivalent widths of Hα and Hβ for the program stars with clearly measurable emission.

Star	$T_{\rm eff}$	Hα			Hβ		
	[K]	(tot)	(phot)	(emi)	(tot)	(phot)	(emi)
HIP 11116	12 240	–7.94	4.20	–12.15	5.23	7.24	–2.00
HIP 26368	9874	5.39	6.83	–1.435	10.8	12.1	–1.28
HIP 29635	11 822	–1.69	5.39	–7.085	7.76	9.55	–1.78
HIP 33509	17 064	–16.4	3.57	–20.06	3.31	6.40	–3.08
HIP 37007	15 093	–5.95	4.53	–10.48	6.06	7.57	–1.50
HIP 39183	11 231	0.65	5.89	–5.235	7.68	8.51	–0.82
HIP 39595	12 234	–1.65	5.68	–7.337	9.12	10.1	–1.03
HIP 46329	14 599	–8.91	4.27	–13.18	5.28	6.85	–1.56
HIP 51491	11 453	4.44	5.94	–1.493	8.39	10.5	–2.12
HIP 80577	11 697	0.43	5.94	–5.503	9.07	10.1	–1.09
HIP 82874	14 099	–6.90	3.93	–10.83	5.13	6.75	–1.61
HIP 87032	11 936	–6.37	6.70	–13.07	7.89	11.1	–3.22
HIP 90096	13 441	3.05	5.20	–2.146	8.56	9.02	–0.45
HIP 90509	13 123	0.44	5.37	–4.925	8.76	9.51	–0.74
HIP 91975	11 951	1.64	5.48	–3.830	7.70	9.45	–1.74
HIP 92038	15 139	–14.4	3.80	–18.23	3.80	5.98	–2.18
HIP 94770	12 721	–2.43	5.12	–7.561	7.70	8.84	–1.13
HIP 94859	15 311	–2.25	4.26	–6.523	6.80	8.12	–1.31
HIP 95109	11 847	–2.64	5.96	–8.601	8.56	10.2	–1.68
HIP 96453	14 338	2.81	4.52	–1.706	5.51	5.77	–0.25
HIP 99457	23 061	–1.37	2.51	–3.889	2.73	3.71	–0.97

Table 5. Statistics of Be stars observed with X-shooter.

Bin name	Early			Σ	Mid				Σ	Late					Σ
Sp. type	B0	B1	B2		B3	B4	B5	B6		B7	B8	B9	A0	A1	
# of all stars	4	10	85	*99*	129	38	112	34	*313*	57	211	347	52	14	*681*
# of Be stars	1	1	1	*3*	3	4	7	7	*21*	9	16	13	13	5	*56*
# of new Be stars	0	0	0	*0*	0	1	3	5	*9*	6	10	8	11	4	*39*
LC V	0	0	1	*1*	1	3	0	1	*5*	2	2	0	1	0	*5*
LC IV	0	1	0	*1*	1	1	5	2	*9*	2	11	5	5	2	*25*
LC III	1	0	0	*1*	0	0	1	4	*5*	4	3	6	7	3	*23*
Ca II emi/abs	0	0	0	*0*	0	0	3	0	*3*	4	5	4	1	4	*18*
Variability detectable?	0	1	1	*2*	1	1	5	6	*13*	6	11	10	10	3	*40*
Hα variable	0	1	0	*1*	1	0	3	5	*9*	2	4	6	2	0	*14*

conclude that binarity is not the responsible mechanism, but suggest some other, not further specified peculiarity of the circumstellar disk.

For young stellar objects the common presence of the Ca II triplet in emission is suspected to be linked to either magnetic processes, accretion (e.g., Kwan & Fischer 2011; Moto'oka & Itoh 2013), or a combination of both. In cataclysmic variables, the formation of the triplet is more specifically traced to external UV irradiation of an optically thin gas (Ivanova et al. 2004). If we combine that with the current understanding of Be stars, which do not show any trace of large-scale magnetic fields, this leaves UV photons formed in accretion shocks as the most promising mechanism to power the Ca II triplet. The self re-accretion from the viscous disk is probably not sufficient, as otherwise almost all Be stars should have Ca II emission.

This leaves binarity as a possible explanation. As Koubský et al. (2012) point out, several known binaries do not show Ca II in their data. However, plain binarity is not sufficient; the companion must also accrete to form the UV flux to excite Ca II. Hence binarity remains a possible hypothesis to explain the infrared Ca II triplet emission.

5. Conclusions

Searching the X-shooter database of telluric standards, 78 Be stars were detected in emission, of which 48 had not been reported before. The sample is strongly biased toward later type Be stars. In some sense, this is an advantage, because later type Be stars, owing to their lack of variability and often less dense disks, are less well studied than earlier type Be stars. In particular, we were able to confirm, or at least strengthen, the following findings and hypotheses:

– The Galactic Be star fraction decreases less dramatically toward the later spectral (sub-)types than previously known

A&A 609, A108 (2018)

numbers suggest. It may even be constant, as proposed by Zorec et al. (2005).
- Late-type Be stars show less variablility of their disks than early-type Be stars.
- Late-type Be stars have less dense disks than early-type Be stars.
- Be stars are more likely to be closer to the TAMS than to the ZAMS.
- The presence of the IR Ca II in emission may be linked to accretion onto a companion, but the emission itself originates from the Be disk proper.

Some of these points either clearly are, or may well be, linked to stellar evolution and its timescales. For instance the lower density of disks around later subtype Be stars could be a natural consequence of their slower evolution, if indeed the disk is the means by which the star stays below critical rotation. The amount of angular momentum to lose over a given time is simply less. The same might explain the lower variability of the later subtypes.

In summary, while late-type Be stars are less well investigated than the earlier type Be stars, it might actually be this lack of "interesting" behavior in them that will enable new insights into the origin and evolution of Be stars.

Acknowledgements. We dedicate this work to the memory of Prof. M. Hamdy. A. Shokry would like to acknowledge the Egyptian Ministry of Higher Education (MoHE) for providing the financial support for his Joint scholarship, as well as the ESO observatory for offering facilities and tools needed through his stay in ESO (Chile), and the Kottamia Center of Scientific Excellence for support. A. Shokry is deeply indebted to Prof. S. Saad for her continued support. R. Townsend acknowledges support from NASA grant NNX12AC72G. D.M.F. acknowledges support from FAPESP grant 2016/16844-1. This research has made use of NASA's Astrophysics Data System Service, as well as of the SIMBAD database, operated at CDS, Strasbourg, France.

References

Aidelman, Y., Cidale, L. S., Zorec, J., & Arias, M. L. 2012, A&A, 544, A64
Andersen, J., & Nordstrom, B. 1983, A&AS, 52, 471
Ardeberg, A. 1979, in IAU Colloq. 47: Spectral Classification of the Future, eds. M. F. McCarthy, A. G. D. Philip, & G. V. Coyne, Ricerche Astronomiche, 9, 389
Baade, D. 2000, in IAU Colloq. 175: The Be Phenomenon in Early-Type Stars, eds. M. A. Smith, H. F. Henrichs, & J. Fabregat, ASP Conf. Ser., 214, 178
Balona, L. A. 1975, MmRAS, 78, 51
Balona, L. A. 1990, MNRAS, 245, 92
Bhatt, H. C., Ashok, N. M., Chandrasekhar, T., & Goraya, P. S. 1984, A&AS, 58, 685
Briot, D. 1981, A&A, 103, 1
Briot, D. 1986, A&A, 163, 67
Buscombe, W. 1970, MNRAS, 148, 79
Carrier, F., Burki, G., & Burnet, M. 2002, A&A, 385, 488
Catanzaro, G. 2013, A&A, 550, A79
Chojnowski, S. D., Whelan, D. G., Wisniewski, J. P., et al. 2015, AJ, 149, 7
Dall, T. H., Foellmi, C., Pritchard, J., et al. 2007, A&A, 470, 1201
Floquet, M., Neiner, C., Janot-Pacheco, E., et al. 2002, A&A, 394, 137
Frémat, Y., Zorec, J., Hubert, A.-M., & Floquet, M. 2005, A&A, 440, 305
Freudling, W., Romaniello, M., Bramich, D. M., et al. 2013, A&A, 559, A96
Ghosh, K. K., Apparao, K. M. V., & Pukalenthi, S. 1999, A&AS, 134, 359
Goraya, P. S., & Tur, N. S. 1988, AJ, 96, 346
Granada, A., Ekström, S., Georgy, C., et al. 2013, A&A, 553, A25
Gray, R. O., & Corbally, C. J. 2002, AJ, 124, 989
Halbedel, E. M. 1996, PASP, 108, 833
Harrington, D. M., & Kuhn, J. R. 2009, ApJS, 180, 138
Henize, K. G. 1976, ApJS, 30, 491
Hiltner, W. A., Garrison, R. F., & Schild, R. E. 1969, ApJ, 157, 313
Huat, A.-L., Hubert, A.-M., Baudin, F., et al. 2009, A&A, 506, 95
Hubert, A. M., & Floquet, M. 1998, A&A, 335, 565
Irvine, N. J. 1975, ApJ, 196, 773
Ivanova, D. V., Sakhibullin, N. A., & Shimanskii, V. V. 2004, Astron. Rep., 48, 476
Jaschek, C., & Jaschek, M. 1992, A&AS, 95, 535
Jaschek, M., Jaschek, C., Hubert-Delplace, A.-M., & Hubert, H. 1980, A&AS, 42, 103
Jaschek, M., Slettebak, A., & Jaschek, C. 1981, Be star terminology, Be Star Newsletter, 4, 9
Kaiser, D. 1987, A&AS, 67, 203
Kogure, T., & Leung, K.-C. 2007, The Seventh Pacific Rim Conference on Stellar Astrophysics, eds. Y. W. Kang, H.-W. Lee, K.-C. Leung, & K.-S. Cheng, ASP Conf. Ser., 362, 260
Koubský, P., Kotková, L., Votruba, V., et al. 2012, ArXiv e-prints [arXiv:1205.2259]
Krtička, J., Owocki, S. P., & Meynet, G. 2011, A&A, 527, A84
Kucewicz, B. 1967, Inform. Bull. Southern Hemisphere, 11, 34
Kuchner, M. J., Silverberg, S. M., Bans, A. S., et al. 2016, ApJ, 830, 84
Kurucz, R. 1969, in Theory and Observation of Normal Stellar Atmospheres, ed. O. Gingerich, 375
Kwan, J., & Fischer, W. 2011, MNRAS, 411, 2383
Lanz, T., & Hubeny, I. 2007, ApJS, 169, 83
Levenhagen, R. S., & Leister, N. V. 2006, MNRAS, 371, 252
Mathew, B., Banerjee, D. P. K., Subramaniam, A., & Ashok, N. M. 2012, ApJ, 753, 13
Mennickent, R. E., & Vogt, N. 1988, A&AS, 74, 497
Merrill, P. W., & Burwell, C. G. 1943, ApJ, 98, 153
Moto'oka, K., & Itoh, Y. 2013, RA&A, 13, 1189
Neiner, C., Hubert, A.-M., & Catala, C. 2005, ApJS, 156, 237
Okazaki, A. T. 1997, A&A, 318, 548
Polidan, R. S. 1976, in Be and Shell Stars, ed. A. Slettebak, IAU Symp., 70, 401
Polidan, R. S., & Peters, G. J. 1976, in Be and Shell Stars, ed. A. Slettebak, IAU Symp., 70, 59
Porter, J. M., & Rivinius, T. 2003, PASP, 115, 1153
Rivinius, T., Carciofi, A. C., & Martayan, C. 2013a, A&ARv, 21, 69
Rivinius, T., Townsend, R. H. D., Kochukhov, O., et al. 2013b, MNRAS, 429, 177
Slettebak, A., Wagner, R. M., & Bertram, R. 1997, PASP, 109, 1
Stagg, C. 1983, Information Bulletin on Variable Stars, 2376
Tolbert, C. R. 1964, ApJ, 139, 1105
Vernet, J., Dekker, H., D'Odorico, S., et al. 2011, A&A, 536, A105
Vieira, R. G., Carciofi, A. C., Bjorkman, J. E., et al. 2017, MNRAS, 464, 3071
Zorec, J., & Briot, D. 1997, A&A, 318, 443
Zorec, J., Divan, L., & Briot, D. 1983, A&A, 126, 192
Zorec, J., Frémat, Y., & Cidale, L. 2005, A&A, 441, 235
Zorec, J., Frémat, Y., Martayan, C., Cidale, L. S., & Torres, A. F. 2007, in Active OB-Stars: Laboratories for Stellare and Circumstellar Physics, eds. A. T. Okazaki, S. P. Owocki, & S. Stefl, ASP Conf. Ser., 361, 539
Zorec, J., Cidale, L., Arias, M. L., et al. 2009, A&A, 501, 297

Appendix E

Revealing the structure of the outer disks of Be stars

Astronomy & Astrophysics manuscript no. 29932JN
March 22, 2017

Revealing the structure of the outer disks of Be stars⋆

R. Klement[1,2], A. C. Carciofi[3], T. Rivinius[1], L. D. Matthews[4], R. G. Vieira[3], R. Ignace[5], J. E. Bjorkman[6], B. C. Mota[3], D. M. Faes[3], A. D. Bratcher[6], M. Curé[7], and S. Štefl⋆⋆

[1] European Southern Observatory, Alonso de Córdova 3107, Vitacura, Casilla 19001, Santiago, Chile
e-mail: robertklement@gmail.com
[2] Astronomical Institute of Charles University, Charles University, V Holešovičkách 2, 180 00 Prague 8
[3] Instituto de Astronomia, Geofísica e Ciências Atmosféricas, Universidade de São Paulo, Rua do Matão 1226, Cidade Universitária, 05508-090, São Paulo, SP, Brazil
[4] MIT Haystack Observatory, off Route 40, Westford MA 01886, USA
[5] Department of Physics & Astronomy, East Tennessee State University, Johnson City, TN 37614, USA
[6] Ritter Observatory, Department of Physics & Astronomy, University of Toledo, Toledo, OH 43606, USA
[7] Instituto de Física y Astronomía, Facultad de Ciencias, Universidad de Valparaíso, Casilla 5030, Valparaíso, Chile

ABSTRACT

Context. The structure of the inner parts of Be star disks ($\lesssim$ 20 stellar radii) is well explained by the viscous decretion disk (VDD) model, which is able to reproduce the observable properties of most of the objects studied so far. The outer parts, on the other hand, are not observationally well-explored, as they are observable only at radio wavelengths. A steepening of the spectral slope somewhere between infrared and radio wavelengths was reported for several Be stars that were previously detected in the radio, but a convincing physical explanation for this trend has not yet been provided.
Aims. We test the VDD model predictions for the extended parts of a sample of six Be disks that have been observed in the radio to address the question of whether the observed turndown in the spectral energy distribution (SED) can be explained in the framework of the VDD model, including recent theoretical development for truncated Be disks in binary systems.
Methods. We combine new multi-wavelength radio observations from the Karl. G. Jansky Very Large Array (JVLA) and Atacama Pathfinder Experiment (APEX) with previously published radio data and archival SED measurements at ultraviolet, visual, and infrared wavelengths. The density structure of the disks, including their outer parts, is constrained by radiative transfer modeling of the observed spectrum using VDD model predictions. In the VDD model we include the presumed effects of possible tidal influence from faint binary companions.
Results. For 5 out of 6 studied stars, the observed SED shows strong signs of SED turndown between far-IR and radio wavelengths. A VDD model that extends to large distances closely reproduces the observed SEDs up to far IR wavelengths, but fails to reproduce the radio SED. Using a truncated VDD model improves the fit, leading to a successful explanation of the SED turndown observed for the stars in our sample. The slope of the observed SEDs in the radio is however not well reproduced by disks that are simply cut off at a certain distance. Rather, some matter seems to extend beyond the truncation radius, where it still contributes to the observed SEDs, making the spectral slope in the radio shallower. This finding is in agreement with our current understanding of binary truncation from hydrodynamical simulations, in which the disk does extend past the truncation radius. Therefore, the most probable cause for the SED turndown is the presence of binary companions that remain undetected for most of our sources.

Key words. Stars: emission-line, Be – Stars: circumstellar matter – Stars: binaries: general – Radio continuum: stars – Submillimeter: stars

1. Introduction

Be stars offer unique possibilities for studying circumstellar disks. Because they are common among the bright, nearby stars – 17% of B-type stars are Be stars (Zorec & Briot 1997) – their disks are among typical targets for modern optical/near-infrared interferometers that have resolved them at the milliarcsec level. As a result, the structure of the inner parts of the disks is now well understood in the framework of the viscous decretion disk (VDD) model, first proposed by Lee et al. (1991) and further developed by, for example, Bjorkman (1997), Porter (1999), Okazaki (2001), and Bjorkman & Carciofi (2005). The central stars rotate close to break-up velocities, and an uncertain mechanism – the so-called Be phenomenon – acts in addition to rotation, leading to episodic or continuous mass ejection from the stellar equator. Subsequently, outflowing, ionised, purely gaseous disks, rotating in a nearly Keplerian way are formed (see Rivinius et al. 2013, for a recent review). In the VDD model, it is the turbulent viscosity that is responsible for the transport of the angular momentum outwards, and therefore for the growth of the disk.

In the last decades, observational techniques such as spectroscopy, linear polarimetry, and optical/near-IR interferometry have been used to constrain the physical structure of VDDs. Combining polarimetric and interferometric measurements, the disk-like structure of the circumstellar matter was unambiguously confirmed (Quirrenbach et al. 1997) and the rotation law was subsequently confirmed to be nearly Keplerian (Meilland et al.

⋆ Based on observations from the Karl J. Jansky Very Large Array collected via programme 10B-143, on observations from APEX collected via CONICYT programmes C-092.F-9708A-2013 and C-095.F-9709A-2015 and on observations from CARMA collected via programme c1100-2013a.
⋆⋆ Deceased

A&A proofs: manuscript no. 29932JN

2007; Wheelwright et al. 2012; Kraus et al. 2012). However, it is important to note that these results apply to the inner parts of VDDs only ($\lesssim$ 20 stellar radii, Vieira et al. 2015), that are responsible for the bulk of the disk emission in the optical and infrared (IR), as well as for the Balmer lines (Carciofi 2011). At larger radii, the disks are detectable only at radio wavelengths.

In this work, we are interested in the overall density structure of VDDs, focusing on the parts outwards of ∼20 stellar radii. We constrain the density structure by compiling the observed spectral energy distribution (SED) from ultraviolet (UV) up to radio wavelengths. Due to the nature of the disk continuum emission – bound-free and free-free emission from the ionized hydrogen in the disk – fluxes at longer wavelengths originate from progressively larger areas of the disk. At the UV wavelengths, the SED usually consists of the stellar photospheric flux only, although in shell stars (Be stars seen close to edge-on), the UV photospheric spectrum can be dimmed by the surrounding disk and also strongly blanketed by the disk line absorption (mostly Fe). At longer wavelengths, the disk contribution to the SED becomes more significant until it dominates the SED in the mid-IR to radio domains. This is well explained in terms of the gas in the disk forming an optically thick pseudo-photosphere, whose size grows with increasing wavelength (see Vieira et al. 2015, for more details on the pseudo-photosphere concept applied to the continuum emission of Be disks).

Radio observations longwards of sub-mm wavelengths are of special interest for studying the outer parts of VDDs, as the disk pseudo-photospheres are larger at these wavelengths. In this work, we revisit the Be stars that were detected by the Very Large Array (VLA) observations at 2 cm by Taylor et al. (1990, six detected stars) and subsequently observed at mm wavelengths using the James Clerk Maxwell Telescope (JCMT) by Waters et al. (1991). The main outcome of the radio measurements was the discovery of an SED turndown, that is, a steepening of the spectral slope somewhere between mid-IR (10 – 60 μm, as measured by the IRAS satellite) and radio wavelengths, in the studied stars. Using a simple wedge-shaped disk model seen pole-on, Waters et al. (1991) were able to reproduce the observed SEDs with the disks having power-law density structure in the form $\rho \propto r^{-n}$, with the exponent n ranging from 2.0 to 3.5. However, to reproduce the SED turndowns, disks truncated at a certain radius (ranging from 26 to 108 stellar radii) had to be used. Although the VDD model was not yet established at that time, it was already suspected that Be envelopes have disk-like shapes that originate from the central star and flow outwards. If the disks are dominated by rotation rather than outflow (as in the VDD model), it would follow that the most likely reason for the disk truncation is the presence of an (unseen) binary companion. However, because Waters et al. (1991) assumed wind-like outflows rather than disks dominated by rotation, they found truncation to be an unlikely explanation for the SED turndown, favoring other possibilities, such as changes in the disk geometry or additional acceleration of the disk material in the outer disk.

In the last decade or so, the VDD model has been firmly established as the framework in which most of the observable properties of Be disks can be explained (at least in their inner parts). Successful VDD reproductions of multi-technique and multi-wavelength observations of individual objects include, for example, ζ Tauri (Carciofi et al. 2009), β CMi (Klement et al. 2015, 2017) and 48 Lib (Silaj et al. 2016). This allows us to interpret the radio observations on a firm physical basis and therefore distinguish between the suggested scenarios to explain the SED turndown.

The goal of the present work is to carefully model the compiled SEDs of the Be stars detected in the radio by Taylor et al. (1990) using the VDD model implemented in the Monte Carlo radiative transfer code HDUST (Carciofi & Bjorkman 2006, 2008). For four of these stars, we have obtained new multi-band measurements in the cm domain, allowing us to study the properties of the SED turndown in detail. With the results of this study we address the question of the origin of the SED turndown, that is, whether it can be explained in the framework of the VDD model, which may be truncated by a binary companion, or if further physical ingredients in the model are needed.

In the following section we focus on the theoretical predictions concerning the structure of the outer disks of Be stars. In Sect. 3 we describe the observations used, and in Sect. 4 we explain the VDD model and the modeling procedure. The following section details the results for the six individual objects and the conclusions follow.

2. The outer parts of Be star disks

In an isolated VDD, the outflow velocity in the inner disk is highly subsonic and grows linearly with the distance from the central star (Okazaki 2001). At a certain point, sometimes called the critical or photo-evaporation radius, the outflow velocity reaches the local sound speed, which marks the transition between a subsonic inner part and a supersonic outer part of the disk. Outwards from this point, it is no longer viscosity but rather the gas pressure that drives the outflow, and the disk becomes angular momentum conserving. This transition may offer an explanation for the SED turndown, as the density decreases much more rapidly past the transonic part. However, the transition is only expected to occur at very large distances from the central star. An approximate relation for the critical radius R_c was derived by Krtička et al. (2011) for isothermal disks:

$$\frac{R_c}{R_e} = \frac{3}{10}\left(\frac{v_{orb}}{c_s}\right)^2, \quad (1)$$

where R_e is the stellar equatorial radius, v_{orb} is the disk orbital speed above the stellar equator and c_s is the speed of sound. The typical values of R_c are approximately 350 and 430 R_* for spectral types B0 and B9, respectively. According to the pseudo-photosphere model of Vieira et al. (2015), for typical disk densities, the pseudo-photosphere radius attains such large values only at wavelengths longer than 10 cm. Unless the disk is extremely dense, this means that only wavelengths longwards of 10 cm can probe the transonic regions. So far, no detections of Be disk emission at these wavelengths have been reported. It follows that the SED turndown is likely unrelated to the existence of a transonic regime in Be disks.

The only known physical mechanism that can truncate the disk at a closer distance to the central star is the tidal influence from an orbiting secondary companion. The effects of such a scenario on the VDD of the primary have recently been explored by smoothed particle hydrodynamics (SPH) simulations, under the assumption that the orbit of the secondary is aligned with the disk (Panoglou et al. 2016). For circular orbits, the influence of the secondary has two important effects on the Be disk. The first is the truncation of the disk at a distance close to the 3:1 resonance radius, which is much smaller than the orbital separation. Outwards of the truncation radius, the density starts to decrease much more rapidly, but these parts can still contribute to the emergent spectrum. The second is the so-called accumulation effect, which causes the parts of the disk inwards of the

Table 1. Details of the IR, sub-mm, and radio observations.

Mission/Telescope	Epoch of observations	$\lambda_{central}$/phot. band	Reference
IRAS	1 – 11/1983	12, 25, 60, 100 μm	Helou & Walker (1988)
VLA	12/1987 – 9/1988, 2/1990, 8/1991	2, 3.6, 6 cm	Taylor et al. (1987, 1990), Apparao et al. (1990), Dougherty et al. (1991b), Dougherty & Taylor (1992)
RAO/NOAO/MKO	4/1988 – 3/1991	*JHKLMN* bands	Dougherty et al. (1991a)
JCMT	8/1988, 8/1989	0.76, 1.1 mm	Waters et al. (1989, 1991)
IRAM	3/1991, 12/1992	1.2 mm	Wendker et al. (2000)
MSX	1996 – 1997	4.29, 4.35, 8.88, 12.13, 14.65, 21.3 μm	Egan et al. (2003)
AKARI	5/2006 – 8/2007	9, 18, 65, 90, 140, 160 μm	Ishihara et al. (2010)
WISE	1/2010 – 11/2010	3.3, 4.6, 12 and 22 μm	Cutri & et al. (2014)
JVLA	10/2010	0.7, 1.3, 3.5 and 6.0 cm	this work
CARMA	9/2013	3 mm	Klement et al. (2015)
APEX/LABOCA	9/2013, 7–8/2015	0.87 mm	this work

truncation radius to have a slower density fall-off (i.e., a smaller radial power law exponent). The accumulation effect has a larger impact with decreasing orbital period, decreasing viscosity, and increasing binary mass ratio. Considering the possibility that the orbit of the secondary is misaligned with respect to the equatorial plane of the disk, both the truncation and accumulation effects become much weaker (Cyr et al. submitted).

The incidence of binarity among Be stars remains an important open issue. The presence of a close binary companion was, in the past, believed to be the cause of the Be phenomenon, although that is not likely the case (Oudmaijer & Parr 2010). However, the evolution of a mass-transferring binary may produce a low-mass subdwarf O or B star (sdO/sdB, the mass donor that was originally the more massive component and is now stripped of its outer layers) and a fast-spinning star (the mass and angular momentum gainer, that is now the primary star). It is expected that at least some Be stars may have formed in this fashion. Owing to their lower luminosity, sdO/sdB companions are difficult to detect and only five Be+sdO/sdB systems have been reported so far: φ Per (Gies et al. 1998), FY CMa (Peters et al. 2008), 59 Cyg (Peters et al. 2013), o Pup (Koubský et al. 2012), and HR 2142 (Peters et al. 2016). They were revealed by periodic signatures in the UV spectra and by traveling emission components in the emission lines of the Be star caused by radiative interaction of the hot sdO/sdB star with the outer disk of the Be star. Other common companions of Be stars are neutron stars, which may emit X-rays as they accrete some of the matter from the disk of the Be primary. Other compact companions should include black holes and white dwarfs, although only one such system has been confirmed (Be star + black hole system HD 215227; Casares & Jonker 2014). The companions that are hardest to detect, though they are possibly common, are low-mass main-sequence stars.

Searching for binary companions using radial velocity (RV) shifts of spectral lines is complicated by their large rotational broadening. The exceptions from this rule are shell stars, which have narrow absorption lines in the centers of broad emission lines formed in the disk and thus orbiting companions are more easily detectable. Searches for binary companions of Be stars using speckle interferometry (Mason et al. 1997) and direct imaging with adaptive optics (Roberts et al. 2007; Oudmaijer & Parr 2010) led to the conclusion that the incidence of binaries among Be stars is around 30%. However, these results apply only for companions that are farther than 0.1 arcsec ($\sim$ 20 au for the most nearby targets), with a maximum magnitude difference of 10 mag in the I and K-bands. That means that Be companions such as main sequence objects of spectral classes F and cooler or sdO/sdB stars are not detectable with these techniques. Such binary companions would remain invisible, but could, in principle, be revealed through their influence on the density structure of the disk of the primary. If prevalent, the truncation of Be disks by such companions could be the cause of the observed turndown in the SEDs. Considering additional indirect evidence, line emission in the IR Ca triplet has been suggested to indicate binarity in Be stars (see, e.g., discussion by Koubský et al. 2011). Also, in known Be binaries in a close orbit (e.g., γ Cas), the Hα line often shows no clear peaks or symmetry, which is thought to indicate disturbances in the disk due to the orbiting companion.

3. Observations

The primary dataset used for the modeling is the SED measurements, namely the absolutely calibrated UV spectra and photometric measurements from visual to radio wavelengths. The secondary dataset contains visual spectra and polarimetry. The spectra were used to search for RV variations that could be assigned to the presence of an orbiting companion. The emission line profiles and the polarimetry were used to check for variability in the disk throughout the last decades.

The epochs, wavelengths, and references of the IR, sub-mm, and radio photometric measurements are given in Table 1. The epochs of the observations span over three decades. Since Be disks are often highly variable, this may introduce errors in our solutions. Nevertheless, the data for each target were still combined into a single dataset, which then represents average properties of the disk over the last decades. For more details on the variability of individual targets, and how it affects the solution, we refer to Sect. 5.

3.1. Ultraviolet spectra

For the UV part of the spectrum, data from the International Ultraviolet Explorer (IUE)[1] and the Wisconsin Ultraviolet Photo-Polarimeter Experiment (WUPPE)[2] were used. For the IUE spectra, large aperture measurements were used in all cases due to the problems with absolute flux calibration of the small aperture measurements. When available, we preferred low-

[1] https://archive.stsci.edu/iue/
[2] https://archive.stsci.edu/wuppe/

A&A proofs: manuscript no. 29932JN

Table 4. Newly acquired radio observations from JVLA (0.7, 1.3, 3.5 and 6.0 cm).

Star	F at 0.7 cm [mJy]	F at 1.3 cm [mJy]	F at 3.5 cm [mJy]	F at 6.0 cm [mJy]
η Tau	2.09 ± 0.30	0.852 ± 0.090	0.237 ± 0.024	0.1432 ± 0.0098
EW Lac	<0.83 (3σ)	0.351 ± 0.077	0.133 ± 0.023	0.089 ± 0.012
γ Cas	1.65 ± 0.15	0.710 ± 0.057	0.201 ± 0.016	0.128 ± 0.011
ψ Per	3.47 ± 0.26	1.284 ± 0.083	0.435 ± 0.022	0.241 ± 0.012

dispersion spectra. The data show very little or no temporal variation for all stars and were therefore averaged for modeling purposes.

3.2. Visual and IR photometry

To compile all the available visual and IR photometric measurements, we made use of the Virtual Observatory SED Analyser[3] (VOSA; Bayo et al. 2008) and the VO Spectral Analysis Tool[4] (VOSpec; Arviset et al. 2008). These tools search the available catalogs and compile the SED for a given object. The visual domain catalogs that VOSA and VOSpec searched and that we subsequently used in this study include those of Ducati (2002), Hipparcos (Perryman et al. 1997), Mermilliod & Mermilliod (1994) and Tycho-2 (Høg et al. 2000). For the IR domain, data from the space mission MSX (MSX6C Infrared Point Source Catalog; Egan et al. 2003) was used.

In the near-IR domain we made use of $JHKLMN$ magnitudes measured at three observatories: the University of Calgary Rothney Astrophysical Observatory (RAO) 1.5 m telescope, the National Optical Astronomy Observatory (NOAO), Kitt Peak 1.3 m telescope and the MKO 0.6 m telescope (Dougherty et al. 1991a). In the mid-IR domain, we used available data from IRAS (Helou & Walker 1988), AKARI (AKARI/IRC mid-IR all-sky Survey; Ishihara et al. 2010), and WISE (Cutri & et al. 2014) satellites. The catalog flux values were color-corrected in the same way as described by Vieira et al. (2017). For β CMi we also used data from the Spitzer Space Telescope (SST; Su et al. 2006). IR measurements corresponding to upper limits were discarded.

We note that for the star β Mon A, the visual and IR photometry actually corresponds to the combined photometry of the three components, all of which are Be stars of similar spectral types. This may introduce additional errors in our solution.

3.3. Radio observations

3.3.1. Sub-millimeter observations

For the star β Mon A, we used a new APEX measurement from the bolometer camera LABOCA (Siringo et al. 2009) at the wavelength of 870 μm. The observed flux is 23.5 ± 3.5 mJy. The separation between the A and B components is 7.1 arcsec. When centered on the A component, the B component falls inside the FWHM of the LABOCA beam, which is equal to 19.2±3 arcsec. Although close to the edge of the FWHM, the B component may still slightly contribute to the observed flux.

For β CMi, we also have an APEX/LABOCA measurement, that was originally published in Klement et al. (2015). However, we newly reduced the data using Crush[5] version 2.32-1 (Kovács 2008), with the updated flux value for β CMi being 38.6 ± 3.1 mJy. This value remains consistent within the error bars with the value used previously. For a more detailed description of the APEX/LABOCA measurements, see Sect. 2.2 of Klement et al. (2015). For β CMi, we also use the flux at 3 mm as measured by CARMA (see Table 1 of Klement et al. 2015).

3.3.2. Millimeter observations

At mm wavelengths, we used the previously published JCMT measurements of Waters et al. (1989, 1991) and the IRAM measurements of Wendker et al. (2000).

3.3.3. Centimeter observations

The previously published radio fluxes at cm wavelengths were taken from the VLA observations presented by Taylor et al. (1987, 1990), Apparao et al. (1990), Dougherty et al. (1991b) and Dougherty & Taylor (1992).

New radio observations of four stars were obtained with the Karl G. Jansky Very Large Array (JVLA) of the National Radio Astronomy Observatory in October, 2010 (Table 4). Each star was observed at four different wavelengths (6.0 cm, 3.5 cm, 1.3 cm, and 0.7 cm) in the C configuration (baselines ~ 0.035 – 3.4 km). For all four observing bands, the WIDAR correlator was configured using a setup that provided two sub-bands, each with a 128 MHz bandwidth, 64 spectral channels, and dual circular polarizations. Typical on-source integration times for each star were ~65, 13, 4, and 3.5 minutes at 6.0 cm, 3.5 cm, 1.3 cm, and 0.7 cm, respectively, with the exception of γ Cas, where a second observation of comparable duration was obtained at each of the three shortest wavelengths. Observations of each star were interspersed with observations of a neighboring bright point source to serve as a complex gain calibrator, and each session included an observation of 3C48 at the appropriate observing band(s) to serve as an absolute flux density and bandpass calibrator. Data reduction was performed using the Astronomical Image Processing System (AIPS; Greisen 2003) and followed standard procedures for continuum data obtained with the WIDAR correlator as described in the AIPS Cookbook[6]. The data were loaded into AIPS directly from the archival science data model (ASDM) files using the Obit software package (Cotton 2008). However, the default calibration ('CL') tables were recreated to update the gain and opacity information. The antenna positions were also updated to the best available values.

For all of the data obtained for this program it was necessary to perform an initial delay correction using a short (~1 minute) segment of data from the flux/bandpass calibrator. Following the excision of poor-quality data, the data weights were calibrated based on the system power measurements from each antenna using the AIPS task TYAPL. The absolute flux density scale was

[3] http://svo2.cab.inta-csic.es/theory/vosa/
[4] http://esavo.esa.int/vospec/
[5] http://www.submm.caltech.edu/~sharc/crush/index.html
[6] http://www.aips.nrao.edu/cook.html

determined using the time-dependent 3C48 flux density values from Perley & Butler (2013). Calibration of the bandpass and the frequency-independent portion of the complex gains was subsequently performed using standard techniques. At the two highest frequencies, the gain calibration was performed in two steps, first solving only for the phases using a solution interval of ∼10 seconds. Following the application of these corrections, a second iteration solved for both amplitude and phase. The flux densities determined for each of the complex gain calibrators observed in the present study are summarized in Table 2 (online only).

Imaging was performed using the AIPS task IMAGR with robust +1 weighting of the visibilities. Table 3 (online only) provides a summary of the resulting properties of the image and the synthesized beam. Flux densities for each of the target stars were then determined based on Gaussian fits to these images using the AIPS task JMFIT). All of the stars were spatially unresolved, hence the measured peak flux density is taken to represent the total flux.

3.4. Visual spectroscopy

Visual domain spectra for the program stars were obtained from the following archives:

- Unpublished HERos data, see Štefl & Rivinius (2005).
- The ELODIE archive described by Moultaka et al. (2004).
- The ESPaDOnS archive at CADC[7]. ESPaDOnS is mounted at the CFHT on Hawaii and described by Donati et al. (2006).
- The TBL/Narval archive[8]. NARVAL is a copy of the ESPaDOnS instrument, adapted to the 2 m TBL.
- The BeSS database (Neiner et al. 2011). However, data from this source were not used for velocity measurements; only for equivalent width (EW) measurements and general trend descriptions.

3.5. Visual polarimetry

Visual spectropolarimetric measurements were taken from the archives of the HPOL spectropolarimeter[9] mounted on the Pine Bluff Observatory (PBO) 36" telescope (Meade et al. 2012).

4. SED modeling

4.1. Model description

The adopted model of a Be star system consists of a combination of a fast rotating central star and a VDD.

The central star is approximated by a spheroidal, rotationally oblate shape that is gravity darkened according to the von Zeipel law (von Zeipel 1924). Its surface is divided into a number of latitude bins, and each one is assigned with a model spectrum (Kurucz 1979) corresponding to the local values of $T_{\rm eff}$ and $\log g$.

The rotating central star is thus completely described by four independent parameters: mass M, polar radius $R_{\rm p}$, luminosity L, and rotation rate W. The W parameter is defined as $W = v_{\rm rot}/v_{\rm orb}$, where $v_{\rm rot}$ is the rotational velocity at the stellar surface and $v_{\rm orb}$ is the Keplerian orbital velocity directly above the stellar surface. The gravity darkening exponent β that appears in the classical form of the gravity darkening law, $T_{\rm eff} \propto g^{\beta}$ (von Zeipel 1924), is a function of W as given by Espinosa Lara & Rieutord (2011).

[7] http://www.cadc-ccda.hia-iha.nrc-cnrc.gc.ca/en/
[8] tblegacy.bagn.obs-mip.fr/narval.html
[9] http://archive.stsci.edu/hpol/

The VDD model is adopted in a simplified parametric form, in which the density structure follows a power law decrease in the radial direction and has a hydrostatic equilibrium structure in the vertical direction:

$$\rho(r,z) = \rho_0 \left(\frac{r}{R_{\rm e}}\right)^{-n} \exp\left(-\frac{z^2}{2H^2}\right), \quad (2)$$

where r and z are respectively the radial and vertical cylindrical coordinates, ρ_0 is the density of the disk close to the stellar surface, $R_{\rm e}$ is the equatorial radius of the rotationally deformed central star, n is the density exponent, and H is the disk scale height. The disk flares with the following dependence of the disk scale height H on the distance r from the star:

$$H(r) = H_0 \left(\frac{r}{R_{\rm e}}\right)^{3/2}, \quad (3)$$

where $H_0 = c_{\rm s} v_{\rm orb}^{-1} R_{\rm e}$ is the pressure-supported scale height at the base of the disk, $c_{\rm s} = [(k_{\rm B} T_{\rm k})/(\mu m_{\rm a})]^{1/2}$ is the isothermal sound speed, $k_{\rm B}$ is the Boltzmann constant, $T_{\rm k}$ is the gas kinetic temperature, μ is the mean molecular weight, and $m_{\rm a}$ is the atomic mass unit. $T_{\rm k}$ is the parameter that determines the scale height, and we choose it to correspond to 60% of the effective temperature at the stellar equator, following Carciofi & Bjorkman (2006).

For $n = 3.5$, this structure represents the subsonic parts of an isolated, isothermal VDD in a steady-state (when mass from the central star was fed to the disk at a constant rate for a sufficiently long time) and composed purely of hydrogen (Bjorkman & Carciofi 2005). However, there are effects that can alter the value of n. Local non-isothermalities in the disk can affect both the flaring exponent and the radial density fall-off (Carciofi & Bjorkman 2008), while a non-steady mass feeding rate (Haubois et al. 2012), and the accumulation effect caused by a close orbiting companion (Panoglou et al. 2016) can also affect the density profile in quite complicated ways. For instance, Haubois et al. (2012) found that a forming disk (i.e., a disk being actively fed by the star but that has not yet reached a steady-state configuration) has a sharp density profile, which, if approximated by a power-law, results in n larger than 3.5; conversely, a dissipating disk (i.e., a disk that is no longer being fed and is therefore accreting back to the central star) has a much flatter density exponent ($n \approx 3.0$). Density exponents smaller than 3.5 are also believed to ensue from the accumulation effect in Be binaries. In this regard, varying n in our models allows us to accommodate these processes in the studied targets.

The only remaining free parameter of the disk is its outer radius $R_{\rm out}$. If not set to a very high number corresponding to a steadily fed isolated disk, this parameter roughly corresponds to the truncation radius caused by the tidal influence of a possible binary companion. In this work, we adopt a sharp truncation, in which no material exists past $R_{\rm out}$. Detailed hydrodynamic calculations, however, show that this is not a realistic assumption, because some material spills over past the truncation radius. This material may still contribute to the disk observables (Panoglou et al. 2016).

To compare the model with observations, we additionally need the value of interstellar reddening $E(B-V)$ and two geometrical parameters: the inclination angle i (0° for pole-on orientations) and the distance d.

4.2. Modeling procedure

To calculate the synthetic observables, we employ the code HDUST (Carciofi & Bjorkman 2006, 2008). All the objects are

A&A proofs: manuscript no. 29932JN

Table 5. Adopted model parameters.

Star	Spectral type[a,b]	Mass[c] [$M_\odot$]	Distance[d] [pc]	Inclination [°]
β CMi	B8 Ve	3.5[e]	49.6	43[e]
η Tau	B7 IIIe	3.4	123.6	41[f]
EW Lac	B3 IVe-shell	6.1	252	80[b,g]
ψ Per	B5 IIIe-shell	4.4	178.9	75[h]
γ Cas	B0.5 IVe	13.2	168.4	42[i]
β Mon A	B4 Ve-shell	5.1	208	70[b,g]

Notes.
[(a)] Slettebak (1982); [(b)] Rivinius et al. (2006); [(c)] Harmanec (1988); [(d)] van Leeuwen (2007); [(e)] Klement et al. (2015); [(f)] Tycner et al. (2005); [(g)] This work; [(h)] Delaa et al. (2011); [(i)] Stee et al. (2012).

Table 6. Derived model parameters.

Star	R_p [$R_\odot$]	R_e [$R_\odot$]	L [$L_\odot$]	$\log\rho_0$ [g cm^{-3}]	n	R_{out} [R_e]	R_c [R_e]	$E(B-V)$
β CMi	2.8 ± 0.2	4.20	185 ± 5	$-11.78^{+0.18}_{-0.30}$	2.9 ± 0.1	40^{+10}_{-5}	400	$0.01^{+0.02}_{-0.01}$
η Tau	8.0 ± 0.5	10.56	1750 ± 50	$-12.23^{+0.12}_{-0.16}$	3.0 ± 0.4	40^{+10}_{-5}	140	0.06 ± 0.02
EW Lac	4.5 ± 0.5	5.94	3500 ± 100	$-11.60^{+0.12}_{-0.18}$	2.2 ± 0.1	100^{+30}_{-20}	360	$0.11^{+0.04}_{-0.03}$
ψ Per	5.5 ± 0.5	7.26	2100 ± 100	$-11.48^{+0.10}_{-0.12}$	2.5 ± 0.1	100^{+5}_{-15}	250	$0.08^{+0.01}_{-0.02}$
γ Cas	7.0 ± 0.5	9.24	19000 ± 500	$-10.48^{+0.10}_{-0.12}$	3.3 ± 0.1	35 ± 5	560	$0.04^{+0.03}_{-0.02}$
β Mon A	4.0 ± 0.5	5.28	4500 ± 100	$-10.60^{+0.19}_{-0.18}$	$3.0^{+0.2}_{-0.1}$	110 ± 40	380	0.11 ± 0.04

Notes. The best-fit model parameters of the central star (R_p, L), the disk ($\log\rho_0$, n, R_{out}), and the interstellar medium ($E(B-V)$). The calculated values of R_e (for given W), and R_c (Eq. 1) are also listed.

modeled as a combination of a fast-rotating central star surrounded by a VDD. The code uses the Monte Carlo method to solve the radiative transfer, radiative equilibrium, and statistical equilibrium in 3D geometry for the given density and velocity distributions for pure hydrogen gas. For details on the hydrodynamics of VDDs, we refer to Carciofi (2011) and Krtička et al. (2011).

The modeling procedure is similar to the one tested by Klement et al. (2015) when using a multi-technique and multi-wavelength dataset. In the present work we used only the SED flux measurements to constrain the models. As this limits the constraining ability of the modeling, we keep several parameters fixed, specifically the stellar mass, rotation rate, inclination and distance, and we focus instead on determining the parameters that are best constrained by the SED structure, namely the interstellar reddening, the stellar radius and luminosity, the disk parameters (ρ_0, n) and the outer disk radius.

The multi-epoch data were combined into a single dataset, as the variability of the studied stars was found to be reasonably low. Where signs of variability are present, the combined data represent average properties of the disks in the last decades (for details see the results for individual targets in Sect. 5).

We started by searching the literature for spectral type classifications of the programme stars. The spectral types were used to fix the masses of the central stars as given by Harmanec (1988) for the fundamental parameters of main sequence B-type binaries. The rotation rate was kept at the typical value of $W = 0.8$ (Rivinius et al. 2013). This value corresponds to a R_e/R_p ratio of 1.32. The gravity darkening exponent was correspondingly set to 0.1728, as given by Espinosa Lara & Rieutord (2011). The distances to the stars were taken from the Hipparcos measurements (van Leeuwen 2007), and the inclinations from interferometric studies, when available. For the shell stars, we assumed $i > 70°$.The adopted parameters are listed in Table 5.

Interstellar reddenning presents an additional model parameter $E(B-V)$, which needs to be determined in order to be able to compare the observations to the model. We used the 2200 Å absorption bump (caused by the interstellar medium) to determine the $E(B-V)$ of the programme stars (we refer to Zagury 2013, for discussion of the origin of the bump). During the procedure the observed UV spectra are dereddened using the reddening curve of Fitzpatrick (1999) with $E(B-V)$ as a free parameter, until the 2200 Å bump disappears and the spectrum becomes flat in that region. For the extinction R_V we used the standard value of 3.1 (Savage & Mathis 1979). Although values other than 3.1 may be observed in nebular and star-forming regions, for nearby field stars such deviations are less likely. The uncertainties of the determined values of the $E(B-V)$ parameter were inferred by a Markov Chain Monte Carlo (MCMC) method provided by the emcee Python module[10] (Foreman-Mackey et al. 2013).

We proceed to the remaining physical parameters of the central star, namely the polar radius R_p and luminosity L. As discussed in Klement et al. (2015), for non-shell stars or shell stars with tenuous disks, the disk has very little influence on the observed UV spectrum. In such cases and within a reasonable parameter range, changing R_p (which in effect means changing the effective temperature as well) influences the slope of the model UV spectrum only, while changing L influences mainly its level. This allows us to constrain these two parameters independently by computing a grid of purely photospheric, fast-rotating models (similar to Klement et al. 2015). Furthermore, for tenuous disks, the visual and near-IR parts of the SED are also devoid of disk influence. The wavelength interval used to determine R_p and L was therefore selected on a case-by-case basis (we refer to Sect. 5 for details on individual targets).

The best-fit R_p and L parameter combination was determined via χ^2 minimization, where for the best-fit model $\chi^2 = \chi^2_{min}$. Since we were dealing with SED modeling, where both the wavelengths and fluxes span many orders of magnitude, we used

[10] available online at `http://dan.iel.fm/emcee` under the MIT License

the logarithmic version of χ^2:

$$\chi^2_{\rm mod} = \sum_{i=1}^{N} \left(\frac{\log F_{\rm obs,i} - \log F_{\rm mod,i}}{F_{\rm err,i}/F_{\rm obs,i}} \right)^2 , \quad (4)$$

where $F_{\rm obs}$ is the observed flux, $F_{\rm mod}$ is the model flux, $F_{\rm err}$ is the observed flux error, and N is the total number of fitted data points. The uncertainties of the best-fit parameters were estimated from the $\Delta\chi^2_{0.683} = \chi^2_{\rm mod} - \chi^2_{\rm min}$ contour corresponding to the 68.3% confidence level (1-σ), where $\Delta\chi^2_{0.683}$ is a function of the number of degrees of freedom of the fit (we refer to, e.g., Chapter 11 of Bevington & Robinson 1992). In some cases the parameter uncertainties turned out to be lower than the step size adopted for the parameter grid. Since the quality of the model fit was already sufficient for the aims of this work, we did not put in the computational effort to further fine-tune the model parameters and thus lower the uncertainty estimates, and we instead conservatively selected the corresponding step size as the parameter uncertainty.

The disk itself is non-isothermal with a temperature structure computed by HDUST, but its density structure is not solved self-consistently with the temperature solution and remains the same throughout the simulation. For such a simplified VDD model we need only three free parameters to fully describe it: the base density ρ_0, the density exponent n, and the disk outer radius $R_{\rm out}$. We set an upper limit to the $R_{\rm out}$ parameter, so that it cannot exceed the value of the critical radius $R_{\rm c}$ estimated by means of Eq. (1), in which the sound speed $c_{\rm s}$ was computed using the mass-averaged temperature of the disk.

In our model, we assume a single value of n throughout the whole disk and by doing so we are neglecting local non-isothermal density effects in the disk. VDD theory predicts a temperature minimum to occur in the inner parts of the disk due to its high opacity to the stellar radiation. However, since we are interested in the overall density structure of the VDD, of which the inner non-isothermal part is only a small fraction, these effects are not important for our analysis.

The modeling procedure was executed as follows. First, we fixed $R_{\rm out}$ to an intermediate value of 50 stellar radii, and a grid of models with ρ_0 and n in the range $1{\times}10^{-13}$ – $1{\times}10^{-10}$ g cm^{-3} and 1.5 – 5.0, respectively, was computed. To determine the parameters ρ_0 and n, we fit the model grid to the part of the SED where the disk contribution is significant, but not to the long wavelength radio data, that are sensitive to the disk size. While dense disks start to contribute to the SED already at visual wavelengths, excess radiation due to a tenuous disk might become observable only at mid-IR wavelengths. Similarly, the truncation effects in very dense disks will influence the SED at shorter wavelengths as compared to less dense disks. Therefore, the SED region used to constrain ρ_0 and n will be different from star to star and will shift towards shorter wavelengths with increasing density of the disk (for details on individual targets see Sect. 5). The uncertainties of the best-fit values of the parameters ρ_0 and n were determined in the same way as for the central star parameters $R_{\rm p}$ and L, described above.

The modeling procedure gets more complicated for shell stars with dense disks. In these cases, the disk reduces the UV flux (and sometimes also portions of the visual and near-IR flux) emitted by the central star and the observed UV spectrum cannot, therefore, be used to constrain $R_{\rm p}$ and L in a straightforward way. We adopted an iterative modeling procedure for such stars: A first look estimate for $R_{\rm p}$ and L was done using the photospheric models only, after which the disk was included in the model to get the first estimates for the disk parameters ρ_0 and n from the IR fluxes. With the values obtained in this way, the magnitude of the influence of the disk on the UV spectrum could be estimated and taken into account for the next iteration of photospheric parameters. After a few such iterations, a satisfactory fit to both the UV and IR parts of the SED was obtained.

After determining the best-fit values of ρ_0 and n, we can proceed to the determination of the $R_{\rm out}$ parameter. As mentioned above, the truncation effects will become detectable at progressively shorter wavelengths with increasing density of the disk. However, with disk sizes $\gtrsim 20\,R_{\rm e}$, the influence does not fall shortwards of sub-mm/mm wavelengths. Therefore, the mm and cm fluxes are suitable for constraining the sizes of dense disks, while cm fluxes only constrain the disk size of the tenuous ones (e.g., β CMi). In the latter case, the sub-mm/mm region was included when searching for the best-fit values of ρ_0 and n. Measurements corresponding to upper limits were used for visual checking, but not for the modeling procedure itself. The uncertainty of the $R_{\rm out}$ parameter was obtained in the same way as for the previously mentioned model parameters.

5. Results

In this section we first review the results for β CMi from Klement et al. (2015). Then we present the results for stars for which we have new JVLA measurements (η Tau, EW Lac, ψ Per, γ Cas), followed by the results for β Mon A, which has new sub-mm data from APEX/LABOCA. We also give a brief overview of what can be learned from the available visual spectroscopy and polarimetry for each target. The derived model parameters for all stars are listed in Table 6. In Table 6 we also include the values of $R_{\rm c}$ calculated using Eq. (1).

5.1. β CMi (HD 58715; HR 2845)

The star β CMi was studied in extensive detail by Klement et al. (2015). As in the present study, the HDUST code was used to model the SED from the UV to the radio, but additionally a large data set of spectroscopic, polarimetric, and interferometric observations was used to further constrain the model. Here we present a slightly adjusted model of the SED produced using an updated version of the HDUST code, which fixed some numerical problems that were slightly affecting the correct computation of synthetic observables. More details on the fixes of the code and the changes regarding the results of modeling of the observables besides the SED are given in Klement et al. (2017).

We recomputed the model and allowed the ρ_0, n and $R_{\rm out}$ parameters to vary in a small interval around the values originally determined by Klement et al. (2015), while keeping the central star parameters the same as in the previous study. The best-fit value of base density ρ_0 remains the same, but a significant change to the model concerns the density exponent n: the SED up to mm wavelengths is now reproduced exceptionally well when using a value of $n = 2.9$. We recall that in the original study, the very inner parts of the disk were compatible with a steeper ($n = 3.5$) density fall-off, while in the remainder of the disk it followed a shallower profile ($n = 3.0$).

Regarding the outer parts of the disk, the original conclusion was that the disk is truncated at a distance of $35^{+10}_{-5}\,R_{\rm e}$, as revealed by the observed radio flux at 2 cm. Here we include three additional VLA measurements at cm wavelengths that are available from the literature. The revised model and additional cm data led to a revised best-fit disk size of $40^{+10}_{-5}\,R_{\rm e}$. The best-fit model is plotted in Fig. 1 as a solid black line, together with the

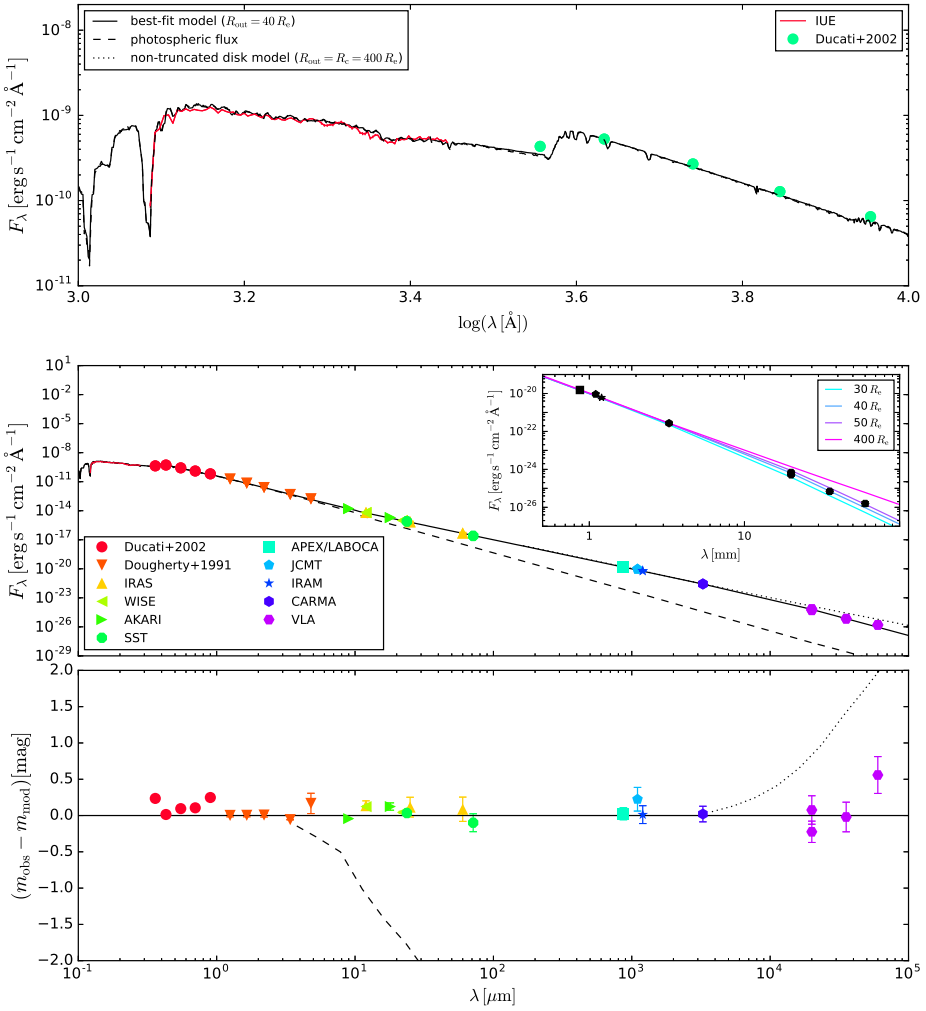

Fig. 1. β CMi. The best-fit model is plotted as the black solid line, the photospheric contribution as the dashed black line, and a non-truncated disk model ($R_{out} = R_c$) as the black dotted line. *Upper:* The SED in the 1000–10000 Å interval. *Middle:* The SED from 0.1 μm to 10 cm. The inset shows model predictions for different disk sizes. The observed fluxes are plotted with error bars, which are smaller than the symbol size in most cases. *Lower:* The residuals structure of the best-fit model with $R_{out} = 40\,R_e$. The photospheric and non-truncated models are also plotted in relation to the best-fit model, highlighting where these models deviate from the best-fit one.

purely photospheric flux (dashed black line) and a non-truncated disk model (dotted black line). The model reproduces the full SED almost perfectly, with the exception of the data point at 6 cm, which lies slightly above our best-fit model.

5.2. η Tau (Alcyone; HD 23630; HR 1165)

This star from the Pleiades cluster has been mostly classified in the literature as a B7IIIe star (Slettebak 1982; Lesh 1968; Hoffleit & Jaschek 1991). The inclination is apparently of an intermediate value. In previous interferometric studies it was quoted

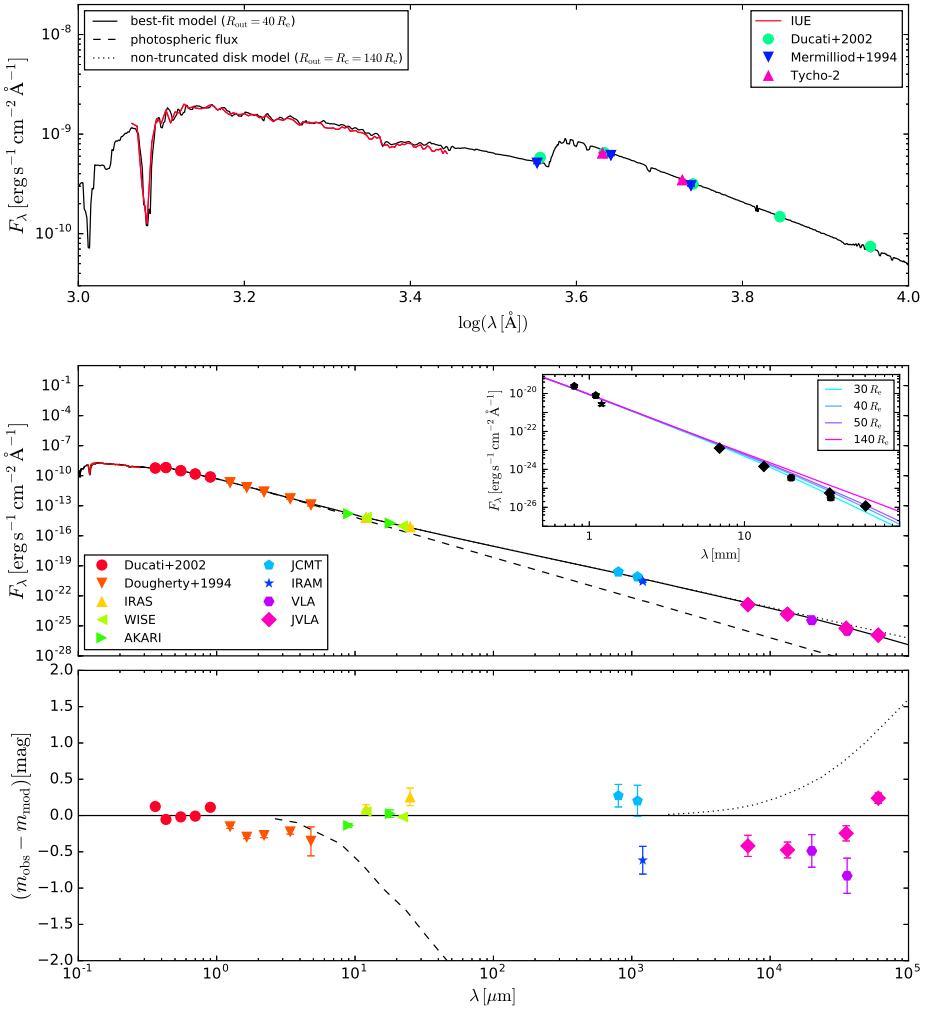

Fig. 2. As in Fig. 1, but for η Tau.

to be higher than 18° (Quirrenbach et al. 1997) and equal to 41° (Tycner et al. 2005). We adopt the latter value for our model.

No companion was revealed in adaptive optics observations (Roberts et al. 2007). A total of 47 spectra suitable for RV measurement were found in the archives. The RV was measured in the Mg II 4481 line. The mean RV is 6.9 ± 2.1 km/s. HEROS measurements around MJD 52000 are on average approximately 4 km/s lower than ESPaDOnS measurements at MJD 55000, but given the different instrument parameters, the values are well compatible and within 3-σ of one another. However, we note that this by no means excludes the possible presence of a binary companion. The IR Ca triplet emission, indicative of binarity, is not present in the spectra.

The spectroscopic data show that the Hα emission was at a constant level of I/I_c = 2.2, and W_λ = −3.5 Å until approximately 2005, and since then steadily decreased by a small but detectable amount to I/I_c = 2.0, and W_λ = −2.5 Å. The spectropolarimetric measurements available from the HPOL database show no change of polarization degree or angle between 1992 and 1999.

From the comparison of IRAS and AKARI/WISE measurements, which are separated in time by around two decades, we also see that the variability of the disk has been relatively low. This is a common feature of late-type Be stars. The comparison of the observed mm fluxes from JCMT and IRAM shows signs of slight variability at mm wavelengths on the time scale of years. The archival VLA and the new JVLA measurements are very much consistent with one another, with the exception of the observed fluxes at 3.6 cm, which however still lie within 2-σ of one another.

The results of the SED modeling of η Tau are plotted in Fig. 2. The non-shell nature of η Tau allows us to use the UV spectrum to determine the central star parameters $R_{\rm p}$ and L without any complications. Moreover, the disk of η Tau is apparently very tenuous and starts to contribute to the observed SED only at around 5 μm. We thus use both the UV spectrum and the visual photometry to constrain $R_{\rm p}$ and L. Changing the disk size influences the cm fluxes only and has a negligible influence on the mm fluxes (as expected for tenuous disks). Therefore, the SED interval from 5 μm to mm was used to find the best-fit values of the disk parameters ρ_0 and n.

The observed radio fluxes are lower than expected from a non-truncated VDD model. The disk size best reproducing the cm data is $R_{\rm out} = 40^{+10}_{-5}\,R_{\rm e}$. We interpret this as a clear sign of truncation of the outer disk. However, a simply truncated VDD does not offer a good fit either, as the observed SED slope in the radio is flatter than the model predicts. This is most easily seen in the residuals of the best-fit model with respect to the radio measurements (bottom panel of Fig. 2).

5.3. EW Lac (HD 21750; HR 8731)

EW Lac was classified as a B3IVe-shell star (Slettebak 1982; Rivinius et al. 2006), and a B4IIIep star (Lesh 1968; Hoffleit & Jaschek 1991). No previous interferometric determination of the disk inclination exists in the literature. However, the shell nature of the star restricts the inclination angles to $\geq$70°. For our study we adopt the value of $i = 80°$, which was found to reproduce well the shapes of the Balmer and Paschen jumps.

EW Lac has shown remarkable variations in its shell line appearance in the past, most notably from 1976 to 1986, and a similar episode lasted from 2007 until 2012 (Mon et al. 2013). The variations are best explained in terms of V/R variability, that is, changes in the peak height ratio of the violet and red side of the emission. Small V/R differences were present in almost all spectra at our disposal, taken from 1998 to 2014. However, beginning in the 2007 to 2014 period, that is, for the last V/R cycle, the amplitudes were greatly enhanced.

There are 13 suitable spectra to measure RVs, from which the presence of a companion could be neither confirmed, nor excluded. Values measured in the Fe II 5169 line obtained from Heros spectra, from MJD 51000 to 52500, are at approximately −22 km/s, while ESPaDOnS values, obtained around MJD 55400, are at −28 km/s. Although this change is very likely real, it is probably due to a change in the global density oscillation of the disk rather than binarity. Also, changes in the Hα equivalent width are due to the variable strength of the central absorption core, rather than changes in the strength of the emitting peaks.

Like for η Tau, the HPOL data, taken from 1989 to 1995, do not show any change in polarization degree or position angle; neither is the infrared Ca triplet observed in emission in our spectra.

Comparison of the IRAS and AKARI/WISE measurements reveals a variation in the IR excess emission that is somewhat stronger than in the other targets in our sample. The mm fluxes observed by JCMT and IRAM are consistent within the respective error bars. The comparison of the VLA and JVLA measurements also reveals a slight discrepancy in that one of the VLA measurements lies a few σ above the JVLA fluxes. The two VLA observations at 2 cm are slightly inconsistent, as the upper limit measurement lies below the detection. This suggests a possible mild variability of cm fluxes on the time scale of a year.

The results of the SED modeling of EW Lac are plotted in Fig. 3. Due to the shell nature of the star and the high value of the disk density, the observed UV spectrum of EW Lac is slightly dimmed by the surrounding disk. The disk excess starts to be significant at a wavelength of around 1 μm, allowing for the inclusion of the visual part of the SED for determining the central star parameters. Since the disk is dense, the IR part of the SED was used to determine ρ_O and n, while the mm and radio part, sensitive to varying the disk size, was used to determine $R_{\rm out}$. The resulting SED fit up to far-IR is satisfactory.

The radio observations, including the mm measurements, are inconsistent with a non-truncated disk. The resulting disk size for the case of simple truncation is $100^{+30}_{-20}\,R_{\rm e}$. Moreover, the new JVLA data set reveals a similar result as given above for η Tau – the observed slope of the SED in the radio is not as steep as would be expected for a simply truncated disk.

5.4. ψ Per (HD 22192; HR 1087)

The star ψ Per has been classified as a B5Ve-shell star (Lesh 1968; Hoffleit & Jaschek 1991), a B4IVe star (Underhill 1979) and also as a B5IIIe star (Slettebak 1982; Rivinius et al. 2006). The inclination angle is > 62° according to Quirrenbach et al. (1997) and 75° ± 8° according to Delaa et al. (2011); for this study we adopt the latter value.

No binary companion is evident (Mason et al. 1997; Delaa et al. 2011). Yet, for this star, the infrared Ca triplet is observed in clear emission in all available spectra covering that region. Like for EW Lac, the shell nature permits the measurement of the RV with a precision of a few dozen m/s. While the RV is varying by approximately 1500 m/s peak to peak, there are not enough spectra to say whether this is due to a companion, that is, clearly periodic, or due to small changes in the disk, in which case changes could be merely cyclic or secular.

For ψ Per, the HPOL data show a clear increase of polarization degree from 0.4% to 0.8% from 1992 to 1994, which then remains at 0.8% until at least 2000. All available spectra were taken in 2000 to 2014, that is, after the polarization changed, and show a strong and stable disk, with $I/I_{\rm c} = 6$ and $W_\lambda = -41$ Å. The V/R ratio of the emission lines is unity; apparent deviations observed, for example, in Fe II 5169, are due to blends.

No variability in the IR excess is revealed by comparing the IRAS and AKARI/WISE data. The mm measurements from JCMT and IRAM are mostly consistent, although one of the JCMT detections lies slightly above the others. The old VLA and the new JVLA data are in good agreement, although the upper limit of Apparao et al. (1990) at 2 cm lies below the subsequent detections. It is unclear whether this is caused by radio variability or by the low signal-to-noise ratio of the observations.

The results of the SED modeling of ψ Per are plotted in Fig. 4. Although ψ Per is a shell star, the disk base density is only of an intermediate value and does not significantly influence the UV and visual part of the SED. Therefore the SED interval up

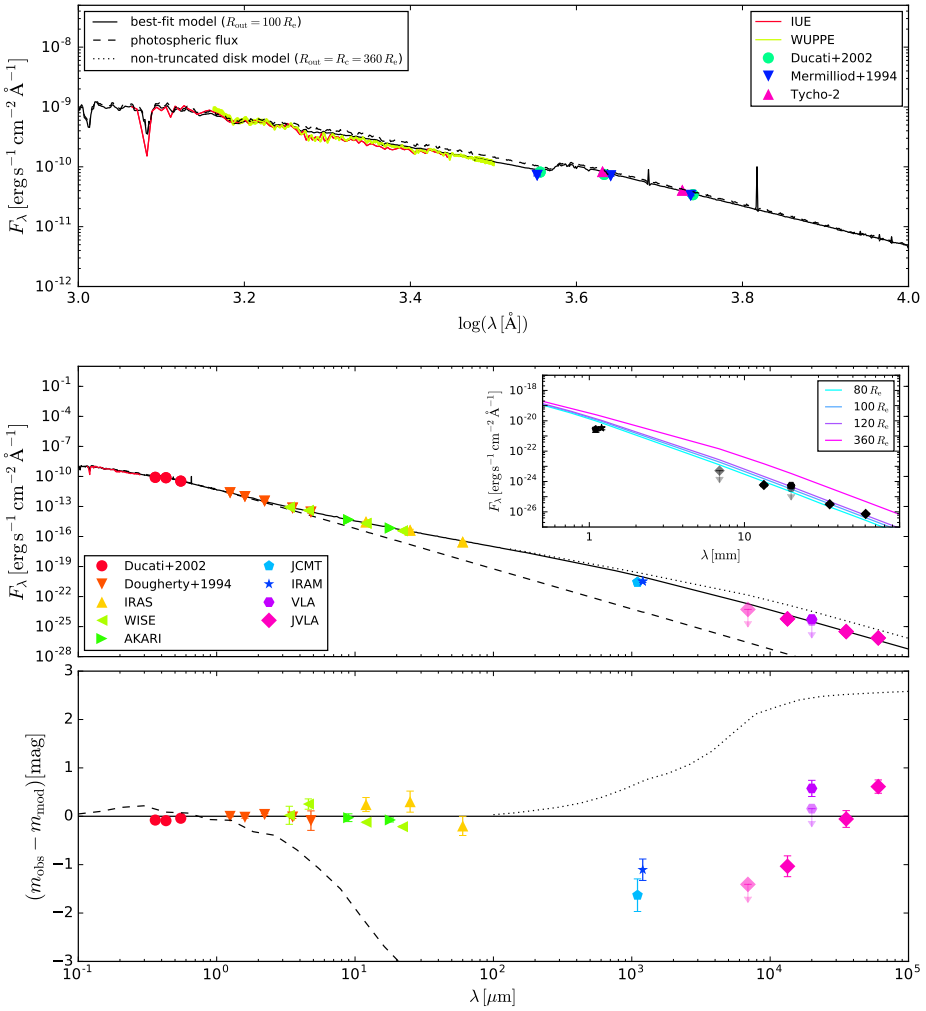

Fig. 3. As in Fig. 1, but for EW Lac.

to 1 micron was used to constrain the central star R_p and L. The disk contribution to the observed SED starts to be significant at near-IR wavelengths. Although the value of ρ_0 is only intermediate, the fact that n is very low makes the disk dense in its outer parts. Correspondingly, the model SED was found to be sensitive to changing the disk size already at mm wavelengths, therefore it was only the IR portion of the spectrum that was used to constrain the disk density parameters. The resulting fit from UV to far-IR wavelengths is exceptionally good.

The observed radio SED slope is once again inconsistent with both a non-truncated and a simply truncated disk. The resulting disk size best reproducing the whole radio data set is $100^{+5}_{-15}\,R_e$. The result again suggests that the disk density fall-off regime changes to a steeper one in the outer parts, but the disk is not simply cut-off, as is assumed in our model.

To this date, ψ Per is the only star that has been angularly resolved in radio (λ = 2 cm) along the semi-major axis of its disk (Dougherty & Taylor 1992). In that study, the Gaussian fit to the azimuthally averaged visibility data indicated a best-fit disk size (FWHM) of 74 mas, corresponding to 392 R_e. In Fig. 5 we plot the original visibility curve of Dougherty & Taylor (1992), along with the curves derived from our models with different disk sizes

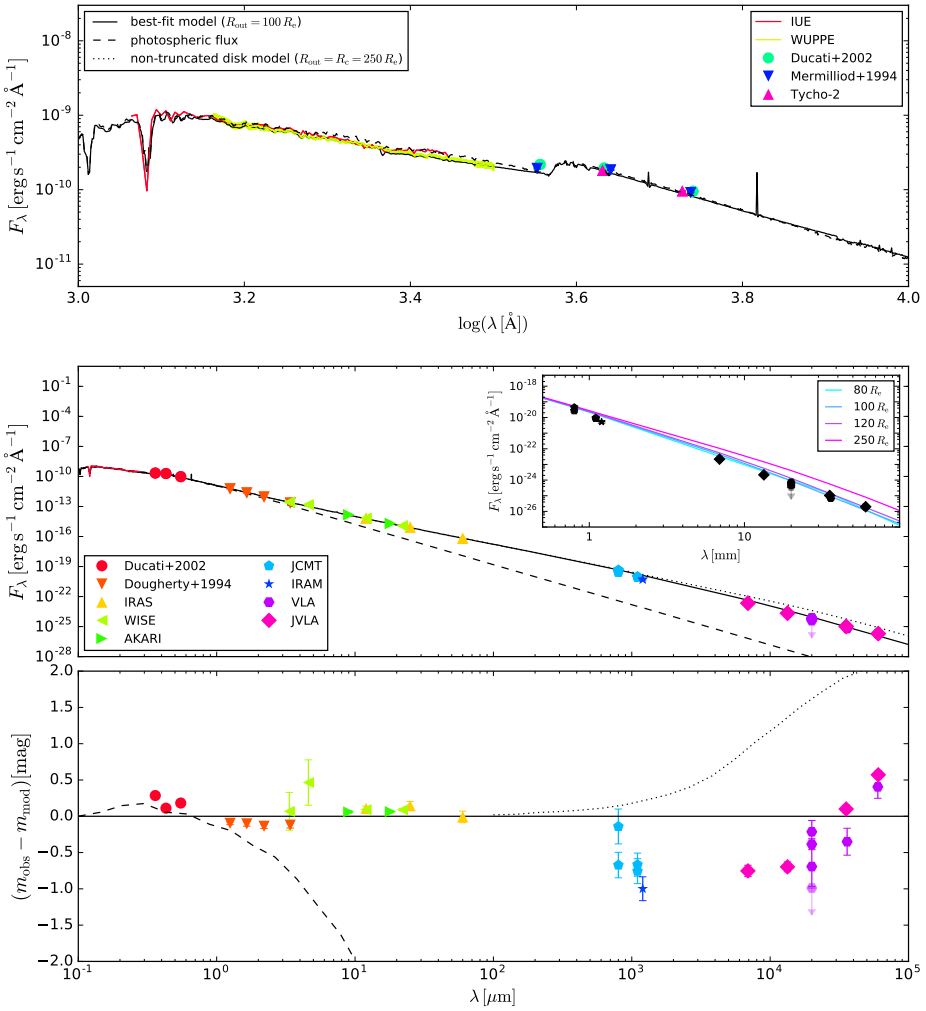

Fig. 4. As in Fig. 1, but for ψ Per.

(azimuthally averaged). Since the absolute flux density values for each of our models differ, we scale the curves so that at zero baseline the visibility is equal to unity. The visibility curve of our best-fit model (R_{out} = 100 R_e) shows that such a disk would not have been resolved by the observations of Dougherty & Taylor (1992), although the model flux density at 2 cm (1190 μJy) is relatively close to the measured value (804 ± 60 μJy). The model with the disk size of 500 R_e shows almost perfect agreement with the shape of the observed visibility curve. However, the flux density of this model (9.31 mJy) overestimates the measured value by more than a factor of 10. As for the apparent disk sizes of our models, 2D Gaussian fits give FWHMs of 29.5 × 20.1 mas and 85.2 × 47.8 mas for the best-fit and the 500 R_e disk models, respectively. The disagreement between our model and the angular size and fluxes of Dougherty & Taylor (1992) cannot be solved by the simple models that we employ, and will be the subject of future research.

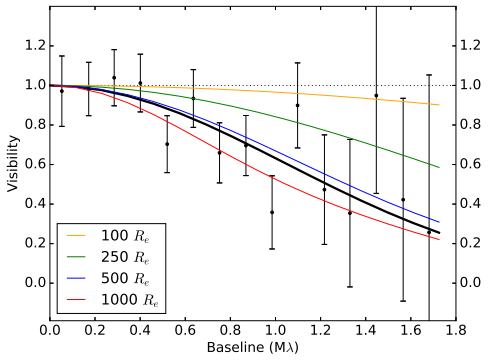

Fig. 5. ψ Per: The azimuthally averaged visibility data of Dougherty & Taylor (1992, black points with error bars) and a Gaussian fit to them (thick black line, FWHM of 74 mas corresponding to 518 R_e) overplotted with the visibility curves derived from our azimuthally averaged models with several different disk sizes indicated in the legend. The dotted line shows the visibility curve of a point source (visibility equal to unity with increasing baseline length).

5.5. γ Cas (HD 5394; HR 264)

The star γ Cas was one of the first two Be stars to be discovered (Secchi 1866). It was identified as an X-ray source and there is an ongoing debate as to the origin of the puzzling X-ray emission properties (e.g., Motch et al. 2015). γ Cas is a known single-line spectroscopic binary. The set of orbital parameters was recently revised by Nemravová et al. (2012), who concluded that the orbit is circular with an RV semi-amplitude of 4.30 ± 0.09 km/s and a period of 203.52 ± 0.08 days. γ Cas has a very complicated observational history, as it has appeared as a shell star, briefly as a normal B star and since a few decades ago as a Be star seen under intermediate inclination (see Harmanec 2002, for details).

γ Cas has been classified in the literature as a B0.5IVe star (Slettebak 1982). For the inclination, we adopt the value of 42°, found in a recent interferometric study by Stee et al. (2012).

In agreement with the suspicion that the infrared Ca triplet may be linked to binarity (Koubský et al. 2011), γ Cas does indeed show emission in these spectral lines. The strength is somewhat lower than that of the Paschen lines that the Ca triplet lines are blended with, but clearly discernible. The shape of the Hα line also seems to indicate binarity, since it often shows no clear peaks or symmetry, which are signs of disturbances in the disk.

Judging from the Hβ profiles, which behave closer to the expectations for a classical Be star than the Hα profiles, γ Cas underwent V/R variability before 2000, which weakened between 2000 and 2005, and is since absent. The available HPOL data, spanning 1991 to 2000, show a constant polarization. Since γ Cas is the brightest Be star in the Northern hemisphere, there is a great wealth of spectroscopic data available from the archives. Here spectra taken between 1996 and 2014 are considered. The value for I/I_c of Hα varied, but remained in the range between approximately 4 and 5. In other words, while the disk of γ Cas is not stable in the same sense as the one of, for instance, ψ Per, it is clearly not currently in a stage of secular build-up or decay, but fluctuating around a certain state.

The IR measurements do however reveal signs of variability, as the IRAS fluxes are several σ below those of AKARI/WISE. The same is true for the observed mm fluxes, as the JCMT and IRAM measurements are discrepant by several σ. This suggests mild variability in the disk, consistent with what is observed in the Hα emission. The VLA and JVLA measurements are in very good agreement, except for the 3.6 cm VLA upper limit which lies slightly below the JVLA detection.

The results of the SED modeling of γ Cas are plotted in Fig. 6. The disk contribution to the observed SED is apparent already at visual wavelengths, therefore we use only the UV spectrum to constrain the central star parameters R_p and L. Owing to the high density of the disk, the observed fluxes from optical to far-IR were used to determine the disk parameters ρ_0 and n. The overall model fit to the observed SED from UV to far-IR region is satisfactory with the exception of the visual and near-IR fluxes, which are overestimated by the model.

The result from the modeling of the radio SED is that the disk is clearly truncated, similar to the previous targets. The disk size best reproducing the radio data is 35^{+5}_{-5} R_e. However, the observed slope of the radio SED is again flatter than the slope of the truncated model.

5.6. β Mon A (HD 45725; HR 2356)

β Mon A is a component of a visual multiple system, with the B and C components separated by 7.1 and 10 arcsec, respectively (Taylor et al. 1990). At such distances the companions cannot have any tidal influence on the disk of the A component (Rivinius et al. 2006). The star has been classified as a B3Ve star (Lesh 1968; Hoffleit & Jaschek 1991), B4Ve-shell star (Slettebak 1982; Rivinius et al. 2006), and a B2III star (Maranon di Leo et al. 1994). Strong V/R variations with a period of 12.5 years have been observed in the past (1930–1960, Taylor et al. 1990).

The shell nature of the star restricts the inclination angle to be close to edge-on. Unfortunately no interferometric studies of this star have been published (although interferometric measurements do exist and are public - Rivinius et al. 2016); the only reference for the inclination is 67° (Frémat et al. 2005). We adopt an inclination of 70° for our model.

There are 48 available spectra taken in four observing seasons between MJD 51000 and 56000. The narrow circumstellar line Fe II 5169 shows small RV variations with an amplitude of approximately 3 km/s. Again, however, it is not clear whether this variation is due to binarity or changes in the disk, since β Mon A is a V/R variable Be star.

No HPOL data are available for β Mon A. Judging from the line emission, the disk is generally strong, with values of I/I_c between 5 and 6. It also underwent a weak V/R cyclic variability in these years. The spectra do show IR Ca triplet emission on a similar level to that of γ Cas.

The disk properties as shown by the observed SED seem to have been relatively stable in the last decades, with only the AKARI measurements being slightly discrepant with respect to those from IRAS and WISE. The sub-mm/mm measurements indicate a slight variability, similar to the previous targets. New JVLA observations are not available for this star and the data set at cm wavelengths consists only of a single VLA detection at 2 cm and three upper limit measurements at 2, 3.6, and 6 cm. The upper limit at 2 cm lies a few σ below the detection, suggesting a mild variability of the radio fluxes.

The results of the SED modeling of β Mon A are plotted in Fig. 7. β Mon A is a shell star and the disk influence is already clear in the UV spectrum, which is slightly dimmed in comparison with a purely photospheric spectrum. The disk of β Mon A is

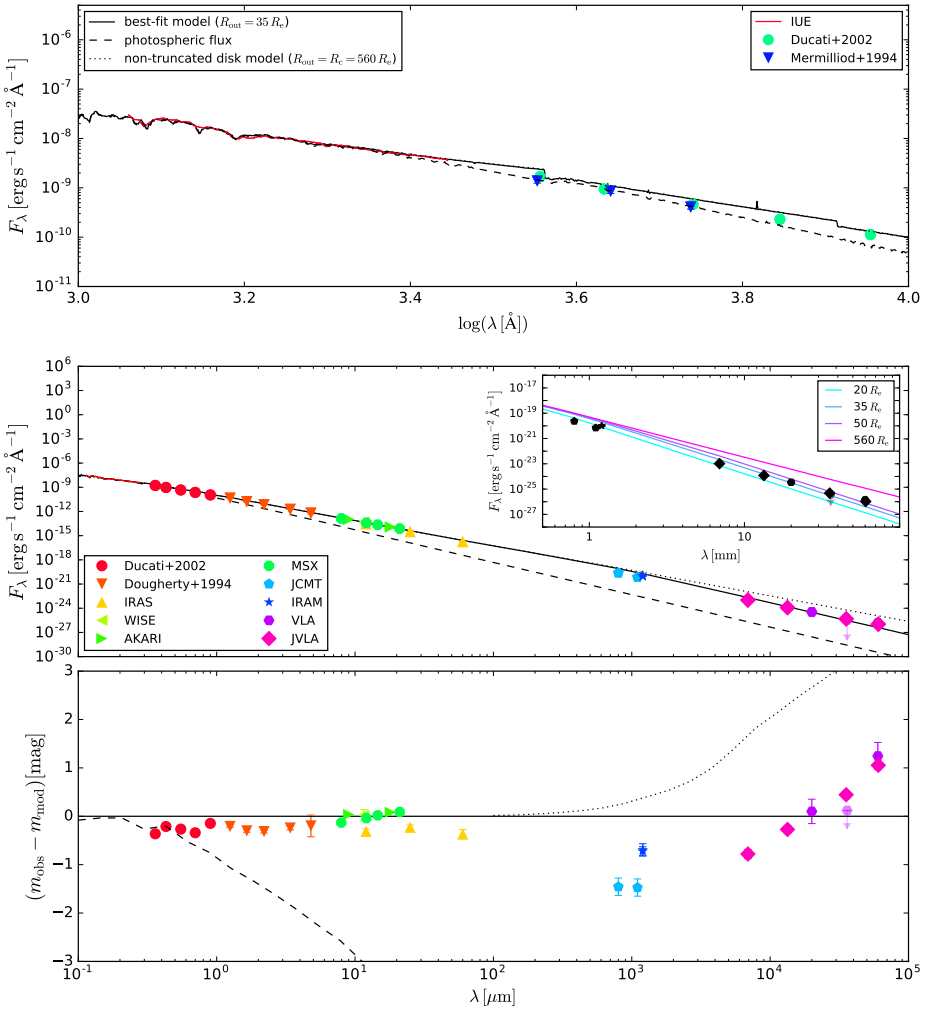

Fig. 6. As in Fig. 1, but for γ Cas.

dense and significant excess radiation is present already at visual wavelengths. Only the IR part of the SED was used to search for the disk parameters, as the disk has a high density. The resulting model SED agrees with the observations reasonably well.

For β Mon A the signs of the disk truncation are the weakest among our targets. However, the APEX/LABOCA and JCMT fluxes lie more than 3-σ below what is expected of a non-truncated disk. The upper limit measurements at 2 and 3.6 cm are also inconsistent with a non-truncated disk. Nevertheless, additional radio measurements are necessary to better constrain the disk size and confirm the signs of truncation. However, even with the available data, the best-fit disk size is $110 \pm 40\,R_e$, which is significantly lower that the critical radius value of $260\,R_e$.

6. Discussion

The VDD model in its parametric form reproduces the observed SED of the studied stars generally well. The resulting values of the density exponent n are in all cases lower than the canonical value of 3.5 derived for flaring isothermal VDDs in steady-state. A possible explanation for this was recently given by Vieira et al. (2017), who studied the IR SEDs of 80 Be stars and determined

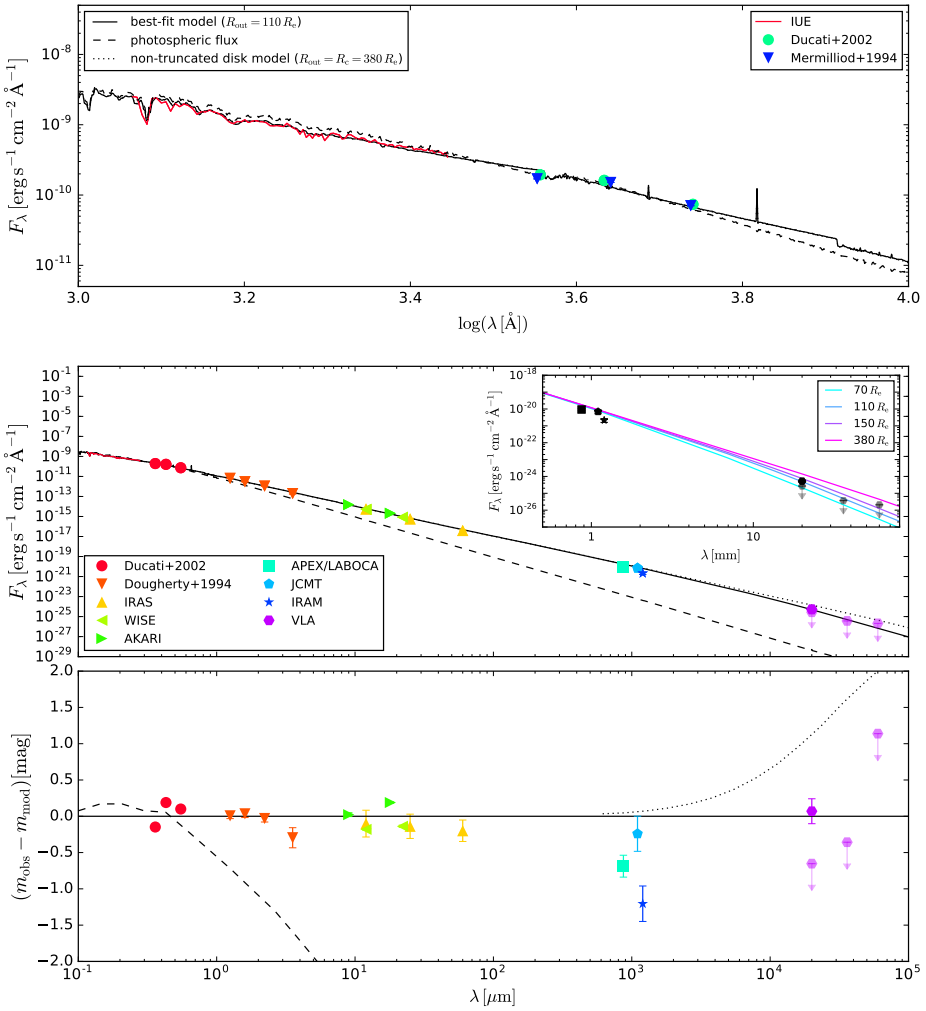

Fig. 7. As in Fig. 1, but for β Mon A.

their ρ_0 and n parameters using a semi-analytic model based on the pseudo-photosphere concept (Vieira et al. 2015). The determined values of n are generally not equal to 3.5, with the majority of the studied disks showing n between 2.0 and 3.0. These results were proposed to be explained by the dynamical state that we see the disks in. According to the dynamical models (Haubois et al. 2012) and assuming additional effects such as cooling by heavier elements (not taken into account in our model), the disks with $n \geq 3.5$ should correspond to disks that are in the process of formation, disks with n between approximately 3.0 and 3.5 are in a steady-state, and disks with $n \lesssim 3.0$ are in the process of dissipation. As presented in Fig. 7 of Vieira et al. (2017), approximately two thirds of the observed Be disks were found to be in the dissipating phase, suggesting that the time scales for disk dissipation are longer than those for disk formation.

Over-plotting the results of the present study on Fig. 7 of Vieira et al. (2017) shows that the $\log \rho_0$ and n parameter combinations determined for the stars in our sample fall within the two central contours corresponding to the probability density of 0.06 (Fig 8). However, contrary to the study of Vieira et al. (2017), the majority of our targets seem to be in steady-state (4 out of 6). This apparent disagreement (which might not be significant

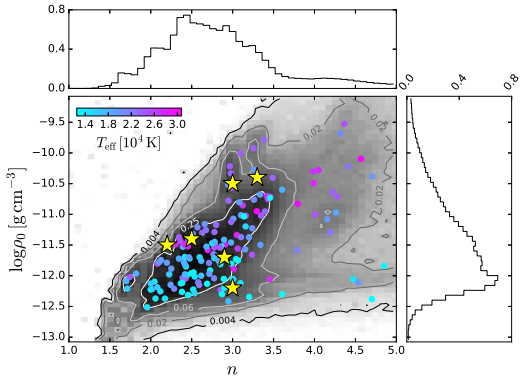

Fig. 8. Results for the ρ_0 and n distributions of the sample of Be stars studied by Vieira et al. (2017). The main panel shows the probability density (gray scale contours), while the upper and left panels show the distributions for the individual parameters. The contour values correspond to the probability density levels. Superimposed as filled circles are the results of Vieira et al. for individual stars (colors indicate the stellar effective temperatures computed by Frémat et al. 2005). Overplotted as yellow star symbols are the results for the stars studied in this work.

given the small number of stars in our sample) is probably due to the fact that Waters et al. (1991) favored Be stars with large infrared and radio excesses in their study. Another apparent inconsistency is that the two targets for which n is well below 3.0 (EW Lac and ψ Per) and should, according to Vieira et al. (2017), be in a dissipation state, also seem to have stable disks over long time-scales. We speculate that if these disks are truncated by unseen binary companions (see below), the shallower density profile might be due to the accumulation effect, which causes the disk density profile to become shallower than the steady-state value (Panoglou et al. 2016).

An SED turndown (i.e., a steepening of the SED slope) is clearly observed between the far-IR and radio wavelengths in five out of the six studied stars. The one exception is β Mon A, for which the presence of an SED turndown is inconclusive.

The results of the modeling show that, to a first approximation, the observed SED turndown can be explained by assuming truncated disks. We recall that there are two physical effects that are predicted to affect the outer disk structure, that could be the cause of the SED turndown: the tidal influence from a close binary companion, or the transonic transition, that occurs when the outflow velocity of the gas in the disk becomes supersonic.

We found that the disk truncation occurs at much smaller distances from the central star than where the supersonic point (the critical radius, $R_{\rm c}$, in Table 6) is expected to lie. Therefore we conclude that the supersonic regime is an unlikely cause for the SED turndown observed in our sample. As mentioned in Sect. 2, the effects of the transonic transition in a typical Be disk are likely to be observable only at even longer wavelengths. The one exception is EW Lac, for which the non-truncated disk model SED structure in the radio (dotted line in the lower panel of Fig. 3) suggests that for this star (and Be stars with similarly dense disks), the effect of the transonic transition may already be observable at cm wavelengths. However, we note that the formula for the critical radius (Eq. 1) is only approximate and the resulting values of $R_{\rm c}$ are therefore uncertain.

The disk sizes determined by our modeling represent sizes of truncated disks that best reproduce the data, but it is clear from the radio SED slope that the situation is not that simple: Some matter seems to overflow beyond the truncation radius (which is generally not equal to our parameter $R_{\rm out}$), from where it non-negligibly contributes to the radio SED. Investigating the role of the material past the truncation radius on the SED will be the subject of a future study.

For the previously studied star β CMi, the presence of the companion was not confirmed at the time of the analysis of Klement et al. (2015). The disk truncation was nevertheless suggested as being caused by the tidal influence of an unseen binary companion, with further observable evidence, such as the Ca triplet in emission, supporting this option (we refer to Sect. 5 of Klement et al. 2015). A follow-up RV analysis of the Hα line led to the detection of the binary, with an orbital period of 170 days and RV amplitude of 2.25 km/s (Dulaney et al. 2017). The value of the detected period, if a circular, coplanar orbit and a 1 $M_\odot$ companion are assumed, indicates a semi-major axis of $\sim 50\,R_{\rm e}$. Based on the results of Panoglou et al. (2016), the truncation radius is expected to lie near the 3:1 resonance with the binary orbit, corresponding to $\sim 25\,R_{\rm e}$. The result that the disk is truncated at $\sim 40\,R_{\rm e}$ rather favors the 3:2 resonance with the orbit as the location of the truncation radius for the case of β CMi.

For the other confirmed binary in our sample, γ Cas, the semi-major axis of the orbit is $a \simeq 1.64$ au (Nemravová et al. 2012), corresponding to $38\,R_{\rm e}$ of our model. However, here the comparison with our best-fit disk size is difficult, since the slope of the radio SED is not reproduced well. This means that if, for example, the cm data were ignored, the mm measurements would point to a much smaller disk size than was derived from the whole radio data set. This is also the case for the remaining objects with new JVLA data (η Tau, EW Lac, and ψ Per).

In conclusion, modeling of the radio SED offers the possibility to indirectly detect previously unknown companions of Be stars. A systematic search for RV periods in stars which show truncation effects (especially shell stars), but for which no companion was reported, is necessary to confirm that it is indeed binary companions that cause the SED turndown by truncating the disk, and not any other so-far undetected mechanism operating in Be star disks. We performed a search for RV variations in the available spectra of the unconfirmed binaries in the sample. However, the data set was limited and the RV amplitudes caused by low-mass companions are likely of the same order as the value 2.25 km/s derived for β CMi for late-type Be stars, and even smaller for earlier types (since the mass ratio is higher). Detection of such RV amplitudes would probably require dedicated high-resolution spectroscopic campaigns and careful analysis similar to the one performed by Dulaney et al. (2017). If the companions are confirmed and are found to be sdO/sdB stars, this may establish a common evolutionary path for Be stars and help confirm a possible cause for Be stars being fast rotators.

We note that the original sample of Waters et al. (1991) was biased towards stars with the flattest spectra, that is, with the least pronounced SED turndowns. The reason is that only stars detected at cm wavelengths were analyzed, while those not detected likely have even more pronounced SED turndowns and therefore stronger signs of truncation.

7. Conclusions

The main conclusions of this work may be summarized as follows:

- The predictions of the VDD model agree very well with the observed SEDs covering the wavelength interval from the UV to the far-IR. This further establishes the VDD model as the best model so far to explain the structure of Be disks.
- Comparison of our results with the ones of Vieira et al. (2017) shows that our sample has a much higher prevalence of steeper density profiles ($n \sim 3$, typically associated with disks in steady-state) than shallower profiles ($n \sim 2$, usually found in Be stars whose disks are dissipating). However, for these latter cases (namely EW Lac and ψ Per) there is evidence that the disks have remained stable over the last decades, suggesting that the shallow density profile may be caused by the accumulation effect due to the unseen companions (Panoglou et al. 2016) rather than due to the disks being in a dissipation phase.
- A clear steepening of the spectral slope at far-IR to radio wavelengths is observed in the whole sample with the exception of β Mon A, for which the measurements are not conclusive. The effect is present both for confirmed binaries (β CMi, γ Cas) as well as for stars for which no companion has yet been reported.
- We propose that the SED turndown is caused by truncation of the disk. The radio data sets are best reproduced by disks truncated at distances of approximately 30–150 stellar radii from the central star. The most plausible explanation for the disk truncation is the presence of (unseen) binary companions, tidally influencing the outer disk.
- Our simple model for truncation, in which the disk is abruptly cut at the truncation radius, cannot explain in detail the shape of the radio SED. This is in line with hydrodynamical simulations that predict that the disk material overflows past the truncation radius. In a future study we will investigate whether or not this extra material can explain the discrepancies found in this work.
- Comparison of our results with the only previous determination of the disk size in radio (Dougherty & Taylor 1992, ψ Per) revealed unexpected inconsistencies. Our model that best fits the radio flux densities is too small to have been resolved by the VLA. Interestingly, it is the model with the disk size of $500\,R_e$ that shows good agreement with the observed shape of the visibility curve. However, this model clearly overestimates the observed flux density.

Acknowledgements. We acknowledge our recently deceased colleague Stanislav Štefl as being the one who came up with the original idea for this project. R.K. would like to acknowledge the kind help of Dietrich Baade in the final stages of preparation of the paper. The research of R.K. was supported by grant project number 1808214 of the Charles University Grant Agency (GA UK). A.C.C. acknowledges support from CNPq (grant 307594/2015-7) and FAPESP (grant 2015/17967-7). R.G.V. acknowledges support from FAPESP (grant 2012/20364-4). D.M.F. acknowledges support from CNPq (grant 200829/2015-7) and FAPESP (grant 2016/16844-1). This work has made use of the computing facilities of the Laboratory of Astroinformatics (IAG/USP, NAT/Unicsul), whose purchase was made possible by the Brazilian agency FAPESP (grant 2009/54006-4) and the INCT-A. This publication is based on data acquired with the Atacama Pathfinder Experiment (APEX). APEX is a collaboration between the Max-Planck-Institut fur Radioastronomie, the European Southern Observatory, and the Onsala Space Observatory The National Radio Astronomy Observatory is operated by Associated Universities, Inc., under cooperative agreement with the National Science Foundation. This publication makes use of VOSA, developed under the Spanish Virtual Observatory project supported from the Spanish MICINN through grant AyA2011-24052. This publication makes use of data products from the Wide-field Infrared Survey Explorer, which is a joint project of the University of California, Los Angeles, and the Jet Propulsion Laboratory/California Institute of Technology, funded by the National Aeronautics and Space Administration. The VLA data presented here were obtained as part of program VLA/10B-143 (AI141). LDM acknowledges support from an award from the National Science Foundation (AST-1516106).

References

Apparao, K. M. V., Rengarajan, T. N., Tarafdar, S. P., & Ghosh, K. K. 1990, A&A, 229, 141
Arviset, C., Barbarisi, I., de La Calle, I., et al. 2008, in Astronomical Society of the Pacific Conference Series, Vol. 394, Astronomical Data Analysis Software and Systems XVII, ed. R. W. Argyle, P. S. Bunclark, & J. R. Lewis, 227
Bayo, A., Rodrigo, C., Barrado Y Navascués, D., et al. 2008, A&A, 492, 277
Bevington, P. R. & Robinson, D. K. 1992, Data reduction and error analysis for the physical sciences
Bjorkman, J. E. 1997, in Lecture Notes in Physics, Berlin Springer Verlag, Vol. 497, Stellar Atmospheres: Theory and Observations, ed. J. P. De Greve, R. Blomme, & H. Hensberge, 239
Bjorkman, J. E. & Carciofi, A. C. 2005, in Astronomical Society of the Pacific Conference Series, Vol. 337, The Nature and Evolution of Disks Around Hot Stars, ed. R. Ignace & K. G. Gayley, 75
Carciofi, A. C. 2011, in IAU Symposium, Vol. 272, Active OB Stars: structure, evolution, mass loss, ed. C. Neiner, G. Wade, G. Meynet, & G. Peters, 325–336
Carciofi, A. C. & Bjorkman, J. E. 2006, ApJ, 639, 1081
Carciofi, A. C. & Bjorkman, J. E. 2008, ApJ, 684, 1374
Carciofi, A. C., Okazaki, A. T., Le Bouquin, J.-B., et al. 2009, A&A, 504, 915
Casares, J. & Jonker, P. G. 2014, Space Sci. Rev., 183, 223
Cotton, W. D. 2008, PASP, 120, 439
Cutri, R. M. & et al. 2014, VizieR Online Data Catalog, 2328, 0
Cyr, I. H., Jones, C. E., Panoglou, D., Carciofi, A. C., & Okazaki, A. T. submitted, MNRAS
Delaa, O., Stee, P., Meilland, A., et al. 2011, A&A, 529, A87
Donati, J.-F., Catala, C., Landstreet, J. D., & Petit, P. 2006, in Astronomical Society of the Pacific Conference Series, Vol. 358, Astronomical Society of the Pacific Conference Series, ed. R. Casini & B. W. Lites, 362
Dougherty, S. M. & Taylor, A. R. 1992, Nature, 359, 808
Dougherty, S. M., Taylor, A. R., & Clark, T. A. 1991a, AJ, 102, 1753
Dougherty, S. M., Taylor, A. R., & Waters, L. B. F. M. 1991b, A&A, 248, 175
Ducati, J. R. 2002, VizieR Online Data Catalog, 2237, 0
Dulaney, N., Richardson, N. D., Gerhartz, C. J., et al. 2017, ArXiv e-prints
Egan, M. P., Price, S. D., Kraemer, K. E., et al. 2003, Air Force Research Laboratory Technical Report AFRL-VS-TR-2003-1589 (Washington: GPO), available as VizieR Online Data Catalog, 5114
Espinosa Lara, F. & Rieutord, M. 2011, A&A, 533, A43
Fitzpatrick, E. L. 1999, PASP, 111, 63
Foreman-Mackey, D., Hogg, D. W., Lang, D., & Goodman, J. 2013, PASP, 125, 306
Frémat, Y., Zorec, J., Hubert, A.-M., & Floquet, M. 2005, A&A, 440, 305
Gies, D. R., Bagnuolo, Jr., W. G., Ferrara, E. C., et al. 1998, ApJ, 493, 440
Greisen, E. W. 2003, Information Handling in Astronomy - Historical Vistas, 285, 109
Harmanec, P. 1988, Bulletin of the Astronomical Institutes of Czechoslovakia, 39, 329
Harmanec, P. 2002, in Astronomical Society of the Pacific Conference Series, Vol. 279, Exotic Stars as Challenges to Evolution, ed. C. A. Tout & W. van Hamme, 221
Haubois, X., Carciofi, A. C., Rivinius, T., Okazaki, A. T., & Bjorkman, J. E. 2012, ApJ, 756, 156
Helou, G. & Walker, D. W., eds. 1988, Infrared astronomical satellite (IRAS) catalogs and atlases. Volume 7: The small scale structure catalog, Vol. 7, 1–265
Hoffleit, D. & Jaschek, C. . 1991, The Bright star catalogue
Høg, E., Fabricius, C., Makarov, V. V., et al. 2000, A&A, 357, 367
Ishihara, D., Onaka, T., Kataza, H., et al. 2010, A&A, 514, A1
Klement, R., Carciofi, A. C., & Rivinius, T. 2017, in The B[e] Phenomenon: Forty Years of Studies, in press, ed. A. Miroshnichenko, S. Zharikov, & D. Korčáková, Astronomical Society of the Pacific Conference Series
Klement, R., Carciofi, A. C., Rivinius, T., et al. 2015, A&A, 584, A85
Koubský, P., Kotková, L., & Votruba, V. 2011, Journal of Physics Conference Series, 328, 012026
Koubský, P., Kotková, L., Votruba, V., Šlechta, M., & Dvořáková, Š. 2012, A&A, 545, A121
Kovács, A. 2008, in Society of Photo-Optical Instrumentation Engineers (SPIE) Conference Series, Vol. 7020, Society of Photo-Optical Instrumentation Engineers (SPIE) Conference Series, 1
Kraus, S., Monnier, J. D., Che, X., et al. 2012, ApJ, 744, 19
Krtička, J., Owocki, S. P., & Meynet, G. 2011, A&A, 527, A84
Kurucz, R. L. 1979, ApJS, 40, 1
Lee, U., Osaki, Y., & Saio, H. 1991, MNRAS, 250, 432
Lesh, J. R. 1968, ApJS, 17, 371
Maranon di Leo, C., Colombo, E., & Ringuelet, A. E. 1994, A&A, 286
Mason, B. D., ten Brummelaar, T., Gies, D. R., Hartkopf, W. I., & Thaller, M. L. 1997, AJ, 114, 2112

Meade, M. R., Whitney, B. A., Babler, B. L., et al. 2012, in American Institute of Physics Conference Series, Vol. 1429, American Institute of Physics Conference Series, ed. J. L. Hoffman, J. Bjorkman, & B. Whitney, 226–229
Meilland, A., Stee, P., Vannier, M., et al. 2007, A&A, 464, 59
Mermilliod, J.-C. & Mermilliod, M. 1994, Catalogue of Mean UBV Data on Stars
Mon, M., Suzuki, M., Moritani, Y., & Kogure, T. 2013, PASJ, 65
Motch, C., Lopes de Oliveira, R., & Smith, M. A. 2015, ApJ, 806, 177
Moultaka, J., Ilovaisky, S. A., Prugniel, P., & Soubiran, C. 2004, PASP, 116, 693
Neiner, C., de Batz, B., Cochard, F., et al. 2011, AJ, 142, 149
Nemravová, J., Harmanec, P., Koubský, P., et al. 2012, A&A, 537, A59
Okazaki, A. T. 2001, PASJ, 53, 119
Oudmaijer, R. D. & Parr, A. M. 2010, MNRAS, 405, 2439
Panoglou, D., Carciofi, A. C., Vieira, R. G., et al. 2016, MNRAS, 461, 2616
Perley, R. A. & Butler, B. J. 2013, ApJS, 204, 19
Perryman, M. A. C., Lindegren, L., Kovalevsky, J., et al. 1997, A&A, 323, L49
Peters, G. J., Gies, D. R., Grundstrom, E. D., & McSwain, M. V. 2008, ApJ, 686, 1280
Peters, G. J., Pewett, T. D., Gies, D. R., Touhami, Y. N., & Grundstrom, E. D. 2013, ApJ, 765, 2
Peters, G. J., Wang, L., Gies, D. R., & Grundstrom, E. D. 2016, ApJ, 828, 47
Porter, J. M. 1999, A&A, 348, 512
Quirrenbach, A., Bjorkman, K. S., Bjorkman, J. E., et al. 1997, ApJ, 479, 477
Rivinius, T., Carciofi, A. C., & Martayan, C. 2013, A&A Rev., 21, 69
Rivinius, T., de Wit, W. J., Demers, Z., Quirrenbach, A., & the VLTI Science Operations Team. 2016, ArXiv e-prints 1602.03457
Rivinius, T., Štefl, S., & Baade, D. 2006, A&A, 459, 137
Roberts, Jr., L. C., Turner, N. H., & ten Brummelaar, T. A. 2007, AJ, 133, 545
Savage, B. D. & Mathis, J. S. 1979, ARA&A, 17, 73
Secchi, A. 1866, Astronomische Nachrichten, 68, 63
Silaj, J., Jones, C. E., Carciofi, A. C., et al. 2016, ApJ, 826, 81
Siringo, G., Kreysa, E., Kovács, A., et al. 2009, A&A, 497, 945
Slettebak, A. 1982, ApJS, 50, 55
Stee, P., Delaa, O., Monnier, J. D., et al. 2012, A&A, 545, A59
Štefl, S. & Rivinius, T. 2005, Publications of the Astronomical Institute of the Czechoslovak Academy of Sciences, 93, 1
Su, K. Y. L., Rieke, G. H., Stansberry, J. A., et al. 2006, ApJ, 653, 675
Taylor, A. R., Dougherty, S. M., Waters, L. B. F. M., & Bjorkman, K. S. 1990, A&A, 231, 453
Taylor, A. R., Waters, L. B. F. M., Lamers, H. J. G. L. M., Persi, P., & Bjorkman, K. S. 1987, MNRAS, 228, 811
Tycner, C., Lester, J. B., Hajian, A. R., et al. 2005, ApJ, 624, 359
van Leeuwen, F. 2007, A&A, 474, 653
Vieira, R. G., Carciofi, A. C., & Bjorkman, J. E. 2015, MNRAS, 454, 2107
Vieira, R. G., Carciofi, A. C., Bjorkman, J. E., et al. 2017, MNRAS, 464, 3071
von Zeipel, H. 1924, MNRAS, 84, 665
Waters, L. B. F., Marlborough, J. M., van der Veen, W. E. C., Taylor, A. R., & Dougherty, S. M. 1991, A&A, 244, 120
Waters, L. B. F. M., Boland, W., Taylor, A. R., van de Stadt, H., & Lamers, H. J. G. L. M. 1989, A&A, 213, L19
Wendker, H. J., Altenhoff, W. J., & Thum, C. 2000, Astronomische Nachrichten, 321, 157
Wheelwright, H. E., Bjorkman, J. E., Oudmaijer, R. D., et al. 2012, MNRAS, 423, L11
Zagury, F. 2013, Astronomische Nachrichten, 334, 1107
Zorec, J. & Briot, D. 1997, A&A, 318, 443

A&A–29932JN, *Online Material p 19*

Table 2. VLA Calibration Sources.

Source	α(J2000.0)	δ(J2000.0)	Date	ν_0 (MHz)	Flux Density (Jy)
J0102+5824[a]	01 02 45.7624	58 24 11.137	21-OCT-2010	4.894	1.321±0.004
			21-OCT-2010	5.022	1.347±0.004
			30-OCT-2010	8.394	1.965±0.006
			30-OCT-2010	8.522	1.969±0.005
			31-OCT-2010	8.394	1.937±0.003
			31-OCT-2010	8.522	1.948±0.003
			30-OCT-2010	22.394	2.28±0.04
			30-OCT-2010	22.522	2.26±0.03
			31-OCT-2010	22.394	2.08±0.02
			31-OCT-2010	22.522	2.09±0.01
			30-OCT-2010	43.342	2.03±0.10
			30-OCT-2010	43.470	2.04±0.10
			31-OCT-2010	43.342	1.82±0.04
			31-OCT-2010	43.470	1.82±0.04
3C48[b]	01 37 41.2994	+33 09 35.132	11-OCT-2010	4.895	5.3854*
			12-OCT-2010	4.895	5.3855*
			21-OCT-2010	4.895	5.3857*
			31-OCT-2010	4.895	5.3859*
			15-OCT-2010	8.395	3.2074*
			30-OCT-2010	8.395	3.2080*
			31-OCT-2010	8.395	3.2081*
			15-OCT-2010	22.395	1.2422*
			30-OCT-2010	22.395	1.2429*
			31-OCT-2010	22.395	1.2430*
			15-OCT-2010	43.215	0.6739*
			30-OCT-2010	43.343	0.6728*
			31-OCT-2010	43.343	0.6728*
J0349+4609[c]	03 49 18.7416	46 09 59.658	31-OCT-2010	8.394	0.5802±0.0005
			31-OCT-2010	8.522	0.5772±0.0005
			31-OCT-2010	22.394	0.410±0.002
			31-OCT-2010	22.522	0.407±0.002
			31-OCT-2010	43.342	0.335±0.005
			31-OCT-2010	43.470	0.333±0.006
J0359+5057[c]	03 59 29.7473	50 57 50.162	11-OCT-2010	4.894	8.56±0.02
			11-OCT-2010	5.022	8.71±0.02
J0403+2600[d]	04 03 05.5860	26 00 01.503	31-OCT-2010	4.894	2.344±0.003
			31-OCT-2010	5.150	2.357±0.004
			15-OCT-2010	8.394	2.190±0.003
			15-OCT-2010	8.650	2.187±0.003
			15-OCT-2010	22.394	1.55±0.01
			15-OCT-2010	22.650	1.56±0.01
			15-OCT-2010	43.214	1.15±0.04
			15-OCT-2010	43.470	1.15±0.04
J2311+4543[e]	23 11 47.4090	45 43 56.016	31-OCT-2010	8.394	0.602±0.001
			31-OCT-2010	8.650	0.605±0.001
			31-OCT-2010	22.394	0.525±0.006
			31-OCT-2010	22.650	0.531±0.007
			31-OCT-2010	43.342	0.43±0.01
			31-OCT-2010	43.598	0.43±0.01
J2322+5057[e]	23 22 25.9822	50 57 51.964	12-OCT-2010	4.894	1.251±0.008
			12-OCT-2010	4.894	1.245±0.008

Notes.
[(*)] Adopted flux density, based on Perley & Butler (2013) [(a)] Secondary gain calibrator for γ Cas. [(b)] Absolute flux density and bandpass calibrator. [(c)] Secondary gain calibrator for ψ Per. [(d)] Secondary gain calibrator for η Tau. [(e)] Secondary gain calibrator for EW Lac. For 3C48, the flux density S_ν as a function of frequency was taken to be $\log(S_\nu) = 1.3332 - 0.7665(\log(\nu)) - 0.1981(\log(\nu))^2 + 0.0638(\log(\nu))^3$, where $\nu_{\rm GHz}$ is the frequency expressed in GHz.

A&A–29932JN, *Online Material p 20*

Table 3. Deconvolved image characteristics for the new VLA Data.

Source	λ [cm]	$\theta_{\rm FWHM}$ [arcsec]	PA [degrees]	rms [μJy beam^{-1}]
γ Cas	6.0	5.4×4.0	−59.3	11.0
γ Cas*	3.5	2.9×2.3	−43.6	16.0
γ Cas*	1.3	1.1×0.89	−29.6	56.4
γ Cas*	0.7	0.63×0.51	−33.7	156
ψ Per	6.0	6.7×4.7	+88.7	12.3
ψ Per	3.5	2.6×2.3	+9.8	21.9
ψ Per	1.3	1.1×1.0	+12.4	83.5
ψ Per	0.7	0.67×0.55	+29.7	252
EW Lac	6.0	6.3×4.6	−89.6	11.7
EW Lac	3.5	2.7×2.2	+35.1	23.4
EW Lac	1.3	1.2×0.9	+30.6	76.5
EW Lac	0.7	0.60×0.53	+57.0	275
η Tau	6.0	4.6×4.1	−3.2	9.75
η Tau	3.5	2.7×2.2	−2.5	23.9
η Tau	1.3	1.0×0.9	+14.9	91.1
η Tau	0.7	0.62×0.52	+56.9	297.5

Notes.
(*) For γ Cas, observations from 2010 October 30 and 31 were combined to make the final maps.

Appendix F

Disk-loss and disk-renewal phases in classical Be stars. II. Constrating with stable and variable disks

The Astrophysical Journal, 786:120 (15pp), 2014 May 10 doi:10.1088/0004-637X/786/2/120

DISK-LOSS AND DISK-RENEWAL PHASES IN CLASSICAL Be STARS. II. CONTRASTING WITH STABLE AND VARIABLE DISKS

Zachary H. Draper[1,2], John P. Wisniewski[3], Karen S. Bjorkman[4], Marilyn R. Meade[5], Xavier Haubois[6,7], Bruno C. Mota[6], Alex C. Carciofi[6], and Jon E. Bjorkman[4]
[1] Department of Physics and Astronomy, University of Victoria, 3800 Finnerty Rd, Victoria, BC V8P 5C2, Canada
[2] Herzberg Institute of Astrophysics, National Research Council of Canada, Victoria, BC V9E 2E7, Canada
[3] HL Dodge Department of Physics & Astronomy, University of Oklahoma, 440 W Brooks St, Norman, OK 73019, USA; wisniewski@ou.edu
[4] Ritter Observatory, Department of Physics & Astronomy, Mail Stop 113, University of Toledo, Toledo, OH 43606, USA; karen.bjorkman@utoledo.edu, jon@physics.utoledo.edu
[5] Space Astronomy Lab, University of Wisconsin-Madison, 1150 University Avenue, Madison, WI 53706, USA; meade@astro.wisc.edu
[6] Instituto de Astronomia, Geofísica e Ciências Atmosféricas, Universitária de São Paulo, Rua do Matão 1226, Cidade Universitária, 05508-900 São Paulo, SP, Brazil; xhaubois@astro.iag.usp.br, carciofi@usp.br
[7] Sydney Institute for Astronomy, School of Physics, University of Sydney, NSW 2006, Australia
Received 2013 December 6; accepted 2014 March 18; published 2014 April 24

ABSTRACT

Recent observational and theoretical studies of classical Be stars have established the utility of polarization color diagrams (PCDs) in helping to constrain the time-dependent mass decretion rates of these systems. We expand on our pilot observational study of this phenomenon, and report the detailed analysis of a long-term (1989–2004) spectropolarimetric survey of nine additional classical Be stars, including systems exhibiting evidence of partial disk-loss/disk-growth episodes as well as systems exhibiting long-term stable disks. After carefully characterizing and removing the interstellar polarization along the line of sight to each of these targets, we analyze their intrinsic polarization behavior. We find that many steady-state Be disks pause at the top of the PCD, as predicted by theory. We also observe sharp declines in the Balmer jump polarization for later spectral type, near edge-on steady-state disks, again as recently predicted by theory, likely caused when the base density of the disk is very high, and the outer region of the edge-on disk starts to self absorb a significant number of Balmer jump photons. The intrinsic V-band polarization and polarization position angle of γ Cas exhibits variations that seem to phase with the orbital period of a known one-armed density structure in this disk, similar to the theoretical predictions of Halonen & Jones. We also observe stochastic jumps in the intrinsic polarization across the Balmer jump of several known Be+sdO systems, and speculate that the thermal inflation of part of the outer region of these disks could be responsible for producing this observational phenomenon. Finally, we estimate the base densities of this sample of stars to be between $\approx 8 \times 10^{-11}$ and $\approx 4 \times 10^{-12}$ g cm^{-3} during quasi steady state periods given there maximum observed polarization.

Key words: circumstellar matter – stars: individual (pi Aquarii, 60 Cygni, 48 Librae, psi Persei, phi Persei, 28 Cygni, 66 Ophiuchi, gamma Casseopia, omega Orionis, FY CMa, 59 Cyg)

Online-only material: color figures, machine-readable tables

1. INTRODUCTION

Classical Be stars are a subset of B-type main sequence stars which are characterized by their rapid rotational velocities ranging from 60% to 100% of their critical rate (Rivinius et al. 2013). They have a geometrically flattened decretion disk that is fed by material from the stellar photosphere as diagnosed from studies of their optical/IR emission lines, polarization, and interferometric signatures (see, e.g., Porter & Rivinius 2003; Stee 2011). A large volume of observations suggest the kinematic properties of these gas disks is best represented by near Keplerian rotation (Hummel & Vrancken 2000; Meilland et al. 2007; Pott et al. 2010; Wheelwright et al. 2012; Kraus et al. 2012). For the most up to date review of Classical Be stars, see Rivinius et al. (2013).

As summarized in Carciofi (2011), the viscous decretion disk model developed by Lee et al. (1991) can explain many of the observational signatures of Be disks, although other models have been explored to explain the structure of these disks (Bjorkman & Cassinelli 1993; Cassinelli et al. 2002; Brown et al. 2008). One key unanswered question in the study of Be disks is what mechanism(s) are responsible for injecting material into these disks. Non-radial pulsations have been suggested to be one contributing factor to supplying material to some of these disks (Cranmer 2009; Rivinius et al. 1998; Neiner et al. 2002), while periastron passage of binary companions may contribute in other systems such as δ Scorpii (Miroshnichenko et al. 2001, 2003). This scenario for δ Scorpii is now questionable given the disk's growth prior to the periastron passage of 2011 (Miroshnichenko et al. 2013). Nonetheless, binarity may play a role in the phenomenon and disk variability. For example, the source of material and angular momentum in non-classical Be stars can be the result of a red giant phase binary transferring material to create a Be+sdO system Gies et al. (1998). Characterizing the evolution of Be stars' mass-loss rates is another promising approach to constrain the disk-feeding mechanism. On short time-scales, Carciofi et al. (2007) noted polarimetric variability in Archernar likely arising from injections of discrete blobs of mass into the inner disk, that subsequently circularize into rings. Studying longer duration disk-loss and disk-regeneration events (Underhill & Doazan 1982; Doazan et al. 1983; Clark et al. 2003; Vinicius et al. 2006; Haubois et al. 2012), including the time-scales (Wisniewski et al. 2010) and statistical frequency (McSwain et al. 2008, 2009) of these episodes, is another way to diagnose the mechanism feeding Be disks.

Polarimetry has been used to study the Be phenomenon for both individual Be stars (Quirrenbach et al. 1997; Wood et al. 1997; Clarke & Bjorkman 1998) and larger statistical

surveys (Coyne & Kruszewski 1969; McLean & Brown 1978; Poeckert et al. 1979; Wisniewski et al. 2007a). It is widely believed that Thompson scattering (free-electron scattering) is the source of polarization in Be stars (Wood et al. 1996a, 1996b; Halonen et al. 2013). Pre- or post-scattering absorption of photons within the disk can imprint wavelength dependent signature on top of the wavelength independent Thompson scattering (Wood & Bjorkman 1995). Because the polarization across the Balmer jump traces material in the innermost regions of disks ($\sim$6 $R_\star$; Carciofi 2011; Halonen & Jones 2013a) and the V-band polarization is a tracer of the total scattering mass of the disk, studying the time evolution of the wavelength-dependence of polarization in Be stars can be used to constrain the time dependence of the mass decretion rate and the α parameter in these systems. Specifically, the slope, shape, and temporal evolution of polarization color diagrams (PCDs) observed in Be systems (Draper et al. 2011) have been theoretically reproduced, for the first time, by time-dependent radiative transfer models in which the mass decretion rate, α parameter, and inclination angle are the primary variables (Haubois et al. 2014). In addition to density changes caused by changes in the mass decretion rate, it has been suggested that PCD diagram loops can also be produced by one-armed density perturbations (Halonen & Jones 2013b).

In this paper, we implement the PCD diagram diagnostic developed in Draper et al. (2011) on a broader sample of Be stars, including systems showing evidence of experiencing disk-loss events and those whose disks appear roughly stable over time. We describe the data sample in Section 2, and discuss the techniques we used to remove the interstellar polarization (ISP) component from each data set in Section 3. We discuss the temporal evolution of each Be disk in PCD diagram parameter space in Section 4, and also detail evidence of variability in the disk position angle (P.A.) in select systems. Finally, we summary the major results of this manuscript in Section 5.

2. OBSERVATIONS AND DATA REDUCTION

The spectropolarimetric data analyzed in this study were obtained by the University of Wisconsin's HPOL spectropolarimeter, mounted on the 0.9 m Pine Bluff Observatory (PBO) telescope. Data obtained before 1995 were recorded using a dual Reticon array detector spanning the wavelength range of 3200–7600 Å with a spectral resolution of 25 Å (Wolff et al. 1996). Beginning in 1995, HPOL's detector was upgraded to a 400 × 1200 pixel CCD camera that provided coverage from 3200 to 6020 Å at a resolution of 10 Å and 5980–10,500 Å at a resolution of 7 Å (Nordsieck & Harris 1996). Further details about HPOL can be found in Nook (1990), Wolff et al. (1996), and Harries et al. (2000).

Data obtained by HPOL were reduced and calibrated using REDUCE, a spectropolarimetric software package developed by the University of Wisconsin-Madison (see Wolff et al. 1996). Routine monitoring of unpolarized standard stars at PBO has enabled the instrumental polarization to be carefully calibrated. The residual instrumental systematic errors depend mildly on the date of the observations, but range from 0.027% to 0.095% in the U-band, 0.005%–0.020% in the V-band, and 0.007%–0.022% in the I-band. At the current time, HPOL data from 1989 to 2000 are available on the STScI MAST archive.[8]

[8] See archive Web site for more up to date details: http://archive.stsci.edu/hpol/

HPOL spectroscopic data were not flux calibrated to an absolute level because of nonphotometric skies typically present during the observations. To mitigate any relative flux offsets between red and blue grating data obtained on the same night, we applied a constant multiplicative factor to the grating with the lower flux in an observation, and then merged the red and blue grating bandpasses.

When available, HPOL observations were supplemented with observations from the Wisconsin Ultraviolet Photo-Polarimeter Experiment (WUPPE) from both the Astro-1 and Astro-2 missions flown on the Space Shuttles Columbia and Endeavor, respectively. WUPPE is a 0.5 m telescope with a spectropolarimeter which simultaneously obtained spectra and polarization from 1500 to 3200 Å with a resolution of about 16 Å. For a more detailed explanation of the instrument see Nordsieck et al. (1994), and Clayton et al. (1997) for a detailed description of the pre-flight and in-flight calibrations.

Additional spectroscopic observations of 66 Oph obtained with the fiber-fed echelle spectrograph mounted on the Ritter Observatory 1 m telescope were also analyzed. These observations were obtained with the default spectrograph setup, yielding $R \sim 26{,}000$. These data were reduced using standard IRAF techniques. A summary of the data used for each star in this study is in Table 1.

3. DATA ANALYSIS

3.1. Interstellar Polarization

Before any robust interpretations of polarization from our classical Be stars can be made, the ISP must be removed. The ISP is due to a dichroic scattering in the interstellar medium (hereafter, ISM) imprinting itself on the intrinsic polarization of the science target. There are three common techniques which are used to characterize the ISP: field stars, emission lines, and utilizing the wavelength dependence of the observed polarization (Wisniewski et al. 2007b). In this paper, we take advantage of the field star and wavelength dependence to diagnose the ISP for our target stars and try to present an improved and streamlined process for determining ISP for spectropolarimetry from long surveys, like HPOL.

3.1.1. 48 Lib

Using our IDL routines, the calibrated HPOL data were processed in a manner similar to the ISP removal process in Quirrenbach et al. (1997) and Wisniewski et al. (2010) to constitute a standardized ISP determination process. We measure the raw Johnson V-band polarization measurements from the spectropolarimetry using Equations (1) and (2),

$$\%P = \int_{\lambda_1}^{\lambda_2} \frac{P(\lambda)F(\lambda)w(\lambda)}{F(\lambda)w(\lambda)} \quad (1)$$

$$\%P_{\rm err} = \frac{1}{\sqrt{n}} \int_{\lambda_1}^{\lambda_2} d\lambda \frac{{\rm Err}(\lambda)F(\lambda)w(\lambda)}{F(\lambda)w(\lambda)}, \quad (2)$$

where $P(\lambda)$ is a Stokes parameter of the spectropolarimetry (Q, U, or P), $F(\lambda)$ is the relative flux, and $w(\lambda)$ is the filter function desired to weight the data. The error measurement is divided by a Poisson statistic, where n is the total number of data points within the wavelength range. This is consistent with the *pfil* command in the REDUCE software code developed for HPOL (Wood et al. 1996a). These raw V-band polarization data are compiled in Table 2 for every target in our sample.

Table 1
Target Star Summary

Star	Spectral Type	$T_{\rm eff}$	Inclination	No. of HPOL Reticon Nights	No. of HPOL CCD Nights	WUPPE
48 Libra	B3Ve	17645 ± 554[1]	~ 90[7,8]	13	7	Astro-2
ψ Persei	B5Ve	15767 ± 509[1]	75 ± 8[4]; 75[6]	9	10	Astro-2
ϕ Persei	B2Vpe	25556 ± 659[1]	84[5]; 72[6]	15	11	Astro-2
28 Cygni	B2.5Ve	18353 ± 516[1]	64[6]	4	31	N/A
66 Ophiuchi	B2Ve	21609 ± 523[1]	48[6]	7	3	N/A
γ Casseopia	B0.5IVpe	26431 ± 618[1]	44[5]; 76[6]	9	14	N/A
ω Orionis	B3IIIe	20200[2]	N/A	10	8	N/A
FY Canis Majoris	B1II	21750 ± 655[1]	55[6]	9	14	N/A
59 Cygni	B1.5Vnne	21750 ± 655[1]	72[5] 73[6]	10	8	Astro-2
60 Cygni	B1Ve	27000[3]	N/A	2	27	N/A
π Aquarii	B1Ve	26061 ± 736[1]	33.6[6]	53	57	Astro-1

Notes. A summary of the spectropolarimetric data analyzed in this paper. Spectral types were adopted from SIMBAD, except for 48 Lib which is identified as B3 in a more detailed study (Stefl et al. 2012). Sources for the effective temperature include [1]Frémat et al. (2005), [2]Cantanzaro (2013), and [3]Koubský et al. (2000). Sources for the disk inclinations include [4]Delaa et al. (2011), [5]Touhami et al. (2013), [6]Frémat et al. (2005), [7]Rivinius et al. (2006), [8]Stefl et al. (2012). The number of observations used for each star during the survey is listed by which detector was used. If the target was observed with the Wisconsin Ultraviolet Photo-Polarimeter Experiment (WUPPE), the mission which took the data is listed.

Table 2
Raw HPOL Data

Target Name	Julian Date	%Q (V-band)	%U (V-band)	%Err	Hα EW
48 Lib	2447679.2	−0.614	−0.497	0.005	−21.5
48 Lib	2448003.2	−0.544	−0.591	0.003	−19.7
48 Lib	2448012.2	−0.575	−0.530	0.006	−20.0

Notes. The raw V-band polarization and Hα equivalent width is presented for every observation of all of our target stars.

(This table is available in its entirety in a machine-readable form in the online journal. A portion is shown here for guidance regarding its form and content.)

When they are not spatially resolved, Be systems exhibit linear polarization along a single, preferred P.A., defined by the orientation of the disk's major axis on the sky. We fit a linear trend through the data in the QU plane to determine this mean disk polarization axis (Figure 1, left column). Then we rotated the entire data set by the mean intrinsic disk angle, thereby putting them into a rotated (Q' U') space. The ISP perpendicular component ($P_\perp$) to the intrinsic polarization, i.e., along the U' axis, in this regime is independent of the intrinsic disk polarization. The Q' axis is comprised of the parallel component of ISP ($P_\parallel$) plus the intrinsic disk polarization.

The U' axis for all observations were then combined with an error weighted mean (Figure 1, middle column). To extend the wavelength coverage of these data, which aids our effort to robustly model the wavelength dependent ISP signature described below, we supplemented our target stars with archival WUPPE data where possible (Table 1). These archival UV data were rotated by the same intrinsic disk angle determined for each star and merged with the optical U' spectropolarimetry. We then fit these U' data with a modified version of the empirical Serkowski law (Serkowski et al. 1975; Wilking et al. 1982),

$$P(\lambda) = P_\perp \exp\left[-K \ln^2(\lambda_{\rm max}/\lambda)\right] \quad (3)$$

$$K = (1.68 \times 10^{-4})(\lambda_{\rm max}) - 0.002 \quad (4)$$

to determine the perpendicular component of ISP. $\lambda_{\rm max}$ can be determined by the wavelength of the Serkowski curves' inflection point at the peak amplitude of ISP. This characteristic Serkowski profile stems from dichroic absorption of the ISM where certain wavelengths are preferentially scattered from dust grains aligned with the galactic magnetic field.

Following the methodology used in Quirrenbach et al. (1997), we compute the ISP$_\parallel$ component by assuming that the P.A. of the total ISP is sufficiently represented by nearby field stars to each of our targets, and then using simple geometry to extract the magnitude of the ISP$_\parallel$ component. For each of our science targets, we generated a field star P.A. estimate (P.A.$_{\rm fs}$) by selecting stars from the Heiles (2000) catalog in the vicinity of each science target (3° maximum separation and within 150 pc of the target) that exhibit no conspicuous intrinsic polarization (Table 3). We separated the V-band polarization for each field star into Q and U components, computed an error weighted mean, and finally used this error weighted mean to compute the final field star P.A. for each science target (Table 3). The error in this P.A. was computed using the standard deviation of QU:

$$\text{P.A.} = 0.5 \tan^{-1}\left(\frac{U}{Q}\right) \quad (5)$$

$$\text{P.A.}_{\rm err} = \frac{\sigma UQ + \sigma QU}{U^2 + Q^2}. \quad (6)$$

Given the amplitude of ISP$_\perp$ and the field star P.A., we compute the amplitude of ISP$_\parallel$ using simple geometry:

$$P_\parallel = \frac{P_\perp}{\tan(2\text{P.A.}_{\rm fs})}. \quad (7)$$

Finally, the total ISP is computed using the amplitude of ISP$_\perp$ and ISP$_\parallel$:

$$P_{\rm ISP} = \sqrt{P_\perp^2 + P_\parallel^2}. \quad (8)$$

With the $P_{\rm ISP}$, $\lambda_{\rm max}$ and P.A.$_{\rm fs}$ the ISP characterization is complete. As a check of the accuracy of our ISP removal, we plot the resultant intrinsic polarization on a Stokes QU diagram and confirm the data's trend passes through the origin (Figures 1(A)–(C), right column) with 48 Lib shown in Figure 1(A). The final ISP values, along with the parallel and perpendicular components, are tabulated in Table 4 for each science star. For 48 Lib, our final ISP parameters of $P_{\rm max} = 0.86\%$ and $\theta = 93°$ are consistent with the ISP P.A. derived from previous field star (82 ± 22) and Hα line depolarization (85 ± 3) studies

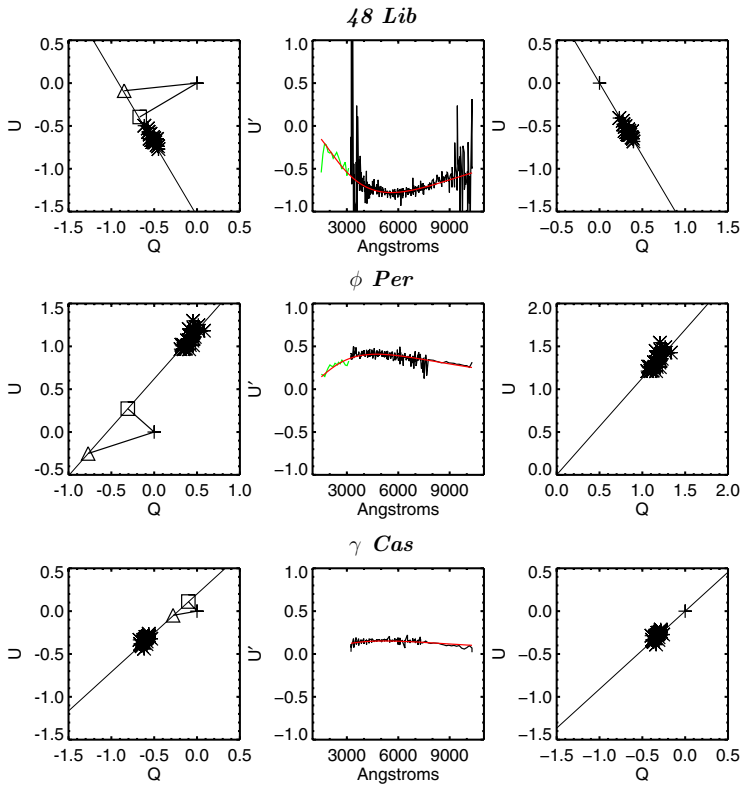

Figure 1. Left panel depicts the raw *V*-band polarization for a target star plotted on a Stokes QU diagram along with the intrinsic disk position angle vector overlaid. Either the best fit linear regression or the multi-epoch polarization change across the Balmer jump was used to define the position angle of the disk major axis. The $ISP_{\perp}$ (square) and ISP_{total} (triangle) vectors are also overlaid. The center panel depicts the wavelength dependence of the U' data (WUPPE data shown in green, HPOL data shown in black), formed by rotating the *V*-band polarization by the P.A. of the disk major axis. The best fit Serkowski law fit (red) parameterizes the $ISP_{\perp}$ and ISP λ_{max} components (Table 4).

(A color version of this figure is available in the online journal.)

(Poeckert et al. 1979) and amplitude of ISP derived from these studies (0.64%–0.73%; Poeckert et al. 1979). Removing this ISP component yields the time-dependent intrinsic polarization behavior within our data (Figure 2), which is compiled in Table 5 for all targets in our sample.

3.1.2. ϕ Per

When the intrinsic polarization angle was not well determined, the ISP removal process described in Section 3.1.1 failed, as diagnosed by the combined U' data set exhibiting a Balmer jump instead of a characteristic Serkowski curve. For ϕ Per this breakdown occurred because the source exhibited minimal variability in its intrinsic polarization levels, such that the raw data were not well fit by a linear trend on the QU diagram (see Figure 1(a)). To mitigate this, instead of using the *V*-band polarization to determine the intrinsic P.A. on the QU diagram we used the raw polarization data across the Balmer jump 3200–4000 Å. The differing opacity across the Balmer jump imprints a change in amplitude of linear polarization across the jump. Plotting the polarization across the Balmer jump in QU space helps to differentiate the intrinsic polarization of the disk, thereby allowing us to fit these data with a linear trend to derive the intrinsic disk P.A. Once the intrinsic disk P.A. was determined, we adopted the ISP P.A. of Quirrenbach et al. (1997) and determined the ISP parameters using the rest of the procedures described in Section 3.1.1. Our total ISP polarization, $P_{max} = 0.76\%$, was similar to that found by Quirrenbach et al. (1997), 0.82%. The resultant time-dependent intrinsic polarization of ϕ Per is shown in Figure 2(a) and Table 5.

3.1.3. γ Cas

Like ϕ Per, the long-term stability of γ Cas's disk necessitated use of its polarization across the Balmer jump to characterize the intrinsic disk P.A. (Figure 1(a)). We adopted the field star P.A. used by McLean & Brown (1978) and Quirrenbach et al. (1997; see Table 4). The final ISP parameters we derived, $P_{max} = 0.31\%$ and $\theta = 95^{\circ}$ (Table 4), were consistent with those derived by Quirrenbach et al. (1997), $P_{max} = 0.26\%$ and $\theta = 95^{\circ}$. The time-dependent intrinsic polarization of γ Cas is shown in Figure 2(a) and Table 5.

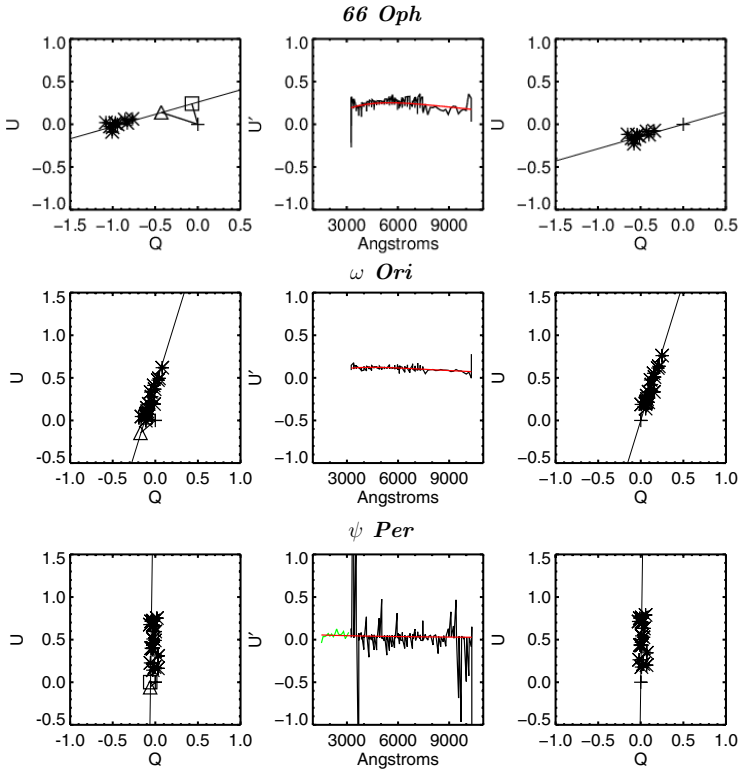

Figure 1. (Continued)

3.1.4. 66 Oph

We adopted the same ISP method used for 48 Lib on 66 Oph. After defining the major axis of the disk by fitting a linear regression to the *V*-band polarization data plotted in a QU diagram (Figure 1(b)), we determined $ISP_{\perp}$ by fitting a Serkowski law to the U' data and $ISP_{\parallel}$ from the P.A. of nearby field stars (Table 3). The final ISP parameters we derived, $P_{max} = 0.45\%$ and $\theta = 81^{\circ}$ (Table 4), were consistent with those derived by Poeckert et al. (1979) from field star and Hα line depolarization, $P_{max} = 0.51\%$–0.52% and $\theta = 82 \pm 3$–86 ± 19. The time-dependent intrinsic polarization of 66 Oph is shown in Figure 2(b) and Table 5.

3.1.5. ω Ori

ω Ori exhibited significant *V*-band polarization variability, which enabled us to determine the P.A. of the disk's major axis by fitting a linear regression to these data in the Stokes QU diagram (Figure 1(b)). While we were able to determine $ISP_{\perp}$ by fitting a Serkowski law to the U' data (middle panel, Figure 1(b); Table 4), the field star P.A. estimates for this source varied from 20 to 165 (Table 3), with an average value of $36^{\circ} \pm 9.^{\circ}7$. Previous estimates of the ISP toward ω Ori indicated that the magnitude of ISP was low (<0.05%; Poeckert et al. 1979 to ∼0.1%, McLean & Brown 1978), and the orientation of this ISP ranged from 151° (Poeckert et al. 1979) to being undetermined (McLean & Brown 1978). Our long temporal baseline of spectropolarimetric data is particularly helpful in constraining the ISP P.A. as Figures 1(b) and 2(b) indicate that ω Ori experienced disk depletion events. Because the variation in the raw *V*-band polarization (Figure 2) passes near the origin in QU space, this excludes our average field star P.A. (36°) from being a viable ISP P.A. Furthermore, an adopted ISP P.A. of 36° would cause the *V*-band polarization and Hα to have an anti-correlated trend with time. Rather the total ISP P.A. must lay in the third quadrant of the QU diagram (90°–135°). We estimate this P.A. to be ∼110°, under the assumption that our lowest polarization data captures the system in a near disk-less state, akin to the scenario considered by Wisniewski et al. (2010). Removing our estimate of the total ISP, $P_{max} = 0.23\%$ and $\theta = 110^{\circ}$, from these data yields the time-dependent intrinsic polarization shown in Figure 2(b) and Table 5.

3.1.6. ψ Per

ψ Per exhibited significant variability in its total *V*-band polarization across the time sampling of our data (Figure 1(b)), enabling us to determine the P.A. of the disk's major axis. The perpendicular component of ISP was weak and poorly constrained by a Serkowski law (middle panel, Figure 1(b)). We adopted a field star P.A. of 112°, yielding final ISP parameters

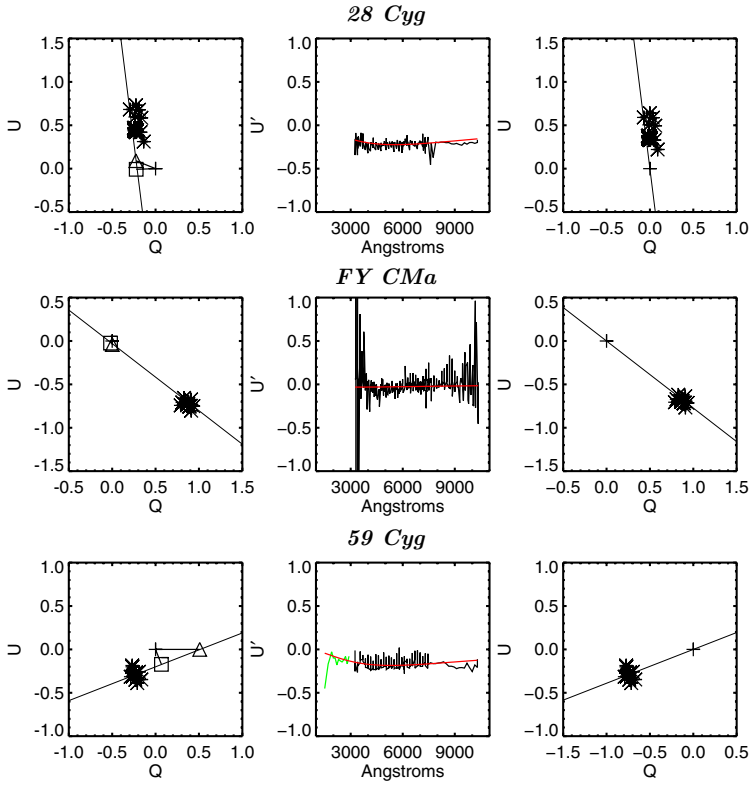

Figure 1. (Continued)

of $P_{max} = 0.09\%$ and $\theta = 112°$. These parameters are generally consistent with those determine by Poeckert et al. (1979; $P_{max} = 0.31\% \pm 0.11\%$–$0.36\% \pm 0.10\%$; $\theta = 128 \pm 13$–129 ± 10) and McLean & Brown (1978; $P_{max} = 0.4\%$ and $\theta = 135°$). However, they are finding a stronger parallel ISP component. Removing this ISP yields the time-dependent intrinsic polarization shown in Figure 2(b) and Table 5.

3.1.7. 28 Cyg

We determined the P.A. of the disk major axis of 28 Cyg by fitting the variation in its *V*-band polarization in the *QU* frame with a linear regression (Figure 1(c)). Previous studies have suggested a weak ISP along the line of sight to 28 Cyg (<0.20%, Poeckert et al. 1979; 0.1%, McLean & Brown 1978), which agrees with our new analysis. We found 28 Cyg had a very weak $ISP_{\perp}$ component (Figure 1; Table 4). Based on a field star P.A. of 79° (Table 3), we determined final ISP parameters of $P_{max} = 0.25\%$ and $\theta = 79°$. Removing this small ISP component yielded the time-dependent intrinsic polarization shown in Figure 2(c) and Table 5.

3.1.8. FY CMa

Both the raw *V*-band polarization (Figure 1(c)) and polarization across the Balmer jump were well fit with a linear regression passing near the origin. This unique situation presents substantial challenges for determining the ISP, as it either implies that the ISP component is zero or it implies that the ISP component is aligned with the intrinsic disk axis. In the latter scenario, one would only be able to robustly determine the ISP during epochs in which FY CMa experienced a complete loss of its disk (see, e.g., Wisniewski et al. 2010). For the purposes of this paper we have assumed the ISP component is small ($P_{max} = 0.04\%$ and $\theta = 136°$). The nominal field star P.A., 136° (Table 3), is ∼20° from the P.A. of the disk major axis, which supports our assumption that the ISP toward FY CMa is not parallel with the intrinsic P.A. The time-dependent intrinsic polarization for FY CMa is shown in Figure 2(c) and Table 5.

3.1.9. 59 Cyg

Like ϕ Per and γ Cas, the long-term stability of 59 Cyg's *V*-band polarization (see Figure 1(c)) forced us to measure the change in polarization across the Balmer jump to characterize the intrinsic disk P.A. We were able to determine $ISP_{\perp}$ by fitting a Serkowski law to the UV and optical U' data (Figure 1(c)); however, the total ISP P.A. suggested by field stars surrounding 59 Cyg ($29° \pm 35°$; Table 3) is unlikely to be correct as this lays parallel to the intrinsic disk P.A. This could only be plausible if the $ISP_{\perp}$ was instead zero. We therefore were unable to

Table 3
Field Star Polarization Data

Target Star	Field Star	Spectral Type	Distance(pc)	%Pol.	% Error	P.A.	P.A. Error
48 Lib	HD 145748	K5III	275.4	0.420	0.035	99.6	2.4
···	HD 144639	F3IV	144.5	1.060	0.048	86.7	1.3
···	HD 145153	K0III	120.0	0.760	0.036	86.3	1.4
···	HD 145897	K3III	104.7	0.310	0.035	111.8	3.2
···	AVG	···	···	···	···	92.93	10.73
ϕ Per	···	···	···	···	···	···	···
ψ Per	HD 23049	K4III	125.9	0.500	0.032	113	1.8
···	HD 21278	B5V	150.0	0.480	0.120	120	7.1
···	HD 20902	F5Iab	162.0	0.410	0.120	100	8.3
···	HD 21428	B3V	168.0	0.287	0.141	127.2	13.8
···	HD 20809	B5V	169.0	0.569	0.102	104	5.1
···	AVG	···	···	···	···	112	11.1
π Aqr	HD 213119	K5III	132	0.23	0.035	110.4	4.4
···	HD 212320	G6III	87	0.39	0.017	160.0	1.2
···	HD 211924	B5III	251	1.17	0.037	140.3	0.9
···	HD 211838	B8V	120	0.46	0.035	138.8	2.2
···	HD 211304	B9	306	0.22	0.035	107.6	4.5
···	HD 211099	B6	417	0.26	0.038	119.2	4.2
···	AVG	···	···	···	···	109.22	1.61
60 Cyg	HD 198915	B6V	475	0.19	0.120	15.0	17.5
ω Ori	HD 36267	B5V	143	0.133	0.026	164.7	5.6
···	HD 37606	B8V	242	0.150	0.032	36.0	6.1
···	HD 38650	B9	352	0.134	0.023	42.0	4.9
···	HD 38900	B9	360	0.074	0.026	20.0	10.0
···	AVG	···	···	···	···	36	9.7
28 Cyg	HD 192383	G5III	109	0.190	0.030	131.2	4.5
···	HD 192934	A0V	109	0.170	0.050	71.1	8.4
···	HD 192182	G8III	113	0.080	0.030	77.3	10.6
···	HD 189751	K1III	155	0.150	0.040	63.5	7.6
···	HD 192124	A5III	156	0.070	0.030	61.6	12.1
···	HD 191046	K0III	159	0.080	0.032	80	11.3
···	HD 193636	A7III	197	0.060	0.060	3.4	26.6
···	HD 191045	K5III	229	0.130	0.032	61.0	7.0
···	HD 192745	A0V	254	0.120	0.050	86.0	11.8
···	HD 194357	B9II	316	0.440	0.032	76.0	2.1
···	HD 227421	A5III	347	0.260	0.080	94.7	8.7
···	AVG	···	···	···	···	79	35
66 Oph	HD 162177	A0	288	0.600	0.060	77.7	2.9
···	HD 162954	B7	288	0.740	0.035	75.7	1.4
···	HD 163592	B8	288	0.820	0.042	92.8	1.5
···	HD 162649	A0	302	0.960	0.073	79.5	2.2
···	HD 164097	A0	302	0.670	0.066	68.8	2.8
···	HD 162993	A0	331	0.630	0.073	73.4	3.3
···	HD 163152	A0	347	0.600	0.073	75.3	3.5
···	HD 163591	B8	347	1.030	0.055	85.8	1.5
···	AVG	···	···	···	···	81	8.5
FY CMa	HD 56094	B2IV	1645	0.310	0.100	126.4	9.2
···	HD 59612	A5I	686	0.460	0.035	159.1	2.2
···	HD 61227	F0II	391	1.140	0.040	125.0	1.0
···	AVG	···	···	···	···	136	18
59 Cyg	HD 202654	B2V	549	0.180	0.200	24.0	29.1
···	BD+44.3627	B3V	504	0.780	0.180	46.0	6.6
···	HD 198915	B6V	475	0.190	0.120	15.0	17.5
···	HD 201836	B5V	246	1.060	0.200	21.0	5.4
···	AVG	···	···	···	···	29	35

Notes. Archival *V*-band polarization data for field stars used in this manuscript, compiled from [1]Mathewson & Ford (1970) and [2]Heiles (2000), are listed. Spectral types for the field stars were obtained from SIMBAD, and distance measurements were obtained from the *Hipparcos* catalog (Perryman et al. 1997).

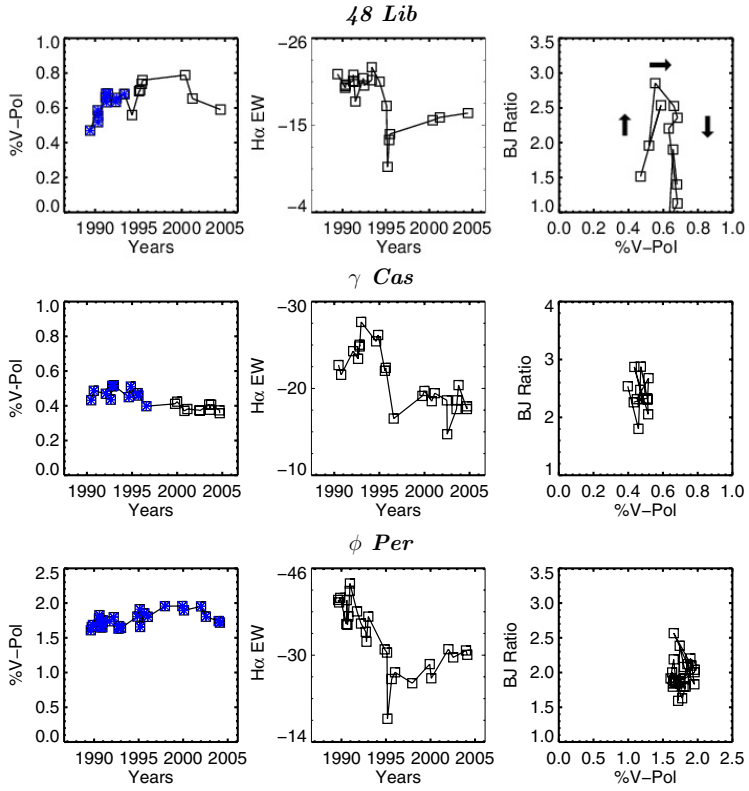

Figure 2. Time evolution of the intrinsic *V*-band polarization of the target stars are in the left panel and the Hα equivalent width (EW) are shown in the center panel. EWs measured by HPOL data are shown in squares while EWs measured from spectra obtained at Ritter Observatory are shown in triangles. The flux offset is due to HPOL not being flux calibrated. The right panel depicts the PCD for the portion of the *V*-band % Pol. data cross-marked in blue on the left panel.
(A color version of this figure is available in the online journal.)

determine a robust total ISP for 59 Cyg. As will be discussed in Section 4.5, we did explore the behavior of 59 Cyg's mostly intrinsic polarization across the Balmer jump (Figure 2(c)) assuming a total ISP around 0°. Specifically, we explored ISP parameter space about this adopted value and confirmed that, even though there is significant uncertainty in the correct total ISP P.A., this did not specifically affect the observed Balmer jump polarization discussed in that section.

3.1.10. 60 Cyg and π Aqr

Wisniewski et al. (2010) already used the total disk loss phases of 60 Cyg and π Aqr to establish well determined ISP parameters for these systems. We applied the IDL code and basic techniques used throughout this paper on these data (see Figures 1 and 2), and adopted the same total ISP P.A. as used in Wisniewski et al. (2010). This enabled us to test the effects of using different binning during the fitting process as compared to the earlier work (e.g., 60 Cyg) as well as the effects of including UV polarimetry and different binning (e.g., π Aqr). As seen in Table 4, the ISP parameters we derive are fully consistent with those reported in Wisniewski et al. (2010).

3.2. Hα Equivalent Widths

To help assess the temporal behavior of the disk systems in our sample, we computed Hα equivalent widths (EWs) from our spectropolarimetric data in the last column of Table 5. We processed HPOL flux data using IDL code that computed EWs using the trapezoid rule:

$$\mathrm{EW} = \sum_{n=\lambda_1}^{\lambda_2} \left(1 - \frac{0.5(F(n)_{\mathrm{line}} + F(n+1)_{\mathrm{line}})}{F_{\mathrm{cont}}}\right) \Delta\lambda, \quad (9)$$

where F_{cont} is the continuum flux computed from 6366 to 6456 Å and 6666 to 6756 Å. The Hα line flux was computed from 6516 to 6606 Å (λ_2 and λ_1).

Minor variations in Hα EWs can be seen in HPOL data that span the change from a Reticon to a CCD detector in 1995. These variations are not considered real, but rather are likely due to the slight change in spectral resolution achieved between the two different instrument configurations (see Section 2). A small number of archival spectroscopic observations of 66 Oph (Table 6), obtained at Ritter Observatory, were also analyzed in

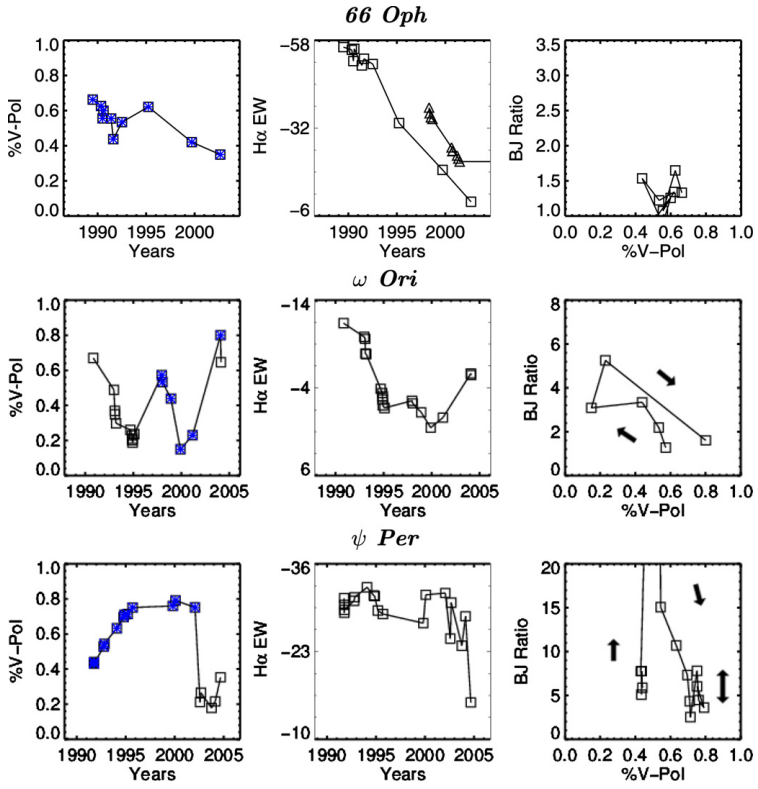

Figure 2. (Continued)

Table 4
Final Interstellar Polarization Parameters

Star	$\%P$	θ	λ_{max}	$\%P_{\perp}$	$\%P_{\parallel}$
48 Lib	0.86	93	5593	−0.78	−0.36
ϕ Per	0.76	99	4539	0.40	−0.65
γ Cas	0.31	95	3786	0.15	−0.27
66 Oph	0.45	81	5466	0.25	−0.37
ω Ori	0.23	110	4442	0.12	−0.19
ψ Per	0.09	112	528	0.065	−0.06
28 Cyg	0.25	79	5496	−0.22	−0.10
FY CMa	0.04	136	3545	−0.03	0.03
59 Cyg	0.51	0	5805	−0.18	0.47
60 Cyg	0.11	41.5	5349	0.08	0.07
π Aqr	0.50	108.7	5123	−0.45	−0.22

Notes. The final parameters for the parallel component ($\%P_{\parallel}$), perpendicular component ($\%P_{\perp}$), and net ($\%P$) interstellar polarization for each of our target stars is compiled.

this paper to supplement the HPOL data. As noted previously by Wisniewski et al. (2010), there is also a flux offset between Hα EWs computed from HPOL and Ritter data, likely owing to the different resolutions of these data. Since we are merely interested in using these data to track the long-term evolution of 66 Oph, this offset does not affect our analysis or interpretations.

Table 5
Intrinsic Polarization

Target Name	Julian Date	$\%Q$ (V-band)	$\%U$ (V-band)	%Err
48 Lib	2447679.2	0.233	−0.410	0.005
48 Lib	2448003.2	0.304	−0.504	0.003
48 Lib	2448012.2	0.273	−0.442	0.006

Notes. The intrinsic V-band polarization is presented for every observation of all of our target stars.

(This table is available in its entirety in a machine-readable form in the online journal. A portion is shown here for guidance regarding its form and content.)

4. DISCUSSION

4.1. Additional Disk-growth and Loss Phases

In Paper I of this series, we analyzed well sampled, long-term spectropolarimetric data for two classical Be stars that clearly underwent a complete disk-loss phase. In this paper, we explore the behavior of a larger sample of classical Be stars, including systems that exhibit disks that are stable over time periods of more than a decade, as well as systems that exhibit at least partial disk-loss/disk-renewal phases. While detailed modeling of each system that exhibits a non-stable disk is clearly necessary and warranted, albeit outside the scope of this paper, we discuss

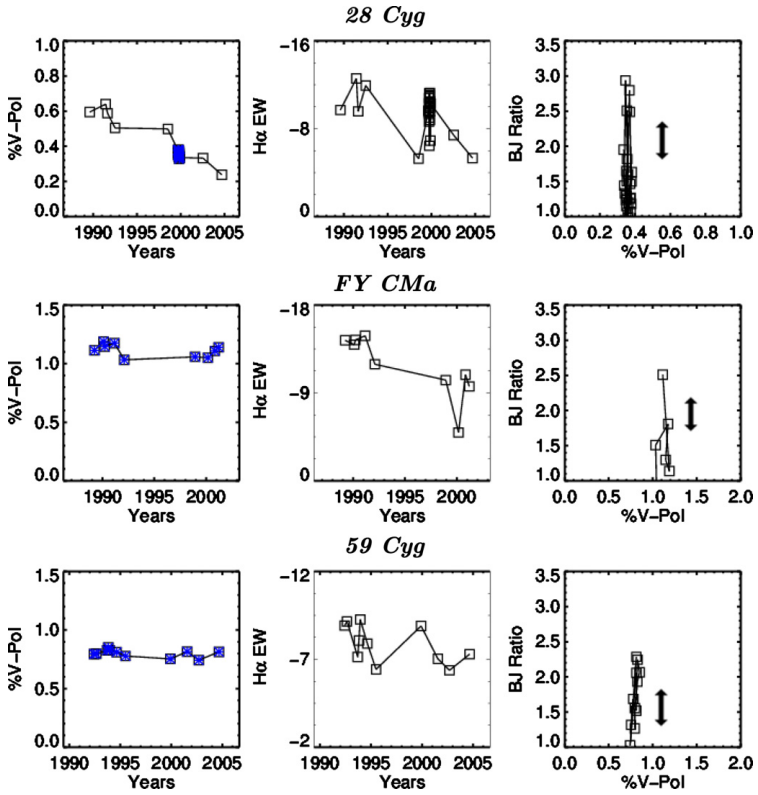

Figure 2. (Continued)

some of the basic observational properties of these systems below.

4.1.1. ψ Per

The intrinsic polarization and Hα EW of ψ Per both exhibit clear evidence of significant variability over the ∼13 yr time coverage of our data (Figure 2(b)). Throughout the early 1990s, the steady increase in the system's intrinsic polarization, lasting for ∼1400 days, accompanied by a small strengthening in its Hα EW is indicative of a growth in density and size of the disk. Although the data sampling is sparse, there is evidence that the disk generally stabilized in strength between 1995 and 2001. Figure 2(b) also exhibits a dramatic, monotonic drop in intrinsic polarization over a period of ∼190 days starting in 2002 August, along with a more gradual, time-delayed, significant decrease in Hα EW. These trends are consistent with a major inside-out clearing of significant mass from the disk (Wisniewski et al. 2010). Since a small level of both intrinsic polarization and Hα emission remained after the event, we characterize this as a incomplete disk-loss event.

Characterizing the time-scale of disk-loss events is important in order to constrain the viscosity parameter, α, assuming the disk dissipates on a viscous time-scale. Equation (19) of Bjorkman & Carciofi (2005) describes such an assumption and can be rewritten to give α as function of the diffusion timescale, $t_{\rm diff}$.

$$\alpha = (0.2\,{\rm yr}/t_{\rm diff})(r/R_\star)^{0.5}. \quad (10)$$

Assuming the bulk of the scattering events producing the observed polarization occurs at a radial distance of ∼5 $R_\star$ and the (partial) disk-loss time-scale of ∼190 days yields $\alpha \sim 0.86$ for ψ Per. This value is intermediate compared to estimates for 60 Cyg (∼0.1; Wisniewski et al. 2010) and robustly measured for 28 CMa (1 ± 0.2; Carciofi et al. 2012). Because the ψ Per disk did not completely clear out, our quoted disk-loss time-scale is a lower limit and correspondingly the quoted α parameter is an upper limit. Clearly, characterizing the viscosity parameter for a larger number of systems is required to assess whether there is a preferred parameter for most Be disks.

4.1.2. ω Ori

The overall steady decline in Hα EW strength throughout most of the 13 yr of coverage in our data set (Figure 2(b)) is indicative of a gradual, albeit incomplete, loss of the system's disk. The ∼1500 day duration decline in intrinsic V-band polarization starting at the beginning of our data set is consistent with a gradual loss of the system's disk. Mirroring the scenario observed in π Aqr reported by Wisniewski et al. (2010), the subsequent ∼1100 day long increase in intrinsic polarization is

Table 6
66 Oph Ritter Data

Julian Date	EW
2450930.9	−38.1
2450952.8	−36.4
2450999.7	−35.2
2451058.6	−34.7
2451777.6	−26.3
2451809.5	−25.2
2451814.5	−25.3
2451987.9	−23.9
2452033.8	−23.0
2452086.8	−22.1
2452105.7	−22.7
2452128.6	−22.3
2452164.5	−21.8
2452450.7	−20.5
2452461.8	−20.3
2452757.8	−15.4
2452792.8	−14.6
2452818.8	−14.2
2452849.6	−15.1
2452876.6	−14.8
2452898.6	−15.1
2453162.8	−12.4
2453187.7	−12.4
2453223.6	−12.3
2453259.6	−12.2
2453553.7	−10.9
2453623.6	−12.2
2453648.5	−11.5

Note. Supplementary Hα EW measurements from spectra of 66 Oph obtained at Ritter Observatory.

likely responsible for the temporary halt in the decline of Hα EW strength between 1995 and 1998 and indicative of temporary replenishment of material to the inner regions of the disk. The cessation of this mass injection to the inner disk is marked by a fast decrease in the intrinsic polarization level, as well as a resumption of the gradual decline in Hα EW. Near the end of our data set, the sharp rise in both intrinsic polarization and Hα EW indicate significant mass injection into the disk. Overall, these disk-loss and growth epochs occurred in the span of 2–4 yr.

4.1.3. 66 Oph

The Hα EW of 66 Oph also exhibited a steady decline throughout the entire 13 yr baseline of our data set (Figure 2(b)). Supplementary Hα EWs from spectra obtained at Ritter Observatory improve the time sampling during the end of our spectropolarimetric data, and confirm that the emission strength decline continues during these epochs. The Ritter EWs end their decline after the last epoch of our spectropolarimetric data (see, e.g., Table 6), suggesting the system's mass-loss rate changed and a complete disk-loss phase was avoided. The intrinsic polarization data (Figure 2(b)) also exhibit a slow decline throughout the 13 yr baseline of the HPOL data, supporting the interpretation of a gradual decline in the disk.

4.2. Intrinsic Polarization Color Diagrams

Draper et al. (2011) noted the evolution of the ratio of the polarization across the Balmer jump versus the *V*-band polarization occasionally traced out distinctive loops in PCD diagrams. Haubois et al. (2014) explored these diagrams in detail with theoretical models. Since the polarization change across the Balmer jump is roughly proportional to the density squared whereas the *V*-band polarization is proportional to the density, PCD diagrams offer a useful method to investigate the evolution of Be disks when spectral type and inclination can be constrained (Haubois et al. 2014). PCD loops observed in 60 Cyg and π Aqr were qualitatively modeled using the radiative transfer code HDUST and one-dimensional hydrodynamical code SINGLEBE by turning the mass decretion rate on and off. Subsequent detailed modeling of PCDs demonstrated that the shape, slope, and time-scale of loops depends on spectral type, inclination angle, the base density of the disk, and the temporal behavior of the mass decretion rate (Haubois et al. 2014). One important conclusion from these modeling efforts is that steady state disks pause at the top of a PCD loop, while the disk is fed by either constant mass-loss or semi-regular mass injections from the star (Haubois et al. 2014). Our steady disk sample broadly reproduces this behavior. For example, both ϕ Per and γ Cas (Figure 2) cluster at high *V*-band polarization and high Balmer jump ratios in their PCDs during their steady-state disk stage.

However, the following systems have deviations from this steady state disk behavior:

4.2.1. 48 Lib

48 Lib exhibits clear evidence of a partial PCD loop (Figure 2(a)) in our data set. The rise in 48 Lib's intrinsic *V*-band polarization (blue points; Figure 2(a)) indicates a disk growth phase, which eventually plateaus into a steady state disk phase. Unlike other steady state disks in our sample that sit at the top of the PCD loop during the steady state, 48 Lib's Balmer jump ratio rapidly drops during this phase. Since 48 Lib is a near edge-on inclination (Rivinius et al. 2006; Stefl et al. 2012), its PCD behavior seems consistent with the modeling scenario outlined in Figure 9 of Haubois et al. (2014). Specifically, these results suggest that 48 Lib was characterized by a high base density ($\approx 10^{-11}$ g cm^{-3}) disk and disk orientation which gives a high opacity. This manifests during the onset of the disk-growth event with a large Balmer jump ratio which later decreases at a nearly constant *V*-band polarization as it approaches a steady state phase. Furthermore it has a steeper decline, which consistent with a later spectral type of B2 to B5 given 48 Lib is B3.

4.2.2. ψ Per

ψ Per experienced a notable rise in intrinsic *V*-band polarization during the early 1990s (blue points; Figure 2(b)) indicating a disk growth phase, that seemingly plateaued during the later part of the decade into a stable phase. ψ Per exhibited a dramatic drop in its Balmer jump polarization as it transitioned to a steady state system. Given the mid spectral type (B5) and near edge-on inclination ($\sim 75^\circ$; Table 1) of the system, like 48 Lib, we suggest that the ψ Per PCD behavior could be caused by the outer regions of the high inclination, high density disk absorbing significant Balmer jump photons at the onset of the disk growth event (Haubois et al. 2014). This is further supported by the fact the polarization blueward of the Balmer jump was nearly zero or essentially optically thick to polarization of the disk.

4.2.3. 28 Cyg

During 28 Cyg's overall long-term decline in disk strength, as measured by its declining intrinsic *V*-band polarization and Hα EW (Figure 2(c)), the system experienced three short, large

jumps in Balmer jump polarization. During a 90 day period when the star was monitored regularly, in some cases nightly, the PCD diagram illustrates three instances where the Balmer jump ratio spiked to >2.5 (compared to the median value of 1.4). The separation between these three peaks was 24 and 18 days respectively. Given its spectral type (B2.5), the Balmer jump polarization is most sensitive to the inner regions of the disk when compared to the *V*-band polarization (Haubois et al. 2014). These Balmer jump ratio spikes (that occur at a constant *V*-band polarization) are likely caused by discrete events in the inner disk. Specifically, we speculate that the spikes stem from stochastic mass injections into the disk.

Although outside the scope of this paper, it is clear that detailed modeling of 48 Lib, ψ Per, and 28 Cyg using codes such as Halonen & Jones (2013a) and Haubois et al. (2014) should be improved and pursued to reproduce the PCD variability observed in these systems. Moreover, given the diagnostic potential for systems experiencing full disk growth/disk-loss episodes (π Aqr, 60 Cyg; Draper et al. 2011) and episodic disk growth (48 Lib, ψ Per, 28 Cyg), it is certainly clear that enhanced observational monitoring of these types of systems should be aggressively pursued. Without consistent temporal monitoring, it can become challenging to constrain the exact time-scale for disk growth and loss events. Our results for 28 Cyg provide quantitative evidence that even high cadence (i.e., nightly) observations yield interesting PCD phenomenon that could be better exploited to diagnose episodic mass injection events.

4.3. One-armed Density Waves

Halonen & Jones (2013b) presented ad hoc model predictions of the effects of global one-armed oscillations (Okazaki 1991, 1997) on the time-dependent linear polarization of Be disks, including models that used a perturbation pattern characterized by a pattern of opposite overdense and underdense regions (Okazaki 1997) and models that used a spiral shaped perturbation pattern as adopted by Carciofi et al. (2009). These models (and those of Carciofi et al. 2009) predict that the *V*-band polarization and polarization across the Balmer jump should exhibit a clear inclination-dependent modulation with phase (Figures 6–8 of Halonen & Jones 2013b), although they will be out of phase with one another due to the different radial locations in the disks over which the scattering events occur in each bandpass. The *V*-band polarization P.A. is also predicted to exhibit complex changes with phase (Figure 10, Halonen & Jones 2013b). Inspite of these predictions, no conclusive observational evidence of this phenomenon has been reported (Carciofi et al. 2009).

γ Cas is known to exhibit V/R variations indicating the presence of a one-armed density feature in its disk, as seen in its phase-folded He I V/R ratios (Figure 3) compiled from data presented in Miroshnichenko et al. (2002). Observations were made at the Ritter Observatory from 1993 to 2002 of the He I at 5876 Å, amongst other lines, with a resolving power of ∼26,000. The line profile was consistently double peaked and had clear V/R variations. γ Cas exhibits a generally stable disk, as diagnosed by its intrinsic polarization (Figure 2(a)), which indicates its inner disk is being supplied by a generally stable decretion rate. It therefore makes an ideal system to search for long-term polarimetric effects related to its one-armed density feature. The intrinsic *V*-band polarization, polarization across the Balmer jump, and *V*-band polarization P.A. phased to the V/R period of the He I data is shown in Figure 3. The intrinsic *V*-band polarization generally exhibits a double-oscillation pattern over one period that is predicted by Halonen & Jones (2013b). The intrinsic polarization across the Balmer jump exhibits variability, albeit no clear indication of the phase-lagged behavior predicted by Halonen & Jones (2013b). The intrinsic *V*-band polarization P.A. suggestively exhibits evidence of cohesive variations as a function of phase, but such variations are an order of magnitude greater than that predicted in the ad hoc models of Halonen & Jones (2013b). We speculate that one reason these data exhibit a stronger indication of the predicted behavior in *V*-band, rather in the Balmer jump polarization, is that the former is less sensitive to small changes in the inner disk caused by changes in the mass decretion rate. We encourage future modeling efforts of this phenomenon to explore the ramifications of abrupt and gradual changes in the mass decretion rate have on the polarization in disks having one-armed density waves.

4.4. P.A. Deviations

Wisniewski et al. (2010) reported numerous instances of the intrinsic polarization of 60 Cyg and π Aqr deviating from their linear trends on a Stokes QU diagram, and found that these deviations in intrinsic polarization P.A. were more prominent during large outburst events. These authors interpreted this behavior as either evidence of the injection and subsequent circularization of new blobs of mass into the inner disk region, similar to that noted in Carciofi et al. (2007), or as evidence of the injection and subsequent circularization of new blobs at an inclined orbit to the plane of pre-existing disk material. Many of the Be systems explored in our current study exhibit generally stable, strong disks over most of the duration of our data set, which suggests we should see analogous evidence of P.A. deviations in our data set. As seen in Figure 4, γ Cas exhibits P.A. deviance as a function of the intrinsic *V*-band polarization in the system. Analogous figures for our other targets are available in the online-version of this paper. Overall, we do see clear evidence of strong P.A. deviations in most of our Be stars even though they cannot be correlated to specific outburst events like 60 Cyg and π Aqr were. The system that exhibits the smallest level of P.A. deviations, ω Ori, is noteworthy as it exhibited evidence of a gradual, albeit incomplete, loss of its disk throughout the time-frame covered by our data. While errors in the ISP estimate could be inducing errors in the intrinsic P.A., we note that the deviations are symmetric about the mean. If there were errors in our P.A. determinations, then one would expect the deviations to be systematically offset to one side of the mean. In general, our results are consistent with systems which have had more precise ISP determinations and time resolved outbursts which suggest the P.A. deviations are also "clumpy" injection events (e.g., 60 Cyg and π Aqr).

4.5. Be+sdO Systems

Three of our targets are known to have a sub dwarf companion, ϕ Per (Gies et al. 1998), FY CMa (Peters et al. 2008), and 59 Cyg (Peters et al. 2013), and all three systems exhibit steady state disks in our data. This apparent stability could be influenced by the sdO truncating these disks to the maximum allowed radius. Interestingly, we do observe significant variability in the polarization across the Balmer jump in both FY CMa and 59 Cyg (Figure 2(c)). We remind the reader that the ISP for 59 Cyg was poorly constrained; however, we explored different assumed total ISP P.A. values (about P.A. = 0) and still observed the jumps in the polarization across the Balmer jump, suggesting that they are likely real.

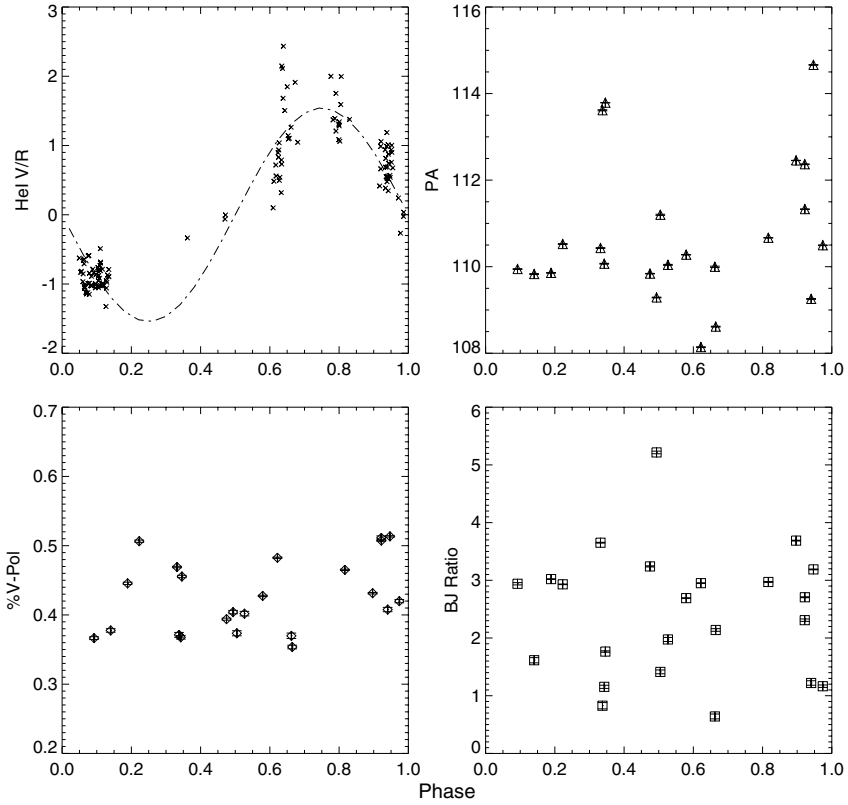

Figure 3. Phase folded He I V/R measurements (adopted from Miroshnichenko et al. 2002; panel (A)), the phase folded intrinsic V-band polarization position angle (panel (B)), the phase folded intrinsic V-band polarization (panel (C)), and the phase folded intrinsic polarization across the Balmer jump (panel (D)) is shown for γ Cas.

As the sdO is likely heating the outer region of the disk nearest its orbital position, we speculate that this outside heating source may inflate the scale height of this region of the disk. Given the short periods of order 29–37 days (Peters et al. 2013), we speculate that when the inflated scale heights of these moderately high inclination disks (Table 1) pass in front of our line of sight with the star, they cause the observed changes in polarization across the Balmer jump. We further speculate that the amount of disk material heated and inflated by ϕ Per's more distant (127 day period) sdO companion may contribute to why this system exhibits no analogous Balmer jump polarization jumps. Higher cadence observations that sufficiently sample the suggested puffed-up outer disk over the orbital period of these systems' sdO companion would help to further establish our interpretation of this observational phenomenon.

4.6. Maximum Polarization

The maximum polarization for a viscous disk in equilibrium is found to be correlated with inclination, spectral type, and base density (Haubois et al. 2014; Halonen & Jones 2013b). In most cases the disks in this sample reach some form of steady state. We then assume that the maximum observed polarization at some point in the 15 yr survey is the maximum polarization of a disk around these stars. Since the effective temperature and inclination can be determined by other means (e.g., spectroscopy and interferometry), we use literature values to then derive the range of base densities for this sample of Be stars (see Table 1). Given the model tracks of Haubois et al. (2014), we find that the base density for these stars lie within 8×10^{-11} to 4×10^{-12} g cm^{-3} (see Figure 5).

Several items are key to interpreting the base density estimates extracted from Figure 5. π Aqr, for example, exhibits a lower maximum V-band polarization than the 4.2×10^{-11} g cm^{-3} base density track compared to other stars having a similar stellar effective temperature (Figure 5; right panel) due in part because the system's inclination angle (33.°6 is lower than that used for the model track) 70°. Similarly, π Aqr exhibits a higher maximum than expected for the 4.2×10^{-11} g cm^{-3} base density track (Figure 5; left panel) compared to other systems having a similar inclination due in part to π Aqr having a warmer stellar effective temperature than adopted for these models. Due to this degeneracy, it likely has a similarly large base density as ϕ Per around 4.2×10^{-11} g cm^{-3}. ψ Per and 59 Cyg have similar

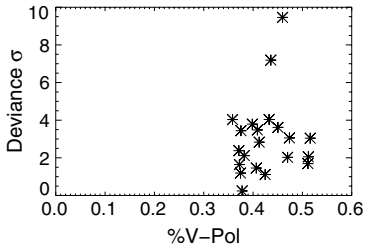

Figure 4. Absolute value of the error weighted deviation (deviance) of every *V*-band polarization of γ Cas from the best fit line defining its intrinsic disk position angle in its *QU* diagram (Figure 1) is plotted as a function of the magnitude of intrinsic *V*-band polarization present in each observation. The sporadic large deviations mimic those reported by Wisniewski et al. (2010). The online version of this manuscript includes corresponding figures for every star in our target list.

maximum polarization and inclination yet have very different effective temperatures. This then requires a low base density of 8.4×10^{-12} g cm^{-3} which exhibits maximum polarization independent of effective temperature. An object like γ Cas, shows behavior similar to that of π Aqr in relation to the model tracks. It is likely limited in maximum polarization due to its low inclination rather then its spectral type, so it is consistent with a low base density of 4.2×10^{-11} g cm^{-3}. Due to the degeneracy and variable nature of some of the stars observed by HPOL, these limits are not meant to be absolute but rather a first look into the disk properties for the class as a whole. Each star will require more detailed modeling, but potentially broader statistics could be applied to a wider sample if polarimetry, spectroscopy, and interferometry can be obtained simultaneously to derive the applicable parameters.

5. SUMMARY

Motivated by the recent discovery of the diagnostic power of PCDs in characterizing the time-dependent mass decretion rate in Be stars (Draper et al. 2011), and the recent theoretical explorations and predictions of the utility of this diagnostic (Halonen & Jones 2013a, 2013b; Haubois et al. 2014), we carefully analyzed the long-term polarimetric behavior of nine additional classical Be stars. Our targets included systems exhibiting evidence of partial disk-loss/disk-growth episodes as well as systems exhibiting long-term stable disks. After characterizing and removing the ISP along the line of sight to each of these targets, we found:

1. Our steady-state Be disk sample (e.g., ϕ Per and γ Cas (Figure 2(a)) tend to simultaneously exhibit high intrinsic *V*-band polarization and high Balmer jump ratios in their PCDs, which confirms the behavior predicted by theory (Halonen & Jones 2013a; Haubois et al. 2014).
2. The PCDs for several later spectral type, highly inclined Be stars in our sample (e.g., 48 Lib and ψ Per, Figure 2) exhibit rapid declines in their Balmer jump ratios at epochs of continuously high intrinsic *V*-band polarizations, which provides the first observational confirmation of this predicted (Haubois et al. 2014) behavior. As noted by Haubois et al. (2014), this phenomenon can be produced when the base density of the disk is very high, and the outer region of the edge-on disk starts to self absorb a significant number of Balmer jump photons.
3. We observe numerous, brief jumps in the intrinsic polarization across the Balmer jump in 28 Cyg, ϕ Per, FY CMa, and 59 Cyg. The high cadence of our 28 Cyg data suggest these jumps are likely caused by stochastic injections of material into the inner disk (of this system). ϕ Per, FY CMa, and 59 Cyg are known sdO systems. We speculate that the sdO companion in these systems might be thermally inflating the outer region of one side of these disks, and that the observed Balmer jump polarization changes might be related to this inflated disk region passing in front of our line of sight as an alternative to blob injection events. We recommend future high cadence observations of these systems over the orbital periods of their sdO companions be obtained to confirm our interpretation.
4. We observe suggestive evidence of coherent variability in the intrinsic *V*-band polarization and polarization P.A. of γ Cas that phases with the orbital period of a known one-armed density structure in this disk, similar to the theoretical predictions of Halonen & Jones (2013b). We speculate that the "astrophysical noise" present in these trends, and our

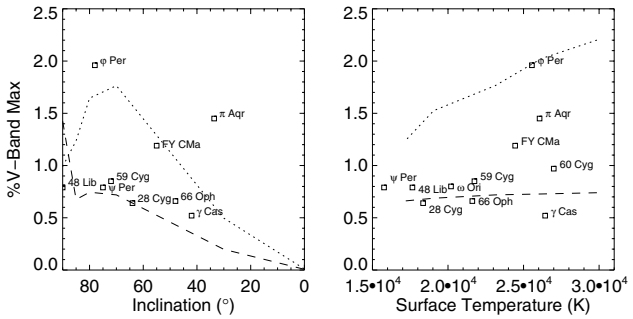

Figure 5. Maximum observed polarization of the target sample is plotted vs. disk inclination, on the left, and effective temperature, on the right, when available. Model tracks are shown for two base densities of 8.4×10^{-12} on the dashed line and 4.2×10^{-11} on the dotted line in g cm^{-3} from Haubois et al. (2014). The model inclination tracks are of a fixed B2 type star ($T_{\rm eff} \approx 23{,}000$ K). Inclination causes polarization to peak at $i = 70°$–$80°$. The model effective temperature tracks are from a fixed inclination of 70°. For low base densities, the effect on maximum polarization by effective temperature is constant where as high density models have a growing linear with higher effective temperature. The polarization maximum is degenerate between the effective temperature and inclination but general limits can be placed on the sample as a whole.

non-detection of the predicted (Halonen & Jones 2013b) phased trend in the polarization across the Balmer jump, could be caused by stochastic changes in the mass decretion rate in this system.

5. We also provide constraints on the base densities of quasi-static disks given our sample. Given the degeneracy between inclination and spectral type with the max polarization, we can only estimate the base densities are within $\approx 8 \times 10^{-11}$ to $\approx 4 \times 10^{-12}$ g cm^{-3}.

We thank the referee, Carol Jones, for helpful comments which improved this paper. We thank Brian Babler for his invaluable assistance with various aspects of HPOL data, and the HPOL and Ritter science teams for support of data acquisition. We also thank Kenneth H. Nordsieck for providing access to the HPOL spectropolarimeter, and Anatoly Miroshnichenko for supplying an electronic copy of his archival γ Cas data. Z.H.D. acknowledges partial support from the University of Washington Pre-MAP program, NSF REU at the University of Toledo, and the Washington Space Grant/NASA Summer Undergraduate Research Program. HPOL and WUPPE observations were supported under NASA contract NAS5-26777 with the University of Wisconsin-Madison. X.H. wants to thank FAPESP for the grant 2009/07477-1. A.C.C. acknowledges support from CNPQ (grant 307076/2012-1) and FAPESP (grant 2010/19029-0). Observations at the Ritter Observatory are supported by the NSF under the PREST grant AST 04-40784. This study has made use of the SIMBAD database, operated at CDS, Strasbourg, France, the NASA ADS service, and the STScI MAST Archive. We also like to thank the Astronauts and Space Shuttle support crews for the successful completion of STS-35 and STS-67 which obtained data presented in this paper.

REFERENCES

Bjorkman, J. E., & Carciofi, A. C. 2005, in ASP Conf Ser. 337, The Nature and Evolution of Disks Around Hot Stars, ed. R. Ignace & K. Gayley (San Francisco, CA: ASP), 75
Bjorkman, J. E., & Cassinelli, J. P. 1993, ApJ, 409, 429
Brown, J. C., Cassinelli, J. C., & Maheswaran, M. 2008, ApJ, 688, 1320
Cantanzaro, G. 2013, A&A, 550, 79
Carciofi, A. C. 2011, in IAU Symp. 272, Active OB Stars: Structure, Evolution, Mass Loss and Critical Limits, ed. C. Neiner et al. (Cambridge: Cambridge Univ. Press), 325
Carciofi, A. C., Bjorkman, J. E., Otero, S. A., et al. 2012, ApJ, 744, 15
Carciofi, A. C., Magalhaes, A. M., Leister, N. V., Bjorkman, J. E., & Levenhagen, R. S. 2007, ApJL, 671, L49
Carciofi, A. C., Okazaki, A. T., le Bouquin, J.-B., et al. 2009, A&A, 504, 915
Cassinelli, J. P., Brown, J. C., Maheswaran, M., Miller, N. A., & Telfer, D. C. 2002, ApJ, 578, 951
Clark, J. S., Tarasov, A. E., & Panko, E. A. 2003, A&A, 403, 239
Clarke, D., & Bjorkman, K. S. 1998, A&A, 331, 1059
Clayton, G. C., Wolff, Michael J., Allen, R. G., et al. 1997, AJ, 114, 1132
Coyne, G. V., & Kruszewski, A. 1969, AJ, 74, 528
Cranmer, S. R. 2009, ApJ, 701, 396
Delaa, O., Stee, Ph., Meilland, A., et al. 2011, A&A, 529, 87
Doazan, V., Franco, M., Rusconi, L., Sedmak, G., & Stalio, R. 1983, A&A, 128, 171
Draper, Z. H., Wisniewski, J. P., Bjorkman, K. S., et al. 2011, ApJL, 728, L40
Frémat, Y., Zorec, J., Hubert, A.-M., & Floquet, M. 2005, A&A, 440, 305
Gies, D. R., Bagnuolo, W. G., Jr., Ferrara, E. C., et al. 1998, ApJ, 493, 44
Halonen, R. J., & Jones, C. E. 2013a, ApJ, 765, 17
Halonen, R. J., & Jones, C. E. 2013b, ApJS, 208, 3
Halonen, R. J., Mackay, F. E., & Jones, C. E. 2013, ApJS, 204, 11
Harries, T. J., Babler, B. L., & Fox, G. K. 2000, A&A, 361, 273
Haubois, X., Carciofi, A. C., Rivinius, Th., Okazaki, A. T., & Bjorkman, J. E. 2012, ApJ, 756, 156
Haubois, X., Mota, B. C., Carciofi, A. C., et al. 2014, ApJ, accepted
Heiles, C. 2000, AJ, 119, 923
Hummel, W., & Vrancken, M. 2000, A&A, 359, 1075
Koubský, S., Harmanec, P., Hubert, A. M., et al. 2000, A&A, 356, 913
Kraus, S., Monnier, J. D., Che, X., et al. 2012, ApJ, 744, 19
Lee, U., Osaki, Y., & Saio, H. 1991, MNRAS, 250, 432
Mathewson, D. S., & Ford, V. L. 1970, MmRAS, 74, 139
McLean, I. S., & Brown, J. C. 1978, A&A, 69, 291
McSwain, M. V., Huang, W., & Gies, D. R. 2009, ApJ, 700, 1216
McSwain, M. V., Huang, W., Gies, D. R., Grundstrom, E. D., & Townsend, R. H. D. 2008, ApJ, 672, 590
Meilland, A., Stee, P., Vannier, M., et al. 2007, A&A, 464, 59
Miroshnichenko, A. S., Bjorkman, K. S., & Krugov, V. D. 2002, PASP, 14, 1226
Miroshnichenko, A. S., Bjorkman, K. S., Morrison, N. D., et al. 2003, A&A, 408, 305
Miroshnichenko, A. S., Fabregat, J., Bjorkman, K. S., et al. 2001, A&A, 377, 485
Miroshnichenko, A. S., Pasechnik, A. V., Manset, N., et al. 2013, ApJ, 766, 119
Neiner, C., Hubert, A.-M., Floquet, M., et al. 2002, A&A, 388, 899
Nook, M. 1990, PhD dissertation, The Univ. Wisconsin-Madison
Nordseick, K. H., Code, A. D., Anderson, C. M., et al. 1994, Proc. SPIE, 2010, 2
Nordsieck, K. H., & Harris, W. 1996, in ASP Conf. Ser. 97, Polarimetry of the Interstellar Medium, ed. W. G. Roberge & D. C. B. Whittet (San Francisco, CA: ASP), 100
Okazaki, A. T. 1991, PASJ, 43, 75
Okazaki, A. T. 1997, A&A, 318, 548
Perryman, M. A., Lindegren, L., Kovalevsky, J., et al. 1997, A&A, 323, 49
Peters, G. J., Gies, D. R., Grundstrom, E. D., & McSwain, M. V. 2008, ApJ, 686, 1280
Peters, G. J., Pewett, T. D., Gies, D. R., Touhami, Y. N., & Grundstrom, E. D. 2013, ApJ, 765, 2
Poeckert, R., Bastien, P., & Landstreet, J. D. 1979, AJ, 84, 812
Porter, J. M., & Rivinius, T. 2003, PASP, 115, 1153
Pott, J.-U., Woillez, J., Ragland, S., et al. 2010, ApJ, 721, 802
Quirrenbach, A., Bjorkman, K. S., Bjorkman, J. E., et al. 1997, ApJ, 479, 477
Rivinius, Th., Baade, D., Stefl, S., Stahl, O., Wolf, B., & Kaufer, A. 1998, A&A, 333, 125
Rivinius, Th., Stefl, S., & Baade, D. 2006, A&A, 459, 137
Rivinius, Th., Carciofi, A. C., & Martayan, C. 2013, A&AR, 21, 69
Serkowski, K., Mathewson, D. S., & Ford, V. L. 1975, ApJ, 196, 261
Stee, P. 2011, in IAU Symp. 272, Active OB Stars: Structure, Evolution, Mass Loss and Critical Limits, ed. C. Neiner et al. (Cambridge: Cambridge Univ. Press), 313
Stefl, S., Le Bouquin, J.-B., Carciofi, A. C., Rivinius, Th., Baade, D., & Rantakyro, F. 2012, A&A, 540, 76
Touhami, Y., Gies, D. R., Schaefer, G. H., et al. 2013, ApJ, 768, 128
Underhill, A., & Doazan, V., eds. 1982, in B Stars with and without Emission Lines, (NASA SP-456; Washington, DC: NASA)
Vinicius, M. M. F., Zorec, J., Leister, N. V., & Levenhagen, R. S. 2006, A&A, 446, 643
Wheelwright, H. E., Bjorkman, J. E., Oudmaijer, R. D., et al. 2012, MNRAS, 423, L11
Wilking, B. A., Lebofsky, M. J., & Rieke, G. H. 1982, AJ, 87, 695
Wisniewski, J. P., Bjorkman, K. S., Magalhaes, A. M., et al. 2007a, ApJ, 671, 2040
Wisniewski, J. P., Draper, Z. H., Bjorkman, K. S., et al. 2010, ApJ, 709, 1306
Wisniewski, J. P., Kowalski, A. F., Bjorkman, K. S., Bjorkman, J. E., & Carciofi, A. C. 2007b, ApJL, 656, L21
Wolff, M. J., Nordsieck, K. H., & Nook, M. A. 1996, AJ, 111, 856
Wood, K., & Bjorkman, J. E. 1995, ApJ, 443, 348
Wood, K., Bjorkman, J. E., Whitney, B. A., & Code, A. D. 1996a, ApJ, 461, 828
Wood, K., Bjorkman, J. E., Whitney, B. A., & Code, A. D. 1996b, ApJ, 461, 847
Wood, K., Bjorkman, K. S., & Bjorkman, J. E. 1997, ApJ, 477, 926

Appendix G

Dynamical evolution of viscous disks around Be stars. II. Polarimetry

The Astrophysical Journal, 785:12 (13pp), 2014 April 10 doi:10.1088/0004-637X/785/1/12

DYNAMICAL EVOLUTION OF VISCOUS DISKS AROUND BE STARS. II. POLARIMETRY

X. Haubois[1,2,3], B. C. Mota[2], A. C. Carciofi[2], Z. H. Draper[4,5], J. P. Wisniewski[6], D. Bednarski[2], and Th. Rivinius[7]
[1] LESIA, Observatoire de Paris, CNRS UMR 8109, UPMC, Université Paris Diderot, 5 place Jules Janssen, F-92195 Meudon, France; xavier.haubois@obspm.fr
[2] Instituto de Astronomia, Geofísica e Ciências Atmosféricas, Universidade de São Paulo, Rua do Matão 1226, Cidade Universitária, São Paulo, SP 05508-090, Brazil
[3] Sydney Institute for Astronomy, School of Physics, University of Sydney, NSW 2006, Australia
[4] Department of Physics and Astronomy, University of Victoria, 3800 Finnerty Road, Victoria, BC V8P 5C2, Canada
[5] Herzberg Institute of Astrophysics, National Research Council of Canada, Victoria, BC V9E 2E7, Canada
[6] H. L. Dodge Department of Physics and Astronomy, University of Oklahoma, 440 West Brooks St Norman, OK 73019, USA
[7] European Organisation for Astronomical Research in the Southern Hemisphere, Casilla 19001, Santiago 19, Chile
Received 2013 November 28; accepted 2014 February 8; published 2014 March 21

ABSTRACT

Be stars exhibit variability for a great number of observables. Putting the pieces of the disk dynamics together is not an easy task and requires arduous modeling before achieving a good fit to the observational data. In order to guide the modeling process and make it more efficient, it is very instructive to investigate reference dynamical cases. This paper focuses on continuum polarimetric quantities and is the second of a series that aims to demonstrate the capacity of deriving the dynamical history and fundamental parameters of a classical Be star through follow-up of various observables. After a detailed study of the different opacities at play in the formation of polarized spectra, we investigate predictions of polarimetric observables in the continuum for different dynamical scenarios. Our models are based on a coupling of a hydrodynamic viscous decretion simulations in a disk and a three-dimensional non-LTE radiative transfer code. Through introduction of the polarization color diagram (PCD), we show that certain combinations of polarimetric observables exhibit features that are characteristic of a mass-loss history. This diagram also enables estimates of fundamental parameters such as the inclination angle, disk density scale, and the α viscous diffusion parameter. We present the PCD as a powerful diagnosis tool to track the dynamical phases of a Be star, such as disk build-up, dissipation, periodic, and episodic outbursts. Finally, we confront our models with observations of four Be stars that exhibited long-term polarimetric activity.

Key words: circumstellar matter – radiative transfer – stars: emission-line, Be – stars: individual (π Aquarii, 60 Cygni, δ Scorpii and ψ Persei) – techniques: polarimetric

Online-only material: color figures

1. INTRODUCTION

Be stars are non-supergiant, early-type stars with a circumstellar (CS) disk that is created from matter ejected from the star. Recent observational facts brought by spectro-interferometry and spectro-astrometry (e.g., Meilland et al. 2012; Wheelwright et al. 2012) support the fact that so far, all studied Be star disks rotate in a Keplerian fashion. This characteristic, together with other observational signatures of the disk outlined in Carciofi (2011), are properties that only the viscous decretion disk (VDD) model can reproduce. This model, first suggested by Lee et al. (1991) and further developed by Bjorkman (1997), Porter (1999), Okazaki (2001), Bjorkman & Carciofi (2005), and Jones et al. (2008), among others, uses the angular momentum transport by turbulent viscosity to lift material into higher orbits, thereby causing the disk to grow in size. This model has already been successfully applied to systems showing stable continuum emission, e.g., ζ Tauri (Carciofi et al. 2009), χ Oph (Tycner et al. 2008), β CMi (Wheelwright et al. 2012), and systems exhibiting a more variable photometric activity (28 CMa; Carciofi et al. 2012). In a recent review paper, Rivinius et al. (2013) discuss in detail the observational and theoretical evidences in support of the VDD scenario for Be stars.

Polarization is a powerful tool to study the geometry of the disk (opening angle, flaring) of Be stars without angularly resolving it. Polarized flux originates from electron scattering off the disk, and is affected by both pre- and post-scattering absorption by H I atoms (Wood et al. 1996; Halonen & Jones 2013a). Since H I opacity depends on the physical state of the gas, studying polarimetric observables at different wavelengths allows one to probe different regions of the disk. In the literature, the polarimetric technique has an established history of providing a unique diagnosis in identifying and studying the detailed CS environments of Be stars (Wood et al. 1997; Carciofi et al. 2007, 2009; Wisniewski et al. 2010; Draper et al. 2011).

Haubois et al. (2012, hereafter Paper I), studied the temporal variability of Be disks, based on SINGLEBE VDD hydrodynamic simulations (Okazaki 2007). SINGLEBE solves the one-dimensional surface density evolution equation for a viscous isothermal Keplerian decretion disk. The effects of variable mass injection rates on the disk structure, and their corresponding effect on the photometry, were studied at different wavelengths and compared to observations. More specifically, we first studied the different timescales that characterize the evolution of the disk surface density and how this surface density responds to changes in mass injection rates. These surface density profiles were used as inputs to the three-dimensional non-LTE Monte Carlo radiative transfer code HDUST (Carciofi & Bjorkman 2006, 2008) that allowed the calculation of photometric observables at various wavelengths. The characteristic shapes of these lightcurves agree qualitatively well with observations, which provide strong circumstantial evidence that viscosity is indeed the mechanism that redistributes matter along the CS disk. The first successful confrontation of theoretical VDD lightcurves with observations was done by Carciofi et al. (2012) for the Be star 28 CMa. To summarize, Paper I provides the reader with a description of the photometric variability from a Be star in the framework of the VDD model. With the present

Table 1
Stellar Main Parameters Used in the Simulations

Parameter	B0	B1	B2	B3	B4	B5
Mass ($M_\odot$)	14.6	11.0	8.6	6.1	5.1	4.4
Polar radius $R_{\rm pole}(R_\odot)$	12.8	9.6	7.5	5.4	4.5	3.8
Equatorial radius $R_\star$ ($R_\odot$)	5.8	4.9	4.3	3.6	3.3	3.0
$W^{\rm a}$	0.53	0.53	0.53	0.53	0.53	0.53
$v_{\rm rot}$ (km s^{-1})	344	325	308	283	272	261
$v_{\rm orb}$ (km s^{-1})	648	613	580	534	512	492
$\Omega/\Omega_{\rm crit}$	0.8	0.8	0.8	0.8	0.8	0.8
Oblateness	1.14	1.14	1.14	1.14	1.14	1.14
Polar temperature (K)	29900	26200	23100	19100	17200	15500
Luminosity ($L_\odot$)	24200	10200	4400	1500	830	467

Note. [a] $W = v_{\rm rot}/v_{\rm orb}$, see Section 2.3.1 of Rivinius et al. (2013).

paper, we aim at exploring the variability of the continuum polarimetric features in the same manner.

In Section 2, we describe the polarigenic mechanisms operating in Be disks. Then, we present the dynamical models we investigated and their signatures on common continuum polarimetric observables. We also show the diagnosis potential of a series of diagrams that we named polarization color diagrams (PCDs) that represent a powerful tool to follow the mass injection history in Be stars (Section 3). Finally, a discussion and a comparison to observed data of these synthetic observables are presented in Section 4 before concluding.

2. POLARIZATION IN Be STAR DISKS

Continuum spectropolarimetric observations of Be stars usually reveal a sawtooth pattern that displays abrupt changes of the polarization close to the H I ionization thresholds (see, e.g., Quirrenbach et al. 1997, for examples of observed polarization spectra). It is useful to review the origin of this pattern to understand precisely the physical processes that control the shape of the polarized spectrum. In this section, we therefore adopt an analytical model to describe a viscous decretion disk surrounding a rotationally deformed and gravity darkened star; see Table 1 for the adopted stellar parameters.

For the disk, we adopted the VDD model in its simplest form; after a sufficiently long and stable period of mass decretion, a viscous disk assumes a power-law density profile given by $\rho = \rho_0 (R_\star/r)^{3.5}$ (Bjorkman & Carciofi 2005), where ρ_0 is the density at the base of the disk. In this study and in the rest of the paper, we keep the disk outer radius fixed at 20 $R_\star$. Thus, in this section we explore the effects of two model parameters in the polarized spectrum: the spectral type of the star and the disk density scale.

Figure 1 shows two theoretical polarized spectra at two different base densities and at an inclination angle of 70°. While the low-density model has a nearly flat spectrum in the optical and near IR, the high-density model displays a steep spectrum with marked changes in the H I ionization thresholds. This behavior can be understood in terms of the relative contribution to the total opacity of each opacity source. Figure 1 shows the total optical depth of the disk, measured in the radial direction along the midplane (orange lines). The contribution of the absorptive (free-free and bound-free) and scattering (Thomson) opacities are also shown.

At low density, the electron scattering opacity, which is wavelength independent, is responsible for most of the total opacity. The resulting polarized spectrum is consequently nearly flat. However, changes in the polarization level do occur close to H I ionization thresholds, and more importantly, at the Balmer discontinuity (0.365 μm). What causes the decrease in the polarization redward of the discontinuities is the increase in the H I opacity. This effect is thoroughly discussed in Wood et al. (1996) and can be understood in terms of pre-scattering (and to a lesser degree, post-scattering) absorption of starlight, that decreases the polarized flux and hence the polarization level, creating an anticorrelated aspect of optical depth and polarization curves. If the density of the disk increases, the electron opacity will increase more or less linearly, as it is proportional to the number density of free electrons (ρ-diagnostics). However, the bound-free and free-free opacities, being roughly proportional to the square of the density (e.g., Equation (A1) and Equation (30) of Bjorkman & Bjorkman 1994), will increase much faster than the electron opacity (ρ^2-diagnostics) so that, at high disk densities (lower panel of Figure 1), the bound-free opacity dominates the total opacity.

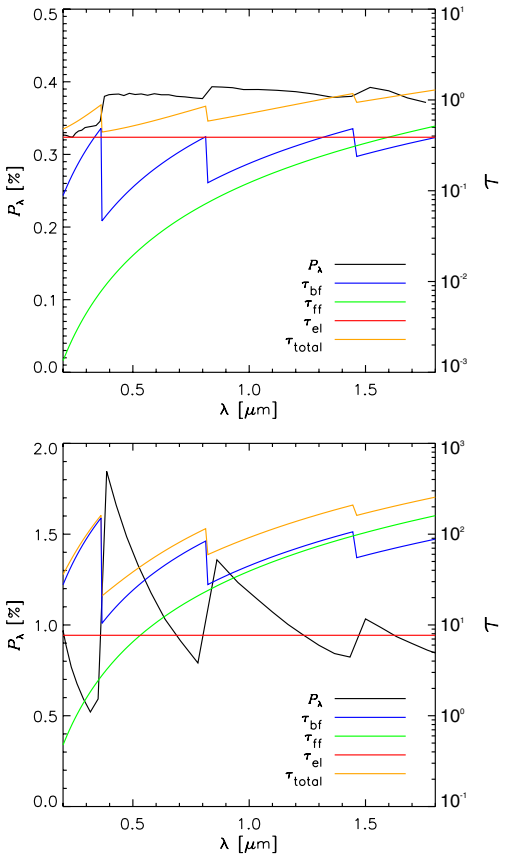

Figure 1. Polarized spectrum and radial optical depth contributions along the midplane. The total optical depth is the sum of the optical depth for each continuum opacity source, as indicated. Upper panel: 4.2×10^{-12} g cm^{-3}; lower panel: 8.4×10^{-11} g cm^{-3}. The inclination angle is 70° and the spectral type is B2.

(A color version of this figure is available in the online journal.)

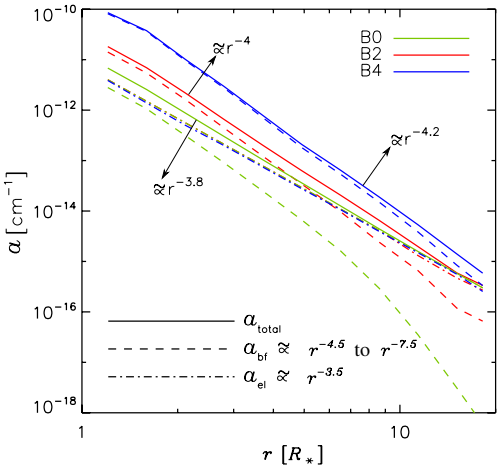

Figure 2. Absorption coefficient redward of the Balmer discontinuity as a function of the distance to the stellar surface. The calculations assume a base density of $\rho_0 = 8.4 \times 10^{-12}$ g cm^{-3} and three spectral types: B0 (green curve), B2 (red curve), and B4 (blue curve). The free–free absorption coefficient is not shown because for short wavelengths, it is much smaller than the other opacities. The electron scattering opacities are very similar for the three spectral types so that their curves overlap. Power-law indexes were estimated for the individual (in the legend) and total (on the graph) absorption coefficients.

(A color version of this figure is available in the online journal.)

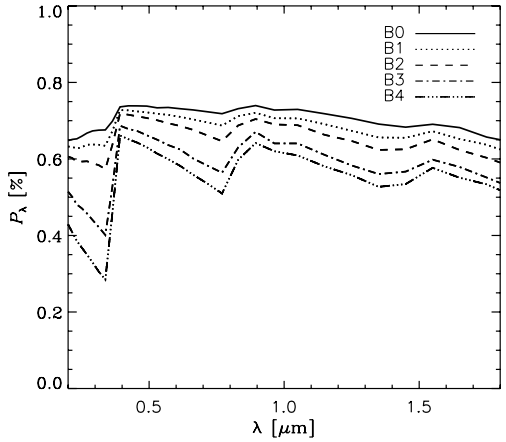

Figure 3. Polarized spectra for five spectral types: B0 (top curve) to B4 (bottom curve). The base density of the disk is 8.4×10^{-12} g cm^{-3}. The inclination angle is 70°.

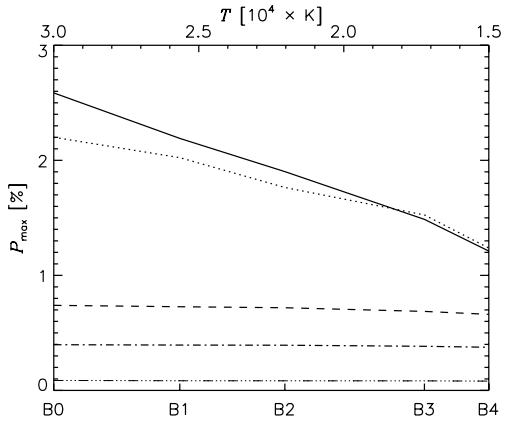

Figure 4. V-band maximum level of polarization vs. the effective temperature of the star for five different base densities and five spectral types. The inclination angle is 70°. From top to bottom: 8.4×10^{-11} g cm^{-3}, 4.2×10^{-11} g cm^{-3}, 8.4×10^{-12} g cm^{-3}, 4.2×10^{-12} g cm^{-3}, and 8.4×10^{-13} g cm^{-3}.

As a result, the polarized spectrum, besides displaying much more pronounced changes in the H I discontinuities, has a quite steep slope that results from the spectral dependency of the bound-free opacity.

In addition to the total radial optical depth, another important quantity in shaping the polarized spectrum is the radial dependence of the opacities or equivalently, absorption coefficients. These are shown in Figures 2 and 16 for a wavelength redward of the Balmer discontinuity. The effects of the spectral type on the absorption coefficients are shown in Figure 2. The slope of the electron absorption coefficient curve, a_{el}, follows roughly the slope of the density ($\propto r^{-3.5}$), because, for the models shown, H I is more than 98% ionized everywhere in the disk (in other words, the ionization fractions are close to unity, and therefore, the electron number density is roughly proportional to the total density). However, the bound-free absorption coefficient, a_{bf}, falls much faster than the electron absorption coefficient. For the B4 model, for instance, $a_{bf} \propto r^{-4.5}$, and no significant difference in slope was found for other spectral types (Figure 2). The value of the radial slope of the bound-free opacity is controlled by the H I level populations, as shown in the Appendix. The actual values of the opacities differ quite markedly for different spectral types: the later the spectral type the larger the opacity. This is explained by the changing ratio between the ionizing UV luminosity versus the total luminosity. Since the electron opacity is essentially the same for the models shown in Figure 2, the large differences in the bound-free opacity implies that the dominant opacity source is different for each spectral type. So, for a B0 star, electron scattering dominates at 0.3647 μm everywhere in the disk, and the opposite is true for the B4 star. An intermediate behavior is seen for the B2 star model: while the bound-free absorption coefficient dominates in the inner disk (up to $\approx 6\ R_\star$), the opacity is controlled by electron scattering in the outer disk.

The resulting effects of the spectral type on the continuum polarization can be seen in Figure 3. The polarized spectrum goes for a relatively flat one for the B0 star (electron scattering dominated) to a steep one, with marked discontinuity at the H I thresholds, for a B4 star at the density considered (bound-free dominated). Another interesting aspect of Figure 3 is the fact that the polarization level for a given wavelength increases with the effective temperature. This is seen more qualitatively in Figure 4, which shows how the V-band maximum polarization of a given model (that happens for an inclination around 70°; Wood et al. 1996) varies with spectral type. For low densities, all models (including the ones for later spectral types) are electron scattering dominated, meaning that electron scattering opacity

is larger than the bound-free opacity in the optical and near-IR continuum (see the Appendix and Figure 16 for an example of how the different opacities changes with changing disk density). This explains why the low density curve in Figure 4 is flat.

As larger densities are considered, two effects concur for the strong dependence of the maximum polarization with spectral type. (1) The relative contribution of the bound-free opacity to the total opacity increases, and it will eventually become the dominating source of opacity in the optical continuum (e.g., bottom panel of Figure 1). Since absorptive opacities decrease the polarization level due to pre- and post-scattering absorption, it follows that the latter spectral types, that are more bound-free dominated, will have lower polarization levels. (2) The total scattering mass of the disk decreases for latter spectral types. For instance, in the high density B2 model of Figure 4, the ionization fraction is about 99%, while for the B4 model it is 91%. These combined effects are so important that the maximum polarization level of the high density B0 model is about 2.5 times larger than the B4 model (Figure 4).

In the above, the relevance of continuum absorption to both the polarization level and the slope of the polarized continuum was discussed. However, Wood et al. (1996) showed that other processes, such as multiple scattering and occultation by the central star, also concur to define the shape of the polarized continuum. These additional processes are not discussed here but they are all self-consistently included in our calculations (Carciofi & Bjorkman 2006). In a recent paper, Halonen & Jones (2013a) also studied the polarization from Be star disks. Based on an self-consistent treatment of the thermal structure of the disk, they performed a radiative transfer in a gaseous disk that feeds a Monte Carlo multiple scattering routine which provides polarization levels for different parameters. Even though a quantitative comparison was not attempted, the results shown in Figure 1 of Halonen & Jones (2013a) are qualitatively similar to the ones we present in this paper.

We conclude that the polarization spectrum carries valuable information about the physical conditions in the circumstellar disk. The polarization level at a given wavelength depends primarily on the total scattering mass of the envelope (number of free electrons), while the "color" of the spectrum (its slope or, equivalently, the size of the polarization change across the H I ionization thresholds) depends on the H I bound-free opacity, which is a strong function of both the disk density and the spectral type. These two polarization features (polarization level and "color") thus carry complementary information. This will be further explored in the next section, particularly through examples of the polarization in the V band (polarization level), P_V, and the polarization level ratio across the Balmer discontinuity (polarization "color"), $P_{\rm BD}$.

3. DYNAMICAL SIGNATURES IN POLARIMETRY

In the last section, we set the stage for explaining the origin of polarized spectra from Be stars using a VDD model in steady state (constant mass decretion rate). However, Be stars are known to be highly variable, and a constant mass decretion rate is likely to be the exception rather than the rule. A much more common situation is a disk whose characteristics are time dependent, in response to variable disk injection rates. To model the polarized signature of a time-dependent VDD, we follow the same approach used in Paper I. In that paper, the photometric variability was studied in detail and it was shown that predictions based on simple, yet realistic, mass injection rate scenarios agree quite well with the correlations observed for both shell and Be stars (we refer the reader to the discussion in Section 5 of Paper I). Here, our goal is to extend that study to the two polarimetric features described in Section 2: the polarization level in the V band and the color of the polarized spectrum as measured either by the polarization change across a H I ionization threshold or by the slope of the polarized spectrum.

Table 2
Time in Years Required to Reach 95% of the Limit Value for $\alpha = 1$

Inclination Angle (deg)	$T_{P_{\rm BD}}$	T_{P_V}	$T_{V\,\rm mag}$
30	1.4	1.9	2.8
70	3.0	3.9	<0.1
80	2.7	4.2	3.4
85	1.0	4.8	7.1
90	0.4	8.4	8.1

For the reader's benefit, we succinctly describe the procedures adopted here; full details are given in Paper I. Using the SINGLEBE code, different dynamical scenarios were built from a given coefficient of viscosity (α, Shakura & Sunyaev 1973) and different histories of the mass injection into the disk: monotonic build-up and dissipation phases of the disk, periodic injection rates, and episodic outbursts. From each hydrodynamic simulation, we obtained a temporal series of surface density profiles for a given dynamical scenario. To transform these structural information into observables, we used the surface density profiles as input to the radiative transfer code HDUST for each epoch of the dynamical scenario we wanted to investigate. This three-dimensional Monte Carlo code produces a full spectral synthesis of a star+disk system with a non-LTE treatment of the level populations and gas temperature and produces output spectra for the Stokes parameters Q and U. Unless mentioned otherwise, the model parameters are the same as presented in Tables 1 and 2 of Paper I. This model, that we call hereafter "the reference model," simulates a B2 star with a disk base density of 8.4×10^{-12} g cm^{-3}. Nevertheless, we also explored the base density and spectral type parameter space and the corresponding values are specified in the figure captions.

3.1. Disk Build-up and Dissipation

3.1.1. V-band Polarization and Balmer Discontinuity

To understand the effects of different dynamical scenarios upon polarimetric observables, we start with a case of an uninterrupted disk build-up and dissipation. The disk build-up is simulated using a constant mass injection rate. The simulation starts without any circumstellar material, and the disk is gradually fed with matter as time goes on. The dissipation is modeled starting with a fully developed disk; mass injection is turned off, and the disk material slowly dissipates both inwardly (re-accretion onto the star) and outwardly. We refer the reader to Paper I for a detailed discussion on how the disk grows and dissipates and the timescales involved.

To explore the two polarimetric features we mentioned at the beginning of the section, we plot in Figure 5 the temporal evolution of P_V and $P_{\rm BD}$ defined as:

$$P_{\rm BD} = \frac{P_{\lambda_{\rm BD+}}}{P_{\lambda_{\rm BD-}}}, \quad (1)$$

where $P_{\lambda_{\rm BD+}}$ and $P_{\lambda_{\rm BD-}}$ are the polarization levels estimated at higher- and lower-wavelength intervals of the Balmer discontinuity, respectively. Results are shown for two α parameters and three inclination angles.

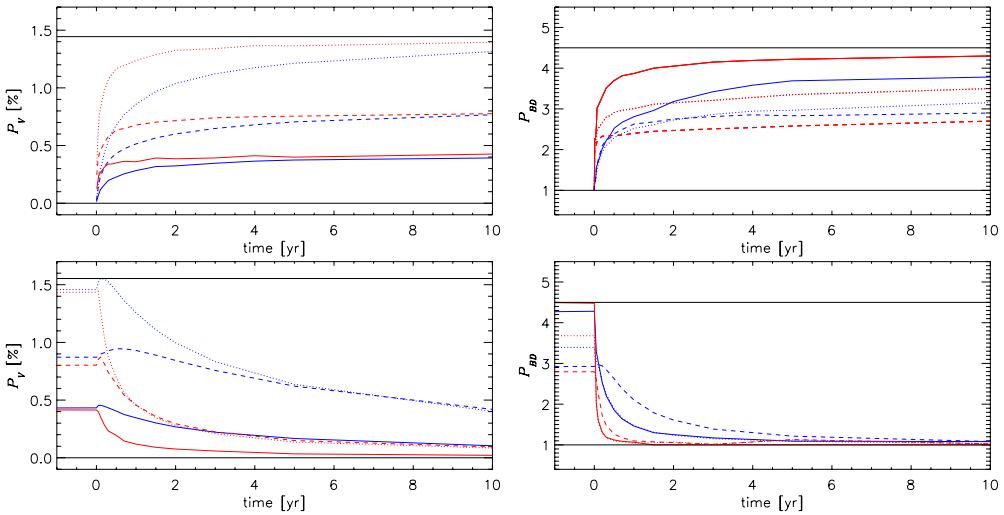

Figure 5. Temporal evolution of P_V (left) and $P_{\rm BD}$ (right) associated with disk build-up (top panels) and dissipation (bottom panels). The solid, dotted, and dashed lines represent the lightcurves for inclination angles of 30° (face-on), 70°, and 90° (edge-on), respectively. The blue and red colors represent models for $\alpha = 0.1$ and 1.0, respectively. The solid black lines indicate the maximum values for each scenario. These curves were obtained using the reference model parameters.

(A color version of this figure is available in the online journal.)

Understanding the build-up phase (upper panels of Figure 5) is straightforward; the polarization level monotonically increases as the disk builds up, approaching a limit value after a time that depends on the α coefficient. This limit value is associated with the fact that even though viscous decretion disks never actually reach steady state, in the case of steadily building disks, their surface density approaches an r^{-2} profile when time goes to infinity (Paper I and references therein). The maximum of the polarization level does not happen for 90° but rather at around 70° (e.g., Wood et al. 1996). Indeed, at high inclinations, photons scattered in directions parallel to the disk plane are much more likely to be absorbed by the disk than photons scattered away from the disk.

The dissipation (lower panels of Figure 5) is characterized by an increase of the P_V signal right after the mass injection has been set to zero (no more mass injected at the base of the disk). This somewhat counterintuitive behavior is explained by the fact that the (unpolarized) emission in the V band decreases soon after the mass injection stops (see Paper I). However, the total polarized flux decreases less rapidly because it is produced in a bigger area in the disk (Rivinius et al. 2013). This causes the polarization fraction to increase. When a sufficient fraction of the disk mass has been dissipated, there is less and less electrons available for Thomson scattering, and the polarization fraction naturally decreases as is the case for $P_{\rm BD}$. These variations are also naturally α and inclination angle dependent. Eventually, all of the polarized signals reach the zero value, when the disk has dissipated all or almost all its scattering mass. As shown in Figure 5, $P_{\rm BD}$ grows and decreases faster than P_V because the former quantity is a ρ^2 diagnostics (depending on the $\tau_{\rm bf}$ opacity), whereas the latter varies linearly with the density (depending on the $\tau_{\rm el}$ opacity.) Hence, $P_{\rm BD}$ responds much faster to changes in density. To further illustrate this point, Table 2 shows the timescales that P_V and $P_{\rm BD}$ need to reach 95% of their limit value for an uninterrupted 50 yr long phase of building up (for $\alpha = 1$). The same timescales for the V-band magnitude are also listed for comparison (taken from Paper I).

3.1.2. Polarization Color Diagrams (PCDs)

From Figure 12 of Paper I, we can see the excess magnitude in different bands stem from different locations in the disk. As demonstrated in Section 2, the same apply for polarimetric features studied in this paper, which probes different disk regions. This offers the possibility of tracking the variations of the local density at different locations in the disk. This fact therefore provides us with an interesting possibility of following viscous processes in Be disks through different dynamical phases such as dissipation, build-up, or outburst phases. Particularly, it is useful to look at the correlation between the polarimetric features $P_{\rm BD}$ and P_V. This correlation was detected observationally in Be stars that underwent build-up and dissipation phases by Draper et al. (2011), which showed that the process of disk growth and dissipation is associated to a loop in a diagram that plots $P_{\rm BD}$ versus P_V. We saw in Section 2 that these quantities respond differently to density changes and are produced in different loci in the disk (although these loci do overlap). We can generalize the concept of this diagram by plotting other combinations of polarimetric observables that also represent a polarized spectrum "color" as a function of polarization level. In analogy to color magnitude diagrams (e.g., Figure 22 of Paper I), this kind of diagram allows us to follow the evolution of Be star disks. We hereafter name this kind of diagram polarization color diagrams (PCD).

Examples of PCDs are shown in Figure 6. The formation of these loops can be described as follows. When the mass injection starts, $P_{\rm BD}$ increases from the value 1 and faster than P_V until it reaches a limit value as seen on Figure 5. At the end of this first phase, the star has generated a large and dense CS disk. The formation path in the PCD corresponds to the

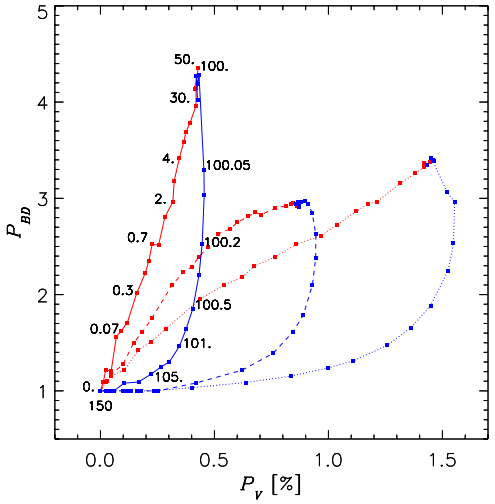

Figure 6. PCDs showing the process of disk growth and dissipation, involving a 100 yr long build-up (in red) and 50 yr dissipation (in blue). The results are shown for three inclination angles (solid line, 30°; dotted line, 70°; and dashed line, 90°). For reference, epochs are marked in years along the curve obtained for 30° and $\alpha = 0.1$. These curves were obtained using the reference model parameters.

(A color version of this figure is available in the online journal.)

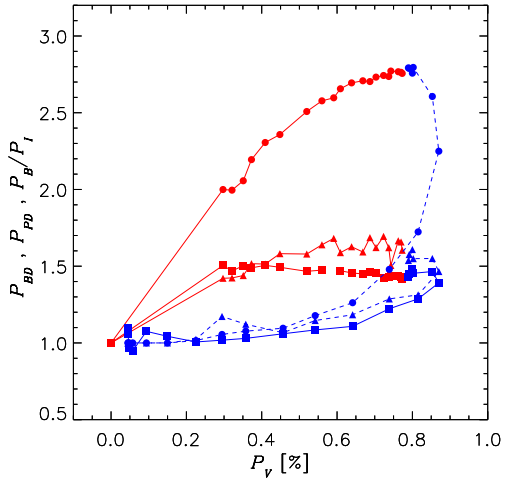

Figure 7. PCDs showing $P_{\rm BD}$ (filled circles), $P_{\rm PD}$ (squares), and P_B/P_I (triangles) as a function of P_V. The red curve shows a 50 yr building up and the blue curve a following 50 yr dissipation phase. The inclination angle is 90° and $\alpha = 1.0$. These curves were obtained using the reference model parameters.

(A color version of this figure is available in the online journal.)

upper part of the loops. When mass injection stops, the inner disk quickly reaccretes back onto the star; this causes a fast drop of $P_{\rm BD}$, which being a ρ^2 diagnostics, responds fast to the density variations. However, as described in the previous section, P_V reacts more slowly to mass injections and increases a bit more until dissipation eventually makes its level drop. The curve then follows a track toward the bottom-left part of the diagram. What follows is a slow secular dissipation of the entire disk along which $P_{\rm BD}$ changes little and P_V diminishes steadily. The detailed shape of the loop depends on the viewing angle, as shown in Figure 6, and also on the value of α.

To generate a PCD, we need to plot a quantity that measures the "color" of the polarized spectrum versus the polarization level at some wavelength. Here, one can employ several quantities to measure the color; for instance, in addition to the polarization change in the Balmer discontinuity, other discontinuities can be used or, alternatively, the slope of the polarized spectrum can be measured directly from the ratio between the polarization values at different bandpasses. An example of different diagrams for the same model can be seen in Figure 7 which compares the use of $P_{\rm BD}$ with the polarization change at the Paschen discontinuity ($P_{\rm PD}$) and the slope of the polarization spectrum as measured by the ratio between the polarization at the B and I bands (P_B/P_I). All diagrams made according to this principle contain roughly the same information in the sense that they enable tracking of the build-up and dissipation phases. For simplicity, from now on, by PCD we refer to the diagram $P_{\rm BD}$ versus P_V.

3.1.3. Diagnostic Potential

Having described the two main features contained in the polarized spectrum (polarization level and color) and how these relate to the disk properties, we now explore the diagnostic potential of polarimetric observations of Be disks, with a focus on the usefulness of the PCDs. Figure 6 already showed that the shape of the loop in the PCD is very sensitive to the inclination angle of the system. Moreover, PCDs are characteristic of the density at the base of the disk and can be used to infer this quantity via VDD modeling. Figure 8 shows the different forms the PCDs can take depending on the density at the base of the disk. The amplitude of the loop in the PCDs is a clear signature of the base density: the loop has a bigger extent for a higher density, whatever the inclination angle. If the disk undergoes an almost constant build-up phase, the top region of the PCD is reached in less than a year (for a viscous coefficient $\alpha = 1$). Provided a few measurements typically spaced by one or two months and with ∼0.1% uncertainties, Figure 8 shows that it is quite straightforward to disentangle between base densities that are different by a factor of three (except maybe at the end of a long-term dissipation phase). We also note that the slope of the PCDs changes with density. For low densities, the slope is smaller and the loop less broad, while for large densities, the slope increases and the loop gets broader. This is a result of the different weight that H I opacity plays in each model.

Interestingly, PCDs exhibit a secondary loop for very high density models ($>1 \times 10^{-10}$ g cm^{-3}) seen close to equator-on (Figure 9). For all of the PCDs presented so far, the tip of the loop roughly corresponded to the end of the disk build-up phase (for example, see Figure 6). This is easily understood from the fact that the higher the density, the higher the polarization change across the Balmer jump (e.g., Figure 1). However, for the models shown in Figure 9, the tip of the loop (labeled point 1) no longer corresponds to the end of the build-up phase (labeled point 2). This phenomenon is characteristic of high-inclination angles ($i > 80$ deg), and the most likely explanation is a rather complex interplay between pre- and post-scattering absorption. Indeed, the two effects cause both a

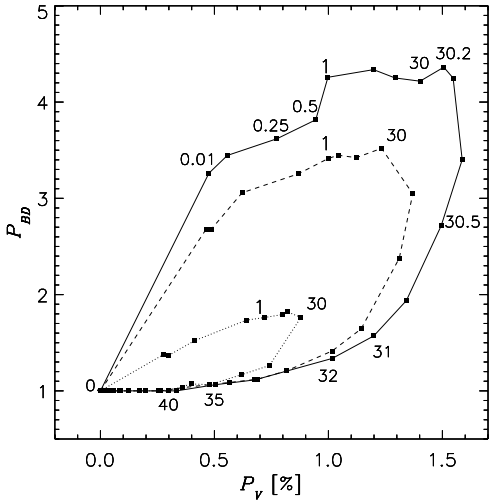

Figure 8. PCD for the reference model with three different base densities: 6×10^{-11} g cm^{-3} (solid line), 3×10^{-11} g cm^{-3} (dashed line), and 1×10^{-11} g cm^{-3} (dotted line). The dynamical scenario involves a B3 star and 30 yr of build-up followed by 30 yr of dissipation. The inclination angle is 85° and $\alpha = 1.0$. The epochs are marked and counted in years for the highest density model. The 1 yr and 30 yr epoch are marked for the three models.

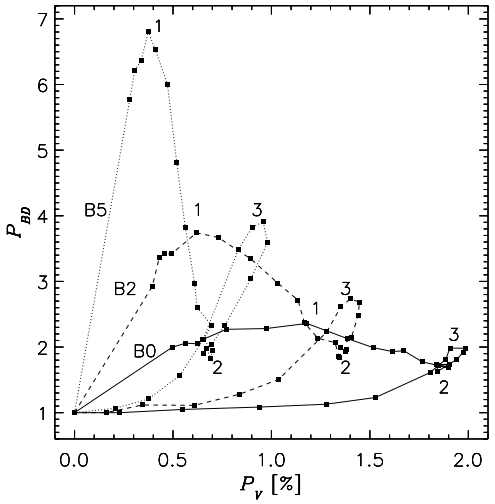

Figure 9. PCDs for three different spectral types (solid for B0, dashed for B2, and dotted for B5) with a dynamical scenario compound of 30 yr of build-up followed by 30 yr of dissipation. The base density is 1×10^{-10} g cm^{-3}. The inclination angle is 90° and $\alpha = 1.0$. Numbers indicate three reference times that help describe the disk evolution in the text. Whereas 1 and 3 represent different epochs depending on the spectral type, the number 2 always marks the stop of mass injection in the disk at $t = 30$ yr.

decrease in the polarization value and a change in the color of the polarized spectrum. However, pre-scattering absorption depends on the conditions of the innermost part of the disk, whereas

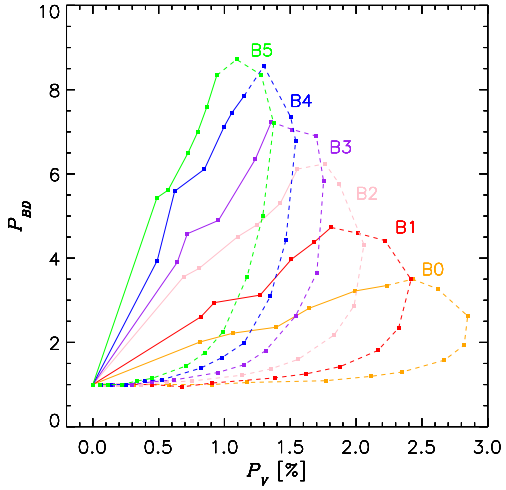

Figure 10. PCD for a central star of different spectral types, as indicated. The scenario is the same as for Figure 8. The solid lines mark the build-up phase, and the dashed lines represent the dissipation phase. The base density is 6×10^{-11} g cm^{-3}. The inclination angle is 70° and $\alpha = 1.0$.

(A color version of this figure is available in the online journal.)

post-scattering absorption follows the conditions at much larger radii. We thus explain Figure 9 as follows: for the onset of the disk formation to point 1, the loops follow a normal behavior. As time passes, $P_{\rm BD}$ grows as a result of the density increase everywhere in the disk. As the disk continues to grow and to become more dense, post-scattering absorption starts to play a role in lowering $P_{\rm BD}$ (point 1 to 2). The track between point 1 and 2 in Figure 9 thus indicates the growing role of the outer disk in absorbing the polarized flux coming from the innermost parts of the disk. When mass injection stops (point 2), P_V increases for reasons already explained in Section 3.1, and $P_{\rm BD}$ also increases due to the smaller post-scattering absorption. At point 3, post-scattering absorption becomes negligible and, at the same time, the $P_{\rm BD}$ also drops due to the lack of density. This is why the $P_{\rm BD}$ level at the top of the secondary loop (point 3) is always smaller than the level at the top of the primary loop (point 1). Finally, the PCD follows a normal track toward $P_{\rm BD} = 1$ and $P_V = 0$, characteristic of an emptying disk. Moreover, since this post-scattering absorption changes the color of the polarized spectrum, the phenomenon we just described is more important for late spectral type stars where the polarization color is more pronounced. From the observational point of view, this example shows that it is not possible to directly associate a value of $P_{\rm BD}$ to a disk density scale, at least for close to edge-on viewing.

Figure 4 showed how the maximum polarization of a given model depends on $T_{\rm eff}$. A strong dependence of the PCD on the central star spectral type is thus to be expected. In Figure 10, we can see that the spectral type impacts the PCD in various ways. Firstly, the range of P_V values plotted in the PCD increases with increasing $T_{\rm eff}$ (in agreement with Figure 4). Secondly, the slope of the PCD increases with decreasing $T_{\rm eff}$. This again can be understood in terms of the relative importance of electron scattering opacity versus H I opacity.

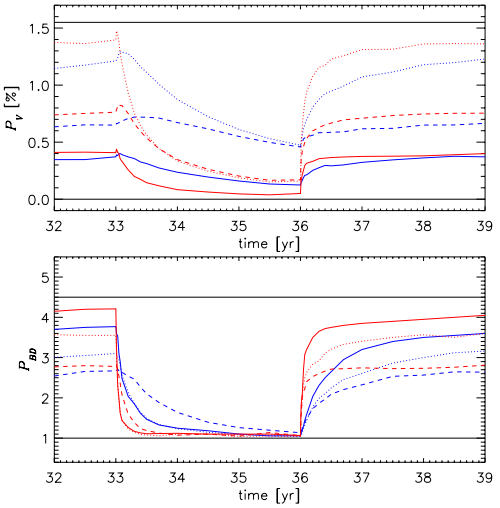

Figure 11. Same as for Figure 5 for the sixth cycle of a periodic mass injection scenario with period of six yr and a duty cycle of 50%. The solid black lines indicate the limit values that are reached for uninterrupted build-up and dissipation phase.

(A color version of this figure is available in the online journal.)

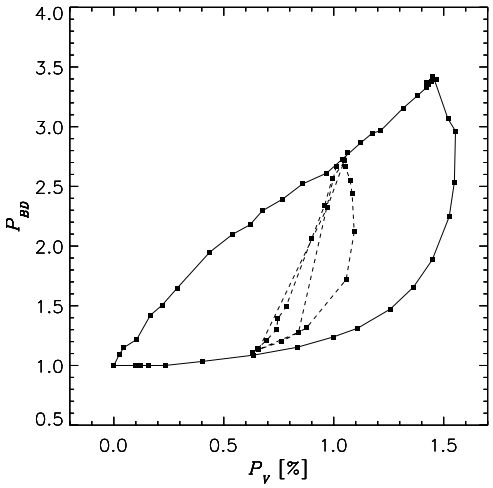

Figure 12. PCD at a 70° inclination angle and $\alpha = 0.1$ for the same dynamical scenario shown in Figure 6 (solid line) and for another one where the mass injection rate is periodically turned on and off every one year (dashed line).

As seen above, the higher the effective temperature, the lower the bound-free opacity for a given density. Also, the lower the bound-free opacity, the smaller the polarization change across the Balmer discontinuity. Therefore, the slope of the loop in the PCD is a good tracer of the bound-free opacity. In view of the results shown in Figures 8 and 9, the diagnostic potential of the PCD as a measure of the disk density depends critically on a good determination of the spectral type of the central star.

Halonen & Jones (2013a) studied the shape of the PCD loops using ad hoc models that simulated the disk growth and dissipation by simply changing the inner and outer radius of the disk while keeping the density slope fixed to its steady state value ($n = 3.5$). A quantitative agreement between this work and their results is not to be expected due to the different disk models used but also because their definition for $P_{\rm BD}$ is based on the difference between polarization levels before and after the Balmer discontinuity instead of the ratio (definition used in the present work).

3.2. Periodic Mass Loss Rate

The previous section dealt with the case of a disk forming when none exists and the dissipation of a fully formed disk. This situation has been already observed in several Be stars. Some examples include π Aqr (a well-documented disk dissipation that started in 1986 can be found in Wisniewski et al. 2010) and the disk growth of ω Ori in the eighties (Sonneborn et al. 1988). In between these limiting cases, most Be stars display either an irregular variability or, what is more rare, a quasi-cyclic variation of the light curve (Sabogal et al. 2008). The best-studied example of the latter case is ω CMa, that displays two to three yr long outbursts separated by four to five yr of quiescence (Štefl et al. 2003). In this section, we explore the polarization signature expected when the mass injection is periodically turned on and off.

A periodical scenario is defined by three parameters, the mass injection rate, the period, and the duty cycle, which indicates the fraction of time in each cycle where the mass injection rate is larger than 0 (see Paper I for details). Figure 11 shows the temporal evolution of P_V and $P_{\rm BD}$ for a periodic mass injection scenario (six-yr period and 50% duty cycle, meaning that mass is continuously injected into the disk for three years every six years). The main difference between this case and the scenarios seen in Section 3.1 is that the disk doesn't totally build and dissipate. The lowest values of P_V and $P_{\rm BD}$ at the end of quiescence are therefore different from 0% and 1, respectively, and the maximum values are less than for an uninterrupted build-up phase (Figure 5). Figure 12 compares the tracks in the PCD of a periodical scenario (one-yr period, 50% duty cycle, dashed curve) to that of a fully formed disk (formation from no previous disk followed by full dissipation, solid curve). The latter case forms a closed loop with maximal extent because at the end of the build-up phase, the disk density approaches a limit value (Paper I), and at the end of the dissipation, the disk matter has been almost completely lost. In the case of a periodical mass injection, however, there are three main differences: (1) the cyclic mass injection prevents the disk density to reach its limit value; (2) at the end of quiescence the disk matter has not yet been fully lost; and (3) a given cycle starts with matter already accumulated in the previous one, so the total disk mass of each successive cycle, at a given phase, is always larger than the previous ones. Observationally, we already saw in Figure 11 that these differences imply that the variations of P_V and $P_{\rm BD}$ will be of a smaller amplitude but it also results in a variation of these curves from cycle to cycle. This last point depends on the parameters of the scenario and is mainly visible for low-period scenarios (i.e., about a year or less for $\alpha = 1.0$). This is well illustrated in Figure 12; the loops in the PCD for a periodic scenario never close, and they are of a smaller amplitude than the loops for fully formed and dissipated disks in which they are confined.

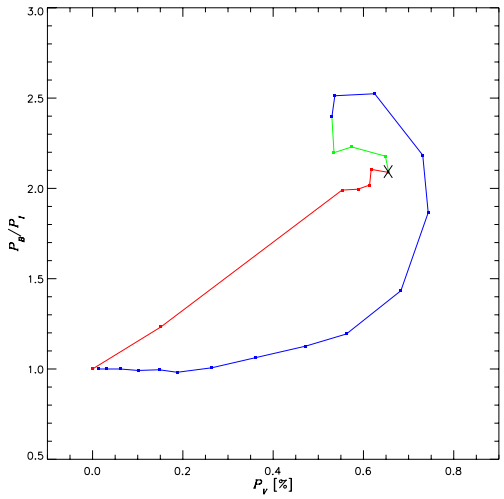

Figure 13. PCD showing P_B/P_I as a function of P_V for a 0.2 yr outburst ($\dot{M} = 3.3 \times 10^{-8}$ $M_\odot$ yr^{-1}, green curve) following a 20 yr long ($\dot{M} = 1.6 \times 10^{-8}$ $M_\odot$ yr^{-1}, red curve) stable period of build-up. The outburst is then followed by a 30 yr dissipation (blue curve). The X point marks the start of the outburst. The parameters are those of the reference model (B2 star). The inclination angle is 39° and $\alpha = 1.0$.

(A color version of this figure is available in the online journal.)

3.3. Episodic Mass Loss Rate

The most common type of variability observed in Be stars is of an irregular nature, which means that the mass injection rate varies with time in a complicated way. One extreme example is the so-called "flickering activity," which is related to short-term variations seen in several observables. Examples of flickering activity can be found in Rivinius et al. (1998; μ Cen, photometry and spectroscopy) and Carciofi et al. (2007; α Eri, polarimetry). The "flickering" is attributed to an enhanced mass injection rate (outburst) that lasts from a few days to several weeks.

To illustrate the effects of an outburst on the polarimetric features, Figure 13 shows a PCD for a dynamical scenario involving a 20 yr long build-up phase followed by a 0.2 yr outburst with a mass injection rate twice higher than for the previous phase. The outburst is then followed by a 30 yr dissipation phase. The first 20 yr of disk formation displays the same signature in the PCD as seen above (red line in Figure 13). After the mass injection rate doubles at $t = 20$ yr, the disk density gradually increases inside-out (see Figure 11 of Paper I for a description on how the disk density evolves with time in this scenario). The signature of the outburst (green curve in Figure 13) in the PCD is quite curious; while P_B/P_I stays essentially the same, P_V initially decreases between epochs 20.01 and 20.1 yr. This can be understood in terms of the sudden increase in the disk continuum emission (Figure 21 of Paper I) as a result of the enhanced densities in the inner disk. After the disk total mass adjusts to the new mass injection rate($\dot{M} = 1.6 \times 10^{-8}$ $M_\odot$ yr^{-1} at epoch 20 yr or so), then P_V increases again. After the end of the outburst, mass injection is turned off ($t = 20.2$ yr) and the model follows a dissipative path in the PCD (blue curve), as seen before. The outburst thus adds an extra outgrowth to the loop compared to a dynamical scenario without any outburst and should be quite well-identified provided a sufficient time coverage of polarimetric observations.

4. COMPARISON OF THE PREDICTIONS WITH OBSERVED DATA

Long-term polarimetric observations of the Be stars 60 Cygni and π Aquarii were obtained with the spectropolarimeter HPOL and revealed several year long disk-loss episodes interrupted by outbursts (Wisniewski et al. 2010). PCDs made out of these measurements showed loop patterns whose general shape was generally well described with viscous disk build-up and dissipation phases (Draper et al. 2011). More recently, Draper et al. (2013) presented a polarimetric follow-up of nine Be stars among which some of them exhibited very characteristic PCD patterns, similar to the ones we showed in the last section.

In this section, we compare our theoretical predictions with PCDs obtained from HPOL measurements for 60 Cygni, π Aquarii, and ψ Persei. We refer the reader to Draper et al. (2013) for further details regarding the observational data. Moreover, we also discuss polarimetric measurements of δ Scorpii made with the IAG polarimeter at the Pico dos Dias Observatory (Bednarski & Carciofi 2012).

4.1. π Aquarii

The PCD of π Aqr presents a very clear observational evidence of a partial loop obtained during a ∼180 day polarimetric flare (Figure 14, left panel). From a pre-existent disk ($P_V = 0.9\%$, $P_{\rm BD} = 1.8$), the loop starts with a build-up phase until it reaches a maximum $P_{\rm BD}$ value of 2.2. After that, an irregular dissipation pattern (with small deviations probably due to short-lived mass injection events) is seen. As already reported in Draper et al. (2011) and in the present paper, the general clockwise loop is well explained by viscous processes. The exact PCD then depends on an interplay between the injected quantity of matter, the inclination angle, the α parameter and a good knowledge of the disk state before the outburst. Such in-depth analysis will be carried out in the future. However, π Aqr being a B1 type star (Slettebak 1982), the range of the observed P_V and $P_{\rm BD}$ values are consistent with the range of the values shown in Figure 10. Since these latter values correspond to maximum values obtained for full build-up and dissipation cases, we conclude that the π Aqr polarimetric observations are compatible with our VDD predictions.

4.2. 60 Cygni

60 Cyg presents a more complex case (Figure 14, middle panel). The first part of the PCD loop forms a clear clockwise loop that is well understood with a classical building-up/dissipation scenario, albeit with an irregular shape, suggestive of possible events of mass injection into the disk. In this part, the slopes are quite high for a B1 spectral type star (Slettebak 1982) when compared with Figure 10. We speculate that this could be a signature of a high base density (i.e., high mass injection rates) and/or low inclination angles. The remaining data points follow a quite irregular track in the PCD, displaying the enigmatic behavior of an increase of $P_{\rm BD}$ with a simultaneous decrease of P_V. The results of Sections 3.1 and 3.3 suggest possible ways to explain such a behavior (e.g., irregular mass injection rates) but the scarcity of the data points prevents any well-founded interpretation.

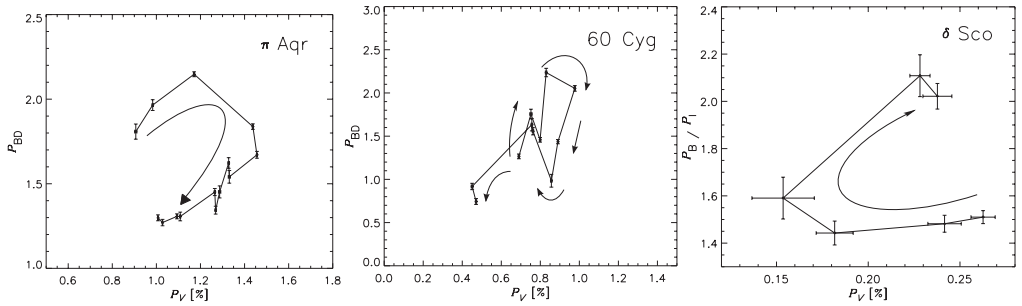

Figure 14. Observed PCDs of π Aqr (left panel) and 60 Cyg (middle panel), from Draper et al. (2013), and PCD of δ Sco (right panel) made from measurements obtained at the IAG polarimeter. For the three PCDs, arrows indicate the chronological succession of epochs.

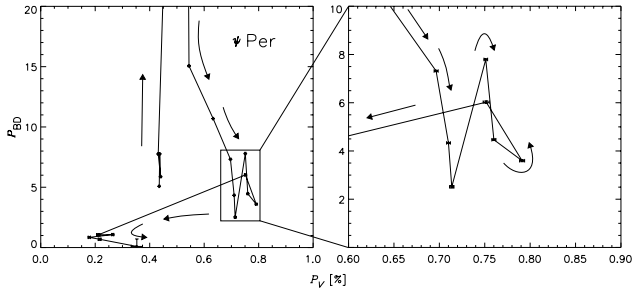

Figure 15. PCD of ψ Per built from HPOL observations that spanned 15 yr.

4.3. δ Scorpii

δ Sco is a B0.2 IVe star with an inclination angle of about 35° (Carciofi et al. 2006). A several-year-long campaign led at the Pico dos dias Observatory (LNA, Brazil) allowed monitoring of the polarimetric activity of δ Sco in the B, V, R, and I filters (Bednarski & Carciofi 2012). At JD $\sim$ 2,445,500, the star was in an intermediary level of activity, having built a large disk over the course of the previous 10 yr, when a photometric increase was observed in 2010 March. Since the star is close to pole-on viewing, this increase is likely associated with a strong outburst (Paper I).

Polarimetric measurements were obtained before, during, and after the 2010 March outburst (Figure 14, right panel). In the PCD, the data shows the following chronological behavior.

1. The P_V level decreases after the photometric outburst had started while the P_B/P_I level stays essentially the same, and
2. as the outburst proceeds, both P_B/P_I and P_V increase.

This behavior is qualitatively very similar to the outburst scenario described in Figure 13. When an outburst happens on top of an already existing disk (which is the case for the 2010 outburst of δ Sco), what is initially seen is a leftward track in the PCD, followed by an up-right track, characteristic of disk build-up and subsequent dissipation. The range of P_V levels are much lower than in Figure 13, which could indicate that the δ Sco disk was not in a very dense state. Even though no attempt is made here to fit the data, it is worth noting that the outburst scenario, as suggested by photometry (Bednarski & Carciofi 2012), is a quite attractive explanation for the unusual track in the PCD seen for δ Sco, which in turn, suggests that this track is consistent with a viscous disk scenario. This certainly deserves further scrutinization.

4.4. ψ Persei

Another observed PCD that we can compare to our models, especially with Figure 9, is ψ Per (B5 star with a disk inclination angle of 75° $\pm$ 8°; Delaa et al. 2011). Figure 15 represents a 15 yr long polarimetric monitoring of this star. The first characteristic of this PCD is the gigantic variation seen in P_{BD} while P_V steadily increases over a period of 10 yr, indicating that the disk is overall building up. The data point which is off scale corresponds to $P_V \sim 0.5$ and $P_{BD} \sim 80$. Second, after P_{BD} decreased, a series of lower amplitude P_{BD} variations are seen (see zoom of Figure 15), until both P_{BD} and P_V decline over a few months. The track that ψ Per follows on the PCD presents many similarities with the curve corresponding to the B5 spectral type in Figure 9. Even though the time-scale and amplitude of the P_{BD} jump is not reproduced specifically by our model, the fact that a high P_{BD} variation is concomitant with a steady increase of P_V supports the fact that ψ Per was experiencing a build-up phase seen at a high-inclination angle and with a very high disk density. We also mention that this peaky shape for a PCD is typical of late-type stars as shown in Figure 9. Moreover, the zoomed panel of Figure 15 also shows a pattern that is very similar to the counter-clockwise secondary loop in the PCD presented in Figure 9. This type of behavior was only observed for models involving an inclination angle of $i >$ 80° and a base density higher than 1×10^{-10} g cm^{-3}. However, we speculate that this sort of PCD could be observed for lower inclination angles if the disk is denser ($\rho_0 > 1 \times 10^{-10}$ g cm^{-3}).

It is important to mention that loop-shaped PCDs can also be qualitatively reproduced using spiral oscillation models as demonstrated in Figure 9 of Halonen & Jones (2013b). In this approach, a one-armed density wave that is confined to a region extending out to 10 $R_\star$ generates distinct shapes for the PCDs as well as characteristic signatures in the polarization angle variation. We conclude by saying that a detailed modeling specific to each observed Be star is needed to understand the origin of the polarimetric variability. PCDs and polarization angle measurements are critical observable quantities to disentangle a scenario involving a variable mass injection rate in an axisymmetric disk (with no polarization angle variation expected) from a scenario including a one-armed oscillation.

5. CONCLUSIONS

In this paper, we first review the mechanisms at the origin of the continuum polarization levels observed for Be stars under the assumption of a steady-state VDD model. For different disk densities and spectral types, we detail how the electron scattering, bound-free, and free-free opacities shape the polarized spectrum. Analyzing these opacities further, we describe how they vary radially to establish the regions of the disk that are electron-scattering dominated and the regions that are bound-free dominated. For low densities (typically 1×10^{-12} g cm^{-3}), all models are electron scattering dominated and the polarization spectrum is roughly flat regardless of the spectral type. For larger densities (typically greater than 1×10^{-11} g cm^{-3}), the bound-free opacity becomes the dominant opacity in the disk, at least in its innermost part. Based on this opacity description, we can define two polarimetric features that depend on different disk properties: P_V, the polarization level in the visible (or any other wavelength), is a measure of the scattering mass of the disk; and $P_{\rm BD}$ (the polarization change across the Balmer jump), a measure of the color of the polarization spectrum, which depends on the relative importance of the bound-free opacity to the total opacity. With a more realistic modeling based on a coupling of hydrodynamics and radiative transfer simulations, we show how these polarimetric features evolve with time for different disk mass injection scenarios. Different mass injection histories (constant, periodic, or episodic) result in specific behaviors of the polarimetric observables. This led us to introduce an extension of the concept of BJV diagrams (Draper et al. 2011) that we named PCD as an analogy to color magnitude diagrams. The PCD plots $P_{\rm BD}$ (or other measure of the polarization color) versus the polarization level. PCDs constitute a powerful diagnosis tool to derive different physical parameters of the disk such as the inclination angle, the viscous coefficient α, the disk base density, and the spectral type of the central star on top of the mass injection history. Typically, the polarimetric features of a star evolving from a diskless phase (normal B star) to a Be phase (with a disk present) and back to a B phase will appear as a loop in the PCD, the upper part of the loop being associated with the disk construction and the lower part with the dissipation. In some particular cases of very high densities and high inclination angles, morphologic variations of the PCDs with the apparition of a secondary loop were found. Albeit the useful diagnostic potential, the morphologies seen in the PCD bear some degeneracy with respect to some parameters. For this reason, we stress that the more observables and better time coverage, the easier it is to infer a dynamical scenario and physical parameters of the system. The theoretical predictions were confronted with observed PCDs of four stars. While π Aqr exhibits quite a clear build-up/dissipation pattern in its PCD, 60 Cyg presents a more irregular case that is likely to be the result of mass injection rate variations. We then analyze the PCD of δ Sco and speculate that it probably represents the polarimetric counterpart of an outburst seen with photometry. Finally, we point out that the huge variations and the counter clockwise structure of ψ Per's PCD can be explained with our predictions for a B5 spectral type star, with a high inclination angle and a high density. However, a detailed modeling needs to be carried out for each specific star in order to achieve an accurate reproduction of the observed PCDs.

X.H. thanks FAPESP for supporting this work through the grants 2009/07477-1 and 2010/19029-0. B.C.M. acknowledges support from CNPq (grant 133338/2012-6). A.C.C. acknowledges support from CNPq (grant 307076/2012-1) and Fapesp (grant 2010/19029-0). D.B. acknowledges support from CNPq (grant 134761/2012-0). This work has made use of the computing facilities of the Laboratory of Astroinformatics (IAG/USP, NAT/Unicsul), whose purchase was made possible by the Brazilian agency FAPESP (grant 2009/54006-4) and the INCT-A.

APPENDIX

THE RADIAL DEPENDENCE OF THE BOUND-FREE ABSORPTION COEFFICIENTS

Figure 2 shows that the radial dependence of the bound-free absorption coefficient is much steeper than the radial dependence of the density itself. A similar figure (Figure 16) compares how the scattering and bound-free absorption coefficients change with changing density for two spectral types. It is interesting to note that the bound-free absorption coefficient becomes dominant on a larger extent of the disk for both base densities for later spectral types.

The radial dependence of the bound-free absorption coefficients in these two figures, consider the expression for the bound-free absorption coefficient in the Paschen continuum ($\lambda_2 < \lambda < \lambda_3$, where $\lambda_2 = 3646$ Å and $\lambda_3 = 8203$ Å are the H I $n = 2$ and 3 photoionization thresholds). Taking into account, for simplicity, only the contributions of H I levels $n = 2$ and 3 to the opacity (e.g., Bjorkman & Bjorkman 1994, Equation (30))

$$a_{\rm bf}(\lambda, r) = n(r)\left[N_2 b_2 \left(\frac{\lambda}{\lambda_2}\right)^3 + N_3 b_3 \left(\frac{\lambda}{\lambda_3}\right)^3\right], \quad \text{(A1)}$$

where the photoionization cross sections are $b_2 = 1.4 \times 10^{-17}$ cm^{-2} and $b_3 = 2.2 \times 10^{-17}$ cm^{-2}, $n(r)$ is the particle number density, and N_2 and N_3 are the fractional occupation numbers of H I.

The H I occupation numbers of the same models shown in Figure 2 and in the left panel of Figure 16 are plotted in Figure 17. N_3 is much smaller than N_2 everywhere in the disk, so, to a first approximation, the contribution of the atoms in this level (and above) can be ignored. Thus, the radial dependence of $a_{\rm bf}$ is thus controlled by the (explicit) radial dependence of $n(r)$ and the (implicit) radial dependence of N_2

$$a_{\rm bf}(\lambda, r) \propto n(r) N_2 \propto r^{-(A+B)}, \quad \text{(A2)}$$

where A is the slope of the density distribution and B is the radial variation of N_2. For a steady-state disk, $A = 3.5$ (Section 2). The value of B is not constant, as is apparent from the fact that the N_2 curves in Figure 17 are not straight lines. However,

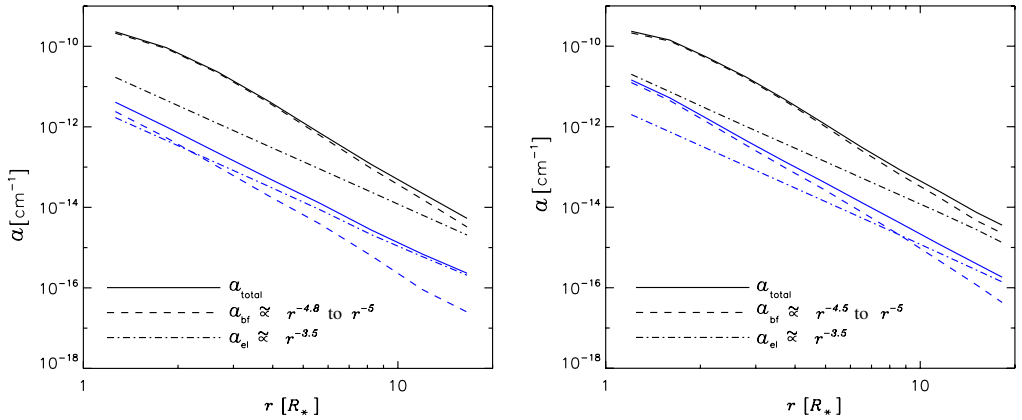

Figure 16. Same as Figure 2 for a B2 star (left) and B3 star (right) and two different base densities: $\rho_0 = 4.2 \times 10^{-11}$ g cm^{-3} in black, and 4.2×10^{-12} g cm^{-3} in blue.
(A color version of this figure is available in the online journal.)

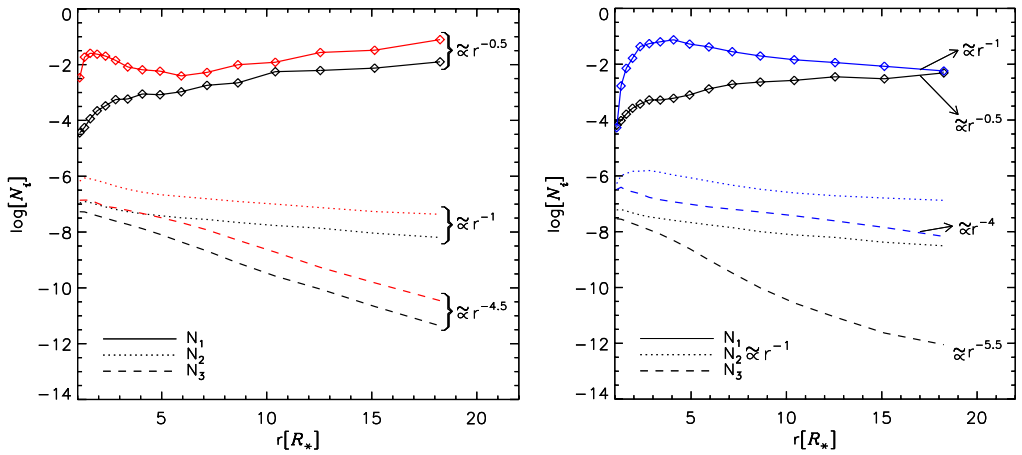

Figure 17. Hydrogen level populations (up to level 3) vs. distance from the star. Left: results for different spectral types (B2 in black and B4 in red) for a steady-state VDD with $\rho_0 = 8.4 \times 10^{-12}$ g cm^{-3}. Right: results for different base densities ($\rho_0 = 4.2 \times 10^{-12}$ g cm^{-3}, black, and 8.4×10^{-11} g cm^{-3}, blue) for a B2 star. Power-law indexes are indicated.
(A color version of this figure is available in the online journal.)

representative values of B can be found by fitting the N_2 with a power law. The results, shown in Figure 17, give $B \sim 1$. Thus, a_{bf} falls approximately as $r^{-4.5}$.

REFERENCES

Bednarski, D., & Carciofi, A. C. 2012, in ASP Conf. Proc. 464, Circumstellar Dynamics at High Resolution, ed. A. Carciofi & Th. Rivinius (San Francisco, CA: ASP), 239

Bjorkman, J. E. 1997, in Stellar Atmospheres: Theory and Observations, ed. J. P. De Greve, R. Blomme, & H. Hensberge (Lecture Notes in Physics, Vol. 497; Berlin: Springer), 239

Bjorkman, J. E., & Bjorkman, K. S. 1994, ApJ, 436, 818

Bjorkman, J. E., & Carciofi, A. C. 2005, in ASP Conf. Ser. 337, The Nature and Evolution of Disks Around Hot Stars, ed. R. Ignace & K. G. Gayley (San Francisco, CA: ASP), 75

Carciofi, A. C. 2011, in IAU Symp. 272, Active OB Stars: Structure, Evolution, Mass Loss, and Critical Limits, ed. C. Neiner, G. Wade, G. Meynet, & G. Peters (Cambridge: Cambridge Univ. Press), 325

Carciofi, A. C., & Bjorkman, J. E. 2006, ApJ, 639, 1081

Carciofi, A. C., & Bjorkman, J. E. 2008, ApJ, 684, 1374

Carciofi, A. C., Bjorkman, J. E., Otero, S. A., et al. 2012, ApJL, 744, L15

Carciofi, A. C., Magalhães, A. M., Leister, N. V., Bjorkman, J. E., & Levenhagen, R. S. 2007, ApJL, 671, L49

Carciofi, A. C., Miroshnichenko, A. S., Kusakin, A. V., et al. 2006, ApJ, 652, 1617

Carciofi, A. C., Okazaki, A. T., Le Bouquin, J.-B., et al. 2009, A&A, 504, 915

Delaa, O., Stee, P., Meilland, A., et al. 2011, A&A, 529, A87

Draper, Z. H., Wisniewski, J. P., Bjorkman, K. S., et al. 2011, ApJL, 728, L40

Draper, Z. H., Wisniewski, J. P., Bjorkman, K. S., et al. 2013, ApJ, in press

Halonen, R. J., & Jones, C. E. 2013a, ApJ, 765, 17

Halonen, R. J., & Jones, C. E. 2013b, ApJS, 208, 3

Haubois, X., Carciofi, A. C., Rivinius, T., Okazaki, A. T., & Bjorkman, J. E. 2012, ApJ, 756, 156

Jones, C. E., Sigut, T. A. A., & Porter, J. M. 2008, MNRAS, 386, 1922
Lee, U., Osaki, Y., & Saio, H. 1991, MNRAS, 250, 432
Meilland, A., Millour, F., Kanaan, S., et al. 2012, A&A, 538, A110
Okazaki, A. T. 2001, PASJ, 53, 119
Okazaki, A. T. 2007, in ASP Conf. Ser. 361, Active OB-Stars: Laboratories for Stellar and Circumstellar Physics, ed. S. Stefl, S. P. Owocki, & A. T. Okazaki (San Francisco, CA: ASP), 230
Porter, J. M. 1999, A&A, 348, 512
Quirrenbach, A., Bjorkman, K. S., Bjorkman, J. E., et al. 1997, ApJ, 479, 477
Rivinius, T., Baade, D., Štefl, S., et al. 1998, A&A, 333, 125
Rivinius, T., Carciofi, A. C., & Martayan, C. 2013, A&ARv, 21, 69
Sabogal, B. E., Mennickent, R. E., Pietrzyński, G., et al. 2008, A&A, 478, 659
Shakura, N. I., & Sunyaev, R. A. 1973, A&A, 24, 337
Slettebak, A. 1982, ApJS, 50, 55
Sonneborn, G., Grady, C. A., Wu, C.-C., et al. 1988, ApJ, 325, 784
Štefl, S., Baade, D., Rivinius, T., et al. 2003, A&A, 402, 253
Tycner, C., Jones, C. E., Sigut, T. A. A., et al. 2008, ApJ, 689, 461
Wheelwright, H. E., Bjorkman, J. E., Oudmaijer, R. D., et al. 2012, MNRAS, 423, L11
Wisniewski, J. P., Draper, Z. H., Bjorkman, K. S., et al. 2010, ApJ, 709, 1306
Wood, K., Bjorkman, J. E., Whitney, B., & Code, A. 1996, ApJ, 461, 847
Wood, K., Bjorkman, K. S., & Bjorkman, J. E. 1997, ApJ, 477, 926

Appendix H

ESO Short-term internship

Project Report: "Binarity and the distribution of rotational velocities in Galactic main-sequence B stars"

Release 2.5

B. C. Mota, C. Martayan, T. Rivinius, D. Moser and A. Shoky

April 15, 2016

CONTENTS

ii

Project Report: "Binarity and the distribution of rotational velocities in Galactic main-sequence B stars", Release 2.5

For several types of stars the distribution of rotational velocities (v sini) is bi- or even multi-modal and is a key tracer of star formation and evolution. Binarity and magnetism are among the main contenders for the explanation. Nominally, the frequency of binaries is a strong function of stellar mass, and the distribution of vsini values appears bimodal in O and A stars and the situation is unclear in B stars (flat or bimodal distribution). But this may be entirely spurious. The sample of telluric standard stars used with X-shooter offers a both large and inexpensive initial database comprising more than a thousand B-type stars. The proposed project aims at consolidating and homogenizing the database, extracting the fraction of binaries and the distribution of v sini for analysis in a star formation and evolution context, and improving the quality of telluric standard stars available for X-shooter and other Paranal instruments.

Full goals:

1. Inspect the data and reduce all spectra with an homogeneous manner and with adapted parameters depending on the sky condition and objects. It is not possible to use the automatically reduced data from the archive because of:

1. the very different sky conditions (extraction problem);
2. the presence of visual binaries/companions (extraction problem);
3. the response curve used is an old one;

2. find the binaries in the sample, looking at the acquisition frames, at the spectra (SB2 or multiple stars from the U to the K band), and with the radial velocity follow-up (SB1);
3. determine if the binaries may have an impact on the evolution and day to day life of the main star of the system;
4. determine the fundamental parameters (T_{eff}, logg, vsini, M, etc) and create observational tracks of the rotational velocity evolution in the Main Sequence for B stars. Determine the chemical abundances. And for the binaries to determine the orbital parameters if possible;
5. provide clean catalogues of telluric standard stars (good spectral classification, no binary) to Paranal and other observatories. This legacy aspect was highlighted by the OPC in its comments;
6. give constraints to the theoretical models and cooperate with the Geneva team lead by G. Meynet.

The purpose of this DGDF is to get some help on items a and b. The project at longer time scale is to obtain a student with Geneva to work on other items and enlarge the cooperation observations/theory.

Project Report: "Binarity and the distribution of rotational velocities in Galactic main-sequence B stars", Release 2.5

CHAPTER

ONE

INTRODUCTION

The B stars represent a significant fraction of massive stars. If only stochastic processes at the time of formation govern the distribution of rotational velocities, the distribution of the latter in any sample of stars of similar age and mass should be smooth and in particular not have multiple maxima. However, exactly the latter is observed in some groups of stars. For both O and A stars the rotational velocity distribution appears to be bimodal. For A main sequence stars (cleaned of binaries and peculiar stars), Royer et al. (2007, A&A,463,671) found this bimodal distribution and explained it by an angular momentum loss and its redistribution in the star before it reaches the main sequence (MS). Zorec & Royer (2012,A&A,537,A120) studied the evolution of A type stars rotational velocities and found 2 different behaviours. The less massive A stars have a monomodal equatorial velocity distribution and have a monotonical acceleration with age during the MS. The most massive A stars show a strong acceleration in the first third part of MS but do not show any angular momentum redistribution in the last third of the MS, which could be related to some differential rotation. Guthrie (1982,MNRAS,198,795) also found a bimodal rotational velocity distribution for late B stars in open clusters while B stars in the field show a flat distribution. The author argues that this difference should come from the way the stars formed.

While Abt et al. (2002, ApJ,573,359) explain that the distributions are massdependent and would be explained by magnetic braking or the presence of lowmass companion or planets. Dufton et al. (2013, A&A, 550, A109) also found for late O to early B in the LMC clusters of the Tarantula region a bimodal or even more complex rotational velocity distribution. They argue that this could be explained by similar mechanism that occurs in A type stars. However, if potential binaries are removed, because the spectral classification has not been performed, one cannot disentangle the effects of stellar evolution from original multi-modal distribution of the rotational velocities.

1.1 Impact on the stellar models

Standard evolutionary tracks do not explain this. The two most relevant additional ingredients are magnetic braking and spin-up in binaries through mass transfer or even mergers. Not only have these properties opposite effects but each of them alone can lead to a bi-modal distribution. Moreover, in binaries, the distribution of angular momentum between spin and orbit introduces an additional complex parameter during the period of their formation. The challenge is to disentangle them, especially if binarity and magnetic-field strength depend on mass. An obvious prerequisite for an improved understanding is to know the initial frequencies of relevant binarity and magnetism. Here, we focus on the binarity of at most moderately evolved B-type stars. In addition this knowledge would possibly also allow understanding some discrepancies between theoretical models of stellar and chemical evolution and some observational results (Hunter et al. 2007,A&A,466,277). Possibly unknown angular momentum transfer phenomenon may have to be discovered and taken into account in the models.

1.2 Binarity

To avoid a bias one must find first the binaries in the sample. The fraction of binaries can reach up to 75 % of O stars (Sana et al. 2012, Sci,337, 444), while the fraction for A-type stars would be around 50 % (Duchene

Project Report: "Binarity and the distribution of rotational velocities in Galactic main-sequence B stars", Release 2.5

& Kraus 2013,ARA&A,51,269) and for F to G type stars this fraction would also be around 55 % (Raghavan et al.,2010,ApJS,190,1). However, the situation for B stars is not so clear and the estimates differ a lot from a study to another. For instance Abt et al. (1990,ApJS,74,551) found about 30 % of spectroscopic binaries in their sample with potentially 40 % more of visual binaries (without certainty whether they are bound or not). Raboud (1996,A&A,315,384) evaluated it in the NGC6231 cluster to be about 52 %, Martayan et al. (2008,A&A,489,459) found a binary fraction of 27 % in NGC6611, while Oudmajer et al. (2010,MNRAS,405,2439) estimated the B binary fraction to range from 22 to 38 % with NACO adaptive optics images. Chini et al. (2012,MNRAS,424,1925) found that the binary fraction varies with the stellar mass and ranges from 80 % for O stars to 60-70 % for early-B stars and 20-40 % for late B stars. Indeed Duchene & Kraus (2013,ARA&A,51,269) indicate a B binary fraction ranging from 40 to 60 %. Recently Nasseri et al. (2013,CEAB,37,51) with a spectroscopic monitoring found a similar B binary fraction ranging from 50% in early types to 15% in late types with orbital periods from 1 to 1000 days. Such a discrepancy between the fraction of O binaries (70-80 %) and B binaries (70-20 %), while for A binaries it is 50 %, is difficult to believe. It would indicate a different star formation mechanism for creating B stars while it is still critical to reduce the angular momentum during the star formation. The obvious possibility to decrease it is to form binaries with stellar or planetary companions.

CHAPTER

TWO

OBSERVATIONAL DATA

2.1 The sample

The sample is based on the observatory project 093.D-0415(A,B,C) PI: Martayan.

1. About 200 B stars were observed in this project.
2. About 2500 science spectra were obtained.
3. 65% complete in term of OBs and time (strongly vary with the run)
   (a) run A: 162 of 190 OBs, 85.3%, 29.1 of 34h, 85.5%
   (b) run B: 116 of 204 OBs, 56.9%, 19.4 of 34h, 57.0%
   (c) run C: 58 of 126 OBs, 46.0%, 9.7 of 21h, 46.2%

In addition to the observations, most of the stars have 1 to 3 spectra in the X-Shooter archive:

- Run A, at least 1 spectrum in the archive, and for run B and run C, generally at least 2 spectra;
- In total each object has about 4 to 6 different epochs of observation;
- The objects were observed under photometric transparency to thick clouds, seeing of 0.6" to 4", Full Moon or no Moon;
- Some of the objects are known to host a binary companion or an exoplanet candidate. They will be used as test bench to probe the radial velocity accuracy and stability of X-Shooter on real data.

2.2 The instrument

X-Shooter is a single target spectrograph for the Cassegrain focus of one of the VLT UTs (Vernet et al. 2011, A&A, 536A, 105), convering, in a single exposure, the spectral range from the UV to the K' band (300-2500 nm) at intermediate spectral resolution (R ~ 4000-17000, depending on wavelength and slit width) with fixed echelle spectral format. The instrument consists of four arms with two cameras, namely: Aquisition and Guinding. The 3 spectroscopic arms cover the ranges:

1. UVB - 300-559.5 nm
2. VIS - 559.5-1024 nm
3. NIR - 1024-2480 nm

Project Report: "Binarity and the distribution of rotational velocities in Galactic main-sequence B stars", Release 2.5

CHAPTER

THREE

TOOLS

In this chapter, we describe the tool used to do the data reduction, and the three python routines developed to study the reduced data: Py-XShooter, PharaohUS, and calc_vsini.

3.1 Reflex

Reflex is the ESO Recipe Flexible Execution Workbench recommended in the reduction of ESO data. This recipe offers some facilities to the user, such as a global graphical vision of the data reduction cascade (workflow), for more details we suggest the reading of Freudling et al. 2013. Briefly, this recipe automatically organizes input files according to their category before run the reduction chain. The user has the option to inspect and interact in each reduction step, having the possibility of rerun any step.

3.1.1 Installation

In order to install the *eso-reflex*, we suggest the procedure described in http://www.eso.org/sci/software/pipelines/reflex_workflows/index.html. After that, it is important to define the amount of memory that will be reserved to the Reflex, it may be done by the command line */bin/esoreflex_set_memory* (p.e. 1024; 2018m).

3.1.2 Reduction

Reflex X-shooter Tutorial can be acessed in ftp://ftp.eso.org/pub/dfs/pipelines/xshooter/. The raw data was reduced following the procedure described in the manual **xshoo-pipeline-manual-12.7.pdf**. The results from this recipe are generally very robust with the default parameters, then, after some attempts to improve the residuals, we have decided to adopt the default parameters in the workflow. Basically, as simple procedure we must access the esoreflex and define the folders where are the raw data and where the results will be saved. After, the data organisation process is done automatically by the recipe. A simple reduction procedure is,

1. Uncompress the data before executing Reflex;
2. $esoreflex &
3. open the X-shooter workflow by clicking on File -> Open File, selecting the file xshoo-2.6.8/xshooter.xml;
4. Tools -> Animate at Runtime, enter the number of milliseconds representing the animation interval (1 ms is recommended);
5. Under “Setup Directories” in the workflow canvas there are seven parameters that specify important directories (green dots). When you have finished, click OK to save your changes;
6. Play start button;
7. Follow the workflow.

Project Report: "Binarity and the distribution of rotational velocities in Galactic main-sequence B stars", Release 2.5

The final products that are copied and renamed are:

1. *<HIERARCH.ESO.OBS.NAME>_SCI_SLIT_FLUX_MERGE1D_<ARM>.fits* - The flux-calibrated, extracted and merged science spectrum. This product is only generated if an appropriate instrument response curve (master or otherwise) was used as an input to the Science Reduction actor.
2. *<HIERARCH.ESO.OBS.NAME>_SCI_SLIT_MERGE1D_<ARM>.fits* - The extracted and merged science spectrum.
3. *<HIERARCH.ESO.OBS.NAME>_SCI_SLIT_MERGE2D_<ARM>.fits* - The merged 2-dimensional science spectrum.
4. *<HIERARCH.ESO.OBS.NAME>_SKY_SLIT_MERGE1D_<ARM>.fits* - The merged 2-dimensional sky spectrum (not for nodding mode data).
5. *<HIERARCH.ESO.OBS.NAME>_SCI_SLIT_IDP_<ARM>.fits* - The corresponding final 1D extracted spectra in a format compatible with the Science Data Product Standard needed to submit files to ESO's Science Archive Facility. The standard itself is described in http://www.eso.org/sci/observing/phase3/p3sdpstd.pdf and tips on how to handle the data with common tools are here http://archive.eso.org/cms/eso-data/help/1dspectra.html.

3.2 PY-XShooter

PY-XShooter is an python routine developed to generate, in an easy way, the desired outputs by the user. This routine depends on several python packages: numpy, matplotlib, astropy, pyfits, gzip, re, scipy, math, astropy, csv, astroquery, aplpy, lineid_plot, pyhdust, pyraf, ureka.

3.2.1 Running

To run the routine is required to define the folders where are the input files (raw data to create the images, tag **input_data_raw**, and the end products data to create the science figures, tag **input_data**). Having defined these folders, the user must define the path where the routine is installed in the tag **commum_folder**.

Having defined properly all folders and options, the code can be runned in terminal by typing

```
ur_setup
python xshooter.py or ipython xshooter.py
```

The routine creates a folder with the following structure for each star observed:

1. Star name
   (a) lines
   (b) sed
   (c) images
   (d) bcd
   (e) vsini

Important: This structure is preserved when is started the second step, i.e. when the routine PharaohUS begins to calculate the stellar parameters (see details in the next section).

Inside the folder **lines**, all given lines (defined in lists for each xshooter arm) are saved separatelly, i.e. one by folder. Each of these folders contains three files: two for the line profile (flux vs wavelength and flux vs velocity) and one showing the temporal evolution of the line equivalent width.

The second folder, **sed**, two files, one with all sed's plotted in only one plot area, and another with the fluxes separeted by arm.

The folder **images** has the aquisition images taken from the raw data. These figures can be used in order to check for potential visual companion.

The folder **bcd** has the results of the BCD analysis (which is not impacted by the circumstellar environment). In this folder, we have a text table with the inferred fundamental stellar parameters (Teff, logg, etc), a figure illustrating BCD procedure, and four figures that show the resulting interpolation for each stellar parameter.

The last folder, **vsini**, contains the results for the independently calculated vsini for each X-Shooter arm.

3.2.2 Some Options

There are five variables that can be modified:

1. interact = 'yes' or 'no'
2. plot_images = True or False
3. plot_sed_lines = True or False
4. delta = 50. #Angstrom

Trought the option *interact*, the user could visualize the normalization by interacting with an iraf window. Then, it is possible to check the quality of the normalization, as well as change some standard adopted parameters.

The option *plot_images* is used for the cases in which the user is not interested in save the aquisition images. If this option is True, the images will be saved automatically in the same folder from that of the science figures.

The option *plot_sed_lines* should be equal True, if you want to generate the science figures (line profiles, SEDs, the BCD analysis results, and inferred stellar parameters).

Delta is the range around the line that must be considered during the simulation. This value must be choosen correctly, otherwise it is possible to take another line during the simulation, instead of the correct one.

Following are the description of the functions in this routine:

py_xshooter.**bcd_analysis**(*obj*, *wave*, *flux*, *flux_norm*, *folder_fig*)
This function performs the BCD analysis.

Parameters

- **obj** – star name (string)
- **wave** – Array with the wavelenghts in Angstrom (numpy array)
- **flux** – Array with the fluxes (numpy array)
- **flux_norm** – Array with the normalized fluxes (numpy array)
- **folder_fig** – folder where the figures will be saved (string)

Star_name star name (string)

Returns D and lambda_0 (BCD parameters)

py_xshooter.**calc_dlamb**(*wave*, *flux*, *center_wave*, *delta*)
This function calculates the shift of the line.

Parameters

- **wave** – Observed wavelenght of the line (float, ex: 6562.81 #AA)
- **flux** – Array with the fluxes (numpy array)
- **center_wave** – Lab central wave (float)
- **delta** – range to be considered around the lamb_obs (float)

Project Report: "Binarity and the distribution of rotational velocities in Galactic main-sequence B stars", Release 2.5

Returns delta lambda (float)

py_xshooter.**create_class_object**(*list_files*, *obj*)
Create object class for all targets in a list.

Parameters **list_files** – list of XShooter fits files (array)

Returns data (class object)

py_xshooter.**create_images**(*list_files*, *folder_fig*)
Plot the images for each observed star from the aquisition images.

Parameters

- **list_files** – list of XShooter fits files (array)
- **folder_fig** – folder where the figures will be saved (string)

Returns images

py_xshooter.**create_list_files**(*list_name*, *folder*, *folder_table*)
Creates a list of the files inside a given folder.

Parameters

- **list_name** – list's name (string)
- **folder** – files' folder (string)

Returns creates a txt file, with the files' paths

py_xshooter.**create_list_stars**(*list_files*)
Create list of the observed stars.

Parameters **list_files** – text list with the files' paths

Returns list of stars (array)

py_xshooter.**create_list_stars_img**(*list_files*)
Create list of the observed stars.

Parameters **list_files** – text list with the files' paths

Returns list of stars (array)

py_xshooter.**create_txt_file**(*x*, *y*, *file_name*)
Create a txt file.

Parameters

- **x** – array with n elements (array)
- **y** – array with n elements (array)
- **file_name** – file's name (string)

Returns txt file

class py_xshooter.**data_object**(*name*, *arm*, *mjd*, *list_files*, *name_ffit*, *wave=None*, *flux=None*, *sigm=None*, *wave_vis=None*, *flux_vis=None*, *sigm_vis=None*, *wave_nir=None*, *flux_nir=None*, *sigm_nir=None*)
Class of the stellar objects. Using this class, we can store for each star a sort of variables, which can be easily accessed.

py_xshooter.**find_nearest**(*array*, *value*)
Find the nearest value inside an array.

Parameters

- **array** – array
- **value** – desired value (float)

Returns nearest value and its index (float)

py_xshooter.**fluxXvel**(*wave*, *flux*, *flux_plus_i*, *central_wave*, *delta*, *label*, *ax*, *fit=None*)
Function to plot a line profile.

Parameters

- **wave** – Observed wavelenght of the line (numpy array)
- **flux** – Array with the fluxes (numpy array)
- **flux_plus_i** – Array with the fluxes add by a constant value (numpy array)
- **delta** – range to be considered around the lamb_obs (float)
- **central_wave** – Lab central wave (float)
- **label** – label to be plotted in the legend
- **ax** – subfigure name (ax, ay or az)
- **fit** – Do nothing (boolean)

Returns velocity and associated flux (arrays)

py_xshooter.**ger_tbdata**(*file_name*)
Creates tbdata from hdulist and check if there is fields.

Parameters **file_name** – fits file (string)

Returns tbdata

py_xshooter.**identify_object**(*file_name*)
Function to identify the object.

Parameters **file_name** – fits file (string)

Returns object name (string)

py_xshooter.**normalize_spectrum**(*wave*, *flux*, *input_file*, *output_folder*, *arm*)
Function of normalization.

Source: http://stsdas.stsci.edu/cgi-bin/gethelp.cgi?continuum :param wave: Array with the wavelenght (numpy array) :param flux: Array with the fluxes (numpy array) :param input_file: fits file (string) :param output_folder: folder where it will be saved the output (string) :return: normalized fits file and normalized flux (output_file.fits)

py_xshooter.**plot_arm_lines**(*data*, *folder_fig*, *folder_temp*, *delta*, *star_name*)
Plot the lines for each star inside the data structure.

Parameters

- **data** – list of XShooter fits files (array)
- **folder_fig** – folder where the figures will be saved (string)
- **delta** – plot parameter (float)
- **folder_temp** – folder of the temporary files (string)

Star_name star name (string)

Returns figures and tables

py_xshooter.**plot_fits_image**(*folder_fig*, *fits_file*, *obj*, *mjd*, *scale=None*, *zoom=None*)
Read a simple txt file.

Parameters

- **folder_fig** – folder where it will be saved the figures (string)
- **fits_file** – name of fits file (string)
- **obj** – object name (string)
- **mjd** – MJD (float)
- **scale** – linear, log, and other options (string)
- **zoom** – Plot a zoom of the image? (boolean)

Returns Image

py_xshooter.**plot_line**(*wave*, *flux*, *center_wave*, *delta*, *vel*, *label*, *ax*, *calc_central_wave*, *save_fig=None*, *fig_name=None*, *gauss_fit=None*)

Function to plot a line profile.

Parameters

- **wave** – Observed wavelenght of the line (float, ex: 6562.81 #AA)
- **flux** – Array with the fluxes (numpy array)
- **center_wave** – Lab central wave (float)
- **delta** – range to be considered around the lamb_obs (float)
- **vel** – parameter for the function fit_line (float)
- **label** – label to be plotted in the legend
- **ax** – subfigure name (ax, ay or az)
- **calc_central_wave** – Do calculate the central wave? (boolean)
- **save_fig** – Save the figure? (boolean)
- **gauss_fit** – Would you like to perform a gaussian fit? (boolean)

Returns figures

py_xshooter.**plot_sed**(*data*, *folder_fig*, *folder_temp*, *star_name*)

Plot the SED for each star inside the data structure.

Parameters

- **data** – list of XShooter fits files (array)
- **folder_fig** – folder where the figures will be saved (string)
- **folder_temp** – folder of the temporary files (string)

Star_name star name (string)

Returns data (class object)

py_xshooter.**print_keys**(*file_name*)

Simple function to print the keys header of a fits file.

Parameters **file_name** – fits file (string)

Returns keys

py_xshooter.**read_fits_star_name**(*file_name*, *typ*)

Read XShooter's fits files.

Parameters

- **file_name** – name of the file in fit extension (string)
- **typ** – define if it will be used to read a image (typ='img')or a

bintable (typ='data'). :return: parameters (object if typ='data', file_name if typ='img')

py_xshooter.**read_fits_xshooter**(*file_name*, *print_obj*)
Read XShooter's fits files.

Parameters **file_name** – name of the file in fit extension (string)

Returns parameters (obj, obs_date, mjd, arm, wave, flux,

sigma, qual, snr, flux_red, sigm_red)

py_xshooter.**read_header**(*file_name*)
Simple function to read the header of a fits file.

Parameters **file_name** – fits file (string)

Returns header

py_xshooter.**read_header_aquisition**(*file_name*)
Read header of the aquisition images.

Parameters **file_name** – name of the fits file (string)

Returns object name (string), MJD (float), xshooter arm (string)

py_xshooter.**read_header_simple**(*file_name*)
Read header of a simple fits file.

Parameters **file_name** – name of the fits file (string)

Returns header_1 (string), header_2 (string)

Note: Somethimes, some fits file exhibit two headers.

py_xshooter.**read_list_files_all**(*table_name*, *folder_table*)
Read list of files in a table, and returns all fits file in an array.

Parameters

- **folder_table** – table's folder (string)
- **table_name** – Table's name (string)

Returns list of files (txt file)

py_xshooter.**read_list_files_star**(*table_name*)
Read list of files listed in a table, and returns the star's fits names in an array.

Parameters **table_name** – Table's name (string)

Returns list of files (txt file)

py_xshooter.**read_norm_fits**(*file_name*)
Read XShooter's normalized fits files.

Parameters **file_name** – name of the fits file (string)

Returns normalized flux (array)

py_xshooter.**read_txt**(*table_name*, *ncols*)
Read a simple txt file.

Parameters

- **table_name** – name of the table
- **ncols** – number of columns

Returns x, y (arrays) or x, y, z (arrays)

py_xshooter.**read_zipfile**(*folder*, *zip_file*)
Read the content of a zip file.

Parameters

- **folder** – folder with the files (string)
- **zip_file** – name of the file

Returns file content

py_xshooter.**remove_negs**(*num_list*)
Removes the negative values from a list.

Parameters **num_list** – array of values (array)

Returns keys

py_xshooter.**smooth_spectrum**(*wave*, *flux*, *doplot=None*)
Smooth the spectrum by convolving with a (normalized) Hann window of 400 points.

Parameters

- **wave** – Array with the wavelenght (numpy array)
- **flux** – Array with the fluxes (numpy array)
- **doplot** – Would you like to see the plot? (boolean)

Returns smoothed flux (array)

py_xshooter.**unzip_file**(*folder*, *folder_table*, *zip_file=None*, *list=None*)
This routine unzip a file or a list of files in a given folder.

Parameters

- **folder** – file's folder (string)
- **zip_file** – file's names (string)
- **list** – to unzipped more than one file put list=True, otherwise False

Returns unzipped file

Example:

folder = '/run/media/sysadmin/SAMSUNG/reduzindo/runC/' folder_table = '/run/media/sysadmin/SAMSUNG/reduzindo/' unzip_file(folder, folder_table, list=True)

3.3 PharaohUS

PharaohUS is an python routine that, given the BCD parameters, uses a Scipy interpolation method (*griddata*) to interpolate the stellar parameters from a stellar grid models. The importance of this interpolator is that it is capable of Interpolate unstructured D-dimensional data.

3.3.1 Some Options

The user can define these parameters:

1. resolution = 1000. # resolution of the color maps
2. read_files = True # If you want to read the files
3. interpol = True # Do you want to execute the interpolation?
4. plot3d = False # Plot 3D maps
5. plot_labels = False # Plot values alongside the points
6. cmap = 'plasma' # color map (many options)
7. interpol_method # 'linear', 'nearest', 'cubic'
8. list_models # Define file with the models data: '1.0_all' #'0.5_all'

3.3.2 Running

To run the routine is necessary to define the folders where are the input files (data tables, tag **folder_table**, and the folder where the data will be saved, tag **folder_results**). Having defined these folders, the user must define the path where the routine is installed in the tag **commum_folder**.

Having defined properly all folders and options, the code can be run in terminal by:

```
ur_forget
python pharaohus.py or ipython pharaohus.py
```

Following are the description of the functions in this routine:

pharaohus.**create_class_object**(*list_files*)
Create object class for all targets in a list.

Parameters **list_files** – list of XShooter fits files (array)

Returns data (class object)

pharaohus.**create_list_files**(*list_name*, *folder*, *folder_table*)
Creates a list of the names inside a given folder.

Parameters

- **list_name** – list's name (string)
- **folder** – files' folder

Returns creates a txt file, with the files' paths

pharaohus.**create_txt_file**(*x*, *y*, *w*, *z*, *h*, *q*, *file_name*)
Create a txt file.

Parameters

- **x** – array with n elements (array)
- **y** – array with n elements (array)
- **file_name** – file's name (string)

Returns txt file

class pharaohus.**data_object**(*name*, *lamb0*, *D*)
Class of the stellar objects. Using this class, we can store for each star a sort of variables, which can be easily accessed.

pharaohus.**find_nearest**(*array*, *value*)
Find the nearest value inside an array.

Parameters

- **array** – array
- **value** – desired value (float)

Returns nearest value and its index (float)

pharaohus.**read_list_files_all**(*table_name*, *folder_table*)
Read list of files in a table, and returns all fits file in an array.

Parameters

- **table_name** – Table's name (string)
- **reflex** – If you want to unzip the files to run reflex

Returns list of files (txt file)

pharaohus.**read_txt**(*table_name*)
Read a simple txt file.

Parameters

- **table_name** – name of the table
- **ncols** – number of columns

Returns x, y (arrays) or x, y, z (arrays)

pharaohus.**read_txt_2**(*table_name*, *ncols*)
Read a simple txt file.

Parameters

- **table_name** – name of the table
- **ncols** – number of columns

Returns x, y (arrays)

pharaohus.**rotate**(*matrix*, *degree*)
Function to rotate a matrix.

Parameters

- **matrix** – matrix (array)
- **degree** – rotation (float)

Returns matrix (array)

3.4 calc_vsini

calc_vsini is an python routine that calculates vsini values for a list of stars. The method uses the rotational broadening pyasl.rotBroad function and the Grids of model atmospheres - Kurucz. The routine reads the effective temperature and logg inferred by the BCD method applied by the Pharaohus routine. Its results are save in the folder *star_name/vsini*.

3.4.1 Some Options

The user can define these parameters:

1. delta = 200 # Range of points to be considered around the central wave;
2. plotchi2_map = True # Plotting the χ^2_{red} map;
3. center_wave_vis = 6562.8 # A choosen line in visible arm ;
4. center_wave_uvb = 4861. # A choosen line in uvb arm;
5. center_wave_nir = 21654. # A choosen line in nir arm;
6. vsini_arr = np.arange(1., 600., 10.) # Range of vsini's to be analysed (unit: km/s);
7. limbdark = np.arange(0,1.1,0.2) # Range of limbdarks to be analysed (dimensionless).

Note: The center waves must be given in Angstrom.

3.4.2 Running

To run the routine it is necessary to define the folders where are the input files (data tables, tag **folder_table**, and the folder where the data will be saved, tag **folder_results**). Having defined these folders, the user must define the path where the routine is installed in the tag **commum_folder**.

Having defined properly all folders and options, the code can be run in terminal by:

```
ur_forget
python calc_vsini.py or ipython calc_vsini.py
```

Following are the description of the functions in this routine:

calc_vsini.**create_class_object**(*list_files*, *obj*)
Create object class for all targets in a list.

Parameters **list_files** – list of XShooter fits files (array)

Returns data (class object)

calc_vsini.**create_list_files**(*list_name*, *folder*, *folder_table*)
Creates a list of the files inside a given folder.

Parameters

- **list_name** – list's name (string)
- **folder** – files' folder (string)

Returns creates a txt file, with the files' paths

calc_vsini.**create_list_stars**(*list_files*)
Create list of the observed stars.

Parameters **list_files** – text list with the files' paths

Returns list of stars (array)

calc_vsini.**cut_spec**(*wave*, *flux*, *err*, *center_wave*, *delta*)
Cut a spectra to a given range.

Parameters

- **wave** – array with the wavelengths (array)
- **flux** – array with the wavelengths (array)

Project Report: "Binarity and the distribution of rotational velocities in Galactic main-sequence B stars", Release 2.5

- **center_wave** – central wavelength (float)
- **delta** – interval to be considered around the central wavelength (float)

Returns cut arrays (x, y, z)

class calc_vsini.**data_object**(*name*, *arm*, *mjd*, *list_files*, *name_ffit*, *wave=None*, *flux=None*, *sigm=None*, *wave_vis=None*, *flux_vis=None*, *sigm_vis=None*, *wave_nir=None*, *flux_nir=None*, *sigm_nir=None*)

Class of the stellar objects. Using this class, we can store for each star a sort of variables, which can be easily accessed.

calc_vsini.**find_nearest**(*array*, *value*)

Find the nearest value inside an array.

Parameters

- **array** – array
- **value** – desired value (float)

Returns nearest value and its index

calc_vsini.**plot_vsini**(*data*, *vsini_arr*, *limbdark*, *folder_fig*, *folder_temp*, *folder_table*, *star_name*, *center_wave_uvb*, *center_wave_vis*, *center_wave_nir*, *delta*, *plotchi2_map*, *lbdc*, *ltem*, *llog*, *lambd*, *prof*)

Plot the SED for each star inside the data structure.

Parameters

- **data** – list of XShooter fits files (array)
- **folder_fig** – folder where the figures will be saved (string)
- **folder_temp** – folder of the temporary files (string)
- **limbdark** – between 0 (no) to 1 (maximum)
- **center_wave** – centre wavelength of the line (float)
- **vsini** – array of possible values of vsini (array)
- **mjd** – modified Julian date (float)
- **star_name** – star name (string)
- **lbdc** – list of wavelengths from the model (array)
- **ltem** – list of temperatures from the model (array)
- **llog** – list of logg from the model (array)
- **lambd** – wavelenghts from the model (array)
- **prof** – fluxes from the model (array)

Returns plots, best vsini, best limbdark, and reduced chi2 values

calc_vsini.**read_fits**(*file_name*)

Read XShooter's fits files.

Parameters **file_name** – name of the file in fit extension (string)

Returns parameters

calc_vsini.**read_fits_star_name**(*file_name*, *typ*)

Read XShooter's fits files.

Parameters

- **file_name** – name of the file in fit extension (string)
- **typ** – define if it will be used to read a image

(typ='img')or a bintable (typ='data'). :return: parameters (object if typ='data', file_name if typ='img')

calc_vsini.**read_fits_xshooter**(*file_name*, *print_obj*)
Read XShooter's fits files.

Parameters **file_name** – name of the file in fit extension (string)

Returns parameters

calc_vsini.**read_list_files_all**(*table_name*, *folder_table*)
Read list of files in a table, and returns all fits file in an array.

Parameters

- **folder_table** – table's folder (string)
- **table_name** – Table's name (string)

Returns list of files (txt file)

calc_vsini.**read_params_star**(*table_name*)
Read the output of the bcd method (txt file).

Parameters **table_name** – name of the table (string)

Returns stellar parameters

calc_vsini.**read_txt**(*table_name*, *ncols*)
Read a simple txt file.

Parameters

- **table_name** – name of the table
- **ncols** – number of columns

Returns x, y (arrays) or x, y, z (arrays)

calc_vsini.**smooth_spectrum**(*wave*, *flux*, *doplot=None*)
Smooth the spectrum by convolving with a (normalized) Hann window of 400 points.

Parameters

- **wave** – Array with the wavelenght (numpy array)
- **flux** – Array with the fluxes (numpy array)
- **doplot** – Would you like to see the plot? (boolean)

Returns smoothed flux (array)

calc_vsini.**vsini_calc_kurucz**(*wvl*, *flux*, *teff*, *logg*, *center_wave*, *flux_err*, *limbdark*, *vsini*, *color*, *folder_fig*, *mjd*, *star_name*, *lbdc*, *ltem*, *llog*, *lambd*, *prof*, *arm*)
Function that calculate vsini using rotational broadening pyasl.rotBroad and the Kurucz Grids of model atmospheres.

Parameters

- **limbdark** – between 0 (no) to 1 (maximum)
- **wvl** – observational wavelength (array)
- **flux** – observational flux (array)
- **flux_err** – observational flux error (array)

- **teff** – effective temperature (float)
- **logg** – gravitational acceleration (float)
- **center_wave** – centre wavelength of the line (float)
- **vsini** – array of possible values of vsini (array)
- **color** – array of colors (array)
- **folder_fig** – folder where the figures will be save (string)
- **mjd** – modified Julian date (float)
- **star_name** – star name (string)
- **lbdc** – list of wavelengths from the model (array)
- **ltem** – list of temperatures from the model (array)
- **llog** – list of logg from the model (array)
- **lambd** – wavelenghts from the model (array)
- **prof** – fluxes from the model (array)
- **arm** – xshooter arm (string)

Returns plots, best vsini, best limbdark, and reduced chi2 values

3.5 Shell Script

There is a option to submit all routines simultaneously. In order to do that, we must turn the file *run_all_eso.sh* executable, and after run it:

```
chmod 777 run_all_eso.sh
./run_all_eso.sh
```

This procedure will start to running the routine PY-XShooter. When it is finished, the routine PharaohUS starts. At this point, all the structure created by PY-XShooter will be preserved and used by PharaohUS as well. Finally, the routine calc_vsini evaluates, for the same data, the vsini values by broadening a model atmospheric profile line (without rotation) until achieve the observational line profile.

CHAPTER

FOUR

PRELIMINARY RESULTS

The results, for each star, are saved in the folder */XShooter/results/star_name/*. Inside each folder *star_name*, it will have five other folders: *lines* (line profiles separed by folder), *SED* (all sed's), *bcd* (the BCD fit done in the balmer jump region), *images* (aquisition images), and *vsini* (vsini fits). Following, we present three examples of output, one for a single B star, one for a binary, and another output showing an example of vsini determination.

4.1 A Simple B star

As mentioned previously, it is created a figure with the smoothed spectra separeted by arm. The lines selected by the user appear in this plot, which helps in the visualization of interesting features. In the case of interest in a single line and about any other information about it, the user can visualize them in the folder *star_name/lines/line_name/*.

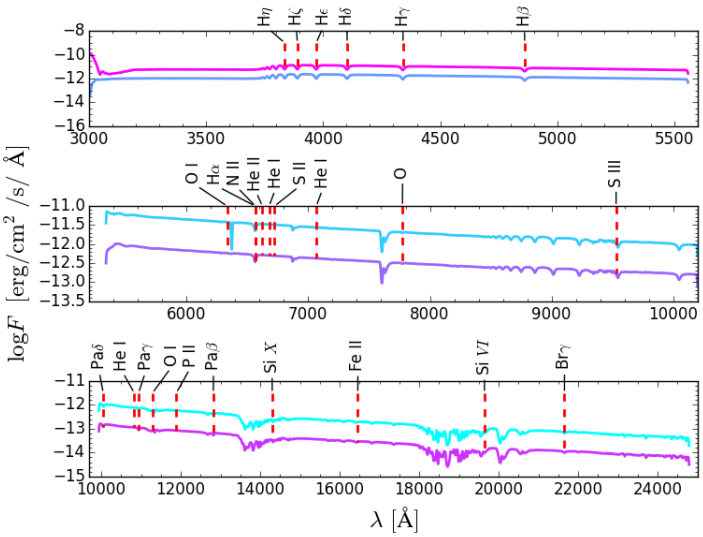

Fig. 4.1: Smoothed SED for all observations by arm for the program star Hip109155.

Beyond the line profiles, the procedure uses the region of the Balmer Jump to determine the input values of the BCD method (see J. Zorec et al. 2009).

Project Report: "Binarity and the distribution of rotational velocities in Galactic main-sequence B stars", Release 2.5

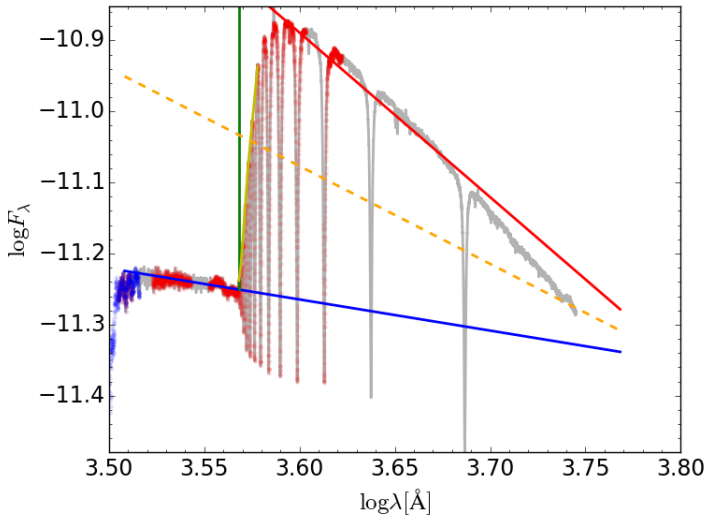

Fig. 4.2: BCD adjust for the program star Hip109155.

After the determination of the parameters (D, λ_0) needed to the BCD method, we execute an interpolation of the stellar parameters. At the end of this step, it generates a table with the inferred stellar parameters.

4.2 v sini

Figure 4.5 shows a example of the procedure adopted to found the vsini. The original line profile (blue curve) is compared with the broadened one, which depends on the values of vsini and limbdark. For each step of the interaction, these values are stored and the it performs a χ^2_{red} minimization (Fig. 4.6).

4.3 Binaries

For the study of binaries, one first step was looking at the raw frames, especially the acquisition images (Fig. 4.7) and some characteristic double-lined spectra (Fig. 4.8), reporting which objects are visible binary with a true or apparent companion from the acquisition images.

The determination of parameters of binary stars will need an implementation of another methods, because, in principle, it is needed a more precise study of the time series of measures. For this task, a more specific tool may be util as the Phoebe Project avaiable at http://www.phoebe-project.org/.

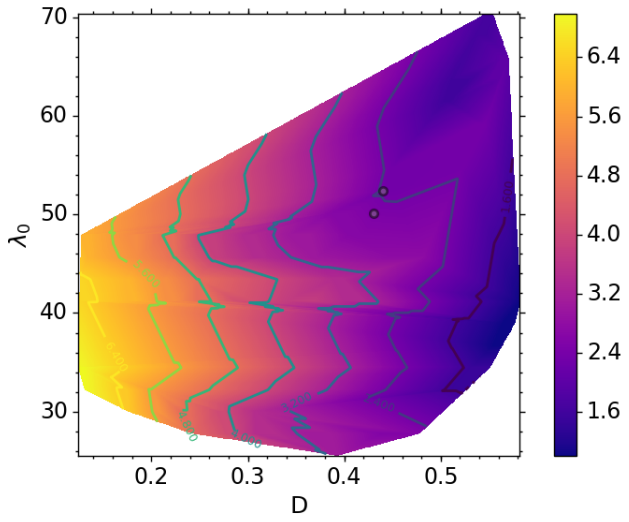

Fig. 4.3: Griddata interpolation of the stellar mass for the program star Hip076442.

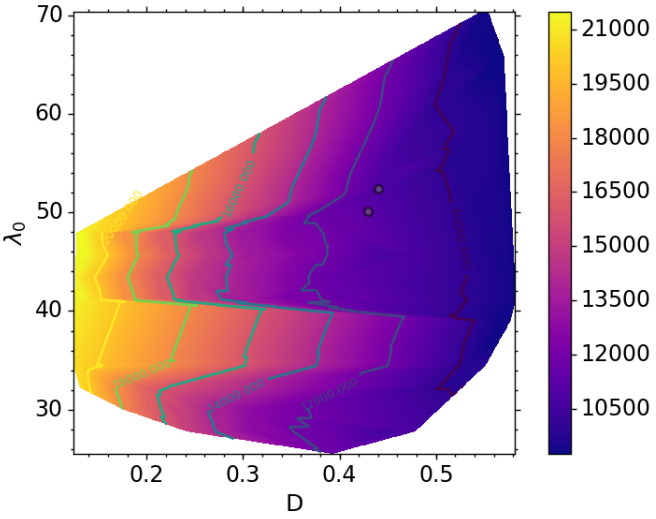

Fig. 4.4: Griddata interpolation of the T_{eff} for the program star Hip076442. The same procedure is done to interpolate the other stellar parameters.

Project Report: "Binarity and the distribution of rotational velocities in Galactic main-sequence B stars", Release 2.5

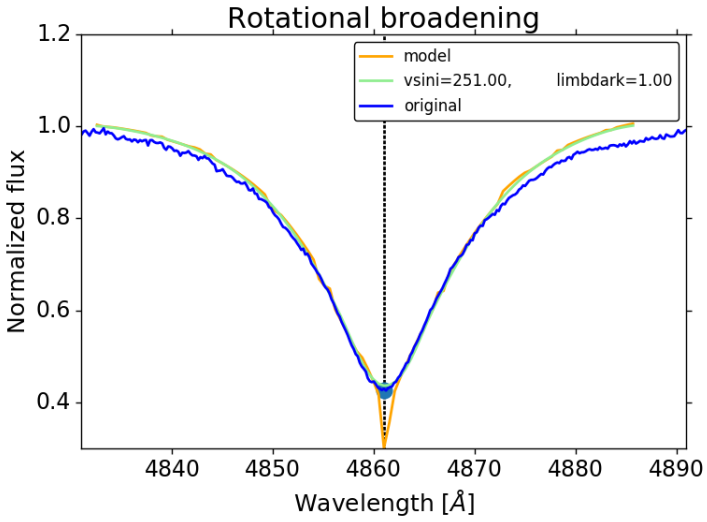

Fig. 4.5: Observational H:math:*alpha* line profile of the star Hip109155 (blue curve), original line profile from the models (orange curve), and best adjust (green curve).

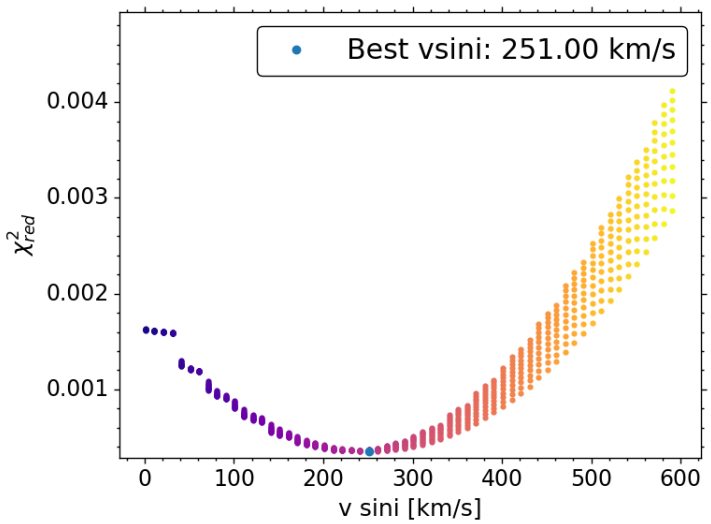

Fig. 4.6: Map of math:*chi*^2_{*red*} showing the best adjust.

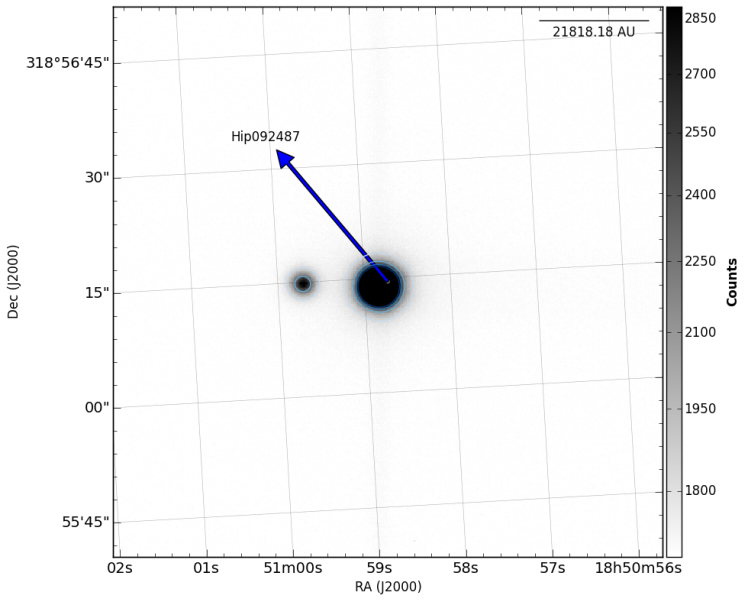

Fig. 4.7: Aquisition image of the program star Hip092487.

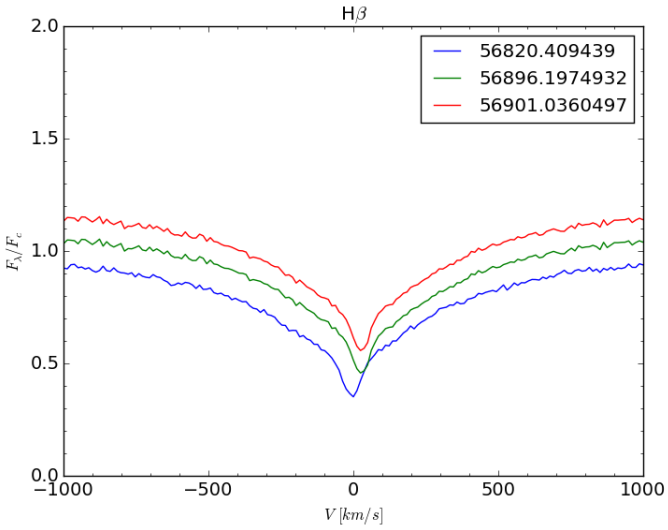

Fig. 4.8: H:math:*alpha* line profile of the program star Hip092487.

Project Report: "Binarity and the distribution of rotational velocities in Galactic main-sequence B stars", Release 2.5

CHAPTER

FIVE

INCOMPLETE TASKS

1. Separete the observations by slit;
2. Improve the normalization;
3. Implement heliocentric correction;
4. Determine parameters of binary systems,

Project Report: "Binarity and the distribution of rotational velocities in Galactic main-sequence B stars", Release 2.5

CHAPTER

SIX

INDICES AND TABLES

- genindex
- modindex
- search

Project Report: "Binarity and the distribution of rotational velocities in Galactic main-sequence B stars", Release 2.5

PYTHON MODULE INDEX

Project Report: "Binarity and the distribution of rotational velocities in Galactic main-sequence B stars", Release 2.5

INDEX

Appendix I

Scientific Initiation Project - Artur Alegre

PROJETO DE INICIAÇÃO CIENTÍFICA

BE-FAVOR: Be Stars - Facilities in VO Research
Uma Ferramenta para a determinação de parâmetros de estrelas Be

Artur C. Alegre & Alex C. Carciofi

9 de outubro de 2016

1 RESUMO

O Observatório Astronômico Virtual (VO) é uma iniciativa internacional liderada pelo IVOA que visa integrar, através de ferramentas interoperacionais, diferentes bancos de dados e diferentes serviços no sentido de modelos, ferramentas de análise e outros.

Neste contexto, nosso trabalho visa disponibilizar uma ferramenta de análise *online* que proporcionará uma interface de integração entre o usuário e ferramentas desenvolvidas pelo grupo de pesquisa BEACON, coordenado pelo professor Dr. Alex C. Carciofi.

Esta ferramenta *online* irá permitir ao usuário estimar as propriedades fundamentais básicas de estrelas Be clássicas a partir de dados fotométricos. A base para esta ferramenta são os dados disponíveis em inúmeras bases de dados do VO, bem como os códigos HDUST de transferência radiativa e o código EMCEE de minimização de múltiplos parâmetros.

2 INTRODUÇÃO: O FENÔMENO BE

Apesar de terem sido descobertas há quase 150 anos por Secchi [1866], estrelas Be continuam sendo verdadeiros enigmas. Estrelas Be clássicas são estrelas que apresentam a maior taxa de rotação entre as estrelas da Sequência Principal [Rivinius, Carciofi, and Martayan, 2013]. Hoje, há consenso na comunidade de que a alta rotação está na base do surgimento dos efeitos peculiares apresentados por estas estrelas.

As características peculiares destas estrelas fazem delas verdadeiros laboratórios de astrofísica estelar, pois podem ser utilizadas para testar teorias sobre discos astrofísicos e sobre os efeitos da rotação sobre a estrela. Além disso, existem várias estrelas Be muito próximas e brilhantes, o que torna o estudo dessas estrelas mais fácil e ainda mais interessante para a Astronomia em geral.

Um dos problemas centrais no estudo de estrelas do tipo Be é a obtenção de parâmetros fundamentais da estrela, tais como massa, idade, taxa de rotação, e inclinação. Suas características particulares tornam essa tarefa difícil: estrelas Be são achatadas em seus polos, apresentam efeito de escurecimento gravitacional e quando vistas de ângulos diferentes apresentam distribuições espectrais de energia (SED) com diferentes características. A característica mais marcante, entretanto, é a presença de um disco circunstelar que altera de forma significativa o espectro estelar.

2.1 O Modelo de Disco de Decréscimo Viscoso

As observações fornecem-nos importantes informações estruturais sobre os discos de Be, que devem ser necessariamente reproduzidas por qualquer teoria que se proponha a descrever como estes discos se formam. Por exemplo, a polarimetria e a interferometria (Quirrenbach et al. [1997]; Wood et al. [1997]) determinaram que os discos são geometricamente finos, enquanto que a espectro-interferometria determinou que o material do disco gira em torno da estrela de forma kepleriana. Até o momento, a única teoria capaz de satisfazer os vínculos observacionais é o modelo de disco de decréscimo viscoso (*viscous decretion disk*, VDD) proposto por Lee [1991] e desenvolvido por outros autores (Porter [1999]; Okazaki [2001]; Bjorkman & Carciofi [2005]).

Este modelo é semelhante ao empregado para discos protoestelares [Pringle, 1981], a diferença primária sendo que discos de Be são *outflowing*, enquanto discos da pré-sequência principal são *inflowing*. No modelo VDD, é suposto que algum mecanismo, ainda desconhecido, injeta material numa velocidade orbital kepleriana na base do disco. Neste ponto, a viscosidade turbulenta começa a atuar, transportando o momento angular do material das regiões internas para as externas do disco.

Este modelo foi aplicado com sucesso a sistemas que apresentam emissão estável contínua tais como as estrelas β CMi [Wheelwright et al., 2012], χ Oph [Tycner et al., 2008] e ζ Tauri [Carciofi et al., 2009]. Destas estrelas, ζ Tauri e β CMi [Klement et al., 2015] foram as únicas estudadas de forma aprofundada, pois tanto Wheelwright et al. [2012] quanto Tycner et al. [2008] usaram um conjunto limitado de dados.

3 Observatórios Virtuais

Nos últimos anos a Astronomia tem apresentado um crescimento de volume e de complexidade de dados sem precedentes. O valor acumulado de dados é da ordem de 100 Pb e vem crescendo a uma espantosa taxa de 2 - 4 Pb/ano. Comparando essa taxa de geração de dados em diferentes áreas da ciência, vemos que a Astronomia está gerando dados no mesmo passo que experimentos na área de Física de partículas, área que recebe muito mais investimentos do que a de Astronomia. Pensando em lidar com essa quantidade enorme de dados foi formada, em junho de 2002, a IVOA - *International Virtual Observatory Alliance* [1], com a missão de facilitar a coordenação e colaboração internacional necessária para o desenvolvimento e

[1] http://www.ivoa.net/

implantação de ferramentas, sistemas e estruturas organizacionais necessárias para permitir a utilização internacional de arquivos astronômicos.

Atualmente o IVOA compreende 19 programas de Observatórios Virtuais espalhados pelo mundo, dentre eles um brasileiro, o BRAVO - *Brazilian Virtual Observatory*, que começou formalmente em 2006. O BRAVO está presente em diversas instituições astronômicas do Brasil.

Nosso grupo já conduz um projeto que visamos integrar ao BRAVO, o BEATLAS (Faes [2015]). Esta ferramenta colocará à disposição da comunidade cerca de 70.000 espectros sintéticos de estrelas Be.

4 MOTIVAÇÃO

Um dos grandes desafios na modelagem de estrelas Be vem sendo abordado pelo doutorando Bruno C. Mota, cujo trabalho, em uma de suas etapas, consiste em determinar os parâmetros estelares de uma grade de estrelas Be austrais. O método desenvolvido para este propósito utiliza espectros da missão IUE[2] que são confrontados com uma grade de modelos fotosféricos que levam em consideração a rotação. Utilizando-se esta grade e a implementação do MCMC[3] no PYTHON - EMCEE[4] - o método retorna dados confiáveis com estimativa de erro robusta dos parâmetros estelares de uma dada lista de estrelas (Fig. 4.1).

Pensando neste problema, nosso projeto, da mesma forma que o BEATLAS, visará disponibilizar esta ferramenta à comunidade, na forma de um VO *service* ligado à infraestrutura do BRAVO, mas hospedado na *homepage* do grupo BeACoN.

5 METODOLOGIA

O projeto possui 2 etapas. Na primeira (Seç. 5.1), efetuaremos a leitura dos dados observacionais diretamente através do servidor. Na segunda (Seç. 5.2), será realizada a implementação da rotina PYTHON de determinação dos parâmetros estelares apresentada na seção 4.

5.1 LEITURA DOS DADOS OBSERVACIONAIS

Uma das preocupações deste projeto é fazer com que o usuário não necessite baixar os dados das estrelas que deseja estudar. Desta maneira, um usuário que busque analisar um conjunto de dados não precisará baixá-los de um serviço de VO e selecioná-los no próprio computador para, em seguida, enviá-los para o servidor analisar: o *web service* fará isto automaticamente.

Esta interface inicial utilizará as coordenadas ou nome de uma estrela para baixar os dados do repositório, graficando-os de forma pré-determinada. Logo, bastará ao usuário apenas selecionar os espectros com os quais deseja trabalhar.

Para tornar possível esta primeira etapa de funcionamento da interface de integração, o aluno de IC deverá, ao longo do início deste projeto, concentrar seus esforços no aprendizado de *web scripting*.

[2] *International Ultraviolet Explorer*
[3] Markov Chain Monte Carlo
[4] Foreman-Mackey et al. [2013]

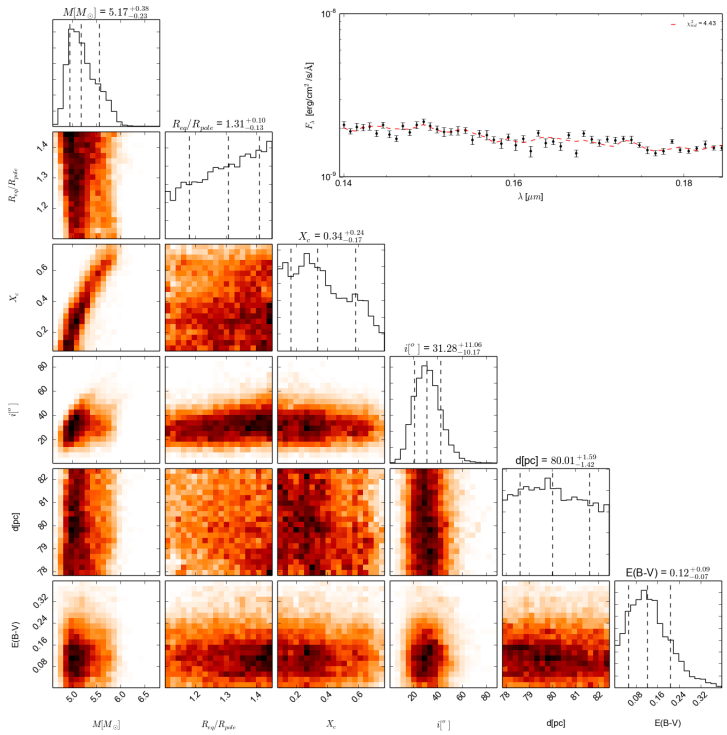

Figura 4.1: Saída do método obtida para a estrela α Columbae. O gráfico acima, à direita, mostra o espectro IUE original (pontos) com o melhor modelo em vermelho. Os gráficos na diagonal mostram a função densidade de probabilidade associada a cada parâmetro. Os mapas de cores mostram a correlação entre cada um dos parâmetros.

5.2 Implementação da rotina Python

A segunda etapa será desenvolver uma inferface de forma a permitir que a rotina PHYTON já existente seja rodada à partir do *web service*. Esta rotina utilizará os dados observacionais selecionados na etapa descrita na seção 5.1 e retornará os parâmetros estelares em uma forma gráfica (Fig. 4.1) juntamente com um arquivo de texto que conterá os melhores melhores parâmetros e com os respectivos erros.

Para isto, o aluno de IC precisará estudar como rodar rotinas PYTHON a partir de páginas *web*, tarefa que exigirá um estudo aprofundado tanto de *web programming* quanto da própria rotina PYTHON em si.

6 RESULTADOS ESPERADOS

Uma vez concluída, o *web service* será uma ferramenta muito útil para a comunidade de estrelas Be clássicas, por permitir obter de forma simples os parâmetros fundamentais da estrela Be a partir de dados observacionais de repositórios *online* e modelos fotosféricos estado-da-arte.

Para o aluno, tal projeto permitirá um estudo aprofundado de PHYTON, *web scripting* e dos protocolos básicos do VO.

REFERÊNCIAS

Secchi, A. 1866, Astronomische Nachrichten, 68, 63

Pringle, J. E. 1981, araa, 19, 137

Lee, R. W. 1991, Presented at the AIP Conference, Portland, ME, 23 Aug. 1991,

Wood, K., Bjorkman, K. S., & Bjorkman, J. E. 1997, apj, 477, 926

Quirrenbach, A., Bjorkman, K. S., Bjorkman, J. E., et al. 1997, apj, 479, 477

Porter, J. M. 1999, aap, 348, 512

Okazaki, A. T. 2001, pasj, 53, 119

Bjorkman, J. E., & Carciofi, A. C. 2005, Astronomical Polarimetry: Current Status and Future Directions, 343, 270

Tycner, C., Jones, C. E., Sigut, T. A. A., et al. 2008, apj, 689, 461

Tycner, C., Jones, C. E., Sigut, T. A. A., et al. 2008, apj, 689, 461

Carciofi, A. C., Okazaki, A. T., Le Bouquin, J.-B., et al. 2009, aap, 504, 915

Wheelwright, H. E., Bjorkman, J. E., Oudmaijer, R. D., et al. 2012, mnras, 423, L11

Rivinius, T., Carciofi, A.C., and Martayan, C.: 2013, *Astronomy and Astrophysics Review* **21**, 69.

Foreman-Mackey, D., Hogg, D. W., Lang, D., & Goodman, J. 2013, pasp, 125, 306

Faes, D. M. 2015, Universidade de São Paulo & Université Nice Sophia Antipolis

Klement, R., Carciofi, A. C., Rivinius, T., et al. 2015, arXiv:1510.01229

Appendix J

BeFaVOr Web Tutorial

Project Report: "Be-FaVOR: Be Stars - Facilities in VO Research. Uma ferramenta para a determinação de parâmetros de estrelas Be"

Release 1.0

Artur Alegre, Alex C. Carciofi e Bruno C. Mota

November 02, 2016

CONTENTS

Project Report: "Be-FaVOR: Be Stars - Facilities in VO Research. Uma ferramenta para a determinação de parâmetros de estrelas Be", Release 1.0

O Observatório Astronômico Virtual (VO) é uma iniciativa internacional liderada pela *International Virtual Observatory Alliance* (IVOA), que visa integrar, através de ferramentas interoperacionais, diferentes bancos de dados e diferentes serviços no sentido de modelos, ferramentas de análise e outros.

Neste contexto, nosso trabalho visa disponibilizar uma ferramenta de análise *online* que proporcionará uma interface de integração entre o usuário e ferramentas desenvolvidas pelo grupo de pesquisa Beacon, coordenado pelo professor Dr. Alex C. Carciofi.

Esta ferramenta *online* irá permitir ao usuário estimar as propriedades fundamentais básicas de estrelas Be clássicas a partir de dados fotométricos. A base para esta ferramenta são os dados disponíveis em inúmeras bases de dados do VO, bem como os códigos HDUST de transferência radiativa e o código EMCEE de minimização de múltiplos parâmetros.

Project Report: "Be-FaVOR: Be Stars - Facilities in VO Research. Uma ferramenta para a determinação de parâmetros de estrelas Be", Release 1.0

CHAPTER

ONE

INTRODUÇÃO

Apesar de terem sido descobertas há 150 anos por Secchi 1866, estrelas Be continuam sendo verdadeiros enigmas. Estrelas Be clássicas são estrelas que apresentam a maior taxa de rotação entre as estrelas da Sequência Principal (Rivinius, Carciofi & Martayan (2013)). Hoje, há consenso na comunidade de que a alta taxa de rotação está na base do surgimento dos efeitos peculiares apresentados por estas estrelas.

Um dos problemas centrais no estudo de estrelas do tipo Be é a obtenção de parâmetros fundamentais da estrela, tais como massa, idade, taxa de rotação e inclinação. Suas características particulares tornam essa tarefa difícil: estrelas Be são achatadas em seus polos, apresentam efeito de escurecimento gravitacional e, quando vistas de ângulos diferentes, apresentam distribuições espectrais de energia (SED) com diferentes características. A característica mais marcante, entretanto, é a presença de um disco circunstelar que altera de forma significativa o espectro estelar.

Buscando uma solução para este problema, o presente projeto visa disponibilizar à comunidade uma ferramenta no formato de um *web service*, isto é, um serviço de Observatório Virtual, ligado à infraestrutura do BRAVO - *Brazilian Virtual Observatory*. O método a ser utilizado por esta ferramenta baseia-se no confronto entre grades de modelos fotosféricos que levam em consideração a rotação e espectros da missão IUE, retornando dados confiáveis com estimativa de erro robusta de parâmetros estelares de uma dada lista de estrelas.

Project Report: "Be-FaVOR: Be Stars - Facilities in VO Research. Uma ferramenta para a determinação de parâmetros de estrelas Be", Release 1.0

CHAPTER

TWO

DADOS OBSERVACIONAIS

2.1 Os dados do IUE

A missão *International Ultraviolet Explorer* (IUE) foi um projeto conjunto entre NASA, ESA e PPARC. Ainda hoje este projeto é entendido como um dos telescópios astronômicos mais produtivos de todos os tempos, ultrapassando as expectativas de seus objetivos originais, dentre estes, a obtenção de espectros de alta resolução de estrelas de todos os tipos espectrais para determinar suas características físicas e fazer repetidas observações de objetos com espectros variáveis.

Os arquivos de espectros do IUE podem ser acessados no sistema da ESA chamado IUE *Newly Extracted Spectra* (INES), cujo objetivo é fornecer à comunidade científica acesso aos espectros do IUE sem que se faça necessário um conhecimento técnico dos instrumentos. Para informações detalhadas sobre o sistema, veja http://sdc.cab.inta-csic.es/ines.

2.2 O *Web Service*

A ferramenta em desenvolvimento utilizará como *input* o nome de uma estrela para automaticamente baixar os dados do repositório *online* do INES e de outros serviços disponíveis e grafică-los de forma pré-derterminada. Desta maneira, não será necessário o usuário baixar os dados das estrelas que deseja estudar em seu computador, selecioná-los e, então, enviá-los de volta ao servidor para serem analisados; bastará apenas selecionar os espectros com os quais deseja trabalhar.

Para construir esta ferramenta, o projeto foi dividido em duas etapas:

1. Elaboração de uma rotina capaz de ler os dados observacionais diretamente através do servidor.

   Esta rotina é a responsável por fazer o *download* automático dos dados buscando no servidor pelo nome da estrela.

2. Implementação da rotina Python de determinação dos parâmetros estelares.

   Esta parte inclui a criação de uma interface que permita ao usuário executar as rotinas de interesse dentro de um ambiente de VO.

Este serviço será hospedado na *homepage* do grupo Beacon, ao lado de outro projeto que visamos integrar ao BRAVO, o BEATLAS (Faes et al. 2017 in prep.), ferramenta que colocará à disposição da comunidade cerca de 70.000 espectros sintéticos de estrelas Be.

Project Report: "Be-FaVOR: Be Stars - Facilities in VO Research. Uma ferramenta para a determinação de parâmetros de estrelas Be", Release 1.0

CHAPTER

THREE

FERRAMENTAS

Nesta seção, são descritas as rotinas Python criadas para leitura dos dados através do servidor: BeFaVOR-Web e TAKE-VIZIER-DATA. Esta última trata-se de uma rotina complementar para habilitar a primeira a buscar por múltiplas estrelas de uma vez.

3.1 BeFaVOR-Web

A rotina BeFaVOR-Web usa como *input* tanto o nome de uma única estrela quanto uma lista de estrelas para realizar uma busca por arquivos de espectros correspondentes no *database* do sistema INES, salvando-os na pasta definida. Em seguida, realiza-se, para a mesma estrela, uma busca no SIMBAD, através do qual obtemos os parâmetros: paralaxe, vsini e suas respectivas incertezas, além da referência bibliográfica para vsini. Também é verificado se a busca na plataforma IRSA-*Galactic DUST Reddening & Extinction* retorna algum valor de avermelhamento E(B-V) para aquela estrela. Caso positivo, o valor é salvo juntamente com os outros parâmetros em uma tabela na pasta definida.

3.1.1 Instalação

Para utilizar esta rotina em sua atual versão é preciso ter instalados os seguintes pacotes:

1. numpy
2. bs4
3. datetime
4. requests
5. selenium
6. astroquery
7. pyhdust
8. matplotlib
9. urllib
10. re
11. random
12. tafile

Os pacotes numerados de 1 a 8 podem ser instalados utilizando o gerenciador de pacotes **pip**, enquanto aqueles de 9 a 12 podem ser instalados pelo comando **apt-get install python3-pacote**.

Project Report: "Be-FaVOR: Be Stars - Facilities in VO Research. Uma ferramenta para a determinação de parâmetros de estrelas Be", Release 1.0

3.1.2 Executando a BeFaVOR-Web

Para rodar a rotina o usuário deve primeiro definir o *path* onde esta encontra-se instalada na tag **commum_folder**, bem como o *path* onde as tabelas serão salvas em **folder_tables**. Recomenda-se utilizar a versão mais atual disponível do Python.

Utilizando como exemplo o IPython 3.0, o código pode ser rodado seguindo os seguintes passos:

1. Abra o terminal e digite o comando: ipython3
2. Vá ao diretório em que a rotina encontra-se instalada;
3. No terminal, digite o comando: run BeFaV0r_web.py
4. A rotina perguntará se o usuário deseja buscar apenas um ou vários alvos. Digite '1' para buscar um único alvo ou 'more' para buscar múltiplos alvos;
5. Caso tenha digitado '1', a rotina perguntará o nome do alvo. Digite o nome da estrela desejada;
6. Caso tenha digitado 'more' a rotina executará a rotina complementar TAKE_VIZIER_DATA que baixará uma série de alvos de acordo com um catálogo pré-definido. Para mais detalhes, veja a descrição da rotina TAKE_VIZIER_DATA na sub-seção seguinte.

Se o usuário tiver buscado por um único alvo, além dos espectros do IUE salvos, a rotina criará um documento de texto com a seguinte estrutura de **linhas**:

1. Nome da estrela
2. Paralaxe
3. Incerteza da paralaxe
4. vsini
5. Incerteza do vsini
6. "Bump"
7. Referência bibliográfica do vsini
8. E(B-V)

"Bump" refere-se à presença de um espectro IUE que cobre a região conhecida como *bump* 2200 Angstron que é utiliza na determinação do valor de E(B-V). Caso retorne "*True*", existe este espectro e, caso retorne "*False*", significa que o espectro não cobre esta faixa espectral e, portanto, o valor é retirado do IRSA.

Se o usuário tiver buscado por múltiplos alvos, além dos espectros do IUE salvos, a rotina criará um documento de texto com uma estrutura de **colunas** pré-determinada pelo usuário. Por exemplo, caso o usuário selecione estrelas do *Bright Star Catalogue*, é possível gerar a seguinte estrutura:

1. Nome da estrela
2. Índice B-V
3. Índice U-B
4. Índice R-I
5. vsini
6. Incerteza B-V
7. Incerteza U-B
8. Incerteza vsini
9. Incerteza R-I

10. Data de observação
11. Tipo espectral

3.1.3 Funções da rotina BeFaVOR-Web

Segue a descrição das funções contidas na rotina BeFaVOR-Web, organizadas em ordem alfabética:

`BeFaVOr_web.`**`create_list_files`**(*list_name*, *folder*, *folder_table*)
Creates a list of the files inside a given folder.

Parameters

- **list_name** – list's name (string)
- **folder** – files' folder (string)

Returns creates a txt file, with the files' paths

`BeFaVOr_web.`**`create_txt_file`**(*data_list*, *file_name*)
Create a txt file.

Parameters

- **data_list** – list of data to be saved (array)
- **file_name** – txt file's name (string)

Returns txt file

`BeFaVOr_web.`**`find_regular_expression`**(*url*, *typ*, *atr*, *expr*)
Search for a specified expression inside a page code and lists all its ocurrences.

Parameters

- **url** – page url (string)
- **typ** – tag (string)
- **atr** – attribute (string)
- **expr** – expression (string)

Returns list of occurences

`BeFaVOr_web.`**`getTitle`**(*url*)
Gets the title of a certain webpage.

Parameters **url** – page url (string)

Returns page title

`BeFaVOr_web.`**`get_attribute`**(*url*, *atr*, *typ*)
Lists all text in a webpage that satisfacts a specified attribute.

Parameters

- **url** – page url (string)
- **atr** – attribute (string)
- **typ** – tag (string)

Returns text containing specified attribute

`BeFaVOr_web.`**`iue_submission`**(*star_name*)
Search in the IUE database for a certain star name.

Parameters **star_name** – name of the star (string)

Returns request of star name in IUE page

`BeFaVOr_web.`**`plot_gal`**(*ra_val*, *dec_val*, *folder_fig*)
Plot in "Galatic Coordinates" (i.e., Mollweide projection).

Parameters

- **ra_val** – right ascencion in RADIANS (float)
- **dec_val** – declination in RADIANS (float)
- **folder_fig** – name of the folder for the figure (string)

Returns saved images

`BeFaVOr_web.`**`read_simbad_coodr`**(*star_name*)
Query SIMBAD for the coordinates of a given star.

Parameters **star_name** – star's name (string)

Returns right ascencion and declination coordinates

`BeFaVOr_web.`**`read_simbad_data`**(*star_name*)
Query SIMBAD for a given star parallax, vsini, bump and references.

Parameters **star_name** – star's name (string)

Returns txt file with star's parallax, vsini, bump, the respective

errors and references for vsini and E(B-V)

`BeFaVOr_web.`**`read_txt`**(*list_name*, *folder*)
Read a given list of star names.

Parameters

- **list_name** – name o txt file containing the list (string)
- **folder** – list's folder (string)

Returns column of the list read

`BeFaVOr_web.`**`retrieve_ebmv_value`**(*star_name*)
Search the INES website for a specified star's E(B-V) value.

Parameters **star_name** – stars's name (string)

Returns E(B-V) value

`BeFaVOr_web.`**`selecting_data`**(*star_name*, *commum_folder*)
Search the INES website for a specified star.

Parameters

- **star_name** – name of the star (string)
- **commum_folder** – name of the folder where the routine is located

Returns request of the star name in INES page

`BeFaVOr_web.`**`show_page_code`**(*url*)
Shows the page code of a certain webpage.

Parameters **url** – page url (string)

Returns page code

BeFaVOr_web.**there_is_a_title**(*url*)
Prints the title of a certain webpage.

Parameters **url** – page url (string)

Returns page title

BeFaVOr_web.**untar**(*fname*)
Decompact a tar file.

Parameters **fname** – name o file to be decompacted (string)

Returns decompacted file

BeFaVOr_web.**unzip**(*zip_file*, *outdir*)
Unzip a given file into the specified output directory.

Parameters

- **zip_file** – name of file to be unziped (string)
- **outdir** – directory of the file (string)

Returns unziped file

3.2 TAKE-VIZIER-DATA

A rotina TAKE-VIZIER-DATA realiza uma busca por catálogos no VizieR. Em seguida, dentro de cada catálogo selecionado, é feita a seleção dos objetos de interesse através de um processo de filtragem por tipo espectral, classe de luminosidade e existência ou não de dados da missão IUE. Deste ponto em diante, a rotina segue os seguintes passos:

1. As estrelas selecionadas no VizieR são buscadas no arquivo do INES;
2. Os espectros daquelas encontradas são salvos no diretório definido;
3. Para cada estrela encontrada no INES, é criado um documento de texto onde são salvos os parâmetros retirados do SIMBAD e (opcional) os parâmetros obtidos dos catálogos lidos por meio do VIZIER.

Detalhes sobre as funções contidas nesta rotina podem ser vistos no anexo do capítulo 6.

Project Report: "Be-FaVOR: Be Stars - Facilities in VO Research. Uma ferramenta para a determinação de parâmetros de estrelas Be", Release 1.0

CHAPTER

FOUR

OUTRAS ATIVIDADES E PERSPECTIVAS

4.1 Atividades complementares

Ao longo do período de duração desta bolsa, além das tarefas diretamente relacionadas a este projeto, também foram realizadas atividades importantes para o desenvolvimento acadêmico, dentre elas destacamos:

1. Participação de reuniões semanais do grupo Beacon, onde são discutidos resultados recentes das pesquisas de seus membros, bem como artigos científicos relevantes para nossa linha de pesquisa;
2. Apresentação de resultados parciais deste projeto na reunião de grupo;
3. Participação de observações astronômicas tanto remotas quanto presenciais no Observatório Pico dos Dias para obtenção de dados polarimétricos e espectroscópicos.

4.2 Tarefas futuras

1. Incorporação das rotinas de leitura de dados em servidores desenvolvidas neste projeto com a rotina Python de determinação de parâmetros estelares que constitui parte do projeto de doutorado do aluno Bruno C. Mota.
2. Desenvolvimento e integração, na *homepage* do grupo Beacon, da interface que permitirá ao usuário executar as rotinas Python criadas ao longo ou anteriormente a este projeto em um ambiente de Observatório Virtual.

Project Report: "Be-FaVOR: Be Stars - Facilities in VO Research. Uma ferramenta para a determinação de parâmetros de estrelas Be", Release 1.0

CHAPTER

FIVE

CONCLUSÕES

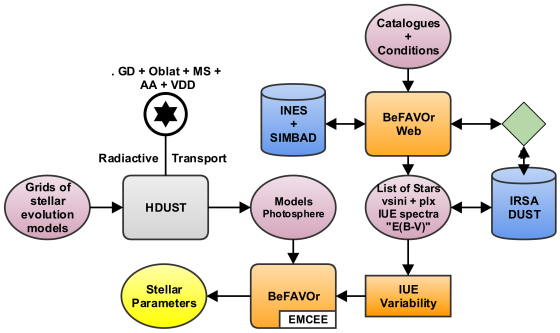

Figure 5.1: Fluxograma simplificado do método desenvolvido.

Na figura _fig1, mostramos uma representação simplificada do método que vem sendo desenvolvido. Neste projeto de iniciação, devenvolvemos o bloco *BeFaVOR web* representado na figura. Em resumo, o usuário necessita apenas selecionar catálogos de interesse, bem como os filtros adequados. A partir deste ponto, a rotina verifica se as estrelas selecionadas possuem dados IUE; caso positivo, dados de paralaxe e vsini são lidos e salvos automaticamente do SIMBAD, juntamente com os espectros do IUE (salvos da plataforma INES). Uma implementação adicional é a verificação da existência de uma região espectral que pode ser utilizada para se determinar o avermelhamento devido ao meio interestelar. Caso ela não exista, a rotina lê e salva uma estimativa do *web service* IRSA. Por fim, o usuário obtêm uma lista de estrelas, com seus respectivos dados de paralaxe, vsini, E(B-V) e incertezas. Estes dados são utilizados na rotina BeFaVOR de determinação dos parâmetros estelares, que está sendo desenvolvida pelo doutorando Bruno C. Mota.

Project Report: "Be-FaVOR: Be Stars - Facilities in VO Research. Uma ferramenta para a determinação de parâmetros de estrelas Be", Release 1.0

CHAPTER

SIX

ANEXOS

6.1 Anexo 1: Rotina BeFaVOr_web

```
# 1) Esta rotina deve ser rodada em ipython3

# ============================================================================
# Importing modules
import numpy as np
from urllib.request import urlopen
from urllib.error import HTTPError
from bs4 import BeautifulSoup
import sys
import re
import datetime
import random
import time
import requests
import math
from selenium import webdriver
from selenium.webdriver.support.ui import Select
import tarfile
from astroquery.simbad import Simbad
import csv
import os
from glob import glob
import pyhdust.phc as phc
import matplotlib.pyplot as plt
from selenium import webdriver
from selenium.webdriver.common.by import By
from selenium.webdriver.support.ui import WebDriverWait
from selenium.webdriver.support import expected_conditions as EC


# ============================================================================
def show_page_code(url):
    '''
    Shows the page code of a certain webpage.

    :param url: page url (string)
    :return: page code
    '''

    html = urlopen(url)
    bsObj = BeautifulSoup(html.read())
```

```
    return bsObj


# ============================================================================
def getTitle(url):
    '''
    Gets the title of a certain webpage.

    :param url: page url (string)
    :return: page title
    '''

    try:
        html = urlopen(url)
    except HTTPError as e:
        print(e)
        return None
    try:
        bsObj = BeautifulSoup(html.read())
        title = bsObj.body.h1
    except AttributeError as e:
        return None
    return title


# ============================================================================
def there_is_a_title(url):
    '''
    Prints the title of a certain webpage.

    :param url: page url (string)
    :return: page title
    '''

    title = getTitle(url)
    if title is None:
        print("Title could not be found")
    else:
        print(title)
    return title


# ============================================================================
def example_try():

    while True:
        try:
            x = int(raw_input("Please enter a number: "))
            break
        except ValueError:
            print("Oops!  That was no valid number.  Try again...")
    return


# ============================================================================
def get_attribute(url, atr, typ):
    '''
    Lists all text in a webpage that satisfacts a specified attribute.
```

```
    :param url: page url (string)
    :param atr: attribute (string)
    :param typ: tag (string)
    :return: text containing specified attribute
    '''

    bsOBJ = show_page_code(url)
    namelist = bsOBJ.findAll(typ, {"class": atr})
    names = []
    for name in namelist:
        nome = name.get_text()
        names.append(nome)

    return names


# ================================================================================
def find_regular_expression(url, typ, atr, expr):
    '''
    Search for a specified expression inside a page code and lists all
    its ocurrences.

    :param url: page url (string)
    :param typ: tag (string)
    :param atr: attribute (string)
    :param expr: expression (string)
    :return: list of occurences
    '''

    html = urlopen(url)
    bsObj = BeautifulSoup(html)
    array = bsObj.findAll(typ, {atr: re.compile(expr)})
    for lista in array:
        print(lista["src"])
    return lista


# ================================================================================
random.seed(datetime.datetime.now())


def getLinks(articleUrl):
    html = urlopen("http://en.wikipedia.org" + articleUrl)
    bsObj = BeautifulSoup(html)
    return bsObj.find("div", {"id": "bodyContent"}).\
        findAll("a", href=re.compile("^(/wiki/)((?!:).)*$"))


# ================================================================================
def get_Link(articleUrl):
    links = getLinks("/wiki/Kevin_Bacon")
    while len(links) > 0:
        newArticle = links[random.randint(0, len(links) - 1)].attrs["href"]
        print(newArticle)
        links = getLinks(newArticle)


# ================================================================================
```

```
def file_submission():
    files = {'uploadFile': open('../files/Python-logo.png', 'rb')}
    r = requests.post("http://pythonscraping.com/pages/processing2.php",
                      files=files)
    print(r.text)
    return


# ========================================================================
def simple_form():
    params = {'firstname': 'Ryan', 'lastname': 'Mitchell'}
    r = requests.post("http://pythonscraping.com/files/processing.php",
                      data=params)
    print(r.text)
    return


# ========================================================================
def file_submission2():
    files = {'uploadFile': open('../files/python.png', 'rb')}
    r = requests.post("http://pythonscraping.com/pages/processing2.php",
                      files=files)
    print(r.text)

    return


# ========================================================================
def iue_submission(star_name):
    '''
    Search in the IUE database for a certain star name.

    :param star_name: name of the star (string)
    :return: request of star name in IUE page
    '''

    ines_site = "http://sdc.cab.inta-csic.es/cgi-ines/IUEdbsMY"
    params = {'object': star_name}
    r = requests.post(ines_site, data=params)
    print(r.text)

    return r


# ========================================================================
def read_txt(list_name, folder):
    '''
    Read a given list of star names.

    :param list_name: name o txt file containing the list (string)
    :param folder: list's folder (string)
    :return: column of the list read
    '''

    list_name = folder + list_name

    cols = np.genfromtxt(list_name, unpack=True, comments='#',
                         delimiter='\t')
```

```
    return cols


# ============================================================================
def untar(fname):
    '''
    Decompact a tar file.

    :param fname: name o file to be decompacted (string)
    :return: decompacted file
    '''

    if (fname.endswith("tar.gz")):
        tar = tarfile.open(fname)
        tar.extractall()
        tar.close()
        print("Extracted in Current Directory")
    else:
        print("Not a tar.gz file: '%s '" % sys.argv[0])


# ============================================================================
def create_list_files(list_name, folder, folder_table):
    '''
    Creates a list of the files inside a given folder.

    :param list_name: list's name (string)
    :param folder: files' folder (string)
    :return: creates a txt file, with the files' paths
    '''

    a = open(folder_table + list_name + ".txt", "w")
    for path, subdirs, files in os.walk(folder):
        for filename in files:
            f = os.path.join(path, filename)
            a.write(str(f) + os.linesep)
    return


# ============================================================================
def create_txt_file(data_list, file_name):
    '''
    Create a txt file.

    :param data_list: list of data to be saved (array)
    :param file_name: txt file's name (string)
    :return: txt file
    '''

    with open(file_name, 'w') as f:
        writer = csv.writer(f, delimiter='\t')
        writer.writerows(zip(data_list))
    return


# ============================================================================
def read_simbad_data(star_name):
    '''
```

```
    Query SIMBAD for a given star parallax, vsini, bump and references.

    :param star_name: star's name (string)
    :return: txt file with star's parallax, vsini, bump, the respective
    errors and references for vsini and E(B-V)
    '''

    customSimbad = Simbad()
    # customSimbad.list_votable_fields() #  to list all avaiable fields
    customSimbad.get_votable_fields()
    customSimbad.add_votable_fields('plx', 'plx_error', 'rot')
    customSimbad.get_votable_fields()
    result_table = customSimbad.query_object(star_name)
    # star = result_table['MAIN_ID']
    star = np.copy(star_name)
    plx = result_table['PLX_VALUE'][0]
    plx_error = result_table['PLX_ERROR'][0]
    vsini = result_table['ROT_Vsini'][0]
    vsini_err = result_table['ROT_err'].item()
    rot_bibcode = result_table['ROT_bibcode']
    bump = True
    ebmv_ref = 0.0

    return star.item(), plx, plx_error, vsini, vsini_err, bump,\
        rot_bibcode.item(), ebmv_ref


# ============================================================================
def read_simbad_coodr(star_name):
    '''
    Query SIMBAD for the coordinates of a given star.

    :param star_name: star's name (string)
    :return: right ascencion and declination coordinates
    '''

    customSimbad = Simbad()
    customSimbad.get_votable_fields()
    result_table = customSimbad.query_object(star_name)

    ra = result_table['RA'][0]
    dec = result_table['DEC'][0]

    return ra, dec


# ============================================================================
def unzip(zip_file, outdir):
    '''
    Unzip a given file into the specified output directory.

    :param zip_file: name of file to be unziped (string)
    :param outdir: directory of the file (string)
    :return: unziped file
    '''

    import zipfile
    zf = zipfile.ZipFile(zip_file, "r")
```

```
    zf.extractall(outdir)
    return


# ============================================================================
def plot_gal(ra_val, dec_val, folder_fig):
    """
    Plot in "Galatic Coordinates" (i.e., Mollweide projection).

    :param ra_val: right ascencion in RADIANS (float)
    :param dec_val: declination in RADIANS (float)
    :param folder_fig: name of the folder for the figure (string)
    :return: saved images
    """

    fig = plt.figure()
    ax = fig.add_subplot(111, projection="mollweide")
    ax.set_xticklabels(['14h', '16h', '18h', '20h', '22h', '0h', '2h', '4h',
                        '6h', '8h', '10h'])

    for i in range(len(ra_val)):
        dec = dec_val[i].replace(' ', ':')
        ra = ra_val[i].replace(' ', ':')

        # list of floats (degrees fraction)
        dec = [phc.dec2degf(dec)]
        ra = [phc.ra2degf(ra)]

        # arrays of floats (radians)
        dec = np.array(dec) * np.pi / 180
        ra = np.array(ra) * np.pi / 180

        ax.scatter(ra, dec)
    plt.savefig(folder_fig + 'galatic_distribution.png')

    return


# ============================================================================
def selecting_data(star_name, commum_folder):
    '''
    Search the INES website for a specified star.

    :param star_name: name of the star (string)
    :param commum_folder: name of the folder where the routine is located
    :return: request of the star name in INES page
    '''

    from pyvirtualdisplay import Display
    display = Display(visible=0, size=(800, 600))
    display.start()

    # now Chrome will run in a virtual display.
    # you will not see the browser.

    # Creating the path
    a = star_name.split()
```

```
# short_star_name = a[0][0] + a[1][0:3]
short_star_name = a[0] + a[1]

# Starting the searching
if os.path.isdir(commum_folder + 'iue/' + short_star_name) is False:
    os.mkdir(commum_folder + 'iue/' + short_star_name)

    folder_data = commum_folder + 'iue/' + short_star_name

    # Define global Chrome properties
    options = webdriver.ChromeOptions()
    prefs = {"download.default_directory": folder_data}
    options.add_experimental_option("prefs", prefs)

    browser = webdriver.Chrome(chrome_options=options)
    # browser = webdriver.Firefox(firefox_profile=fp)

    # Define web source
    ines_site = "http://sdc.cab.inta-csic.es/cgi-ines/IUEdbsMY"

    # Openning it
    browser.get(ines_site)
    # browser.maximize_window()
    # time.sleep(3)

    # Selecting all data
    mySelect = Select(browser.find_element_by_name("limit"))
    mySelect.select_by_value("all")
    # time.sleep(3)

    # Selecting some stars
    browser.find_element_by_name("object").send_keys(star_name)
    browser.find_element_by_name(".submit").click()
    # time.sleep(3)

    # Taking the data
    browser.find_element_by_name("markRebin").click()
    browser.find_element_by_name(".submitNH").click()
    time.sleep(20)
    # browser.close()

    # Unzip files
    outdir = os.getcwd()
    # print(short_star_name)
    # new_path = outdir + '/iue/' + short_star_name + '/'
    os.chdir(folder_data)
    file_list = glob('*')
    if len(file_list) != 0:
        # print(file_list)
        fname = str(file_list[0])
        # print(fname)
        tar = tarfile.open(fname, "r:gz")
        tar.extractall()
        tar.close()
        os.system('rm *.gz')
    os.chdir(outdir)
    browser.close()
```

```
    return


# ============================================================================
def retrieve_ebmv_value(star_name):
    '''
    Search the INES website for a specified star's E(B-V) value.

    :param star_name: stars's name (string)
    :return: E(B-V) value
    '''

    from pyvirtualdisplay import Display
    display = Display(visible=0, size=(800, 600))
    display.start()

    # Define global Chrome properties
    browser = webdriver.Chrome()

    # Define web source
    irsa_site = "http://irsa.ipac.caltech.edu/applications/DUST/"

    # Openning it
    browser.get(irsa_site)
    # wait = WebDriverWait(browser, 180)
    # wait.until(EC.title_contains("title"))

    # Selecting some stars
    browser.find_element_by_name("locstr").send_keys(star_name)
    browser.find_element_by_class_name("tdsubmit").click()

    time.sleep(30)
    ebmv = browser.find_element_by_class_name("tdwhiteleft")
    ebmv = float(ebmv.text)
    browser.close()

    return ebmv

    return ebmv


# ============================================================================
def main():

    num_spa = 75
    print(num_spa * '=')
    print('\nBeFaVOr_Web\n')
    print(num_spa * '=')
# ----------------------------------------------------------------------------

    # Defining folders
    user = input('Who is using? (bmota or artur): ')
    commum_folder = '/home/' + user + '/Dropbox/Artur/BeFaVOr_web/'
    commum_folder_2 = '/home/' + user + '/Dropbox/Artur/BeFaVOr_web/'

    folder_tables = commum_folder + 'tables/'
    folder_tables_2 = commum_folder_2 + 'emcee/' + 'tables/'
```

Project Report: "Be-FaVOR: Be Stars - Facilities in VO Research. Uma ferramenta para a determinação de parâmetros de estrelas Be", Release 1.0

```
    folder_figures = commum_folder + 'figures/'

    table_final = folder_tables + 'list.txt'
    table_final_2 = folder_tables_2 + 'list_final.txt'
# ----------------------------------------------------------------------------

    # Saving the input for the routine Befavour.py
    if os.path.isfile(table_final_2) is True:
        os.system('rm ' + table_final_2)

    if os.path.isfile(folder_figures) is False:
        os.system('rm -r ' + folder_figures)

    if os.path.isfile(folder_figures) is False:
        os.system('mkdir ' + folder_figures)

    if os.path.isfile(table_final) is True:
        os.system('rm ' + table_final)

    os.system('rm -r' + folder_tables)
    if os.path.isdir(commum_folder + 'tables/') is False:
        os.mkdir(commum_folder + 'tables/')
# ----------------------------------------------------------------------------

    # Would you like to run one or a list of stars?
    option = input('\nRun one or more stars: (1 or more) ')

    if option == '1':
        # Saving data from the INES database
        star = input('\nPlease, put the star name: ')
        print('\nSaving data from INES database...')
        selecting_data(star_name=star, commum_folder=commum_folder)

        # Saving SIMBAD stellar data to a table
        print('\nSaving data (plx, vsini) from SIMBAD database...')
        table_file = commum_folder + 'tables/' + star + '.txt'
        folder_tables = commum_folder + 'tables/'
        val = read_simbad_data(star_name=star)

        # Check if there are bump files
        folder_star = commum_folder + 'iue/' + star
        bump = glob(folder_star + 'L*')

        if len(bump) is 0:
            start_time = time.time()
            val = list(val)
            ebmv_bump = retrieve_ebmv_value(star_name=star)
            print(ebmv_bump)
            val[7] = ebmv_bump
            val[5] = False
            val = tuple(val)
            print("--- %s seconds ---" % (time.time() - start_time))

        # Saving the table
        create_txt_file(data_list=val, file_name=table_file)
# ----------------------------------------------------------------------------

    if option == 'more':
```

```
        cols = read_txt(list_name='selected_bn_stars.txt',
                        folder=commum_folder + 'tables_vizier/')

        cols_2 = read_txt(list_name='selected_bn_stars_compl.txt',
                          folder=commum_folder + 'tables_vizier/')

        cols_3 = read_txt(list_name='selected_be_stars.txt',
                          folder=commum_folder + 'tables_vizier/')

        cols_4 = read_txt(list_name='selected_be_bsc_stars.txt',
                          folder=commum_folder + 'tables_vizier/')

        # cols_5 = read_txt(list_name='selected_be_bsc_stars_compl.txt',
        #                   folder=commum_folder + 'tables_vizier/')

        stars = np.concatenate((cols[0], cols_2[0], cols_3[0],
                                cols_4[0]), axis=0)

        # stars = cols_3[0]

# ----------------------------------------------------------------------------

        for i in range(len(stars)):
            star = str(stars[i])
            star = "HD " + star[:-2]
            a = star.split()
            star_2 = a[0] + a[1]
            # Saving data from the INES database
            print(num_spa * '=')
            print('\nStar: %s' % star)
            print('\nSaving data from INES database... %d of %d' %
                  (i + 1, len(stars)))

            selecting_data(star_name=star, commum_folder=commum_folder)

            # Saving SIMBAD stellar data to a table
            print('\nSaving data from SIMBAD database... star: %s\n'
                  % (star))
            table_file = commum_folder + 'tables/' + star + '.txt'
            val = read_simbad_data(star_name=star)

            # Check if there are bump files
            folder_star = commum_folder + 'iue/' + star_2 + '/'

            bump = glob(folder_star + 'L*')
            # print(star_2)
            # print(folder_star)
            # print(bump)
            # print(len(bump))
            if len(bump) is 0:
                start_time = time.time()
                val = list(val)
                ebmv_bump = retrieve_ebmv_value(star_name=star)
                print(ebmv_bump)
                val[7] = ebmv_bump
                val[5] = False
                val = tuple(val)
                print("--- %s seconds ---" % (time.time() - start_time))
```

Project Report: "Be-FaVOR: Be Stars - Facilities in VO Research. Uma ferramenta para a determinação de parâmetros de estrelas Be", Release 1.0

```
                print(val)
            # nan and "--" Filters
            if math.isfinite(val[1]) is True and math.isfinite(val[2]) is True\
               and math.isfinite(val[3]) is True:

                if math.isfinite(val[3]) is True and\
                   math.isfinite(val[4]) is False:
                    val = list(val)
                    val[4] = 0.0
                    val = tuple(val)
                    create_txt_file(data_list=val, file_name=table_file)
                else:
                    create_txt_file(data_list=val, file_name=table_file)
            else:
                print('This Star was excluded!')
# ----------------------------------------------------------------------------

        # Plotting galatic distribution
        ra_val_arr = []
        dec_val_arr = []
        for i in range(len(stars)):
            star = str(stars[i])
            star = "HD " + star[:-2]
            ra, dec = read_simbad_coodr(star_name=star)
            ra_val_arr.append(ra)
            dec_val_arr.append(dec)

        plot_gal(ra_val=ra_val_arr, dec_val=dec_val_arr,
                 folder_fig=folder_figures)

# ----------------------------------------------------------------------------

    # Creating list of files
    create_list_files(list_name='list', folder=folder_tables,
                      folder_table=folder_tables)

    table_final = folder_tables + 'list.txt'
    table_final_2 = folder_tables_2 + 'list_final.txt'

    files = open(table_final)
    files = files.readlines()
    final_table = open(table_final_2, "a+")

    for i in range(len(files)):
        files_2 = open(files[i][:-1])

        lines = files_2.readlines()

        if len(lines) == 8:
            star = lines[0][:-1]
            a = star.split()

            if len(a) >= 2:
                short_star_name = a[0] + a[1]
            else:
                short_star_name = np.copy(a)

            final_table.writelines(('%s\t%s\t%s\t%s\t%s\t%s\n')
```

```
                                    % (short_star_name, lines[1][:-1],
                                       lines[2][:-1], lines[3][:-1],
                                       lines[4][:-1], lines[7][:-1],
                                       lines[5][:-1]))
    final_table.close()
    print(num_spa * '=')
    print('\nFinished\n')
    return


# ============================================================================
if __name__ == '__main__':
    main()
```

6.2 Anexo 2: Rotina TAKE-VIZIER-DATA

```
# ============================================================================
# !/usr/bin/env python
# -*- coding:utf-8 -*-

# Created by B. Mota 2016-02-16 to present...

# import packages

import matplotlib.pyplot as plt
import matplotlib as mpl
import matplotlib.font_manager as fm
import numpy as np
import pyhdust.phc as phc
from astroquery.vizier import Vizier
from astroquery.simbad import Simbad
import csv
import os
# import pyraf
mpl.rcParams.update({'font.size': 18})
mpl.rcParams['lines.linewidth'] = 2
font = fm.FontProperties(size=17)
mpl.rc('xtick', labelsize=17)
mpl.rc('ytick', labelsize=17)
fontsize_label = 18  # 'x-large'

__version__ = "0.0.1"
__author__ = "Bruno Mota"

# ============================================================================
# Parameters that must be defined
user = 'bruno'
num_spa = 75
commum_folder = '/home/' + user + '/Dropbox/Artur/BeFaVOr_web/' +\
    'tables_vizier/'
folder_fig = '/home/' + user + '/Dropbox/Artur/BeFaVOr_web/figures/'

if os.path.isdir(folder_fig) is False:
    os.mkdir(folder_fig)

print(num_spa * '=')
```

```
print('\nTake_VIZIER_data\n')
print(num_spa * '=')


# ============================================================================
def create_txt_file(a, b, c, d, e, f, g, h, i, j, l, file_name):
    '''
    Create a txt file.

    :param a: table's column (array)
    :param b: table's column (array)
    :param c: table's column (array)
    :param d: table's column (array)
    :param e: table's column (array)
    :param f: table's column (array)
    :param g: table's column (array)
    :param h: table's column (array)
    :param i: table's column (array)
    :param j: table's column (array)
    :param l: table's column (array)
    :param file_name: file's name (string)
    :return: txt file
    '''

    with open(file_name, 'w') as k:
        # file.write(('%s\t & \t %s \t & \t %s \t & \t %s \t & \t  %s \t &' +
        #                ' \t  %s \t & \t  %s   \n')
        writer = csv.writer(k, delimiter='\t')
        writer.writerows(zip(a, b, c, d, e, f, g, h, i, j, l))

    return


# ============================================================================
def create_txt_file_compl(a, b, c, d, e, f, g, h, file_name):
    '''
    Create a txt file.

    :param a: table's column (array)
    :param b: table's column (array)
    :param c: table's column (array)
    :param d: table's column (array)
    :param e: table's column (array)
    :param f: table's column (array)
    :param g: table's column (array)
    :param h: table's column (array)
    :param file_name: file's name (string)
    :return: txt file
    '''

    with open(file_name, 'w') as k:
        writer = csv.writer(k, delimiter='\t')
        writer.writerows(zip(a, b, c, d, e, f, g, h))

    return


# ============================================================================
```

```
def main():

    Vizier.ROW_LIMIT = -1  # VIZIER whole catalog
    cat = ['V/50', 'V/36B']
    catalogs = Vizier.get_catalogs(cat)
    catalog = catalogs[0]
    catalog_compl = catalogs[2]

    # Operating with the data
    data = catalog.as_array()
    data_compl = catalog_compl.as_array()

    # Print available data
    data.dtype
    data_compl.dtype

    # Filtering the SpType
    sptype = list(data['SpType'].data)
    sptype_compl = list(data_compl['SpType'].data)
    # indexes = np.where(conc_flux[0] > 0)

    indexes = []
    for i in range(len(sptype)):
        sptyp = sptype[i].decode('UTF-8')
        if len(sptyp) != 0:
            if sptyp[0] == 'B':
                if ('e' in sptyp) is False:
                    if ('IV' in sptyp) is False:
                        if ('IIII' in sptyp) is False:
                            if ('Hg' in sptyp) is False:
                                if ('Mn' in sptyp) is False:
                                    if ('n' in sptyp) is True:
                                        indexes.append(i)

    indexes_compl = []
    for i in range(len(sptype_compl)):
        sptyp_compl = sptype_compl[i].decode('UTF-8')
        if len(sptyp_compl) != 0:
            if sptyp_compl[0] == 'B':
                if ('e' in sptyp_compl) is False:
                    if ('IV' in sptyp_compl) is False:
                        if ('IIII' in sptyp_compl) is False:
                            if ('Hg' in sptyp_compl) is False:
                                if ('Mn' in sptyp_compl) is False:
                                    if ('n' in sptyp_compl) is True:
                                        if ('n' in sptyp_compl) is True:
                                            indexes_compl.append(i)

# ============================================================================
    # Selecting the data with the B stars
    selected_data = data[indexes]
    sptyp_selected = list(selected_data['SpType'])
    name_selected = selected_data['Name']
    hd_selected = selected_data['HD']
    plx = selected_data['Parallax']
    bmv = selected_data['B-V']
    err_bmv = selected_data['u_B-V']
    umb = selected_data['U-B']
```

```
    err_umb = selected_data['u_U-B']
    rmi = selected_data['R-I']
    vsini = selected_data['RotVel']
    err_vsini = selected_data['u_RotVel']
    companions = selected_data['MultCnt']

    selected_data_compl = data_compl[indexes_compl]
    sptyp_selected_compl = list(selected_data_compl['SpType'])
    hd_selected_compl = selected_data_compl['HD']
    plx_compl = selected_data_compl['Plx']
    bmv_compl = selected_data_compl['B-V']
    umb_compl = selected_data_compl['U-B']
    rmi_compl = selected_data_compl['R-I']
    vsini_compl = selected_data_compl['vsini']
    err_vsini_compl = selected_data_compl['u_vsini']


# ============================================================================
    # Checking if there are IUE data
    customSimbad = Simbad()
    customSimbad.TIMEOUT = 2000  # sets the timeout to 2000s

    # see which fields are currently set
    customSimbad.get_votable_fields()

    # To set other fields
    customSimbad.add_votable_fields('measurements')


# ============================================================================
    # Selecting the stars with IUE data
    data = data[indexes]
    obs_iue_date = []
    stars = []
    indexes = []
    print(num_spa * '=')
    print('\nselected stars: %d\n' % len(hd_selected))
    print(num_spa * '=')
    for i in range(len(hd_selected)):
        try:
            star = "HD " + str(hd_selected[i])
            result_table = customSimbad.query_object(star)
            obs_date = result_table['IUE_ObsDate']
            if len(obs_date.item()) != 0:
                print(num_spa * '-')
                print('\n' + star)
                print('%0.2f perc. concluded' % (100 * i / len(hd_selected)))
                print(obs_date)
                obs_iue_date.append(obs_date.item())
                stars.append(star)
                indexes.append(i)
        except:
            pass

    data_compl = data_compl[indexes_compl]
    obs_iue_date_compl = []
    stars_compl = []
    indexes_compl = []
```

```
    print('selected stars compl: %d' % len(hd_selected_compl))
    for i in range(len(hd_selected_compl)):
        try:
            star = "HD " + str(hd_selected_compl[i])
            result_table = customSimbad.query_object(star)
            obs_date = result_table['IUE_ObsDate']
            if len(obs_date.item()) != 0:
                print(num_spa * '-')
                print('\n' + star)
                print('%0.2f perc. concluded' % (100 * i / len(hd_selected)))
                print(obs_date)
                obs_iue_date_compl.append(obs_date.item())
                stars_compl.append(star)
                indexes_compl.append(i)
        except:
            pass

# ============================================================================
    # Selecting the data with the B stars in IUE database

    selected_data = data[indexes]
    sptyp_selected = list(selected_data['SpType'])
    name_selected = selected_data['Name']
    hd_selected = selected_data['HD']
    plx = selected_data['Parallax']
    bmv = selected_data['B-V']
    err_bmv = selected_data['u_B-V']
    umb = selected_data['U-B']
    err_umb = selected_data['u_U-B']
    rmi = selected_data['R-I']
    vsini = selected_data['RotVel']
    err_vsini = selected_data['u_RotVel']
    companions = selected_data['MultCnt']

    selected_data_compl = data_compl[indexes_compl]
    sptyp_selected_compl = list(selected_data_compl['SpType'])
    hd_selected_compl = selected_data_compl['HD']
    plx_compl = selected_data_compl['Plx']
    bmv_compl = selected_data_compl['B-V']
    umb_compl = selected_data_compl['U-B']
    rmi_compl = selected_data_compl['R-I']
    vsini_compl = selected_data_compl['vsini']
    err_vsini_compl = selected_data_compl['u_vsini']


# ============================================================================
    # Plotting correlations

    # Plot B-V vs U-B
    plt.clf()
    plt.scatter(bmv, umb, label='V/50', marker='o')
    plt.scatter(bmv_compl, umb_compl, label='V/36B', color='red', marker='o')
    plt.xlabel(r'(B-V) [mag]')
    plt.ylabel(r'(U-B) [mag]')
    plt.legend()
    plt.savefig(folder_fig + 'bmvVSumb.png')

# ----------------------------------------------------------------------------
```

```
    # Plot R-I vs U-B
    plt.clf()
    plt.scatter(rmi, umb, label='V/50', marker='o')
    plt.scatter(rmi_compl, umb_compl, label='V/36B', color='red', marker='o')
    plt.xlabel(r'(R-I) [mag]')
    plt.ylabel(r'(U-B) [mag]')
    plt.legend()
    plt.savefig(folder_fig + 'rmiVSumb.png')

# ------------------------------------------------------------------------------
    # Plot B-V vs R-I
    plt.clf()
    plt.scatter(bmv, rmi, label='V/50', marker='o')
    plt.scatter(bmv_compl, rmi_compl, label='V/36B', color='red', marker='o')
    plt.xlabel(r'(B-V) [mag]')
    plt.ylabel(r'(R-I) [mag]')
    plt.legend()
    plt.savefig(folder_fig + 'bmvVSrmi.png')

# ------------------------------------------------------------------------------
    # Plot B-V vs vsini
    plt.clf()
    plt.scatter(bmv, vsini, label='V/50', marker='o')
    plt.scatter(bmv_compl, vsini_compl, label='V/36B', color='red', marker='o')
    plt.xlabel(r'(B-V) [mag]')
    plt.ylabel(r'$v \sin i$ [km/s]')
    plt.legend()
    plt.savefig(folder_fig + 'bmvVSvsini.png')

# ==============================================================================

    create_txt_file(a=hd_selected, b=bmv, c=umb, d=rmi, e=vsini,
                    f=err_bmv, g=err_umb, h=err_vsini, i=companions.data,
                    j=obs_iue_date, l=sptyp_selected,
                    file_name=commum_folder + 'selected_stars.txt')

    create_txt_file_compl(a=hd_selected_compl, b=bmv_compl, c=umb_compl,
                          d=rmi_compl, e=vsini_compl, f=err_vsini_compl,
                          g=obs_iue_date_compl, h=sptyp_selected_compl,
                          file_name=commum_folder + 'selected_stars_compl.txt')

# ==============================================================================
    # example
    if False:
        R = np.array((data['Vc'] * 1e5) ** 2 /
                     10 ** data['logg'] / phc.Rsun.cgs)
        L = phc.sigma.cgs * np.array(data['Teff'], dtype=float)**4 * 4 *\
            np.pi * (R * phc.Rsun.cgs)**2 * phc.Lsun.cgs
        M = np.array((data['Vc'] * 1e5)**2 * (R * phc.Rsun.cgs) /
                     phc.G.cgs / phc.Msun.cgs)

# ==============================================================================
if __name__ == '__main__':
    main()
```

CHAPTER

SEVEN

REFERÊNCIAS E INDEX

7.1 Referências

Secchi, A.1866, Astronomische Nachrichten, 68, 63

Rivinius, T., Carciofi, A. C., & Martayan, C.2013, *Astronomy and Astrophysics Review*, 21, 69

Project Report: "Be-FaVOR: Be Stars - Facilities in VO Research. Uma ferramenta para a determinação de parâmetros de estrelas Be", Release 1.0

PYTHON MODULE INDEX

INDEX

Appendix K

Rubinho's Article

***